Improved Recovery Boiler Performance Through Control of Combustion, Sulfur, and Alkali Chemistry

DOE/OIT/Forest Products
American Forest & Paper Association
Brigham Young University
Principal Investigator: Larry Baxter

Contents

Table of Figures

Table of Tables

EXECUTIVE SUMMARY

This project involved the following objectives:

1. Determine black liquor drying and devolatilization elemental and total mass release rates and yields.

2. Develop a public domain physical/chemical kinetic model of black liquor drop combustion, including new information on drying and devolatilization.

3. Determine mechanisms and rates of sulfur scavenging in recover boilers.

4. Develop non-ideal, public-domain thermochemistry models for alkali salts appropriate for recovery boilers

5. Develop data and a one-dimensional model of a char bed in a recovery boiler.

6. Implement all of the above in comprehensive combustion code and validate effects on boiler performance.

7. Perform gasification modeling in support of INEL and commercial customers.

The major accomplishments of this project corresponding to these objectives are as follows:

1. Original data for black liquor and biomass data demonstrate dependencies of particle reactions on particle size, liquor type, gas temperature, and gas composition. A comprehensive particle submodel and corresponding data developed during this project predicts particle drying (including both free and chemisorbed moisture), devolatilization, heterogeneous char oxidation, char-smelt reactions, and smelt oxidation. Data and model predictions agree, without adjustment of parameters, within their respective errors. The work performed under these tasks substantially exceeded the original objectives.

2. A separate model for sulfur scavenging and fume formation in a recovery boiler demonstrated strong dependence on both in-boiler mixing and chemistry. In particular, accurate fume particle size predictions, as determined from both laboratory and field measurements, depend on gas mixing effects in the boilers that lead to substantial particle agglomeration. Sulfur scavenging was quantitatively predicted while particle size required one empirical mixing factor to match data.

3. Condensed-phase thermochemistry algorithms were developed for salt mixtures and compared with sodium-based binary and higher order systems. Predictions and measurements were demonstrated for both salt systems and for some more complex silicate-bearing systems, substantially exceeding the original scope of this work.

4. A multi-dimensional model of char bed reactivity developed under this project demonstrated that essentially all reactions in char beds occur on or near the surface, with the internal portions of the bed being essentially inert. The model predicted composition, temperature, and velocity profiles in the bed and showed that air jet penetration is limited to the immediate vicinity of the char bed, with minimal impact on most of the bed. The modeling efforts substantially exceeded the original scope of this project.

5. Near the completion of this project, DOE withdrew the BYU portion of a multiparty agreement to complete this and additional work with no advanced warning, which compromised the integration of all of this material into a commercial computer code. However, substantial computer simulations of much of this work were initiated, but not completed.

6. The gasification modeling is nearly completed but was aborted near its completion according to a DOE redirection of funds. This affected both this and the previous tasks.

PROJECT DESCRIPTION

Project Objective: The objectives of this project are

1. Determine black liquor drying and devolatilization elemental and total mass release rates and yields.

2. Develop a public domain physical/chemical kinetic model of black liquor drop combustion, including new information on drying and devolatilization.

3. Determine mechanisms and rates of sulfur scavenging in recover boilers.

4. Develop non-ideal, public-domain thermochemistry models for alkali salts appropriate for recovery boilers

5. Develop data and a one-dimensional model of a char bed in a recovery boiler.

6. Implement all of the above in comprehensive combustion code and validate effects on boiler performance.

These objectives were met with the following tasks:

Task 1 Combustion Characterization

The objective of this task is to characterize the drying and devolatilization rates characteristic of at least three different liquors and to encapsulate the results in a computer algorithm/model that describes the transient behavior of black liquor droplets under the range of conditions encountered in commercial recovery boilers.

At least three liquors will be selected for analysis under this task based on their range of organic (hardwood vs softwood) and inorganic (chlorine and potassium content) properties. Priority will be given to covering a broad range of inorganic properties.

Experimental measurements of drying rates, devolatilization rates, and elemental losses during drying and devolatilization will be completed using captive particle techniques. These techniques will involve heating individual droplets/particles under realistic conditions of heat flux and gas environment and observing changes in diameter, temperature, mass, and composition. Experimental approaches may include droplets suspended on thermocouples, levitated droplets, and droplets entrained in flows. High priority will be placed on characterization of the thermal environment (temperature, radiative fluxes, etc.) in which such reactions occur and matching these with those typical of commercial operation. Rates and mechanisms of moisture, carbon, hydrogen, nitrogen, oxygen, sodium, potassium, chlorine, and sulfur loss will be determined by sampling particles and varying extents of reaction and measuring droplet/particle elemental composition and structure. In situ measurements of size and possibly mass may be achievable in several of the experiments. Video records of reactions will be provided that document many of the processes. We anticipate observing much less swelling under rapid heating conditions than has been reported in many literature sources based on experiments primarily conducted under lower heating rates. As part of this task, experiments will be conducted to try to estimate the size distributions of droplets generated from splash plates, with emphasis on characterization of relatively small droplets. As part of this work, we will also review existing liquor devolatilization models. We anticipate writing a fundamentally new model in which volatile yield and devolatilization rate is based on measurable chemical characterizations of the liquor in a manner similar to the CPD model for coal devolatilization.

The primary deliverables from this work include experimentally determined rates and mechanisms of drying and devolatilization and computer algorithms and models that describe each process. Specifically, a relatively comprehensive computer model describing droplet/particle combustion will result in which the physical (size, density) and chemical (heat of reaction, composition, phase) properties of the droplets/particles are predicted as a function of time in arbitrary environments.

Task 2: Sulfur Chemistry

The objective of this task is to characterize the rates and mechanisms of sulfur scavenging from recovery boiler flue gases and to develop analytical expressions for the results.

The disappearance of sulfur from flue gas in a recovery boiler is qualitatively well established, but the rates and mechanisms of such disappearance are generally not understood or understood differently by different authorities in this field. In our estimation, sulfur scavenging and aerosol formation are mechanistically linked. The amount of sulfur (and other elements) in particles and deposits has a large impact on particle melting behavior and other thermal performance. A quantified understanding of sulfur scavenging is necessary to accurately describe aerosol formation. It is possible that such understanding would provide a valuable key to anticipating deposition problems. For example, sulfur disappearance in or near the superheaters may be indicative of largely molten fume and intermediate particles in the flow whereas sulfur disappearance lower in the furnace suggests less troublesome particle properties. We do not believe there are quantitative field techniques available that provide an accurate

measure of sulfur scavenging (based on our own field experience and that of others), but we do believe that the disappearance of sulfur correlates strongly with a rapid increase in fume in the boiler. As part of this project, we will attempt to verify this correlation by field measurement. We note, however, that such measurements are difficult at best.

The primary deliverable from this task is an algorithmic description and computer code that predicts sulfur disappearance and aerosol formation in a recovery boiler. This model will describe the conditions under which sulfur is scrubbed from the gas phase in a manner that allows it to be incorporated into a comprehensive computer code. If resources allow, we will extend the model to include a complete aerosol formation description, although this is not necessary (or promised) for the remainder of this project to succeed.

Task 3: Alkali Chemistry

The objective of this task is to develop a fundamentally based predictive algorithm that is capable of predicting phase diagram behavior for alkali salt mixtures. This algorithm will be capable of indicating the liquid fraction, vapor pressures, and chemical composition of alkali (sodium and potassium) sulfate/carbonate/chloride mixtures over the range of compositions of importance to recovery boiler operation (dominant sodium sulfate and carbonate with minor amounts of chlorine and potassium). The predictions will be compared with published experimental phase diagrams. We view existing experimental results as sufficient in scope and depth to provide validation of these predictions and we do not intend to experimentally determine of verify the accuracy of existing data. We do intend to critically review the existing literature to determine the consistency and accuracy of the published data.

We intend to develop non-ideal solution behavior according to lattice-type models for this exercise. These models are capable of dealing with both the physical and electro-chemical interactions of the electrolytic solutions formed from these salts. We do not anticipate having to extend the lattice model to the quasi-chemical models, but will do so if we are not successful with lattice models. We also intend to review alternative approaches and will base the thermo-chemical model on the best available approach.

The primary deliverables from this task include a published algorithm, a companion PC-based, stand-alone computer program, and a comparison of predicted results with published experimental results.

Task 4: Bed Combustion Characteristics

The objective of this task is to characterize black liquor char bed combustion rates and mechanisms. Experiments at both laboratory and mill scale will be performed in addition to the bed modeling. The primary deliverables include (1) an algorithmic char bed combustion rate and mechanism description; and (2) a one-dimensional bed combustion model. The fundamental chemical processes needed to complete this work (vaporization, devolatilization, thermochemistry, etc.) will be coordinated with similar work being conducted in the remainder of this project.

Task 5: Reconcile Results with Commercial Operation

The objective of this task is to reconcile all of the experimental and modeling work discussed above with commercial behavior by incorporating the algorithms into a comprehensive computer code and demonstrating the impact on predicted commercial performance. The existing comprehensive code of Babcock & Wilcox will be used as the starting point for this work. The subroutines and algorithms developed under this project will be publicly available, but the entire comprehensive code will not be publicly available under this project.

AEROSOL FORMATION MODEL

Abstract

This document describes the development and validation of a computer code written to predict aerosol composition, size, and number for multi-component systems and its application to black liquor recovery boilers. This research is based on fundamental principles governing aerosol dynamics and chemistry. The output from this simulation is compared full-scale recovery boiler results (Lind, Rumminger et al. 2000; Baxter, Lind et al. 2001). Typically the predicted size distributions and particle compositions lie within the experimental uncertainty in particle size, amount, and composition if provisions for pre-existing particles and mixing are provided (inclusion of a single empirical parameter in the nucleation term).

This code would be most effectively used in conjunction with computational fluid dynamics codes for black liquor combustion or gasification to predict fume formation and subsequent deposition as a function of operating conditions, fuel properties, and boiler design. Additionally, the code predicts important aspects of sulfur chemistry in recovery boilers, specifically the scrubbing of SO_2 from the gas phase and formation of sulfates in aerosol phases. This tool predicts the amounts, sizes and composition of aerosols and the composition and concentration of remaining vapors under arbitrary boiler conditions.

Symbols and Terms

β	coefficient of coagulation	n_i	particles in section *i*
C_i	heat capacity coefficient	P_0	atmospheric pressure (as reference)
$\Delta C_p(T)$	change in heat capacity	p_1	partial pressure of a species
$\Delta H(T)$	change in enthalpy	p_d	pressure at particle surface
ΔH^o	reference enthalpy	P_{sat}	vapor pressure

d	(denotes a differential quantity)	R	universal gas constant
d_p	particle diameter	SR	saturation ratio
d*	Kelvin diameter	σ	surface tension
D_{AB}	diffusivity	T	temperature
D_p	particle diameter	T_b	normal boiling point
e (or exp)	Euler's constant	T_c	critical temperature
I	nucleation current	T□	(1- T_r)
k	Boltzmann's constant	T_m	Melting point
λ	gas phase mean-free path	T_r	reduced temperature
μ	viscosity	v_i	total volume of section i
m_p	particle mass	V_m	molecular volume
N_A	Avogadro's number	V_p	particle volume

Introduction

Aerosols are small (sub-micron) particles formed mainly in combustion processes by the vaporization and subsequent re-condensation of volatile, inorganic compounds. Cloud formation is an example of an aerosol process. However, unlike clouds, most aerosol-generating processes produce negative effects on both the process that forms them and the environment. Aerosols represent major process and emissions issues for essentially all systems employing low-grade fuel (coal, biomass, and black liquor). An accurate, predictive understanding of aerosol formation and chemistry would substantially improve the efficiency and environmental performance of many processes.

Black-liquor-fired recovery boilers generate higher numbers of aerosol particles than any other major boiler design. Vapors formed principally during high-temperature black liquor char reactions pass through the boiler, eventually forming aerosols during and concomitant excessive fouling, especially in the condenser pass regions. The role of sulfur chemistry during this process is not well understood, or at least there is little consensus regarding its role, although it is a significant issue, and knowing whether this happens at the bed of the boiler, in the flue gas, or if it happens at all could provide controls that could improve boiler operation and design. Furthermore, aerosol escape into the atmosphere poses serious environmental concerns that could be more effectively remedied with a better understanding of aerosol behavior.

Others have developed models with comparisons to data and analysis of impacts on sulfur chemistry similar to the work reported here (Kauppinen, Mikkanen et al. 1993;

Mikkanen, Kauppinen et al. 1994; Jokiniemi, Pyykonen et al. 1996). This work is part of a larger project that includes gas-phase species measurements and already completed particulate sampling to determine the impacts of sulfur on fume formation and deposition in recovery boilers. This issue was identified as a critical need in a white paper produced at the end of an international conference on recovery boilers in Bar Harbor, Maine.

Although possible, it is extremely difficult to measure the composition of gases in the boiler due to the high temperatures inherent to the system. Additionally, if not measured *in situ*, the sulfate formations are impossible to determine due to the changes to the sample once extracted from the stream. Separate projects are addressing these experimental issues. This project provides an analytical and modeling tool in the form of a computer simulation that predicts the size distribution, composition, and number of particles for aerosol species in the boiler, including the formation of sulfates. This new code, written in object-oriented C++ borrows strongly from previous work as is described below. This predictive tool should provide a better understanding of aerosol behavior and a better analytical capability when compared to experimental results. The simulation is capable of dealing with both single- and multi-constituent condensation and particle formation. Predicting the formation of proven harmful aerosol particles should provide information useful in determining environmental and operational counter-measures that will be simultaneously safer and more economical.

The data made available by this simulation, specifically applied to black-liquor-fired recovery boilers, which lend themselves to investigation by this method, could prove beneficial in counter-acting degrading effects produced by aerosol particles. Predictions of this type are also useful for all other low-grade fuel systems, i.e. biomass- or coal-fired boilers, as well as in advanced materials systems (such as particle-assisted chemical vapor deposition processes).

Theory

Extensive research performed in the aerosol dynamics field indicates that the basic behaviors of aerosol particles are effectively described by a series of coupled differential equations that modify two general characteristics of aerosols: particle number and particle size. For aerosol modeling to be useful, it must provide the number of aerosol particles, the size distribution, their concentration, and the composition in the condensed phase.

The phenomena that modify the first category (particle number) are nucleation (also referred to as homogeneous condensation), coagulation, and agglomeration. For describing the second category (particle size), equations for heterogeneous condensation, agglomeration, and coagulation are required (coagulation and agglomeration affect both categories, as will be shown). Composition is determined for multi-component systems and is especially relevant to black-liquor systems, which are notorious for producing a wide range of chemical species. Some authors indicate that composition can be assumed constant for particles of identical size when coagulation effects are minimal (Jokiniemi, Pyykonen et al. 1996; Pyykonen and Jokiniemi 2000).

Generally, computer simulations are written from an Eulerian reference frame, that is, from the perspective of an observer. This type of code involves extensive iteration techniques to resolve divergence and instability and therefore can potentially require large amounts of processing time. Modeling aerosol dynamics, however, is more appropriately approached from a Lagrangian reference frame, wherein the code tracks the progress of the system by calculating conditions at discrete time increments. In the case of aerosol dynamics, the simulation behaves as if there were a "cloud" of particles whose path is traced from time step to time step.

The size distribution of this aerosol cloud can be discretized to track particle growth as done in the MAEROS models (Gelbard 1984; Gelbard, Fitzgerald et al. 1998). This method of tracking aerosol particles has been generally accepted as the most efficient method for the past two decades (Gelbard and Seinfeld 1980; Gelbard 1990; Gelbard, Fitzgerald et al. 1998). Non-discretized models, as well as "moving-sectional" models (wherein the sectional divisions change with changes in the aerosol mean diameter) have been proposed as alternative methods for tracking aerosol growth (Gelbard, Fitzgerald et al. 1998). The model described in this paper uses the traditional sectional method as used in MAEROS.

Nucleation

The process whereby aggregate gaseous molecules combine to form particles large enough to remain stable at system conditions is called Nucleation. Nucleation is, physically, the result of collisions between molecules whose thermodynamic energies are low enough that they remain associated after the collision. Although theoretically a real gas begins to nucleate at the dew point, this is actually statistically infrequent, and thus nucleation usually begins at sub-cooled temperatures. Once nucleation kernels are available in the condensed phase, however, the effect progresses very rapidly given the increased available surface area. Increased surface area increases the rate of nucleation because molecular kinetic energy is more easily dissipated on a surface that is very large compared to the molecule.

Nucleation can also be defined as collisions occurring between molecules in the same phase and is therefore also called homogeneous condensation (the collision of molecules in different phases is considered in the condensation section and is often referred to as heterogeneous condensation). A particle is considered stable, and therefore is classified as "condensed," once molecules condense onto the particle at an equal or faster rate than they evaporate. The smallest diameter of a particle that is stable at these conditions is called the Kelvin diameter and is defined by the relationship,

$$d^* = \frac{4\sigma V_m}{kT \log\left(S_R\right)} \qquad (1)$$

Where σ is the surface tension, V_m is the molecular volume, k is the Boltzmann constant, T is the temperature (in Kelvin), and S_R is the saturation ratio. S_R is defined as,

$$S_R = \frac{P_i}{P_{sat}} \qquad (2)$$

Where P_i is the partial pressure and P_{sat} is the vapor pressure. Once molecules combine to form a particle that has a diameter equal to or greater than the Kelvin diameter, it is assumed that this particle is stable. Therefore, the nucleation equation, see Equation (3), is the rate at which particles having the Kelvin diameter are formed. The Kelvin diameter has a strong dependence on the saturation ratio, a value of significance in governing aerosol dynamics. Accurate values for the saturation ratio depend heavily on accurate calculations of the vapor pressure (P_{sat}), which, considering that most aerosol phases will generally be multi-constituent, becomes problematic. This issue is addressed below in the section "Vapor Pressure."

Nucleation, the key governing effect in aerosol dynamics, is extremely important because it provides condensation surfaces for high-energy, gas-phase molecules. The following equation (Friedlander 2000) describes the rate of formation of new particles by homogeneous condensation,

$$\frac{dn_p}{dt} = 2\left[\frac{p_1}{(2\pi m_p kT)^{\frac{1}{2}}}\right] \cdot \left(n_1 v_m^{\frac{2}{3}}\right) \cdot \left(\frac{\sigma v_m^{\frac{2}{3}}}{kT}\right) \cdot \exp\left[\frac{-16\,\pi\sigma^3 v_m^2}{3(kT)^3 \cdot (\ln S_R)^2}\right] \qquad (3)$$

The differential term is sometimes represented by I and referred to as a "current" (a rate of particles entering the condensed phase). The n_1 term is a unit-less molecular concentration in the gas phase of the condensing species and is the same as S_R.

Coagulation

Coagulation, as has been mentioned, influences the aerosol phase in two ways. It affects both the size of the already-condensed particles as well as the overall number of condensed particles. Coagulation is determined by calculating the frequency of collisions between particles that result in formation a new particle. This phenomenon is identical to agglomeration in principle, the two main assumptions being that, during coagulation, it is assumed that the newly formed particle retains a spherical shape and that the volumes of the colliding particles are additive. This assumption is good for very small particles, that is, for particles whose projected area is approximately spherical. For almost all liquid particles, the most thermodynamically stable form is a sphere anyway.

Both of these assumptions hold true for most aerosol systems. Although particles become "large" (micron size, or possibly larger) in black-liquor systems, the species are generally liquid during collisions in boiler-regions of interest, implying that the most thermodynamically stable configuration for black-liquor particles is spherical. Thus, simple coagulation should be sufficient for black-liquor systems. Biomass systems however are known to consistently produce particles of non-spherical shape.

For the sake of simplicity, it is assumed that only binary collisions occur (higher order collisions are statistically infrequent and would be negligible anyway). The equation for

the change in particle number based on coagulation effects, (Hinds 1999; Friedlander 2000), is,

$$\frac{dn_k}{dt} = \frac{1}{2}\sum_{i+j=k}\beta(V_i, v_j)n_i n_j - n_k\sum_{i}^{\infty}\beta(v_i, v_k)n_i \qquad (4)$$

where n_k is the number of particles in the k^{th} section, and V_i is the volume of a particle in the i^{th} section. β is a coefficient of coagulation dependant on particle volume and the viscosity (μ) of the condensed phase and is given in Equation (5).

$$\beta(v_i, v_j) = \frac{2kT}{3\mu}\left(\frac{1}{v_i^{\frac{1}{3}}} + \frac{1}{v_j^{\frac{1}{3}}}\right)\cdot\left(v_i^{\frac{1}{3}} + v_j^{\frac{1}{3}}\right) \qquad (5)$$

Coagulation has the greatest effect on aerosol systems when large numbers of small particles are present. As particle size increases (or particle number decreases through coagulation and agglomeration) the effects of coagulation diminish. By the mechanism of coagulation, all aerosol systems would eventually be brought into an equilibrium condition where the size distribution is constant, or "self-preserving."

Agglomeration

Agglomeration deals with collisions that do not result in spherical particles and in which the colliding particles do not themselves have to be spherical. Agglomeration is an observable phenomenon and often results in long chains of particles of varied sizes and compositions, but is less important in black-liquor systems than in biomass. Currently, agglomeration is not handled by this simulation.

The phenomenon does pose several unique difficulties for computer modeling, especially when using the discrete sectional method, as agglomerated particles can grow to very large, non-spherical dimensions. Adding agglomeration effects would not be trivial, but would improve modeling results.

Condensation

Condensation is a process very similar to nucleation whereby gaseous molecules collect on a condensation-surface, the aerosol phase particles in this case. This can occur between gas-phase species and liquid-phase species and is hence called heterogeneous condensation. Condensation occurs more readily than nucleation because energy is more rapidly and easily dissipated when one of the colliding particles is much larger than the other. A gas phase molecule below the dew point colliding with a condensed particle of significantly greater diameter is very likely to condense onto the particle surface.

Condensation occurs due to a pressure gradient between the partial pressure of a species in the bulk gas and the pressure of the species at the surface of a particle (approximated by the vapor pressure). Particle growth rate is therefore limited by diffusion of particles through the gas for particles larger than the mean free path. However, for particles smaller than the mean free path, growth is limited by the diameter of the particle, that is,

the transfer of gas-phase molecules to the particle surface. The equation for diffusion-limited condensation (Friedlander 2000) is,

$$\frac{dv}{dt} = \frac{2\pi D_{AB} d_p V_m}{kT}\left(p_1 - p_d\right) \qquad \text{for } d_p < \lambda \qquad (6)$$

where D_{AB} is the diffusivity of the gas phase into the aerosol phase, p_1 is the partial pressure of the species in the gas phase, and p_d is the pressure at the surface of the particle (assumed to be the vapor pressure). When the velocity of the particulate phase approaches the velocity of the gas phase, Stokes flow can be assumed around the particle and the equation for diffusion-limited growth, differing only from Equation (6) by a constant, becomes,

$$\frac{dv}{dt} = \frac{D_{AB} d_p V_m}{2000kT}\left(p_1 - p_d\right) \qquad \text{for } d_p < \lambda \qquad (7)$$

This assumption is valid for an aerosol system, as sub-micron particles entrained in the gas phase approach very nearly the velocity of the gas itself. With this in mind, the Stokes flow assumption is probably the correct method to use of the two diffusion-limited options.

Diameter-limited growth is described (Friedlander 2000) by the equation,

$$\frac{dv}{dt} = \frac{2\pi d_p^2 v_m}{\left(2\pi m_p kT\right)^{\frac{1}{2}}}\left(p_1 - p_d\right) \qquad \text{for } d_p > \lambda \qquad (8)$$

where it is apparent that particle diameter (the squared term) has large influence on the differential term. It should be noted that both rate expressions calculate the same growth rate.

The condensation equations find a change in volume for each particle based on the pressure driving force caused by the gradient between the partial pressure and the vapor pressure. As with nucleation, condensation is a strong function of vapor pressure.

Vapor Pressure

For ideal systems, the vapor pressure for a mixture can be determined from a weighted average for each species based on the pure species' vapor pressure. However, this is generally incorrect for real systems, and in the case of aerosol systems generated from the combustion of black liquor in which there are large amounts of alkali salts, it becomes very inaccurate.

To determine vapor pressure correctly it is necessary to account for non-ideal thermodynamic behavior that would provide the vapor pressure of mixtures from the Gibb's free energy of these mixtures. A model of this kind would require extensive work and an ideal approximation can be used to determine vapor pressures for aerosol systems in spite of the inaccuracy.

The vapor pressure of the aerosol phase is calculated based on the weighted average of each species present in the condensed phase and the corresponding pure vapor pressure of each species as shown in equation (9).

$$P_{sat,mix} = \sum_{i}^{n} x_i P_{sat,i} \qquad (9)$$

Where n is the number of components in the aerosol phase and x is the mass fraction of species i.

The difficult part of this equation is in finding the vapor pressure of each species. This is obtained by using a seven-coefficient fit (McBride and Gordon, 1996) for the heat capacity and then, using the Clausius-Clapeyron equation (where the molar change in volume is not constant), the vapor pressure is found with,

$$P_{sat}(T) = P_0 e^{\int_{T_0}^{T} \frac{\Delta H}{RT^2} dT} \qquad (10)$$

where T_0 is a reference temperature and P_0 is a reference pressure. P_0 is usually taken to be atmospheric pressure since this assumption makes finding T_0 significantly easier than it otherwise would be. The reference temperature is found by employing the thermodynamic equilibrium principle that the Gibb's Free Energies of two phases are equal at the phase transition temperature, and that the phase change that occurs for substances changing from the gas to the liquid phase at atmospheric pressure (P_0) also occurs at the boiling point (which will become T_0 in this case). Finding this temperature from heat capacity fits requires a minor iteration scheme. A relatively fast way to obtain this value is to employ Newton-Raphson and Bisection numerical methods (Burden, Faires, and Reynolds, 1981).[1]

Once T_0 is obtained, it becomes necessary only to integrate the enthalpy change to find the vapor pressure. The integration is performed as shown by the following series of equations in which the integrand of the Clausius-Clapeyron equation is shown to stem from the formula for the change in enthalpy, which in turn comes from the integrated change in the heat capacity with respect to temperature.

$$\frac{C_p(T)}{R} = \sum_{i=0}^{7} c_i T^{i-2} \qquad (11)$$

$$\frac{\Delta H(T)}{R} = \Delta H^{\circ} + \int_{T_0}^{T} \Delta C_p(T) dT \qquad (12)$$

[1] No more rigorous method is required because the thermodynamic functions of enthalpy and entropy are relatively mild functions of temperature.

$$\int_{T_b}^{T} \frac{\Delta H}{RT^2}\,dT = \frac{c_0}{2T^2} - \frac{c_1}{T}\left(1+\ln T\right) + c_2 \ln T + \sum_{i=3}^{8} \frac{c_i T^{i-1}}{\geq \left(i^2 - 3i + 2\right)} - \frac{\Delta H^\circ}{T} \qquad (13)$$

In Equations (12) and (13), the term ΔH^o is a reference enthalpy normalized by the ideal gas constant (McBride and Gordon, 1996). Note that Equation (13) is the exponent in the Clausius-Clapeyron relationship and T_b is the reference temperature, found by the method described previously for finding T_0.

Results and Discussion

The simulation should be used to predict the behaviors of real-life systems to obtain a more complete understanding of what happens in recovery boilers. For this model to be reliable, however, it is necessary that its output be validated based on experiment. It is difficult to compare aerosol data because it is difficult to measure aerosol data. This is one of the main reasons a predictive method would be so useful. However, comparisons have been made with full-scale experiments (Lind, Rumminger et al. 2000; Baxter, Lind et al. 2001).

Figure 1 shows the relative effectiveness of the Clausius-Clapeyron vapor-pressure predictions with tabulated data for the vapor pressure of ethanol from 273 to 413 Kelvin (the maximum error is -2.24%). The model predicts the normal boiling point of ethanol to be 354 Kelvin, while the tabulated value is 351 Kelvin. It is important to note that the vapor pressures obtained by the simulation are not truly representative of real systems, but are only idealized approximations. Therefore, it becomes imperative that a thermodynamically reliable method be employed to truly model any system with accuracy. However, since this capability is not yet available, comparisons were made with inaccurate data.

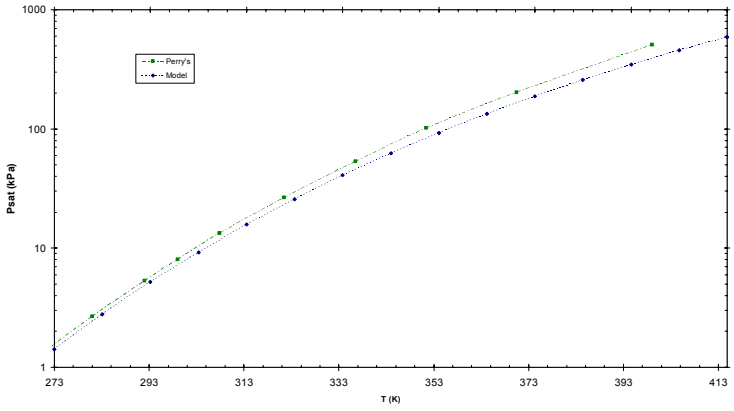

Figure 1. Ethanol vapor pressure curve: comparison between model prediction and values tabulated in Perry's Chemical Handbook, 50th ed.

With accurate values of vapor pressure, the model can be used to determine aerosol formation under given boiler conditions. Conditions in a recovery boiler do not change uniformly across a cross-section. With this in mind, two sets of data are presented, one

for an ideal boiler in which system conditions change uniformly, and one for a non-ideal boiler in which conditions are not uniform for a given cross section. The non-ideal conditions for the second case are arbitrarily determined based on the experimental data.

The composition data are virtually identical for both simulation cases and are shown in Figure 2 as compared with experimental measurements. One of the main goals of this research is to predict effectively the formation of sulfates in boilers and therefore, accurately predicting sulfur content becomes significant. The results shown in Figure 2 are normalized for the four species listed (sulfur, chlorine, potassium and sodium). Hydroxide content was not included.

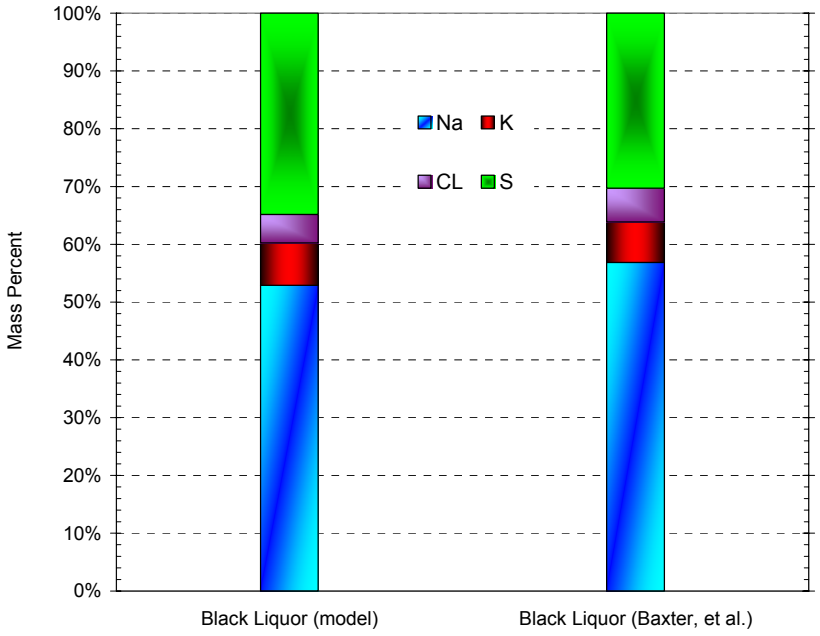

Figure 2. Aerosol composition: comparison between simulation and experiment (Lind, Rumminger et al. 2000; Baxter, Lind et al. 2001). Residence time is 4.0 seconds – taken from char bed to primary super-heater.

Composition is a strong function of initial concentration, especially in the case of black-liquor where virtually all of the alkali species in the vapor phase are scrubbed out by vapor condensation. It is clear from Figure 2 that the black-liquor model very nearly predicts measured compositions exactly. There is an average error of 0.9% in the composition predictions.

The size distribution is the most difficult prediction to make but is important because it affects the fluid dynamics of the particles in the boiler. Additionally, particle size can be a determining factor in environmental remediation requirements and techniques. Figure 3 shows the correlation between experimentally measured size-distributions (by particle impaction devices, see Baxter, *et al.* (2000) for measurement methods) compared with model predictions for black liquor for an ideal boiler condition.

There is obvious deviation from expected results in the prediction. One of the significant factors that influences boiler operation is incomplete mixing (often resulting in definite striations in the gas phase) of the flue gas, resulting in varied temperatures at equal locations. This prediction does not account for non-ideal mixing. A second significant factor is the formation of sulfate compounds as a function of temperature. The model has no way of thermodynamically predicting whether sodium hydroxide or sodium sulfate is more favorable at a given temperature. Because of this, the point where the sulfate becomes stable is arbitrarily chosen.

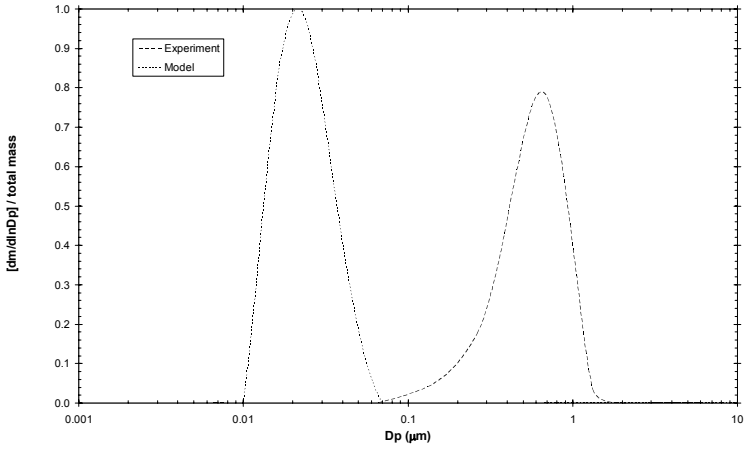

Figure 3. Aerosol particle size distribution for an ideal boiler: comparison between simulation and experiment (Lind, Rumminger et al. 2000; Baxter, Lind et al. 2001). Residence time is 4.0 seconds.

In spite of the poor correlation in Figure 3, it is encouraging to note that the model correctly predicts that the aerosol distribution will be all of one diameter. Considering the theory that the vapor condensation effects approach the upper size limit asymptotically and that the rate of growth slows exponentially with increasing particle diameter, the expected result is more likely to resemble the model prediction in shape (i.e. all of the mass should be found in one size diameter section). Literature data (Lind, Rumminger et al. 2000; Baxter, Lind et al. 2001) indicate a large peak at 0.7 μm and smaller peaks at 0.26 and 1.31 μm (physical diameters).[2]

Figure 4 shows the particle size distribution for an arbitrary non-ideal boiler. For the non-ideal case, sodium sulfate became stable at a higher temperature (1075 K) than is generally accepted as the sub-cooled and thermodynamically stable temperature (1058 K). This modification allowed for some of the sulfate to nucleate while most remained in the vapor phase. In the ideal case, in which sodium sulfate is assumed to become stable at a sub-cooled temperature, the sulfate nucleates into many small particles very

[2] Note that all diameters shown in this investigation are reported as physical diameters, not the aerodynamic diameters reported by Baxter (2000). Conversion to physical diameter was made with the specific gravity, assumed to be 2.3. The simulation calculates real diameters.

rapidly, in less than a tenth of a second in fact, and the size distribution is therefore skewed to the smaller range as shown in Figure 3. The nucleation rate was reduced by a factor of 100,000 to account for particles nucleating at varied temperatures along the boiler streamlines.

It is important to note that the correction factors included to account for non-ideality were chosen to fit the measured data, so the fit is very good. In this case, the predicted diameter at the maximum peak is in error by 0.82% from the measured data, whereas in the uncorrected case, the maximum peak is in error by approximately 97%.

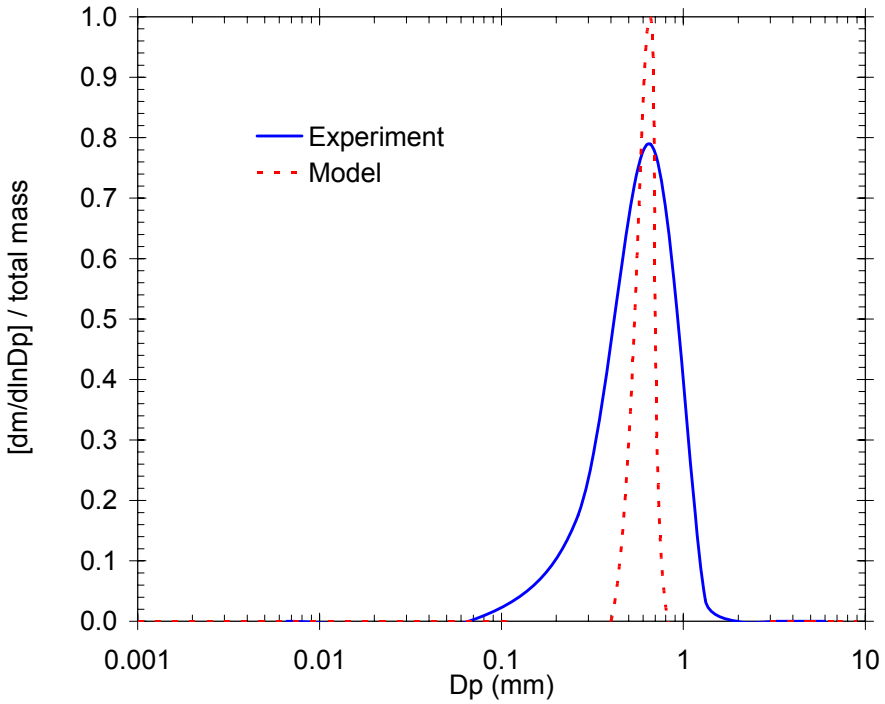

Figure 4. Aerosol particle size distribution for a non-ideal boiler: comparison between simulation and experiment (Lind, Rumminger et al. 2000; Baxter, Lind et al. 2001). Residence time is 4.0 seconds.

Concentration predictions were identical for both the corrected and uncorrected cases. Figure 5 shows the prediction of condensed phase concentration in grams of aerosol per normal cubic meter over a 4.0 second residence time. The model predicts concentration to within 2.1% accuracy. Although most of the alkali is bonded to hydroxide during vaporization at the char bed, very little hydroxide is found in the aerosol. This is due to "sulfur scrubbing," that is, the conversion of, say, sodium hydroxide to sodium sulfate. Virtually all of the sulfur in the gas phase is "scrubbed" by the vapor-phase sodium.

Sodium sulfate, as mentioned previously, becomes thermodynamically favorable over sodium hydroxide at around 1058 K, which is also near the melting point of sodium

sulfate but above the melting point of sodium hydroxide (594 K). This means that once the sulfate is formed, it immediately and rapidly condenses into small aerosol particles, which subsequently become condensation surfaces for other vaporized species in the gas phase, whereas the hydroxide would have remained in the vapor phase. This process accounts for the small amount of hydroxide in the aerosol phase.

Note that the values Figure 5 do not directly relate to the composition percents in Figure 2, as these are not normalized by the same species (Figure 2 is normalized by hydroxide and oxygen, Figure 5 is normalized only by hydroxide). The temperature range for the test was 1223.15 to 673.15 K (the corresponding range reported by Baxter was 950 to 400ºC).

Particle number is a value that is strongly influenced by nucleation (just as the size distribution is). From the data, it is expected that there are approximately 2.74 x 10^{13} aerosol particles per normal cubic meter (calculated from the specific gravity, the average diameter, and the concentration per normal cubic meter). The uncorrected model predicts 5.08 x 10^{17} particles per normal cubic meter, which is in serious error. The corrected model, on the other hand, does significantly better. It predicts 2.92 x 10^{13} particles per normal cubic meter, which is in error by only 6.8%.

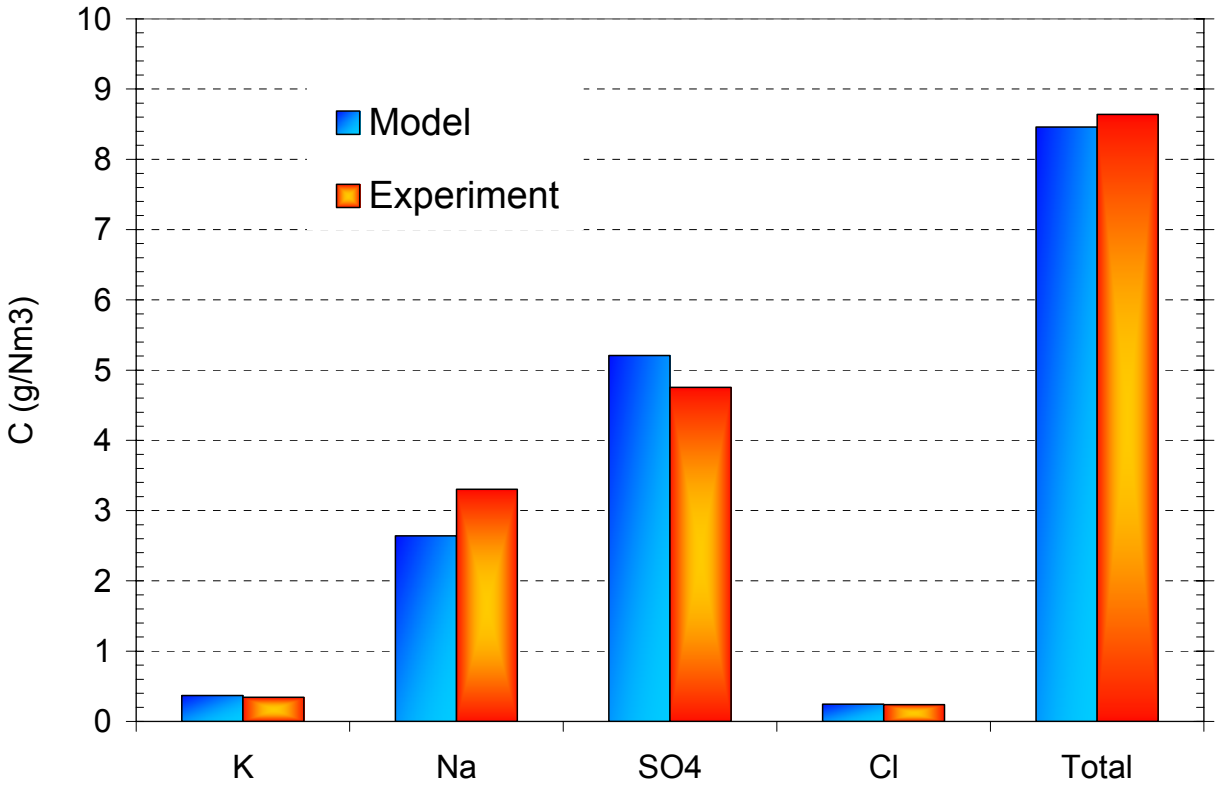

Figure 5. Aerosol concentration: comparison between simulation and experiment (Lind, Rumminger et al. 2000; Baxter, Lind et al. 2001). Residence time is 4.0 seconds.

Conclusions and Recommendations

The model herein described can predict composition, mass and number concentration, and the shape of the particle size distribution for aerosol species in black-liquor-fired recovery boilers. When combined with experimental programs that provide measured particulate and gaseous results from laboratory and commercial facilities, the new data should provide new information with possible implications in improving the efficiency and life of recovery boilers. Additionally, this research verifies the current hypothesis that the initial vapor concentration of alkali salts and sulfates, and gas temperature are the principle factors affecting aerosol formation.

The disagreement between the uncorrected size distribution predictions and the experimental results would be resolved by incorporating the model into a CFD code that would calculate sulfate formation based on thermodynamics, and by including a more rigorous, non-ideal thermodynamic equilibrium submodel into this model.

Two major assumptions of the current model are (1) that the vapor pressures for a mixture behave ideally (This will have an important effect on transport to the surface of aerosol particles), and (2) that sodium sulfate becomes thermodynamically stable at 1058 K. The model uses this assumption to determine when the gas-phase sulfates are scrubbed by vaporized sodium hydroxide. Both of these assumptions can be improved by incorporation of non-ideal thermochemical equilibrium codes suitable for alkali salts, as is being developed in a companion project.

This research would be measurably enhanced by further work in three areas. First, work in non-ideal thermodynamic interactions for liquid-salt mixtures would certainly improve the reliability of aerosol-phase predictions, including sulfate scrubbing from the vapor phase. Secondly, preexisting particles, whose origin lies outside the scope of this model, should have a profound impact on the relative rates of condensation vs. nucleation and must be separately modeled. Finally, accounting for non-ideal mixing, either through further research or by incorporating the model into a CFD code, should help resolve discrepancies between predicted and measured size distributions.

CHAR BED COMBUSTION

Abstract

This paper describes the development of a three-dimensional computer code that predicts fluid mechanics, heat and mass transfer and chemical kinetics within a reacting char bed and its application to black liquor. Finite-volume equations estimate pressure drop through porous media with the Ergun equation, a semi-empirical equation based on Darcy's law, to predict fluid flow. Gas and particle temperatures are calculated using established albeit mostly empirical heat transfer correlations together with heat released/absorbed by chemical reactions. The model predicts air flow, including penetration depth into the bed and heat transfer between the bed and the surrounding gases. A companion project collecting experimental information from laboratory and commercial scale beds should provide experimental data for validation in the near future. In the absence of such data, current validation consists only of qualitative analysis of quantitative predictions. This model has not yet been incorporated into a comprehensive computer code, but its use in such codes is illustrated based on previous work coupling simpler bed models with CFD codes.

Introduction

Black liquor is a biomass fuel generated during wood pulping. It is rich in both organic and inorganic materials. Recovery boilers process the fuel to recover the pulping chemicals and the energy in the organic fraction of the fuel. These boilers operate with a char bed on top of a smelt layer at the bottom of the boiler. Air jets trained at several locations around the char bed provide locally oxidizing conditions that generate heat and drive char combustion reactions. In addition, black liquor char reacts with water and carbon dioxide in endothermic reactions to produce hydrogen and carbon monoxide. The bulk of the char bed maintains reducing conditions, where reduction reactions convert the spent pulping chemicals (mainly fully oxidized sodium salts) back to reduced forms that eventually recycle to the pulping equipment. The range of stoichiometries, temperatures, physical states (gas liquid and solid), compositions, and velocities create a tremendously complex environment in and around the char bed. The momentum, heat, and mass transfer rates in such beds are poorly understood. Nevertheless, the char bed is the primary means by which both chemical and heat recovery take place. In addition, the char bed is potentially responsible for much of the fume (Tavares, Tran et al. 1998) and possibly intermediate-sized particle (Kochesfahani, Tran et al. 2000) formation (Tamminen, Kiuru et al. 2002) that leads to major downstream issues of deposition and pluggage. Finally, char beds and their cooling rates play central roles in safety and emergency operations relating to recovery boilers(Grace 1999; Grace, Tran et al. 2002). Efficient performance of recovery boilers depends critically on char bed behavior. This investigation focuses on developing and eventually validating a quantitative tool that captures most of this complexity and is useful for detailed engineering calculations.

Several investigators report recovery boiler and char bed models and data at varying levels of detail (Warnqvist 1994; Yang, Horton et al. 1994; Blasiak, Tao et al. 1997; Lee and Nichols 1997; Wessel, Parker et al. 1997; Dasappa and Paul 2001; Sutinen, Karvinen et al. 2002; Fjellerup, Henriksen et al. 2003). Most of the models and the data

address surface phenomena, with several notable cases coupling the surface description into complete boiler simulations (Yang, Horton et al. 1994; Blasiak, Tao et al. 1997; Wessel, Parker et al. 1997). A current research program is underway that focuses on experimental and theoretical descriptions of char beds at both laboratory and commercial scale. This document describes the progress in the theoretical analysis.

This investigation develops a comprehensive model of the bed region, accounting for momentum, heat and mass transfer of gas, liquid and solid phases, with homogeneous and heterogeneous global kinetic models including, oxidation, gasification and volatile combustion.

Particular attention is given to air flow patterns, and bed penetration depth. Understanding how gases flow through a bed and the penetration depth of jets leads to a better understanding of bed chemistry and behavior.

Theory/Methods

This investigation reports development of a computer code that models a black liquor bed as a three-dimensional, porous, multiphase, media. The code predicts the steady-state shape of the bed based on droplet arrival at the surface and consumption in the bed (when coupled to a liquor injection model) but for the purposes of this document, which does not include the liquor injection model, the bed assumes the fixed shape of a downward-opening paraboloid. The bed is divided into discrete volumes (discretized). We have developed and applied new numerical techniques potentially capable of greatly improving the accuracy and flexibility of this type of calculation (Robinson, Junker et al. 2002), but the focus here is now the bed behavior, not the numerics, so we present a classical solution in this document. Values of temperature, composition, flow, and reaction rate are calculated at each node in the grid using a finite volume method (Versteeeg and Malalasekera 1995). The finite volume method defines the mathematical relationships between the properties at the nodes based on substation of algebraic equations for derivatives in differential equations. These are presented briefly here for this application. The generalized equation describing energy, mass and momentum transport appears as Equation 1.

$$\frac{\partial(\rho\phi)}{\partial t} + \vec{\nabla} \bullet (\rho\phi\vec{v}) = \vec{\nabla} \bullet (\Gamma\vec{\nabla}\phi) + S_{\phi} \qquad 1$$

The first term represents accumulation of the property φ at a point and is zero for steady-state solutions. The second term describes convective transport. The first term to the right of the equals sign represents diffusive transport and last term represents sources (generation/destruction) for the property φ. The values for the general equation for each of the transport equations appear in Table I. Substituting finite volume relationships for the gradient and divergence terms, the equation can be reduced to an algebraic expression involving the unknown φ values. This is written in matrix form and solved numerically. Iterative solutions are required because of nonlinear dependencies and couplings in the equations and, in our case (as is very common), because the

exceptionally efficient Thomas algorithm is used to invert the matrix, which causes the non-tridiagonal elements of the leading matrix to be transferred to the right side.

Table I General transport equation parameters.

Property	ϕ	Γ	S_ϕ
Pressure	P	$\frac{\delta \cdot \alpha \cdot \rho}{\mu}$	$-r_A$
Mass/Mass Fraction	x	$\rho \cdot D_{AB}$	$-r_A$
Energy/Enthalpy	$c_P \cdot T$	$\rho \cdot \alpha$	$\Delta H_{rxn} + q'''_{conv} + q'''_{rad}$

The foundation of the model is the solution to the gas flow and velocity profiles in the bed. In this document, results from an uncommon approach to the gas flow solution appear relative to traditional CFD solutions. In porous media, wall boundary layer forces, rather than shear forces internal to the gas, dominate flow patterns. Consequently, the gas flow model is based upon Darcy's law as opposed to Navier-Stokes-style equations. The result is similar to the modeling of underground flows through porous rock, as is done in petroleum reservoir modeling. A reasonably detailed discussion of this approach is included here whereas the rest of the CFD equations are set up and solved in a manner that can be found in any number of CFD texts (Versteeeg and Malalasekera 1995).

Darcy's law predicts how pressure drops through the bed as a function of permeability (α), bulk gas velocity (v_∞) and dynamic viscosity (μ). Specifically,

$$\nabla P = \frac{\mu}{\alpha} \cdot v_\infty \qquad 2$$

The computer code uses the Ergun equation (see Equation 3), a semi-empirical correlation based upon Darcy's law. It is a valid prediction of pressure drop in flow regimes from laminar to turbulent (Bird, Stewart et al. 2002).

$$-\nabla P = 150 \cdot \left(\frac{\mu \cdot v}{{D_p}^2} \right) \cdot \frac{(1-\varepsilon)^2}{\varepsilon^3} + \frac{7}{4} \cdot \left(\frac{\rho \cdot v^2}{D_p} \right) \cdot \frac{1-\varepsilon}{\varepsilon^3} \qquad 3$$

Rearranging the terms in Equation 3 leads to a form that looks similar to Darcy's law with the addition of a turbulence factor (δ) (Bird, Stewart et al. 2002).

$$-\vec{\nabla}P = \frac{\mu}{\delta \cdot \alpha} \cdot \vec{v} \quad (4)$$

where,

$$\alpha = \frac{D_p^2}{150} \cdot \frac{\varepsilon^3}{(1-\varepsilon)^2} \quad (5)$$

$$\beta = \frac{7}{4} \cdot \frac{1}{D_p} \cdot \frac{(1-\varepsilon)}{\varepsilon^3} \quad (6)$$

$$\delta = \left(1 + \frac{\beta \cdot \rho \cdot \alpha \cdot v}{\mu}\right)^{-1} \quad (7)$$

Equation 4 can be combined with the continuity equation (see Equation 8) to create a function that gives the pressure as a function of position.

$$\vec{\nabla} \bullet (\rho \cdot \vec{v}) = S \quad (8)$$

$$\frac{\delta \cdot \alpha \cdot \rho}{\mu} \cdot \nabla^2 P = S \quad (9)$$

Equation 9 now resembles the diffusion term of the general transport equation (see Equation 1), lends itself easily to the finite volume method. With the pressure solution, gas velocities result from a rearranged form of Equation 4.

The gas velocities form the basis for the rest of the model. Using the general transport equation and the velocity field from the pressure solution, heat and mass transfer throughout the bed can be predicted.

For both the gas and the solid phases, the general transport equation is implemented with relevant source terms. For the gas phase, the energy transport equation source terms include the heat of reaction from the homogeneous kinetics and convection between the gas phase and the solid phase. The solid phase includes an equal but opposite source term from convection with the gas phase, heats of reaction from the heterogeneous kinetics, and radiation from the surrounding environment. These source terms and boundary conditions determined by geometry and external flows complete the specification for the energy equation. Mass transport in the gas phase is solved in a similar manner with reaction rates as source terms.

Mass transport in the condensed phase requires a different approach. Movement of the solid phase in the bed occurs according to a simple mass balance. At steady state, the rate at which mass flows down into an individual cell in the bed is equal to the rate of overall consumption of mass in the cell plus the net rate at which mass flows out of the particular cell. This mass balance results in a term for the solid velocity at the face of each node (see Equation 10).

$$v_k = \frac{v_{k-1} \cdot \rho_{k-1} \cdot A_{k-1}}{\rho_k \cdot A_k} - \frac{r_{Ak} \cdot \forall_k}{\rho_k \cdot \mathrm{A}_k} \qquad 10$$

where,

v is velocity

k is the cell index from bottom to top

ρ is the solid density

A is cross-sectional area perpendicular to the direction of flow

$\forall$ is cell volume

$-r_A$ is the rate of mass consumption

The shape of the bed is directly defined, with the assumption that fuel feeds the bed at the boundaries at the rate at which it is consumed in the direction of gravity below the surface. The downward flow of the fuel is solved only in the vertical (gravity-oriented) dimension, with the assumption that there is no lateral movement within the bed. The geometry of the bed adapts to the source terms at the surface, which allows the bed to define its own shape based upon the fuel feed rate and liquor dispersion model. Density and porosity of the bed are defined as functions of the fuel composition.

The model includes global kinetics for char oxidation and char gasification by water and carbon dioxide. Reactions are implemented through source terms in the transport equation. Gasification reactions are modeled using published kinetics (Li and Vanheiningen 1989; Li and Vanheiningen 1990; Li and Vanheiningen 1991; Backman, Frederick et al. 1993; Frederick, Wag et al. 1993; Vanheiningen, Arpiainen et al. 1994; Lee and Nichols 1997; Saviharju, Moilanen et al. 1998; Sutinen, Karvinen et al. 2002) that include mechanisms catalyzed by the inorganic salts present in the liquor. Gas phase reactions include carbon monoxide conversion and volatiles combustion. Submodels are also included which model pyrolysis, evaporation and melting of inorganic material and will soon be extended to advanced devolatilization models being developed under a companion project.

Results

The three-dimensional nature of the predictions produced by this code are especially difficult to display and discuss in traditional, black-and-white graphical formats. This discussion highlights results from relatively simple examples and focuses on issues of practical interest.

The first several results presume a bed shape of a downward-opening parabola and air jets located at the midpoint of each of four walls around the bed. The bed is 3.7 m wide and deep and 1.4 m tall. One of the key considerations is the extent of jet penetration and fluid dynamics in the bed.

Figure 6 illustrates the pressure profile across a bed at its axis of symmetry (through the center of the bed) that has air jets impinging on the bed surface from four sides. The jets collinear with the axis of this plot dominantly impact these results. This profile is at the bottom of the bed. The pressure differences illustrated are too small to appreciably impact chemical quantities such as vapor pressures or reaction rates, but they impart large velocity gradients in the gases that move through the bed. In this simple case, the profile is symmetric, as would be expected for a symmetrically defined problem.

The total gas speed (magnitude of the velocity vector) along the same location is illustrated as Figure 7. As seen, the speed profiles closely follow the pressure profiles, although the speed is more closely proportional to the square root of the velocity gradient than to the velocity gradient itself.

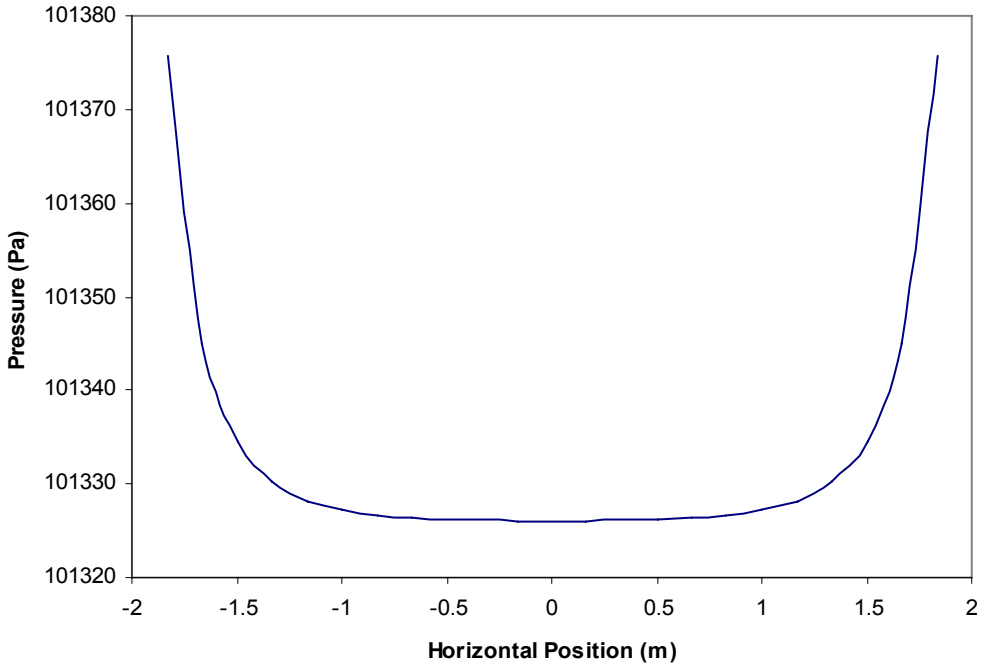

Figure 6 Pressure profile across a bed at the axis of symmetry with jets impinging on the bed surface from both sides.

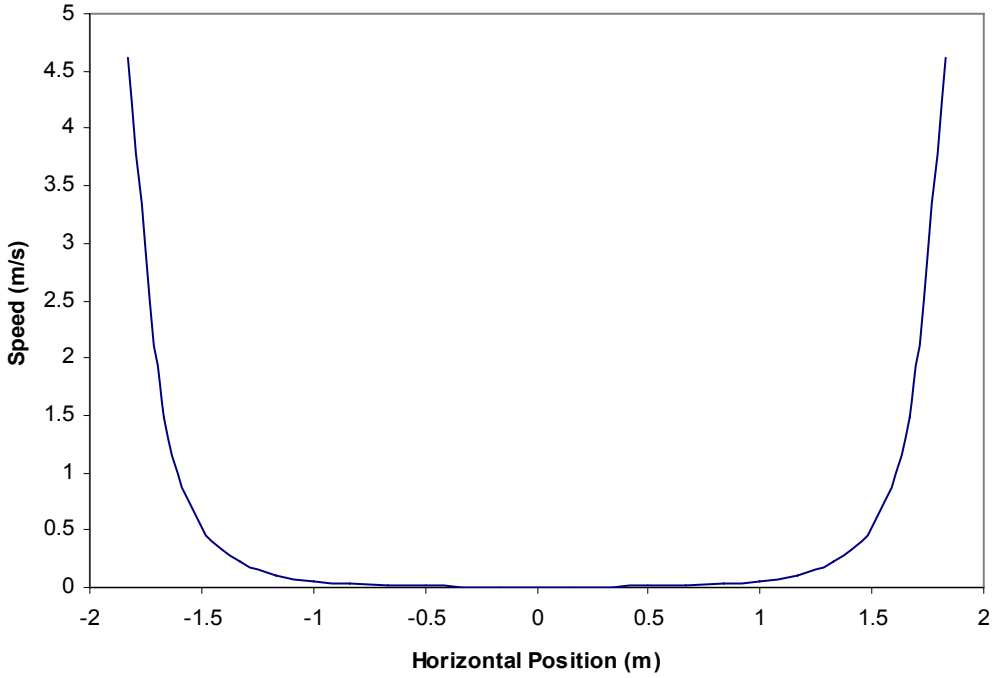

Figure 7 Pressure profile across a bed at the axis of symmetry with jets impinging on the bed surface from both sides.

The center of the bed has essentially no gases moving through it, in part because this illustration is for the bottom of the bed where there are no convective velocities rising from below, and in part because the bed prevents gases from completely penetrating into its porous structure. A general characterization is that the jet speed decays to about twelve percent of its value at the bed surface in the first foot of its depth.

The next series of illustrations are presented in the form of surface plots. These three-dimensional depictions represent the value of the variable as height in the vertical direction. These figures indicate variation in the dependent variables (velocity, pressure, speed, etc.) as functions of two dimensions as a continuous surface, the elevation of which is proportional to the value of the variable. The surface includes a grid that helps indicate its structure and variation. In addition, the original versions of these surfaces are color coded according to the value of the variable, with the highest values being violet and the colors progressing as through a rainbow from highest to lowest, the lowest being red.

In these cases the two dimensions are the two horizontal coordinate dimensions of the three dimensional bed. Values of selected variables will be illustrated at different vertical locations, with each plot showing the spatial variation of the variable in a horizontal section of the bed. Contour plots of the same data are projected onto planes above and below the surface plots and in some cases may aid in interpreting the trends. The bottom contour plot is continuously color coded according to the scheme for the surface plot to aid in its interpretation. Only the lines of the top contour plot are shown

so as to avoid obscuring the surface illustration. However, these lines are also color coded. As little additional clutter as possible is added to the plots. For example the axes are not labeled or even shown. Quantitative values of the peak values and other key locations are provided in the text and sometimes in the figure captions. In all cases, the independent variables include the full extent of the two horizontal dimensions of the bed.

A surface plot of the velocity (signed single component of the velocity vector) at the base of the bed appears as Figure 8. This view is for the velocity component in the coordinate direction that runs from the lower right to the upper left of the illustration. The two jets oriented in this coordinate direction impinge on the bed along the lower right and upper left border producing velocity peaks on the border. The actual peaks have been truncated to allow a better display of the rest of the velocity field structure. The value of zero velocity is midway along the vertical axis of the surface, and most of the bed has a velocity of near zero. However, the positive (upward ranging) velocities of the jet impacting on the bed on the lower right are flanked by two negative velocity peaks on either side. These spikes represent gases that impinge on the bed, penetrate a short distance, and return at relatively high velocities along the edges of the impinging jet but in the opposite direction.

The structure in the velocity profile seen along the lower left and upper right edges of the plot has a similar origin. The jets along these walls impinge on the bed with this component of velocity being zero. The impacting jets expand rapidly in the bed as they slow. This component of velocity remains zero on the centerline of the jets, but the jet expansion creates relatively large values of velocity lateral to the main jet outside of this centerline. In total, the impinging jets induce significant velocities over a relatively small portion of the total bed. The other horizontal component of the velocity is identical to that shown in Figure 8 except that it is rotated ninety degrees around the horizontal axis.

The vertical velocity component at the base of the bed appears in Figure 9. Again, the peak values of this component have been truncated. All four impinging jets generate identical vertical velocity components in the bed, although the magnitude is smaller than the horizontal components, with peak values of 0.75 m/s and the highest values seen in the figure at 0.1 m/s.

These figures indicates that jet impingement into the bed primarily results in outgassing in the immediate vicinity of the jet impact with minimal penetration in either the direction of the jet or in the vertical direction. Parametric variations in bed porosity, jet velocity, and similar parameters indicate that this qualitative conclusion is generally accurate although the quantitative details change. For example, bed porosity increases result in higher in-bed initial velocities but almost identical decay patterns when the velocity profiles are scaled by the peak (initial) in-bed velocity. More simply stated, the jet horizontal velocity decays to about 12% of its initial value in the first foot of bed depth over a wide range of bed porosities. However, the initial in-bed velocity of the jet depends strongly on bed porosity.

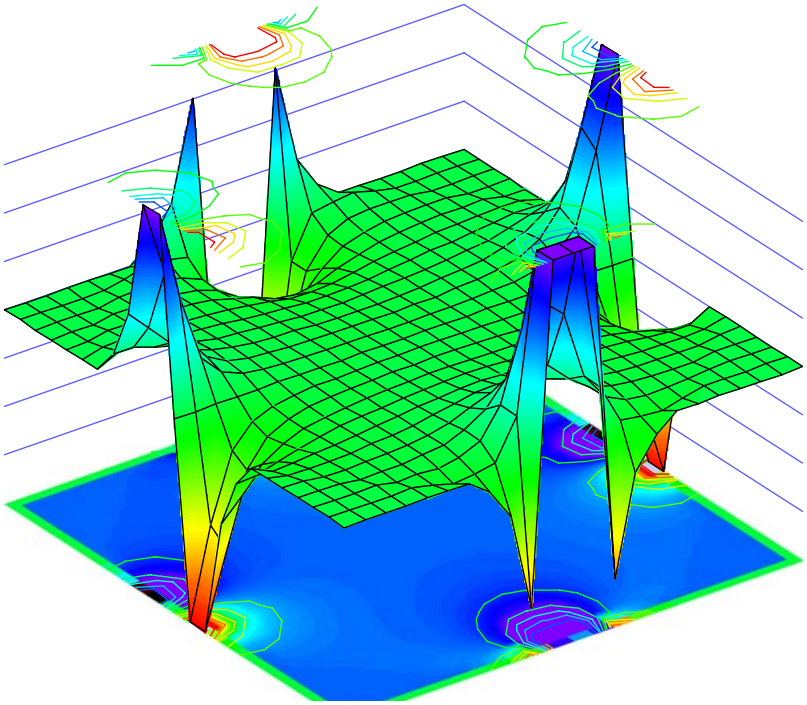

Figure 8 Surface plot of a horizontal component of velocity at the base of the bed, with contour plots of the same data appearing at planes at the top and bottom of the figure. The peak magnitude of the horizontal component of the velocity (which is truncated in this figure) is nearly 5 m/s.

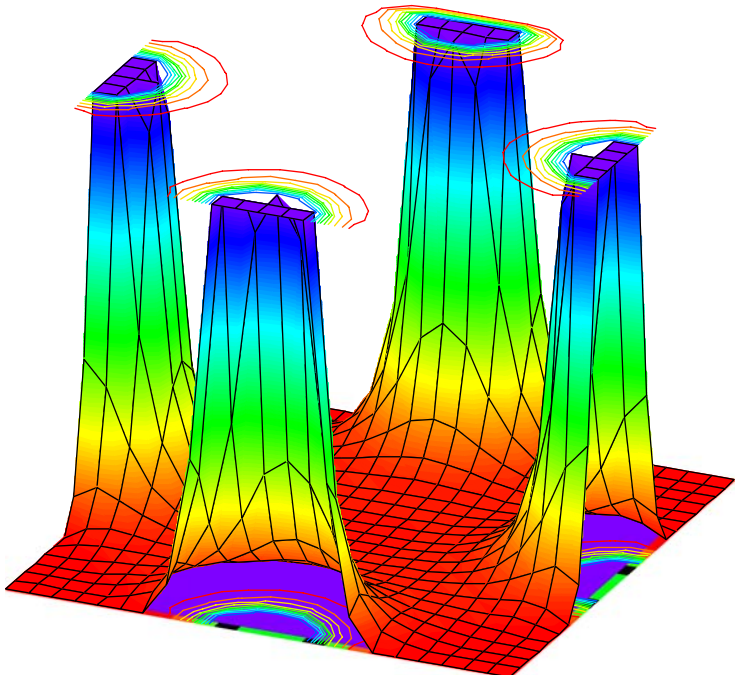

Figure 9 Surface and contour plots of the vertical velocity component near the base of the bed as a function of horizontal position. The peak value of this velocity component (which is truncated in this figure) is approximately 0.75 m/s. The maximum value seen illustrated here is 0.1 m/s.. Compare with Figure 11 and Figure 13.

Two practical conclusions result from this analysis. The first is that the great majority of the base of the bed is minimally impacted by the impinging jets along the outside. The second is that the center of the base of the bed in any case experiences minimal gas velocity gradients and represents a relatively stagnant region.

Figure 10and Figure 11 illustrate similar data for a vertical section of the bed approximately half-way between the base and the top of the bed and above the primary air ports (jets directed at the base of the bed. Several features of these plots differ from those at the bottom of the bed. First, peak in-bed velocities are much lower than at the base of the bed. The peak values of the horizontal velocity components are +/- 0.03 m/s and those of the vertical component are 0.05 m/s. Additionally, all velocities in the horizontal directions are oriented out of the bed. In the case of Figure 10, the negative values on the lower right indicated velocities are directed in the negative coordinate directions, which is out of the bed in this region. Positive values in the upper left also indicate velocities are directed in the positive coordinate direction, which is also out of the bed in this region. Even though the jets penetrate the bed in the region of the jets but cause outgassing in this region, the influence of the jects on the in-bed velocities propagates to this level of the bed. Figure 11 illustrates the vertical component of velocity as a function of position. In this region, the gases exhibit significantly higher velocities above the jets compared to other regions of the bed, albeit these velocities are still quite low. The vector sum of both horizontal components of the velocity shows a pattern similar to that of Figure 11 and indicates that both the horizontal and vertical velocity component of velocity remain strongly influenced by the jets even in regions physically distant from the jets.

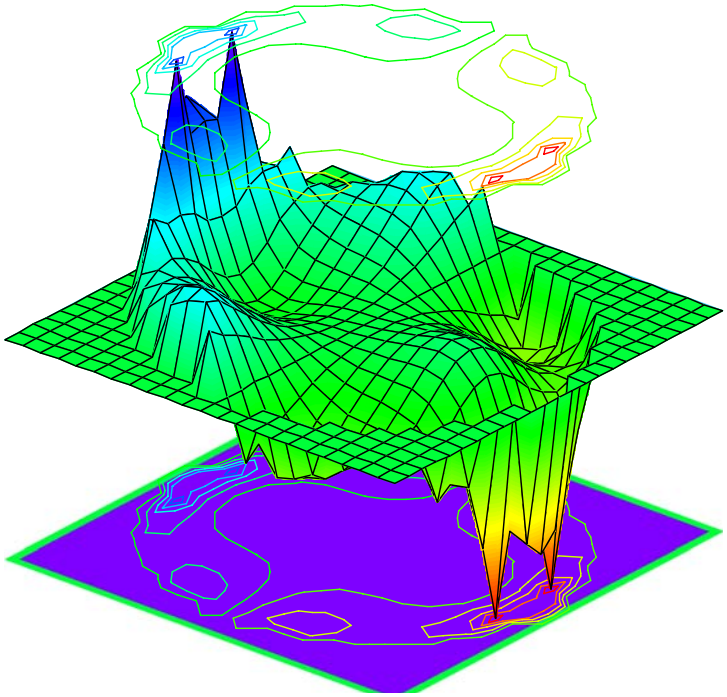

Figure 10 Surface and contour plots of the horizontal component of velocity in the bed viewed from the same perspective as Figure 8. The spatial dimensions represent a point approximately halfway between the bed base and its top. The peak value of this velocity component is approximately 0.03 m/s and has not been truncated in this view.

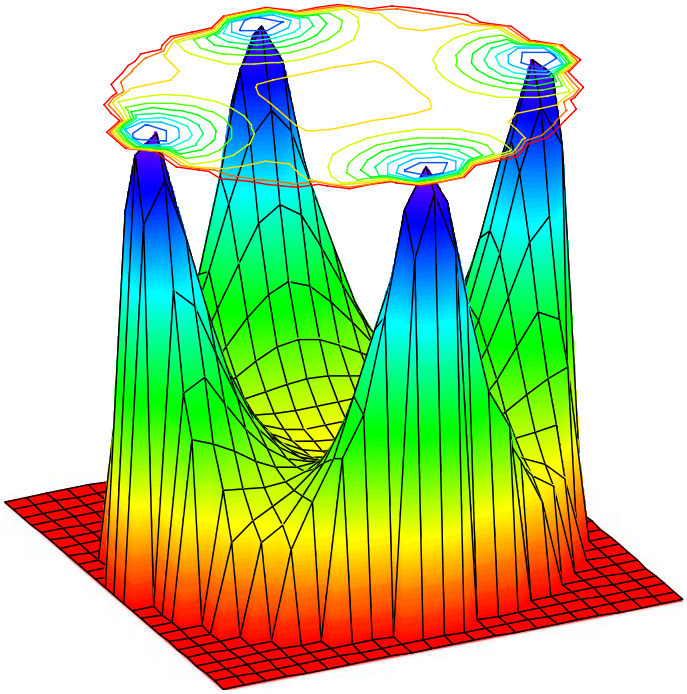

Figure 11 Surface and contour plots of the vertical velocity component in a horizontal plane near the vertical center of the bed as a function of horizontal position. The peak value of this velocity component (which is not truncated in this figure) is approximately 0.05 m/s. Compare with Figure 9 and Figure 13.

Near the top of the bed, the in-bed velocities are lower still and the influence of the jets wanes. Figure 12 and Figure 13 illustrate data similar to that considered in the previous figures but for a horizontal plane near the top of the bed. As is seen, peak velocities fall to about 0.01 m/s but are still uniformly directed out of the bed. The influence of the jets on the in-bed velocities is minimal, although not completely absent, in these plots.

Three major aspects of this project remain to be completed. These include resolution of some numerical issues associated with the condensed-phase reactions, verification with reliable experimental data, and incorporation in a comprehensive computer code. Substantial progress has been made in each of these areas and will be summarized briefly here.

Some final issues with condensed-phase kinetics remain to be resolved in this code before the predictions can be considered sufficient for comparison with data. However, these are relatively small details. Essentially all in-bed properties not discussed here follow logically from the velocity plots. For example, the only velocities of sufficient magnitude for oxygen to reach char surfaces and react directly with the char are in the immediate vicinity of the jet impingement locations. The oxygen in these regions is rapidly consumed, with minimal penetration into the bed (much less than even the velocity profile penetration). Heat release from oxygen reaction with char is substantial in the immediate regions of the jets, but in all other regions char is consumed by endothermic gasification reactions principally with H_2O and CO_2. Therefore, with the exception of the jet regions, the temperatures in the bed should be lower than the surrounding gas and decreasing toward the center of the bed in a manner somewhat similar to the vertical velocity plots. The hottest portions of the bed are near the jets even though the gases in the jets themselves are relatively cool. The rest of the bed heating occurs from external gases through convection. A complete, standalone bed model with its own multi-dimensional graphics package should be completed shortly with all reactions (gas- and condensed-phase) heat transfer, mass transfer, and fluid mechanics incorporated.

These predicted features of bed behavior require experimental verification to verify their usefulness. A companion project, also being reported in this meeting, is developing these experimental data and the data will be used with the model to develop an advanced understanding of bed behavior.

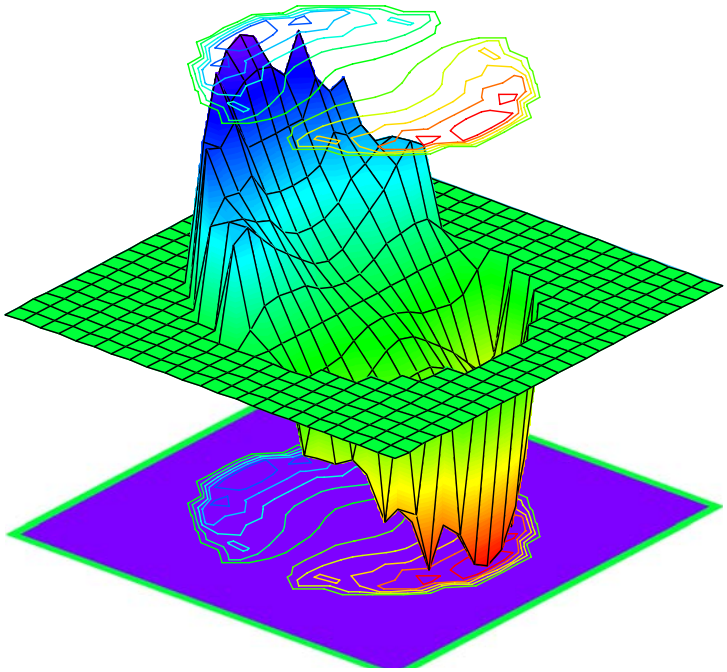

Figure 12 Surface and contour plots of the horizontal component of velocity in the bed viewed from the same perspective as Figure 8 and Figure 10 but at a point near the top of the bed. The peak value of this velocity component is approximately 0.006 m/s and has not been truncated in this view.

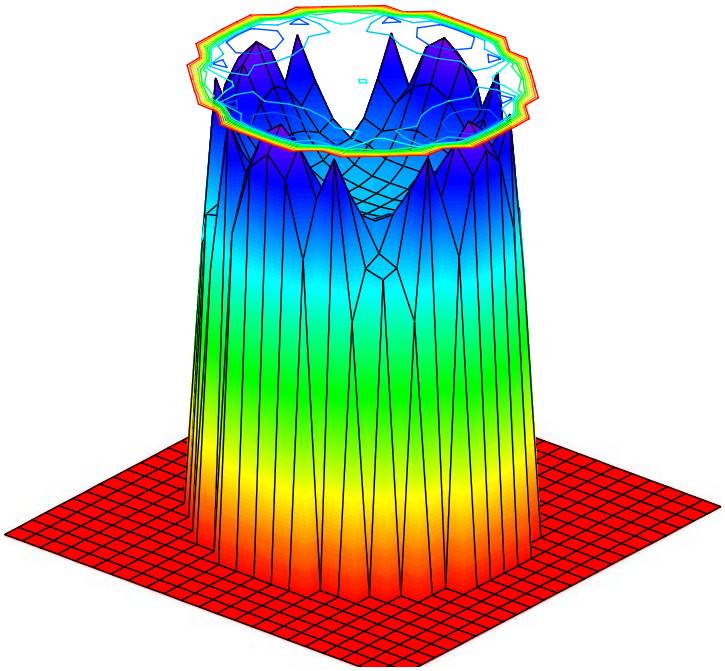

Figure 13 Surface and contour plots of the vertical velocity component in a horizontal plane near the top of the bed as a function of horizontal position. The peak value of this velocity component (which is not truncated in this figure) is approximately 0.015 m/s. Compare with Figure 9 and Figure 11.

Less sophisticated but multi-dimensional bed computer models have already been developed and incorporated into computational fluid mechanics codes. These codes predict the impacts of particle entrainment from a bed, deposition patterns on walls and heat exchangers, particle conversion rates, etc. The ultimate goal of this work is to provide a general-purpose, fully three-dimensional computer description of the bed in a format usable both as a standalone code and as part of a more comprehensive description of a boiler.

Conclusion

A three-dimensional black liquor bed combustion model provides some insight into possibly dynamic behavior internal to recovery boiler beds. The model suggests that the central portion of the base of the bed is largely quiescent, with relatively low gas velocities and temperatures. The jets impinging on the bed near this location penetrate the bed no further than about one foot (0.3 m). the majority of the gases impinging on the bed return by reverse flow and create an annular reverse flowing jet around the impinging jet. The jet impingement regions are the only regions where sufficient convective velocities exist to create boundary layers thin enough for oxygen to directly oxidize carbon. The remainder of bed experiences carbon conversion through gasification reactions, primarily with H_2O and CO_2. Since the gasification reactions are endothermic, the only heat sources internal to the bed are in the regions of the jets. The remainder of the bed is heated through convection and radiation from the gases and particles surrounding the bed.

Essentially everywhere except at the jet impingement locations, there is a net outflow of gas in bed. The velocities of the gases leaving the bed are low everywhere except around the jets and decrease with increasing height in the bed. Gas velocity profiles inside the bed are influenced by the jets at most locations, with gas outflow being noticeably higher on average at regions directly above the jets than in other regions. This influence wanes and is barely noticeable at the top of the bed.

A companion project is developing experimental data describing bed combustion behavior with which these results can be compared. The combination of the two projects will undoubtedly lead to modifications of both experimental designs and theoretical descriptions, especially in the area of particle reactions. The eventual result of this work will include a stand-alone computer code capable of describing bed combustion and a code that can be incorporated into more comprehensive computer simulations.

PARTICLE REACTIVITY

Abstract

Experimental and theoretical investigations indicate how particle shape and size influence biomass combustion rates. Experimental samples include flake-like, cylinder-like, and equant (nearly spherical) shapes with similar particle masses and volumes but different surface areas. These samples passed through a laboratory reactor in a nitrogen atmosphere and a maximum reactor wall temperature of 1600 K. A separately developed computer and image analysis system determined particle surface-area-to-volume ratios based on three orthogonal particle silhouettes. Experimental data indicate that equant particles react more slowly than the other shapes, with the difference becoming more significant as particle mass increases and reaching a factor of two for particles less than 1 mm in diameter.

A one-dimensional particle model simulates the rapid pyrolysis process of particles with different shapes. The model characterizes particles in three basic shapes (sphere, cylinder, and flat plate). With the particle geometric information (particle aspect ratio, volume, and surface area) included, this model can be modified to simulate the devolatilization process of biomass particles of any shape. Model simulations of the three shapes agree nearly within experimental uncertainty with the data. Model predictions extended to a wider range of sizes predict the effects of shape and size on yields and overall mass conversion rates. The near-spherical particle losses mass most slowly and its conversion time significantly differs from those of flake-like particles and cylinder-like particle when particle equivalent diameter increases. Little difference exists between the cylinder- and plate-like particles. Low-ash fuels yield up to 95% volatiles during high-temperature pyrolysis. Both particle shape and size affect the product yield distribution. Near-spherical particles exhibit lower volatile and higher tar yields relative to aspherical particles with the same mass. Volatile yields decrease with increasing particle size for particles of all shapes.

Introduction

At least two compelling forces drive global interest in renewable energy supplies: (1) increasing concern about environmental impacts associated with fossil fuels and nuclear energy; and (2) increasing anxiety regarding the security and longevity of fossil fuel resources. One potential strategy that addresses both concerns is the supplementing traditional, dominantly fossil fuels with renewable biomass fuels, since biomass fuels come from indigenous sources and can be essentially CO_2-neutral (considering the carbon cycle in atmosphere) if derived from sustainable cultivation practices. Thermal conversion (combustion and gasification) represents the most common commercial utilization of biomass. Black liquor and hog fuel used at pulp and paper mills represent by far the largest contributions to non-hydro renewable energy in the country. Both current and future technologies employed in the pulp and paper industry benefit from more accurate understanding of the processes occurring in the conversion systems. This investigation focuses on issues common to most conversion systems – particle combustion characteristics.

Black liquor and biomass particles commonly have more irregular shapes and much larger sizes than pulverized coal or other entrained-flow, low-grade fuels, with typical aspect ratios between 2 and 15. Larger particle sizes establish the potential for large internal temperature and composition gradients that complicate combustion models. At present, particle models used in computational fluid dynamics (CFD) codes and elsewhere generally assume spherical, isothermal biomass particles (Fletcher, Haynes et al. 2000; O'Dowd, Gera et al. 2001). Furthermore, various particle shapes result in different particle exterior surface-area-to-volume ratios, which are essential to heat and mass transfers and further affect the devolatilization and oxidation rates. Spheres represent an extreme case with lowest surface-area-to-volume ratios if any shape.

A substantial experimental and modeling literature for biomass particle pyrolysis processes exists, with varying kinetic mechanisms and related parameters. A one-step global model, which is described by one global reaction suffices for relatively simple applications (Nunn, Howard et al. 1985; Varhegyi, Antal et al. 1989; Antal and Gabor 1995; Antal, Varhegyi et al. 1998; Guo and Lua 2000). The drawback of the one-step model is that it cannot predict the variation of total mass or individual product yield distributions with temperature and heating conditions. Typical wood applications use one- or two-stage multiple reaction models (Thurner and Mann 1981; Font, Marcilla et al. 1990; Di Blasi 1998; Brown, Dayton et al. 2001; Babu and Chaurasia 2003). Two-step models include a primary stage, during which wood thermally decomposes to produce light gases, tars, and chars, and a secondary stage, during which tars undergo additional cracking to produce gases. Much more sophisticated devolatilization models exist (Niksa, Kerstein et al. 1987; Solomon, Fletcher et al. 1993), including some under development by this research group (Pond, Fletcher et al. 2003), and these will be incorporated into this analysis in the future, but the present simple models are adequate to illustrate the impacts of shape and size on particle conversion.

Biomass particle models usually include mass, energy, and momentum transport equations (Chan, Kelbon et al. 1985; Shen, Lui et al. 1991; Di Blasi 1994; Di Blasi 1996; Di Blasi 1996; Di Blasi 1997; Miller and Bellan 1997; Liliedahl and Sjostrom 1998; Jalan and Srivastava 1999; Gronli and Melaaen 2000; Janse, Westerhout et al. 2000; Brown, Dayton et al. 2001; De Diego, Garcia-Labiano et al. 2002; Hagge and Bryden 2002). Few of these particle models simulate aspherical shapes but several are suitable for incorporation into CFD codes. The paucity of experimental data suitable for validating these model predictions compromises the potential contributions of such models to engineering or scientific investigations.

This investigation summarizes experimental devolatilization conversion rates for sawdust particles of three shapes in an entrained-flow reactor together with a model that predicts these data nearly within their experimental uncertainty. A particle model is developed to simulate the devolatilization of biomass particle of any shape. Effects of particle shape and size on devolatilization behaviors are investigated over a wider range of conditions than are available from experimental data to evaluate overall impacts of aspherical shapes in practical applications.

Experimental Method

Fuel Properties

The samples used in this study are sawdust particles with same volume and different shapes. Three shapes are considered: flake-like, cylinder-like, and near-spherical. The sawdust was first separated using sieves, then aerodynamically classified. Finally, different aspect ratios were separated by sieves again. The samples were put in an oven at 90^{o}C for two hours before feeding. To measure the particle surface area and volume, three images were taken from three orthogonal directions for the particle. The particle volume and surface area were calculated using a 3D shape reconstruction code, which is developed in the combustion lab at Brigham Young University. The particle volume was verified by measuring over 2000 particles with the particle density known as 650 kg/m^3. The samples are shown in Figure 14. Other data of the samples are tabulated in Table II.

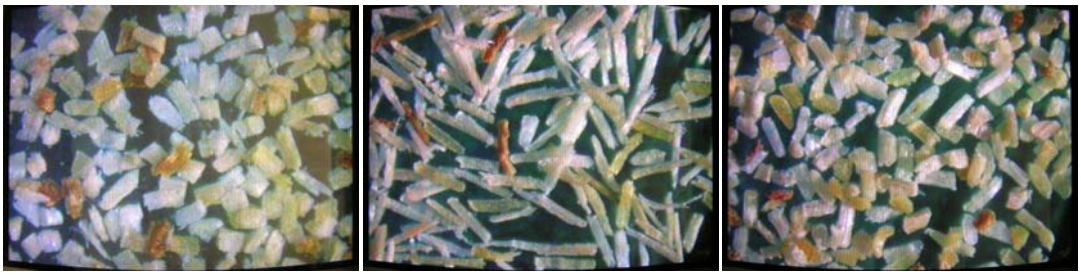

(a) flake-like particle (b) cylinder-like particle (c) near-spherical particle

Figure 14 Photographs of sawdust particles of different shape.

An entrained flow reactor is used in this study. As is shown in Figure 15, the reactor includes feeding section, reactor body, collection section, and separation section. The feeding section consists of a syringe feeder and a water-cooled feeding probe, which can obtain a feeding rate as low as 1.0 gm/hr. An electrically heated preheater can heat the secondary gas up to 500^{o}C before it enters the reactor. The reactor body is electrically heated using Kanthal super heating elements, providing a maximum wall temperature of 1650 K. The reactor also provides up to 0.5 seconds residence time, and the residence time can be changed by adjusting the relative distance between the feeding probe and collection probe. When particle reaches the collection probe at the bottom of the reactor, it will be quenched down by nitrogen gas. The flow rate ratio of the quench nitrogen and the secondary gas is about 7 ~ 10. Char will be collected in the first cyclone separator, which has a cutting point of 25 μm. The second cyclone separator has a cutting point of 5 μm, which is capable of collecting most of the condensed tar. Finally, the very fine particles are collected in the filter. The pore size of the filter is 1 μm.

Table II Sample properties

Sample	Flake-like	Cylinder-like	Equant

Volume ($\times 10^{-11}$ m^3)	1.697	1.682	1.794
Equivalent diameter (mm)	0.32	0.32	0.325
Surface area ($\times 10^{-7}$ m^2)	4.91	4.79	3.438
Aspect ratio	4.0 (width/thickness)	6.0	1.65

Experimental Setup and Procedure

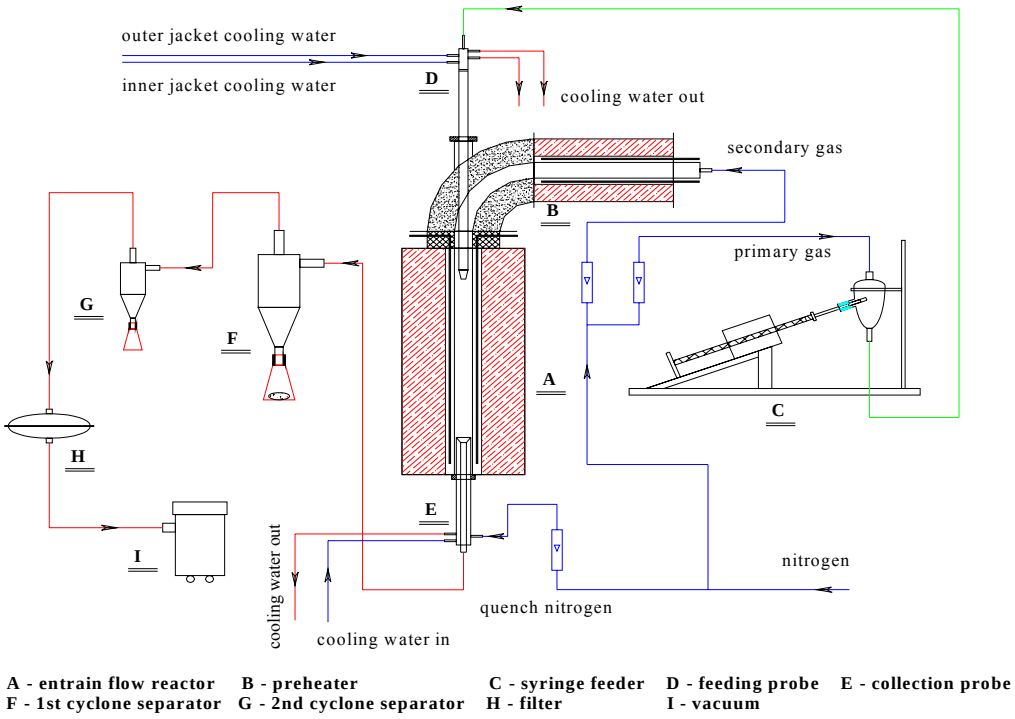

Figure 15 Entrained flow reactor schematic diagram.

With the sawdust samples prepared above, devolatilization experiments are conducted on this entrained flow reactor in nitrogen environment. Mass loss data as functions of residence time have been collected.

Description of the Mathematical Model

When the biomass particle is traveling through the entrained flow reactor, it is exposed to both radiation and convective heat transfer. This devolatilization process involves the heating of raw biomass or organic materials in the absence of oxidizer, the thermal degradation of the biomass components, mass transport of the devolatilization products in the particle by means of advection and diffusion, and blowing of the gas products at

the surface of the particle. The two-stage wood pyrolysis kinetics model, shown in Figure 16, is chosen for this particle model since it is capable of predicting the product yields and distribution variations with temperature and heating rate which are significantly influenced by particle shape and size.

Moisture in wood is divided into two categories. Free moisture vaporizes from the surface at a rate determined by the surface vapor pressure, the moisture in the bulk flow (zero in these experiments) and the surface area of the particle. The particles used in these experiments were dried prior to use to maximize the particle size that can react in our residence-time-limited reactor. Drying of this nature removes all of the free moisture. Additionally, some moisture is chemically bound in the fuel in a variety of ways. This moisture does not vaporize in a manner similar to free moisture. Four basic methods, including a thermal model, describe wood drying under combustion heat fluxes (Bryden and Hagge 2003). A chemical reaction using an Arrhenius expression with zero activation energy describes the release of this moisture, consistent with recommendations from the literature. Figure 17 illustrates the drying scheme of moisture.

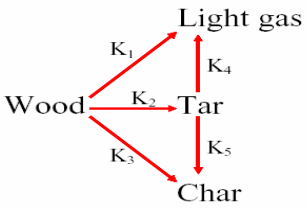

Figure 16 Reaction scheme for thermal decomposition of biomass

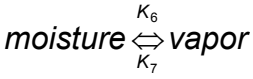

Figure 17 Drying scheme of moisture.

In addition to this simple devolatilization model, under this project we modified the CPD devolatilization model to include parameters suitable for black liquor, with the following results.

Results

Selection of Chemical Structure Parameters for the CPD model

This section describes how chemical structure parameters were selected. A summary of recommended values based on the literature is shown in Table 3.

Table 3 Structural Parameters used in the CPD model for biomass materials

Parameter	MW_{c1}	M_δ	p_o	$\sigma + 1$
Cellulose	81	22.67	1.0	3.0
Hardwood hemi-	77.5	21.5	1.0	3.0

cellulose				
Softwood hemi-cellulose	81	22.67	1.0	3.0
Hardwood Lignin	208	39	.71	3.5
Softwood Lignin	186	34	.71	3.5
Kraft Lignin	195	22	.71	3.5

Lignin

Structural parameters for lignin were determined from representative chemical structures and equations. Lignin comprises of a lattice-like structure of coniferyl, coumaryl and sinapyl alcohol base units. These alcohols were considered as the base clusters for lignin, and average MW_{cl}, M_σ, $\sigma + 1$ and p_o were determined.

Initial kinetic parameters for lignin were identified from pervious work. Serio and coworkers(Serio 1997) and Sheng and coworkers (Sheng and Azevedo 2002) both identified values for lignin kinetic parameters, which helped fix ranges for the CPD model.

Black Liquor

Black liquor was looked at as both a combination of Kraft lignin and residual carboxylic acids and as a composite. Kraft lignin was studied theoretically and structural parameters taken from the chemical structures. Although no exact structure of Kraft lignin is available, representative models were used. Dried black liquor samples were sent to the University of Utah and studied using ^{13}C NMR analysis (Solum 2002). Structural parameters were determined for the composite black liquor using CP/MAS and dipolar dephasing techniques previously developed for coal (Solum, Pugmire et al. 1989). A summary of the NMR analysis is listed in Table 4.

The coordination number ($\sigma + 1$) found theoretically for Kraft lignin was 3.5, compared to the value of 4 used by Sricharoenchaikul (Sricharoenchaikul 2001), whereas the NMR analysis yielded a value of 3.6. The value of $p_0 = 0.33$ obtained from the NMR analysis did not seem correct. The percolation threshold for a lattice is defined as $p = 1/\sigma$, which is the point at which the bridges are broken up to the point that no connected lattice exists. The percolation threshold for the value of $\sigma + 1$ measured is therefore 0.38; this indicates that the measured value of p_0 is not feasible. The black liquor sample analyzed was mixed with silica gel in order to permit feeding into various experiments; this may have caused problems with the NMR measurement. In a similar manner, the measured value of M_δ seemed too high, based on comparison with theoretical lignin values.

Table 4 Measured chemical structure parameters for a Kraft black liquor

Symbol	Definition	Value

f_a	aromaticity	0.59
C	# of carbons on a cluster	6
σ+1	# of bridges per cluster	3.6
p_o	Percent intact bridges	0.33
$M_{\square}$	Molecular weight per side chain	60
M_{cl}	Molecular weight per cluster	292

Cellulose

Although cellulose and hemi-cellulose are composed of chains of linked sugars, they lack aromatic rings like lignin and coal. It is expected that during pyrolysis these sugar rings will break and evolve into light gases, and therefore modifications needed to be made to apply the CPD model to these components. Base clusters for cellulose and hemi-cellulose were defined as the fixed anomeric carbon and attached hydrogen. There are three attachments, all intact bridges, one ether bridge and two bridges that comprise the sugar ring with attached side chains. These adjustments produce the expected nearly complete pyrolysis with low tar and high light gas yields. Table 3 shows the structural parameters for hard- and softwood lignin, cellulose, hemi-cellulose, Kraft lignin, as well as the black liquor composite parameters from NMR.

Black Liquor Drop Combustion Experiments

Optimized CPD model calculations are shown in this section for black liquor, lignin, and cellulose. The lignin and cellulose calculations were performed with the eventual objective in mind to build models of any black liquor sample based on the constituent compounds (mainly lignin and hemicellulose). A summary of the kinetic parameters used in the model calculations presented below is given in Table 5 at the end of this section.

Black Liquor Devolatilization Parameters

The value of p_0 determined from the ^{13}C NMR experiments was lower than the percolation threshold, and therefore could not be used. The value of p_0 used in the black liquor predictions was set to 0.71, since values for black liquor should be similar to lignin (see Table 3). For similar reasons, the value of M_δ was set to 0.37, which is the average between the hardwood and softwood lignin in Table 3.

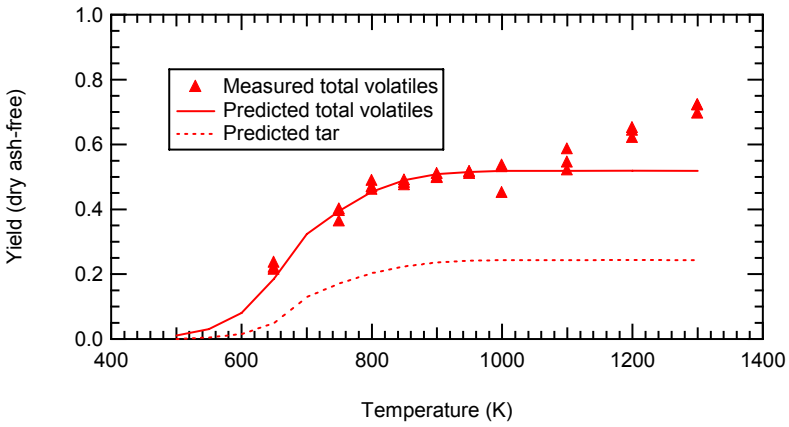

Figure 18 Comparison of CPD model calculations with black liquor pyrolysis data from a furnace. Calculations were performed with a heating rate of 100 K/s and a 10 minute hold time at each final temperature.

The other chemical structure parameters were taken from the NMR analysis. The value of c_0 was left at zero in the absence of tar data. The initial kinetic parameters were set to the values used for coal, and then the value of E_g was changed to fit the black liquor pyrolysis data from the furnace experiments. Model calculations were performed using a heating ramp of 100 K/s followed by a 10 minute hold time. The resulting model calculations are compared with the data in Figure 18. In this figure, all of the data points are shown instead of the average for each temperature. The predicted tar yields are also shown, but no data were available from this experiment.

The model agrees with the total volatile yield data until a temperature of 1050 K, where mineral reactions take place. The following mineral reactions are suggested by Whitty (Whitty 1997).

$$Na_2CO_3 + 2C \rightarrow 2Na + 3CO \quad (1)$$

$$Na_2CO_3 + C \rightarrow 2Na + CO + CO_2 \quad (2)$$

These reactions are not well understood, and must be studied further before incorporation into modeling efforts.

In summary, the results displayed in Figure 18 show that the CPD model can accurately describe black liquor pyrolysis. More data and varying heating rates are required to better validate the model and parameters. Tar data would also help to evaluate this and other models.

Lignin

Sheng and Azevedo (Sheng and Azevedo 2002) used heated grid data from previous MIT experiments (Nunn, Howard et al. 1985) to determine kinetic parameters for lignin pyrolysis. The sample used in the experiments was a milled wood lignin from a sweet gum hardwood (*Liquidambar styraciflua*). Samples were heated at 1000 K/s to the final temperature, followed immediately by cooling at 200 K/s with no hold time at the maximum temperature. The reactor was operated at a pressure of 5 psig. Optimization of CPD parameters for this set of data was

performed using OptdesX. The values of chemical structure parameters and kinetic parameters suggested Sheng and Azevedo (Sheng and Azevedo 2002) were used as initial guesses for this optimization. Initial optimization runs showed that the model was rather insensitive to E_c, and so this parameter was set to zero. However, it was quickly determined that this particular set of data could be fit with many different combinations of parameters. It was then decided to start with the original coal-independent kinetic parameters from the CPD model, which were optimized to match yields based on both temperature and heating rate. For this set of numerical experiments, p_0 was set to be that of lignin (0.71), and M_δ was set to be that of the average between the softwood and hardwood lignin (37).

The kinetic parameters for coal are not adequate for describing the pyrolysis of this type of lignin. In particular, the value of ρ (the ratio of bridge scission to char bridge formation) of 0.9 was too low to permit calculation of the large tar yields reported by Nunn and coworkers (Nunn, Howard et al. 1985). A value of 3.9 was determined to be the optimal value to match this data set. In addition, the activation energy for gas release had to be lowered slightly in order match the temperature at which the gas release occurred.

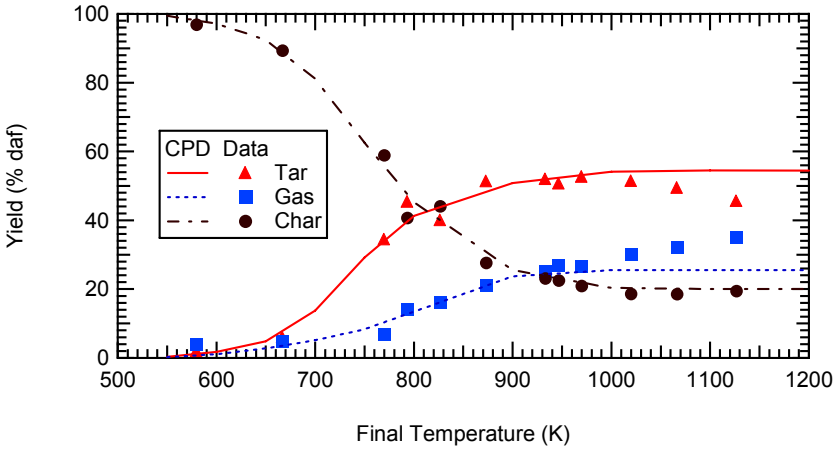

Figure 19 Comparison of predicted and measured tar and light gas yields for lignin. Data are from Nunn, et al. (1985). CPD calculations were made for conditions of 1000 K/s with no hold time and a 200 K/s cooling ramp.

The results in Figure 19 demonstrate that the CPD model is capable of predicting lignin pyrolysis behavior. The data at temperatures above 950 K show secondary reactions of the tar to form more gas, and are not modeled here with the CPD model. However, the model agrees with the char yield at these higher temperatures (which is 100 minus the total volatiles yield). The parameter selection used in the calculations is not considered unique; comparison with additional data sets would greatly improve model evaluation.

Cellulose

Coefficients for the CPD model to describe cellulose pyrolysis were also developed using data from Brown et al. (Brown, Dayton et al. 2001) obtained in a laminar entrained flow reactor (LEFR). The particle temperature histories were taken from some modeling work performed by Brown et al. (Brown, Dayton et al. 2001). Heating rates ranged from 1400 to 3200 K/s,

depending on the temperature. A hold time of 0.3 s was used, with a cooling ramp of 1200 K/s after the hold time to reach a final temperature of 300ºC. The data showed high total volatile yields, reaching 100% near 850 K. The model was fine-tuned through adjustments of the kinetic parameters. The fact that no char remained at high temperatures suggested that the formation of char bridges in the CPD model was an unnecessary step for cellulose. Therefore, the value of □ (the bridge scission to char bridge formation ratio) was set to an artificially high value of 100 to prevent char formation. This high value of ρ had the effect of a large predicted tar yield. However, the molecular weight per cluster in the cellulose was only 80, so this tar yield actually represents gases with molecular weights in the 80 (monomers) to 160 (dimers) amu range. These molecular weights are quite consistent with the mass spectrometry data presented by Brown and coworkers (Brown, Dayton et al. 2001). The value of the activation energy for light gas evolution was also lowered substantially to fit these data. The resulting CPD calculations are shown versus the measured volatile yield data in Figure 5.

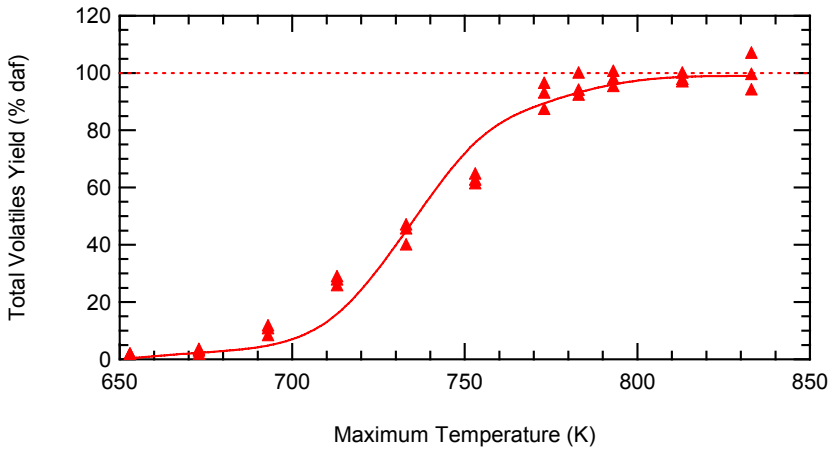

Figure 20 CPD model calculations (solid line) compared with cellulose pyrolysis data (points) of Brown and coworkers (Brown, Dayton et al. 2001; Brown, Dayton et al. 2001). The dashed line represents 100% volatiles.

The coefficients used in the CPD model yielded slightly lower predictions than observed in the experiments at 713 K and slightly higher predictions than observed at 753 K. However, the overall agreement seems reasonable. In fact, the model agreement shown in Figure 5 is better than the models presented in Brown's paper (Brown, Dayton et al. 2001).

It is assumed that hemi-cellulose will behave similarly to cellulose, with only minor changes in the structural parameters. Additional data for both cellulose and hemi-cellulose are needed to test the universality of the CPD with these biomass fuels.

Table 5 shows the kinetic parameters used in the CPD model to match pyrolysis data for coal, black liquor, lignin, and cellulose. The coal parameters were based on extensive comparison with pyrolysis data as a function of coal type, heating rate, temperature, pressure, and residence time. The fact that only one change was made to these parameters to match the black liquor data is very encouraging, but not conclusive until comparisons with additional data. The lignin comparison is interesting because of the very close agreement, but is not totally applicable to the partially reacted lignin thought to be found in black liquor. The cellulose parameters are

interesting for black liquor in that they may be similar to parameters that would describe hemicellulose pyrolysis.

Table 5 CPD Kinetic Parameters for Coal, Black Liquor, Lignin, and Cellulose

Kinetic Parameter	Coal	Black Liquor	Lignin	Cellulose
E_b, kcal/mol	55.4	55.4	54	55.4
A_b, s^{-1}	2.6×10^{15}	2.6×10^{15}	2.6×10^{15}	2.0×10^{17}
σ_b, kcal/mol	1.8	1.8	4.0	1.8
E_g, kcal/mol	69	60	66	42
A_g, s-1	3.0×10^{15}	3.0×10^{15}	3.0×10^{15}	8.23×10^{15}
σ_g, kcal/mol	8.1	8.1	4.8	3.0
ρ	0.9	0.9	3.9	100
E_c, kcal/mol	0	0	0	0
E_{cross}, kcal/mol	65	65	65	65
A_{cross}, s^{-1}	3×10^{15}	3×10^{15}	3×10^{15}	3×10^{15}

Assumptions included in the mathematical model described below include:

- all properties are assumed to be transient and one dimensional;
- local thermal equilibrium exists between the solid and gas phase in the particle, so temperatures and their gradients are the same for the solid and gas;
- gases behave as ideal gases, including both relationships between pressure, temperature, and specific volume and dependence of heat capacity on temperature only;
- particle aspect ratios and shapes do not change during devolatilization – a simplifying assumption for this case but not required by the model in general;

- heat and mass transfer at particle boundaries increase relative to that of a sphere by the ratio of the particle surface to that of a volume-equivalent sphere.

In the particle model, the particle shapes are represented by a parameter n. A spherical particle is described by n = 2, cylinder particle n = 1, and flat plate particle n = 0. Before the biomass particle enters the reactor, it is assumed that it is filled by inert gas. So there are totally seven species are considered in the model: biomass, char, moisture, light gas, tar, water vapor, and inert gas. The mass conservation of each species, the momentum, and the total energy equations are illustrated in equations (1) - (10).

The biomass temporal mass balance contains three consumption terms, one each for the reactions to light gas, tar, and char, where all terms in this expression and most terms in the following expressions are functions of both time and position.

$$\frac{\partial \rho_B}{\partial t} = -(K_1 + K_2 + K_3)\rho_B \qquad 1$$

Similarly, the char temporal mass balance contains two source terms, one from the conversion of biomass to char and one for the char yield from the secondary reactions of tar

$$\frac{\partial \rho_C}{\partial t} = K_3 \rho_B + \varepsilon K_5 \rho_T \qquad 1$$

The temporal moisture mass balance contains a loss associated with conversion to vapor and a source term associated with water vapor readsorption into the particle, the latter having an explicit dependence on gas velocity as suggested by the literature (Bryden and Hagge 2003)

$$\frac{\partial \rho_M}{\partial t} = -K_6 \rho_M + \varepsilon K_7 \rho_g Y_V u \qquad 1$$

The conservation equations for all gas-phase components (light gas, water vapor, tar, and inert gas) include temporal and spatial gradients and source terms and can be written as follows

$$\frac{\partial}{\partial t}\varepsilon \rho_g Y_i + \frac{1}{r^n}\frac{\partial}{\partial r}(r^n \varepsilon \rho_g Y_i U) = \frac{1}{r^n}\frac{\partial}{\partial r}(r^n \varepsilon D_{eff,i} \rho_g \frac{\partial Y_i}{\partial r}) + S_i \qquad 1$$

where $i = T$ for tar, G for light gas, V for water vapor, and I for inert gas and source terms are defined as follows

$$S_T = K_2 \rho_B - \varepsilon K_4 \rho_T - \varepsilon K_5 \rho_T \qquad S_G = K_1 \rho_B + \varepsilon K_4 \rho_T \qquad 1$$
$$S_V = K_6 \rho_M - K_7 \varepsilon \rho_g Y_V u \qquad S_I = 0$$

The total gas-phase continuity equation is defined as the sum of these species and has the form

$$\frac{\partial}{\partial t}\varepsilon\rho_g + \frac{1}{r^n}\frac{\partial}{\partial r}(r^n \varepsilon\rho_g u) = S_g \qquad 1$$

where

$$S_g = K_1\rho_B + K_2\rho_B - \varepsilon K_5\rho_T + K_6\rho_M - \varepsilon K_7\rho_g Y_V u \qquad 1$$

The gas-phase velocity in the particle obeys a Darcy-law-type expression

$$u = -\frac{K}{\mu}\frac{\partial P}{\partial r} \qquad 1$$

where

$$P = \frac{\rho_g R_g T}{M_W} \qquad 1$$

and M_W is the mean molecular weight and the permeability is expressed as a mass-weighted function of the individual solid-phase permeabilities

$$K = {\rho_B}\big/{\rho_{B,0}}\, K_B + \left(1 - {\rho_B}\big/{\rho_{B,0}}\right)K_C \qquad 2$$

Arrhenius expressions describe the temperature dependence of the kinetic rate coefficients for reactions 1-6 illustrated in Figure 16and Figure 17

$$K_i = A_i \exp\left(-{E_i}\big/{RT}\right) \qquad 2$$

The energy conservation equation describes

$$\begin{aligned}&\frac{\partial}{\partial t}\left[\left(\rho_B\hat{H}_B + \rho_C\hat{H}_C + \rho_M\hat{H}_M\right) + \varepsilon\rho_g\left(Y_G\hat{H}_G + Y_I\hat{H}_I + Y_T\hat{H}_T + Y_V\hat{H}_V\right)\right]\\ &+\frac{1}{r^n}\frac{\partial}{\partial r}\left[r^n\varepsilon\rho_g U\left(Y_G\hat{H}_G + Y_T\hat{H}_T + Y_I\hat{H}_I + Y_V\hat{H}_V\right)\right] = \frac{1}{r^n}\frac{\partial}{\partial r}\left(r^n k_{eff}\frac{\partial T}{\partial r}\right)\\ &+\frac{1}{r^n}\frac{\partial}{\partial r}\left[r^n\rho_g\varepsilon\left(D_{eff,T}\frac{\partial Y_T}{\partial r}\hat{H}_T + D_{eff,G}\frac{\partial Y_G}{\partial r}\hat{H}_G + D_{eff,V}\frac{\partial Y_V}{\partial r}\hat{H}_V + D_{eff,I}\frac{\partial Y_I}{\partial r}\hat{H}_I\right)\right]\end{aligned} \qquad 2$$

where

$$\hat{H}_i = \hat{H}_{i,f}^0 + \int_{T_0}^{T} Cp_i dT \qquad 2$$

and subscript *i* represents each of the four gas-phase components as before.

This form of the energy equation relates to standard theoretical analyses (Bird, Stewart et al. 2002) for multi-component systems. In Equation 23, the first term represents the energy accumulation; the second term represents energy convection; the third term (first term after the equals sign) accounts for conduction heat transfer, and the last term accounts for energy associated with diffusion of species in the gas phase,. The last term generally contributes only negligibly to the overall equations and is commonly justifiably ignored.

The effective particle thermal conductivity includes radiative and conductive components with some theoretical basis (Robinson, Buckley et al. 2001; Robinson, Buckley et al. 2001) and with empirical verification for wood (Janse, Westerhout et al. 2000).

$$k_{eff} = k_{cond} + k_{rad} \qquad 2$$

where the particle structure is assumed to be close to the upper limit for thermal conductivity, that is, is assumed to have high connectivity in the direction of conduction,

$$k_{cond} = \varepsilon k_{gas} + (1-\varepsilon)\left(\rho_B / \rho_{B,0} \; k_B + \left(1 - \rho_B / \rho_{B,0} \right) k_C \right) \qquad 2$$

and where radiation contributes approximately to the third power of the temperature

$$k_{rad} = \frac{\varepsilon \sigma T^3 d_{pore}}{\omega} \qquad 2$$

Initial conditions are assumed from experimental conditions for a non-reacting particle. That is, at $t = 0$,

$$\begin{aligned} &P(t=0,r) = P_{atm} \\ &T(t=0,r) = 300\,K\,(typically) \\ &u(t=0,r) = 0 \\ &Y_l(t=0,r) = 1 \\ &Y_T(t=0,r) = Y_V(t=0,r) = Y_G(t=0,r) = 0 \end{aligned} \qquad 2$$

Boundary conditions at the particle center are determined by symmetry, that is, at $r = 0$

$$\left.\frac{\partial P}{\partial r}\right|_{t,r=0} = 0 \Rightarrow u(t, r=0) = 0$$
$$\left.\frac{\partial T}{\partial r}\right|_{t,r=0} = 0 \qquad 2$$
$$\left.\frac{\partial Y_I}{\partial r}\right|_{t,r=0} = 0$$

Boundary conditions at the particle outer surface are defined by external conditions of pressure, heat and mass flux, and

$$P(t, r=r_p) = P_{atm},$$
$$\left.\frac{\partial Y_i}{\partial r}\right|_{r=t,r_p} = 0 \qquad 2$$
$$k_{eff}\left.\frac{\partial T}{\partial r}\right|_{r=t,r_p} = \theta_T h_f R_{SA}\left(T_f - T\right) + R_{SA}\omega\sigma\left(T_w{}^4 - T^4\right)$$

where θ_T represents the blowing factor (Bird, Stewart et al. 2002). R_{SA} represents the exterior surface area ratio, which is the surface area of the particle divided by the characteristic surface area as follows

$$R_{SA} = SA/(4\pi R_P{}^2)$$
$$R_{SA} = SA/(4\pi R_P{}^2 AR) \qquad 3$$
$$R_{SA} = SA/(4R_P{}^2 AR^2)$$

for spheres, cylinders, and flat plates, respectively

Each shape employs heat transfer coefficients developed for that particular shape. Correlations suitable for andom particle orientation during flight appear in the literature for some particles. Where such a model is not available the characteristic length of the particle is calculated using the average length of the particle. For near-spherical particle, Masliyah's prolate spheroid model (Masliyah and Epstein 1972) provides a suitable correlation, as indicated in Equation 31.

$$Nu = 1.05 + 0.6\,\mathrm{Re}^{0.65}\,\mathrm{Pr}^{0.33} \qquad 3$$

Cylinders at low Reynolds numbers adopt the correlation of Kurdyumov (Kurdyumov and Fernandez 1998) (see Equation 32). Expression for W_0 and W_1 appear in detail in the literature (Kurdyumov and Fernandez 1998).

$$Nu = W_0(\mathrm{Re})\mathrm{Pr}^{0.33} + W_1(\mathrm{Re}) \quad 3$$

The heat transfer coefficient of flat plate is shown in Equation 33

$$Nu = 0.644\,\mathrm{Re}^{0.5}\,\mathrm{Pr}^{0.343} \quad 3$$

The kinetic parameters for wood pyrolysis found in literatures vary over a wide range. They are usually measured at low to moderate temperature (usually < 900 K). No high-temperature kinetic data for the two-stage scheme have been reported. Font et al. (Font, Marcilla et al. 1990) presented kinetic data for the three primary reactions that are found to be comparable to what Nunn et al. (Nunn, Howard et al. 1985) reported for the single reaction kinetic data for hardwood in the high-temperature range (573 ~ 1373 K). Font et al.'s results are used in this model. The pre-exponential factors, activation energy, and heat of reactions of all the reactions used in this model appear in Table VI.

Table VI Kinetic parameters of wood pyrolysis process

Reaction no.	frequency factor (s^{-1})	activation energy (kJ/mol)	reference	Heat of reaction kJ/kg	reference
1	1.52×10^{7}	139.2	(Font, Marcilla et al. 1990)	-418	(Chan, Kelbon et al. 1985)
2	5.85×10^{6}	119	(Font, Marcilla et al. 1990)	-418	(Chan, Kelbon et al. 1985)
3	2.98×10^{3}	73.1	(Font, Marcilla et al. 1990)	-418	(Chan, Kelbon et al. 1985)
4	4.28×10^{6}	107.5	(Liden, Berruti et al. 1988)	42	(Koufopanos, Papayannakos et al. 1991)
5	1.0×10^{5}	107.5	(Di Blasi 1993)	42	(Koufopanos, Papayannakos

					et al. 1991)
6	5.13×10^{10}	88	(Bryden and Hagge 2003)	-2,440	(Bryden and Hagge 2003)
7	$T < 95$ ℃ $k_7 = 125cm^{-1}$ $T > 95$ ℃ $k_7 = 0cm^{-1}$		(Bryden and Hagge 2003)	2,440	(Bryden and Hagge 2003)

The physical properties of the biomass particles significantly affect the heat and mass transfer process (Raveendran, Ganesh et al. 1995; Di Blasi 1997). In this work, temperature-dependent heat capacity correlations are used for all species. The heat capacity of biomass and char adopt the model suggested by Merrick (Merrick 1983). Gronli et al. (Gronli and Melaaen 2000) suggested a correlation for tar heat capacity, which is based on some typical pyrolysis tar components (closely related to benzene). All physical properties are listed in Table VII.

Table VII Physical properties of biomass particles

Variable	Value	Reference
Wood density ρ_B	650 kg/m^3	
Porosity ε	0.4	
Emissivity ω	0.75	
Permeability K	$K_B = 0.01$ Darcy	(Gronli and Melaaen 2000)
	$K_C = 10$ Darcy	(Gronli and Melaaen 2000)
Thermal conductivity k	$k_{gas} = 0.026$ W/m.K	(Kansa, Perlee et al. 1977)
	$k_B = 0.11$ W/m.K	(Lee, Chaiken et al. 1976)
	$k_C = 0.071$ W/m.K	(Lee, Chaiken et al. 1976)
Pore size d_{pore}	3.2×10^{-6} m	(Janse, Westerhout et al. 2000)

Molecular weight M	M_T = 145 kg/kmol	(Janse, Westerhout et al. 2000)
	M_G = 31 kg/kmol	(Janse, Westerhout et al. 2000)
	M_I = 28 kg/kmol	
	M_V = 18 kg/kmol	
Viscosity μ	$\mu_{gas} = 3\times10^{-5}$ Pa.s	(Kansa, Perlee et al. 1977)
Diffusivity D_{eff}	$D_{eff} = 1.0\times10^{-6}$ m^2/s for all	(Chan, Kelbon et al. 1985)
Heat capacity Cp (J/kg.K)	$Cp_B := \left(\frac{1000R_g}{7.72}\right)\cdot\left(g\left(\frac{380}{T}\right) + 2\cdot g\left(\frac{1800}{T}\right)\right)$	(Merrick 1983)
	$Cp_C := \left(\frac{1000R_g}{11.3}\right)\cdot\left(g\left(\frac{380}{T}\right) + 2\cdot g\left(\frac{1800}{T}\right)\right)$	(Merrick 1983)
	Where, $g(x) = \frac{x^2 e^x}{(e^x - 1)^2}$	
	$Cp_T = -100+4.4\times T-0.00157\times T^2$	(Gronli and Melaaen 2000)
	$Cp_G = 770+0.629\times T-0.000191\times T^2$	(Gronli and Melaaen 2000)
	$Cp_I = 950+0.188\times T$	(Gronli and Melaaen 2000)
	Cp_M = 4180	
	Cp_V = 2220	

The mass conversion equations of biomass, char, and moister are solved using fourth-order Runge-Kutta method. Control volume (finite volume) [Patankar 1980] method is applied to solve the gas species mass conservation equations and energy conservation equations. A power-law scheme and the SIMPLE algorithm are used to accelerate the convergence of the solution procedure.

Results and Discussions

The wall and gas temperatures measured by type B thermocouples during sawdust pyrolysis experiments appear in Figure 21. Based on these average temperature profiles of reactor and gas,

the mathematical model simulates the devolatilization process of the sawdust particle with the specific shapes described in the sample preparation section. Figure 22 illustrates the mass loss history of the three samples. Both the experimental data and model predictions show that the near-spherical particle losses mass most slowly compared with the other two shapes, while the flake-like particle devolatilizes slightly faster than cylinder-like particle. For each of the three samples, the slope of the model prediction is found to be steeper than that of the experimental data. This can be explained by the fact that an imperfect size and/or shape distribution of the sample may exist, even though the samples are considered to be very uniform after the delicate sample preparation procedure. These variations in shape and size tend to smooth the observed curve of mass loss vs. time as the small particles react faster than the larger particles.

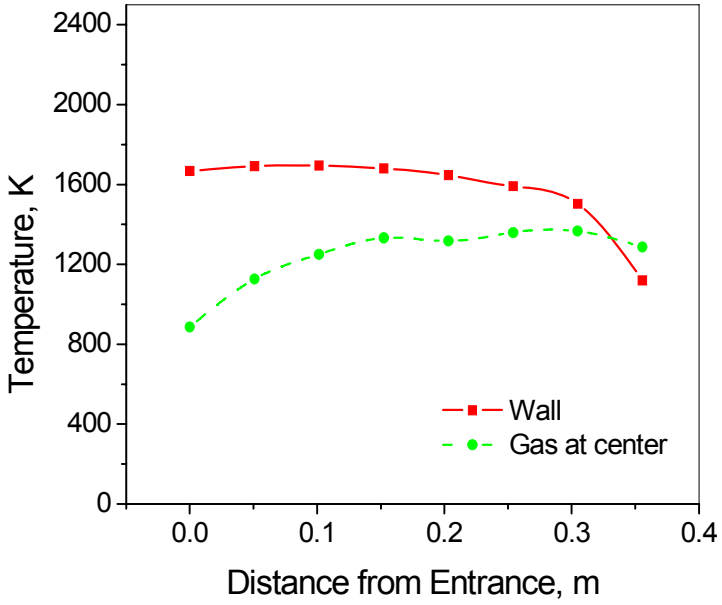

Figure 21 Reactor wall temperature and gas temperature at center

The data and the model agree quantitatively that near-spherical particles react more slowly than do less symmetrical particles. The mass losses differ by as much as a factor of two during most of the particle histories based on both the predictions and the measurements. These data indicate that at these relatively small sizes, asphericity plays a significant role in overall conversion.

The experimental data and model predictions also show that the near-spherical particles yield slightly lower volatiles relative to the other shapes. This is caused by a combination of different particle temperature histories due to the particle shape and longer average path lengths for tars to travel in spherical particles compared to the aspherical counterparts. The flake-like and cylinder-like particles have larger surface area and smaller thickness, which result in a higher heating rate and faster heat and mass transfer to the particle. The predicted surface and center temperatures for the three samples are illustrated in Figure 23. As expected, the near-spherical particle heats up slower than the other two shapes.

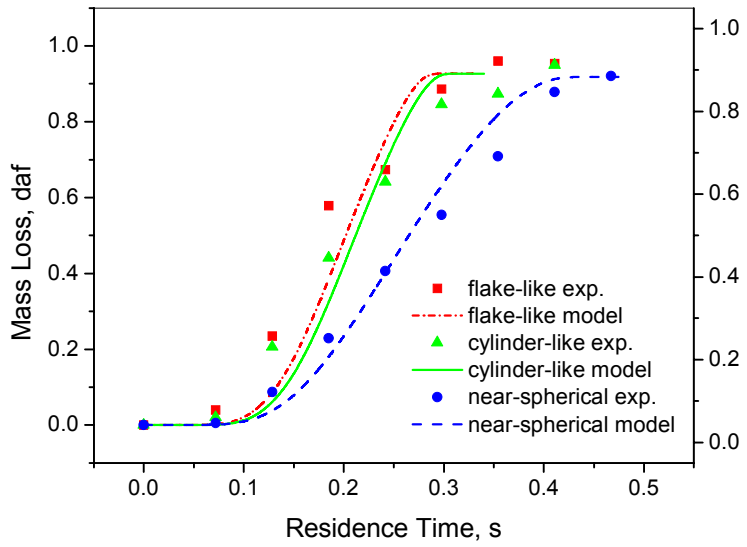

Figure 22 Mass loss histories of sawdust particles with different shapes

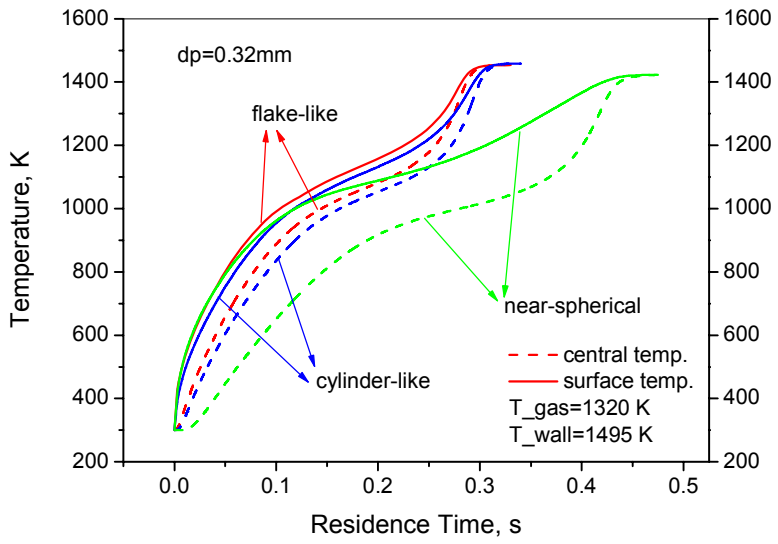

Figure 23 Particle temperature history comparison

The particle size of the samples used in the experiment is limited by the reactor length since it can only provide a maximum residence time of about 0.5 seconds. However, the model developed and validated against the nominal 300 μm particle data can provide estimates for larger particle behavior. Assuming the same aspect ratios for all of the three particles with different shapes, the conversion times predicted as a function of equivalent diameter appear in Figure 24. Pyrolysis conversion time increases with increasing equivalent diameter as would be expected. Additionally, conversion time difference between spherical and aspherical particles

increases with increasing particle size. In addition, the effects of particle shapes and sizes on volatile yields are investigated using the model. As shown in Figure 25, the volatile yield of near-spherical decreases with increasing particle size. Both flake-like and cylinder-like particles behavior similarly.

The effect of particle shape on conversion time and product distribution should be more apparent for large particles than small particles. Large particles that sustain substantial internal temperature and composition gradients transfer heat and mass at rates that scale with surface area. Spheres have the lowest surface area to volume ratio of all shapes and should therefore transfer heat and mass at slower rates than aspherical particles of the same volume/mass. By contrast, particles with little or no internal temperature and compositions gradients transfer mass and heat at rates proportional to total particle volume. These typically small particles are less sensitive to shape than are larger particles of the same material in the same environment. These data and the analyses quantify these theoretical trends and indicate that particles as small as 0.3 mm equivalent diameter experience significant differences in conversion rate. This renders spheres poor choices for many if not most biomass fuels. This concept is similar to but not identical with using a Biot number to determine when internal temperature (and composition) gradients are significant. The Biot number determines when internal temperature (and composition) gradients can be ignored (Bi < 0.1) but does not in itself help determine how to treat the impacts of shape on such gradients when they shouldn't be ignored.

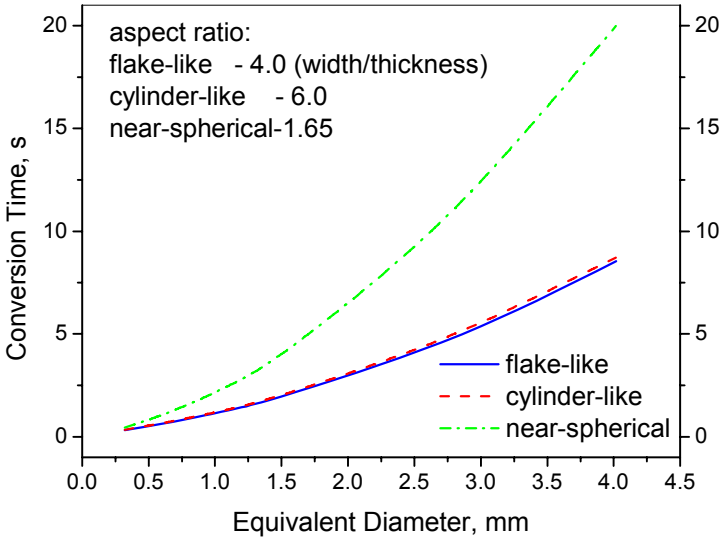

Figure 24 Conversion time vs. particle equivalent diameter

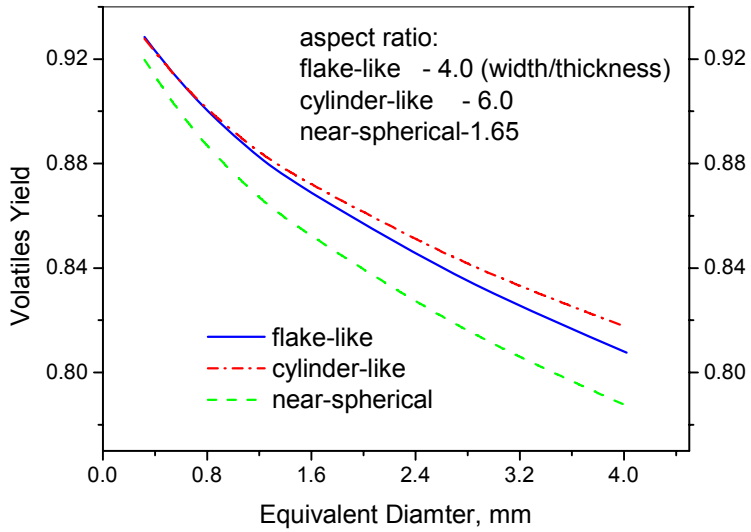

Figure 25 Volatile yields comparison of various particle shape and size

Conclusions

Both experimental and theoretical investigations indicate the impact particle shape and size have on overall particle reactivity. Experiments conducted on biomass particles at relevant temperatures and a variety of well-characterized shapes indicate that particle shape impacts overall reaction rates relative to those of spheres with the same mass/volume by factors of two or more at relatively small sizes. Theoretical models developed and validated against the data indicate that the impact of shape increases with increasing size and is much greater at sizes relevant to black liquor and biomass utilization in the pulp and paper industry. Generally speaking, spherical mathematical approximations for fuels that either originate in or form aspherical shapes during combustion poorly represent combustion behavior when particle size exceeds a few hundred microns. This includes a large fraction of the particles in both biomass and black liquor combustion.

Nomenclature

A_i	pre-exponential factor, s^{-1}
AR	aspect ratio,
Cp	heat capacity, $J.kg^{-1}.K^{-1}$
d_{pore}	pore diameter, m
D_{eff}	effective diffusivity, $m^2.s^{-1}$
E_i	activation energy, $J.mol^{-1}$

h_f	heat transfer coefficient, $W.m^{-1}.K^{-1}$
$\hat{H}$	enthalpy, $J.kg^{-1}$
k	thermal conductivity, $W.m^{-1}.K^{-1}$
K	permeability, m^2
K_i	rate constant, s^{-1}
M	molecular weight, $kg.kmol^{-1}$
M_W	gas average molecular weight, $kg.kmol^{-1}$
n	shape factor
Nu	Nusselt number,
P	pressure, Pa
Pr	Prandtl number
r	radius coordinate, m
Re	Reynolds number
R_g	universal gas constant, $J.mol^{-1}.K^{-1}$
Rp	particle radius, m
R_{SA}	surface area ratio,
t	time, s
SA	surface area
S_i	source term
T	temperature, K
u	gas velocity, $m.s^{-1}$

Y	mass fraction,
Greek symbols	
ε	porosity,
μ	viscosity, Pa.s
ρ	density, $kg.m^{-3}$
σ	Boltzman constant, $W.m^{-2}.K^{-4}$
ω	emissivity,
$-\Delta H$	heat of reaction, $J.kg^{-1}$
Subscript	
0	initial value or reference state
B	biomass
1, …, 7	reaction
C	char
con	conductivity
g	gas phase
G	light gas
I	inert gas
M	moisture
rad	radiation
V	water vapor
T	tar

BLACK LIQUOR REACTIVITY

Abstract

Black liquor is an intermediate product of pulp production. Recovery boilers process black liquor to recover the inorganic material for recycling in the mill and to generate electricity and steam. Black liquor droplet combustion rates and mechanisms dictate many aspects of recovery boiler performance.

This investigation documents new experimental data on single droplet pyrolysis and combustion in a laboratory furnace that mimics many of the essential features of commercial boilers (temperature, composition, droplet size, etc.). These experiments monitored single droplets placed on a thermocouple wire and suspended from a mass balance. Simultaneous video images and pyrometry data provide mass loss and internal temperature data. These investigations provide an extensive data set from which to validate a model and insight into the mechanisms of combustion. Particles burning in air expel small particles from the particle during the entire combustion process, though ejection rates during the late stages of char combustion are higher than during other stages. In addition, char burning begins almost the instant the particles entered the reactor; showing significant overlap with drying and devolatilization.

A transient, 1-dimensional, single-droplet model describes droplet combustion. This model solves the momentum, energy, species continuity, and overall continuity equations using the control volume method. The model uses the power-law scheme for combined advection diffusion, and a fully-implicit scheme for the time steps. It predicts internal velocities, gas and solid temperatures (assumed equal), pressure, and composition. Pressure and velocity equations use Darcy's Law for flow through a porous medium. This model describes the flame region by extending the control volume into the gas phase. Modeling results show the large effect of swelling on all particle properties.

Introduction

During papermaking, a mixture of sodium hydroxide (NaOH), sodium carbonate (Na_2CO_3) and sodium sulfide (Na_2S) at elevated temperatures dissolves lignin in wood chips, releasing insoluble cellulose fibers in a process called digestion. The lignin acts as a binder in the wood to hold the fibers together and constitutes about 30% of the wood mass. Lignin has several detrimental impacts on paper; so after digestion, it is washed from the cellulose fibers. The digester effluent stream containing mostly dissolved lignin-based organic materials and spent alkali salts is called black liquor and is referred to as weak black liquor in the state that it leaves the digester. Evaporators concentrate the weak black liquor to strong liquor with 65-85 % solids content to promote its combustion. The so-called solids refer to the non-water portion of the liquor – they form solids after complete drying of the liquor, but essentially all of these so-called solids are either dissolved or in suspension in the liquor. In the concentrated or strong black liquor, the solids mainly comprise sodium salts and lignin-based organics in solution with some precipitates and impurities as suspended solids and small amounts of potassium, chlorine, silica, and other impurities. These last impurities come from inorganic components and contaminants in the wood and collectively represent the non-process elements. Recent trends increase the solids content of strong black liquor to 80-85% to decrease the possibility of water-smelt explosions and increase the throughput of the recover boiler.

For a paper mill to be profitable and environmentally acceptable, the black liquor must be processed to recycle the valuable and otherwise environmentally aggressive inorganic salts. Separating the salts from the organics and recovering heat from the latter represents the primary role of a recovery boiler – it recovers chemicals and heat. Because of the heat recovered, black liquor is the second largest renewable energy source in the US, after hydropower. The lower section of the recovery boiler provides the reducing environment that reduces the oxidized components of black liquor to active solubilizing agents that eventually return to the digester.

Black liquor impinges on a splash plate as it enters the boiler, forming droplets in the range of 0.5 to 5 mm in diameter. As these droplets pass through the boiler, they undergo different stages of combustion. The stages include drying, devolatilization, char burning, and smelt (molten inorganic matter) formation. Normally some devolatilization and most char burning and smelt formation occur after the droplet has fallen to the bottom of the boiler onto the char bed. A fraction of the droplets become entrained in the combustion gases of the recovery boiler and combust in suspension. These droplets are those that are initially 2 mm or smaller.

Black liquor is unique among major low-grade fuels in amount and composition of inorganic species that it contains. As can be seen from Table 8, black liquor consists of about 20% sodium. About half of this sodium is in the form of inorganic salts, and the other half is in the form of acidic functional groups such as carboxylates and phenolates. During combustion, black liquor generates sodium-containing vapors that, in turn, form submicron-sized inorganic particles or aerosols. These particles, known as fume, contain sodium carbonate (Na_2CO_3), and sodium sulfate (Na_2SO_4) with smaller amounts of sodium chloride (NaCl) and other sodium- and potassium-containing species. Fume formation depends strongly on furnace temperature and furnace oxygen content. Field experiments indicate that the majority of fume forms from entrained black liquor particles while some forms from the sub-stoichiometric char bed or smelt in the bottom of the boiler.

Table 8: Typical Black Liquor Composition

Element	Wt. % of Solids
C	33.8
H	2.90
O	34.8
S	3.80
Na	21.8
K	1.20
Cl	0.20
N	0.10
Other	1.4

The current investigation focuses on the black liquor droplets entrained by flue gases and that burn in suspension in the recovery boiler. As shown later, both the inorganic content of the liquor and the substantial swelling that occurs during combustion dramatically affect these droplets. The investigation includes both experimental and modeling efforts of single particle combustion. Both the experimental data and the model give insight into the combustion process.

Literature Review

This chapter summarizes results from various investigations on topics related to this thesis. It also includes a more critical review of the work done by Le-ong Teng "Elvin" Ip, who previously worked on this project. His work appears in his dissertation, *Comprehensive Black Liquor Droplet Combustion Studies*. His investigations included experimental work on black liquor droplets to obtain data on droplet size, shape, internal and surface temperature, and mass loss during combustion and pyrolysis. A numerical model of black liquor droplet combustion quantitatively predicts similar data, based largely on related work conducted by Hong Lu focusing on biomass particles. During his investigation, Ip also obtained qualitative and quantitative data of intermediate sized particle (ISP) formation. Aside from the investigation of ISP formation, the current thesis improves considerably on the data model pioneered by Ip and Lu.

Droplet Combustion Experiment

Many different techniques characterize black liquor combustion and pyrolysis. The technique of most importance to this work is single particle combustion and pyrolysis. Hupa et al. pioneered this work. They studied black liquor particles by suspending them on a thin platinum wire or on a thermocouple and placing them in a muffle furnace. By placing the black liquor droplet on a thermocouple, they measured the internal droplet temperature during the burn. They also used a video camera to record the burning droplet and measure particle size and burning times. Frederick et al. used a two-color pyrometer to measure the surface temperature of the particle during combustion and pyrolysis. Ip used a similar technique except that his furnace gases were not stagnant. He also incorporated a mass balance to measure particle mass during burning. The main disadvantage to this technique is that the wire on which the droplet rests can significantly impact the heat transfer to the particle.

Molecular Beam Mass Spectrometry

Another technique used in black liquor droplet combustion investigations is molecular beam mass spectrometry (MBMS). An MBMS received its name from the sampling port of the instrument. The sampling port usually consists of a series of two or three nozzles (or skimmers). The inlet orifices to each of these nozzles cause choked flow behavior. The gases expand nearly adiabatically through a shock wave. In well constructed nozzles, this expansion causes significant cooling and decreases internal energy. This cooling rapidly quenches the gases and minimizes reactions. The decrease in internal energy causes the molecules to be more resistant to fragmentation after being ionized. The series of orifices decrease the pressure of the system to the appropriate operating conditions of the mass spectrometer (10^{-5}-10^{-8} Torr). Thus the series of orifices allows near-real-time and essentially *in situ* sampling of combustion or pyrolysis gases into the mass spectrometer. This series of inlet skimmers, if properly aligned, allows condensable species to remain in the gas phase at temperatures well below their condensation temperatures because of the absence of a nucleation surface. Figure 26 shows a diagram of the double skimmer

assembly used by Ip and associates. In this configuration, both skimmers create choked-flow, adiabatic expansion of the gases. If the centerlines of both are aligned, the molecules emitted from the second are all traveling in nominally the same direction at near sonic-velocities and form a beam of molecules, that is, a molecular beam.

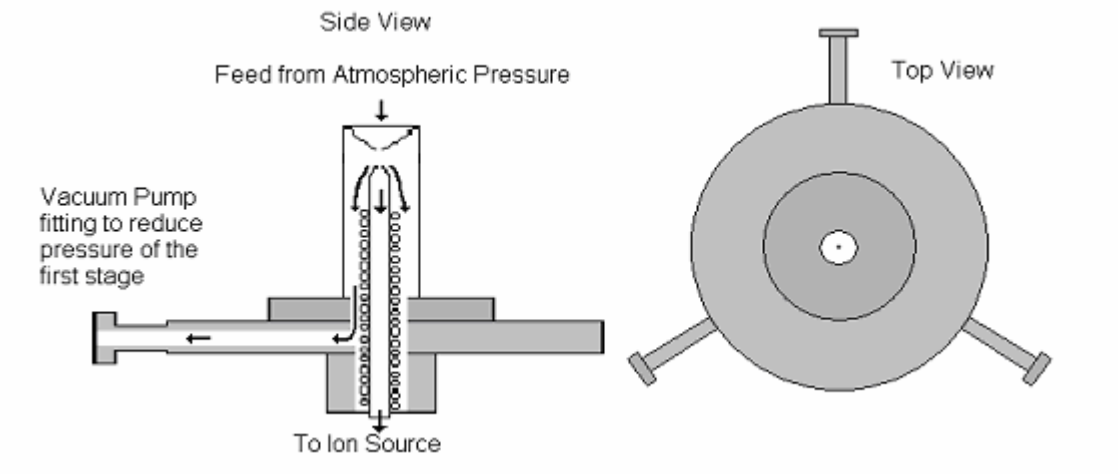

Figure 26: Double Skimmer Assembly Used for MBMS

Ip's group had significantly modified an electro-spray mass spectrometer to meet the requirements of the MBMS. These modifications included changing the electro-spray ion source to an electron impact ion source, rewiring the mass spectrometer for the new source, adding power supplies, cutting and welding a new flange onto the mass spectrometer vacuum chamber, updating the data system, and rebuilding parts of the skimmer assembly. The author was primarily responsible for all of these modifications.

The benefits of using such a mass spectrometer are limited. The mass spectrometer is a semi-quantitative instrument because many factors influence the mass spectra. These include operating pressure, electron energy, quadruple tuning, and the ion source. Electron energy affects ionization efficiency and ion fragmentation. In tuning the quadrupole, trade-offs between signal intensity and spectral resolution force some compromises in each. These variables make it difficult to get absolute species concentration from the mass spectrometer, requiring difficult calibrations of the mass spectrometer at the conditions used in the experiments. However, a mass spectrometer can measure relative change in species concentration versus time easily and accurately.

Swelling During Drying and Devolatilization

Black liquor dramatically swells during drying and devolatilization. The gases created upon heating the black liquor create bubbles that expand or inflate the particle. This swelling drastically impacts particle heating rates, drag/trajectory, mass transfer, and reaction rates. Various investigations indicate what variables impact the extent of droplet swelling. The most important of these variables is reportedly the lignin to carbohydrate ratio. Black liquor experiences maximum swelling around a ratio of 50/50. Black liquor swelling decreases

irreversibly when its pH decreases by adding acid. Wintoku et al. proposed a swelling model based on first principles, yet their model was not consistent with data.

Flame Region Surrounding a Droplet

Many different flame models have been derived from mass and energy balances assuming complete or partial combustion, usually infinite kinetics, and constant or average diffusivities in the flame layer. These assumptions allow computation of heat and mass fluxes from the devolatilizing particle. When implementing this type of model, one must assume whether the flame is present or not. Verrill et al. assumed that a flame was present when the Reynolds number was less than one. Järvinen's model uses a flame model when the Damkohler number exceeds three.

Bryden used a different approach to solving the flame layer problem. The domain of the control volume extends into the gas phase, including a stagnant film boundary layer. In the outer-most shell, the concentrations of the gas species and the temperature equal the bulk gas conditions. In this approach, the flame reaction kinetics and mass transfer clearly indicate—from the high temperature and decreased oxygen content in the film layer—whether a flame is present or not. One of the major variables in this approach is the film thickness, or the distance from the droplet surface to the bulk gas. Mass and heat transfer decrease with increasing film layer thickness. Bryden did not explain how he determined the boundary layer thickness.

Inorganic Chemistry

Inorganic species play an important role during black liquor combustion. They aid in char conversion, capture gas-phase sulfur species, and ultimately account for much of the fouling in a recovery boiler. Inorganic species are the major component of fume and intermediate sized particle (ISP), which conglomerate and ultimately account for the deposit formation in a boiler, which depends strongly on furnace temperature and oxygen content. Black liquor is typically about 20% sodium and 1% potassium. Although most investigations have concentrated on sodium species, it is generally assumed that potassium species follow the same mechanisms as their sodium equivalents. Furthermore, combinations of sodium and potassium or of chlorides and sulfates form eutectics and other solutions that impact both deposition rates and deposit properties. Of the inorganic species, sulfates and carbonates form the largest fractions. Included with Equations (0-1) and (0-2) are the molar heat of reaction, $\Delta\tilde{H}_{rxn}$, and the molar Gibb's energy of reaction $\Delta\tilde{G}_{rxn}$ for reference.

$$Na_2S + 2O_2 \rightarrow Na_2SO_4 \qquad \Delta\tilde{H}_{rxn,25\,°C} = -1020\frac{kJ}{mol}$$
$$\Delta\tilde{G}_{rxn,1000\,°C} = -886\frac{kJ}{mol} \quad \Delta\tilde{H}_{rxn,1000\,°C} = -982\frac{kJ}{mol} \qquad (0\text{-}1)$$

$$\frac{(2-f)}{2} Na_2SO_4 + 2C_f \rightarrow \frac{2-f}{2} Na_2S + 2 \cdot f \cdot CO + 2 \cdot (1-f) \cdot CO_2$$

$$where \quad 0 \le f \le 1.0 \qquad \Delta\tilde{H}_{rxn,25\,^\circ C} = 200 \frac{kJ}{mol} \qquad (0\text{-}2)$$

$$\Delta\tilde{G}_{rxn,1000\,^\circ C} = -270 \frac{kJ}{mol} \quad \Delta\tilde{H}_{rxn,1000\,^\circ C} = 161 \frac{kJ}{mol}$$

Sulfur Containing Inorganic Species

Black liquor typically contains about 4% sulfur. Of this sulfur, initially about 40% is sulfate, 35% is thiosulfate, and 25% is organic sulfur. Thiosulfate decomposes almost immediately upon heating and thus is not an active participator during the rest of the combustion process. The organic sulfur forms H_2S and COS, but can be recaptured through reactions with different fume species. Sulfate acts as a carbon conversion catalyst through a mechanism referred to as the sulfide/sulfate cycle (Reactions (0-1) and (0-2)). These reactions are extremely important in the char bed where simultaneous sulfate reduction and carbon oxidation are essential. In a reducing environment sulfide is more thermodynamically stable than sulfate; however, in an oxidizing environment the opposite is true.

Carbonates

In an investigation on fume formation, Li and van Heiningen studied the decomposition of sodium carbonate in black liquor under different environments. They observed that carbon reduces carbonate and that this process releases sodium vapor, Reaction (0-3). They were able to obtain a kinetic rate expression in a nitrogen environment. They observed that both CO and CO_2 suppress sodium carbonate decomposition, but did not acquire reaction kinetics for the decomposition reaction when these species are present. Gairns et al. found that sodium carbonate decomposition increased sharply between 800-900 ºC, but disappeared entirely by introducing 15% CO_2 at 900 ºC. In addition to sodium release due to sodium carbonate decomposition, Frederick and Hupa found that between 23-35% of the sodium is released during pyrolysis. Others later proposed that this sodium release is due to small particles being ejected from the droplets.

$$Na_2CO_3 + 2 \cdot C \rightarrow 2 \cdot Na + 3 \cdot CO \qquad \Delta\tilde{H}_{rxn,25\,^\circ C} = 1240 \frac{kJ}{mol} \qquad (0\text{-}3)$$

$$\Delta\tilde{G}_{rxn,1000\,^\circ C} = 239 \frac{kJ}{mol} \qquad \Delta\tilde{H}_{rxn,1000\,^\circ C} = 1130 \frac{kJ}{mol}$$

Motivation

The current investigation builds upon the work of the research mentioned previously in this chapter. This investigation incorporates both modeling techniques as well as single droplet experiments to understand the mechanisms of black liquor droplet combustion. This document outlines two types of single droplet experiments. These experiments utilize techniques similar to those developed previously, including work with a molecular beam mass spectrometer, using

thermocouples to measure internal droplet temperature during combustion, and a pyrometry technique to measure surface temperature. In addition to these techniques, this project developed new techniques for surface temperature measurement, mass measurement, and data synchronization.

The model developed during this investigation incorporates various sub-models to account for the phenomena explained in this chapter. This document explains how the model quantifies swelling of black liquor, the sulfate/sulfide cycle, carbonate decomposition, and the presence of a flame. By using both experiments and modeling, this investigation reveals some of the important mechanism of black liquor combustion.

Research Objectives

Original Status of Project

Because some of the objectives of this project represent a continuation of the works of Ip and Lu in previous projects, this section explains the status at the end of the previous project.

Experiment Synchronization and Improvement

The PACE XR440 Pocket Logger used for recording temperature has a problematic synchronization mechanism, resulting in time stamps that are off by 2-4 seconds. This required a new synchronization method. Previously, the camera software did not supply a time stamp for the images; so camera data could not be synchronized accurately with the rest of the data. Convective forces and the movement of the balance resulted in poor balance measurements and required the development of improved experimental procedures. Large amounts of data from each run required the development of a macro to open the data files, manipulate the data to put it in user-friendly form, compile the data into one comprehensive spreadsheet, and graph the data.

Experimental Data

Prior to this thesis work, simultaneous data were collected for a single droplet experiment; however due to the problems stated in the previous section, the data could not be synchronized accurately. Previous experiments may have also lacked furnace characterization, such as accurate flow rate and furnace wall temperature estimations. These parameters are essential to compare model predictions with the experimental data. In the current thesis, a task includes collecting simultaneous mass, internal and surface temperatures, and size data for 3 different liquors at temperatures between 650 and 800 ºC.

Single Particle Model

Lu, with some help from Ip, developed a particle combustion model for biomass combustion. However, various assumptions needed to be relaxed to predict black liquor droplet combustion accurately. First, because black liquor experiences significant swelling, a swelling model needed to be added. While many experiments characterize the extent of particle swelling (volumes increase by more than 100 times in many cases), no consistent, theoretical, quantitative predictive techniques exist to characterize this behavior. Most of the swelling models include only correlations of swelling as a function of mass loss or of volatile loss. Second, up to the beginning of this project there was no model to account for the flame that surrounds the particle. Experimental observations indicate there is typically a flame present during parts of devolatilization and char burning. Third, inorganic chemistry and transport become important during black liquor combustion, as explained below. Others have developed inorganic reaction mechanisms and kinetic parameters that needed to be included in the model. This inorganic model would facilitate the prediction of fume formation, which is essential in corrosion and deposition calculations. Fourth, during devolatilization black liquor produces much more char than does biomass. Previously, biomass parameters described black liquor devolatilization. In addition, other properties such as particle porosity, emissivity, and internal surface area and mechanisms such as drying needed to be implemented or updated to describe black liquor better.

Tuning and Adjusting the MBMS Mass Spectrometer

Prior to the work in this thesis, the mass spectrometer was not capable of detecting inorganic species. Further work needed to be performed to troubleshoot the MBMS and better tune the instrument.

Objectives of Current Investigation

The ultimate goal of this research is to understand more fully the combustion characteristics of single black liquor particles. To achieve this goal, the project includes both experimental and modeling efforts. The following three goals describe the objective in more detail:

Digitally synchronize simultaneous collection of internal temperature, video, and mass measurement data, improve experimental procedures, and build a macro that will handle the data manipulation to provide reasonably comprehensive and comparable experimental documentation of particle reaction histories.

Collect comprehensive experimental data with sufficient accuracy and detail that they provide discriminating model validation, that is, are sufficiently accurate to indicate successes and failures of model predictions within their uncertainties.

Develop an existing combustion model to include inorganic species, particle swelling, and a flame model.

Some experimental techniques such as the color-band method and MBMS on suspended black-liquor droplets are new to the field. In addition, some aspects of the data such as simultaneous mass loss, particle shape, and temperature data for suspended droplets, represent new techniques. The combination of data from these experiments contributes significant new information to the current database and understanding of black liquor droplet combustion.

Experimental Approach

The experimental portion of this project involved substantial experimental design and trouble shooting. Experimental facilities used in this project include purchased equipment (cameras, temperature data logger, temperature controllers, and relays), newly designed and constructed equipment (single-particle furnace), rebuilt equipment, the last category including an MBMS built from portions of an abandoned, non-molecular-beam mass spectrometer and a spare detector. This chapter summarizes the experimental methods and the features of the equipment used in the project.

Experimental Materials and Methods

Five liquors formed the suite of fuels used in this project. Their compositions are indicated in Table 9. These liquor samples were all from industrial paper mills.

The first two liquors, A and B, are softwood liquors and come from a mill in the Northwest United States. Liquor A came with very high solids-content (>95%), and Liquor B came with about 50% solids. The other three liquors, C, D, and E, were softwood/hardwood mixed liquors and came from different mills. Liquor C came with 55% solids, Liquor D came with about 70% solids, and Liquor E came with 77% solids. All liquors were concentrated to at least 70% solids content prior to use. Two types of experiments comprise the experimental portion of in this project: droplet combustion experiments and MBMS experiments. In the droplet experiments, drying increased the black liquors B and C to about 70% solids content while the other liquors remained at the concentrations shown in Table 9.

Table 9: Compositions of Black Liquors Used in the Project

Elements	Black Liquor				
	A	B	C	D	E
C	35.6	36.0	39.3	38.6	37.5
H	3.34	3.48	3.64	3.52	3.63
O (by difference)	36.6	33.3	33.5	35.6	35.0
S	4.06	3.49	2.69	3.47	3.92
Na	18.8	22.0	18.4	17.38	18.23
K	1.50	1.26	2.2	0.87	1.39
Cl	0.10	0.55	0.22	0.53	0.36
Initial %Solids	95	50	55	70	77

	Softwood	Softwood/hardwood

Droplet Combustion Experiment

The first type of experiment was a droplet combustion experiment. The equipment used in this experiment includes a furnace built at BYU (Figure 27), three SVS Vistek CCD cameras, a Pace Scientific XR440 Pocket Logger and associated thermocouple (for internal temperature measurement), a Scientech SA 310 mass balance, and a Thermolyne 21100 tube furnace (used to preheat the gas). The furnace is equipped with six view ports oriented in three orthogonal directions. These view ports are for video and pyrometry imaging. They are all viewed in the same plane in the figure to better illustrate the furnace construction, but in fact the axis of the horizontal port is perpendicular to the page.

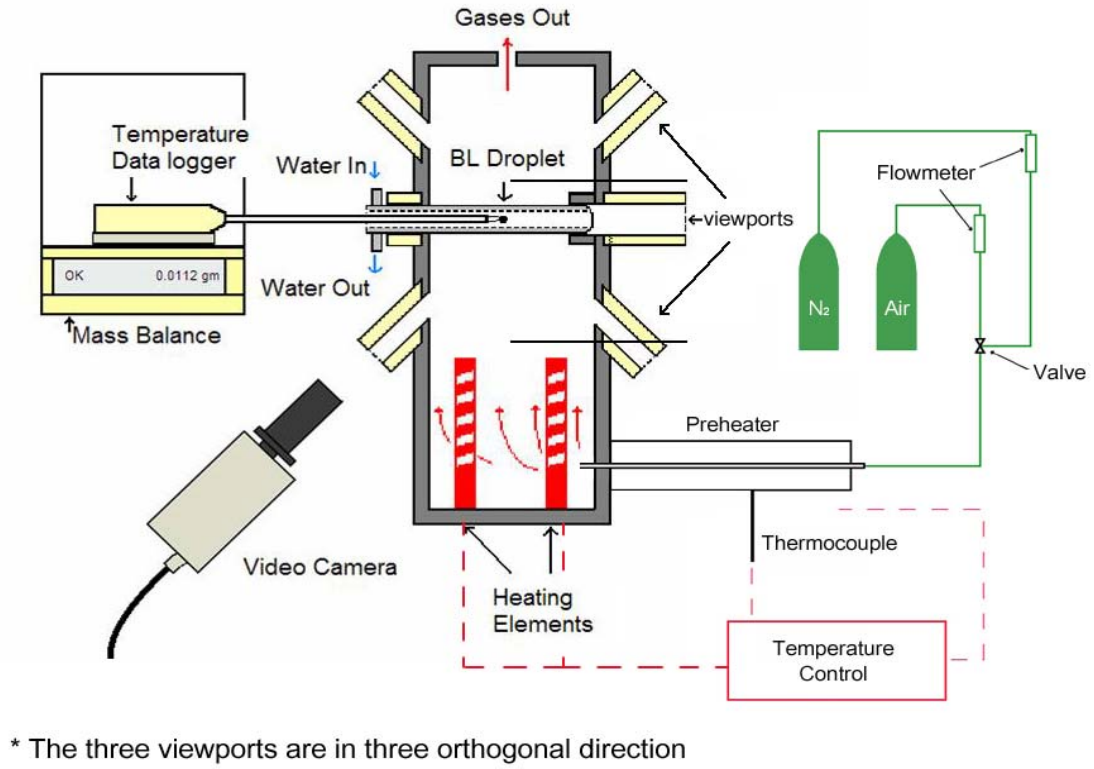

Figure 27: Setup for the Droplet Combustion Experiment

Four silicon carbide electrical resistance-heating elements from Kanthal Globar positioned at the bottom of the furnace heat the furnace. A K-type thermocouple provides feedback to a Watlow 5-10 V controller and two Continental solid-state relays to control the 110 V potential to heating elements. The system includes a water-cooled jacket that slides into the middle of the furnace to provide a shielded environment for the particles during setup. Two rotameters control the gas flow to the furnace, one manufactured by Cole Palmer and the other by Dwyer. A mass flow

meter calibrates both. The cameras, the mass balance and the pocket logger connect to a single computer for synchronization purposes. More detailed descriptions of the furnace, the mass balance, and the cooling jacket, as well as a novel technique of using video imaging from a single camera for pyrometry measurement, appear in Ip's dissertation.

During each experiment, a 1.5 – 4 mm black liquor droplet suspended on a thermocouple burned in the furnace. Simultaneous collection of so many parameters complicates the experimental procedures and makes each experiment somewhat tedious, but the procedures provide unique and comprehensive data. The temperature measurement recorder did not connect directly to the computer (by design), and its synchronization with the remaining data appears in Section 0.

Typical experiments proceeded as follows: A weighed droplet was placed on an approximately 0.01 inch diameter type K thermocouple. The thermocouple was attached to the temperature logger and positioned in the balance. The thermocouple-droplet assembly rolled toward the furnace until the droplet reached the center of the furnace, inside the water-cooled jacket. After the mass balance oscillations stopped, mass measurement and camera measurement were initialized, and the cooling jacket was pulled from the furnace.

With the cooling jacket removed, the droplet almost immediately experiences the hot gases of the furnace. The droplet then dries, and either pyrolyzes in an inert environment or devolatilizes and oxidizes in an oxidizing environment. Experiments include runs in either air or nitrogen environments. During each experiment, the data logger records temperature at a rate of 20 Hz, the mass balance recorded mass at 18-19 Hz, and the camera's images were stored at about 15 Hz.

After the droplet finishes reacting, the particle is removed and the mass and internal temperature data are compiled onto a single spreadsheet. From the images, the particle's horizontal and vertical lengths are measured by counting the pixels from one side of the particle to the other. The absolute lengths are found by using the known view point tube diameter as a reference. Because the droplet is located midway between the two view point tubes, the scaling factor for the droplet is simply the average of scaling factors calculated for the two view point tubes. This paper will report geometric mean diameter, which is the square root of the product of the horizontal and vertical lengths of the particle. The surface temperature measurements come from two points on the particle surface. At the beginning of a run, these data may be far from representative or random, because the pyrometry technique only measures in the high temperature range. Both surface temperature and size data were recorded at 0.5 Hz.

Synchronization Method

As mentioned previously, the Pocket Logger used to collect temperature data inaccurately records time in terms of both initial time and time increments. Corrections to these errors enable accurate synchronization of thermocouple temperature measurements with video, mass loss, and related data from the computer. Before each experimental run, the Pocket Logger was initialized and a thermocouple was attached to it. The signal from this thermocouple was split between the Pocket Logger and a National Instruments computer board controlled by a LABVIEW program. The LABVIEW program then records the temperature of the thermocouple and a corresponding time stamp from the computer. A flame is then placed under the thermocouple and removed. This temperature spike provides sufficient information to compare the data from the National

Instruments board and the Pocket Logger. The thermocouple reported only to the pocket logger during the remaining experiment, with computer leads disconnected to avoid biasing weight measurements.

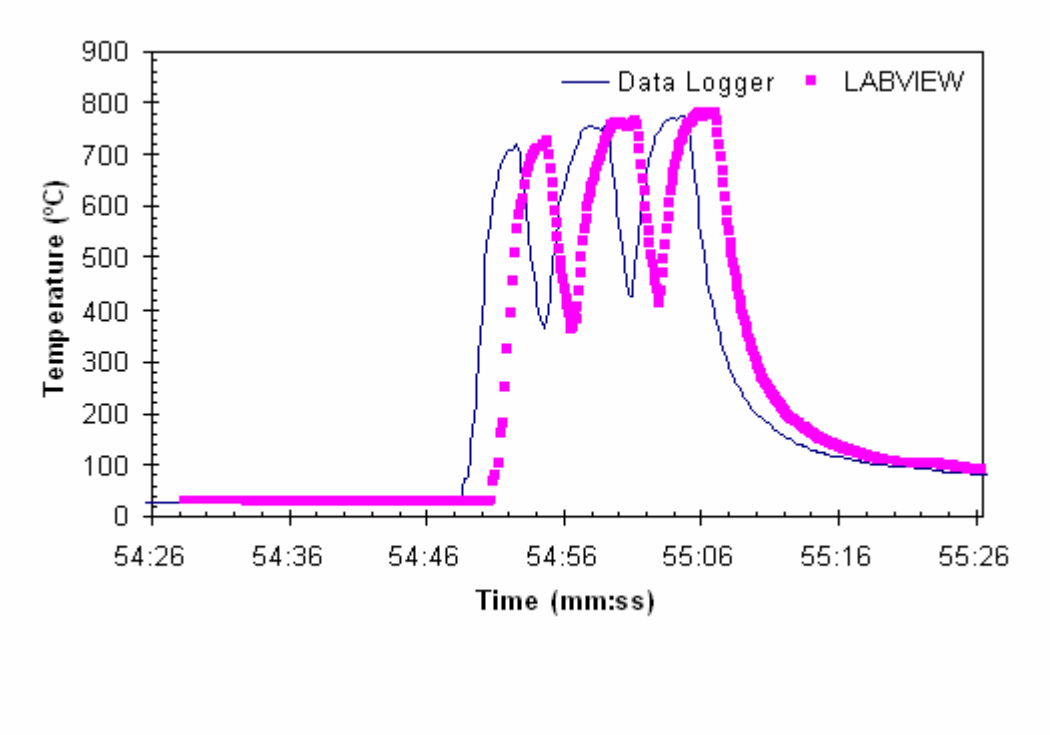

Figure 28: Comparison of LABVIEW and Pocket Logger Time Stamp

In comparing the two images, a time correction can be given to the Pocket Logger data (Figure 28). In the particular case of Figure 28, 2.2 seconds is added to the Pocket Logger time stamp. The second problem comes from the time mechanism in the Pocket Logger. It is as if the Pocket Logger's clock is slightly slower than a standard clock. Figure 29 shows how this slowly skews the data to the right of the LABVIEW data. A simple equation corrects the Pocket Logger for both of these problems. Where t is the actual time, t_{TS} is the time stamp, $t_{TS,0}$ is the Pocket Logger's initial time stamp, γ is the first correction factor, and t_{cor} is the second correction factor.

$$t = t_{TS,0} + (t_{TS} - t_{TS,0}) \cdot \gamma + t_{cor} \qquad (0\text{-}4)$$

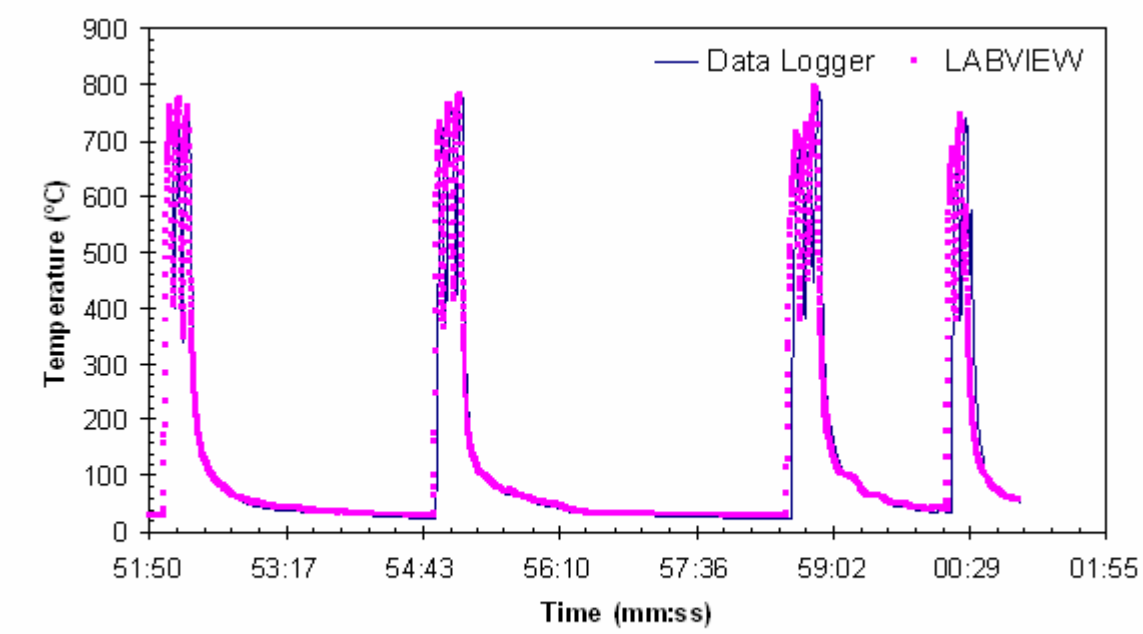

Figure 29: LABVIEW and Pocket Logger Time Stamp Comparison

Optical Pyrometer and Color-Band Method

The Color-Band Method for optical pyrometry was developed by Lu and Ip, and a detailed explanation of this method is given by Ip. Typically, a CCD camera uses four types of sensors: one that is sensitive to blue, one that is sensitive red, and two that are sensitive to green. Lu and Ip developed Equation (0-5), which describes how the camera's pixel value, *DN*, relates to the temperature based on a few simplifying assumptions, where *DN* is the digital number describing the intensity of one color of light. The sensitivity of each type of sensor can be described as a function of wavelength by a function called the spectral responsivity, $S(\lambda)$. The emissive power per unit wavelength, $E(\lambda,T)$, of an object is described by Plank's Law, where $E(\lambda,T)$ is the product of the surface emissivity and the blackbody radiation per steradian. The pixel value is the integral of the product of $E(\lambda,T)$ and $S(\lambda)$ times the lens and camera setting factors, Equation (0-5). In Equation (0-5), τ is the lens transmission factor, D is the lens diameter, d is the distance between the object and the sensor, a is the pixel area, X is the magnification, and Δt is the camera exposure time. The technique takes advantage of multiple color bands to simplify the measurement. By taking the ratio of the pixel values for different color sensors, the lens and camera setting factors cancel in the equation, Equation (0-6).

$$DN = \tau \frac{\pi}{4} \frac{D^2}{d^2} \frac{a^2}{X} \Delta t \int_{\lambda_1}^{\lambda_2} S(\lambda) E(\lambda, T) d\lambda$$

$$\text{where} \quad E(\lambda, T) = \varepsilon \frac{c_1 \lambda^{-5}}{e^{c_2 / \lambda T} - 1} \qquad \text{(0-5)}$$

$$\frac{DN_G}{DN_R} = \frac{\int_{\lambda_1}^{\lambda_2} S_G(\lambda) E(\lambda, T) d\lambda}{\int_{\lambda_1}^{\lambda_2} S_R(\lambda) E(\lambda, T) d\lambda} \qquad \text{(0-6)}$$

The main advantages of this technique include accuracy, relatively high signal to noise ratios because of the integrations, inexpensive equipment, and simple implementation. One of the major drawbacks for combustion application is that flames that surround an object interfere with the temperature measurement. However, this is not unique to color-band pyrometry. Two- and single-color pyrometries also may not penetrate the flame layer obtain a surface temperature.

Balance Response

Because the balance does not respond instantaneously to changes in weight, a simple investigation determines the representative response time for a change in mass. A small jar was placed on the balance, and the camera focused on the jar. A medicine dropper dripped water into the jar one drop at a time. A single computer recorded both the mass measurement and the video. The camera's time stamp recorded the instant that the droplet touched the bottom of the jar to within ±0.08 seconds. Figure 30 shows that the balance does not respond at all to a step change for approximately 0.75 seconds. The balance then takes an additional 0.65 seconds to reach its steady value. The average total response time for six runs was 1.3 seconds. This investigation reveals two important characteristics of the mass measurement, first that the changes that occur within a 1.3 second interval cannot be resolved. Secondly, a time delay will be seen in all measurements. To correct for the second characteristic, a 1.3 second adjustment was made to all mass measurements.

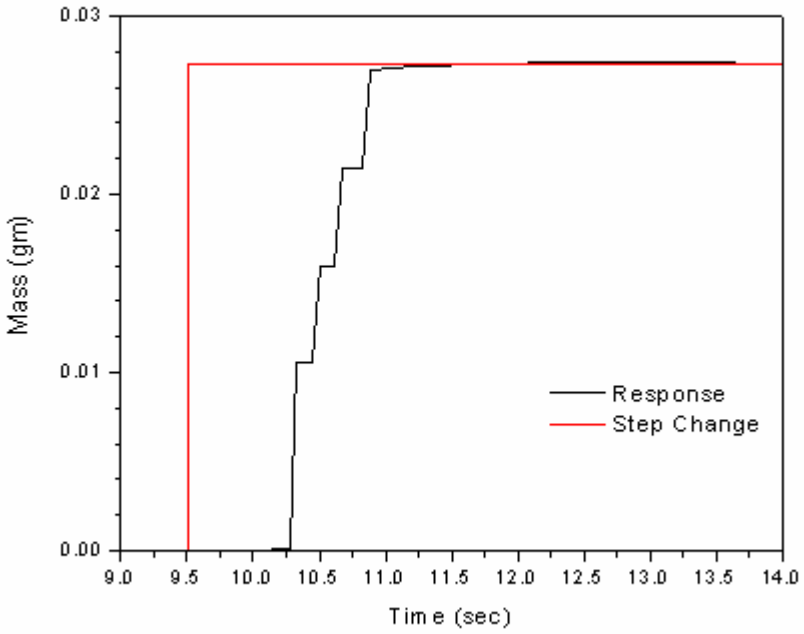

Figure 30: Balance Response to Step Change

Results and Discussion: Droplet Combustion

This chapter discusses the experimental results of the single droplet combustion experiments. Experiments yielded insight into interactions between droplet swelling, mass loss, and temperature changes. Observations also show mechanisms that will be important in modeling, especially a surface char "regeneration" mechanism.

Simultaneous Mass Loss, Size, Internal and Surface Temperature

The experimental data collected offer many insights into the combustion behavior of black liquor.

Figure 31 shows the results from a 45-mg black liquor A droplet in 750 ºC air. The droplet's size changes significantly during the combustion process. The droplet's radius increases rapidly during drying and especially devolatilization. Afterwards, the droplet shrinks as the char burns out.

The thermocouple temperature curve shown by pink squares ascends quickly at first, up to a plateau at about 130 ºC. Water evaporation from this salt-saturated fuel leads to this plateau. After the water evaporates from the droplet, the temperature again increases. Initially the temperature increases slowly; the gases that are evolved during devolatilization decrease the heat transfer to the particle. Also, local gas evolution in the particle decreases heat transfer locally. Once devolatilization is complete, the temperature increase is more rapid due to the combined effects of no gas evolution, smaller mass and larger surface area. The center temperature increases to a maximum near the end of char burning. This maximum temperature measured by

the thermocouple usually corresponds closely with the time that the smelt bead collapses onto the thermocouple. The temperature then drops slowly to a steady-state temperature in the furnace somewhere between the local gas and furnace wall temperatures. This temperature decrease is slow for two reasons. First, by this point the particle has shrunk to its smallest volume, thus the smallest surface area. Second, exothermic sulfide oxidation reactions continue after char burning, further slowing the temperature change.

Similar mechanisms affect the mass loss. Mass loss during drying is slower than during devolatilization. Devolatilization causes the most rapid mass loss. Char burning, associated with a slower mass loss, follows devolatilization. The surface temperature measurements, as explained in Section 0, are picked at two nonrandom points. The cameras can only accurately determine high temperatures (> 600 K). This means that during the early stages of combustion, the reported temperatures are biased towards the maximum temperatures found on the surface. The temperature measurements tend to show that although there is a large variance in the surface temperature, the maximum surface temperature tends to stay nearly constant throughout most of the combustion process. As a disclaimer, some of the reported surface temperatures are a couple hundred degrees above the average surface temperatures. These temperature measurements may have been affected by flame interference.

Another phenomenon revealed by the surface temperature measurement is the beginning of char burning on the surface. As shown in

Figure 31, for a very dry black liquor droplet (95% solids), surface char burning starts while the internal temperature of the particle is still near the boiling point of water. This creates very large temperature gradients inside the droplet of at least 280 ºC/mm. The surface temperature measurement is always higher that that of the thermocouple-measured internal temperature, even as the droplet reaches a pseudo-steady combustion regime. This is likely due to the thermocouple leads being cooled by the ambient gases. Because the thermocouple leads are exposed to the surrounding gas, the leads conduct heat away from the thermocouple bead, decreasing the temperature measurement.

After the initial shrinking of the particle, the particles shown in

Figure 31 and Figure 32 swell again. This secondary swelling may indicate that there is residual char or black liquor solid material leftover when the smelt collapses onto it. The smelt reactions with the residual then cause vapors to be released, expanding the particle once again.

Figure 32 and Figure 33 show similar trends to those described above. The droplet in Figure 33 has a higher moisture content (70% solids). This leads to a later initial char burning time compared with the droplet of Figure 32. The droplet in Figure 32 started char burning after only about 1 ½ seconds. There was an interesting mass increase at the char burning shown in Figure 32. Although this may only be a result of turbulence around the particle, it raises the question of how much mass increase might result from sulfide oxidation during smelt oxidation. It is likely that the mass of the particle increases during smelt oxidation.

A summary of some of the main combustion characteristics are summarized for six runs in Table 10. The reported times for drying, devolatilization, and total combustion time are ballpark estimates since there was significant overlap of the stages of combustion for each of the runs.

Table 10: Experimental Runs

Characteristics		Liquor Type					
		D	A	A	E	D	E
Solids Content	(%)	70	95	95	70	70	70
Initial Mass	mg	59.3	44.8	23.2	27.9	41.9	26.6
Particle Volume	10^{-8} m^3	4.09	2.78	1.44	1.92	2.89	1.83
Velocity	m/s	0.217	0.35	0.367	0.217	0.32	0.32
Max TC Temperature	(ºC)	926	1063	1001	939	935	971
Gas Temperature	(ºC)	715	750	800	710	662	650
Maximum Swelling	(r/r_{ini})	2.52	2.81	2.55	3.32	3.8	2.68
Drying Time	(s)	7	5	3	3*	7	6
Devolatilization Time	(s)	17	13-15	7-9	7-11	10-16	10
Total Combustion Time	(s)	22	21	13-15	15	21	16

TC is thermocouple. *Thermocouple may have come out of droplet

Figure 31: 44.8 mg Droplet of Black Liquor A in 750 ºC Air, Gas Velocity=0.35 m/s, 95% Solids

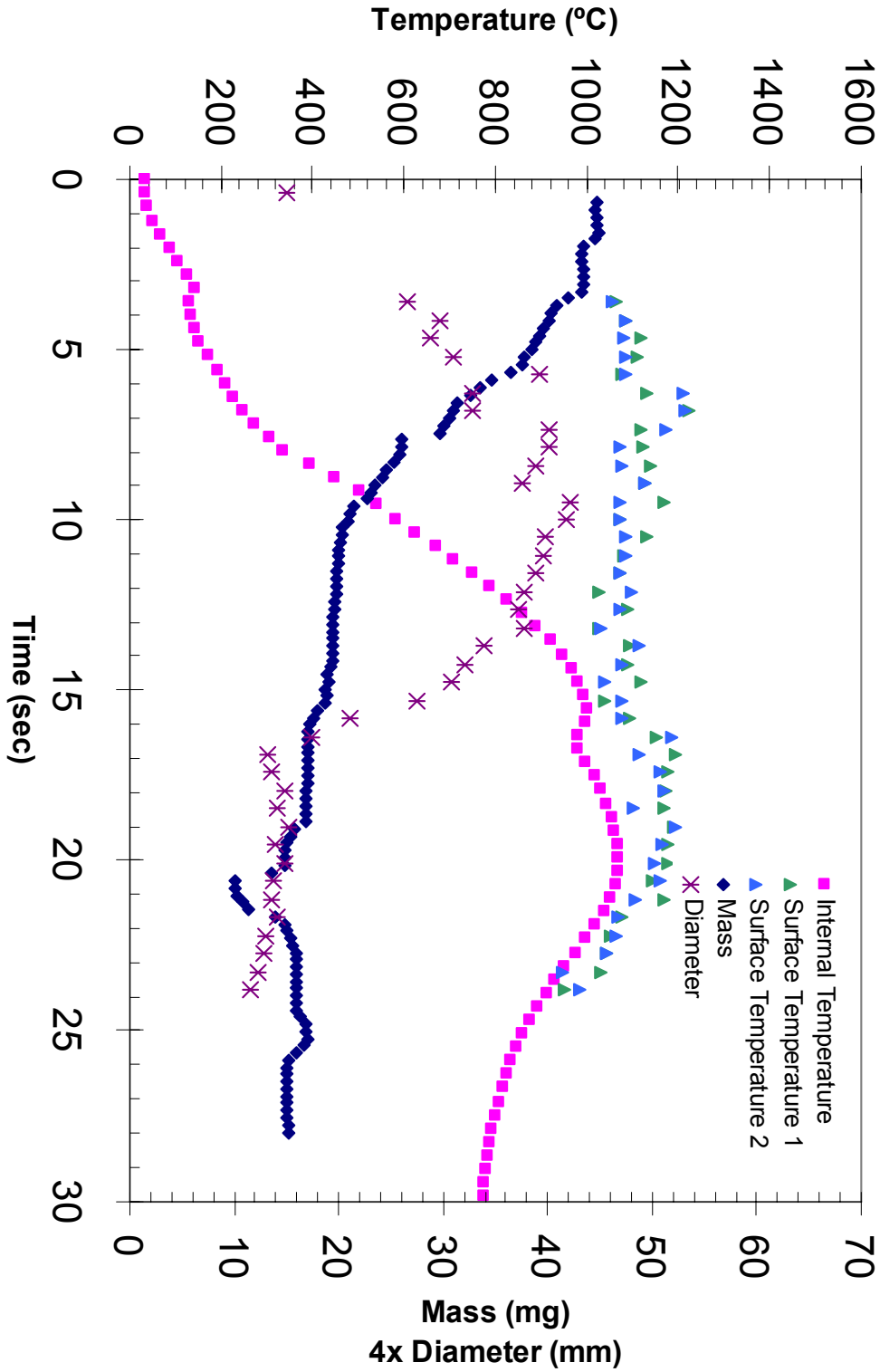

Figure 32: 23.2 mg Droplet of Black Liquor A in 800 ºC Air, Gas Velocity=0.367 m/s, 95% Solids

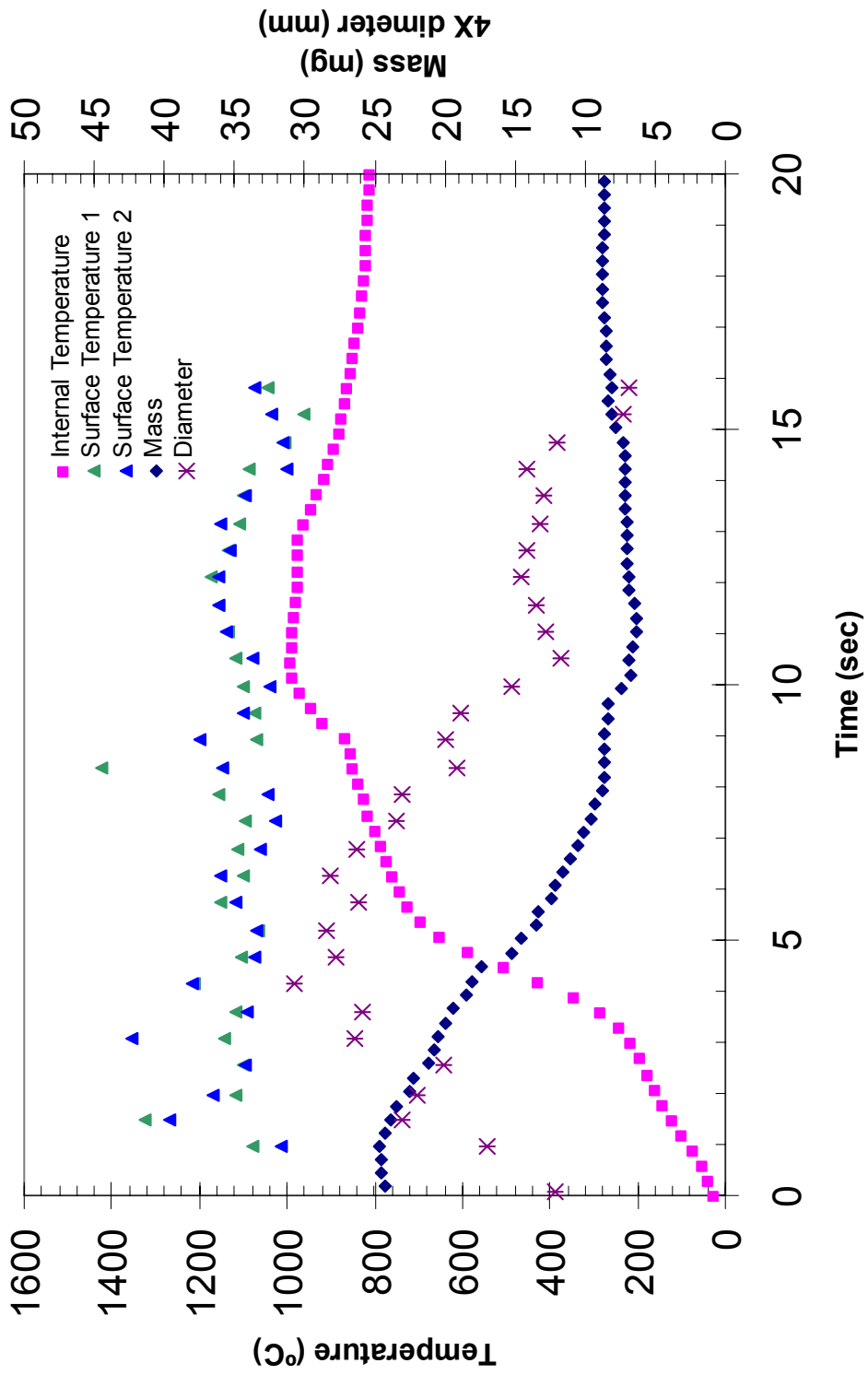

Figure 33: 59.3 mg Droplet of Black Liquor D in 715 ºC Air, Gas Velocity=0.217 m/s, 70% Solids

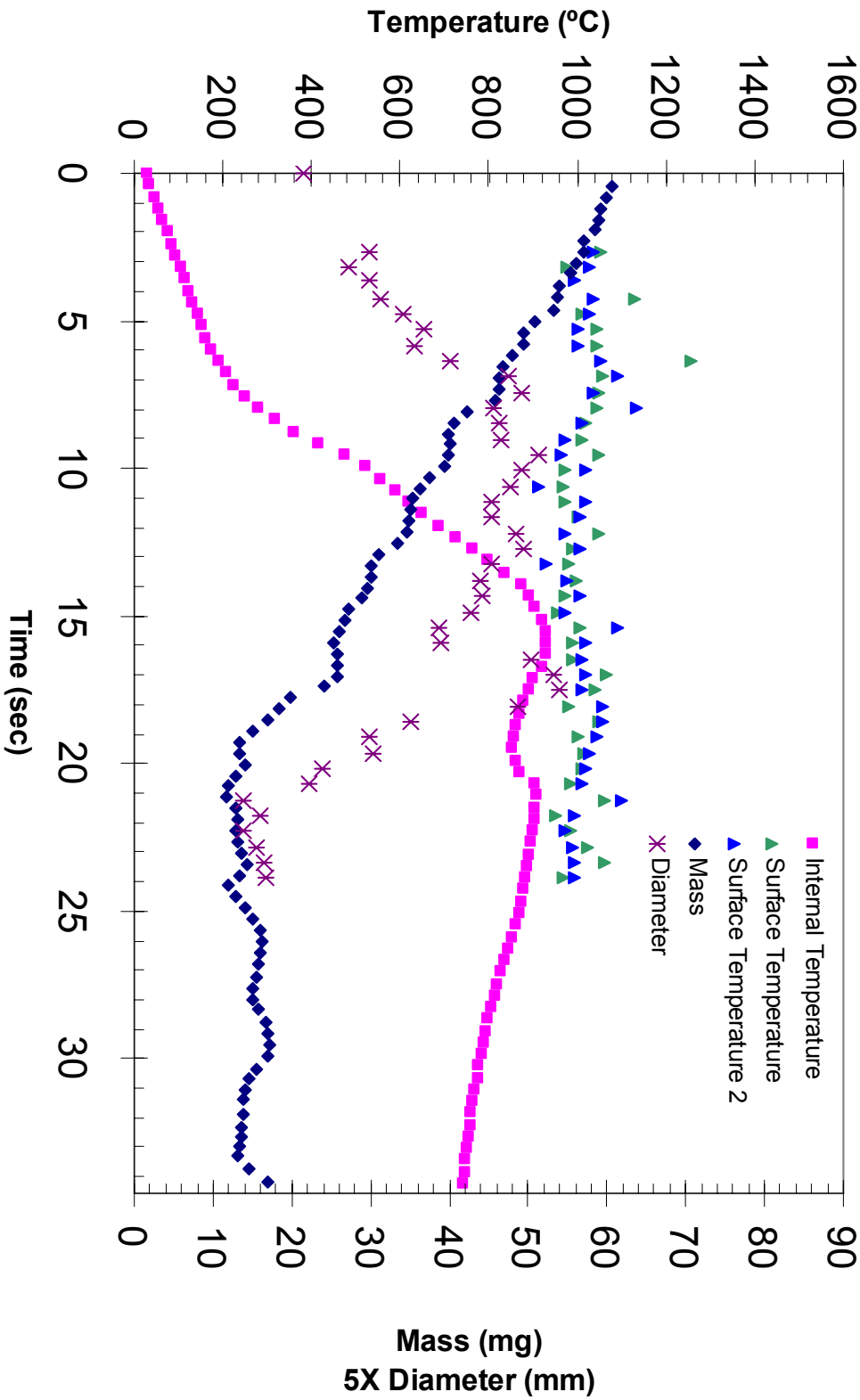
Temperature (ºC)
0
200
400
600
800
1000
1200
1400
1600
Time (sec)
0
5
10
15
20
25
30
Mass (mg)
5X Diameter (mm)
0
10
20
30
40
50
60
70
80
90
Internal Temperature
Surface Temperature
Surface Temperature 2
Mass
Diameter

Video Observations

Video images reveal further information on combustion mechanisms. Video images during drying and devolatilization reveal that particle conditions are highly two- or three-dimensional. This particular furnace is bottom heated and has a constant gas flow around the particle. During devolatilization, a bright orange-yellow flame develops near the droplet as shown in Figure 34.

During devolatilization, the droplet becomes very porous. Char burning exposes these large voids. As the char burns, the remaining smelt forms beads that agglomerate on the droplet surface. As char burning continues, the smelt beads grow by agglomeration. This agglomeration seems to minimize the mass- and heat-transfer barrier that the smelt may have imposed if it did not agglomerate. This means that instead of oxidizer having to diffuse through a thin stagnant layer of a smelt to penetrate to the char; the char is constantly exposed on the surface. This has significant modeling implications as discussed later. This mechanism for exposing new char to the surface is called the char regeneration mechanism. Figure 35 illustrates this mechanism. It shows how a large void opens near the center of the droplet and eventually exposes new char on the surface.

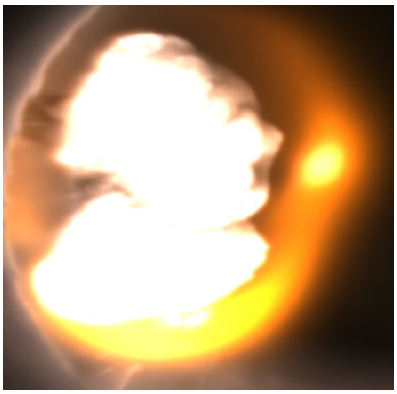

Figure 34: Yellow Flame around Droplet during Devolatilization

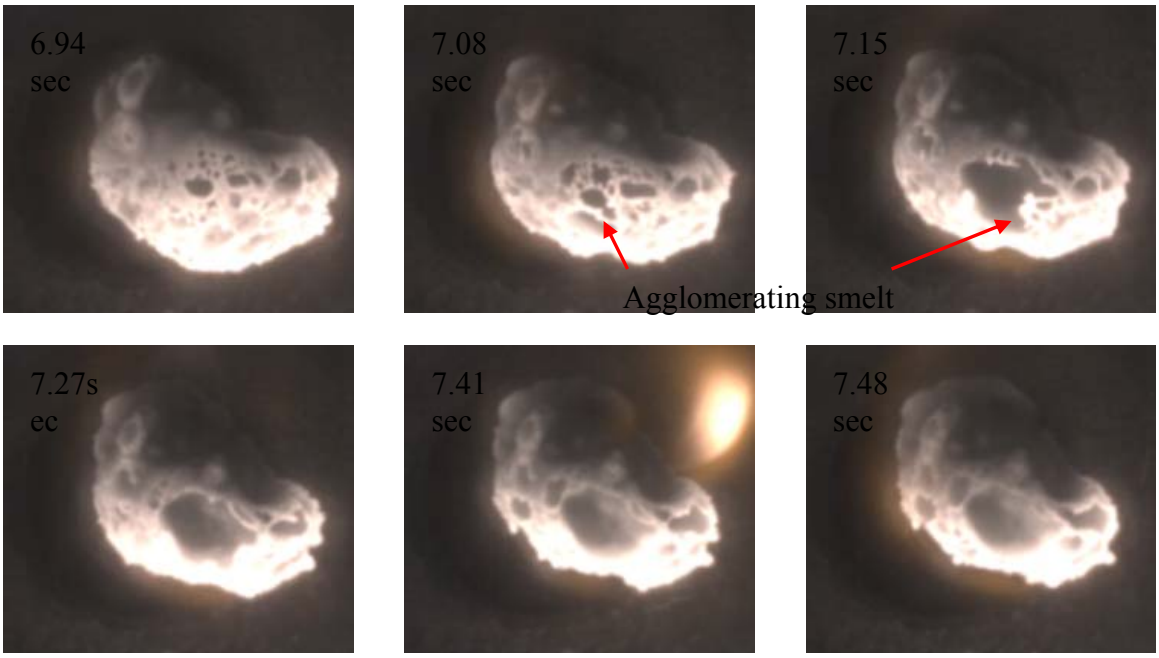

Figure 35: Successive Images during Char Burning, 26.6 mg Droplet of Black Liquor E in 650 ºC Air, 0.32 m/s Gas Velocity, 70% Solids. (Numbers Indicate Total Elapsed Burn Time.)

As the droplet completes char burning, smelt agglomeration exposes large voids in the particle center formed during devolatilization. The size of these voids is roughly the same order of magnitude as the entire particle. This mechanism may greatly aid the speed of char burning because it allows surrounding gases to enter close to the center of the particle. The structure of the droplet may also add to the turbulent convection around the particle, hence aiding mass transfer.

Figure 36: Large Voids during Char Burning, Very Large Droplet of Black Liquor A, 95% Solids, in 800 ºC Air

At oxidation temperatures, the particle's interior structure melts. The droplet begins to collapse upon itself and agglomerate into one large bead. Thus, the opening of large voids in the center of the particle may result in a rapid volume change, such as appears in

Figure 31. When the droplet collapses, the unburned char reacts with liquid sodium carbonate and sodium sulfate, causing rapid gas release.

This rapid gas release may be the cause of intermediate sized particles being ejected. Near the end of char burning, the droplet releases burning intermediate sized particles (ISP) easily seen by the cameras. Although these particles occasionally appear throughout most of the combustion process, Figure 37 shows the spectacular event that sometimes characterizes the end of char burning. This large release of ISP is consistent with Ip's observations. Lien et al. observed that in char beds ISP formation increases with bed temperature. In their experiments, increasing inlet oxygen concentration increased bed temperature. Increased oxygen on the bed could oxidize inorganic species. Thus, their results may also point toward ISP formation from a reaction of oxidized inorganics with char.

Ip et al. also found that increasing the moisture content of the liquor decreased the ISP formation. Increased moisture content leads to increased auto-gasification. During gasification, no oxygen is present in the char layer, and the sulfate/sulfide cycle is broken because the sulfide does not oxidize back to sulfate. (See Section 0 for more information on the sulfate/sulfide cycle.) This decrease in oxidized inorganic species could be the cause of decreased ISP formation in initially wet particles.

The two pictures in Figure 37 record the same particle at the same time using identical cameras and lenses but with different aperture settings. The left image shows only one particle leaving the droplet, but the other image shows hundreds of particles leaving the droplet. The right image indicates the particle is nearly exploding. The left image indicates only minor surface reactions occurring. (However, if the left image is manipulated, such as inverting the colors as in Figure 38, more particles can be seen.) The distinct difference between these two images illustrates how difficult ISP ejection may be to quantify using visual approaches. Conclusions derived from visual observations that more ISP form at higher temperatures should be highly suspect. Being able to see the ISP depends strongly on their temperature and camera settings. Ejection at lower combustion temperatures or during the early stages of combustion would therefore be more difficult to validate visually due to the cooler temperature of the ISP.

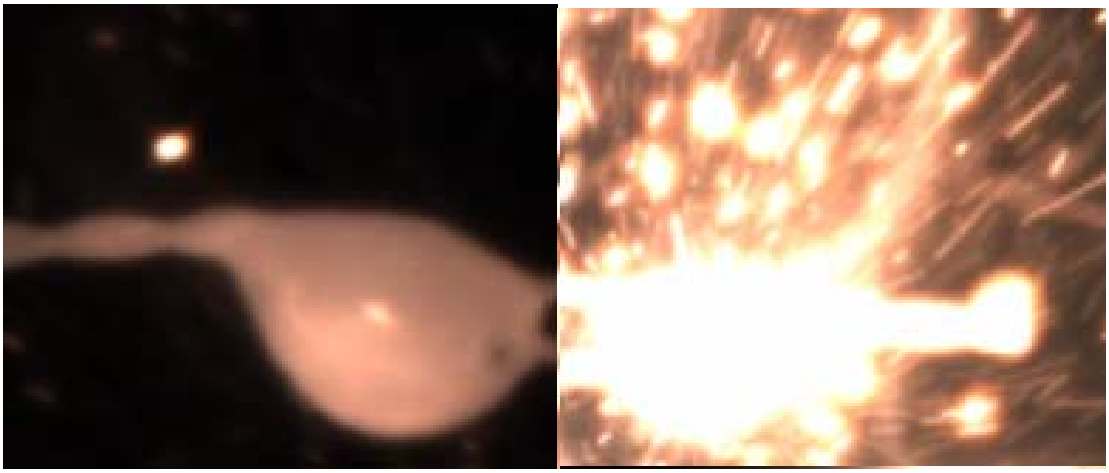

Figure 37: ISP Ejection After Char Burning, Two Simultaneous Images, Very Large Droplet of black Liquor A, 95% Solids, in 800 ºC Air.

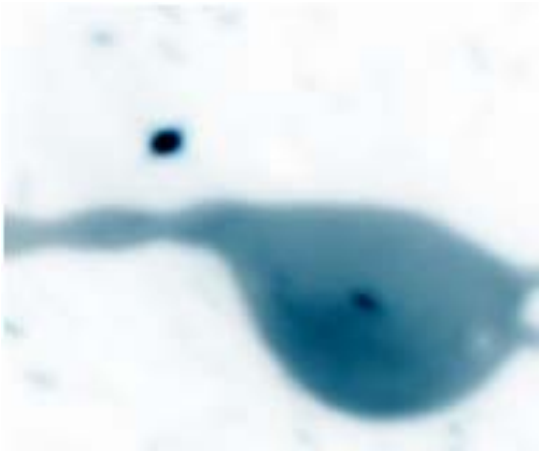

Figure 38: ISP Ejection After Char Burning, Very Large Droplet of Black Liquor A, 95% Solids, in 800 ºC Air (Colors Inverted)

Droplet Model Description and Development

Modeling combustion processes entails solving transport equations, Equations (0-7), (0-8), and (0-9), using a control-volume method. The model calculations reported here result from modifications of a code that was originally developed for biomass particle combustion written primarily by Lu and partially by Ip. Many simplifications had to be made to the model because of incomplete understanding of all of the mechanisms and kinetic parameters required by a highly detailed model as well as for computation time considerations. Nevertheless, even the simplified model provides significantly more detail than those commonly used to describe black liquor combustion. In this model, heat and mass transfer are described by a 1-dimensional model for arbitrary shapes; however, so far when considering black liquor the code is only configured for a spherical shape. The model uses the power-law scheme to solve the combined advection-diffusion problem. The term "advection" is used in this document to describe flow in the radial direction. Darcy's law for flow through a porous medium and the continuity equations are solved using the SIMPLE (Semi-implicit Method for Pressure Linked Equations) algorithm. The model predicts transient temperature, velocity, pressure, composition, reaction rate, mass- and heat-transfer rates, and related data as a function of one spatial dimension. This dimension is the radius in the case of spherical particle and the equations use r for the independent variable describing it.

$$\frac{\partial}{\partial t}\varepsilon\rho_g Y_i + \frac{1}{r^n}\frac{\partial}{\partial r}\left(r^n \varepsilon\rho_g Y_i u\right) = \frac{1}{r^n}\frac{\partial}{\partial r}\left(r^n \varepsilon D_{eff,i}\rho_g \frac{\partial Y_i}{\partial r}\right) + S_i \qquad (0\text{-}7)$$

$$\frac{\partial}{\partial t}\left[\sum_i \rho_i \hat{H}_i + \sum_k \rho_k \hat{H}_k + \varepsilon\rho_g \sum_j Y_j \hat{H}_j\right]$$
$$+ \frac{1}{r^n}\frac{\partial}{\partial r}\left[r^n \varepsilon\rho_g u \sum_j Y_j \hat{H}_j\right] = \frac{1}{r^n}\frac{\partial}{\partial r}\left(r^n \lambda_{eff}\frac{\partial T}{\partial r}\right)$$
$$+ \frac{1}{r^n}\frac{\partial}{\partial r}\left[r^n\left(\rho_g \varepsilon \sum_j D_{eff,j}\frac{\partial Y_j}{\partial r}\hat{H}_j + D_{eff,k}\frac{\partial \rho_k}{\partial r}\hat{H}_k\right)\right] \qquad (0\text{-}8)$$

where,

$\hat{H}_I = \hat{H}^0_{I,f} + \int_{T_0}^{T} Cp_I(T)dT$, I is any species involved

$$\frac{\partial \rho_g}{\partial t} + \frac{1}{r^n}\frac{\partial}{\partial r}\left(r^n \varepsilon\rho_g u\right) = S \qquad (0\text{-}9)$$

□	Porosity	S	Source term due to reactions
□$_g$	Gas density	C_p	Heat Capacity

Y	Species mass fraction	$\hat{H}$	Enthalpy
u	Gas velocity	$\hat{H}^0_{l,f}$	Standard heat of formation
D_{eff}	Effective diffusivity	T	Temperature
t	Time	n	Coordinate system factor
i	Any solid-phase species	j	Any gas-phase species
k	Free or bound water	□	Condensed-phase species density
λ_{eff}	Effective thermal conductivity		

The integer variable n changes with the coordinate system that best describes the shape and ranges from 0 to 2. For example, a sphere corresponds to a value of two for n. This enables the code to perform calculations for other shapes

Because of swelling during black liquor combustion, the internal radiation heat transfer becomes important. The solid-phase thermal conductivity of black liquor, λ_S, depends on temperature and composition as indicated in Equation (0-10).

$$\lambda_S = \left(1.44\times10^{-1}\cdot\left(T-273.15\right)+0.58-0.335\cdot Y_S\right)\frac{W}{m\cdot K} \qquad (0\text{-}10)$$

Temperature, T, is in Kelvin, and Y_S is the mass fraction of the solids. This conductivity combines with the conductivity of the gas, λ_g, and radiative properties to form an effective thermal conductivity which, when using a diffusion approximation for cubic pores and an opaque cube pore model, is expressed as in Equation (0-11).

$$\lambda_{eff} = \lambda_S\left(1-\varepsilon^{2/3}\right)+\frac{\varepsilon^{2/3}}{\frac{1-\varepsilon^{1/3}}{\lambda_S}+\frac{\varepsilon^{1/3}}{\lambda_g}}+\frac{16\sigma T^3}{3a_R}\varepsilon \qquad (0\text{-}11)$$

A value of 850 m^{-1} for a_R, known as the Rosseland mean absorption coefficient, was given by Järvinen based on a sensitivity analysis. The pressure outside of the particle is assumed constant at ambient pressure; thus, to find velocities, in the boundary layer only the continuity equation is solved. Equation (0-12) is Darcy's Law, where μ is the gas viscosity, η is the permeability, and P is pressure.

$$u = -\frac{\eta}{\mu}\frac{\partial P}{\partial r} \qquad (0\text{-}12)$$

Boundary Conditions and Flame Layer

Symmetry boundary conditions apply at the center of the particle (all gradients are assumed to be zero). The model has two options for the boundary conditions at the particle edge. The first option is to use standard heat- and mass-transfer correlations to calculate the Nusselt and Sherwood numbers, as shown in Equations (0-13) & (0-14), to calculate the mass and heat transfer coefficients to the surface. This option is best for pyrolysis calculations because it reduces calculation time. The second option is to extend the calculation domain past the solid surface into the gas phase. This gas-phase portion is described by a stagnant-film model. At the edge of the film, the conditions are considered to be the same as the bulk conditions in the reactor.

$$Nu = 2.0 + 0.6 \cdot Re^{1/2}\, Pr^{1/3} \qquad (0\text{-}13)$$

$$Sh = 2.0 + 0.6 \cdot Re^{1/2}\, Sc^{1/3} \qquad (0\text{-}14)$$

Nu	Nusselt number	Re	Reynolds number
Sh	Sherwood number	Sc	Schmidt number

This second option is better for combustion modeling because it solves the transport equations in the region immediately surrounding the particle, or the boundary layer, thus resolving the gas properties near the particle surface, including the flame that often located there. Unlike small-particle (pulverized-coal, for example) combustion, reactions in particle boundary layer commonly occur during black liquor combustion. The boundary layer thickness is approximately proportional to the particle diameter and black liquor and many biomass particles are large enough that flames occur in the boundary layer and provide thermal feedback to the particles. Specifically, during devolatilization and char burning, significant amounts of combustibles evolve from the particle. If the boundary layer is very thin (relative to the reaction distance of the gas-phase components), these species simply diffuse from the surface and burn in the bulk gas. However, when the boundary layer is thick, these species burn within the boundary layer, thus reducing the oxidizer concentrations at the surface. When a flame is present during char burning, the combustion products, such as CO_2 and H_2O, diffuse back to the surface to gasify the char.

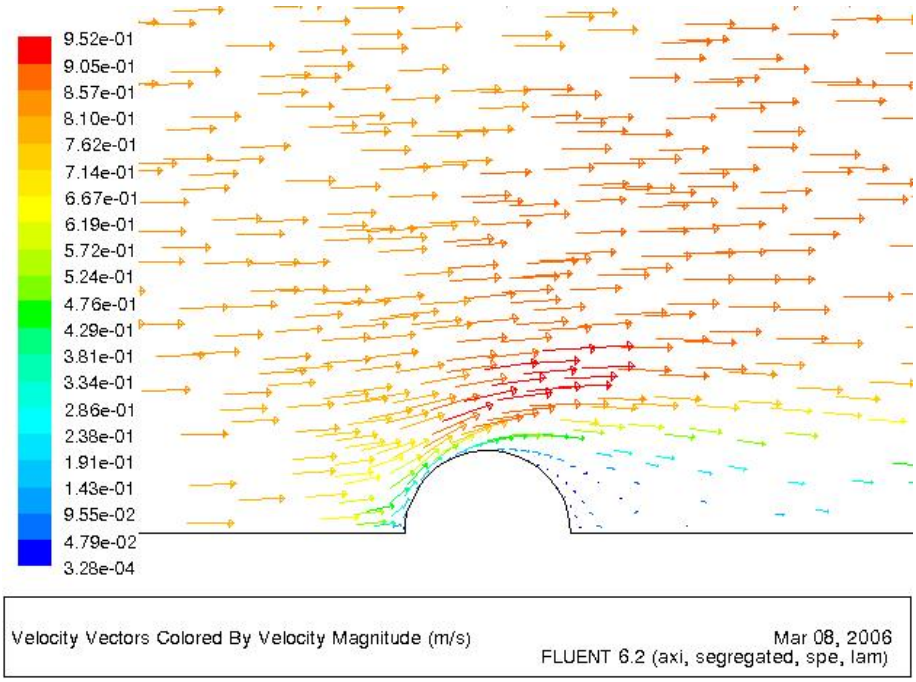

Figure 39: FLUENT™ Plot of Velocity Vectors of Air Flow around a Particle

The gas flow around a sphere is really at least 2-dimensional, as is shown in Figure 39. This figure shows theoretical calculations using Fluent™ that describe typical fluid mechanics of a sphere entrained in a gas with a different velocity. On the upwind side of the sphere there is a stagnation point. On the sides of the sphere, there is a more fully developed boundary layer, and on the downwind side of the sphere, there is a recirculation zone. This flow pattern creates non-uniform heat and mass transfer around the sphere. However, with a two-dimensional model (assuming the flow is axisymmetric around the particle), the flame zone surrounding the particle could be described by simply setting the boundary conditions at an arbitrarily long distance from the particle and solving the transport equations.

For a one-dimensional model, the flame zone surrounding the particle is not so easily described because flow in only one direction can be considered. For this reason, the boundary layer in the model is described by a stagnant film. For a one-dimensional model in spherical coordinates, the radial direction, *r*, does not capture the effect of bulk airflow around the particle except by changing the film thickness, which is the distance from the particle surface to the bulk conditions. With the bulk conditions set at an arbitrarily long distance from the particle (i.e. very thick film), a one-dimensional model can only accurately predict the boundary layer characteristics when the bulk gas is stagnant. However, by placing the bulk conditions closer to the particle, the heat and the mass transfer rates accurately describe overall particle conditions even if axial flow is ignored and variations in the second dimension are ignored. The crucial variable is the film thickness. By increasing this distance, the temperature and species gradients decrease, and thus heat and mass transfer decrease.

It is also important to note that instead of describing the heat and mass transfer at each point on the particle surface, a 1-D model can only describe the average heat and mass transfer. The *Nu* and *Sh* correlations, shown above, work well for describing the average heat and mass transfer in a non-reacting boundary layer. The method developed for predicting the film thickness utilizes the accuracy of these correlations.

Estimating the film thickness, involves several assumptions. The first assumption is that standard heat and mass transfer correlations in conjunction with the stagnant-film model accurately describe mass and heat transfer and hence can be used to predict the film thickness. Associated with this assumption are assumptions of a quasi-steady-state process, no angular flow (only radial flow) in the film, and no gas production sources in the film. The definition of the overall mass-transfer coefficient to a particle is given in Equation (0-15).

$$-\rho_g D_{AB} \left.\frac{dY_i}{dr}\right|_{r=r_0} = h_m \theta_m \bar{\rho}_g \left(Y_{i,0} - Y_{i,L}\right) \qquad (0\text{-}15)$$

θ_m is the correction factor for advection from the particle, sometimes called the blowing factor, and the subscripts *0* and *L* represent the conditions at the surface and in the bulk, respectively. Because of these assumptions, the concentration profile for inert species in the film can be derived from the steady-state advection-diffusion equation. Another assumption is that the product of density and the diffusivity is constant in the film. In the calculations below, an average value is used denoted with an over-bar, $\overline{\rho_g D_{AB}}$. Finally, the film thickness for both reacting and non-reacting species is assumed the same. The differential equation for steady-state advection-diffusion without a source term yields an exact solution when coupled with the overall continuity equation. Equation (0-16) is the solution to this equation when solved in spherical coordinates. (Note: By continuity, the product of density, velocity and the radius squared is a constant in the boundary layer, i.e. $\rho_g u r^2$ = constant.)

$$\frac{Y_i - Y_{i,L}}{Y_{i,0} - Y_{i,L}} = \frac{exp\left[\dfrac{\rho_g u r^2}{\overline{\rho_g D_{AB}}}\left(\dfrac{1}{r_0} - \dfrac{1}{r}\right)\right] - exp\left[\dfrac{\rho_g u r^2}{\overline{\rho_g D_{AB}}}\left(\dfrac{1}{r_0} - \dfrac{1}{r_L}\right)\right]}{1 - exp\left[\dfrac{\rho_g u r^2}{\overline{\rho_g D_{AB}}}\left(\dfrac{1}{r_0} - \dfrac{1}{r_L}\right)\right]} \qquad (0\text{-}16)$$

The derivative of Equation (0-16) yields an expression for the concentration/density gradient at the particle surface, $dY_i/dr|_{r=r0}$. By substituting this expression for $dY_i/dr|_{r=r0}$ into Equation (0-15) and solving for r_L, the thickness of the film can be calculated. For very low bulk velocities, this calculation yields very large quantities for the film thickness. However, in the code, the film thickness is limited to ten times the particle diameter.

$$\Delta r = r_L - r_0 = \left[\frac{1}{r_0} - \frac{\overline{\rho_g D_{AB}}}{\rho_g u r^2} ln\left(1 + \frac{\rho_g u r^2}{r_0^2 \bar{\rho}_g h_m \theta_m} \frac{\left[\rho_g D_{AB}\right]_{r=r0}}{\overline{\rho_g D_{AB}}}\right)\right]^{-1} - r_0 \qquad (0\text{-}17)$$

This equation has a singularity when the velocity equals zero. However, by applying L'hopital's rule or by re-deriving this equation and ignoring the advection term, this problem can be eliminated. The result of the film thickness for low velocities is given in Equation (0-19).

$$\Delta r = \frac{-Sh \cdot \overline{\rho_g D_{AB}}}{2\left(D_{AB} \cdot \rho_g\right)_{r_0}} \left(\frac{1}{r_0} - \frac{Sh \cdot \overline{\rho_g D_{AB}}}{2 \cdot r_0 \cdot \left(D_{AB} \cdot \rho_g\right)_{r_0}} \right)^{-1} - r_0 \qquad (0\text{-}18)$$

The film thickness calculated from Equations (0-17) and (0-18) is only valid for mass transfer problems, and a different film thickness must be calculated for heat transfer. The derivation for the heat transfer film thickness is analogous to the derivation for the mass transfer film thickness. The additional assumptions are that the heat capacity and the thermal conductivity, λ, in the film are taken to be the average heat capacity and the average thermal conductivity, respectively.

$$\Delta r = \left[\frac{1}{r_0} - \frac{\overline{\lambda}}{\rho_g u r^2 \overline{C_p}} ln\left(1 + \frac{\rho_g u r^2 \overline{C_p}}{r_0^2 h_T \theta_T} \frac{(\lambda)_{r=r0}}{\overline{\lambda}} \right) \right]^{-1} - r_0 \qquad (0\text{-}19)$$

$$\Delta r = \frac{-Nu \cdot \overline{\lambda}}{2 \cdot (\lambda)_{r_0}} \left(\frac{1}{r_0} - \frac{Nu \cdot \overline{\lambda}}{2 \cdot r_0 \cdot (\lambda)_{r_0}} \right)^{-1} - r_0 \qquad (0\text{-}20)$$

The most impressive results from using this method for calculating the film thickness are that it preserves the analytical solution for non-reacting steady-state advection-diffusion problems, and that the effects of the flame inside the boundary layer can be predicted from the model. After implementing this method for determining the film thickness into the particle model, this method was tested to determine how well it worked for a particle during pyrolysis. Because there are no significant gas-phase reactions in the boundary layer during pyrolysis, the droplet model predictions based the method described above should be very similar to model predictions based on heat and mass transfer correlations during the transient and should converge to the same steady-state temperature at the end. The following figure shows the predicted particle surface temperature when each of the methods are employed in the droplet model. The predictions show that by specifying the thermal and mass transfer film thicknesses in the manner described above, the model still accurately predicts heat and mass transfer for the simple case of pyrolysis.

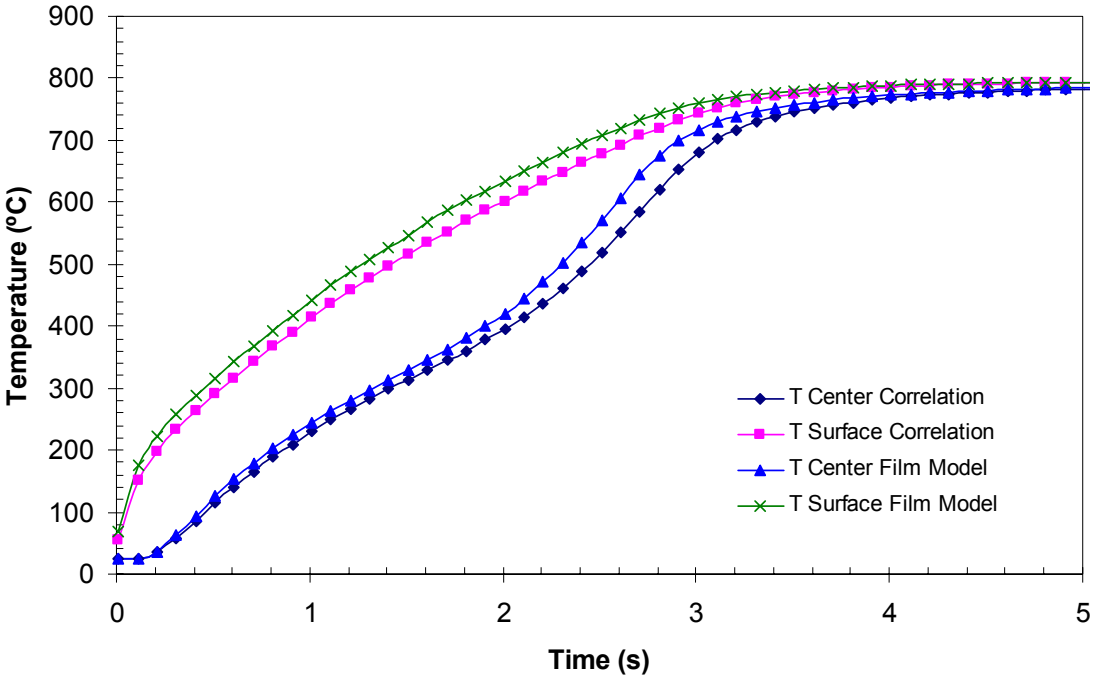

Figure 40: Comparison of Stagnant Film Model with Standard Correlations Model for a 2-mm Droplet Pyrolyzing in 800ºC Nitrogen

Swelling and Drying Models

One of black liquor's most unique characteristics is that during devolatilization a droplet swells to between 3-5 times its original diameter. The large impact this has on the structure may be more apparent when considering the implication for particle density for a nominally spherical particle. An increase in size by a factor of 5 coupled with a decrease in mass through devolatilization by, say, a factor of 2 implies a change in particle density by a factor of 250. To account for swelling, a swelling submodel makes the shell volume a function of the evaporation of moisture, devolatilization conversion, and char conversion. Each shell volume swells or shrinks independently of the rest. This model does not consider the droplet to be necessarily more porous near the center as some authors contend is the case. This model appears as Eq. (0-21). This model was taken from Järvinen, but this investigation modified it to include shrinking during char burnout.

$$v = v_{ini} \cdot \left(\beta_M + (\beta_B - \beta_M) \cdot \left(1 - \frac{m_B}{m_{B,ini}} \right) + (\beta_C - \beta_B) \frac{char\_consumed}{m_B + char\_produced} \right) \qquad (0\text{-}21)$$

v	Droplet volume	β_M	Volume ratio for drying
v_{ini}	Initial volume	β_B	Volume ratio after devolatilization

m_B	Mass of Black Liquor Solid	$\square_C$	Volume ratio after char burning
char_produced	Mass of char produced	$m_{B,ini}$	Initial Mass of Black Liquor Solid
char_consumed	Mass of char consumed		

The variable *char_consumed* is the integral of the rate of char consumption with respect to time, and *char_produced* is the integral of the rate of char production with respect to time. The ratio of these numbers approaches unity from below, but not necessarily monotonically, as conversion increases. The βs can be considered to be the ratios of the volume to the initial volume for drying, devolatilization, and smelt oxidation.

In this submodel, swelling during drying is instantaneous. Hupa et al. showed that swelling during drying is initially very fast, but then practically stops for the rest of drying. Instantaneous swelling during drying may reasonably approximate the real behavior. Because the model assumes that there is a zero initial concentration of char in the particle, some basis has to be used to know how much shrinking has occurred during char consumption. This model uses the total char production as that basis. By using the total char production as the basis, as opposed to the char concentration during the previous time step, the shrinking model is more linear with char conversion. However, due to overlap between devolatilization and char burning, the particle starts shrinking before it finishes swelling; thus, the degree of swelling specified by the β_B will not occur. To match swelling with experimental data iterating on β_B is necessary.

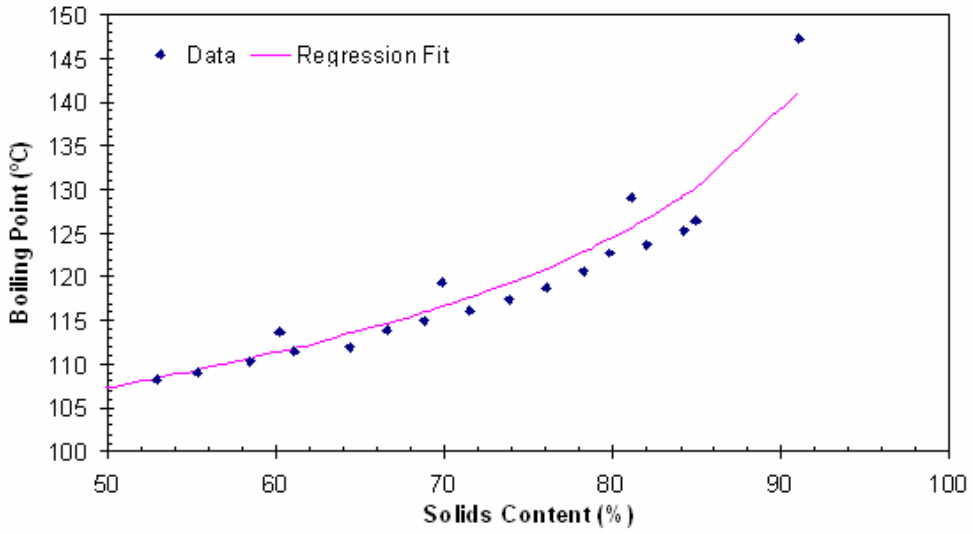

Figure 41: Boiling Point Model Regression

The drying model uses a modified Raoult's Law approach. Boiling point data provided a basis for an "effective" mole fraction for the black liquor as a function of moisture content. The regression is shown in Figure 41 and resulted in Equation (0-22). In this equation, P_{H_2O} is the partial pressure of water, and $P_{H_2O}^{sat}$ is the vapor pressure.

$$P_{H_2O} = 0.0716 \cdot (1 - Y_S)^{0.609} P_{H_2O}^{sat} \qquad (0\text{-}22)$$

Pyrolysis Model

The pyrolysis material in black liquor solids (B) devolatilizes into light gases, tar (T), and char (C). The tar converts into either light gas or char. Although this process is conceptually accurate, it does not preserve elemental conservation. Char in this model has the properties of graphite. The light gases are assumed to be a mixture of 1.9% H_2, 39.6% CO, 20.9% CO_2, 24.9% H_2O, and 12.7% light hydrocarbons. Thermodynamic properties of tar describe tar.

Because no devolatilization kinetics parameters were available for black liquor with the proposed mechanism, parameters were regressed from available literature data. A zero dimensional model was made of a single black liquor droplet during pyrolysis along with a code that performs nonlinear least squares using the Gauss-Newton method. Pyrolysis data from Jing et al provived benchmark kinetic information. The model parameters were adjusted until the differences between the data and predictions was minimized. The resulting model predictions appear with the data in Figure 42. Model assumptions are described in Appendix I.

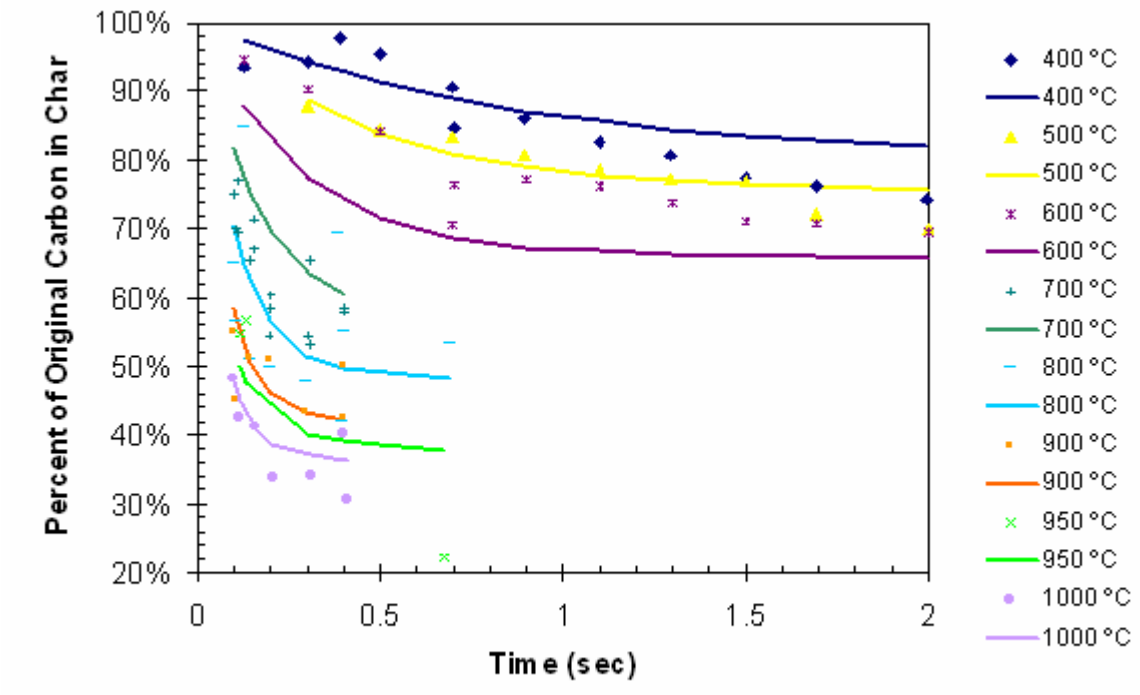

Figure 42: Results of Devolatilization Regression

Char Regeneration

The diffusivity model accounts for the porosity, ε, and the tortuosity, τ, the later is assumed to be 1.5, Equation (0-23). Near the end of char burning the smelt becomes molten. The molten smelt's porosity approaches zero and has a diffusivity orders of magnitude lower than the gas diffusivity. However, because the smelt agglomerates into beads, the underlying char structure is continuously exposed to the surrounding gases. To account for this mechanism, mass from the neighboring cell is added to the outermost cell during char oxidation. When 80% of the char has been consumed from the outermost cell, small amounts of adjacent cell are added to it to maintain the 80% char consumption until 99.9% of the particle is contained within the outermost shell. This rate of cell combination is consistent with Järvinen's conclusions.

$$D_{eff} = \frac{D_{combined} \cdot \varepsilon}{\tau} \qquad (0\text{-}23)$$

Table 11: Heat Capacities and Heats of Formation

Species	C_p (J·kg^{-1}·K^{-1})	Ref.	ΔH_f (J/mol)
B	$\frac{1000 \cdot R_g}{7.72}\left(\frac{exp\left(\frac{380}{T}\right)}{\left(\frac{T}{1800}exp\left(\frac{380}{T}\right)-1\right)^2}+\frac{2\,exp\left(\frac{1800}{T}\right)}{\left(\frac{T}{1800}exp\left(\frac{1800}{T}\right)-1\right)^2}\right)$	[**Error! Reference source not found.**]	-2.88E5*
C	$\frac{1000 \cdot R_g}{11.3}\left(\frac{exp\left(\frac{380}{T}\right)}{\left(\frac{T}{1800}exp\left(\frac{380}{T}\right)-1\right)^2}+\frac{2\,exp\left(\frac{1800}{T}\right)}{\left(\frac{T}{1800}exp\left(\frac{1800}{T}\right)-1\right)^2}\right)$	[**Error! Reference source not found.**]	1.317E6**
Tar	Same as benzene on a mass basis		4.20E4

*Based on an average heat of devolatilization between 500-800K of -80 kJ/kg.

**Based on Bryden's measurement of heats of char oxidation.

***Based on $\Delta H_{rxn,298K}$ for Tar → Char where char is pure graphite.

Thermodynamics and Kinetics

The model attempts to make all of the thermodynamics completely consistent, meaning that each species includes thermodynamically consistent heat of formation and heat capacity values. Enthalpies of pure species come from heat capacity and heats of formation information in the Gordon-McBride Thermodynamics Database. Tar is assumed to have the heat capacity of

benzene on a mass basis. The heat capacities and heats of formation of char (C), black liquor solids (B), and tar (T) appear in Table 11. All of the heats of reactions are calculated from the enthalpies of the species. All phases (gases and mixture) form ideal solutions. Initial species compositions come from softwood liquor data given by Järvinen et al. as shown in Table 12.

Table 12: Black Liquor Initial Composition

Species	wt%
B	68.78
Na_2S	0.00
K_2S	0.00
Na_2SO_4	1.38
K_2SO_4	0.10
Na_2CO_3	27.30
K_2CO_3	2.10
NaCl	0.31
KCl	0.02

For simplicity, the condensed-phase species enthalpies were forced to be continuous functions of temperature, even across phase transitions. Figure 43 shows an example of the resulting enthalpy as a function of temperature when this assumption is enforced for sodium carbonate.

All reaction kinetics (other than pyrolysis reactions, see Section 0) for the model come from literature. Table 13 shows the kinetics and their respective references. In this table, species concentration, C_i, has units of mols/m^3; MW_i is in kg/mol; r_i is in kg/m^3; and all rate expressions are in units of kg(of the first reactant)/m^{3}s.

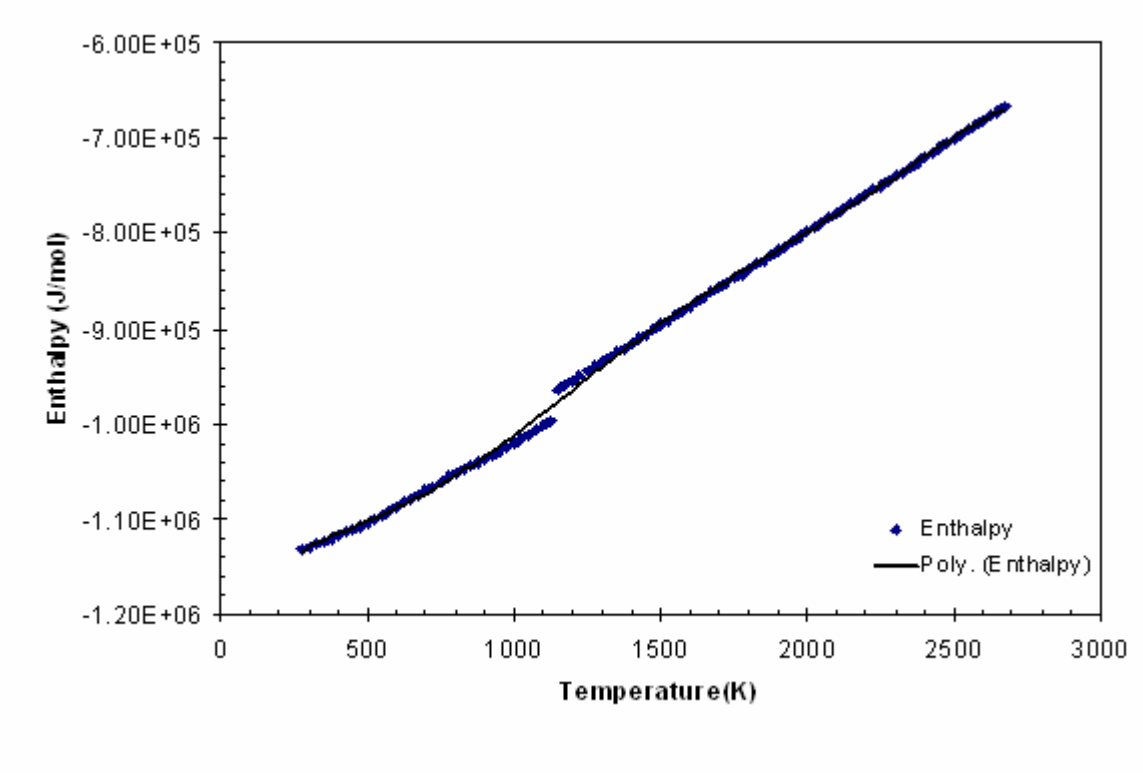

Figure 43: Estimated Enthalpy of Sodium Carbonate

Sodium Carbonate Equilibrium Model

In their original investigation of sodium carbonate decomposition, Li and Van Heiningen found that sodium carbonate was stabilized by the presence of carbon dioxide and carbon monoxide. Yet since then, no one has found reaction kinetics for the reverse reaction to sodium carbonate decomposition. To account for the stabilization of sodium carbonate by carbon monoxide and carbon dioxide, the model modified the original rate expression to be Equation (0-24).

$$-r_{Na2CO3} = k_{18} \cdot \left(C_{Na2CO3} - C^{eq}_{Na2CO3} \right) \qquad (0\text{-}24)$$

Table 13: Chemical kinetics

#	Reaction	Rate Expression (all units kg, mol, m, s, K)	E_i	A	n
1	B → light gas	$k_1(T) \cdot \rho_B$	6.40E7	1.4E5	0
2	B → Tar	$k_2(T) \cdot \rho_B$	9.85E7	1.33E5	0
3	B → Char	$k_3(T) \cdot \rho_B$	1.39E	1.16E	0

			7	5	
4	Tar → light gas	$k_4(T)\cdot\rho_g\cdot Y_T$	4.28E6	1.08E5	0
5	Tar → Char	$k_5(T)\cdot\rho_g\cdot Y_T$	1.00E5	1.08E5	0
6	Water evaporation	$SA_{M,ini}\cdot h_{m,p}\cdot\frac{\rho_{H_2O}}{\rho_{H_2O,ini}}\cdot\left(\frac{P^{sat}_{H_2O}\cdot M_{H_2O}}{R_g\cdot T}-\left(\rho_g\cdot Y_{H_2O}\right)\right)$	-	-	-
7	Bound water evaporation	$k_7(T)\cdot\rho_{BM}$	5.13E10	8.80E4	0
8	½O_2 + C → CO	$R_{SA,C}\cdot SA_{C,V}\cdot k_8(T)\cdot\rho_{O_2}$	0.658	7.48E5	1
9	C + CO_2 → 2CO	$SA_{C,m}\cdot k_9(T)\cdot\rho_C\cdot C_{CO_2}/\left(C_{CO_2}+3.4C_{CO}\right)$	3.92E5	2.50E5	1
10	C + H_2O → CO + H_2	$SA_{C,m}\cdot k_{10}(T)\cdot\rho_C\cdot C_{H_2O}/\left(C_{H_2O}+1.42C_{H_2}\right)$	1.60E4	2.10E5	1
11	CO + 1/2 O_2 → CO_2	$k_{11}\cdot\rho_g\cdot Y_{CO}\cdot C_{O_2}{}^{0.25}\cdot C_{H_2O}{}^{0.5}$	3.98E8	1.67E5	0
12	H_2 + ½O_2 → H_2O	$k_{12}\cdot\rho_g\cdot Y_{H_2}\cdot C_{O_2}{}^{1.42}$	2.28E8	1.71E5	0
13	$C_6H_{6.2}O_{0.2}$* + 2.9O_2 → 6.0CO + 3.1H_2	$k_{13}\cdot C_T{}^{0.5}\cdot C_{O_2}\cdot P^{0.3}\cdot MW_T$	20892	80235	1
14	2C + Na_2SO_4 → Na_2S + 2CO_2	$k_{14}\cdot\left(\frac{C_{Na_2SO_4}}{C_{Na_2SO_4}+C_{Na_2S}+C_{Na_2CO_3}}\right)^{1.4}\cdot C_C MW_{Na_2SO_4}$	3.79E3	7.81E5	0

15	$K_2SO_4 + 2C \rightarrow K_2S + 2CO_2$	$k_{15}\left(\frac{C_{K_2SO_4}}{C_{K_2SO_4}+C_{K_2S}+C_{K_2CO_3}}\right)^{1.4} C_c MW_{K_2SO_4}$	3.79E3	7.81E5	0
16	$Na_2S + 2O_2 \rightarrow Na_2SO_4$	$k_{16} R_{SA,Na_2S} \cdot SA_{C,V} \cdot C_{O_2} \cdot MW_{Na_2S}$	6.235 E3	7.81E5	0
17	$K_2S + 2O_2 \rightarrow K_2SO_4$	$k_{17} R_{SA,K_2S} \cdot SA_{C,V} \cdot C_{O_2} \cdot MW_{K_2S}$	6.235 E3	7.81E5	0
18	$Na_2CO_3 + 2C \rightarrow 2Na + 3CO$	$k_{18} \cdot \left(\rho_{Na_2CO_3} - \rho^{eq}_{Na_2CO_3}\right)$	1.00E9	2.44E5	0
19	$K_2CO_3 + 2C \rightarrow 2K + 3CO$	$k_{19} \cdot \rho_{K_2CO_3}$	1.00E9	2.44E5	0
20	$NaCl_{(s,l)} \rightarrow NaCl_{(v)}$	$SA_{C,V} \cdot h_{m,p} \cdot \left(\frac{\rho_{NaCl}}{\rho_{tot}} \frac{P^{sat}_{NaCl} \cdot M_{NaCl}}{R_g \cdot T} - \rho_g \cdot Y_{NaCl}\right)$	-	-	-
21	$KCl_{(s,l)} \rightarrow KCl_{(v)}$	$SA_{C,V} \cdot h_{m.p} \cdot \left(\frac{\rho_{KCl}}{\rho_{tot}} \frac{P^{sat}_{NaCl} \cdot M_{KCl}}{R_g \cdot T} - \rho_g \cdot Y_{KCl}\right)$	-	-	-
22	$Na_{(v)} + H_2O \rightarrow NaOH_{(v)} + \frac{1}{2}H_2$	$k_{23} \cdot C_{Na} \cdot C_{H_2O} \cdot MW_{Na}$	1.629 E5	1.0E7	0

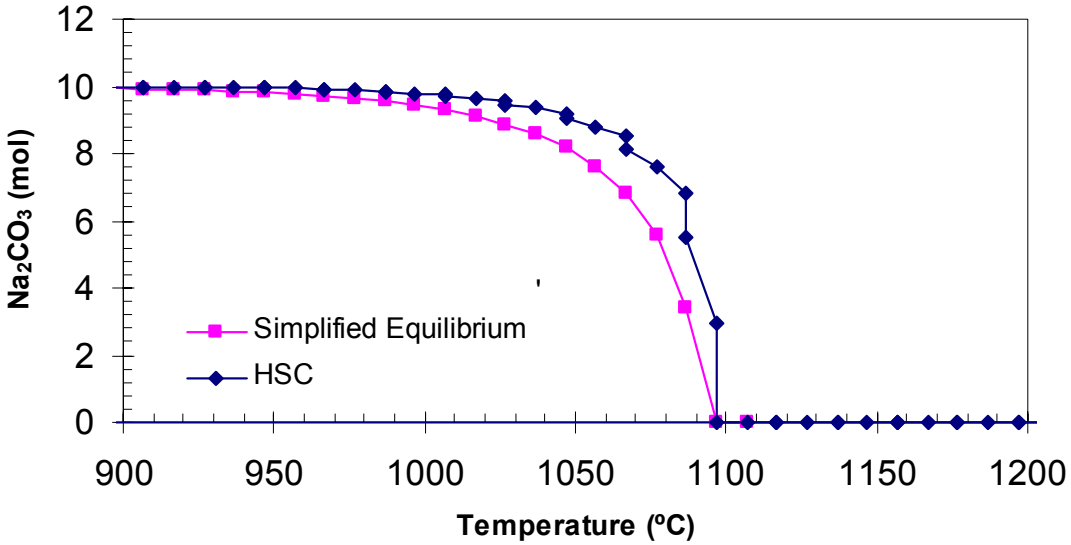

Figure 44: Sodium Carbonate Equilibrium at 50 mol of Nitrogen per initial mol of Na_2CO_3

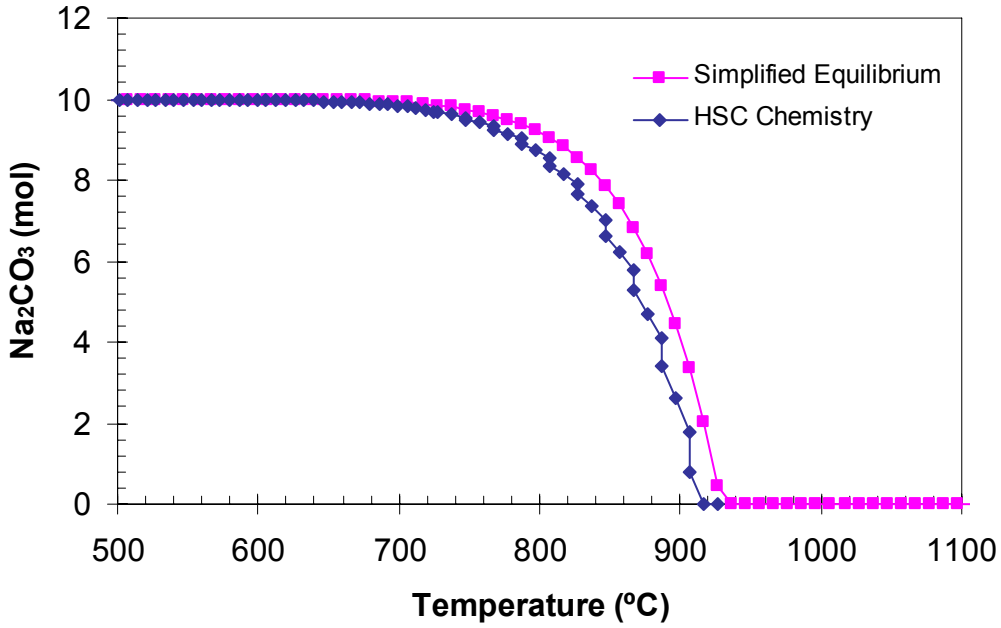

Figure 45: Sodium Carbonate Equilibrium at 1 mol of Nitrogen per initial mol of Na_2CO_3

The equilibrium concentration of sodium carbonate was calculated two different ways. The first way utilized HSC Chemistry 5.11© software, where N_2, Na(v), Na(l), C(pure carbon), CO, and CO_2 were included in the equilibrium calculations. The second way simply uses Gibbs energy to

calculate the equilibrium constant for the reaction shown in Equation (0-25). These two equilibrium calculations were compared and the simplified equilibrium calculation was deemed adequate, and included in the model, see Figure 44 and Figure 45.

$$Na_2CO_3 + C\,(carbon) \leftrightarrow 2Na_{(v)} + CO_2 + CO \qquad (0\text{-}25)$$

Model Limitations

A one-dimensional droplet model has several limitations. As explained previously, the boundary layer surrounding the particle is non-uniform. Also, the particle temperatures and composition vary with angular and radial position. Commonly, a particle's windward edges are hotter and burn out sooner than the leeward edges. Additionally, non-uniformity in furnace conditions leads to non-uniform particle heating.

As shown in Figure 46 particle shapes are far from spherical and the impact of the shape on conversion time and other properties can be dramatic. Capturing some of these complexities, such as the windward tendencies to burn out sooner and hotter than the leeward sides, lies within the grasp of multi-dimensional models, but others, such as the bizarre and rapidly changing shapes, depend on unknown and possibly stochastic processes that may prove very difficult to theoretically capture.

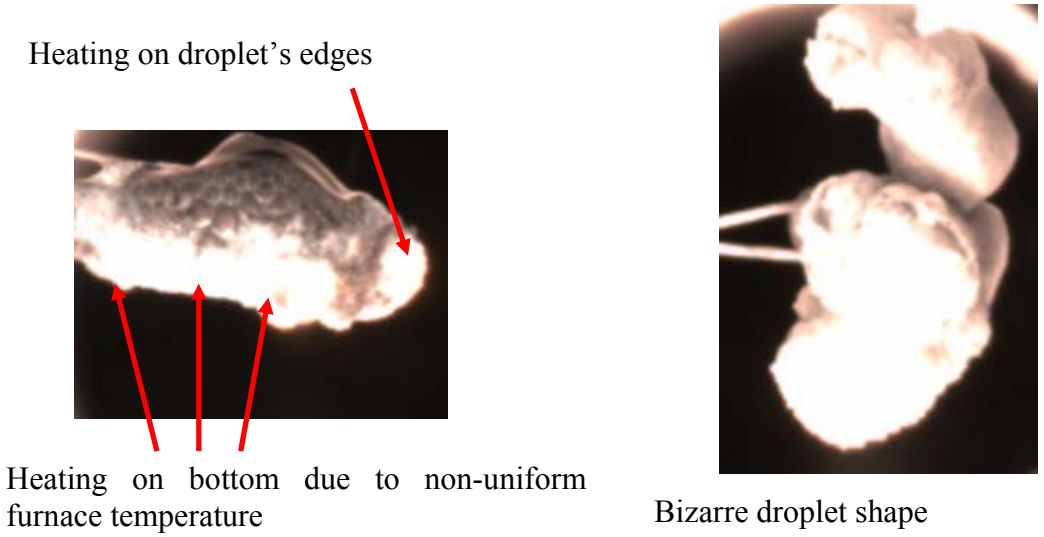

Figure 46: Illustration of Non-Ideal Behavior of Black Liquor Droplets

Modeling Results and Discussion

This chapter compares model predictions with the experimental data from the furnace and illustrates the effects of different assumptions on model predictions.

Comparison of Model Results with Experimental Data

This section discusses experimental data as compared to model predictions and problems associated with both. Additional comparisons appear in Appendix B.

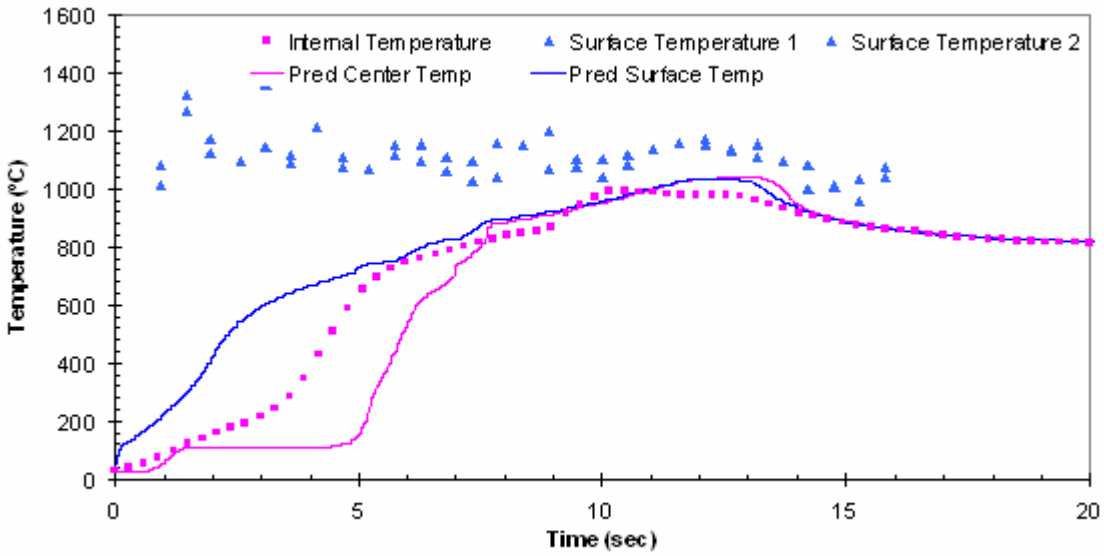

Figure 47: Temperature Profile for a 23.2 mg Droplet of BL A at 800 ºC in Air, Gas Velocity=0.37 m/s, 95% Solids

Figure 47 compares predicted to measured temperatures, the latter measured by the thermocouple (internal) and the camera pyrometry (surface) techniques. The temperature is a good indicator of the dominate combustion stage as well as the extent of conversion of the droplet. In this case, the model accurately predicts the stages of combustion; the internal temperature measurement lies between the predicted center and surface temperature during drying and devolatilization and follows a similar trend to the measured temperature during char burning and smelt oxidation. If the end of smelt oxidation is taken to be the final bump in the temperature curves (between 13-14 seconds), the model and the measured overall conversion times agree within less than 4 %.

The measured and predicted surface temperatures disagree substantially, especially in the early stages of combustion. As mentioned previously, the measured surface temperatures during particle heating are limited to regions of high temperature and are therefore biased toward high temperatures. Ip showed in his work that large temperature variations occur on the surface of the particle (about 400-500 ºC during char burning). However, measurements show no temperatures as low as the predicted temperatures.

One of the major assumptions in the model is that the gas species in the particle are in thermal equilibrium with the surrounding particle. This assumption results in dramatic cooling of the char surface by the escaping pyrolysis gases. Because of the large pore size in black liquor char, it is possible that path of escaping gas is not sufficiently tortuous to cause thermal equilibrium with the char. If the thermal equilibrium assumption were relaxed, it would increase the predicted temperature gradient and increase the predicted surface temperature. Considering the large pore size and the measured temperature gradients in the droplet, it appears that this assumption is not validated.

Figure 48 illustrates measured and predicted droplet mass histories. Predicted and measured droplet mass follow the same trend, but are offset by about 0.3 seconds. For this run, the droplet's initial and final weights were 23.2 and 8.5 mg, respectively. The model predicted a final mass of 6.5 mg for the droplet.

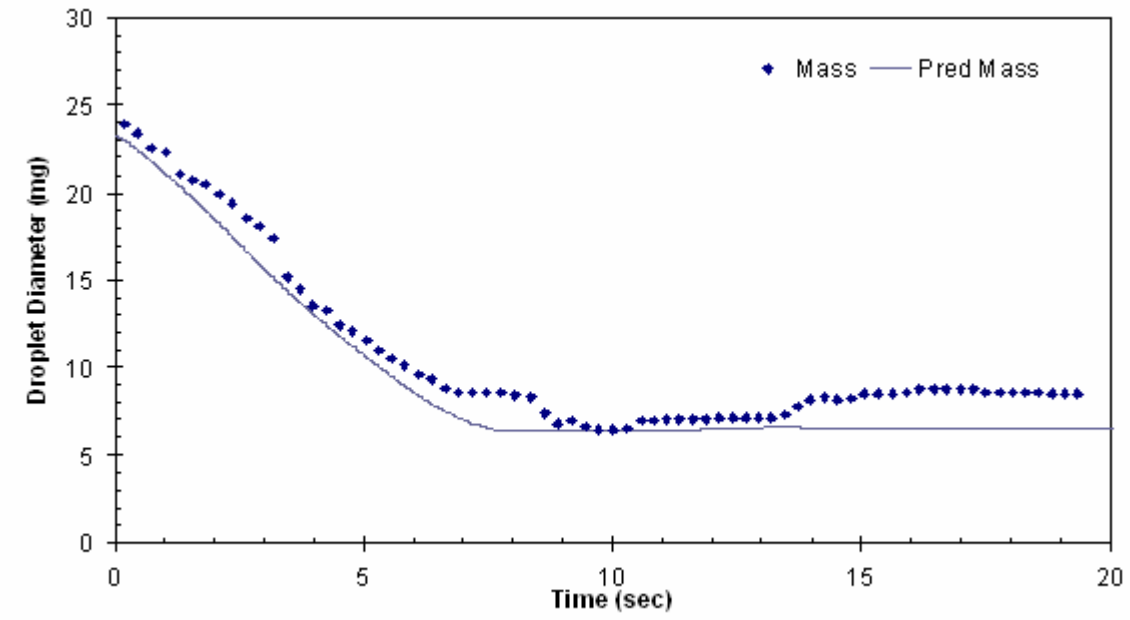

Figure 48: Particle Mass for a 23.2 mg Droplet of Black Liquor A at 800 ºC in Air, Gas Velocity=0.37 m/s, 95% Solids

Figure 49 illustrates predicted and measured particle diameters. Although the model appears to over-predict swelling at the beginning of drying, the first point shown on the graph is the diameter of the droplet based on the droplets mass. As shown in previous studies, the droplet swelling is almost immediate. The maximum predicted diameter is higher than that measured probably causing the predicted size decreases more rapidly than the measurements. The maximum size prediction could easily be corrected by iterating on the swelling coefficient. Droplet swelling behavior varies radically from sample to sample despite many efforts to homogenize the material and control conditions. Even though average swelling behaviors can be estimated with correlations, there appears to be inherent stochastic variations in the swelling behavior between droplets.

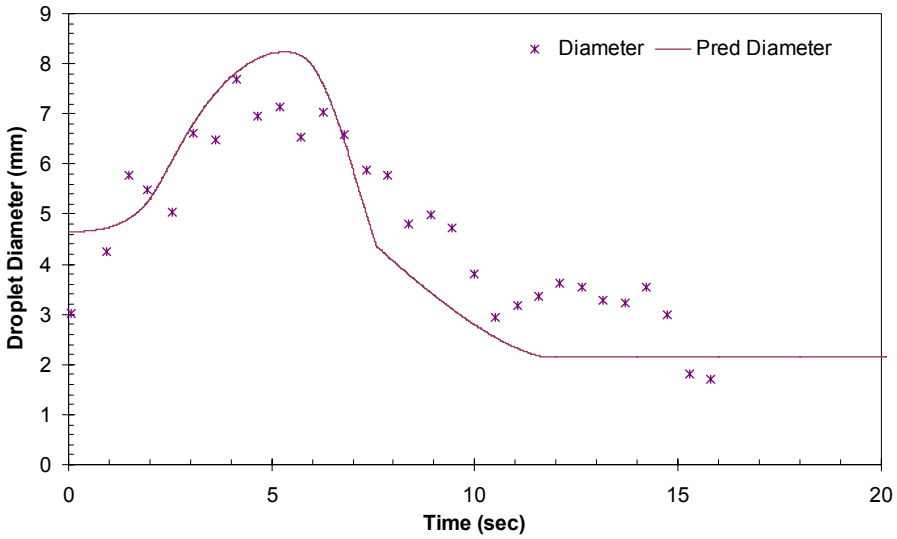

Figure 49: Particle Size for a 23.2 mg Droplet of Black Liquor A at 800 ºC in Air, Gas Velocity=0.37 m/s, 95% Solids

Effect of Typical Assumptions on Model Results

Black liquor combustion involves extreme behaviors in many respects compared to other low-grade fuels. With typically 30% moisture, it contains similar moisture to other biomass fuels. It experiences extreme changes in size and density. With a typical volume increase of 35 times its original volume and an associated mass loss of 50%, the particle's density decreases by up to two orders of magnitude between the initial value and the point of maximum swelling. The considerable swelling during periods of rapid heating contributes to large internal temperature gradients. The large quantity of inorganic species tends to increase the reactivity of black liquor very significantly, whereas in most fuels the ash can be assumed inert.

The following graphs show the effects of some modeling assumptions on black liquor combustion. The assumptions that have been included in this investigation are lumped capacitance (or an isothermal particle), no swelling, inert inorganic species, and no flame. This analysis relaxes each assumption sequentially to show the relative importance of each phenomenon. Table 14 indicates which assumptions are made for each prediction for a 2-mm particle in 1073 K air. The swelling model assumed β_B was assigned a value of 22. (see Section 0) The first prediction has the most simplifying assumptions and is the simplest model, and the last prediction has the fewest assumptions and is the most sophisticated and accurate.

Table 14: Modeling Assumptions Included in Prediction

	Prediction Number				
Assumptions	1	2	3	4	5
No Flame	Y	N	N	N	N

No Swelling	Y	Y	N	N	N
Isothermal	Y	Y	Y	N	N
Inert Ash	Y	Y	Y	Y	N

Figure 50 shows the predicted droplet surface temperature during burning under different assumptions. Prediction 1 has the slowest overall conversion time. Prediction 2 shows the effect of a flame on the particle. The flame increases the surface temperature during devolatilization by 70 ºC. The overall conversion time is almost identical for the first two predictions, Figure 51 shows that the flame accelerates devolatilization and decelerates char burning, leading to largely offsetting influence on overall particle conversion time. During devolatilization, a flame forms inside the boundary layer, producing higher particle heat fluxes, thus accelerating devolatilization. During char burning, partial oxidation of carbon monoxide consumes some of the oxygen that would otherwise react at the surface. Because char gasification with carbon dioxide and water is slower than oxidation with oxygen, char burning decelerates. Prediction 3 shows the effect of swelling on the particle's reactivity. Swelling decreases conversion time by half (from 11.5 s down to 5.5 s). Of all of the modeling assumptions, swelling has the most dramatic effect on the conversion time. Prediction 4 shows the effect of the isothermal assumption. Internal temperature gradients tend to increase the estimated conversion time, in this case by about 0.5 seconds.

Prediction 5 shows the impact of the inorganic chemistry. The inorganic species reactions increase particle temperature during char burning. The inorganic species reactions also increase the overall conversion time. This increase in conversion time is somewhat counterintuitive considering it involves including additional char consuming reactions. It occurs for two reasons. First, the inorganic species decrease the particle size during char conversion. During the early part of char conversion, sulfate reacts with char to produce CO_2 and sulfide. This char conversion decreases droplet size, thus decreasing total mass transfer (though increasing mass flux). Second, the sulfate/sulfide cycle is less efficient in its oxygen use than is direct oxidation of char with O_2. Although the sulfate donates all of its oxygen to char, the product of this reaction is CO_2, which is much less reactive than O_2, and much of the carbon leaves the droplet as CO_2. In the case of direct oxidation of char with O_2, much of the carbon leaves the particle as CO.

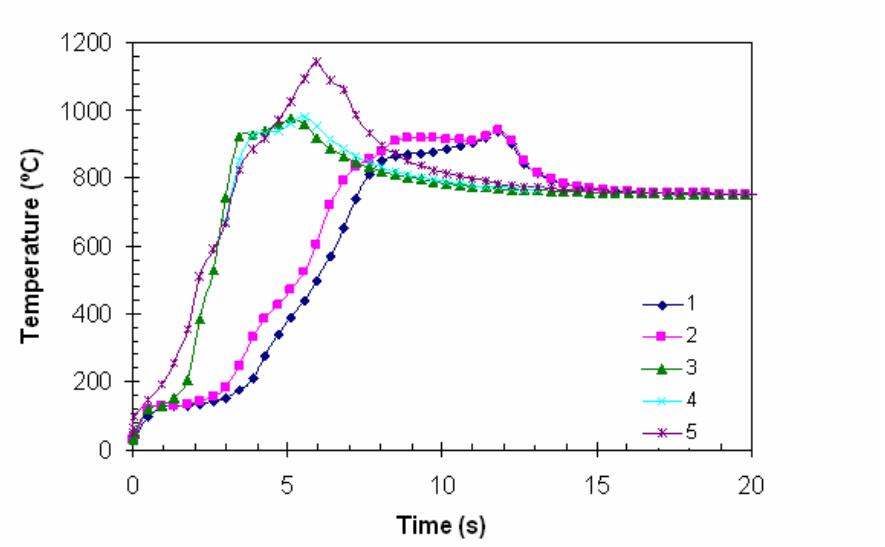

Figure 50: Surface Temperature Predictions of a 2-mm Droplet in 750 ºC Air and 0.2% Water Vapor, Gas Velocity .30 m/s

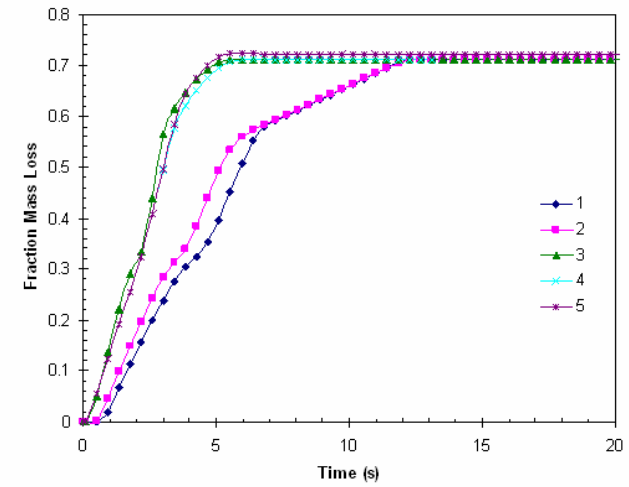

Figure 51: Predicted Fractional Mass Loss of 2-mm Droplet in 750 ºC, Air and 2% Water Vapor, Gas Velocity .30 m/s

Prediction 5 indicates a large temperature spike due to the sulfide oxidation. After char conversion, the particle cools slower for prediction 5 because of sulfide oxidation reactions that continue after char burning.

Comparison to MBMS Data

The molecular beam mass spectrometer sampled the off-gases from the burning particle. If the off-gas sample is a representative sample, then the water peak should indicate the relative water evaporation rate plus the hydrogen oxidation rate. In addition, if one assumes complete combustion, the carbon dioxide concentration indicates the rate of carbon loss. Integration of these peaks over time yields the fractional water loss and carbon loss from the droplet.

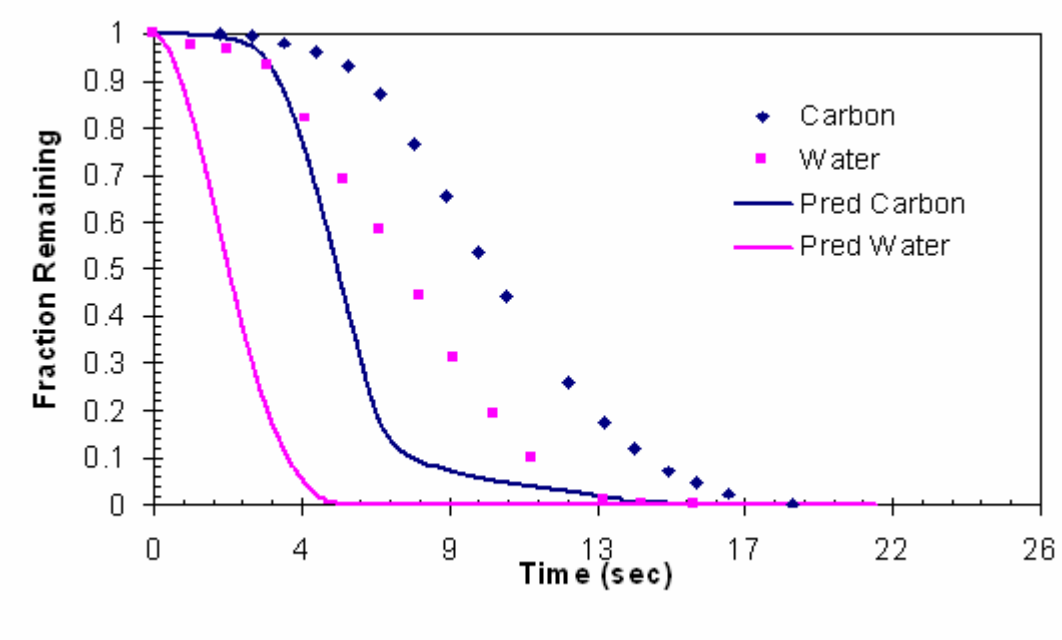

Figure 52: Fraction Carbon and Water Remaining in a 17.3 mg Droplet of Black Liquor D in Air at 750 ºC, Gas Velocity = 0 m/s, Solids=70%

Figure 52 illustrates carbon and water fractions remaining in the droplet as measured by the MBMS compared to those predicted by the model. Obvious discrepancies appear between the measurements and the model predictions. The major difference is a time shift between the model predictions and the measurements by approximately 5-6 seconds. This discrepancy arises from the residence time of gases in the sample train prior to entering the MBMS. Not only is the measurement approximately 5-6 seconds behind the prediction, but the total times for evaporation and carbon conversion are 5-6 seconds longer than those predicted. This indicates that there could be about 5-6 seconds of mixing before the sample is measured. However, the difference in the shape of the curves may indicate that there is a mechanism that is not accurately accounted for in the model. This issue could be resolved by changing the gas flow patterns in the furnace.

Sulfate/Sulfide Cycle

The sulfate/sulfide reactions, as explained in Section 0, oxidize char. From the model prediction, this mechanism is the most significant mechanism for char conversion by an inorganic species. Figure 53 shows the model prediction of the major inorganic species and indicates that carbonate decomposition is minimal during combustion at the specified conditions. On the other hand, the sulfate decreases to approximately 23% of its initial mass and then re-oxidizes after char conversion is complete. Sulfate oxidation accounts one-sixth of the char conversion to carbon dioxide.

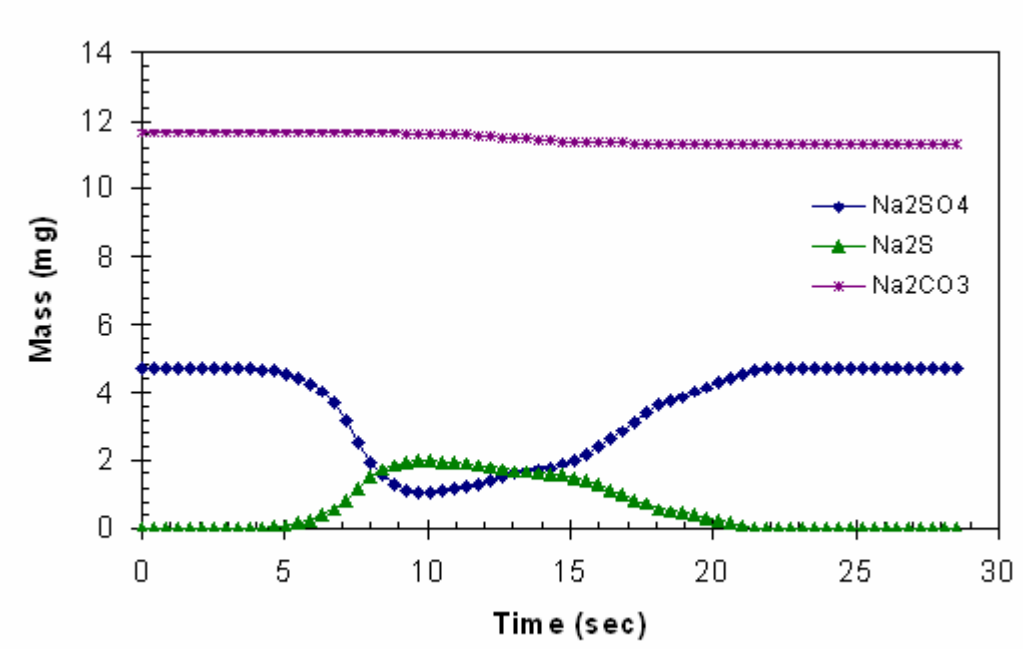

Figure 53: Major Inorganic Species for a 23.2 mg Droplet of Black Liquor A at 800 ºC in Air, Gas velocity=0.37 m/s, 95% Solids

Conclusions and Recommendations

This chapter summarizes the general conclusions to the thesis, including results derived from the both the experimental and the modeling results. It will also give recommendations for future work.

General Conclusions

Experimental data from a novel single droplet reactor include simultaneous internal temperature, surface temperature, size, imaging and mass data. These simultaneous data offer insight into black liquor combustion mechanisms and provide computer code validation information. They are especially useful because of accurate furnace characterization (gas flow rates and furnace temperature). These mechanisms include, but are not limited to, particle drying, swelling, devolatilization, heatup, oxidation, and smelt agglomeration.

Particle drying can be modeled using a modified Raoult's Law expression, where the mole fraction of water is replaced by a mass fraction expression. Mole fractions are difficult to define when dealing with black liquor and similar natural components. The model predictions agreed with measurements within their uncertainty limits.

New particle devolatilization parameters were regressed and validated. Devolatilization parameters yielded accurate amounts and rates of char and gas formation, as is further indicated from the prediction accuracy of char burnout times.

Char burnout time predictions and measurements are in good agreement. Most chars burn at or near diffusion limited conditions, therefore these data provide little information on char burnout kinetics. They are representative of commercially significant char particle sizes and conditions.

An expression for the film thickness was developed for a one-dimensional flame layer that both predicts the presence of a flame and accurately accounts for species steady-state heat/mass transfer in inert environments.

Large internal temperature gradients, greater than 280 ºC/mm, form during combustion (typically during drying/devolatilization). The model, however, does not predict such large temperature gradients in the particle. This discrepancy possibly arises from the model assumption that the gas and the condensed phases are in thermal equilibrium. Because of the large pores, the path of escaping gases may not be sufficiently tortuous to cause thermal equilibrium. This assumption may lead to another model deficiency, that the maximum predicted surface temperature is consistently lower (never higher) than the measured surface temperature, by approximately 50-150 ºC.

When considering chemical equilibrium, the presence of carbon monoxide and carbon dioxide make sodium carbonate reactions with char almost negligible below 800 ºC. However, sodium sulfate reactions with char are not reduced significantly by equilibrium considerations, and the sulfate/sulfide cycle is an important mechanism in char conversion.

Smelt agglomeration during char burning exposes new char to the droplet surface. This mechanism minimizes the heat- and mass-transfer resistance to the char. To account for this mechanism in the model, neighbor nodes gradually donate mass to the outer cell, thus allowing char to be present in the surface cell throughout all of char burning.

Predictions change significantly as modeling assumptions change. Swelling strongly impacts reaction rates, decreasing overall conversion times by approximately 50%. Inorganic chemistry, internal temperature gradients, and the flame boundary layer also impact overall reaction rates by measurable amounts.

Recommendations

Future work on the model should include work to increase the speed of the code to make it more useful. When modeling industrial-scale recovery boilers, modern CFD codes trace thousands of particles. To be useful, a single-particle code has to run in less than a second. If the heating value of the black liquor could be specified as an input to the code, this would also be beneficial.

The current devolatilization mechanism does not require the conservation of elemental species, and for this reason it does not conserve energy. For example, during the devolatilization, black liquor can form char, tar, or to light gases. Char and light gas have very different empirical formulas; so depending on the reaction kinetics, the black liquor produces more carbon (in char) or more oxygen and hydrogen (in light gases). In addition, conservation of species and energy are not enforced in boundary layer. Between each time step, the boundary layer can either shrink or swell. The nodes are re-dispersed evenly throughout the boundary, but the initial temperature and the species concentrations are assumed to be what they were during the previous time step. Future work should be performed to remedy these problems.

Future work on the mass spectrometer should include changing the flow characteristics around the droplet to decrease the mixing with stale gas. In addition, orifice sizes and/or pumping design should change to allow the alignment of the skimmer orifices; this would increase the probability of detecting inorganic species.

Zero-dimensional Model Assumptions

A zero-dimensional transient model was built to regress pyrolysis kinetics. Starting points for the regression were taken from Font et al. and from a modification of their data, which better fit the char yields measured by Webster. Because very small droplets were used in the experiments, various new modeling assumptions could be implemented:

Heating rates were unaffected by the heat of devolatilization

Radiation was included

The particle size was initially 70 microns. (email from Kristiina Iisa, a Principal Research Engineer at the Georgia Tech, co-author of the papers reporting the kinetics data)

The particles swell from 2.7-3.0 times the initial diameter. (email from Kristiina Iisa)

Advection accounted for in the heat transfer

Carbonate decomposition controlled by forward reaction rate only. (Good assumption in environment was high in inert gases.)

No tar re-condensation

31.2% initial inorganic species

Carbonate formation is accounted for by initial carbonate composition

Carbonate and Sulfate reaction kinetics are those developed by van Hieningen

Explicit scheme for temperature calculation

Fully-implicit scheme for species continuity

Tar composition is that of benzene

Results and Modeling Predictions

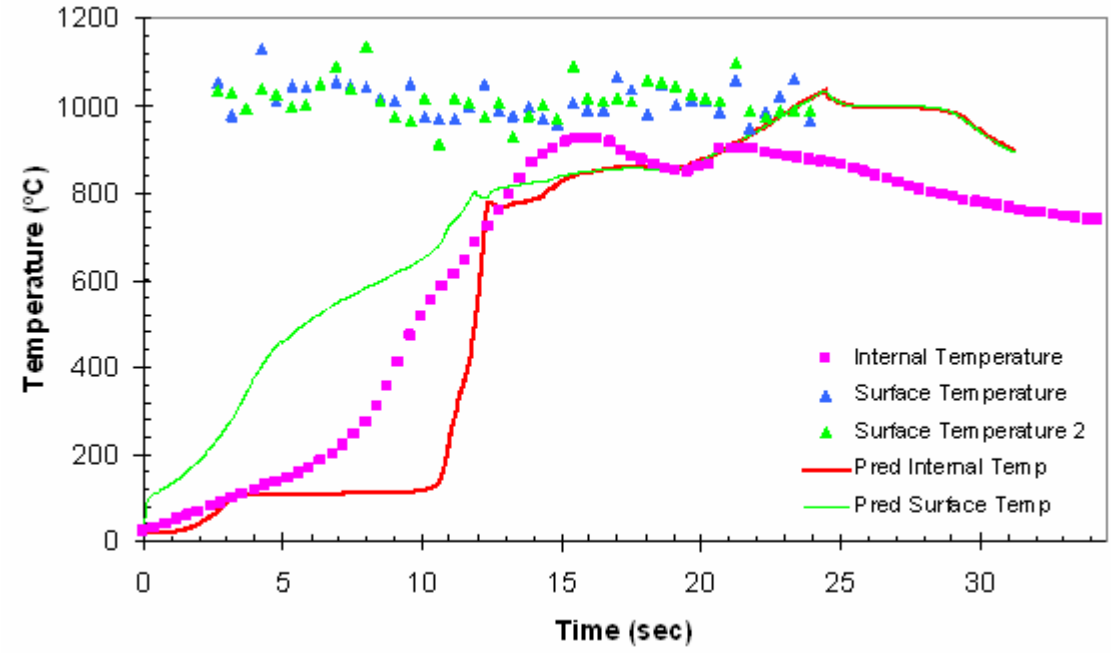

Figure 54: Temperature Profile for 59.3 mg Droplet of Black Liquor in 715 ºC Air, Gas Velocity=0.217 m/s, 70% Solids

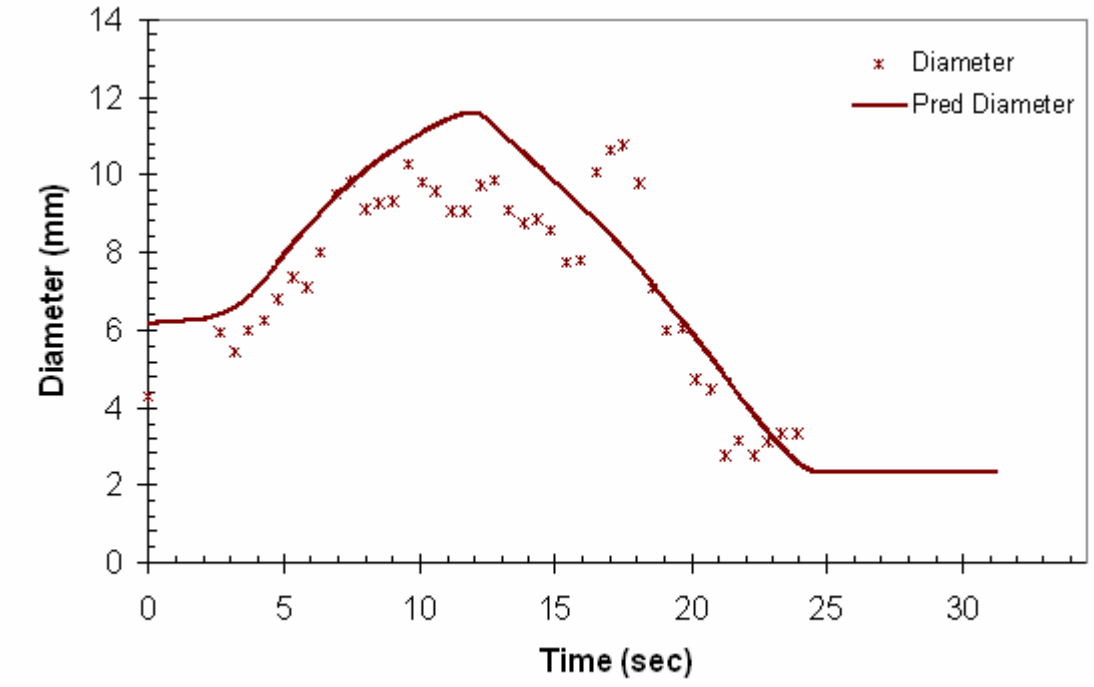

Figure 55: Diameter for 59.3 mg Droplet of Black Liquor D in 715 ºC Air, Gas Velocity=0.217 m/s, 70% Solids

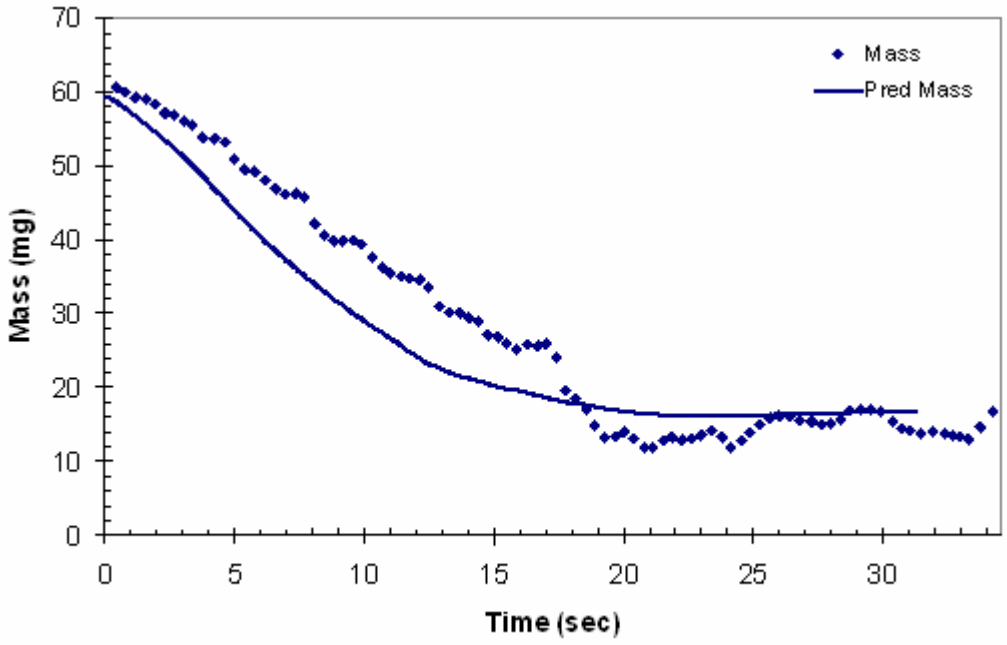

Figure 56: Mass for 59.3 mg Droplet of Black Liquor D in 715 ºC Air, Gas Velocity=0.217 m/s, 70% Solids

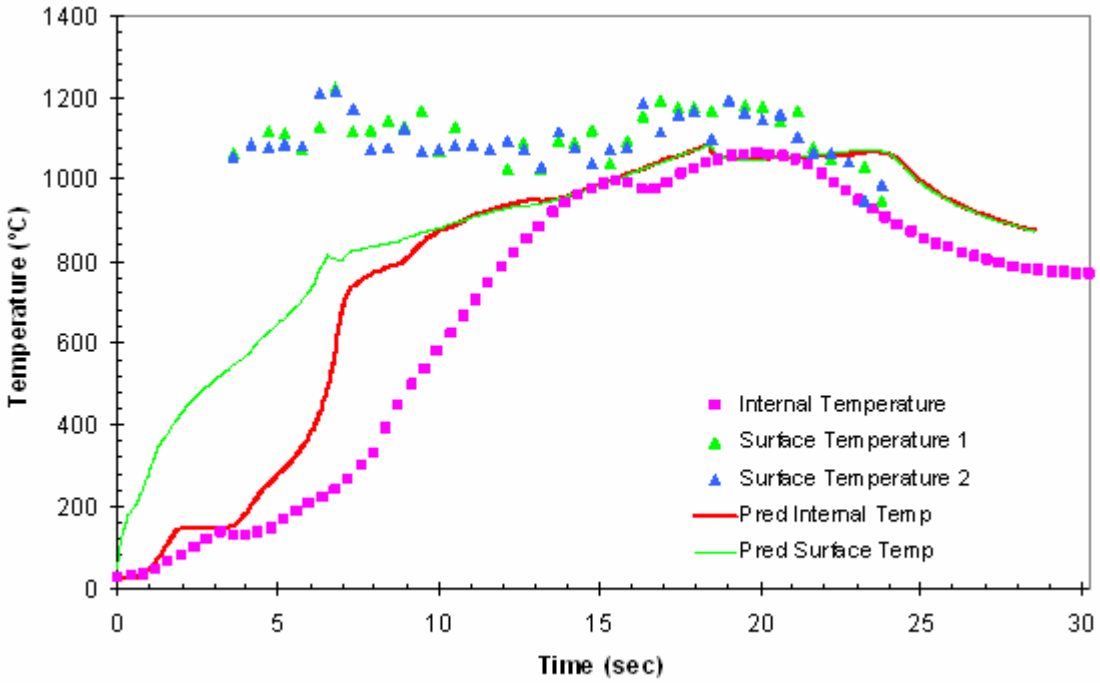

Figure 57: Temperature Profile for 44.8 mg Droplet of Black Liquor A in 750 ºC Air, Gas Velocity=0.35 m/s, 95% Solids

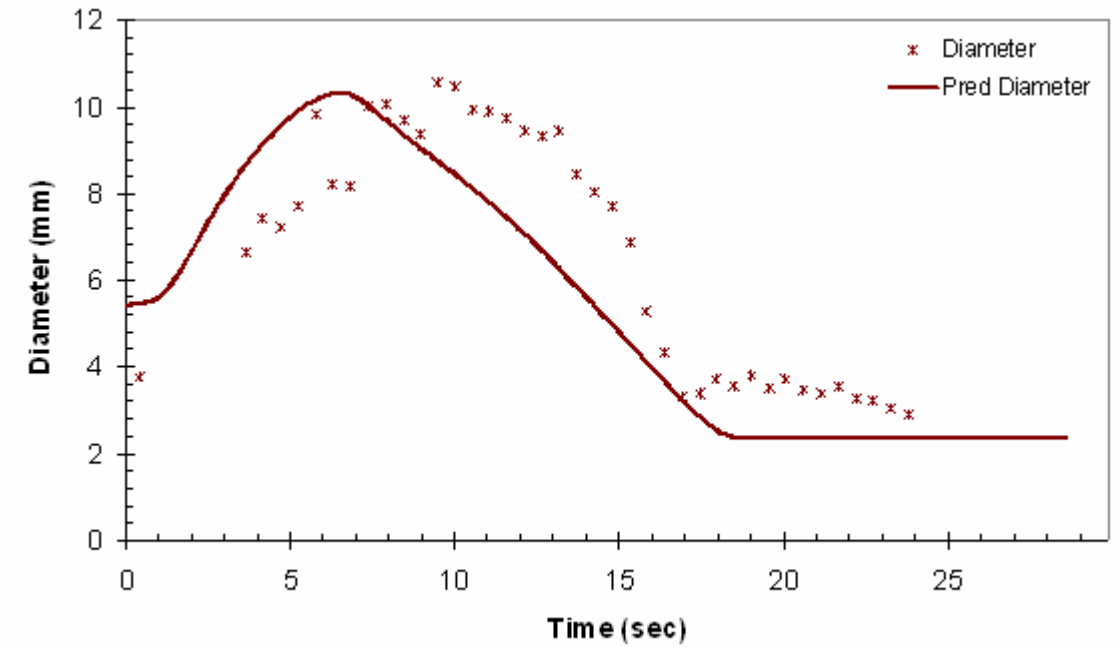

Figure 58: Diameter for 44.8 mg Droplet of Black Liquor A in 750 ºC Air, Gas Velocity=0.35 m/s, 95% Solids

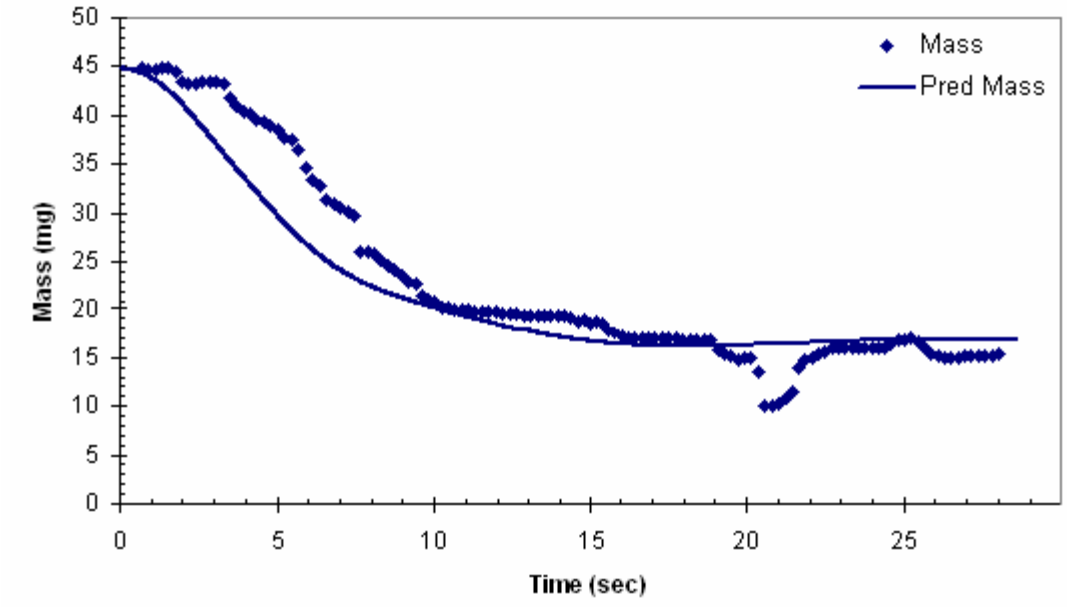

Figure 59: Mass for 44.8 mg Droplet of Black Liquor A in 750 ºC Air, Gas Velocity=0.35 m/s, 95% Solids

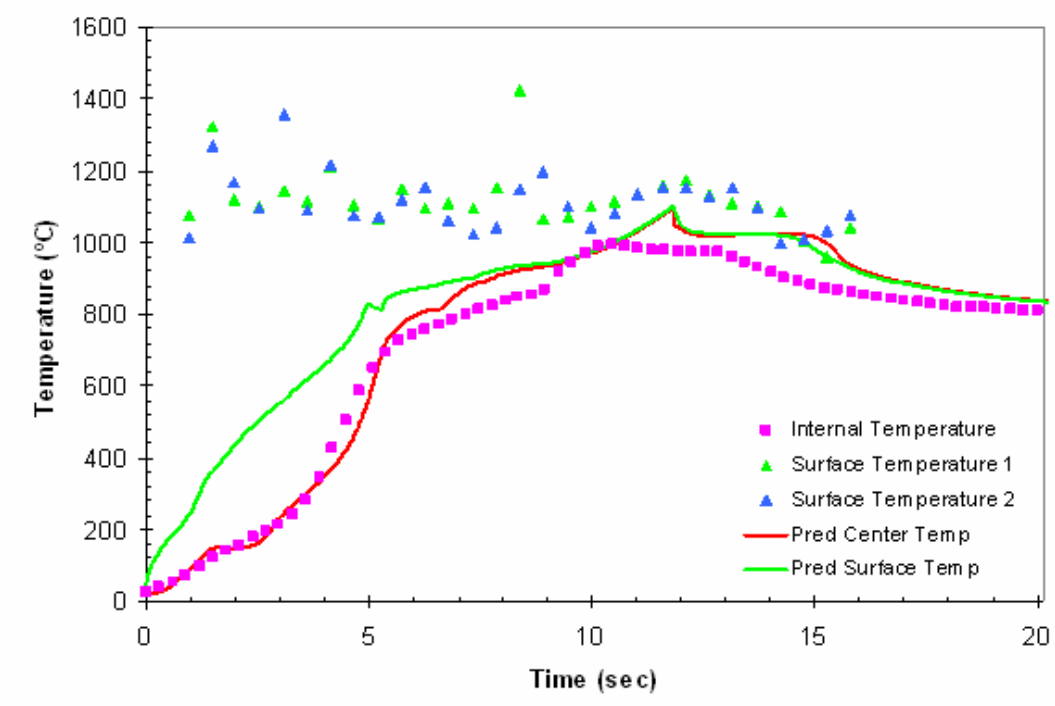

Figure 60: Temperature Profile for 23.2 mg Droplet of Black Liquor A in 800 ºC Air, Gas Velocity=0.367 m/s, 95% Solids

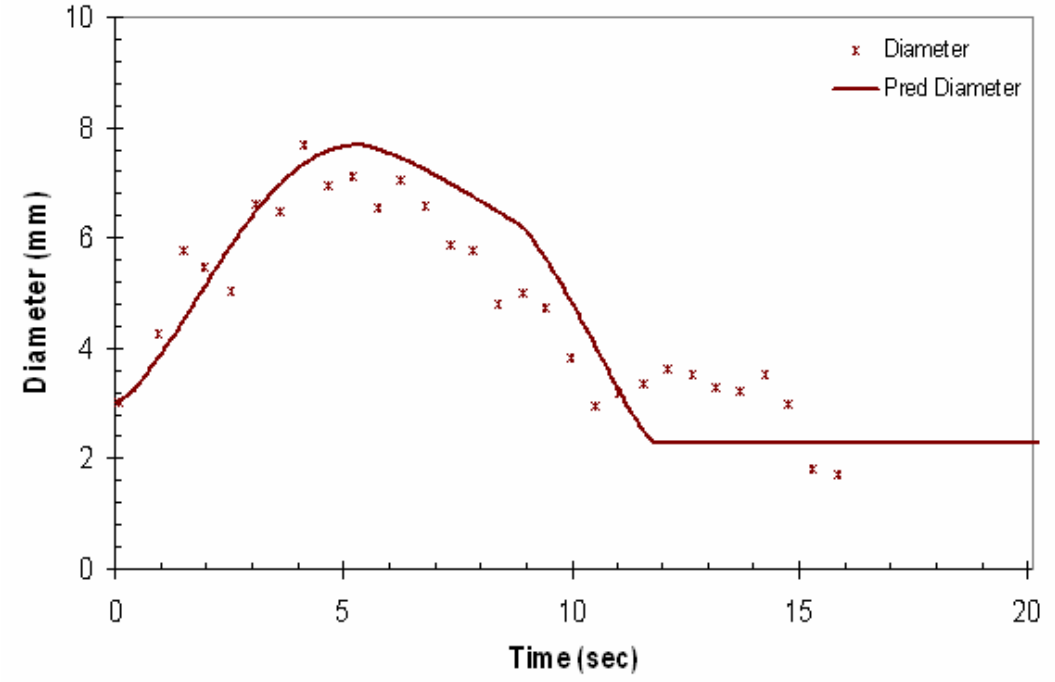

Figure 61: Diameter for 23.2 mg Droplet of Black Liquor A in 800 ºC Air, Gas Velocity=0.367 m/s, 95% Solids

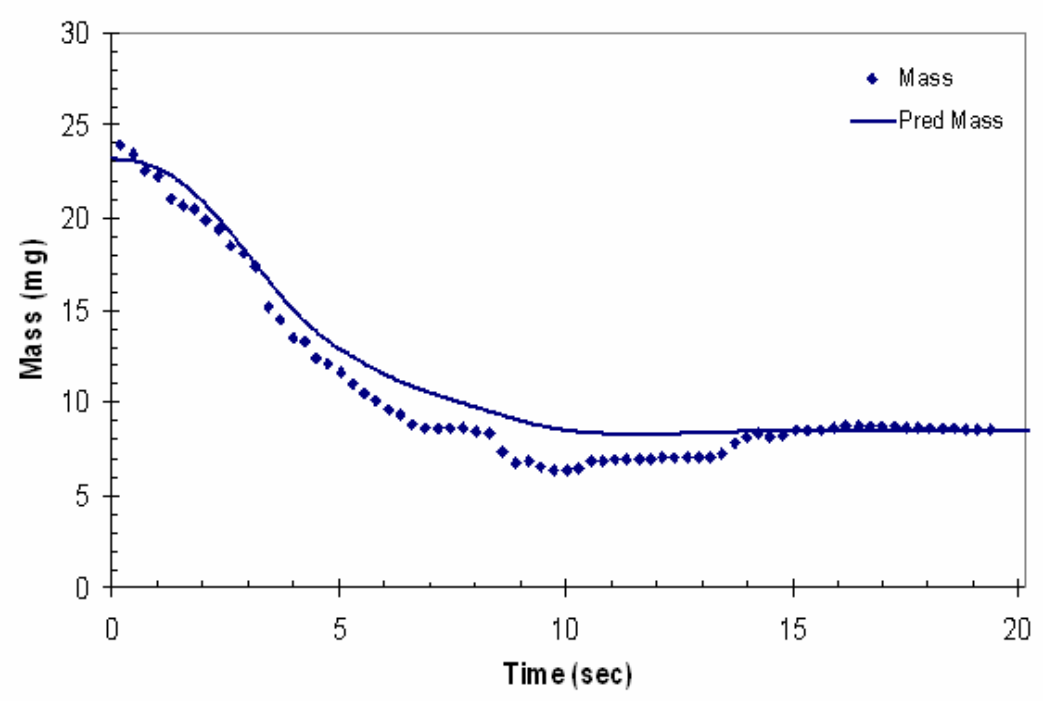

Figure 62: Mass for 23.2 mg Droplet of Black Liquor A in 800 ºC Air, Gas Velocity=0.367 m/s, 95% Solids

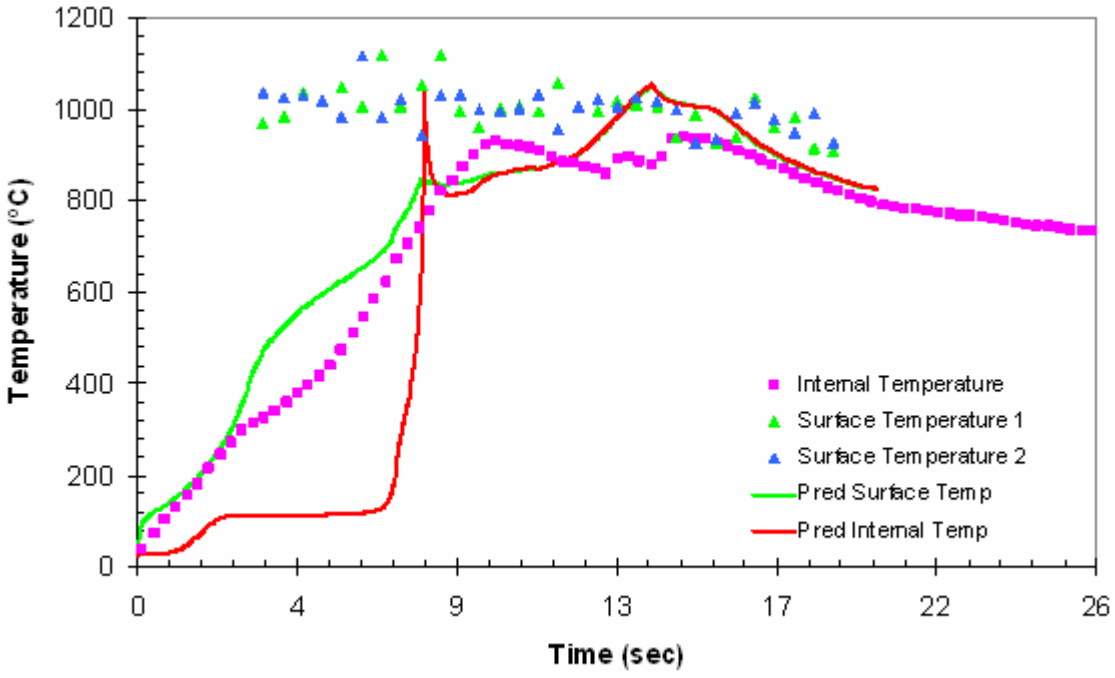

Figure 63: Temperature Profile for 27.9 mg Droplet of Black Liquor E in 715 ºC Air, Gas Velocity=0.217 m/s, 70% Solids

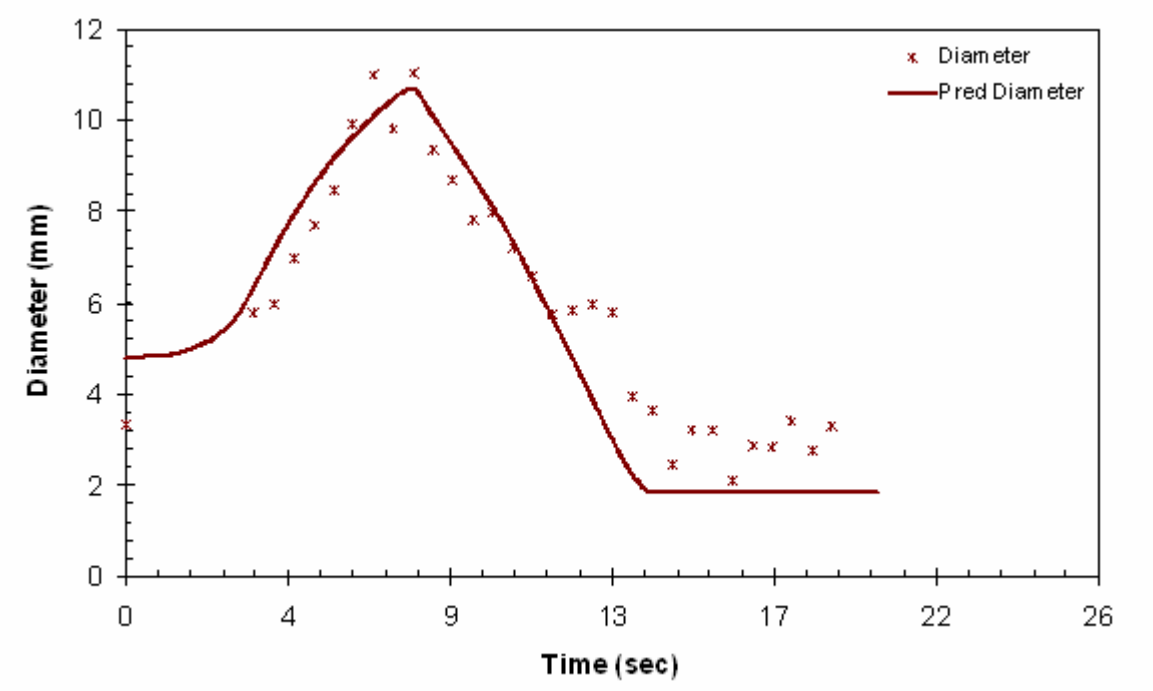

Figure 64: Diameter for 27.9 mg Droplet of Black Liquor E in 715 ºC Air, Gas Velocity=0.217 m/s, 70% Solids

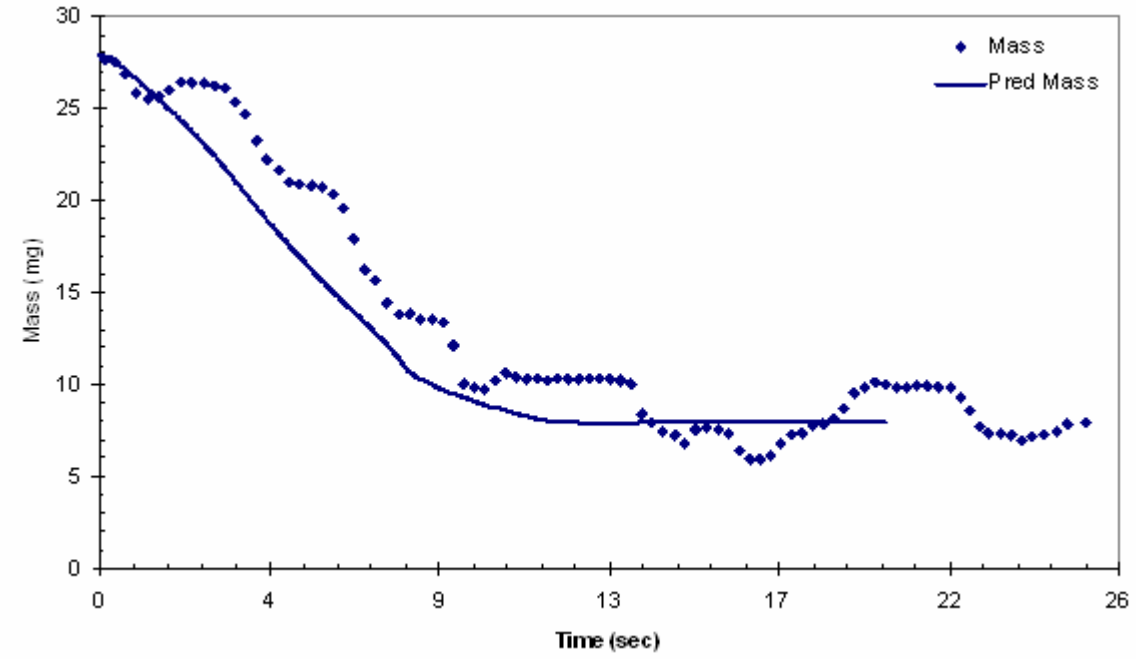

Figure 65: Mass for 27.9 mg Droplet of Black Liquor E in 715 ºC Air, Gas Velocity=0.217 m/s, 70% Solids

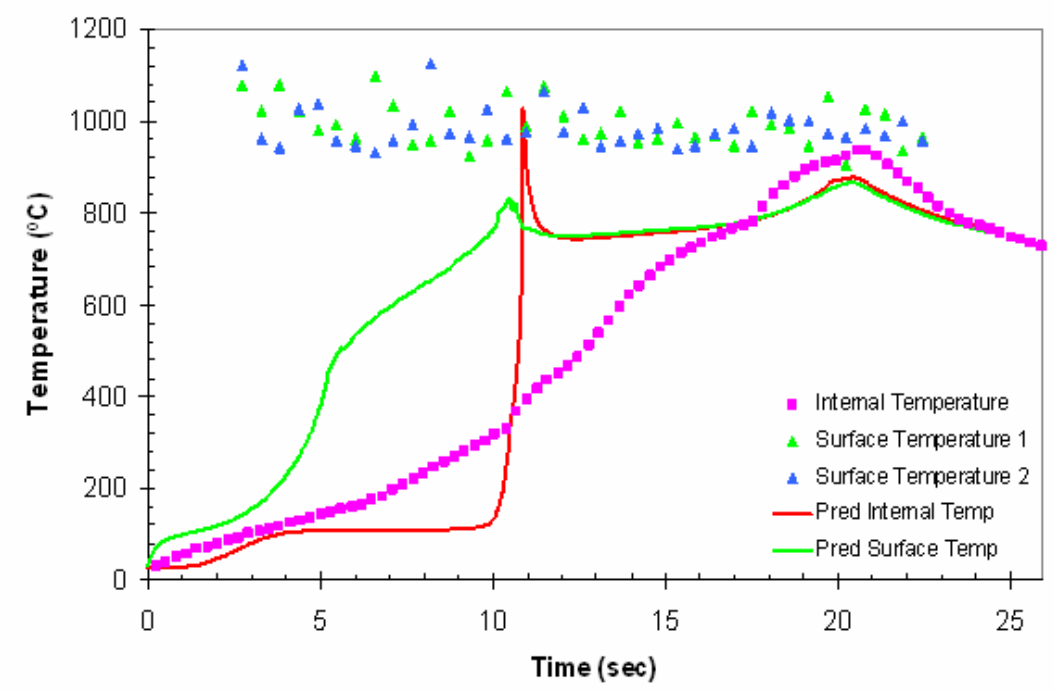

Figure 66: Temperature Profile for 41.9 mg Droplet of Black Liquor D in 662 ºC Air, Gas Velocity=0.32 m/s, 70% Solids

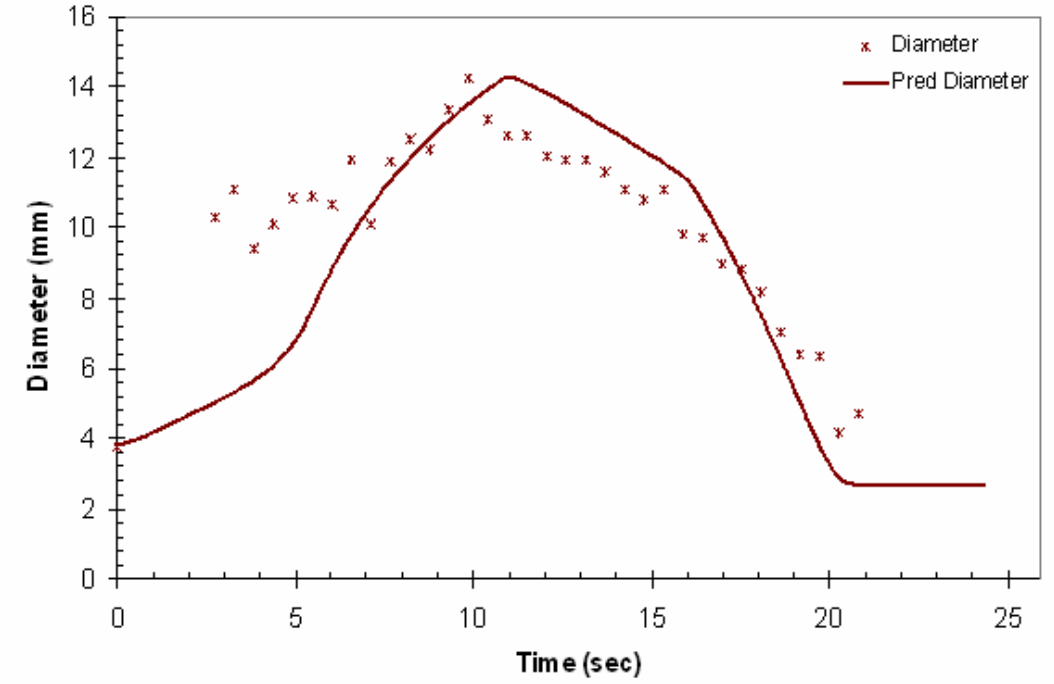

Figure 67: Diameter for 41.9 mg Droplet of Black Liquor D in 662 ºC Air, Gas Velocity=0.32 m/s, 70% Solids

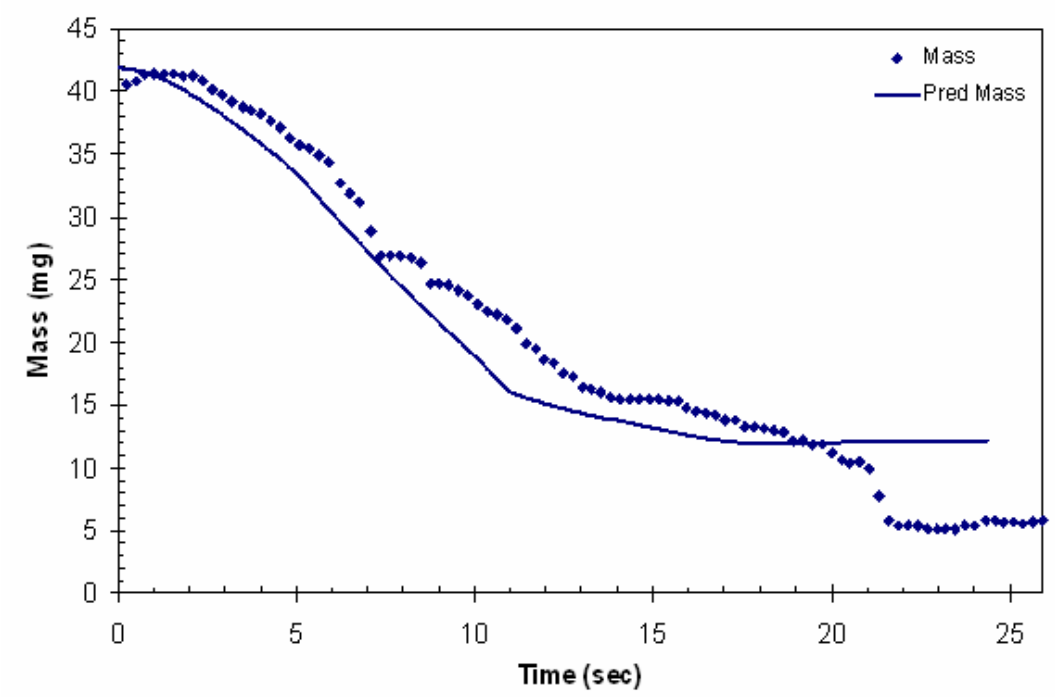

Figure 68: Mass for 41.9 mg Droplet of Black Liquor D in 662 ºC Air, Gas Velocity=0.32 m/s, 70% Solids

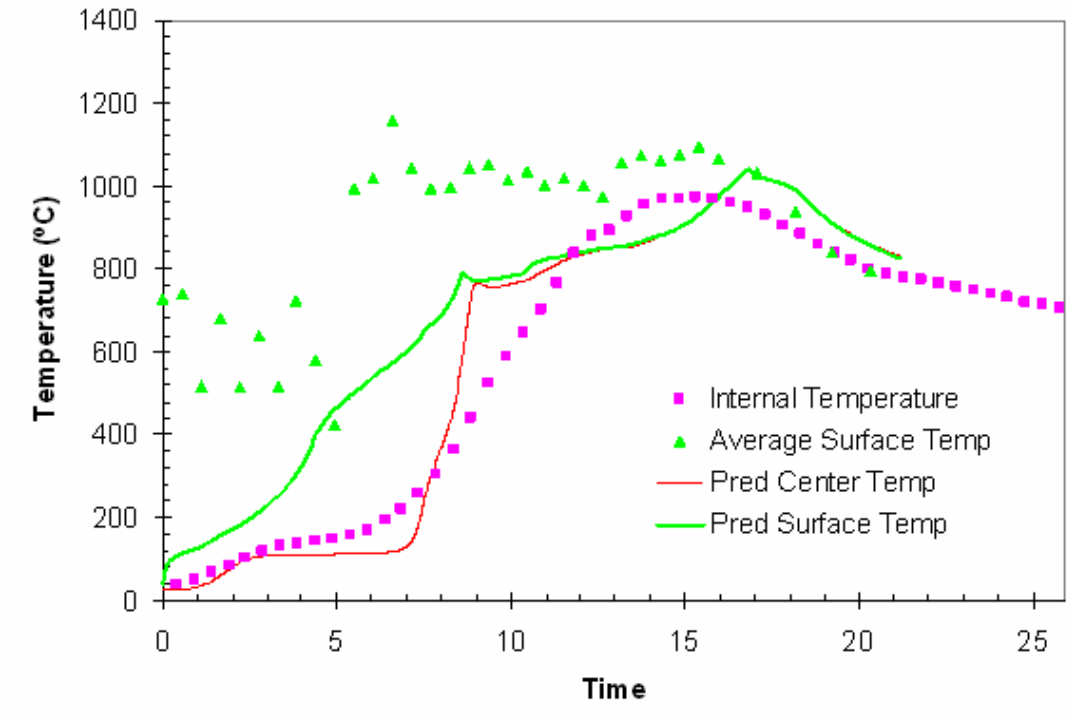

Figure 69: Temperature Profile for 26.6 mg Droplet of Black Liquor E in 650 ºC Air, Gas Velocity = 0.32 m/s, 70% Solids

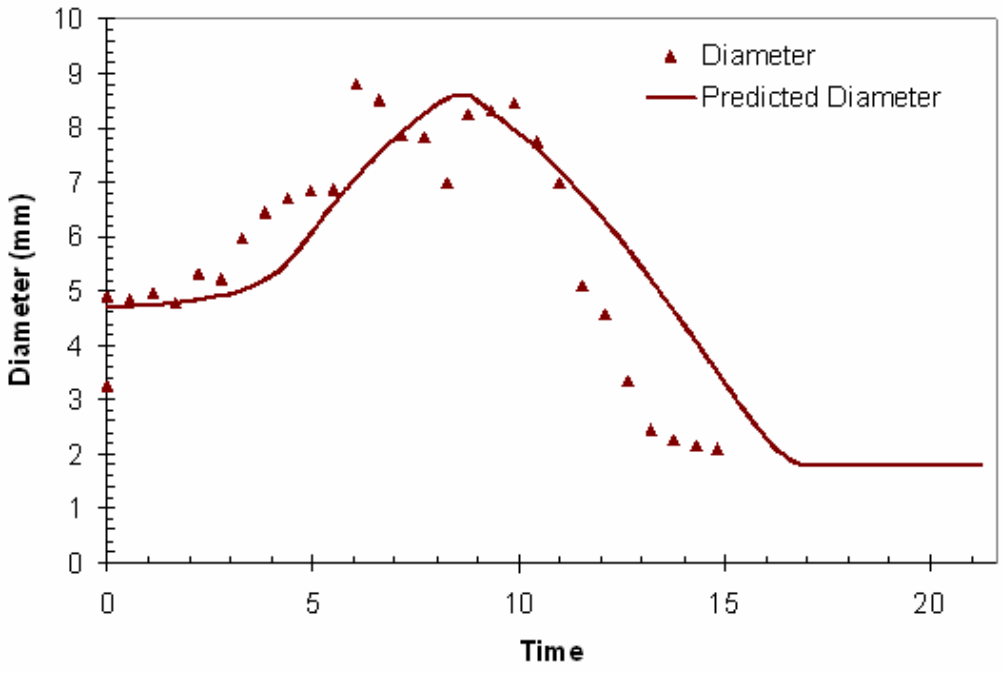

Figure 70: Diameter for 26.6 mg Droplet of Black Liquor E in 650 ºC Air, Gas Velocity = 0.32 m/s, 70% Solids

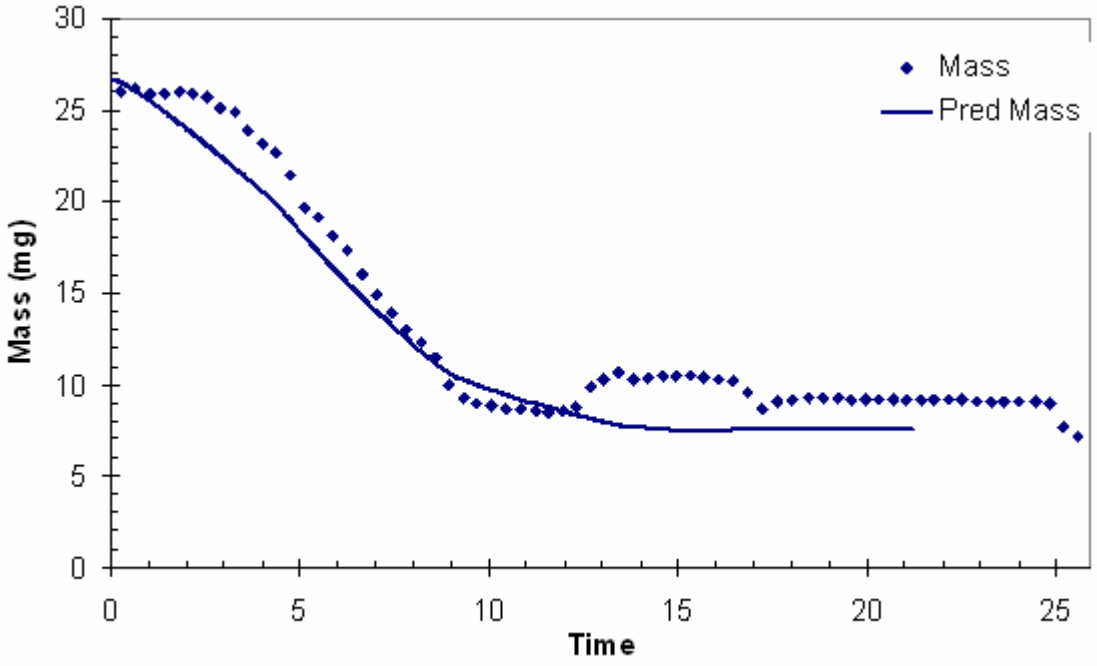

Figure 71: Mass for 26.6 mg Droplet of Black Liquor E in 650 ºC Air, Gas Velocity = 0.32 m/s, 70% Solids

Particle Combustion Code Manual

Introduction

This manual is intended to be useful as a guide to the user as well as the beginning programmer of particle combustion code. The code is meant to be a comprehensive 1-D particle model of all of the combustion process including drying, devolatilization, char burning, and for black liquor, smelt oxidations. The model describes both the processes that occur on the inside of the particle as well as inside the flame layer that surrounds the particle during devolatilization and char burning. It provides a summary of the approach used in the code to solve the system of governing partial differential equations as well as an explanation of the submodels used by the code. This manual can also be used as a reference to locate kinetic information and definitions of variables found in the code. The manual also contains a list of questions and explanations that may come up while becoming familiar with the code.

The code is based on the control volume method, and it uses the nomenclature from Patankar's book, *Numerical Heat Transfer and Fluid Flow*. It uses the power-law scheme for advection-diffusion terms, the SIMPLE algorithm for continuity/momentum, and the fully-implicit scheme for the transient term. (All of these are described in Patankar.)

The code is written in C++ and when running creates text output files for the values of all of the major variables. These output files contain the variable values at a specified time interval for each of the nodes. As a note, this code was built to describe both biomass and black liquor combustion. So some kinetic parameters and submodels will apply to one or the other, but not both. To avoid confusion, whatever applies only to biomass or only to black liquor will be specifically mentioned

Black Liquor Considerations

Black liquor combustion differs from and is generally more complex than most low-grade fuels, coal, biomass, and solid waste being the most typical examples of other low-grade fuels. For example, during drying and pyrolysis, the organic portion of black liquor converts from a liquid to a solid. During char burning, black liquor organic and inorganic material partially mix as a molten smelt and finally converts back to a solid as the smelt cools. Black liquor contains approximately 30% inorganic material while biomass ash contents ranges from less than 1 % for many clean heartwoods to over 20% for many clean herbaceous materials. Coal ash contents range less widely, typically hovering between 6 and 11 % (with some notable exceptions for lignites). However, in all cases the inorganic reactions with organic material during biomass and coal combustion are far less significant than during black liquor combustion. Reactions involving these inorganic species increase the complexity of the problem. During pyrolysis, black liquor swells to approximately 3-5 times the original diameter. This dramatically changes the heat and mass transfer both inside and to the particle.

Control Volume Approach

The control volume approach is one of the most widely utilized approaches for numerically solving systems of partial differential equations. This approach involves taking the calculation domain and breaking it up into control volumes. The governing partial differential equations are solved by integrating these equations over each of these smaller control volumes. The partial differential equations for the combustion model include the following: species continuity

equations, the energy conservation equation, and the overall continuity equation coupled with Darcy's Law. Each of the equations will be described in further detail later. To illustrate the control volume method on a simple case, a spherical 1-D heat conduction problem with a generic source term, S, will be employed.

$$\frac{1}{r^2}\frac{d}{dr}\lambda \cdot \mathrm{r}^2 \frac{\mathrm{dT}}{\mathrm{dr}} + S = 0 \qquad \text{(0-26)}$$

To solve this equation, the sphere is separated into control volumes of imaginary concentric shells. Nodes are located at the center of each control volume as illustrated in Figure 72. Now Equation (0-26) must be linearized. By multiplying through by r^2 and then integrating the differential equation over the control volume, Equation (0-27) is obtained, where the east and west control surfaces are indicated with lowercase e and w, respectively, see Figure 73. To integrate the source term, S, it is often assumed that the source term is constant over the control volume and evaluated at the conditions found at the node.

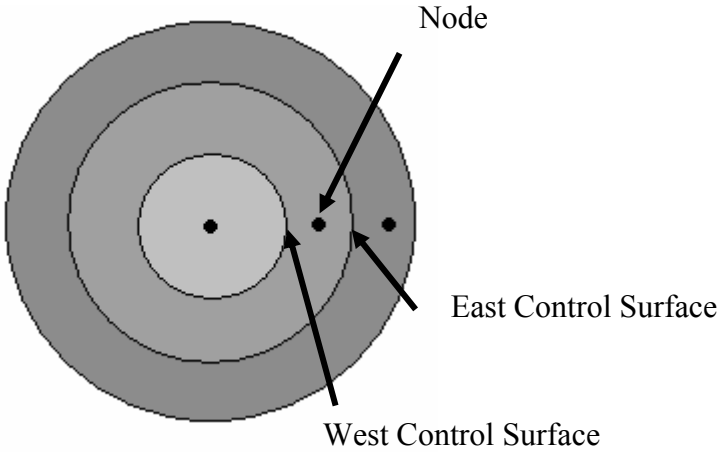

Figure 72: Particle Broken into Control Volumes

$$\int_{r_w}^{r_e}\left(\frac{d}{dr}\lambda \cdot r^2 \frac{dT}{dr} + S \cdot r^2\right)dr = 0$$
$$\left(\lambda \cdot r^2 \frac{dT}{dr}\right)_e - \left(\lambda \cdot r^2 \frac{dT}{dr}\right)_w + \frac{S}{3}\cdot\left(r_e^3 - r_w^3\right) = 0 \qquad \text{(0-27)}$$

Now, assuming that the remaining derivatives can be approximated with a linear profile between nodes, the partial differential equation becomes an algebraic equation:

$$\lambda_e \cdot r_e^2 \frac{(T_E - T_P)}{\delta r_e} - \lambda_w \cdot r_w^2 \frac{(T_P - T_W)}{\delta r_w} + \frac{S}{3} \cdot \left(r_e^3 - r_w^3\right) = 0 \qquad (0\text{-}28)$$

The subscripts W and E represent the adjacent west and east nodes, respectively, and P represents the node point of the current control volume. By integrating (0-26) in a similar manner for the adjacent nodes, a system of algebraic equations is formed. When the boundary conditions are specified, the system consists of an equal number of equations and unknowns. For 1-D problems, this system of equations can be solved very efficiently using a tri-diagonal matrix algorithm (the Thomas algorithm as described by Patankar).

The source term, S, in many cases is dependent on the temperature in the cell. Since the goal is to linearize the differential equations, the source term should also be linearized:

$$S = S_P \cdot T_P + S_C \qquad (0\text{-}29)$$

When solving the system of linear equations, it is convenient to solve for T_p and then put the equation into a standard form.

$$\left(\frac{\lambda_e \cdot r_e^2}{\delta r_e} + \frac{\lambda_w \cdot r_w^2}{\delta r_w} - \frac{S_P}{3} \cdot \left(r_e^3 - r_w^3\right)\right) \cdot T_P = \frac{\lambda_e \cdot r_e^2}{\delta r_e} \cdot T_E + \frac{\lambda_w \cdot r_w^2}{\delta r_w} T_W + \frac{S_C}{3} \cdot \left(r_e^3 - r_w^3\right) \qquad (0\text{-}30)$$

Standard Form

$$a_P T_P = a_E T_E + a_W T_W + b \qquad (0\text{-}31)$$

where

$$a_E = \frac{\lambda_e \cdot r_e^2}{\delta r_e}$$

$$a_W = \frac{\lambda_w \cdot r_w^2}{\delta r_w} \qquad \text{(0-32)}$$

$$a_P = a_E + a_W - Sp\frac{\left(r_e^3 - r_w^3\right)}{3}$$

$$b = \frac{Sc}{3} \cdot \left(r_e^3 - r_w^3\right)$$

Temporal and Spatial Grids

Node Spacing

This code uses a one dimensional grid and follows an east/west nomenclature, see Figure 73. The node of interest in the diagram below is labeled *P* with nodes *W* and *E* as its neighbors. The dashed lines represent the surfaces of the control volume. The variables dr_w and dr_e are variables that respectively represent the distances from the center of the node to the center of the adjacent west and east nodes. The variable Δr is the width of the control volume or the distance between the two control volume surfaces. In most cases, the control volume surfaces are located midway between the nodes. At the boundaries (the particle's center and surface), there are "half cells," where the node is located at the boundary.

Typically, the nodes are equally spaced inside the particle. Outside the particle (in the flame region), the nodes are also equally spaced; however, they are spaced differently than the inside nodes. The code calculates and stores the values of species concentrations, pressure, gas density, porosity, and temperature for each node location. The array index *1* corresponds with the cell in the center of the particle. For example, *den_CC[1]* corresponds to the char density in the center of the particle. The index *NR* corresponds with the cell at the outer boundary. To achieve this equal spacing, the control volumes have to be redefined after each time step because of the non-uniform swelling and shrinking of the particle.

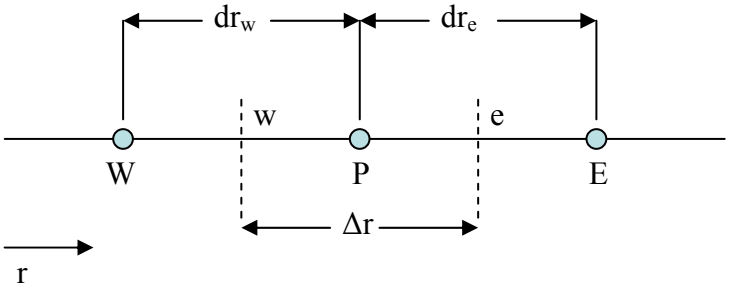

Figure 73: Grid-Point Cluster for the One-Dimensional Problem

The variables r_p, r_e, and r_w represent the locations of the cell center (node location), east cell boundary and west cell boundary, respectively. The code also keeps track of a variable that is similar to the volume of the control volume, *dv* and *dv_prev*, where the post script *prev* denotes the value at the previous time step. These variables originate from the integration of r^n that appears in the transport equations, see Equation (0-33). In this equation, n is 0 for Cartesian coordinates, 1 for cylindrical and 2 for spherical. For stability, the grid for the velocity is staggered from the pressure, meaning that velocities are calculated and stored at the control volume surfaces.

$$\int_{rw}^{re} r^n dr = \frac{r_e^{n+1} - r_w^{n+1}}{n+1} = dv \qquad (0\text{-}33)$$

The Time Step

The variable *time* represents the time of the current time step. While *time* = 0, no calculations are made, but all of the property arrays are initialized. The variable *dt* represents the time step. All time variables are in seconds. To improve convergence the time step can be changed as well as under-relaxation factors. Currently the code uses a constant time step of 0.001 seconds.

Properties Initialization

Each node has a label, starting from *1* for the inner most point to *NNRR* for the outer most point, where the variable *NNRR* is specified by the programmer but is always greater than 2. Properties such as temperature and concentration are stored in arrays. Two extra points are added to each of these arrays. One of these points, the *0* point, is not used at all. The reason for this is to set the origin of all of the arrays at one because of the preference of the programmer. Also the *NNRR+1* point is not used. Changing the origin to zero and deleting the *NNRR+1* location from the arrays would decrease the memory requirement of the code if that becomes an issue.

For the first time step all of the properties are set to their initial values. After convergence of each time step, the parameter values are stored in arrays with the postscript *_0*, *0*, or *_prev* for use during the subsequent time step. Variables that carry the postscript *_ini* store the initial values of the properties.

Gas-phase Species Continuity Equation

Because the conservation equations for all gas-phase components include temporal and spatial gradients and source terms that follow the same form, it is appropriate to first treat the species continuity equation in general. Afterwards, subsections will cover the source terms for some of the individual species. Equation (0-34) is the species continuity equation in spherical coordinates, where Y_j represents the mass fraction of species j in the gas phase, ρ_g represents the gas density, ε is the porosity, and D_{eff} is the effective diffusivity in the particle. The first term is referred to as the transient term and accounts for the change in concentration with time. The second term is the advection term. The third term is the diffusion term, and the last term is the source term. The source term accounts for chemical reactions or condensation/evaporation of species. This section will describe the assumptions made when each of the terms is descretized.

$$\frac{\partial}{\partial t}\varepsilon\rho_g Y_j + \frac{1}{r^n}\frac{\partial}{\partial r}(r^n \varepsilon\rho_g Y_j u) = \frac{1}{r^n}\frac{\partial}{\partial r}(r^n \varepsilon D_{eff,j}\rho_g \frac{\partial Y_j}{\partial r}) + S_j \qquad (0\text{-}34)$$

The Transient Term

The method used to solve the transient equations is the fully-implicit method. Originally the code solved the condensed-phase species equations using the Runge-Kutta method. The use of a combination of the fully-implicit method for the vapor phase and Runge-Kutta for the condensed phase caused numerical instability; so, the condensed-phase method changed to be solved using the fully-implicit method. The stability of fully-implicit method in comparison with explicit or semi-implicit methods is addressed by Patankar. In the fully-implicit method, only the transient term involves variables from the previous time step. The transient term can be integrated as shown in Equation (0-35).

$$\frac{1}{\Delta t}\int_{r_w}^{r_e}\int_{t}^{t+\Delta t} r^n \frac{\partial}{\partial t}\varepsilon\rho_g Y_j\, dt\, dr \rightarrow \frac{1}{\Delta t}\left[\begin{array}{l}\left(\frac{r_e^{n+1}+r_w^{n+1}}{n+1}\varepsilon\rho_g Y_j\right) \\ -\left(\frac{r_e^{n+1}+r_w^{n+1}}{n+1}\varepsilon\rho_g Y_j\right)_{prev}\end{array}\right] \qquad (0\text{-}35)$$

$$= \frac{1}{\Delta t}\left[\left(dv\varepsilon\rho_g Y_j\right) - \left(dv\varepsilon\rho_g Y_j\right)_{prev}\right]$$

Note that the "volume" term, dv, and the porosity, ε, are evaluated at the previous time step and at the current time step. For both biomass and black liquor, the volume changes with time. For black liquor, the porosity also changes with time. In layman's terms, the transient term describes the change in accumulation of the species in the control volume. Without accounting properly for the changing volume and porosity, the species continuity equations cause numerical instability.

In the code, the coefficients for the mass fraction at the current time and the previous time are *ap1* and *ap0*, respectively, as shown in Equation (0-37).

$$ap1 = \frac{dv\varepsilon\rho_g}{\Delta t}$$
$$ap0 = \frac{\left(dv\varepsilon\rho_g\right)_{prev}}{\Delta t} \qquad (0\text{-}36)$$

The Advection and Diffusion Terms

Combining the advection and the diffusion terms leads to more compact equation discretization and better approximations for the nearly exponential concentration gradients. Currently, the code uses the power-law approximation as described by Patankar. This approach is sufficient because in a one-dimensional model there is no false diffusion due to oblique gridding. Patankar derives this method in general for any combined advection-diffusion problem for any transport equation of the form shown in Equation (0-37). The symbol ϕ represents any transport variable (i.e. Y_i or T). Γ represents the exchange coefficient (i.e. ρD_{AB} or λ). The variable ρ represents density in the case of mass transfer and the product of density and heat capacity for heat transfer.

$$\frac{\partial}{\partial x}\rho u\phi = \frac{\partial}{\partial x}\Gamma\frac{\partial \phi}{\partial x} \tag{0-37}$$

This form is valid for any steady-state problem without a source term, but is a good approximation for any problem. To simplify the derivation, Patankar defined three variables that represent the flow strength, F; the diffusion conductance, D; and the dimensionless Peclet number, P.

$$\begin{aligned} F &\equiv \rho u \\ D &\equiv \frac{\Gamma}{\delta x} \\ P &\equiv \frac{F}{D} \end{aligned} \tag{0-38}$$

The particle code uses the flow strength and the diffusion conductance variables quite extensively for both mass and heat transfer. Patankar shows that Equation (0-37) can be solved exactly, and that the concentration gradient is exponential in form. Thus an exponential approximation would be warranted if it were not so computationally expensive. Instead, an expression that approximates the exponential but that is less computationally expensive forms the basis of the power-law scheme. For the case expressed above, the power-law scheme yields the following coefficients to ϕ.

$$a_E = D_e \cdot max\left[0, \left(1 - \frac{0.1 \cdot |F_e|}{D_e}\right)^5\right] + max[0, -F_e]$$
$$a_W = D_w \cdot max\left[0, \left(1 - \frac{0.1 \cdot |F_w|}{D_w}\right)^5\right] + max[0, F_e] \qquad (0\text{-}39)$$
$$a_P = a_E + a_W + (F_e - F_w)$$

In summary, the power-law scheme provides an accurate representation of the combined advection-diffusion problem, and it is less computationally demanding than the exponential scheme.

The Source Term

To improve convergence speed, a source term, S, that depends on the parameter ϕ can be linearized to $S = Sc + Sp \cdot \phi$ by using a first-order Taylor's series approximation. This yields $Sc = S^* - (dS/d\phi)^* \cdot \phi^*$ and $Sp = (dS/d\phi)^*$, where the asterisk, *, denotes the last iteration value. For example, given $S = 4 - 5 \cdot \phi^3$, the linearization of S with respect to ϕ would yield $Sc = 4 + 10 \cdot \phi^{*3}$ and $Sp = -15 \cdot \phi^{*2}$. Sp must always be negative to avoid possible instability and an unrealistic solution. If Sp is positive, then some other linearization scheme should be used such as $Sc = S$ and $Sp = 0$.

Standard Form

With all of the terms linearized, the species continuity equation can be put in standard form, Equation (0-40).

$$a_P \cdot Y_j = a_E \cdot Y_{j+1} + a_W \cdot Y_{j-1} + b$$
$$a_E = D_e \cdot max\left[0, \left(1 - \frac{0.1 \cdot |F_e|}{D_e}\right)^5\right] + max[0, -F_e]$$
$$a_W = D_w \cdot max\left[0, \left(1 - \frac{0.1 \cdot |F_w|}{D_w}\right)^5\right] + max[0, F_e] \qquad (0\text{-}40)$$
$$ap1 = \frac{dv\varepsilon\rho_g}{\Delta t}$$
$$ap0 = \frac{\left(dv\varepsilon\rho_g\right)_{prev}}{\Delta t}$$
$$b = Sc \cdot dv + ap0 \cdot Y_{j,0}$$
$$a_P = a_E + a_W + Sp + ap + (F_e - F_w)$$

Condensed-phase Species Continuity

The condensed-phase species continuity equation, Equation (0-41), does not contain terms for advection and diffusion. As explained above the fully-implicit method is also used for the condensed-phase time integration, Equation (0-42).

$$\frac{\partial \rho_i}{\partial t} = S_i \text{ where } i \text{ is for condensed-phase species} \tag{0-41}$$

$$\int_{r_w}^{r_e}\int_{t}^{t+\Delta t}\left(\frac{1}{\Delta t}\frac{\partial r^n}{\partial t}\rho_i - r^n S\right)dtdr = 0 \rightarrow$$
$$\frac{1}{\Delta t}\left[(dv\cdot\rho_i)-(dv\cdot\rho_i)_{prev}\right] = dv\cdot S \tag{0-42}$$

Biomass or Black Liquor Solid Continuity

The symbol B in the code refers to the black liquor solids portion of the particle, or in other words, the non-char organic portion. The temporal mass balance of B contains three consumption terms, one each for the reactions to light gas, tar, and char. Kinetic rate expressions as well as kinetic parameters are found at the end of this manual in Table 16 and Table 17.

$$\frac{\partial \rho_B}{\partial t} = -(K_1+K_2+K_3)\rho_B \rightarrow$$
$$\frac{1}{\Delta t}\left[(dv\cdot\rho_B)-(dv\cdot\rho_B)_{prev}\right] = dv\cdot -(K_1+K_2+K_3)\rho_B \tag{0-43}$$

Char Continuity

The char temporal mass balance contains two production source terms, one from the conversion of biomass to char and one for the char yield from the secondary reactions of tar. But many depletion source terms which makes it one of the most complicated source terms. As explained above the source terms should be linearized to increase convergence speeds. However instead of using the derivative of the source term for Sp, a slightly different simplified method was employed that seems to work well. For all of the source terms that are dependant on the conservation variable $Sp = S^*/\phi$.

Moisture Density Continuity

Moisture is the only condensed-phase species in the code that is allowed to diffuse, Equation (0-44). The advection component of the equation is considered to be negligible. That is the reason that the flow strength, F, is set to zero. The temporal moisture mass balance contains a

loss associated with conversion to water vapor. This conversion process is described in section **Error! Reference source not found.**.

$$\frac{\partial \rho_k}{\partial t} = \frac{1}{r^n}\frac{\partial}{\partial r}\left(r^n D_{eff,k} \frac{\partial \rho_k}{\partial r} \right) + S_k \text{ where k is for moisture} \qquad (0\text{-}44)$$

Water Vapor Continuity

The water vapor continuity equation is especially important during the drying stage. The moisture in the particle is divided up into two different types: bound moisture and free moisture. The free moisture uses the vapor pressure and the mass transfer coefficient in the pores to describe evaporation as shown in Equation (0-45). Typically Raoult's Law is used to describe the vapor-liquid equilibrium. However, since the mole fraction is unknown, two different assumptions were made, one for biomass and another for black liquor. For biomass, the mole fraction was assumed to always be one which yields Equation (0-45). For black liquor a correlation was developed between the solids content, Y_S, and the mole fraction. The ratio of the moisture density to the initial density is used to correct the surface area of the droplet.

$$\frac{dm_{FM}}{dt} = SA_{M,ini} \cdot h_m \cdot \frac{\rho_{FM}}{\rho_{FM,ini}} \cdot \left(\frac{P_{H_2O}^{sat} \cdot MW_v}{R_g \cdot T} - \rho_g \cdot Y_v \right) \qquad (0\text{-}45)$$

$$\frac{dm_{FM}}{dt} = SA_{M,ini} \cdot h_m \cdot \frac{\rho_{FM}}{\rho_{FM,ini}} \cdot \left(\frac{0.0716 \cdot (1 - Y_S)^{0.609} P_{H_2O}^{sat} \cdot MW_v}{R_g \cdot T} - \rho_g \cdot Y_v \right) \qquad (0\text{-}46)$$

The internal mass transfer coefficient, h_m, is determined by a simple algorithm given in Incropera and DeWitt, Equation (0-45). The effective diffusivity, D_{eff}, is discussed in more detail in section 0.

$$h_m = 3.66 \cdot \frac{D_{eff}}{d_{pore\_hydraulic}} \qquad (0\text{-}47)$$

The bound moisture evaporation is described by the following rate expression.

$$\frac{dm_{BM}}{dt} = k_7 \rho_{BM} \tag{0-48}$$

Total Gas Phase Continuity

The total gas-phase continuity equation is defined as the sum of all of the gas species, Equation (0-49). The source term, S_g, includes chemical reactions that involve both gas phase and condensed-phase species. Inside the particle, this equation is solved simultaneously with Darcy's law to solve for the pressures. At the particle surface and in the boundary layer, the pressure is assumed to be constant, ambient pressure. In the boundary layer, because the pressure is specified, the velocities are solved using only the continuity equation.

$$\frac{\partial}{\partial t}\varepsilon\rho_g + \frac{1}{r^n}\frac{\partial}{\partial r}(r^n \varepsilon \rho_g u) = S_g \tag{0-49}$$

Energy Conservation Equation

Energy equation for particle combustion is shown below in equation (0-50).

$$\frac{\partial}{\partial t}\left[\sum_i \rho_i \hat{H}_i + \sum_k \rho_k \hat{H}_k + \varepsilon\rho_g \sum_j Y_j \hat{H}_j\right] + \frac{1}{r^n}\frac{\partial}{\partial r}\left[r^n \varepsilon \rho_g u \sum_j Y_j \hat{H}_j\right]$$
$$= \frac{1}{r^n}\frac{\partial}{\partial r}(r^n k_{eff}\frac{\partial T}{\partial r}) + \frac{1}{r^n}\frac{\partial}{\partial r}\left[r^n\left(\rho_g \varepsilon \sum_j D_{eff,j}\frac{\partial Y_j}{\partial r}\hat{H}_j + D_{eff,k}\frac{\partial \rho_k}{\partial r}\hat{H}_k\right)\right] \tag{0-50}$$

where,

$\hat{H}_I = \hat{H}^0_{I,f} + \int_{T_0}^{T} Cp_I(T)dT$, I is any species involved

i = any species or component in the solid phase

j = any species or component in the gas phase

k = free water and bound water

To solve this equation together with other mass transfer equations, the variable enthalpies need to be converted to temperatures, which are more convenient than enthalpies for property calculations.

Substituting the enthalpy expression of each species or component into the above equation results in Equation (0-51)

$$
\begin{aligned}
&\sum_i \hat{H}^0_{i,f}\frac{\partial \rho_i}{\partial t}+\sum_k \hat{H}^0_{k,f}\frac{\partial \rho_k}{\partial t}+\sum_j \hat{H}^0_{j,f}\frac{\partial}{\partial t}\left(\rho_g \varepsilon Y_j\right)\\
&+\frac{\partial}{\partial t}\left(\sum_i \rho_i \int_{T_0}^{T} Cp_i dT+\sum_k \rho_k \int_{T_0}^{T} Cp_k dT+\rho_g \varepsilon \sum_j Y_j \int_{T_0}^{T} Cp_j dT\right)\\
&+\sum_j \hat{H}^0_{j,f}\frac{1}{r^n}\frac{\partial}{\partial r}\left[r^n \varepsilon \rho_g u Y_j\right]+\frac{1}{r^n}\frac{\partial}{\partial r}\left[r^n \varepsilon \rho_g u \sum_j Y_j \int_{T_0}^{T} Cp_j dT\right]=\frac{1}{r^n}\frac{\partial}{\partial r}(r^n k_{eff}\frac{\partial T}{\partial r}\\
&+\sum_j \hat{H}^0_{j,f}\frac{1}{r^n}\frac{\partial}{\partial r}\left(r^n \rho_g \varepsilon \sum_j D_{eff,j}\frac{\partial Y_j}{\partial r}\right)+\sum_k \hat{H}^0_{k,f}\frac{1}{r^n}\frac{\partial}{\partial r}\left(r^n \sum_k D_{eff,k}\frac{\partial \rho_k}{\partial r}\right)\\
&+\frac{1}{r^n}\frac{\partial}{\partial r}\left[r^n\left(\rho_g \varepsilon \sum_j D_{eff,j}\frac{\partial Y_j}{\partial r}\int_{T_0}^{T} Cp_j dT+\sum_k D_{eff,k}\frac{\partial \rho_k}{\partial r}\int_{T_0}^{T} Cp_k dT\right)\right]
\end{aligned}
\qquad (0\text{-}51)
$$

Continuity equations of all species appear below in Equations (0-34), (0-41), and (0-44). The heat of formation of each species at standard state is independent of temperature and any other variables. By multiplying each species continuity equation by its species heat of formation at standard state times, and then subtracting these equations from Equation (0-51), the following equation will be obtained.

$$
\begin{aligned}
&\sum_i \hat{H}^0_{i,f}S_i+\sum_k \hat{H}^0_{k,f}S_k+\sum_j \hat{H}^0_{j,f}S_j\\
&+\frac{\partial}{\partial t}\left(\sum_i \rho_i \int_{T_0}^{T} C_{p,i} dT+\sum_k \rho_k \int_{T_0}^{T} C_{p,k} dT+\rho_g \varepsilon \sum_j Y_j \int_{T_0}^{T} C_{p,j} dT\right)\\
&+\frac{1}{r^n}\frac{\partial}{\partial r}\left[r^n \varepsilon \rho_g u \sum_j Y_j \int_{T_0}^{T} C_{p,j} dT\right]=\frac{1}{r^n}\frac{\partial}{\partial r}(r^n k_{eff}\frac{\partial T}{\partial r})\\
&+\frac{1}{r^n}\frac{\partial}{\partial r}\left[r^n\left(\rho_g \varepsilon \sum_j D_{eff,j}\frac{\partial Y_j}{\partial r}\int_{T_0}^{T} C_{p,j} dT+\sum_k D_{eff,k}\frac{\partial \rho_k}{\partial r}\int_{T_0}^{T} C_{p,k} dT\right)\right]
\end{aligned}
\qquad (0\text{-}52)
$$

The source term S of each species can be expressed in terms of reaction rates, as explained in equation (0-53). Substituting these source terms into the first three terms in equation (0-52) yields equation (0-54).

Table 15: Reactions Described in the Model

1	Biomass → light gas	13	$H_6C_6O_{0.2} + 2.9O_2 \rightarrow 6CO + 3H_2$
2	Biomass → Tar	14	$Na_2SO_4 + 2C \rightarrow Na_2S + 2CO_2$
3	Biomass → Char	15	$K_2SO_4 + 2C \rightarrow K_2S + 2CO_2$
4	Tar → Light Gas	16	$Na_2S + 2O_2 \rightarrow Na_2SO_4$
5	Tar → Char	17	$K_2S + 2O_2 \rightarrow K_2SO_4$
6	Free water ↔ water vapor	18	$Na_2CO_3 + 2C \rightarrow 2Na + 3CO$
7	Bound water → water vapor	19	$K_2CO_3 + 2C \rightarrow 2K + 3CO$
8	$C + 1/2\ O_2 \rightarrow CO$	20	$NaCl_{(s,l)} \rightarrow NaCl_{(v)}$
9	$C + CO_2 \rightarrow 2CO$	21	$KCl_{(s,l)} \rightarrow KCl_{(v)}$
10	$C + H_2O \rightarrow CO + H_2$	22	$Na_2SO_4 + 4CO \rightarrow Na_2S + 4CO_2$
11	$1/2\ O_2 + CO \rightarrow CO_2$	23	$Na + H_2O \rightarrow NaOH + 0.5\ H_2$
12	$H_2 + 1/2\ O_2 \rightarrow H_2O$		

$$S_B = -(r_1 + r_2 + r_3)$$

$$S_C = r_3 + r_5 - r_8 \frac{2M_C}{M_{O_2}} - r_9 \frac{M_C}{M_{CO_2}} - r_{10} \frac{M_C}{M_{H_2O}} - r_{14} \frac{2M_C}{M_{Na2SO4}} - r_{15} \frac{2M_C}{M_{K2SO4}} - r_{18} \frac{2M_C}{M_{Na2CO3}} - r_{19} \frac{2M_C}{M_{Na2CO3}}$$

$$S_A = 0$$

$$S_{FM} = -r_6$$

$$S_{BM} = -r_7 \qquad (0\text{-}53)$$

$$S_{CO2} = r_{11} \frac{M_{CO_2}}{M_{CO}} - r_9 + (r_1 + r_4)\alpha_{CO_2} + r_{14} \frac{2M_{CO_2}}{M_{Na_2SO_4}} + r_{15} \frac{2M_{CO_2}}{M_{K_2SO_4}}$$

$$S_{CO} = r_8 \frac{2M_{C0}}{M_{O_2}} + r_9 \frac{2M_{CO}}{M_{CO_2}} + r_{10} \frac{M_{CO}}{M_{H_2O}} + r_{13} - r_{11} + (r_1 + r_4)\alpha_{CO} + r_{18} \frac{3M_{CO}}{M_{Na_2CO_3}} + r_{19} \frac{3M_{CO}}{M_{K_2CO_3}}$$

$$S_{O_2} = -r_8 - r_{11}\frac{M_{O_2}}{2M_{CO}} - r_{12}\frac{M_{O_2}}{2M_{H_2}} - r_{13}\frac{2.9M_{O_2}}{M_{HC}} - r_{16}\frac{2M_{O_2}}{M_{Na_2S}} - r_{17}\frac{2M_{O_2}}{M_{K_2S}}$$

$$S_{H_2} = r_4\alpha_{H_2} + r_{10}\frac{M_{H_2}}{M_{H_2O}} - r_{12} + r_{13}\frac{3M_{H_2}}{M_{HC}} + r_{23}\frac{0.5M_{H_2}}{M_{Na}}$$

$$S_{vapor} = r_4\alpha_{H_2O} + r_6 + r_7 - r_{10} + r_{12}\frac{M_{H_2O}}{M_{H_2}} - r_{23}\frac{M_{H_2O}}{M_{Na}}$$

$$S_{HC} = r_2 + r_4\alpha_{HC} - r_5 - r_{13}$$

$$S_{Na_2SO_4} = -r_{14} + r_{16}\frac{M_{Na_2SO_4}}{M_{Na_2S}}$$

$$S_{K_2SO_4} = -r_{15} + r_{17}\frac{M_{K_2SO_4}}{M_{K_2S}}$$

$$S_{Na_2S} = r_{14}\frac{M_{Na_2S}}{M_{Na_2SO_4}} - r_{16}$$

$$S_{K_2S} = r_{15}\frac{M_{K_2S}}{M_{K_2SO_4}} - r_{17}$$

$$S_{Na_2CO_3} = -r_{18}$$

$$S_{K_2CO_3} = -r_{19}$$

$$S_{Na} = r_{18}\frac{M_{Na}}{M_{Na_2CO_3}} - r_{22}$$

$$S_{K} = r_{19}\frac{M_{K}}{M_{K_2CO_3}}$$

$$S_{NaCl(v)} = r_{20}$$

$$S_{NaCl(l,s)} = -r_{20}$$

$$S_{KCl(v)} = r_{21}$$

$$S_{KCl(l,s)} = -r_{21}$$

$$S_{NaOH} = -r_{22}$$

$$\sum_i \hat{H}^0_{i,f} S_i + \sum_k \hat{H}^0_{k,f} S_k + \sum_j \hat{H}^0_{j,f} S_j = -\sum_m r_m \Delta H^0_m$$

where, m is reaction index $= 1, ..., 21$

ΔH^0_m is the heat of reaction at standard state, which is the enthalpy of reactants substract that of products (0-54)

So, equation (0-52) becomes to equation (0-55).

$$\begin{aligned}
&\frac{\partial}{\partial t}\left(\sum_i \rho_i \int_{T_0}^{T} C_{p,i} dT + \sum_k \rho_k \int_{T_0}^{T} C_{p,k} dT + \rho_g \varepsilon \sum_j Y_j \int_{T_0}^{T} C_{p,j} dT \right) \\
&+ \frac{1}{r^n} \frac{\partial}{\partial r}\left[r^n \varepsilon \rho_g u \sum_j Y_j \int_{T_0}^{T} C_{p,j} dT \right] = \frac{1}{r^n} \frac{\partial}{\partial r}\left(r^n k_{eff} \frac{\partial T}{\partial r} \right) + \sum_m r_m \Delta H^0_m \\
&+ \frac{1}{r^n} \frac{\partial}{\partial r}\left[r^n \left(\rho_g \varepsilon \sum_j D_{eff,j} \frac{\partial Y_j}{\partial r} \int_{T_0}^{T} C_{p,j} dT + \sum_k D_{eff,k} \frac{\partial \rho_k}{\partial r} \int_{T_0}^{T} C_{p,k} dT \right) \right]
\end{aligned} \tag{0-55}$$

Now, the above equation needs to be transformed to a generalized form so that it can be solved for temperature using control volume method. With the transformation described in equations (0-56), the first term in equation (0-55) can be expressed as equation (0-57)

$$\begin{aligned}
&\frac{\partial}{\partial t}\left(\rho_i \int_{T_0}^{T} C_{p,i} dT \right) = \rho_i \frac{\partial}{\partial t}\left(\int_{T_0}^{T} C_{p,i} dT \right) + \int_{T_0}^{T} C_{p,i} dT \frac{\partial \rho_i}{\partial t} \\
&\frac{\partial}{\partial t}\left(\int_{T_0}^{T} C_{p,i} dT \right) = C_{p,i} \frac{\partial T}{\partial t} \\
&\frac{\partial}{\partial t}\left(\rho_i C_{p,i} T \right) = \rho_i C_{p,i} \frac{\partial T}{\partial t} + T C_{p,i} \frac{\partial \rho_i}{\partial t} + T \rho_i \frac{\partial C_{p,i}}{\partial t} \\
&\frac{\partial}{\partial t}\left(\rho_i \int_{T_0}^{T} C_{p,i} dT \right) = \rho_i C_{p,i} \frac{\partial T}{\partial t} + \int_{T_0}^{T} C_{p,i} dT \frac{\partial \rho_i}{\partial t}
\end{aligned} \tag{0-56}$$

$$\frac{\partial}{\partial t}\left(\rho_i \int_{T_0}^{T} C_{p,i} dT\right) = \frac{\partial}{\partial t}\left(\rho_i C_{p,i} T\right) + \left(\int_{T_0}^{T} C_{p,i} dT - TC_{p,i}\right)\frac{\partial \rho_i}{\partial t} - T\rho_i \frac{\partial C_{p,i}}{\partial t} \tag{0-57}$$

$$\begin{aligned}&\frac{\partial}{\partial t}\left(\varepsilon \rho_j Y_j \int_{T_0}^{T} C_{p,j} dT\right) = \\ &\frac{\partial}{\partial t}\left(\varepsilon \rho_j Y_j C_{p,j} T\right) + \left(\int_{T_0}^{T} C_{p,j} dT - TC_{p,j}\right)\frac{\partial \varepsilon \rho_j Y_j}{\partial t} - T\varepsilon \rho_j Y_j \frac{\partial C_{p,j}}{\partial t}\end{aligned} \tag{0-58}$$

Similarly, the advection term and the diffusion term in equation (0-55) can be replaced by equations (0-59), (0-60), (0-61).

$$\begin{aligned}&\frac{1}{r^n}\frac{\partial}{\partial r}\left[r^n \varepsilon \rho_g u Y_j \int_{T_0}^{T} C_{p,j} dT\right] = \frac{1}{r^n}\frac{\partial}{\partial r}\left(r^n \varepsilon \rho_g u Y_j C_{p,j} T\right) \\ &+ \left(\int_{T_0}^{T} C_{p,j} dT - TC_{p,j}\right)\frac{1}{r^n}\frac{\partial}{\partial r}\left[r^n \varepsilon \rho_g u Y_j\right] - \frac{1}{r^n}\left(r^n \varepsilon \rho_g u Y_j T\right)\frac{\partial C_{p,j}}{\partial r}\end{aligned} \tag{0-59}$$

$$\begin{aligned}&\frac{1}{r^n}\frac{\partial}{\partial r}\left(r^n \rho_g \varepsilon D_{eff,j}\frac{\partial Y_j}{\partial r}\int_{T_0}^{T} C_{p,j} dT\right) = \frac{1}{r^n}\frac{\partial}{\partial r}\left[r^n \rho_g \varepsilon D_{eff,j}\frac{\partial Y_j}{\partial r} C_{p,j} T\right] \\ &\left(\int_{T_0}^{T} C_{p,j} dT - TC_{p,j}\right)\frac{1}{r^n}\frac{\partial}{\partial r}\left[r^n \rho_g \varepsilon D_{eff,j}\frac{\partial Y_j}{\partial r}\right] - \frac{1}{r^n}\left(r^n \rho_g \varepsilon D_{eff,j}\frac{\partial Y_j}{\partial r} T\right)\frac{\partial C_{p,j}}{\partial r}\end{aligned} \tag{0-60}$$

$$\begin{aligned}&\frac{1}{r^n}\frac{\partial}{\partial r}\left(r^n D_{eff,k}\frac{\partial \rho_k}{\partial r}\int_{T_0}^{T} C_{p,k} dT\right) = \frac{1}{r^n}\frac{\partial}{\partial r}\left[r^n D_{eff,k}\frac{\partial \rho_k}{\partial r} C_{p,k} T\right] \\ &\left(\int_{T_0}^{T} C_{p,k} dT - TC_{p,k}\right)\frac{1}{r^n}\frac{\partial}{\partial r}\left[r^n D_{eff,k}\frac{\partial \rho_k}{\partial r}\right] - \frac{1}{r^n}\left(r^n D_{eff,k}\frac{\partial \rho_k}{\partial r} T\right)\frac{\partial C_{p,k}}{\partial r}\end{aligned} \tag{0-61}$$

The heat capacity of each species is usually just a function of temperature, and is not related with time and position. In the current physical model, the temperature is a function of both time and position, so the heat capacity would change with time and position. The following transformations are made, as illustrated in equations (0-62) and (0-63).

$$\frac{\partial C_p}{\partial t} = \frac{\partial C_p}{\partial T}\frac{\partial T}{\partial t} \tag{0-62}$$

$$\frac{\partial C_p}{\partial r} = \frac{\partial C_p}{\partial T}\frac{\partial T}{\partial r} \tag{0-63}$$

Substituting equations (0-56) - (0-61) back into equation (0-55), and simplifying the resulted equation with equations (0-52) - (0-55) and (0-62) - (0-63), equation (0-55) becomes equation (0-64).

$$\begin{aligned}
&\frac{\partial}{\partial t}\left[\left(\sum_i \rho_i C_{p,i} + \sum_k \rho_k C_{p,k} + \rho_g \varepsilon \sum_j Y_j C_{p,j}\right)T\right] \\
&+ \frac{1}{r^n}\frac{\partial}{\partial r}\left\{\left[r^n \varepsilon \rho_g \left(u\sum_j Y_j C_{p,j} - \sum_j D_{eff,j}\frac{\partial Y_j}{\partial r}C_{p,j}\right) - r^n \sum_k D_{eff,k}\frac{\partial \rho_k}{\partial r}C_{p,k}\right]T\right\} \\
&= \frac{1}{r^n}\frac{\partial}{\partial r}\left(r^n k_{eff}\frac{\partial T}{\partial r}\right) + \sum_m r_m \Delta H_m^0 + \sum_l \left(C_{p,l}T - \int_{T_0}^{T} C_{p,l}dT\right)S_l \\
&+ \left(\sum_i \rho_i \frac{\partial C_{p,i}}{\partial T} + \sum_k \rho_k \frac{\partial C_{p,k}}{\partial T} + \varepsilon\rho_g \sum_j Y_j \frac{\partial C_{p,j}}{\partial T}\right)T\frac{\partial T}{\partial t} \\
&+ \left[\left(\sum_j Y_j \frac{\partial C_{p,j}}{\partial T}u - \sum_j D_{eff,j}\frac{\partial Y_j}{\partial r}\frac{\partial C_{p,j}}{\partial T}\right)\varepsilon\rho_g - \sum_k D_{eff,k}\frac{\partial \rho_k}{\partial r}\frac{\partial C_{p,k}}{\partial T}\right]T\frac{\partial T}{\partial r}
\end{aligned} \tag{0-64}$$

Substitute equation (0-53) into the third term on the right side of equation (0-64), the following equation is obtained.

$$\begin{aligned}
&\sum_l \left(C_{p,l}T - \int_{T_0}^{T} C_{p,l}dT\right)S_l = \sum_m r_m \left(\sum_{reac}\Psi_{reac}\int_{T_0}^{T} C_{p,reac}dT - \sum_{prod}\Psi_{prod}\int_{T_0}^{T} C_{p,prod}dT\right) \\
&+ \sum_m r_m \left(\sum_{prod}\Psi_{prod}C_{p,prod} - \sum_{reac}\Psi_{reac}C_{p,reac}\right)T
\end{aligned} \tag{0-65}$$

Where, Ψ is the stoichiometric factor of each species in a specific reaction m. So, a final general form of the energy equation, which can be solved by control volume method, is obtained in equation (0-66).

$$
\begin{aligned}
&\frac{\partial}{\partial t}\left[\left(\sum_i \rho_i C_{p,i} + \sum_k \rho_k C_{p,k} + \rho_g \varepsilon \sum_j Y_j C_{p,j}\right) T\right] \\
&+ \frac{1}{r^n}\frac{\partial}{\partial r}\left\{\left[r^n \varepsilon \rho_g \left(u \sum_j Y_j C_{p,j} - \sum_j D_{eff,j} \frac{\partial Y_j}{\partial r} C_{p,j}\right) - r^n \sum_k D_{eff,k} \frac{\partial \rho_k}{\partial r} C_{p,k}\right] T\right\} \\
&= \frac{1}{r^n}\frac{\partial}{\partial r}\left(r^n k_{eff} \frac{\partial T}{\partial r}\right) + \sum_m r_m \left(\sum_{reac} \Psi_{reac} \int_{T_0}^{T} C_{p,reac} dT - \sum_{prod} \Psi_{prod} \int_{T_0}^{T} C_{p,prod} dT\right) \\
&+ \sum_m r_m \left(\sum_{prod} \Psi_{prod} C_{p,prod} - \sum_{reac} \Psi_{reac} C_{p,reac}\right) T + \sum_m r_m \Delta H_m^0 \\
&+ \left(\sum_i \rho_i \frac{\partial C_{p,i}}{\partial T} + \sum_k \rho_k \frac{\partial C_{p,k}}{\partial T} + \varepsilon \rho_g \sum_j Y_j \frac{\partial C_{p,j}}{\partial T}\right) T \frac{\partial T}{\partial t} \\
&+ \left[\left(\sum_j Y_j \frac{\partial C_{p,j}}{\partial T} u - \sum_j D_{eff,j} \frac{\partial Y_j}{\partial r} \frac{\partial C_{p,j}}{\partial T}\right) \varepsilon \rho_g - \sum_k D_{eff,k} \frac{\partial \rho_k}{\partial r} \frac{\partial C_{p,k}}{\partial T}\right] T \frac{\partial T}{\partial r}
\end{aligned}
\tag{0-66}
$$

Effective Thermal Conductivity

Because of the very high temperatures and porous structures of biomass and black liquor, radiative heat transfer must be accounted for inside the particle. The effective thermal conductivity includes radiation and conduction components with some theoretical basis, Equation (0-68). The particle structure is assumed to be close to the upper limit for thermal conductivity, that is, it is assumed to have high connectivity in the direction of conduction. Radiation contributes approximately to the third power of the temperature.

$$\lambda_{eff} = \lambda_{cond} + \lambda_{rad} \tag{0-67}$$

$$\lambda_{cond} = \varepsilon \lambda_{gas} + (1-\varepsilon)\left[\frac{\rho_B}{\rho_{B,0}} \lambda_B + \left(1 - \frac{\rho_B}{\rho_{B,0}}\right) \lambda_C\right] \tag{0-68}$$

$$\lambda_{cond} = \frac{\varepsilon \sigma T^3 d_{pore}}{\omega} \tag{0-69}$$

For black liquor the effective thermal conductivity is calculated differently. Because of the swelling during black liquor combustion, the internal radiation heat transfer becomes very important. Various studies have been done to model this form of heat transfer. First of all the thermal heat capacity of the black liquor itself can be calculated using Equation (0-70), where T is in Kelvin, and Y_S is the mass fraction of the solids.

$$\lambda_S = \left(1.44\times10^{-1}\cdot\left(T-273.15\right)+0.58-0.335\cdot Y_S\right)\frac{W}{m\cdot K} \quad (0\text{-}70)$$

Siegel et al. and Verrill et al. used a diffusion approximation for cubic pores and an opaque cube pore model. This model is given by Equation (0-71). The Rosseland mean absorption coefficient, a_R, was estimated by Järvinen to be 850 m^{-1}.

$$\lambda_{eff} = k_S\left(1-\phi^{2/3}\right)+\frac{\phi^{2/3}}{\frac{1-\phi^{1/3}}{\lambda_S}+\frac{\phi^{1/3}}{\lambda_g}}+\frac{16\sigma T^3}{3a_R}\phi \quad (0\text{-}71)$$

Continuity and Darcy's Law Equation

Simple Algorithm

To calculate the pressure terms in the momentum equation, the momentum equation and the continuity equations are solved simultaneously following the SIMPLE algorithm (Semi-Implicit Method for Pressure-Linked Equations). The model uses Darcy's Law to calculate the gas velocities, because it adequately describes fluid flow in a porous medium. The pressure outside of the particle is assumed to be constant; thus, the gas velocities in the boundary layer are solved using only the continuity equation. Equations (0-72) and (0-73) are respectively Darcy's Law and the continuity equation, where μ is the gas viscosity and K is the permeability. The permeability depends on the condensed-phase composition. This section goes through the 7 steps of the SIMPLE, described by Patankar.

$$u = -\frac{K}{\mu}\frac{\partial P}{\partial r} \quad (0\text{-}72)$$

$$\frac{\partial \varepsilon\rho_g}{\partial t}+\frac{1}{r^2}\frac{\partial}{\partial r}\left(r^2\varepsilon\rho_g u\right)=S \quad (0\text{-}73)$$

Steps of the SIMPLE algorithm

Guess the pressure field, P^*. The guessed pressure field is simply the pressure at the end of the last iteration.

Solve the momentum equation (Darcy's Law) to obtain the velocity, u^*, from Equations (0-74)-(0-76), where η_w is the ratio of biomass to the initial biomass, char, and ash; K_m, K_W, and K_C are

the permeability of the particle cell, wood and char respectively, and the viscosity is of the gas phase.

$$\eta_w = \left(\frac{\rho_{B,w}}{\rho_{B,ini} + \rho_{C,ini} + \rho_{ash,ini}} \right) \tag{0-74}$$

$$u_w^* = -\frac{K_m(\eta_w) \cdot (P^*_P - P^*_W)}{\mu_w \cdot dr_w} \tag{0-75}$$

$$K_m(\eta_w) = \eta_w \cdot K_W + (1-\eta_w) \cdot K_C \tag{0-76}$$

Solve the P' equations, where P' is the pressure correction. To derive the pressure correction equation, P' is substituted into Darcy's Law to find the corrected velocity, Equation (0-77). Then use the control volume method to linearize the continuity equation and substitute in the velocity correction to obtain Equation (0-79).

$$u_e = u_e^* - \frac{\eta_e}{\mu_e} \frac{\left(P_E' - P_P'\right)}{\Delta r_e} \tag{0-77}$$

$$\frac{1}{\Delta t}\left(\rho_P dv - \rho_P^0 (dv)_{prev}\right) + \left[(\rho r^n)_e \left(u_e^* - \frac{\eta_e}{\mu_e} \frac{\left(P_E' - P_P'\right)}{\Delta r_e} \right) \right] - \left[(\rho r^n)_w \left(u_w^* - \frac{\eta_w}{\mu_w} \frac{\left(P_P' - P_W'\right)}{\Delta r_w} \right) \right] = \frac{S_g}{\varepsilon} dv \tag{0-78}$$

This equation when put in standard form is the following:

$$a_P P_P' = a_E P_E' + a_W P_W' + b$$

$$a_E = \left(\rho r^n\right)_e \frac{\eta_e}{\mu_e} \frac{1}{\Delta r_e} \qquad (0\text{-}79)$$

$$a_W = \left(\rho r^n\right)_w \frac{\eta_w}{\mu_w} \frac{1}{\Delta r_w}$$

$$a_P = a_E + a_W$$

$$b = \left(\frac{\rho_P}{\Delta t} + \frac{S_g}{\varepsilon}\right) \frac{r_e^{n+1} - r_w^{n+1}}{n+1} - \frac{\rho_P^0}{\Delta t} \left(\frac{r_e^{n+1} - r_w^{n+1}}{n+1}\right)_{prev}$$

$$+ \left[\left(\rho r^n u^*\right)_e - \left(\rho r^n u^*\right)_w\right]$$

The pressure correction equations are solved simultaneously using the Thomas Algorithm.

Calculate P by adding P' and P^*.

$$P_P = P_P^* + P_P' \qquad (0\text{-}80)$$

Calculate u from its starred values using the velocity-correction formula.

$$u_e = u_e^* + u_e^* - \frac{\eta_e}{\mu_e} \frac{\left(P_E' - P_P'\right)}{\Delta r_e} \qquad (0\text{-}81)$$

Solve an iteration of the other partial differential equations.

Treat the corrected pressure P as a new guessed pressure P^*, return to step 2, and repeat the whole procedure until a converged solution is obtained.

Boundary Conditions

The center velocity is specified to be zero. At the particle surface or at the edge of the boundary layer, the velocity is calculated by integrating the continuity equation. Equation (0-82) shows the

descretized form of the integrated continuity equation, where S_g is the source term that describes the mass increase in the gas phase due to reactions.

$$u_e = \left(dv \cdot S_g - \frac{(dv \cdot \rho_g \cdot \varepsilon - dv_{prev} \rho_{g,0} \cdot \varepsilon_0)}{\Delta t} + r_w{}^n \cdot \rho_{g,w} \cdot u_w \right) \cdot \frac{1}{r_e{}^n \cdot \rho_{g,e} \cdot \varepsilon_e} \qquad (0\text{-}82)$$

For the outer boundary condition, the pressure is set equal to the ambient pressure since the node lies directly on the surface of the particle. The pressure gradient at the particle's center is specified to be zero, as shown in Equation (0-83).

Boundary Conditions

Symmetry Boundary

Boundary conditions at the particle center are determined by symmetry, that is, at $r = 0$ Equation (0-83) applies.

$$\left.\frac{\partial P}{\partial r}\right|_{t,r=0} = 0 \Rightarrow u(t, r=0) = 0 \qquad (0\text{-}83)$$

$$\left.\frac{\partial T}{\partial r}\right|_{t,r=0} = 0$$

$$\left.\frac{\partial Y_l}{\partial r}\right|_{t,r=0} = 0$$

Surface Boundary Conditions

Initially heat and mass transfer correlations were used to determine the heat and the mass transfer to the particle. Later a boundary layer was added to the model to better estimate the effects of the flame that sometimes surrounds the particle. Although the flame region has been added, the mass transfer correlation option is still included in the code. To choose this option the user must specify the number of nodes inside the particle, *NR*, to be the same as the total number of nodes, *NNRR*.

Because of the uniqueness of the cell at the border between the solid and gas phase, a brief explanation is warranted. This border cell is half in the gas phase and half in the condensed phase. The node lies right on the boundary. To make this work, each half of this cell is integrated separately. The source terms are evaluated separately, etc.

The convection boundary condition

If this model is to be included into a CFD code, then the conditions of the gas surrounding the particle will be specified by the CFD code. When there are no significant reactions in the boundary layer, standard heat and mass transfer correlations can then be used to determine the surface fluxes. The following derivation shows how the transport equations are solved at the boundary. This derivation adopts the same nomenclature explained in the species continuity section, Section 0, and used in Patankar's derivation for the exponential scheme for solving the combined advection-diffusion problem. The transport equation can be written as follow for the steady-state advection-diffusion problem without a source term.

$$\left(F\phi - \Gamma\frac{\partial\phi}{\partial x}\right)_e - \left(F\phi - \Gamma\frac{\partial\phi}{\partial x}\right)_w = 0 \qquad \text{(0-84)}$$

As mentioned earlier the analytical solution to this problem is an exponential equation. However, at the boundary the flow strength, F, is calculated by solving the momentum and continuity equations, and the diffusive strength is specified by correlation. By including the transport correlation and transforming the western advection-diffusion term to its exponential solution (0-84) becomes the following:

$$\left(F_P\phi_P + h_m\theta_m\left(\phi_P - \phi_\infty\right)\right) - F_W\left(\phi_P + \frac{\phi_W - \phi_P}{exp(P_e) - 1}\right) = 0 \qquad \text{(0-85)}$$

This equation can now be cast into standard form to solve for the coefficients of ϕ_W and ϕ_P.

The Boundary Layer Thickness

During pyrolysis and char burning, the particle releases a significant amounts of combustibles. These combustibles then burn in the particle's wake or in a flame surrounding the particle. This model uses an approach similar to that of Bryden to solve the flame layer problem. The domain of the control volume is simply extended into the gas phase. In the outer-most shell, the concentrations of the gas species and the temperature equal the bulk gas conditions. One of the major variables in this approach is the thickness of the boundary layer, or the distance from the droplet surface to the bulk gas. By increasing the thickness of the boundary layer, the mass transfer is decreased.

If the boundary layer is very thin, these species simply diffuse from the surface and burn in the bulk. However, if the boundary layer is thick enough, typical of a large slow moving particle, the combustibles burn within the boundary layer, thus depleting surface oxygen concentration. During char burning, the combustion products, CO_2 and H_2O, diffuse back to the surface to

gasify the char. One of the problems faced in creating this code is to estimate the thickness of this boundary layer.

Various assumptions can be made in estimating the boundary layer thickness. The first assumption is that standard mass transfer correlations can be used to estimate the thickness of the boundary layer. (Associated with this assumption is the assumption of a quasi-steady-state process and no gaseous sources in the boundary layer.) Another assumption is that there is a linear concentration profile between the surface of the particle and the infinity conditions for an inert species. With these assumptions, the following is derived:

$$-\rho_g D_{AB} \frac{\left(Y_{i,L} - Y_{i,0}\right)}{\Delta x} = h_m \theta_m \left(Y_{i,0} - Y_{i,L}\right) \tag{0-86}$$

From this derivation Δx, the thickness of the flame zone, is solved easily.

$$\Delta x = \frac{\rho_g D_{AB}}{h_m \theta_m} \tag{0-87}$$

Equation (0-87) was originally used by the model. However, another assumption is that the concentration profile is not linear but follows an exponential curve that can be derived for steady-state convection/diffusion without a source term. As stated previously the partial differential equation for steady-state convection/diffusion without a source term can be solved exactly. The following is a derivation for how the estimate of the boundary layer thickness would be made under this assumption starting with the exact solution to the PDE in Cartesian coordinates using the nomenclature from Patankar. (Equation (0-89) is the exact solution.)

$$\frac{\phi - \phi_0}{\phi_L - \phi_0} = \frac{\exp(Px/L) - 1}{\exp(P) - 1} \tag{0-88}$$

From Equation (0-88), the concentration gradient at x=0 can be found by taking derivative of Equation (0-88) with respect to x, solving for $d\phi/dx$, and evaluating the expression at x=0.

$$\left.\frac{d\phi}{dx}\right|_{x=0} = \frac{\left(\phi_L - \phi_0\right)}{\exp(P) - 1} \cdot \frac{P}{L} = \frac{\left(\phi_L - \phi_0\right)}{\exp(P) - 1} \cdot \frac{\rho u}{\Gamma} \tag{0-89}$$

In this expression, the Peclet number, P (defined in Equation (0-38)), contains the Δx, which is the boundary layer thickness. The gradient, $d\phi/dx|_{x=0}$, is related to the standard transport coefficient. Equation (0-89) shows this relationship. The over-bar denotes an average value in the boundary layer. Solving for Δx now just requires a little bit of algebra, Equation (0-91). The boundary layer thickness can be similarly solved for in cylindrical and spherical coordinates, respectively Equations (0-92) and (0-93). Equation (0-94) is the equation for the heat transfer boundary layer thickness

$$-\overline{\Gamma}\left.\frac{d\phi}{dx}\right|_{x=0} = -\overline{\Gamma}\left[\frac{(\phi_L - \phi_0)}{exp(\rho u \Delta x/\overline{\Gamma}) - 1}\cdot\frac{\rho u}{\overline{\Gamma}}\right] = \overline{\rho} h_m \theta_m (\phi_0 - \phi_L) \tag{0-90}$$

$$\Delta x = \frac{\overline{\Gamma}}{\rho u} ln\left(\frac{\rho u \Gamma_{r=r0}}{\overline{\rho} h_m \theta_m \overline{\Gamma}} + 1\right) \tag{0-91}$$

$$\Delta r = r_0\left(1 - \frac{\overline{\rho} h_m \theta_m}{\rho v_r r}\right)^{-\frac{\rho D_{AB}}{\rho v_r r}} - r_0 \tag{0-92}$$

$$\Delta r = \left[\frac{1}{r_0} - \frac{\overline{\rho D_{AB}}}{\rho v_r r^2} \ln\left(1 + \frac{\rho v_r}{\overline{\rho} h_m \theta_m}\frac{[\rho D_{AB}]_{r=r0}}{\overline{\rho D_{AB}}}\right)\right]^{-1} - r_0 \tag{0-93}$$

$$\Delta r = \left[\frac{1}{r_0} - \frac{\overline{k}}{\rho v_r r^2 \overline{C_p}} ln\left(1 + \frac{\rho v_r \overline{C_p}}{h_f \theta_T}\frac{[k]_{r=r0}}{\overline{k}}\right)\right]^{-1} - r_0 \tag{0-94}$$

For very low air flow rates around the particle these expressions may cause numerical problems. Therefore an approximation used for the boundary layer thickness for low flowrates is the limit of these equations above as the velocity approaches zero. To obtain the low velocity limit for these equations, L'Hopital's rule must be utilized.

Initial Conditions

Initial conditions are assumed from experimental conditions for a non-reacting particle. That is, at $t = 0$,

$$\begin{array}{cc} P(t=0,r) = P_{ambient} & Y_V = Y_{V,Equilibrium\ with\ particle\ moisture} \\ T(t=0,r) = 300K\ (\text{typically}) & Y_l(t=0,r) = 1 \quad (\text{Inside the particle}) \\ u(t=0,r) = 0 & Y_T(t=0,r) = Y_V(t=0,r) = Y_G(t=0,r) = 0 \end{array} \tag{0-95}$$

Under-relaxation factors

Under-relaxation factors are used to increase convergence. Under-relaxation factors are used for the following variables: temperature, pressure, gas-phase mass fractions of O_2, light gas, tar, CO, CO_2, H_2O, NaCl, and KCl, and condensed-phase concentrations of char, black liquor solids (B), moisture (M), Na_2CO_3, K_2CO_3, Na_2SO_4, K_2SO_4, Na_2S, K_2S, NaCl, and KCl.

Properties

Gas Density

The ideal gas law determines the gas density using an average molecular weight for the total gas phase:

$$\rho_{gas} = \frac{P}{R_g \cdot T} \cdot MW_{tot} \tag{0-96}$$

$$MW_{tot} = \sum_{i=1}^{n} X_i \cdot MW_i \tag{0-97}$$

The mole fraction, X, depends on the mass fraction, Y, through the following equation:

$$X_i = \frac{\left(\frac{Y_i}{MW_i}\right)}{\left(\sum_{k=1}^{n} \frac{Y_k}{MW_k}\right)} [=] \frac{\left(\frac{mol_i}{mass_{tot}}\right)}{\left(\frac{mol_{tot}}{mass_{tot}}\right)} [=] \frac{mol_i}{mol_{tot}} \tag{0-98}$$

Because both the numerator and the denominator are normalized by the total mass of the gas phase (for a given volume), they cancel to simplify the equation. Combining the above formulas yields the final version of the gas density equation.

$$\rho_{gas} = \frac{P}{R_g \cdot T} \cdot \sum_{i=1}^{n} \left[MW_i \cdot \frac{\left(\frac{Y_i}{MW_i}\right)}{\left(\sum_{k=1}^{n} \frac{Y_k}{MW_k}\right)} \right] \tag{0-99}$$

Effective Pore Diffusivity

The effective pore diffusivity is a function of the bulk diffusivity, the Knudsen diffusivity, the porosity, and the tortuosity. Equation (0-100) indicates how the Knudsen diffusion coefficient depends on pore size, temperature, and molecular properties. Knudsen diffusion involves collisions with pore walls rather than collisions with other gas molecules.

$$\left(D_K\right)_A = 9.71 \times 10^3 \cdot \left(\frac{d_{pore}}{2}\right) \cdot \left(\frac{T}{MW_i}\right)^{0.5} \cdot \frac{cm \cdot \left(\frac{gm}{mol}\right)^{0.5}}{s \cdot K^{0.5}} \tag{0-100}$$

The reciprocal of the diffusion coefficient represents a transport resistance. To find the total resistance associated with both normal and Knudsen diffusion, the transport resistance of each is considered to be in series. Thus the equation for the combined diffusivity takes the form:

$$\frac{1}{D_{combined}} = \frac{1}{D_{AB}} + \frac{1}{(D_K)_A} \tag{0-101}$$

Total transport depends on both diffusivity and structural parameters; the latter includes porosity and tortuosity.

$$D^0_{eff} = \frac{D_{combined} \cdot \varepsilon_p}{\tau} \tag{0-102}$$

In the biomass model, the porosity, ε, and the tortuosity, τ, do not depend on time. However, during char burning the pore size increases, and the ash offers practically no resistance to the diffusivity. To account for this, the effective diffusivity results from a mass-weighted average of the D^0_{eff} calculated as shown above and the bulk diffusivity, D_{AB}, based on the ash fraction, Y_{ash}.

$$D_{eff} = Y_{ash} \cdot D_{AB} + (1 - Y_{ash}) \cdot D^0_{eff} \tag{0-103}$$

Because black liquor ash is molten, it is nonporous. The effective diffusivity can therefore be calculated by Equation (0-104).

$$D_{eff} = D^0_{eff} \tag{0-104}$$

Porosity

The porosity of the biomass remains constant at 0.6. Because of the drastic volume change, the porosity of the black liquor has to be calculated. By assuming ideal mixing and constant true densities, the porosity becomes a function only of the true and material densities (Equation (0-105)) and approaches unity during droplet swelling.

$$\varepsilon = 1 - \sum_j \frac{\rho_j}{\rho_{j,true}} \tag{0-105}$$

Thermodynamic Properties

The thermodynamic properties needed for this code include the enthalpies of formation, entropies of formation for equilibrium calculations, and the heat capacities of the species. Ideally, from these values, all of the heats of reactions are calculated. However, for species such as char or black liquor solids most literature does not contain heat of formation data; instead literature

sources commonly provide heats of reaction or combustion data. To derive a consistent set of thermodynamic data, various assumptions had to be made.

The heat capacity for char, black liquor solids, and biomass are calculated based on empirical formulas that depend on elemental composition C, H, and O. The heats of formation of these species at 298 K depend in rather simple ways on literature values of the heats of reaction for pyrolysis for B and char conversion for char. For example, the molar heat of formation of char, $\Delta\tilde{H}^0_{c,f}$, was found from Equation (0-105), where the value for the heat of reaction was provided by Bryden. The heat capacity of the tar was assumed to be the same as the heat capacity of benzene. The enthalpy of formation of tar was calculated from the literature value for the heat of reaction of tar to CO_2.

$$C + \tfrac{1}{2}O_2 \rightarrow CO$$
$$\Delta\tilde{H}^0_{c,f} = -\Delta\tilde{H}^0_{rxn} + \Delta\tilde{H}^0_{CO,f} - 0.5\Delta\tilde{H}^0_{O2,f} \qquad \text{(0-106)}$$

Most of the inorganic species undergo a condensed-phase phase transformation in the temperature range of combustion. Instead of writing different continuity equations for the various condensed-phase species, the thermodynamic data were manipulated to fit one continuous equation for the species enthalpy. The heat capacity of the species is the derivative of this curve.

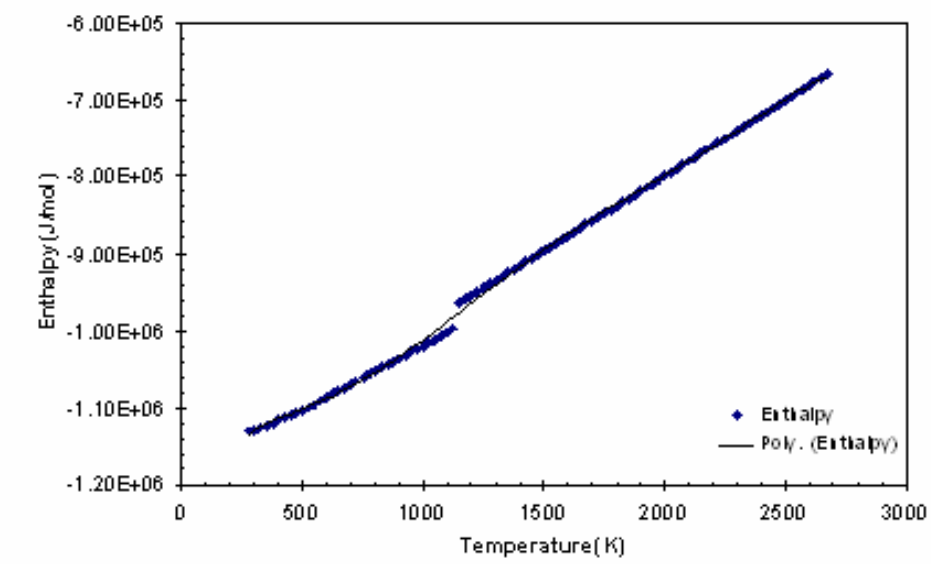

Figure 74: Fitted Enthalpy Curve for Sodium Sulfide

All of the species enthalpies are fitted to 6th order polynomials. Polynomial expressions for the heats of reactions at any given temperature result from multiplying these polynomials by the appropriate stoichiometric factors and combining them. Heats of mixing and other non-idealities are ignored in this formulation.

The Swelling Models

One of black liquor's most unique characteristics is that it swells to between 3-5 times its original diameter during combustion. To account for this, the swelling submodel makes the shell volume a function of the evaporation of moisture, conversion of organic material, and char conversion. Two different models have been implemented to describe swelling of black liquor as well as shrinking associated with char burning. The model developed by Hong Lu follows the differential equation:

$$\frac{\partial v}{\partial t} = \frac{v_0}{1 + dt \cdot \left(\left(\frac{\beta_M - 1}{M0} \right) \frac{dM}{dt} m + \left(\frac{\beta_B - 1}{B0} \right) \frac{dB}{dt} b + \left(\frac{\beta_C - 1}{C0} \right) \frac{dC}{dt} c \right)} \qquad (0\text{-}107)$$

Where v_0 is the volume during the previous time step, dt is the time step, and b is a volume factor. $M0$ and $B0$ represent the initial densities of moisture and biomass, respectively. $C0$ is the char density at the previous time step. The variables are m, b, and c are factors that are set to either 0 or 1 depending whether the species that they represent are present. For example, if the particle's moisture content is initially zero, m is set to zero to prevent swelling due to moisture evaporation. This model also includes some logic so that it does not cause shrinking if there is water condensation in the particle.

In the current investigation, Roberts developed a submodel that describes swelling and shrinking. This model can be described by the following equation:

$$v = v_{ini} \cdot \left(\beta_M + (\beta_B - \beta_M) \cdot \left(1 - \frac{\rho_B v}{B0} \right) + (\beta_C - \beta_B) \frac{char\_consumed}{\rho_B v + char\_produced} \right) \qquad (0\text{-}108)$$

Where $char\_consumed$ is the integral of the rate of char consumption with respect to time, and $char\_produced$ is the integral of the char production rate with respect to time. This equation is quadratic and can be solved directly for v.

There are two main differences in these two submodels. In the Lu submodel, swelling occurs gradually during drying, but in the Roberts submodel, swelling during drying is instantaneous. Hupa et al. showed that swelling during drying is initially very fast, but then practically stops for the rest of drying. So instantaneous swelling during drying may be a fairly good approximation of real behavior. The second difference involves shrinking during char burning. Because the model assumes zero initial concentration of char in the particle, some type of basis has to be used to determine how much shrinking occurs during char consumption. Lu's model uses the previous time step's concentration of char as this basis while the Roberts model uses the total (integrated) char production. By using the total char production as the basis as opposed to the char concentration during the previous time step, the shrinking model is more linear with char conversion and behaves more reasonably during periods of simultaneous char production and consumption.

Equilibrium Calculations

The reaction of char with sodium carbonate requires the use of an equilibrium calculation. The equilibrium concentration of sodium carbonate is calculated from the equilibrium relationship in Equation (0-109). Both sodium carbonate and char are assumed to have an activity of unity; therefore, Equation (0-110) must be satisfied. However, this equation is subject to physical constraints, and in the code, logic is built in so that none of the species concentrations will be negative.

$$Na_2CO_3 + C \leftrightarrow 2Na_{(v)} + CO_2 + CO \tag{0-109}$$

$$K_{eq} = \frac{\left(n_{Na,0} + 2\xi\right)^2 \left(n_{CO_2} + \xi\right)\left(n_{CO} + \xi\right)}{\left(n_{tot} + 4\xi\right)^4} \left(\frac{P}{1\,atm}\right)^4 \tag{0-110}$$

Code Algorithm

This section does not explain all of the code details but summarizes its main features.

Initializes the output files

Initializes a few variables according to moisture content

Calculates surface area and volume of particle based on shape

More output file initialization

Sets all of the previous time step values to zero

Initializes the all of the main variables—porosity outside of the particle set to 1

Determines the initial dv of each control volume in the particle

Begins the loop for the time steps

Calculates Sherwood and Nusselt numbers for the particle and the boundary layer thickness(*BLT*)

Calculates the position of each of nodes and the control surfaces

Stores the values of the previous time step for the parameters

Calculates the volume change

Starts the main loop for the iterations on the single time step

Assumes that the pressure or temperature are the slowest variables to converge

Convergence is determined by the sum of the pressure correction terms or the sum of the temperature change in an iteration

If there is no convergence after a pre-set number of iterations the program gives an error message and the code moves on.

Calculates the pressures and the velocities based on the SIMPLE algorithm

Equation

Black Liquor Equations for the solid phase

Char consumption

Char production

solid phase density

Char

Biomass

Sodium Species

Potassium Species

Biomass calculation for Char, Biomass, and Ash

Gas-phase Continuity Equations

Moisture Equation

Oxygen Equation

Sodium Equation

Potassium Equation

Sodium Chloride (gas phase) equation

Potassium Chloride (gas phase) equation

Hydrogen Equation

Water Vapor Equation

Carbon Dioxide Equation

Carbon Monoxide Equation

Tar Equation

Inert Gas Equation

Temperature (Energy) Calculation

Gas Density Calculation

Particle Size Change Calculation—including redistribution of nodes and control surfaces

End of main loop for a single time step

Calculates the amount of ash that falls from the particle

Calculates variables to be output

Outputs variables

Thermodynamic Data Calculations

Heat Capacity

Enthalpy

Derivative of Heat Capacity

Transport Properties

Permeability

Kinetics

Rate Constants

Rate Expressions

Energy Equations Routines

More transport functions

Other functions

Questions/Answers

The following section contains a list of questions and answers that came up while Warren Roberts was first learning how to use the particle code model. These questions were given to Hong Lu, the original author, and his responses appear below:

How does the pressure correction work? Explained in the SIMPLE algorithm section, Section 0.

How does the evaporation model account for composition? (How would I determine the vapor pressure using Roault's Law since the boiling point changes with composition?)—For biomass, the composition is only factored in to determine the wet surface area. For black liquor, the composition is accounted for using a mass fraction instead of a mole fraction. This is explained in the Water Vapor Continuity section.

The pressure terms are under-relaxed but not the velocity terms?—This is a consequence of the SIMPLE algorithm.

What is the area ratio? This is the ratio of the char density to the total solid phase density. This is calculated because not all of the solid species are reactive. The ash for example does not react.

Do we need to correct the diffusivity for the pressure of 0.86 atm (ambient pressure in Provo)? The diffusivity is not a strong function of pressure.

How can the mass fractions be negative? Why should you allow them to be so? By properly linearizing the source terms and using the fully implicit scheme, this problem should no longer exist. As well since the overall species continuity equation is solved, solving all of the species continuity equations over-specifies the calculation. Now the nitrogen continuity equation is solved by difference.

Does star mean the previous iteration?—Yes, this is nomenclature used by Patankar, especially in dealing with the source terms.

Why doesn't N_2 have a heat capacity?—It does; "I" stands for inert or N_2.

Is there a way to define global variables to be used in the subroutines?—Define them before the main section of the code.

What is den_ash_final? den_ash_final is set to be 500 kg/m^3 for biomass, however, there is a different final ash density for black liquor ash that is dependent on inorganic species content.

How does the size change work?—Explained in the sections on the swelling and shrinking models, Section 0.

Under what conditions can the shrinking be skipped?—If all of the char is completely changed to ash.

What is the order for finding the density of the biomass, char, etc?—The order doesn't matter, but the ash is now found by a mass balance.

To speed things up we can get rid of the moisture equation after drying is complete.

Are the other kinetic parameters for a sensitivity analysis? There are many kinetic parameters saved in the comments in the document. The extra kinetic parameters are parameters found in literature, but the ones currently used in the model are the ones that have been found to best match the data through trail and error.

What is *fsp*?—*fsp* refers to the fiber saturation point. This is the point at which the pores of the biomass have dried out from any excess water; *fsp* should be much lower for black liquor.

What do we do about the effective diffusivity during drying? The temperature, the pressure and the ash content are set to be the same as biomass parameters. These values make sense because during drying the biomass has not yet been converted.

Elvin's dissertation said that the velocity is a factor in the water condensation, is this true? This was the old model and is no longer used.

Should there be a blowing factor involved with the internal mass transfer of the water during the drying stage? Maybe, but we must find a model that will converge as well.

How does the extension into the flame region work? The cell on the boundary of the particle and the boundary layer is divided into two parts. The first half is condensed phase and the second half is gaseous. Because of this split the conservation equations are integrated over each half separately.

Is the reason that there is no boundary blowing factor due to the fact that the continuity equation takes care of the boundaries? Yes, the blowing factor calculations are used to determine the thickness of the boundary layer. This indirectly affects the mass and the heat transfer.

What is the FEI_m in the particle code model? Why is this calculated using average bulk properties? This is ϕ described by Bird's Transport phenomena for the blowing factor calculation. In working with boundary layers, some of the parameters must be averaged over the whole boundary layer.

Why do you multiply by the porosity when you are finding the blowing factor? This must be the velocity is an absolute velocity as opposed to a superficial velocity. Why the porosity at NR+1? Would not this equal 1? The porosity at this point is 1, but the velocity, calculated by Darcy's Law, is the correct velocity.

Why is Sc_cal = 0 for oxygen? As mentioned in a previous question, the linearization of the source terms is not an exact Taylor series approximation, instead sometimes Sp is found by dividing S by the dependent variable.

Why isn't the boundary set to be the edge of the solid gas interface instead of the middle of the cell?—Either way works.

How is the gas density determined at the boundary cell?—The gas density is the true density anyway; so it can be found using the ideal gas law without any consideration of the different porosities in the two halves of the cell.

I don't see an enthalpy for the ash? There is no function to calculate this enthalpy for biomass.

Is there a problem with the ash density equation? How does this work? For biomass, ash is determined by mass balance. For black liquor ash is the sum of the inorganic species.

Table 16: Summary of Reaction Kinetics—Temperatures in K, Pressure in Pa, Where $k = A \cdot T^n \exp(-E_A/R_g T)$

	Reaction	Pre-exponential Factor, A_i	Units on Rate Constant, k_i	Activation Energy, E_A	n
1	Biomass → light gas	$5.175 \cdot 10^4$	Hz	$9.1533 \cdot 10^4$	0
		$1.30 \cdot 10^8$	Hz	$1.40 \cdot 10^5$	0
		$1.11 \cdot 10^{11}$	Hz	$1.77 \cdot 10^5$	0
		$1.44 \cdot 10^4$	Hz	$8.86 \cdot 10^4$	0
		$1.52 \cdot 10^7$	Hz	$1.39 \cdot 10^5$	0
		$1.43 \cdot 10^4$	Hz	$8.86 \cdot 10^4$	0
2	Biomass → Tar	$4.18 \cdot 10^2$	Hz	$3.732 \cdot 10^4$	0
		$2.00 \cdot 10^8$	Hz	$1.33 \cdot 10^5$	0
		$9.28 \cdot 10^9$	Hz	$1.49 \cdot 10^5$	0
		$5.85 \cdot 10^6$	Hz	$1.19 \cdot 10^5$	0
		$3.39 \cdot 10^4$	Hz	$6.897 \cdot 10^4$	0
		$4.13 \cdot 10^6$	Hz	$1.13 \cdot 10^5$	0
		$3.38 \cdot 10^4$	Hz	$6.90 \cdot 10^4$	0
3	Biomass → Char	$5.80 \cdot 10^1$	Hz	$3.011 \cdot 10^4$	0
		$2.91 \cdot 10^2$	Hz	$6.10 \cdot 10^4$	0
		$3.05 \cdot 10^7$	Hz	$1.25 \cdot 10^5$	0
		$2.98 \cdot 10^3$	Hz	$7.31 \cdot 10^4$	0
		$7.38 \cdot 10^5$	Hz	$1.07 \cdot 10^5$	0
		$7.59 \cdot 10^2$	Hz	$4.90 \cdot 10^4$	0
		$7.38 \cdot 10^5$	Hz	$1.06 \cdot 10^5$	0

Table 13 continued					
		$2.91 \cdot 10^{2}$	Hz	$6.10 \cdot 10^{4}$	0
4	Tar → Light Gas	$4.28 \cdot 10^{6}$	Hz	$1.08 \cdot 10^{5}$	0
		$2.60 \cdot 10^{6}$	Hz	$1.08 \cdot 10^{5}$	0
		$8.60 \cdot 10^{4}$	Hz	$8.78 \cdot 10^{4}$	0
5	Tar → Char	$1.00 \cdot 10^{5}$	Hz	$1.08 \cdot 10^{5}$	0
		$1.00 \cdot 10^{6}$	Hz	$1.08 \cdot 10^{5}$	0
		$7.70 \cdot 10^{4}$	Hz	$8.78 \cdot 10^{4}$	0
		$1.00 \cdot 10^{6}$	Hz	$1.08 \cdot 10^{5}$	0
6	Free Water Evaporation	Equilibrium/Mass Transfer Controlled			0
7	Bound Water Evaporation	$5.13 \cdot 10^{10}$	Hz	$8.80 \cdot 10^{3}$	0
8	$C + 1/2\ O_2 \rightarrow CO$	0.658	$\frac{1}{m^2 \cdot s}$	$7.48 \cdot 10^{4}$	1
9	$C + CO_2 \rightarrow 2CO$	3.42	$\frac{1}{m^2 \cdot s}$	$1.297 \cdot 10^{5}$	1
		$3.92 \cdot 10^{8}$	$\frac{gm}{m^2 \cdot s}$	$2.50 \cdot 10^{5}$	0
10	$C + H_2O \rightarrow CO + H_2$	3.42	$\frac{1}{m^2 \cdot s}$	$1.297 \cdot 10^{5}$	1
		$1.60 \cdot 10^{7}$	$\frac{gm}{m^2 \cdot s}$	$2.10 \cdot 10^{5}$	0
11	$1/2\ O_2 + CO \rightarrow CO_2$	$2.24 \cdot 10^{12}$	$\rho_{H2O} \leq 0 \quad \frac{kg \cdot m^{0.75}}{s \cdot kmol^{1.25}}$ $\rho_{H2O} > 0 \quad \frac{kg \cdot m^{2.25}}{s \cdot kmol^{1.75}}$	$1.671 \cdot 10^{5}$	0

Table 13 continued					
12	$H_2 + 1/2\ O_2 \rightarrow H_2O$	$5.13 \cdot 10^{12}$	$\frac{m^{4.26}}{kmol^{1.42} \cdot s}$	$1.713 \cdot 10^{5}$	0
13	$HC + O_2 \rightarrow CO + H_2$	$10^{4.32} * P_0^{0.3}$	$\frac{m^{1.5}}{s \cdot kmol^{0.5}}$	$8.024 \cdot 10^{4}$	1
		$10^{4.32}$	$\frac{m^{1.5}}{s \cdot kmol^{0.5}}$	$8.024 \cdot 10^{4}$	0.3
14	$Na_2SO_4 + 2C \rightarrow Na_2S + 2CO_2$	$3.79 \cdot 10^{3}$	Hz	$7.81 \cdot 10^{4}$	0
15	$K_2SO_4 + 2C \rightarrow K_2S + 2CO_2$	$3.79 \cdot 10^{3}$	Hz	$7.81 \cdot 10^{4}$	0
16	$Na_2S + 2O_2 \rightarrow Na_2SO_4$	$1.645 \cdot 10^{3}$	$\frac{m^3}{mol \cdot s}$	$7.483 \cdot 10^{4}$	1
17	$K_2S + 2O_2 \rightarrow K_2SO_4$	$1.645 \cdot 10^{3}$	$\frac{m^3}{mol \cdot s}$	$7.483 \cdot 10^{4}$	1
18	$Na_2CO_3 + 2C \rightarrow 2Na + 3CO$	$1.00 \cdot 10^{9}$	Hz	$2.44 \cdot 10^{5}$	0
19	$K_2CO_3 + 2C \rightarrow 2K + 3CO$	$1.00 \cdot 10^{9}$	Hz	$2.44 \cdot 10^{5}$	0
20	NaCl Evaporation	Equilibrium/Mass Transfer Controlled			
21	KCl Evaporation	Equilibrium/Mass Transfer Controlled			
23	$Na + H_2O \rightarrow NaOH + 0.5\ H_2$	$1.807 \cdot 10^{7}$	$\frac{m^3}{mol \cdot s}$	$1.858 \cdot 10^{5}$	0.5
*Bolded used only for black liquor; where $k = A \cdot T^n \cdot \exp(E_i / R_g T)$.					

Table 17: Summary of Rate Expressions and Logic

1	Biomass → light gas $Rate_1 = \begin{cases} \rho_B > 0 & k_1(T)\cdot\rho_B \\ \rho_B \le 0 & 0 \end{cases}$
2	Biomass → Tar $Rate_2 = \begin{cases} \rho_B > 0 & k_2(T)\cdot\rho_B \\ \rho_B \le 0 & 0 \end{cases}$
3	Biomass → Char $Rate_3 = \begin{cases} \rho_B > 0 & k_3(T)\cdot\rho_B \\ \rho_B \le 0 & 0 \end{cases}$
4	Tar → Light Gas $Rate_4 = \begin{cases} \rho_{tar} > 0 & k_4(T)\cdot\rho_{tar} \\ \rho_{tar} \le 0 & 0 \end{cases}$
5	Tar → Char $Rate_5 = \begin{cases} \rho_{tar} > 0 & k_5(T)\cdot\rho_{tar} \\ \rho_{tar} \le 0 & 0 \end{cases}$
6	Water evaporation $Rate_6 = \begin{cases} Biomass & SA_{M,ini}\,\frac{\rho_{FM}}{\rho_{FM,ini}}\cdot hm_{pore\_vapor}\cdot\left(\frac{P^{sat}_{H2O}\cdot MW_{vapor}}{R_g\cdot T} - \left(\rho_{gas}\cdot Y_{vapor}\right)\right) \\ Black\ Liquor & SA_{M,ini}\,\frac{\rho_{FM}}{\rho_{FM,ini}}\cdot hm_{pore\_vapor}\cdot\left(\frac{0.0716\cdot\left(1-Y_S\right)^{0.609}P^{sat}_{H2O}\cdot MW_{vapor}}{R_g\cdot T} - \left(\rho_{gas}\cdot Y_{vapor}\right)\right) \end{cases}$
7	Bound Water Evaporation $Rate_7 = k_7\rho_{BM}$
8	C + 1/2 O_2 → CO

	$$Rate_8 = \begin{cases} \rho_{O2} \le 0 & 0 \\ \rho_{O2} > 0 & area\_ratio \cdot SA_{char} \cdot k_8(T) \cdot \rho_{O2} \end{cases}$$
9	$C + CO_2 \rightarrow 2CO$ *Biomass* $$Rate_9 = \begin{cases} \rho_{CO2} \le 0 & 0 \\ \rho_{CO2} > 0 & area\_ratio \cdot SA_{char} \cdot k_9(T) \cdot \rho_{CO_2} \cdot \dfrac{MW_C}{MW_{CO_2}} \end{cases}$$ *Black Liquor* $$Rate_9 = \frac{R_{SA,c} \cdot SA_C \cdot k_9(T) \cdot \rho_C \cdot \rho_{CO_2} / MW_{CO_2}}{\left(\rho_{CO_2} / MW_{CO_2} + 3.4\, \rho_{CO} / MW_{CO}\right)}$$
10	$C + H_2O \rightarrow CO + H_2$ *Biomass* $$Rate_{10} = \begin{cases} \rho_{H_2O} \le 0 & 0 \\ \rho_{H_2O} > 0 & area\_ratio \cdot SA_{char} \cdot k_{10}(T) \cdot \rho_{H_2O} \end{cases}$$ *Black Liquor* $$Rate_{10} = \frac{R_{SA,c} \cdot SA_C \cdot \rho_C \cdot k_{10}(T) \cdot \rho_{H_2O} / MW_{H_2O}}{\left(\rho_{H_2O} / MW_{H_2O} + 3.4\, \rho_{H_2} / MW_{H_2}\right)} \cdot \frac{MW_{H_2O}}{MW_C}$$
11	$1/2\ O_2 + CO \rightarrow CO_2$ $$Rate_{11} = \begin{cases} \rho_{O_2} \le 0 \text{ or } \rho_{CO} \le 0 & 0 \\ \rho_{CO} > 0 \ \&\ \rho_{O_2} > 0 & \begin{cases} \rho_{H2O} \le 0 & k_{11} \cdot \left(\dfrac{\rho_{CO}}{MW_{CO} \cdot 1000}\right) \cdot \left(\dfrac{\rho_{O_2}}{MW_{O2} \cdot 1000}\right)^{0.25} \cdot 10^3 \cdot MW_{CO} \\ \rho_{H2O} > 0 & k_{11} \cdot \left(\dfrac{\rho_{CO}}{MW_{CO} \cdot 10^3}\right) \cdot \left(\dfrac{\rho_{O_2}}{MW_{O_2} \cdot 10^3}\right)^{0.25} \cdot \left(\dfrac{\rho_{H_2O}}{MW_{H_2O} \cdot 10^3}\right)^{0.5} \cdot 10^3 \cdot MW_{CO} \end{cases} \end{cases}$$
12	$H_2 + 1/2\ O_2 \rightarrow H_2O$ $$Rate_{12} = \begin{cases} \rho_{O2} \le 0 \ \&\ \rho_{H_2} \le 0 & 0 \\ \rho_{O2} > 0 \ \&\ \rho_{H_2} > 0 & \left(k_{12}(T) \cdot \left(\dfrac{\rho_{H_2}}{MW_{H_2} \cdot 1000}\right) \cdot \left(\dfrac{\rho_{O_2}}{MW_{O_2} \cdot 1000}\right)^{1.42}\right) \cdot MW_{H_2} \cdot 1000 \end{cases}$$
13	$H6.2C5.8 + 2.9O_2 \rightarrow 6.0CO + 3.1H_2$ $$Rate_{13} = \left(k_{13}(T) \cdot \left(\frac{\rho_T}{MW_T \cdot 1000}\right)^{0.5} \cdot \left(\frac{\rho_{O_2}}{MW_{O_2} \cdot 1000}\right)\right) \cdot MW_T \cdot 1000$$

14	$Na_2SO_4 + 2C \rightarrow Na_2S + 2CO_2$ $Rate_{14} = \left(k_{14}(T) \cdot \left(\frac{\rho_{Na_2SO_4}}{MW_{Na_2SO_4} \cdot \left(\frac{\rho_{Na_2SO_4}}{MW_{Na_2SO_4}} + \frac{\rho_{Na2S}}{MW_{Na_2S}} + \frac{\rho_{Na_2CO_3}}{MW_{Na_2CO_3}} \right)} \right)^{1.4} \cdot \frac{\rho_C}{MW_C} \right) \cdot MW_{Na_2SO_4}$
15	$K_2SO_4 + 2C \rightarrow K_2S + 2CO_2$ $Rate_{15} = \left(k_{15}(T) \cdot \left(\frac{\rho_{K_2SO_4}}{MW_{K2SO4} \cdot \left(\frac{\rho_{K_2SO_4}}{MW_{K_2SO_4}} + \frac{\rho_{K_2S}}{MW_{K_2S}} + \frac{\rho_{K_2CO3}}{MW_{K_2CO_3}} \right)} \right)^{1.4} \cdot \frac{\rho_C}{MW_C} \right) \cdot MW_{K_2SO_4}$
16	$Na_2S + 2O_2 \rightarrow Na_2SO_4$ $Rate_{16} = \left(k_{16}(T) \cdot SA \cdot \left(\frac{\rho_{Na_2S}}{MW_{Na_2S}} \right) \cdot \left(\frac{\rho_{O2}}{MW_{O_2}} \right) \right) \cdot MW_{Na_2S}$
17	$K_2S + 2O_2 \rightarrow K_2SO_4$ $Rate_{17} = \left(k_{17}(T) \cdot SA \cdot \left(\frac{\rho_{K2S}}{MW_{K_2S}} \right) \cdot \left(\frac{\rho_{O_2}}{MW_{O_2}} \right) \right) \cdot MW_{K_2S}$
18	$Na_2CO_3 + 2C \rightarrow 2Na + 3CO$ $Rate_{18} = \left(k_{18}(T) \cdot \left(\frac{\rho_{Na_2CO_3}}{MW_{Na_2CO_3}} \right) \right) \cdot MW_{Na_2CO_3}$
19	$K_2CO_3 + 2C \rightarrow 2K + 3CO$ $Rate_{19} = \left(k_{19}(T) \cdot \left(\frac{\rho_{K_2CO_3}}{MW_{K_2CO_3}} \right) \right) \cdot MW_{K_2CO_3}$
20	$NaCl(s,l) \rightarrow NaCl(v)$

	$Rate_{20} = SA_{fsp} \cdot hm_{pore\_vapor} \cdot \left(\frac{\rho_{NaCl}}{\rho_{Solid\_phase}} \frac{P_{NaCl}^{sat} \cdot MW_{NaCl}}{R_g \cdot T} - \rho_{gas} \cdot Y_{NaCl} \right)$
21	KCl(s,l) → KCl(v) $Rate_{21} = SA_{fsp} \cdot hm_{pore\_vapor} \cdot \left(\frac{\rho_{KCl}}{\rho_{Solid\_phase}} \frac{P_{KCl}^{sat} \cdot MW_{KCl}}{R_g \cdot T} - \rho_{gas} \cdot Y_{KCl} \right)$
23	$Na + H_2O \rightarrow NaOH + 0.5\ H_2$ $Rate_{23} = \left(k_{23}(T) \cdot \left(\frac{\rho_{Na}}{MW_{Na}} \right) \cdot \left(\frac{\rho_{H_2O}}{MW_{H_2O}} \right) \right) \cdot MW_{Na}$
$SA_{C,V}$=10^6m^2/m^3; $SA_{C,m}$=1.6·10^5m^3/kg; $SA_{M,ini}$=2.26·10^4m^2/m^3;	

Table 18: Nomenclature of the Particle Model

Symbol in Manual	Symbol in Code	Meaning
a_R		Rosseland mean absorption coefficient, m^{-1}
A_i	A1-A23	Pre-exponential factor
AR	AR	Aspect Ratio
B		Black liquor solids
C		Char
		Concentration, $mol \cdot m^3$
C_p	Cp	Heat capacity, $J \cdot kg^{-1} \cdot K^{-1}$
d_{pore}		Pore diameter, m
D_{eff}	Deff	Effective diffusivity, $m^2 \cdot s^{-1}$
E()		Surface emissivity Function
E_i	E1–E23	Activation energy, $J \cdot mol^{-1}$
f	f_CO	Fraction of CO produced
h_f	hf	Heat transfer coefficient, $W \cdot m^{-2} \cdot K^{-1}$
h_m	hm	Mass transfer coefficient, $m \cdot s^{-1}$
$\Delta\tilde{G}_{rxn}$	DeltaG	Molar Gibbs energy of reaction, $J \cdot mol^{-1}$
$\hat{H}$	H	Specific enthalpy, $J \cdot kg^{-1}$
$\Delta\hat{H}_{rxn}$	DeltaH1-23	Specific heats of reaction, $J \cdot kg^{-1}$
$\Delta\tilde{H}_{rxn}$	Not used	Molar heats of reaction, $J \cdot mol^{-1}$
k	Kc	Thermal conductivity, $W \cdot m^{-1} \cdot K^{-1}$
K	K	Permeability, m^2
k_i	k1–k23	Rate constant

MW_i	M	Molecular weight, $kg \cdot kmol^{-1}$
MW_{tot}		Gas average molecular weight, $kg \cdot kmol^{-1}$
n	n	Shape factor, n=0 Cartesian, n=1 cylindrical, n=2 spherical
Nu	Nu	Nusselt number
P	Pres	Pressure
		Peclet number
F	F	Flow conductance
D	D	Diffusion conductance
		Lens diameter
D_{AB}	D_	Binary diffusivity, $m \cdot s^{-2}$
D_{eff}		Effective diffusivity, $m \cdot s^{-2}$
D_K		Knudsen diffusivity, $m \cdot s^{-2}$
Pr	Pr	Prandtl number
r	r	Radius coordinate, m
		Reaction rate, $kg \cdot m^{-3} \cdot s$
Re		Reynolds number
R_g	R_g	Universal gas constant, 8.3145 $J \cdot mol^{-1} \cdot k^{-1}$
Rp	Rp	Particle radius, m
R_{SA}	Surface_Area_Ratio	Surface area ratio, $R_{SA,i} = \rho_i / \rho_{tot}$
SA	Sa	Surface area
S		Source term
Sc	Sc	Source term linearization
		Schmidt number
Sh	Sh	Sherwood number

Sp	Sp	Source term linearization parameter S = *Sp·Tp* + *Sc*
t	time	Time, s
T	T	Temperature, K
u	U	Gas velocity, $m \cdot s^{-1}$
Y	Y	Mass Fraction
fsp	fsp	Fiber saturation point
X		Magnification
X_i		Mole fraction
v	Volume	Particle volume
Greek Symbols		
α	shrinking_factor	Shrinking factor
□		Time stamp correction factor
ε	porosity	Porosity
□		Transport variable
□	K	Permeability
□		Wavelength, m
		Thermal conductivity, $W \cdot m^{-1} \cdot K^{-1}$
μ	Viscosity	Viscosity, Pa·s
ρ	den	Density, $kg \cdot m^{-3}$
σ	Boltzmans	Boltzmann constant, $W \cdot m^{-2} \cdot K^{-4}$
ω	emissivity	Emissivity
η		Ratio of biomass to the initial black liquor solid (or biomass), char and ash
θ	theta	Blowing factor

τ	tortuosity	Tortuosity
		Lens transmission factor
Subscript		
0	0	Initial value or reference state
		Surface (reference position)
B	B, Biomass, BB	Biomass
		Blue
1, …, 21	1, …, 21	Reaction
C	C, Char	Char
Combined		Combined
con	k	Conductivity
Cor		Correction
e	e	East control volume surface
eff		Effective
g	gg	Gas phase
G	G, GG, Gas	Light gas
		Green
I	I, Inert	Inert gas
L		far edge of boundary layer
m		Mass transfer
M	M	Moisture
r		r-direction
R		Red

rad		Radiation
V	V, Vapor	Water vapor
S		Solid phase
T	T, TT	Tar
		Thermal
tot	tot	Total condensed phase
TS		Time stamp
w	w	West control volume surface
Superscript		
sat		Vapor pressure
V	V	Water vapor

PARTICLE SIZE AND SHAPE EFFECTS ON COMBUSTION

Abstract

This investigation provides a comprehensive analysis of entrained-flow biomass combustion processes. Experimental and theoretical investigations indicate how particle shape and size influence biomass combustion rates. Experimental samples include flake-like, cylinder-like, and equant (nearly spherical) shapes with similar particle masses and volumes but different surface areas. Samples of small (less than 500 μm) particles passed through a laboratory entrained-flow reactor in a nitrogen/air atmosphere and a maximum reactor wall temperature of 1600 K, while large samples reacted in suspension in a single particle furnace operated at similar conditions as the entrained-flow reactor. A separately developed computer and image analysis system determined particle surface-area-to-volume ratios based on three orthogonal particle silhouettes. Experimental data indicate that equant particles react more slowly than the other shapes, with the ratio in time required for complete combustion becoming more significant as particle mass increases and reaching a factor of two or more for particles larger than 1 mm in diameter (which includes most particles in commercial application).

A color-band, non-contact pyrometry developed in this project measured particle surface temperatures and flame temperatures during pyrolysis and char burning processes, This technique employs widely available and relative inexpensive cameras and detectors such as charge-coupled devices (CCD) and complementary metal oxide semiconductor (CMOS) cameras. The camera-measured temperature data agree with black body calibration data within the accuracy of the data (± 20°C) and with thermocouple-measured data and model predictions within the repeatability of the data (± 50 °C) in most cases. This pyrometry measures the temperature distribution on the particle surface with a resolution limited only by the camera detector and optical system, and the resulting temperature information provides 3-D particle surface temperature data reconstructed from the three orthogonal particle silhouettes using the particle shape reconstruction algorithm in the computer and image system.

A one-dimensional, transient particle combustion model simulates the drying, pyrolysis, and char oxidation and gasification processes of particles with different shapes. The model also predicts the shrinking/swelling and surrounding flame combustion behaviors of a single particle. This model characterizes particles in either one of three basic shapes (sphere, cylinder, and flat plate) or, with the particle geometric information (particle aspect ratio, volume, and surface area) included, the model simulates combustion of biomass particles of any shape. Model simulations of the three shapes agree nearly within experimental uncertainty with the data. For biomass particle devolatilization processes, model predictions extended to a wider range of sizes predict the effects of shape and size on yields and overall mass conversion rates. The near-spherical particle loses mass most slowly and its conversion time significantly differs from those of flake-like particles and cylinder-like particles as particle equivalent diameter increases. Little difference exists between the cylinder- and plate-like particles.

Both particle shape and size affect the pyrolysis product yield distribution. Near-spherical particles exhibit lower volatile and higher tar yields relative to aspherical particles with the same mass. Low-ash fuels yield up to 95% volatiles during high-temperature pyrolysis. Volatile yields decrease with increasing particle size for particles of all shapes.

Model simulations show that the flame increases the predicted particle temperature by about 100 K during char burning stage compared with that of a flame-neglected model, while it slightly influences the particle temperature during the late stage of biomass devolatilization and early char oxidation. No difference is resulted before flame is formed.

Acknowledgements

I wish to express my sincere thanks to those who helped in completion of this thesis. First of all I would like to thank my advisor, Professor Larry Baxter, for his kind guidance, helpful suggestions, and encouragement. Truly concerned for welfare of others and committed to excellence in both research and teaching, he is a leader in engineering education. I would like to thank Dr. Thomas Fletcher for his assistance in the particle combustion model development. Appreciation is also expressed to Dr. Dale Tree for suggestions and discussions in the color-band pyrometry development and the entrained-flow reactor design.

Financial support from various offices of DOE and Sandia National Laboratories is gratefully acknowledged.

Thanks go to Elvin Ip, Warren Roberts, and Andrew Mackrory for their help and valuable discussions. It's a great experience to work with them. Contributions of my other co-workers for this project are also greatly appreciated: Luke Werret, Justin Scott, Gregory Peirce, Kelly Echols, Paul Foster, Bryan Ripa, and Todd Gunderson.

I would like to thank my mom, Changyu Qu, and my parents-in-law, Zhihuang Zhao and Zhongliu Li, without whose assistance and encouragement this work would not have been possible.

Finally and most importantly, I would like to thank my wife, Yi Li, for her love, understanding, support, and encouragement

Nomenclature

a	—	Pixel/cell area of CCD or CMOS sensor, m^2 Ash content,
A	—	Pre-exponential factor, s^{-1}; area, m^2;
AR	—	Aspect ratio, /
B	—	Radiance, $W.Sr^{-1}.m^{-2}.nm^{-1}$
BLT	—	Boundary layer thickness, m
C_1, C_2	—	Constants in Planck's law
Cp	—	Heat capacity, $J.kg^{-1}.K^{-1}$
d	—	Working distance, m
d_{pore}	—	Pore diameter, m
D	—	Lens diameter, m
D_{eff}	—	Effective diffusivity, $m^2.s^{-1}$
D_{AB}	—	Molecular diffusivity, $m^2.s^{-1}$
D_K	—	Knudson diffusivity, $m^2.s^{-1}$
DN	—	Digital number / pixel intensity,
E	—	Photon energy, J Irradiance on sensor, $W.nm^{-1}$
E_i	—	Activation energy, $J.mol^{-1}$
F	—	Geometric configuration factor,
g	—	Camera gain value,
h	—	Planck's constant, 6.626068×10^{-34} $m^2.kg.s^{-1}$
h_f	—	Heat transfer coefficient, $W.m^{-1}.K^{-1}$

h_m	—	Mass transfer coefficient, $m.s^{-1}$
$\hat{H}$	—	Enthalpy, $J.kg^{-1}$
k	—	Rate constant, devolatilization reaction — s^{-1}; heterogeneous reaction — $m.s^{-1}$
K	—	Thermal conductivity, W/m.s
M	—	Molecular weight, $kg.kmol^{-1}$
M_W	—	Gas average molecular weight, $kg.kmol^{-1}$
n	—	Shape factor
Nu	—	Nusselt number,
p	—	Pressure, Pa
Pr	—	Prandtl number,
q	—	Radiant energy flux, $J.m^{-2}$
r	—	Radius coordinate, m Reaction rate, $kg.m^{-3}.s^{-1}$
Re	—	Reynolds number
R, R_g	—	Universal gas constant, $J.mol^{-1}.K^{-1}$
Rp	—	Particle radius, m
R_{SA}	—	Surface area ratio,
t	—	Time, s
S_a	—	Particle specific surface area, $m^2.m^{-3}$
SA	—	Surface area, m^2
S_i	—	Source term in conservation equation

T	_	Temperature, K
u	_	Gas velocity, $m.s^{-1}$
v	_	Volume, m^3
x	_	Conversion,
X	_	Area ratio of effective sensor over light source,
Y	_	Mass fraction,
Z	_	Interpolated third coordinate of reconstructed particle surface point, m

Greek symbols

α	_	Proportional factor,
β	_	Particle/droplet swelling/shrinking factor,
□	_	Porosity,
γ	_	Gas specific heat ratio,
□	_	Viscosity, Pa.s
□	_	Permeability, Darcy
□	_	Wavelength, nm
θ	_	Blowing factor,
□	_	Density, $kg.m^{-3}$
□	_	Stefan-Boltzman constant, $W.m^{-2}.K^{-4}$
□	_	Emissivity,
τ	_	Transmitter,
Ω	_	Solid angle, Sr

□H	_	Heat of reaction, $J.kg^{-1}$
Δt	_	Camera exposure time, s

Subscript

0	_	Initial value or reference state
A	_	Ash
B	_	Biomass
C	_	Char
con	_	Conductivity
g	_	Gas phase
G	_	Light gas
HC	_	Hydrocarbon
i	_	Species or component in solid phase
j	_	Species or component in gas phase
k	_	Species or component in liquid phase
I	_	Inert gas
M	_	Moisture
rad	_	Radiation
V	_	Water vapor
T	_	Tar
w	_	Wall

Introduction

During the last two decades, a growing interest developed in renewable energy sources. There are two driving forces for this interest: (1) the increasing concern about the environmental impact of fossil and nuclear energy sources; and (2) the increasing anxiety regarding the security and longevity of fossil fuel.

The threat of regional and global climate change (global warming) may require significant reduction in the emissions of greenhouse gases — most notably CO_2. One potential strategy for reducing such emissions is the replacement of fossil fuels with renewable biomass fuels. Renewable fuels can be essentially CO_2-neutral (considering the carbon cycle in the atmosphere) if derived from sustainable cultivation practices with minimal fossil fuel requirements. Unlike fossil fuels, biomass fuels can be renewable and CO_2-neutral in the sense that the CO_2 generated by biomass utilization is removed from the atmosphere by the plants that replace the fuel, closing the carbon loop on a short timescale. If the biomass is renewably produced (as is generally the case in developed nations), there is little net increase in atmospheric CO_2 content. Since most biomass, including essentially all biomass residue, decays in any case, often producing methane and other decomposition products that greatly exceed the potency of CO_2 as greenhouse gases, use of biomass residues as fuel has the potential of actually decreasing greenhouse gas impacts, not just being neutral (Mann 2001).

Today, various forms of biomass energy account for nearly 6 % of all energy consumed in the U.S., and 47 % of renewable energy used in the U.S (EIA 2003), as illustrated in Figure 75.

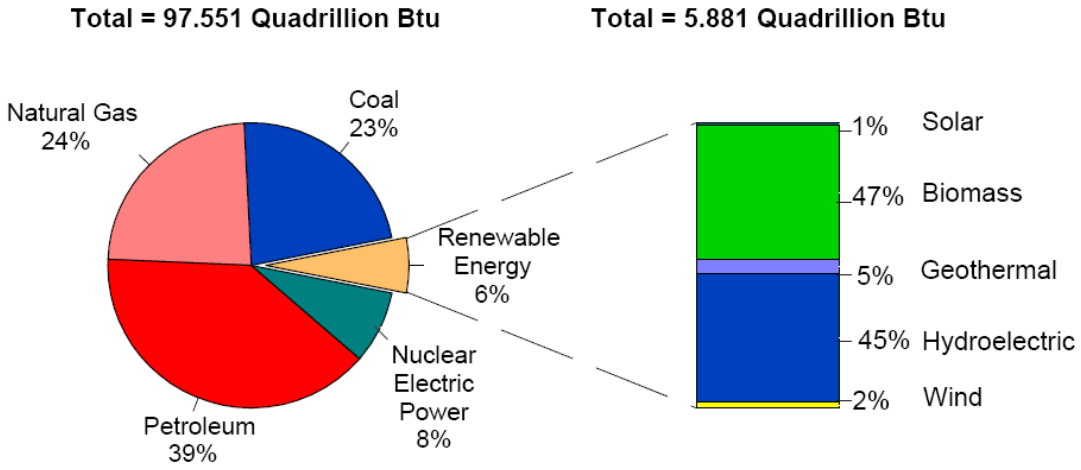

Figure 75 The role of renewable energy consumption in the nation's energy supply, 2002 (EIA 2003)

Biomass represents about 80 % of non-hydro renewable energy generated in the US. Additionally, biomass energy represents among the least costly renewable energy options in many cases (Baxter 2005). Biomass meets a variety of energy needs, including generating electricity, heating homes, and providing process heat for industrial facilities. Biomass can be utilized with the following approaches:

Direct combustion to produce steam and generate electricity;

Gasification to produce combustible gas, which may drive a high-efficiency, combined-cycle gas turbine if current technical roadblocks are resolved;

Pyrolysis to obtain pyrolysis oil and different kinds of chemicals;

Thermal or chemical conversion to transportation fuels, such as ethanol, methanol, and Fischer-Tropsch fuels.

Of these uses, by far the largest use is conversion to steam for process use and power generation.

For biomass to achieve its potential as an energy resource, further research is needed throughout the biomass energy production chain from plant genetics to fuel processing (Baxter 2005) due to a major problem: the relatively low power generation efficiency of biomass power plants (typically 12~25%, but 33~38% for cofiring in a coal-fired power plant), which partially makes biomass energy more expensive than fossil fuel energy. Therefore, new approaches are likely required to substantially increase the efficiency of the conversion of biomass to heat and power. The identification and design of these novel approaches require fundamental understanding of the unique combustion characteristics of biomass fuels.

Coal combustion research represents a relatively mature science in that a lot of promising models have been developed to describe coal devolatilization and oxidation processes, and comprehensive models and CFD codes are available to predict the performance of coal-fired boilers. However it is unreasonable to apply these models directly for biomass combustion, since biomass is much different from coal in both physical and combustion properties.

Some major property differences between biomass and coal are listed in Table 19 (Baxter 2000).

Table 19 Properties comparison of coal and biomass fuel (Baxter 2000)

	Density (kg/m^3)	Size (mm)	Shape	H/C (molar)	O/C (molar)	Heating value (MJ/kg)	Volatile (%)
Coal	~1300	~0.1	spherical	~0.8	0.02~0.4	~25	40+
Biomass	~500	~3.0	irregular	~1.5	0.4~1.0	~16	80+

All of these major property differences make biomass combustion behavior dramatically different from that of coal. Advanced high-efficiency biomass conversion technologies may take advantage of some of the above biomass unique characteristics and further research is needed for biomass combustion.

The large variations in biomass particle sizes and shapes play significant roles in biomass combustion. For small size particles, such as pulverized coal, the Biot number (hL/k) is generally much less than one, justifying the assumption of uniform intra-particle temperature and concentration distributions. But biomass particles, with a typical size of 3 mm and particle-gas heat transfer coefficient of 30 W/m K generally have Biot numbers of about 0.769, which makes the uniform temperature and concentration distribution assumption no longer valid during

combustion. Larger particle sizes establish the potential for large internal temperature and composition gradients (Lu, Robert et al. 2006), which complicate combustion models.

Furthermore, various particle shapes result in different particle exterior surface area to volume ratios and non-uniform heat fluxes in the particle, which can further affect the devolatilization and oxidation rates. Figure 76 shows the surface area ratios of cylinder and disc-plate over a spherical particle with unit volume as functions of aspect ratio. Both the cylinder and disc-plate have higher surface-area-to-mass ratios than does a sphere, and the difference increases with increasing aspect ratio. At high-temperature and high-heating-rate conditions in entrained-flow systems, these phenomena may dominate the overall conversion process. Therefore, particle shape strongly impacts commercial biomass conversion systems.

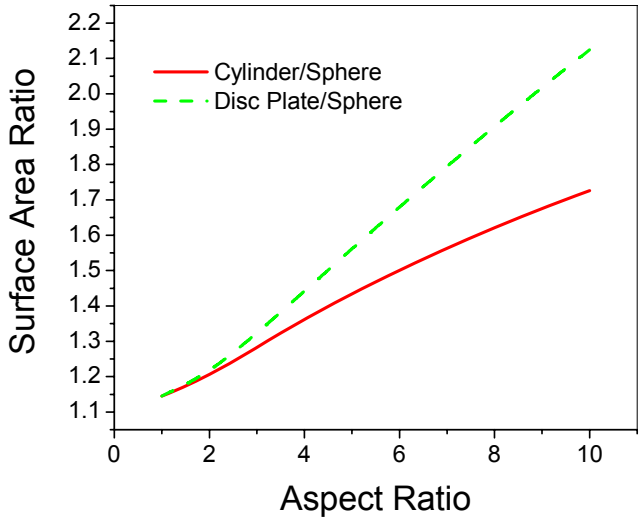

Figure 76 Surface area ratios of aspherical particles with different aspect ratios over spherical particle with same volume.

Literature Review

This literature review is divided into four sections. Section 1 describes biomass composition and chemical structure. In Section 2, the pyrolysis mechanisms and kinetics of biomass and biomass components are summarized, including biomass particle conversion models. Section 3 discusses influences of various factors on biomass pyrolysis, including temperature, heating rate, particle size and shape, and inorganic contents. Section 4 discusses biomass char oxidation processes, char reactivity and related issues.

Biomass Composition

Biomass contains many compounds, but the dominant chemical species can be categorized as cellulose, hemicellulose, and lignin. Several minor components, including lignans, volatile oils, tannins, resins, proteins, etc. complete the organic fraction of the fuel. The inorganic fractions include both biologically active materials, such as potassium and chlorine, particulate materials biologically incorporated into the plant, such as silica, and adventitious material included in the form of soil, process-related compounds such as clay in paper, and often impurities unrelated to

biomass itself ranging from wastes (nails, paint, bottles, pipes, refrigerators, etc.) to process or shipping components (bale wires, mill blades, etc.). As a group, the inorganic materials represent ash-forming components. Each of these major components is discussed separately below.

Cellulose

Cellulose represents about 50 wt% of biomass, ranging from about 30 wt% for some trees and nut shells to over 90 wt% for cotton balls and similar materials. Cellulose typically comprises less than 10,000 anhydroglucose sugar units as indicated in Figure 77, containing 49 wt% oxygen. Its chemical formula is $(C_6H_{10}O_5)_n$, and there are covalent bond, hydrogen bond and Van Der Waal forces within the polymer. It is a glucose-based polysaccharide, illustrated below in Figure 77. A note of passing significance to this project is that the mer of a cellulose polymer contains two, not one, glucose units because of the geometric arrangement of the units relative to one another.

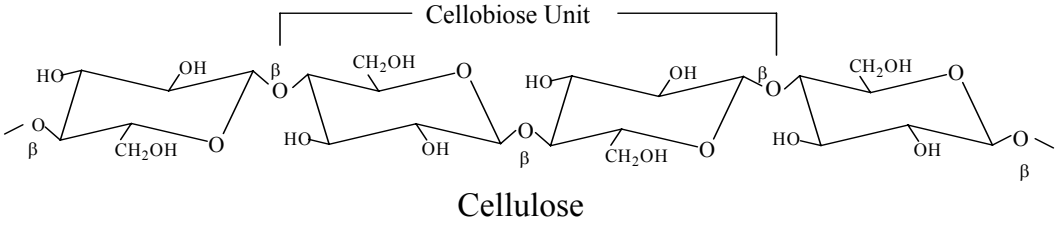

Figure 77 Chemical structure of cellulose (Northey 1998)

Hemicellulose

Hemicellulose accounts for about 25 wt% of biomass in many plants. Hemicellulose and extractives are chemically similar to cellulose except that they are not polymers in that they have no consistently recurring monomer unit and they are much shorter, with a degree of polymerization (DP) between 100~200. Hemicellulose includes several carbohydrate monomers (heteropolysacharides), mainly heterogeneously linked by six-carbon and five-carbon anhydro-sugars, with the five-carbon sugar containing about 54 wt% oxygen by mass.

The chemical structure of some major hemicelluloses (including galacto-glucomannans, arabinoglucuronoxylan, glucurono-xylans, and glucomannan) found in hard wood and soft wood appear in Figure 78 (Northey 1998).

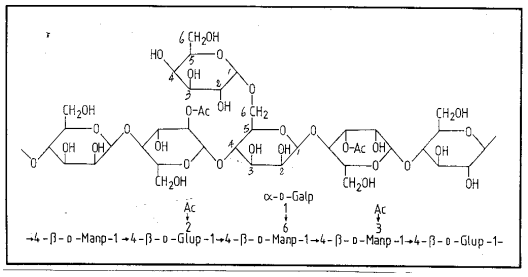

(a) galactoglucomannans

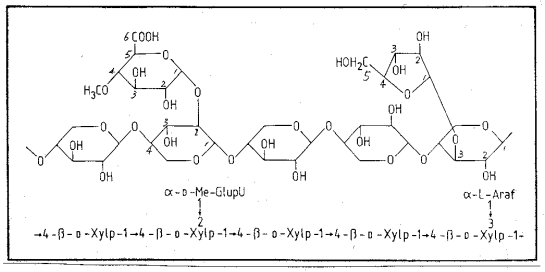

(b) arabinoglucuronoxylan

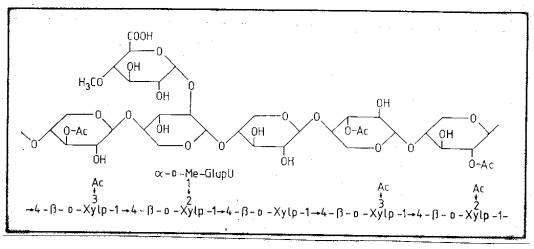

(c) glucuronoxylans

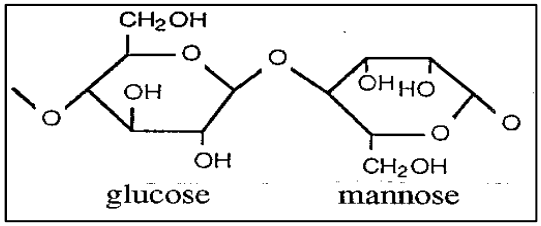

(d) glucomannan

Figure 78 Chemical structures of some typical hemicelluloses (Northey 1998)

Lignin

Lignin contributes about 25 wt% of biomass mass, with generally higher contents in woody material and generally lower contents in herbaceous material. Lignin is a branched, long-chain molecule similar to polymers except that it has a variety of monomer components, mostly derived from phenylpropane units and joined by carbon-carbon and ether linkages. Lignin appears to be a primarily random, three-dimensional polymer of 4-propenyl phenol (p-coumaryl alcohol), 4-propenyl-2-methoxy phenol (guaicyl alcohol), and 4-propenyl-2, 5-dimethoxy phenol (syringl alcohol). Figure 79 (a) (Abreu, Nascimento et al. 1999) illustrates their chemical structures. Lignin can also be represented as coniferyl ($C_{10}H_{12}O_3$), p-coumaryl ($C_9H_6O_3$), and sinapyl ($C_{11}H_{14}O_4$) alcohols (see Figure 79 (b) (Stenius 2000)).

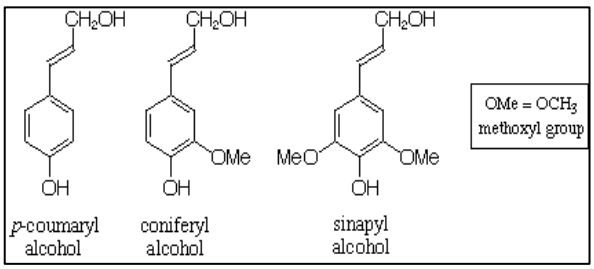

(a) structure one (Abreu, Nascimento et al. 1999)

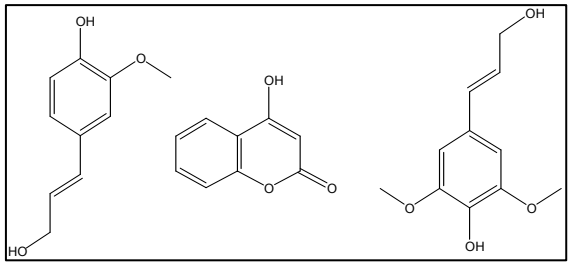

(b) structure two (Stenius 2000)

Figure 79 Three compounds comprising the bulk of lignin

The ratio of these phenols in lignin is a function of the plant species and ecosystems (Stenius 2000). Normal softwood lignins are usually referred to as "guaiacyl lignins" because the

structural elements are derived principally form trans-coniferyl alcohol (more than 90%), with the remainder consisting mainly of trans-p-coumaryl alcohol. In contrast, hardwood lignins, generally termed “guaiacyl-syringyl lignins”, are mainly composed of trans-coniferyl alcohol and trans-sinapyl alcohol-type units in varying ratios (about 50% of trans-coniferyl alcohol and about 50% of trans-sinapyl alcohol). The major linkage in lignin, the arylglycerol-β-aryl ether substructure, comprises about half of the total inter-unit linkages. The oxygen content of these lignin model compounds ranges between 12-29 wt%, much lower than cellulose or hemicellulose. One chemical structure model of softwood lignin is proposed in Figure 80.

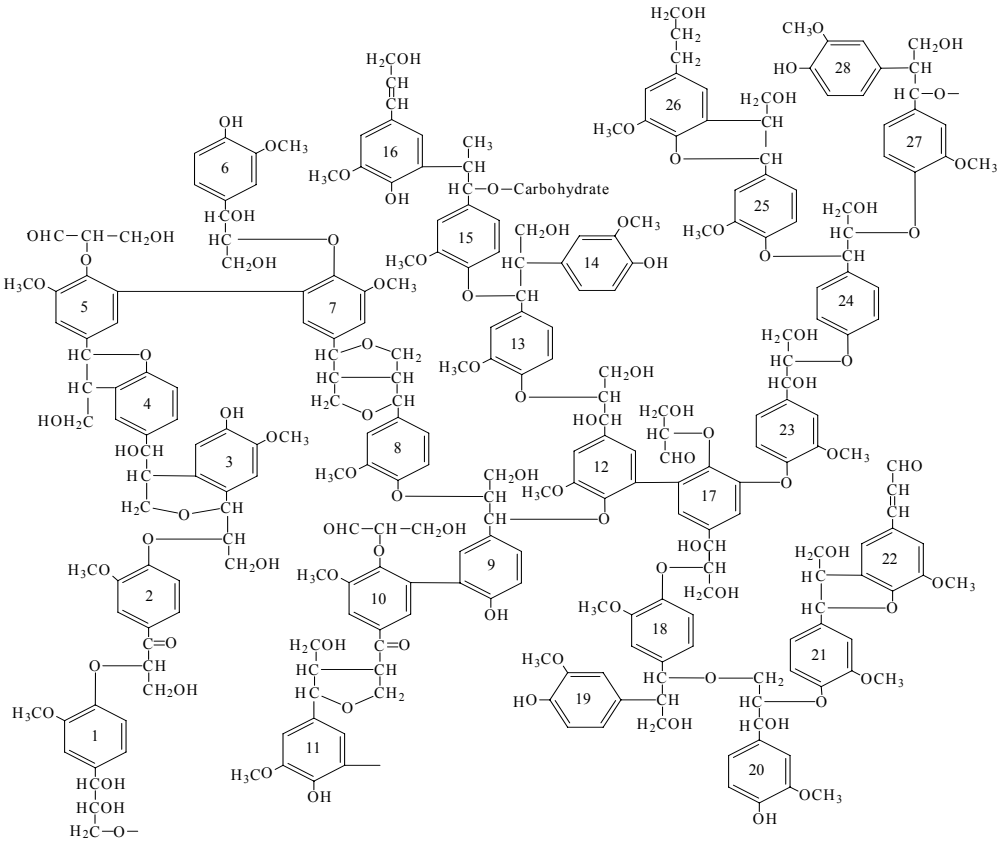

Figure 80 The model of chemical structure of lignin (Northey 1998)

Mechanism and Kinetics of Biomass Pyrolysis

Currently, the exact pyrolysis mechanisms of biomass are not clear, but substantial literature sources on biomass devolatilization kinetics and mechanisms are available. Cellulose thermal decomposition models, together with phase changes and tar production, provide a framework from which a lot of investigators have developed mathematical descriptions of biomass devolatilization.

In general, kinetic models of biomass pyrolysis process can be grouped into three main categories:

One-step reaction, successive reactions, or two-stage models;

Chemical structure-based models;

Superposition models, which are based on the kinetics of individual component (cellulose, hemicellulose and lignin) of biomass.

One-step reaction, successive reactions or two-stage model

Some simple models of cellulose devolatilization appear in the literature. Broido and Nelson suggested a competitive reaction model for large cellulose samples (see Figure 81 (a) (Broido and Nelson 1975)), followed by a multi-step model (see Figure 81 (b) (Broido 1976)) reported by Broido; and a third multi-step model by Bradbury, Sakai, and Shafizadeh (Bradbury, Sakai et al. 1979) (see Figure 81 (c)). All of these models were usually used to describe low- or medium-temperature and low-heating-rate pyrolysis conditions. They are not applicable for simulating biomass conversion because they assume a constant ratio of the char to volatiles yield and cannot be extended to systems different from the one on which they were based.

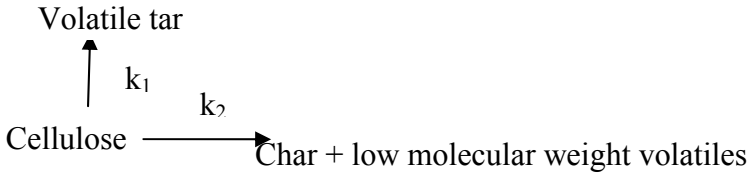

(a) Broido and Nelson model (Broido and Nelson 1975)

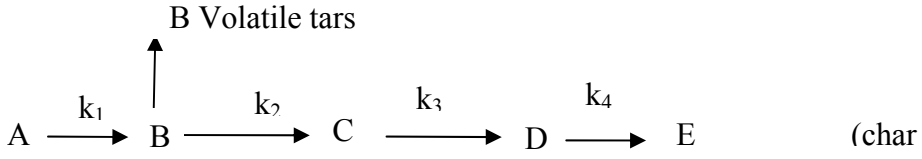

(b) Broido multi-step model (Broido 1976)

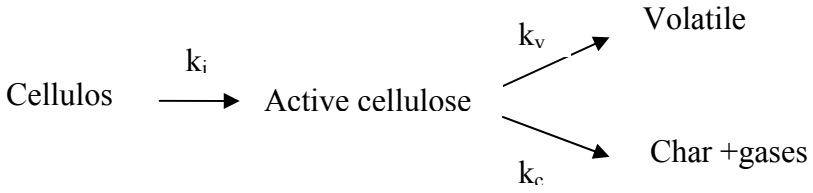

(c) Broido multi-step model (Bradbury, Sakai et al. 1979)

Figure 81 Some basic cellulose pyrolysis models

Two-stage models (Di Blasi 1996) can be profitably applied to simulate thermal conversion since they include the description of the primary degradation of solid and the secondary degradation of

primary pyrolysis products. A typical wood pyrolysis two-stage model appears in Figure 82. The secondary degradation discussed here are the reactions occurring within the biomass particle between vapor phase and the solid, not the secondary cracking reactions of the vapor phase at high temperature, where tar will further react and produce soot and light gas.

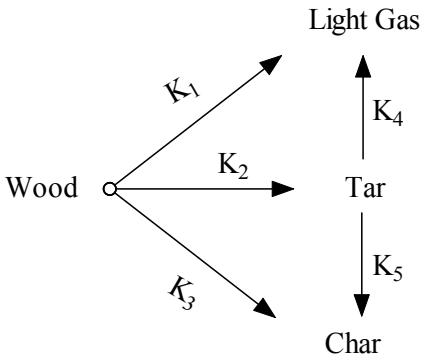

Figure 82 Two-stage wood pyrolysis model (Di Blasi 1996)

A similar mechanism considering secondary reactions was used by Jalan and Srivastava (Jalan and Srivastava 1999). The model appears in Figure 83 and accounts for the secondary reaction between the volatile, gas, and char.

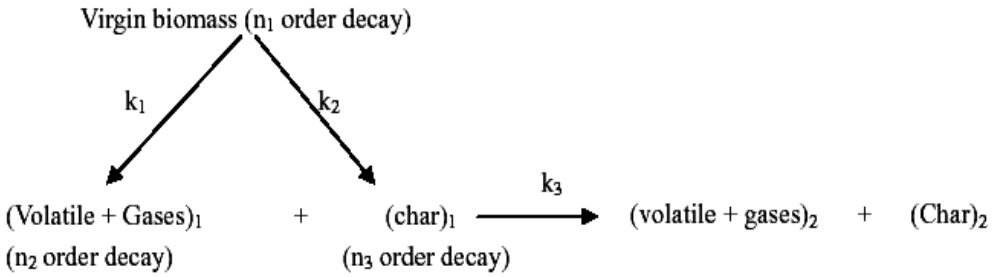

Figure 83 Srivastava pyrolysis model (Jalan and Srivastava 1999)

In these models, k_i is the reaction rate constant, which can be expressed as the Arrhenius formula: $k = A*exp(-E/RT)$. A is the pre-exponential factor; E is the apparent activation energy; R is the universal gas constant and T is the temperature. All reactions are assumed to be first-order. With a few modifications, these models have been widely used to predict the pyrolysis characteristics of biomass and its components.

Chemical Structure Model

In recent years, chemical structures have played more significant roles in the description of thermal decomposition of fuels, especially for coal combustion. Three recent models, Functional-Group-Depolymerization Vaporization Cross-linking Model (FG-DVC), FLASHCHAIN, and Chemical Percolation Devolatilization (CPD) (Fletcher, Kertein et al. 1992; Fletcher, Pond et al. 2003) have been developed with parameters defined at least in part by chemical composition of the fuel. The fuel chemical structures can be characterized by NMR, FTIR or standardized

(typically ASTM) procedures. As a group, these models illustrate how the chemical forms of fuel influence its thermal decomposition. They can also predict the amount of tar formation and cross-linking, the latter representing condensed-phase reactions that lead to the formation of a relatively non-reactive char.

With some modification of the FG-DVC coal devolatilization model, Chen and Charpenay (Chen, Charpenay et al. 1998) applied it to model biomass pyrolysis kinetics. Biomass chemical structure data were collected from ultimate, proximate and TG-FTIR analyses. This model was demonstrated to have predictive capacity when extrapolated to modestly high heating rate conditions (10^3 K/sec). The predicted overall weight loss and CO_2 yields agree very well with experimental data, but not for other species. The observed discrepancies could result from the secondary reactions and/or catalytic role of inorganic material, so improvements are needed to properly account for effects of inorganic material and secondary reactions.

Niksa (Niksa 2000) investigated the rapid devolatilization of diverse forms of biomass with a bio-FLASHCHAIN model. Given the proximate and ultimate analyses and thermal history and pressure, the model reportedly predicts the complete primary product distribution, though this claim seems exaggerated given the significant influence of inorganic material on yields and rates (discussed later) which is not among the input parameters.

Superposition Model

More sophisticated approaches to describe biomass devolatilization kinetics involve superposition of the behavior of typical biomass components such as lignin, cellulose, and hemicellulose (Koufopanos, Maschio et al. 1989; Koufopanos, Papayannakos et al. 1991; Raveendran, Ganesh et al. 1996; Miller and Bellan 1997; Orfao, Antunes et al. 1999). In these models, biomass components in the mixture behave in the same way as they do separately or with weak interactions. In Miller's (Miller and Bellan 1997) work, the pyrolysis of general biomass materials was modeled via a superposition of cellulose, hemicellulose and lignin kinetics. All three of the primary biomass components are modeled with multi-step kinetics involving both competitive primary pyrolysis and secondary tar decomposition reactions. Their model results agree well with micro-particle data, but discrepancy exists for macro-particles, as illustrated in Figure 84. This spherical particle model results suggest that particle shape (geometry) plays an important role during biomass thermal decomposition.

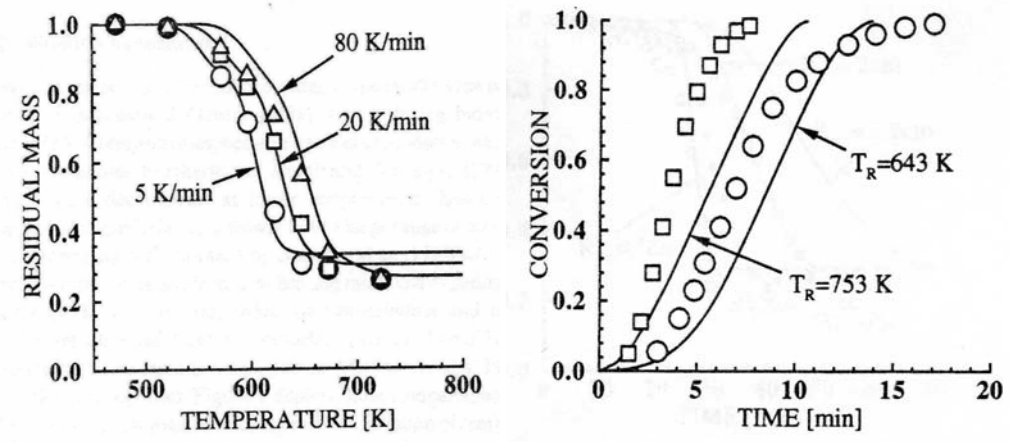

(a) Micro-particle (b) Macro-particle

Figure 84 Comparisons of superposition model predictions with experimental data for micro-particle and macro-particle

Based on the chemical structure of each biomass component, Demirbas (Demirbas 2000) proposed individual pyrolysis mechanism for cellulose, hemicellulose and lignin. In his cellulose mechanism scheme, the kinetics of the reaction proceeds through three distinct stages of pyrolysis. In the first stage, a rapid decomposition takes place with a weight loss that increases with rising temperature. In the second stage, decomposition and volatilization occur. Finally, hemicellulose reacts more readily than cellulose during heating, and undergoes rapid thermal decomposition. Lignin decomposition includes cleavage of aliphatic C-O bonds, aromatic C-O bonds and side-chain C-C bonds. All these mechanism are limited to low-temperature pyrolysis processes.

This is an appealing approach since cellulose thermal decomposition has been widely studied and satisfying data are available, and the composition (the weight fraction of cellulose, hemicellulose, and lignin) of biomass can be estimated based on ultimate and proximate analysis and heating value.

Factors Affecting Biomass Pyrolysis

Generally speaking, biomass pyrolysis characteristics are influenced by the chemical and physical properties (composition, inorganic content, density, thermal conductivity, heat capacity, particle size and shape) of biomass, as well as operating conditions such as temperature, pressure, and heating rate.

Composition

Pyrolysis yields and product distributions are mainly determined by the composition of the original biomass. Usually cellulose has the lowest char yield; lignin produces highest char yield; hemicellulose has a medium char yield, as shown in Figure 85 (Miller and Bellan 1997). The tar yield is associated with that of char, exhibiting the opposite trends.

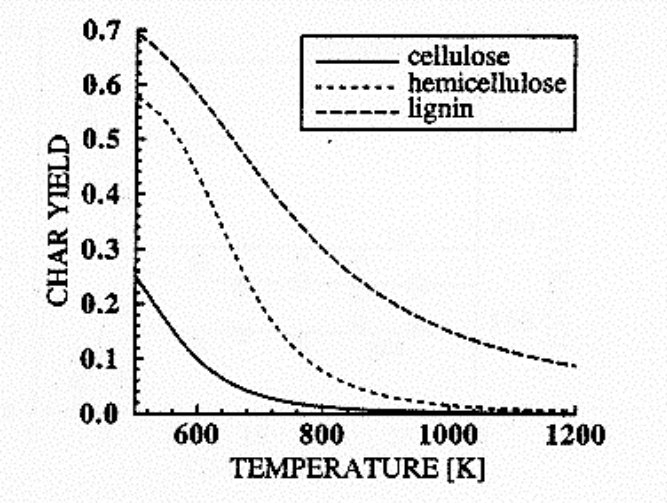

Figure 85 Char yields as a function of temperature for primary biomass components (Miller and Bellan 1997)

Physical properties, temperature and heating rate

Colomba (Di Blasi 1997) investigated the influences of physical properties on biomass devolatilization. A detailed particle energy and mass transport model was used to predict the effects of density, thermal conductivity, and permeability to gas flow and specific heat capacity. For conversion in a thermally thick regime (intra-particle heat transfer control), it was found that variations in the physical properties mainly affect the reactivities of secondary reactions of tar vapors and the conversion time. The highest sensitivity is associated with the biomass density and the char thermal conductivity.

Miller and Bellan (Miller and Bellan 1996) performed a parametric investigation using a spherically symmetric particle pyrolysis model. The effects of reactor temperature, heating rate, porosity, initial particle size and initial temperature on char yields and conversion times were illustrated. The largest effect of the heating rate was observed in the variation of the conversion times for both cellulose and wood. An increase in heating rate decreased both the char yield and the conversion time. Additionally, both char yield and conversion time are increasing functions of initial particle size, as shown in Figure 86 (Miller and Bellan 1996), where conversion time refers to time to reach 90% conversion. The char yield increase is due to the secondary reactions between tar vapor and solid in the particle and the lower temperature heatup.

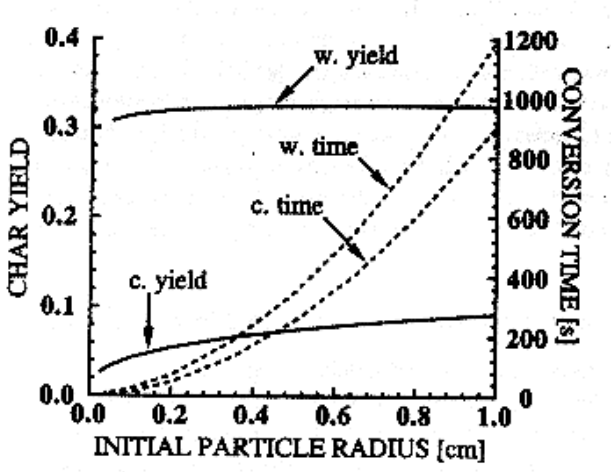

Figure 86 Char yield and conversion time of cellulose and wood vs. initial particle size (Miller and Bellan 1996) (w --- wood, c – cellulose)

Baxter and Robinson (Baxter and Robinson 2000) applied engineering models of kinetics, heat transfer, and mass transfer to predict the effects of particle size and density, shape, internal temperature gradients, and composition. The results of mass loss history of biomass particles were compared with data collected from several highly instrumented furnaces. Drying and devolatilization are found to be primarily heat-transfer controlled whereas oxidation is found to be primarily mass-transfer controlled for most biomass of practical concern. In their later research, they found devolatilization removes most of the mass. Under rapid, high-temperature

pyrolysis conditions, up to 95 wt% of the mass is released during devolatilization, significantly more than ASTM tests.

The effects of particle size, reactor heating rate, and final reactor temperature were theoretically and experimentally investigated by Blasi (Di Blasi 1996). Similar results were obtained: large particle size increases char yields; higher heating rates result in higher volatile yields and lower char yields (see Figure 87). His researech indicates three main regimes of solid-fuel pyrolysis: the thermally thick, the thermally thin, and the pure kinetic regime. The pure kinetic limit involves only particles at least one order of magnitude smaller than those allowing conversion in the thermally thin regime, except at very low temperatures.

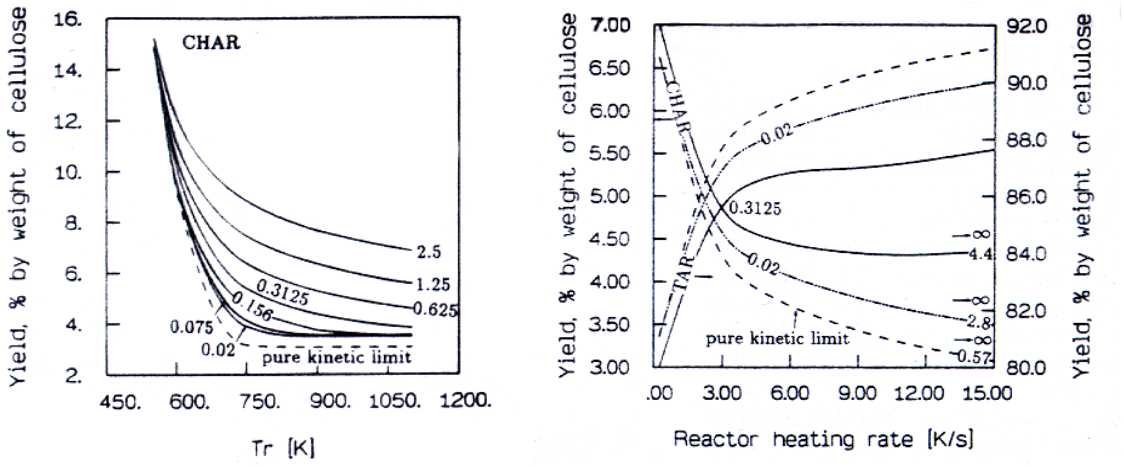

Char yield vs. reactor temperature for different particle size

(b) Char and tar yield vs. heating rate for different particle size

Figure 87 Effects of particle size and heating rate on char and tar yields (Di Blasi 1996)

Particle shape and size

As for particle shape, usually a spherical particle shape is assumed in modeling works for convenience. Other particle shapes have been considered. Jalan and Srivastava (Jalan and Srivastava 1999) studied pyrolysis of a single cylindrical biomass particle, and particle size and heating rate effects were investigated. In Horbaj's model (Horbaj 1997) and Liliddahl's model (Liliedahl and Sjostrom 1998) , a particle geometric factor was introduced to account for the particle shape, which can deal with a prism (or slab), a cylinder (or rod), and a sphere.

In 2000, Janse and Westerhout (Janse, Westerhout et al. 2000) simulated the flash pyrolysis of a single wood particle. To investigate the influence of particle shape, simulations have been carried out with spherical, cylindrical and flat particle shapes (see Figure 88 (Janse, Westerhout et al. 2000)).

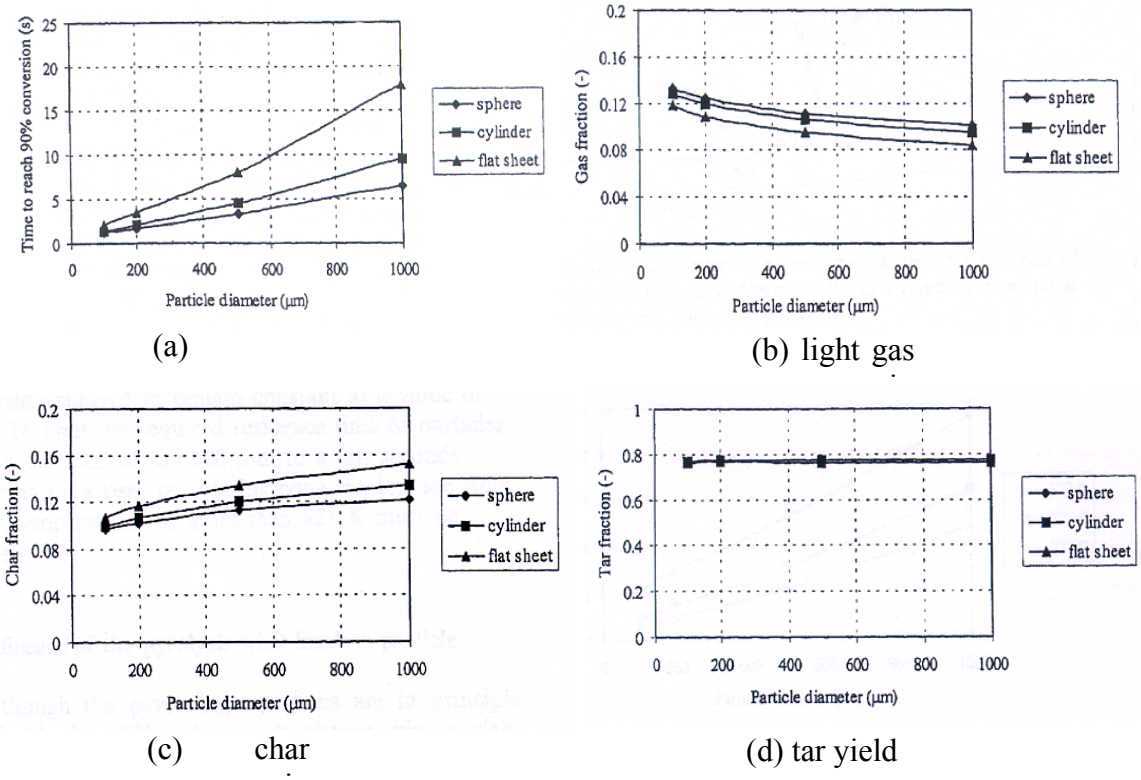

Figure 88 Effects of particle shape and size on conversion time and char, tar, and light gas yields during biomass pyrolysis (Janse, Westerhout et al. 2000)

Results show that spherical particles react most quickly compared to other particle shapes if the characteristic size is taken as the minium particle dimension. The higher surface-area-to-volume ratio of spherical particles on this basis explains this observation; flat particles react most slowly. In the work reported later in this document, the characteristic dimension is taken as the spherical-equivalent diameter – the diameter of a sphere with the same volume/mass as the aspherical particle. As will be shown, using the spherical-equivalent diameter results in the opposite trend – spherical particles react most slowly. There is no inconsistency in these results, just a difference in basis of comparison. At small particle diameters (typically less than 200 micron), the rate of reaction becomes dominant and the different particle shapes exhibit nearly equal conversion times. Flat particles seem to yield less gas and more char. This research also showed that an increase in particle diameter (or conversion time) caused no change in bio-oil yield, a slight decrease in gas yield and slight increase in char yield. This might be due to the low reactor temperature (surface temperature 823 K) they used to simulate this process.

Inorganic material

Inorganic material combined with organic components strongly influence biomass pyrolysis kinetics, total char yield, and char oxidation kinetics due to its catalytic role. Some investigators in the biomass (and coal) communities refer to such material as mineral matter. Inorganic material is a more precise term as much of the material in low-rank coals and biomass does not have mineral characteristics but is largely atomically dispersed in the organic matrix. However, this distinction is rarely recognized in the literature and the two terms can be assumed to be

synonymous in most papers. Numerous investigations have been carried out using washed and doped samples of actual fuels and pure biopolymers (e.g., cellulose, lignin, xylan), but the mechanistic details of inorganic material impacts on devolatilization remain unclear (Antal and Gabor 1995). It is clear that removal of inorganic material, particularly compounds containing sodium and potassium, increases tar yield and decreases light gas yield. The total yields (ASTM) of char and volatiles differ among different biomass (Raveendran, Ganesh et al. 1995; Jensen, Dam-Johansen et al. 1998), as indicated in Table 20.

Table 20 Influences of ash on pyrolysis products distribution (wt %)

	Volatile		Char		Tar		Light gas	
	U	D	U	D	U	D	U	D
Coconut coir	70.5	68.5	29.5	31.3	29.4	36.2	41	32.5
corn cob	79.9	87.1	20.1	12.9	37.4	43.4	42.5	43.6
Groundnut shell	72.9	72.5	27.1	27.5	40.5	45.9	32.5	26.6
Rice husk	82.9	75.6	17.3	24.4	41.2	57.4	41.5	18.2
Wood	80.9	86.4	19.3	13.6	22.6	40.1	58	46.4

U–untreated, D–demineralizated

Williams and Horne (Williams and Horne 1994) found that even low concentrations of metal salt significantly affect thermal degradation of cellulose and the production of residual char. Removal of inorganic material also influences the kinetics of the process. For high-temperature and high-heating-rate conditions, little data have been obtained regarding the influence of inorganic materials on biomass pyrolysis.

Char Reactivity and Oxidation

Coal char reactivity and oxidation processes enjoy an extensive literature developed during the last decades. Char, either from coal or biomass, is usually considered to be mainly composed of carbon, containing far fewer heteroatoms (O, H, S, and N) than the fuels from which they derive but nonetheless retaining some heteroatoms and in any case having structures and reactivity very different from graphite. In this sense, the chemical structure of biomass char is similar to coal char, but large physical differences exist between them, such as density, thermal conductivity, porosity, surface area, and particle shape and size.

With birch wood chars obtained from a free-fall tubular reactor and a thermobalance, Chen et al. (Chen, Yu et al. 1997) studied the char reactivity with carbon dioxide and steam in the thermobalance. It was found that the reaction rates of the char were strongly affected by the particle temperature history during char formation. Chars obtained from rapid pyrolysis possessed higher reactivity (2.3-2.4 times higher) in the reaction with carbon dioxide or steam compared with chars from slow pyrolysis. In other words, kinetic rates of char increase with increasing particle heating rate during the thermal decomposition process.

The reactivity of two kinds of biomass chars from Southern pine and switchgrass was investigated by Wornat et al. (Wornat, Hurt et al. 1999). Results showed that at early stages of char conversion, both of the chars were quite reactive. However, their reactivity decreased somewhat during char conversion as more reactive carbon is preferentially depleted and the inorganic constituents of the chars underwent physical and chemical transformations that render them less catalytically active. They also found that even with small biomass char particle (75-106 micron), the irregular morphologies and their wide range of burning rates made a more rigorous and detailed kinetic analysis quite difficulty.

Results from Di Blasi et al.'s research (Di Blasi, Buonanno et al. 1999) indicate that in the kinetically controlled regime (low temperature ~873 K) and under non-isothermal conditions (10, 20-80 K/min heating rate), the reactivities (*dm/dt*) of three biomass chars (wheat straw, olive husks and grape residues) increased with conversion first, reaching a maximum, and decreased or remained constant then increased again as a function of conversion. A one-step global model interprets the mass loss curves in their work with conversion-dependent parameters. Again at low temperature in a TGA, Adanez and his coworkers (Adanez, de Diego et al. 2001) determined combustion reactivities of five biomass chars with a combined method, with similar results.

In the chemically controlled oxidation regime, Zhang et al. (Zhang, Dukhan et al. 1996) concluded that the total porosity of biomass char increased from an initial value of 0.6-0.76 to a final value of 0.83-0.88; the particle shrinkage of char was the result of the increased ordering of the graphitic microstructures in carbons with increased carbon conversion.

All the previously-cited investigations were conducted at low or medium temperature ranges and with a relatively small particle size. Generally speaking, during biomass char oxidation of relevance to this investigation, oxygen diffusion to a particle surface dominates the net biomass oxidation rates in practical combustion systems due to the relatively large size and rapid kinetics of biomass chars and the high temperatures of entrained-flow systems. Predictions of diffusion-limited burning of non-spherical biomass particles cannot be accurately accomplished by standard models without accounting for the geometric influences (Baxter and Robinson 2000). Investigations including particle shape and size and accounting for surface-area-to-volume ratios, are required to predict accurate heat transfer (and hence devolatilization) and oxidation rates of biomass particles and chars. This investigation addresses this issue.

Objectives and Approach

Objectives

The objective of this project is to develop experimental and modeling descriptions of non-spherical particle/droplet combustion and to demonstrate their applicability to biomass-fired, entrained flow boilers.

This overall objective includes experimental and theoretical components as follows:

Establish a comprehensive database including burning rate and thermal decomposition rate of a single biomass particles with differing shapes and sizes;

Develop a comprehensive particle combustion model, including particle drying, devolatilization, and char gasification and oxidation processes, based on the experimental data and theoretical

analysis. The model will also accounts for the effects of particle/droplet shape and size, reactor temperature, heating rate, and local environment (temperature, oxygen concentration, slip velocity, etc.).

Approach

The objectives of this project will be met by completing the following tasks.

Construction of an entrained-flow reactor

An entrained-flow reactor will be built that can generate the following data as functions of time during biomass combustion: particle surface temperature, size and shape, velocity, residence time, and mass loss. The reactor provides up to 3.0 seconds of residence time, a maximum wall temperature of 1500 K, and optical accesses for an imaging system at three positions along the reactor. *In situ* techniques will generate all of these data except particle mass, which will be based on particle sampling.

Particle imaging system

To measure the particle surface temperature, particle shape, and size change during combustion process, an imaging system is built to take three images simultaneously from three orthogonal directions during heat up and combustion. This system includes three CCD or complementary metal oxide semiconductor (CMOS) cameras, three image acquisition cards, and a high-performance computer. The color cameras are of high speed, high sensitivity, and at least three channels (typically red, green, and blue). The imaging system can record videos for the complete combustion process of a single particle in a single-particle reactor, and capture images for particles traveling in the entrained-flow reactor at different residence time.

3-D particle shape reconstruction algorithm development

Due to irregular shapes of biomass particle, a three-dimensional particle shape reconstruction algorithm is to be developed and coded. By combining the three particle images taken from three orthogonal directions into a three-dimensional computer-generated particle shape, the particle surface area, volume, and shape can be approximately determined. Such an algorithm leads to time-resolved measurement of the surface-area-to-volume ratio and similar important particle properties.

Color-band pyrometry development

For a particle traveling in the entrained-flow reactor or a particle undergoing shrinking/swelling during combustion, a non-contact pyrometry is preferred to measure its surface temperature. In this project, a color-band pyrometry (first-ever applied to particle combustion) will be developed and applied. With images taken by the imaging system, the local particle surface temperature can be calculated by the image pixel intensity ratio of any two of the three channels (red, blue, and green) by assuming gray body radiation for the particle. If the particle surface temperature is lower than reactor wall temperature, the reflection effect on the particle surface will be considered in the calculation and this may limit the useful range of the device. The local surface temperature can also be superimposed on the 3-D particle shape model generated by the shape

reconstruction algorithm, resulting in pixel-by-pixel temperature data for most of the 3D particle reconstruction.

Data collection and analysis

With a single-particle reactor, which is similar to a thermogravimetric analyzer but with a much higher heating rate, and the entrained-flow reactor system built in this project, experiments for the drying, devolatilization, and oxidation processes of biomass particles with different shapes and sizes will produce mass loss and temperature data from which kinetic rate constants for both devolatilization and oxidation models can be determined. Particle mass, surface temperature, center temperature, particle surface area and volume will be measured using techniques developed in this project. The data will be reconciled with the model.

Develop a comprehensive solid/droplet particle combustion model.

For the particle drying process, a mass and heat transfer coupled model will be used to simulate the evaporation and recondensation of moisture in the particle. Biomass devolatilization kinetics is to be a two-step global scheme model. Detailed particle mass and heat transfer models including kinetics, particle physical properties (including particle size and shape) and surrounding gas phase properties, will be developed to describe the particle drying, devolatilization, char gasification and oxidation processes. For biomass char oxidation, this is generally a diffusion-controlled process due to the typically large particle size. In this case, a simple mass transport model, instead of a complex one, may be used. However, oxidation kinetic expressions will be included in the model with some simplifying assumptions. Specifically, intrinsic, single-step surface kinetics will be used. Our expectation is that even global kinetics will have little impact on the diffusion-limited burning rates. However, shape and size will impact such rates substantially. Based on the above three sub-models, a comprehensive particle combustion model will be developed.

Experimental Method

Pyrolysis and combustion experiments were conducted in a single-particle reactor and an entrained-flow reactor for wood samples of different sizes and shapes. Experimental data, including particle mass loss, surface temperature, internal temperature, and particle size change were collected.

Samples

Four types of biomass samples have been prepared and used in this investigation. Sawdust particles with size ranged from 300 to 500 μm were prepared for the entrained-flow reactor since its maximum residence time is 3.0 seconds; large size wood dowel particles with size ranged from 3 mm to 12 mm were used for the single-particle reactor so that the samples can be suspended using thermocouple wire; knees and stalks of wheat straw were also prepared and burned in the single-particle reactor.

Sawdust Particles

Sawdust particles have broad distributions both in size and shape. Three shapes were prepared in this project: near-spherical, flake-like, and cylinder-like. For each shape, samples with more than two different sizes were prepared. To obtain enough sample with uniform properties for each

specific shape and size, sawdust was first separated using sieves, then aerodynamically classified. Finally, different aspect ratios were separated by sieves again. The detailed preparation procedure appears in four steps, as illustrated in Appendix A.

With this procedure, sawdust particle samples with fairly uniform shape and size have been prepared. Two sets of samples were used to conduct pyrolysis and combustion experiments in the entrained-flow reactor. The particle volume and surface area were calculated using the 3-D particle shape reconstruction algorithm developed in this project. The particle volume and surface-area-to-volume ratio of each shape was verified by measuring over 2000 particles and assuming an average particle density of 650 kg/m^3, consistent with the literature (Koufopanos, Papayannakos et al. 1991; Miller and Bellan 1997). Particle shapes are pictured in Figure 89. Other particle properties appear in Table 21 and

Table 22. The samples were put in an oven at 90 °C for two hours before feeding.

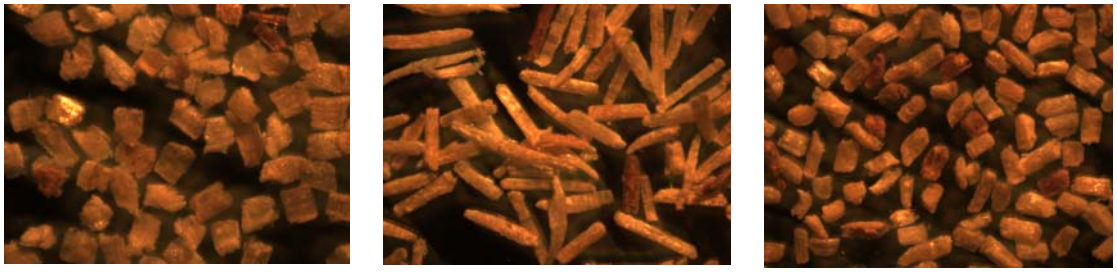

(a) flake-like particle (b) cylinder-like particle (c) near-spherical particle

Figure 89 Photographs of sawdust particles of different shapes

Table 21 Properties of sawdust sample set I

Sample	Flake-like	Cylinder-like	Equant
Volume ($\times 10^{-11}$ m^3)	1.697	1.682	1.794
Equivalent diameter (mm)	0.32	0.32	0.325
Surface area ($\times 10^{-7}$m^2)	4.91	4.79	3.44
Aspect ratio	4.0 (width/thickness)	6.0	1.65

Table 22 Properties of sawdust sample set II

Sample	Flake-like	Cylinder-like	Equant
Volume ($\times 10^{-11}$ m^3)	1.88	1.97	1.99

Equivalent diameter (mm)	0.33	0.34	0.34
Surface area ($\times 10^{-7} m^2$)	5.26	5.25	4.1
Aspect ratio	3.8 (width/thickness)	5.8	1.5

Wood Dowel Particles

The single-particle reactor uses larger wood particles. Three regular shapes, cylinder, disc, and near-sphere, were obtained by cutting poplar dowel rod to different aspect ratios. Particle diameters ranged from 3 mm to 12 mm. Aspect ratios (AR=length/diameter) ranged near 1.0 for spheres, 0.2 to 0.125 for discs, and 5.0 to 8.0 for cylinders. Figure 90 illustrates typical samples.

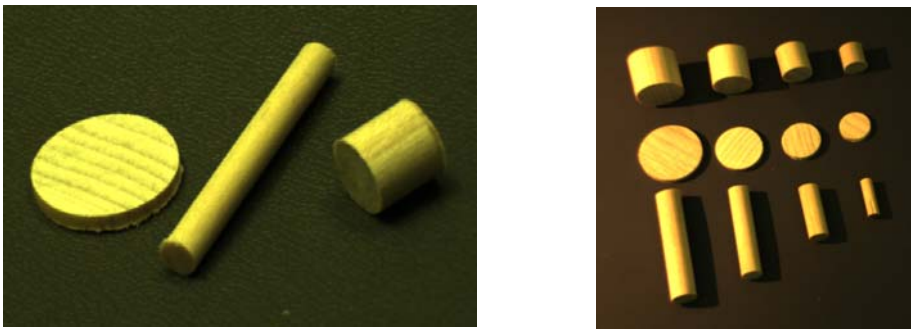

(a) Different shape (b) Different sizes

Figure 90 Poplar dowel particle samples

Two sets of poplar dowel particles were used in this investigation. Sample data are tabulated in Table 23 and Table 24. Moisture content of the samples is about 6%. To study the drying behavior of biomass particle, samples with different moisture contents were also prepared by soaking samples in water.

Table 23 Properties of poplar dowel particle sample set I

	Diameter (inch)	AR
Near-sph	0.25, 0.3	1.0

	ere	75,0.5
Disc	0.188,	0.125 (thickness/diameter) 0.375,0.75
Cylinder	0.125,	8.0 (length/diameter) 0.188,0.25

Table 24 Properties of poplar dowel particle sample set II

	Diameter (inch)	AR
Near-sphere	0.125 - 0.625	1.0

e		
Disc	0.125 – 1.0	0.2 (thickness/diameter)
Cylinder	0.125 – 0.438	5.0 (length/diameter)

Wheat straw samples

Wheat straw knees and stalks with same mass have been prepared. The particle mass is about 0.04 gm. Stalks appear to be larger than knees due to density difference, as shown in Figure 91. The diameter of knee is about 4 mm, and ~4 × ~ 12 for stalks.

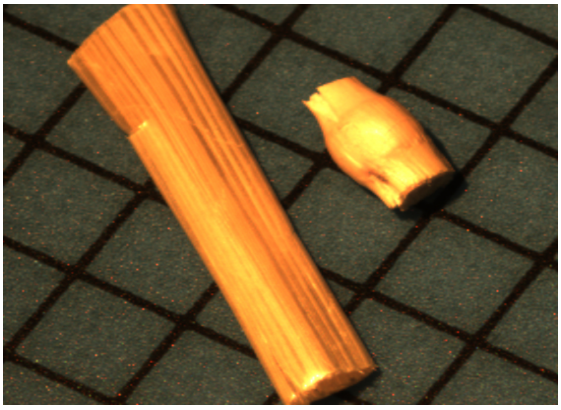

Figure 91 Wheat straw samples: knee and stalk

Experimental Setups

Devolatilization and combustion experiments used both entrained-flow and single-particle reactors, both facilities designed and built as part of this project. The entrained-flow reactor focused on small particles and the single-particle reactor focused on large particles.

Entrained-flow Reactor

The process diagram of the entrained-flow reactor designed and built as part of this project appears in Figure 92. The experimental setup consists of six parts: a particle feeding system, a secondary gas preheater, an entrained-flow reactor body, a sample collection and separation system, an imaging system, and a temperature control system. Each of the above six parts is explained in detail.

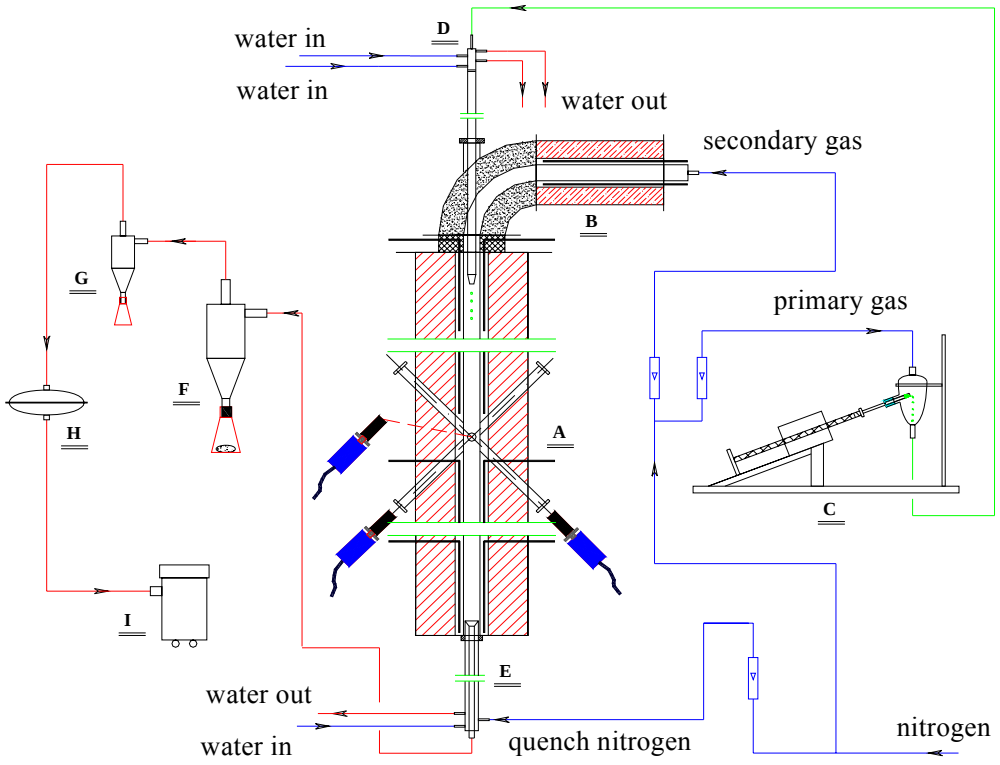

A - entrain flow reactor B - preheater C - syringe feeder D - feeding probe
E - collection probe F - 1st cyclone separator G - 2nd cyclone separator
H - filter I - vacuum

Figure 92 Process diagram of the entrained-flow reactor

In this project, two entrained-flow reactor configurations were used: a short one with only one section and no imaging system and a longer one with four sections and an imaging pyrometry.

A syringe feeder regulated biomass feed rate, with biomass particles entrained in entering the reactor through the feed probe. The preheater heats secondary gas heated to 1400 K as it flows into the top of the reactor. The reactor heats biomass samples as they undergo drying, devolatilization, gasification, and oxidation. A water-cooled nitrogen quench probe collects char which is subsequently separated from entrainment gases by two cyclone separators in series. The distance between the feed probe and the collection probe and the entraining air flow fix particle residence time in the reactor. Particle mass loss was determined by either weighing both the initial total mass of the feedstock samples and the collected char samples in the first cyclone separator or by an ash tracer method. The ash tracer method assumes ash is a conserved particle property (does not vaporize or otherwise leave the particle). Under such assumptions, the total ash content indicates the mass loss as follows

$$m_0 a_0 = ma, \tag{14}$$

$$\frac{m}{m_0} = \frac{a_0}{a}, \tag{15}$$

$$1 - \frac{m}{m_0} = 1 - \frac{a_0}{a}, \tag{16}$$

where, m and a are total sample mass and ash content respectively. The subscript 0 stands for initial state. A specific single inorganic component can also be used to calculate the mass loss with the total ash contents replaced by the component contents in Equation (16).

The imaging system described below provides particle surface temperature and particle velocity.

Separate valves and choked-flow orifices control and meter primary gas, secondary gas, and quench gas flow rates according to the Equation (17) (Saaddjian, Midoux et al. 1996).

$$m^* = A^* \frac{p_0}{\sqrt{T_0}} \sqrt{\left(\frac{\gamma}{R}\right)\left(\frac{2}{\gamma+1}\right)^{(\gamma+1)/(\gamma-1)}}, \tag{17}$$

where, m^* is the gas mass flow rate, A^* is the orifice cross-sectional area where Mach number is 1, p_0 and T_0 are stagnation pressure and temperature respectively, γ is gas specific heat ratio, and R is the gas constant.

A LabVIEW program records and monitors all gas flow rates and temperature distributions along the reactor and in the preheater.

Particle feeding system

The feeding system, as shown in Figure 93, comprises a feed-rate-control motor, a syringe feeder, a vibrator, a funnel, and a water-cooled feed probe. The particle feed rate is controlled by a computer program through the control motor. The vibrator helps maintain a constant feed rate. This system reliably feeds material as slow as 1.0 gm/hr. Particle samples, carried by the primary gas, enter the reactor through the feed probe. The feed probe is 1.27 meters long, with a 3 mm inner diameter and 25 mm outer diameter. Two water jackets control the probe and sample temperatures before they enter the reactor. The detailed structure of the feed probe appears in Figure 94. Figure 95 shows the assembly of the feed probe.

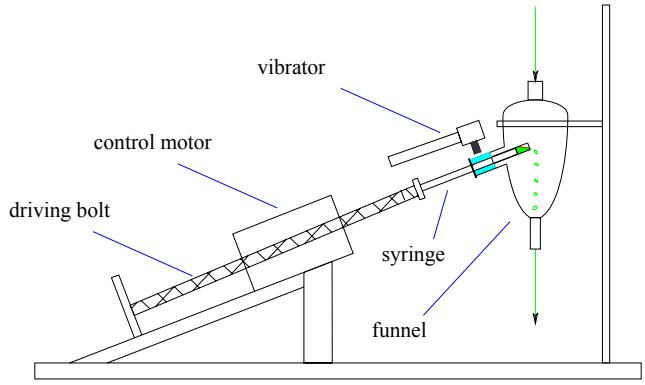

Figure 93 The biomass syringe feeding system for the entrained-flow reactor

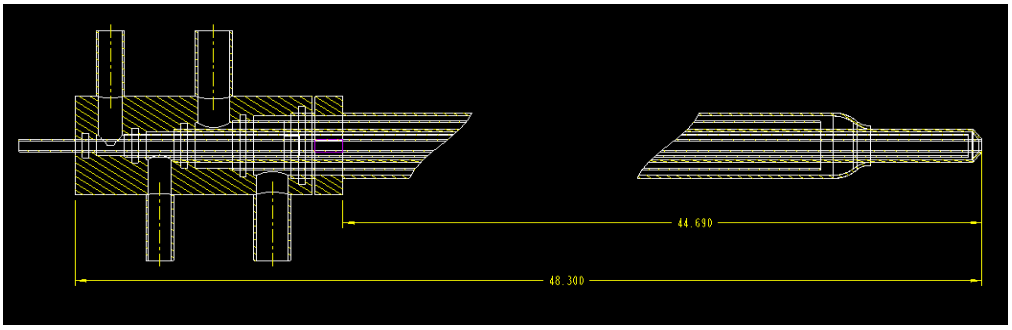

Figure 94 Feed probe structure design drawing

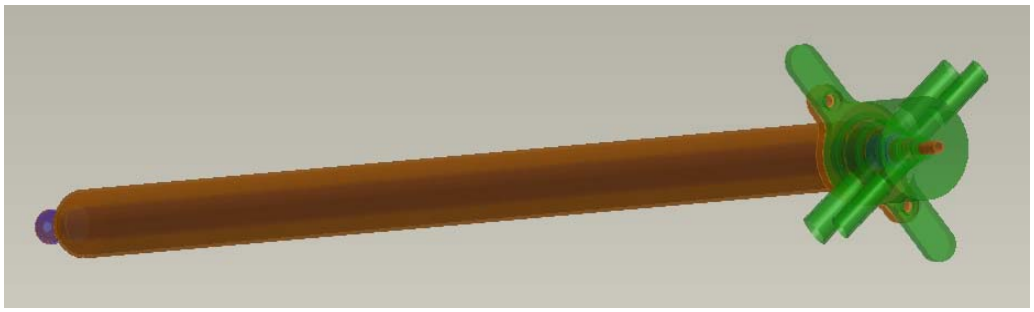

Figure 95 Assembly of the feed probe

Preheater

A preheater controls the secondary gas temperature, typically comparable to the reactor temperature. The preheater uses a Globar heating rod, which heats the crushed ceramics packed in the gap between the recrystallized silicon carbide tube and the refractory cast in the steel cylinder. The crushed ceramics heat secondary gas as it flows through. Specifications of the preheater appear in Table 25. The structure appears in Figure 96 in detail. The preheater wall can be heated to 1400 K. A Silicon Controlled Rectifier (SCR) coupled with a temperature controller maintains temperature setpoints.

Table 25 Preheater specifications

Diameter (inch)	12.7
Length (inch)	32
Heating element	Globar SiC SGR
Inner tube material	Re-crystallized SiC Halsic-R

Entrained-flow reactor

Recrystallized SiC tubes of 60 mm OD and 50 mm ID line the reactor main body. The reactor is 1.8 m long, providing a residence time of up to 3 seconds. The reactor insulation includes one layer of alumina fiber board and two layers of high-temperature blankets. Molybdenum disilicide Kanthal Super heating elements placed between the reactor tube and the inner alumina fiber board control the reactor temperature. The design calls for a maximum outer surface temperature of 50°C. The entrained-flow reactor can reach wall temperatures up to 1600 K and a particle heating rate of 10^3~10^4 K/s. The temperature profile along the reactor is controlled separately by adjusting wall temperatures in each of four sections of the reactor with SCR temperature controllers.

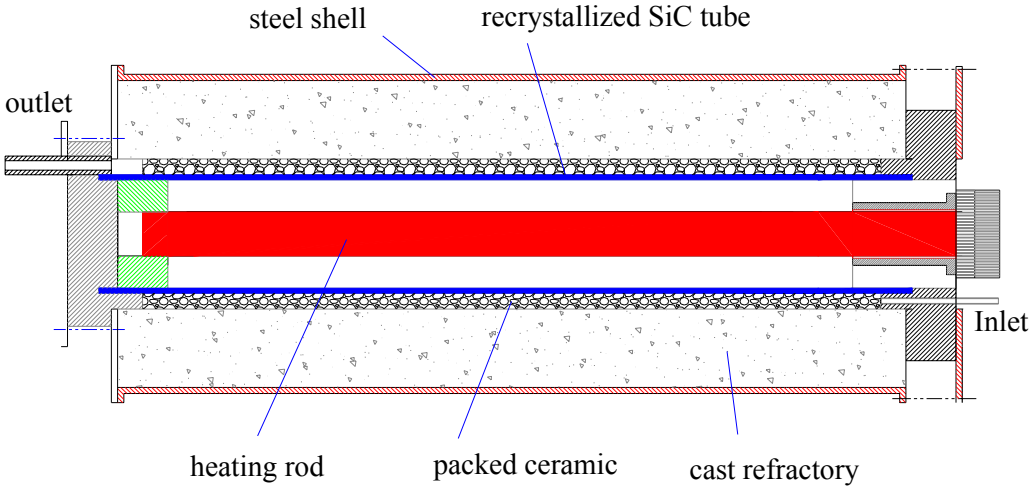

Figure 96 Schematic diagram of the preheater for the entrained-flow reactor

Windows at three levels along the reactor body provide optical access, allowing three orthogonal measurements of particle surface temperature and particle shape with CCD/CMOS cameras. These windows divide the reactor into four sections. Each of the windows provides optical access for image acquisition from three orthogonal directions, as shown in Figure 97. Quartz window glass seals the outside end of each view port. Supported by a SiC plate, each window section includes six view tubes and a short collar tube.

Figure 97 Window section with optical accesses in three orthogonal directions

A detailed structural photo of the reactor body appears in Figure 98. In each of the four sections of the reactor, four U-shaped heating elements hang over refractory bricks immediately adjacent the recrystallized SiC reactor tube, with about 20 mm separation. Four pieces of short reactor tubes reduce thermal expansion stresses compared to a single piece, and these are pinned together through three collar tubes.

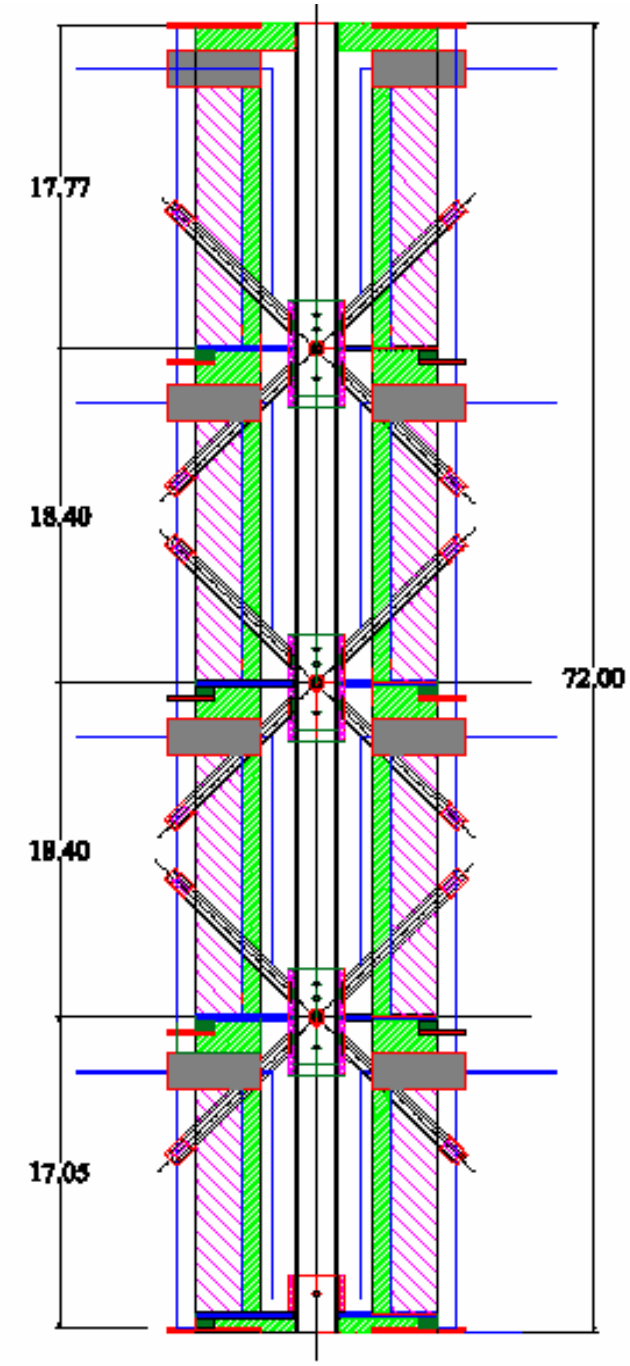

Figure 98 Schematic diagram of the entrained-flow reactor main body

Four steel plates support the reactor body. The plates are located below the four SiC plates and welded to four metal uprights. The base of the four uprights is bolted into the floor and the tops are secured by four cables. Figure 99 illustrates the assembly of the entrained-flow reactor body supported by the four uprights.

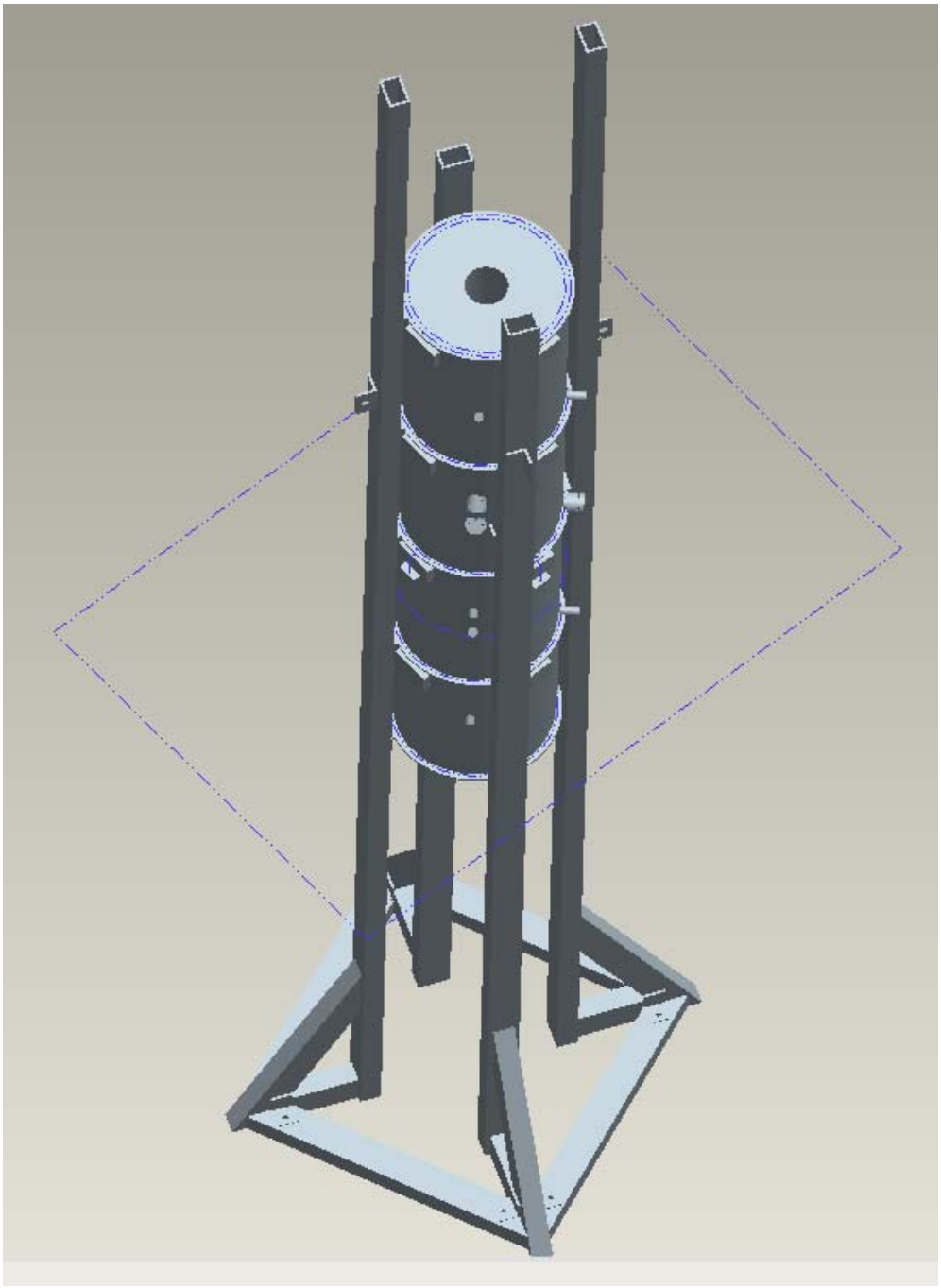

Figure 99 Assembly of the entrained-flow reactor

Specifications of the entrained-flow reactor are listed in Table 26.

Table 26 Entrained-flow reactor specifications

Height (m)	1.8

Outer diameter (m)	0.4
Inner diameter (mm)	50
First layer insulation	Rescor 3360UHT
Secondary layer insulation	Rescor 3370UHT
Third layer insulation	Rescor 370
Heating elements	2-shank Kanthal Super ST and N 6/12 mm
View tube material & size	
Reactor tube material & size	Re-crystallized SiC Type Halsic-R
Collar tube material & size	
Supporting plate material & size	

Sample collection and separation system

The particle collection system includes a water-cooled collection probe, two cyclone separators in sequence, and a filter assembly. A Venturi vacuum pump drives flow through this system. The hot gas and particles enter the collection probe, quenched by nitrogen gas or air introduced through the end of the collection probe. The volume flow rate ratio of the quench gas to the hot gas is about 7:1. A water-bath heat exchanger appears between the filter and Venturi vacuum to cool the exhaust gas.

A detailed structure of the collection probe appears in Figure 100 and its assembly appears in Figure 101.

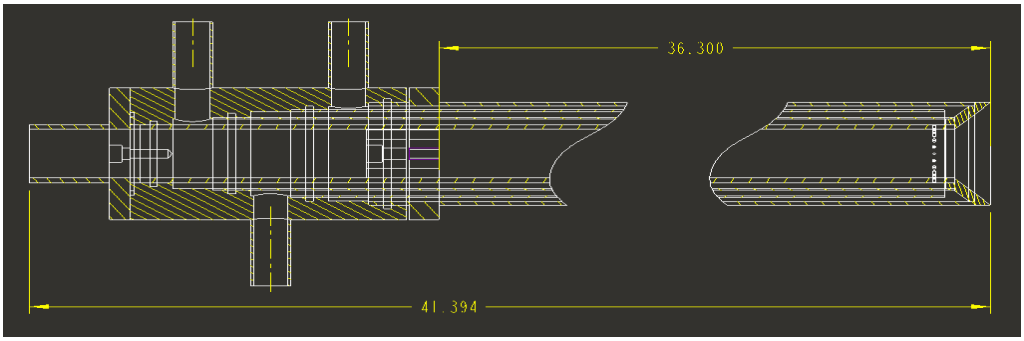

Figure 100 Collection probe structure design drawing

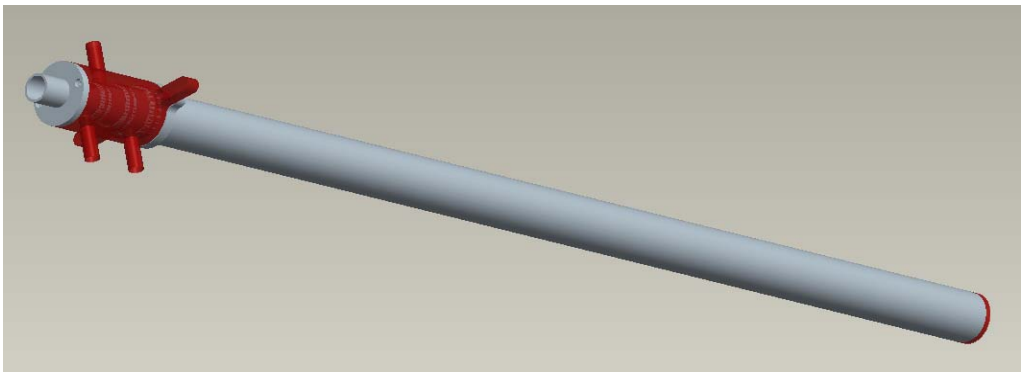

Figure 101 Assembly of the collection probe

The cyclone separators have design cut points of 20 μm and 5μm, respectively. The filter pore size is 1μm. With sawdust samples sized from 300 μm to 500 μm, most of the char samples appear in the first cyclone separator (99 %). Soot and condensed tar sometimes appear on the filter membrane. The cyclone separator drawing appears in Figure 102 (only the 20 μm cut point one), and Figure 103 shows the assembly.

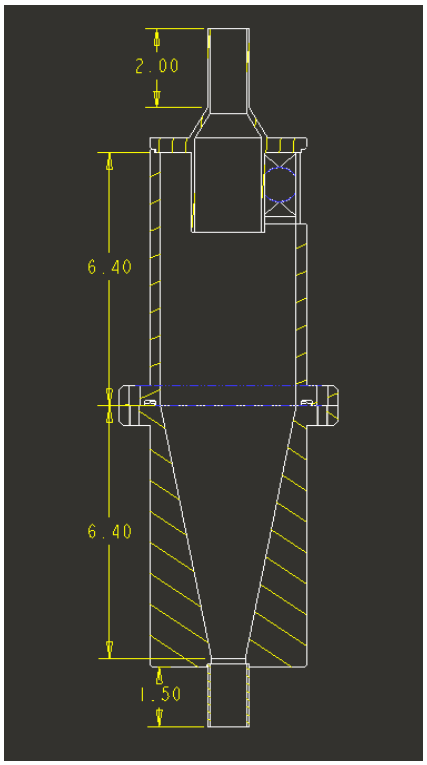

Figure 102 Cyclone separator structure design drawing

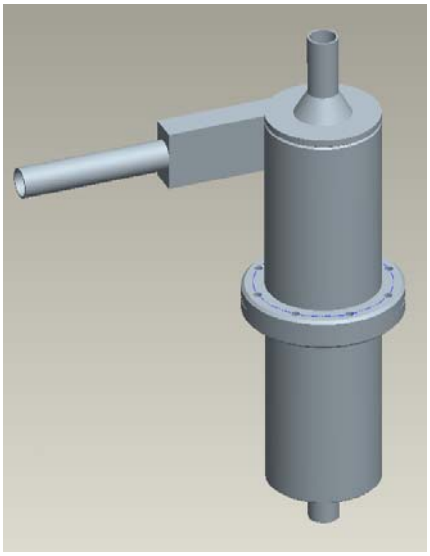

Figure 103 Assembly of the cyclone separator

Imaging system

The imaging system includes three cameras, three image acquisition boards, cameral control and image processing software, and a high-performance computer. When taking videos or images, the three cameras image along three mutually orthogonal directions. The imaging system can record up to two-minute videos with full resolution (1036x1024), and longer record time can be obtained at reduced resolution. The camera uses a SONY ICX285AQ CCD sensor with microlenses, which is more sensitive in the near infrared (NIR) range than traditional CCD sensor. The electrical shutter speed is as short as 62 μs. Detailed components specifications of the imaging system appear in Table 27.

Table 27 Components and specifications of the imaging system

Camera	SVS-285CSL, 10 bit, shutter speed, frame rate
CCD sensor	Sony ICX285AQ, Cell size 6.45x6.45 μm, Resolution 1036x1024
Lens model	Computar MLH-10X
Image acquisition board	Epix Inc. PIXCI D2X
Camera control software	XCAP2.0
Computer configuration	XEON CPU 3.06 G Hz, 3.5G RAM

The three cameras are pre-focused on the center of reactor through the window section, which is the cross-point of the three optical paths. The recorded videos undergo shape reconstruction analysis (explained later) and temperature analysis (also explained later) to yield a three-dimensional shape and surface temperature computer image.

Temperature control system

The reactor wall temperatures in each of four sections behave independently. Each section has 4 U-shaped 90^{o}-bent Kanthal Super heating elements and the power output can be adjusted by the transformer and SCR controllers to regulate temperature. Two three-phase SCR controllers and two three-phase transformers control the 12 heating elements in the top three sections of the reactor according to the setpoints on a three fuzzy logic controllers. Each of the 6 heating elements is star-connected with the three-phase transformer. The bottom section is controlled by a single-phase SCR controller a single-phase tranformer and an additional fuzzy logic controller with the 4 heating elements connected in series. Specifications of each component of the temperature control system are listed in Table 28.

Table 28 Components and specifications of the temperature control system

Temperature controller	FuzyPro 1/16 DIN
SCR controller	Halmar Electronics Inc., 3P-4860-CL-D
	Single phase: AVATAR B2P -24-60, SCR71Z-230
Transformer	Matra Electric Inc. Model 90165346K, 480-70Y/40.4
	Single phase: Olsun Electrics Corp. H-115 208-50/60

Single-particle reactor

A single-particle reactor with the same optical access features, designed and built by Ip (Ip 2005), was used to conduct biomass particle devolatilization and combustion experiments on particles whose conversion/residence times exceed those of the entrained-flow reactor. The detailed structure explanation of the reactor can be found in Ip's thesis (Ip 2005).

Figure 104 schematically illustrates the experimental reactor for the single-particle combustion investigations. Single biomass particles of various shapes (equant, disc, and cylinder) and diameters (3 - 12 mm) suspended on type-B thermocouples provide simultaneous size, shape, internal temperature, external temperature, and mass loss data. A wireless data logger, from PACE Scientific (Model XR440), records internal/center temperature data from the thermocouple at 20 Hz. The data logger, thermocouple, and biomass particle rest on top of a balance (Model SCIENTECH SA310IW). A small hole about the size of the thermocouple wire (~0.01 inch) through the center the particle provides access for the bead at the particle center. The balance records mass loss data at a resolution of 0.1 mg and an accuracy of $\pm$0.2 mg. The imaging system and optical pyrometer focus on the surface and record physical changes in shape/size and surface temperature data. An experiment begins with the balance, data logger and biomass sample entering the reactor. The data logger, the balance, and the imaging system begin recording data simultaneously, synchronized within 0.1 second. During devolatilization, a second thermocouple pressed against the particle surface records particle surface temperature in addition to the imaging system measurements. To reduce the influence of thermal conduction on surface temperature measurement, a shallow and narrow groove in the particle surface housed the wire.

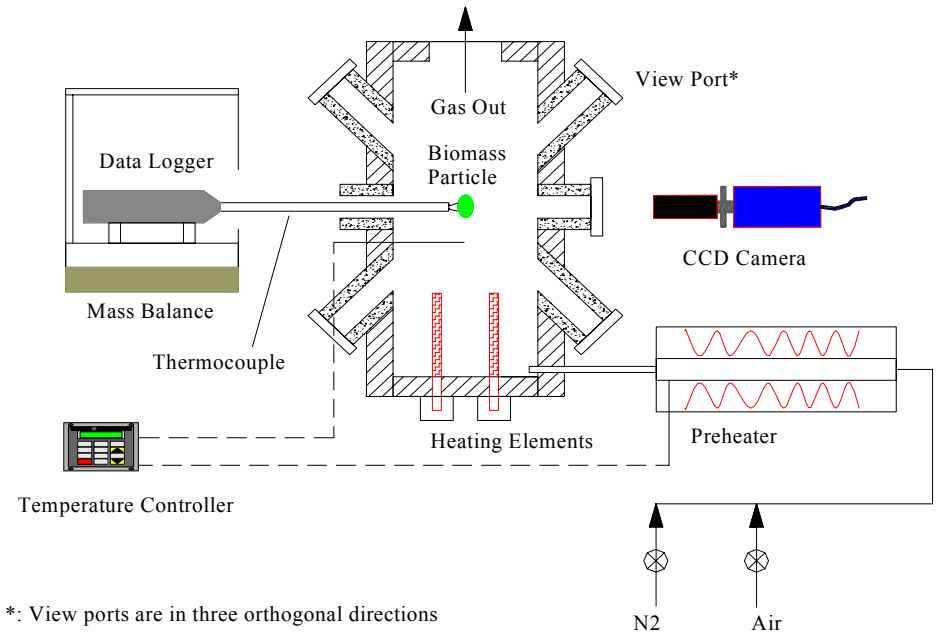

Figure 104 Schematic diagram of the single-particle reactor

This single-particle reactor provides time-resolved, simultaneous mass loss, surface and internal temperatures, size, and shape data during pyrolysis and combustion processes.

Color-Band Pyrometry Development

Non-contact surface temperature measurements provide significant advantages for particles traveling in the entrained-flow reactor or particle undergoing shrinking/swelling or surrounded by flames or other reacting gases in the single-particle reactor. Traditionally, two-color pyrometry provides such data. The disadvantages of this traditional technique include a complicated, expensive, and sensitive imaging system including Photo Multiplier Tubes (PMT) and notch filters, a lack of particle shape information, relatively low signal strengths, crude estimates of size, and no spatial resolution of temperature data. This project developed and applied a conceptually similar but simpler technique that addresses these all of these issues. This is the first-ever application of this technique to particle combustion to our knowledge. The technique, named multi-color band pyrometry, appears in detail below.

Color-Band Pyrometry Principles

Black body spectral radiance (Ingle Jr. and Crouch 1988), expressed as $B_\lambda^b = C_1\lambda^{-5}/\left(e^{C_2/\lambda T}-1\right)$, forms the basis of Planck's law. For a gray body: $B_\lambda = \varepsilon_\lambda B_\lambda^b$, where $\varepsilon(\lambda)$ is the spectral emissivity. The total radiance is $B = \int_0^\infty B_\lambda d\lambda$. In the wavelength range between λ_1 and λ_2, the total radiance is $B = \int_{\lambda_1}^{\lambda_2} B_\lambda d\lambda$. For a typical pyrometry setup illustrated in Figure 105, the solid angle is $\Omega = \pi D^2/4d^2$, where D is the lens (receptor) diameter, and d is the working distance between the lens and the light source .

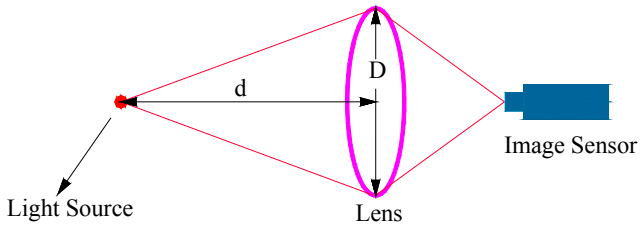

Figure 105 Schematic diagram of the color-band pyrometry

Assuming the total effective extended source area is A_1, the spectral radiant power and total radiant power incident on the lens is $\Phi_{i,\lambda} = B_\lambda A_1 \pi D^2/4d^2$, and $\Phi_i = BA_1 \pi D^2/4d^2$.

If the transmittance (which is the is the ratio of the total radiant or luminous flux transmitted by a transparent object to the incident flux, usually given for normal incidence) of the optical system is τ_λ, the spectral energy incident on the imaging sensor will be $\Phi_{i,\lambda,sensor} = B_\lambda \tau_\lambda A_1 \pi D^2/4d^2$. With an effective image area of A_2 on the imaging sensor, which corresponds to the effective extended light source area, and a pixel/cell area of a on the CCD or CMOS sensor, the spectral irradiance obtained by a specific pixel/cell will be $E_\lambda = B_\lambda \tau_\lambda a A_1 \pi D^2/4d^2 A_2$. Generally, A_2/A_1 is proportional to the magnification factor of the lens, and here we can use X to replace it.

Usually there are two methods to describe the spectral sensitivity/responsivity, S_λ, of an imaging sensor. One is quantum efficiency (QE, electrons/photon), which is the photon-to-electron conversion efficiency; the other one uses the energy to electron conversion efficiency. In addition, the electron to digital number (pixel intensity) conversion is related the gain value of the CCD or CMOS camera.

The energy of a photon with specific frequency or wavelength is $E = hc/\lambda$. If QE is used as the spectral sensitivity/responsivity, with an exposure time of Δt, the digital number (DN) or pixel intensity of any pixel in the image is calculated by Equation (18) for an ideally performing (perfectly linear) black-and-white CCD or CMOS camera based on the optical system and camera characteristics illustrated above.

$$DN = \alpha \cdot \frac{\pi}{4} \cdot \left(\frac{D}{d}\right)^2 \cdot f(g) \cdot \frac{a}{X} \cdot \Delta t \cdot \int_{\lambda_1}^{\lambda_2} \varepsilon_\lambda \tau_\lambda S_\lambda \cdot \frac{C_1 \cdot \lambda^{-5}}{e^{C_2/\lambda \cdot T} - 1} \cdot \left(\frac{h \cdot c}{\lambda}\right)^{-1} \cdot d\lambda \quad (18),$$

where, α is a proportional factor which ensures the units consistent for the equation, and $f(g)$ is a function of gain value of the camera; all other variables are explained earlier and in the nomenclature.

The spectral radiances of the object surface from the lowest wavelength to the highest wavelength that can be detected by the image sensor all contribute to the pixel intensity, by contrast to only two narrow wavelengths in traditional two-color pyrometry. This dramatically increased the signal strength.

If the spectral responsivity uses the energy to electron conversion efficiency, $(h \cdot c/\lambda)^{-1}$ needs to be removed from the above equation, as shown in Equation (19). This equation can be simplified if spectral emissivity is independent of wavelength.

$$DN = \alpha \cdot \frac{\pi}{4} \cdot \left(\frac{D}{d}\right)^2 \cdot f(g) \cdot \frac{a}{X} \cdot \Delta t \cdot \int_{\lambda_1}^{\lambda_2} \varepsilon_\lambda \tau_\lambda S_\lambda \cdot \frac{C_1 \cdot \lambda^{-5}}{e^{C_2/\lambda \cdot T} - 1} d\lambda \qquad (19)$$

By far the most common method of rendering color images in commercial digital cameras involves creating a color filter mosaic array (CFA) on top of a light intensity (black-and-white) imager. In most cases, a 3-color, red-green-blue (RGB) pattern appears in the CFA, though there are other options, including 3-color complementary YeMaCy arrays, mixed primary/complementary colors, and 4-color systems where the fourth color is white or a color with shifted spectral sensitivity. One manufacturer (Foveon) uses a system that separates color based on penetration depth of the signal in the silicon detector with no mosaic filter.

A Bayer filter mosaic, as shown in Figure 106, represents the most commonly used CFA for arranging RGB color filters on a square grid of photo sensors. This term comes from the name of its inventor, Bryce Bayer of Eastman Kodak, and refers to the particular arrangement of color filters used in most single-chip digital cameras. Bryce Bayer's patent called the green photo sensors luminance-sensitive elements and the red and blue ones chrominance-sensitive elements. He used twice as many green elements as red or blue to mimic the human eye's greater resolving power with green light. These elements are referred to as samples and after interpolation become pixels.

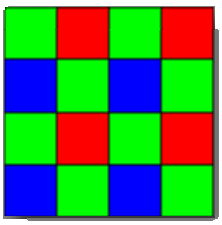

Figure 106 Bayer filter color pattern (Canavos 1984)

There are a number of different ways the pixels are arranged in practice, but the pattern shown in Figure 106 with alternating values of red (R) and green (G) for odd rows and alternating values of green (G) and blue (B) for even rows is very common. The raw output of Bayer-filter cameras is referred to as a Bayer Pattern image. Since each pixel is filtered to record only one of the three colors, two-thirds of the color data are missing from each, as illustrated in Figure 107. The green is usually read out as two separate fields or as one field with twice as many points.

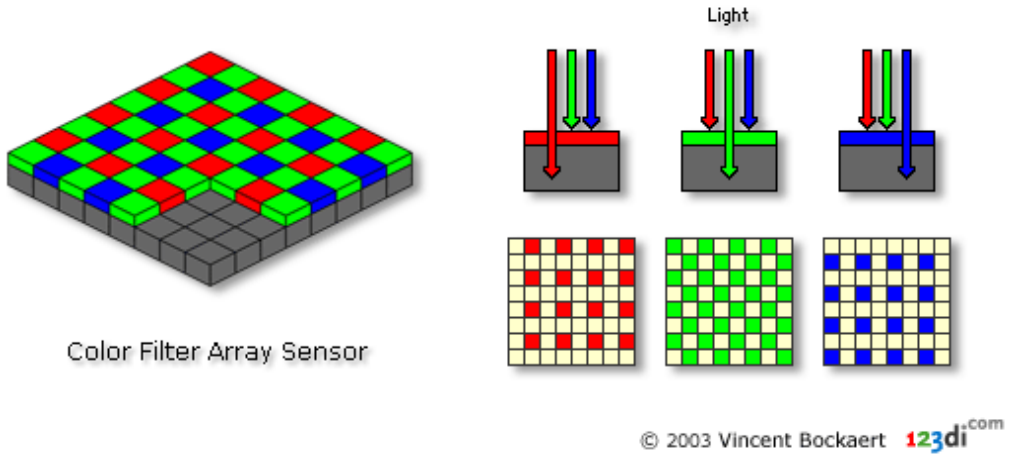

Figure 107 Color image reconstruction from a Bayer filter (Chang, Mournigham et al. 1991)

A demosaicing algorithm interpolates a complete RGB set for each point and produces the RGB image. Many different algorithms exist and they are one of the distinguishing factors in commercial cameras that otherwise often use the same sensors. The simplest is the bilinear interpolation method. In this method, the red value of a non-red pixel is computed as the average of the adjacent red pixels, and similar for blue and green.

With the Bayer filter in front of the CCD or CMOS sensor, sensor spectral responsivity can be measured for each individual color. As a result, the pixel intensity (or digital number) of the red color/channel is correlated with object temperature and red color/channel spectral responsivity as shown in Equation (20), and similarly for the other two colors/channels.

$$DN_{Red} = \alpha \cdot \frac{\pi}{4} \cdot \left(\frac{D}{d}\right)^2 \cdot f(g_{Red}) \cdot \frac{a}{X} \cdot \Delta t \cdot \int_{\lambda_1}^{\lambda_2} \varepsilon_\lambda \tau_\lambda S_{\lambda,Red} \cdot \frac{C_1 \cdot \lambda^{-5}}{e^{C_2/\lambda \cdot T} - 1} d\lambda \qquad (20)$$

Occasionally, a manufacturer provides the color or black-and-white spectral responsivity of CCD or CMOS cameras. To calculate the object surface temperature, Equation (20) applies to each color (typically RGB) channels. Assuming both spectral emissivity and spectral transmission are independent of wavelength and setting the gain value of each color to be the same, a new equation with only one (implicit) unknown – the temperature – results, as shown in Equation (21). This is the basic equation for the color-band method. Any two of the three channels/colors can be used to calculate the object surface temperature based on the pixel intensity of each color. This technique is flexible. The camera doesn't have to be focused on the surface of the object for a reliable temperature, though it does have to focused for reliable spatial distributions of temperature and, in all cases, only pixels with light that originates from the surface are valid pixels for temperature measurement. Images with poor focus contain many pixels with mixed particle-background light. In addition, working distance, lens aperture size, and exposure time all provide additional adjustable parameters that impact signal level. It is not necessary to measure

working distance and aperture size. Only exposure time might be needed, which can be controlled and read through the camera control software.

$$\frac{DN_{Blue}}{DN_{Red}} = \frac{\int_{\lambda_1}^{\lambda_2} S_{\lambda,Blue} \cdot \frac{C_1 \cdot \lambda^{-5}}{e^{C_2/\lambda \cdot T} - 1} d\lambda}{\int_{\lambda_1}^{\lambda_2} S_{\lambda,Red} \cdot \frac{C_1 \cdot \lambda^{-5}}{e^{C_2/\lambda \cdot T} - 1} d\lambda} \quad (21)$$

CMOS-Camera-Based Color-Band Pyrometry

In this project, a CMOS camera from EPIX Inc. (model SV2112) was first used to measure black-body temperature (Mikron Model M330). The camera uses a PixelCam™ ZR32112 CMOS sensor. Spectral responsivities of each color/channel, as well as the monochrome, are shown in Figure 108. The IR filter in front of the CMOS sensor in the camera was removed to obtain maximum response from the camera since near-infrared signal is critical at low temperature measurements, as indicated by Planck's law.

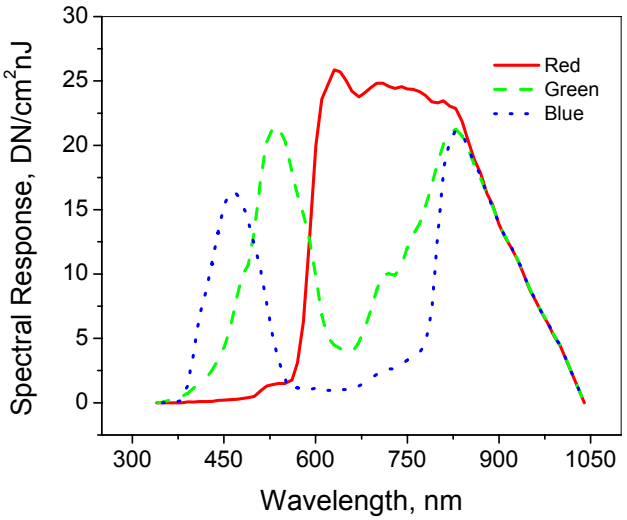

Figure 108 Spectral responsivity of the ZR32112 CMOS sensor (Cannon, Brewster et al. 1999)

Using the spectral responsivity curves obtained from the manufacture and without calibrating the SV2112 CMOS camera, temperatures of a black body were measured by both a type-K thermocouple and the CMOS camera. The XCAP image acquisition and process software provided Pixel intensity of each color. The junction-compensated-thermocouple data compared with the camera measurements appear in Figure 109.

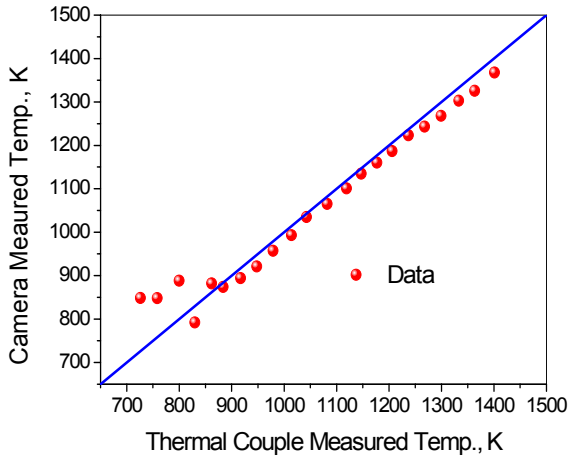

Figure 109 Temperature comparison of thermocouple and CMOS camera measurements

When the black-body temperature was higher than 900 K, the differences between the camera-measured temperature data and the thermocouple results were less than 50 K. Due to the spectral responsivity similarity of the three colors/channels in the near IR range (λ>800 nm) where low temperature radiation dominates, the camera measurements differ by more than 100 K from the black-body temperature and are scattered at temperatures below 900 K. Figure 110 illustrates this issue, the data for which are based on Equation (21). When the black-body temperature is lower than 900 K, the pixel intensity ratio of any two colors/channels approaches 1.0, making accurate temperature measurement difficult.

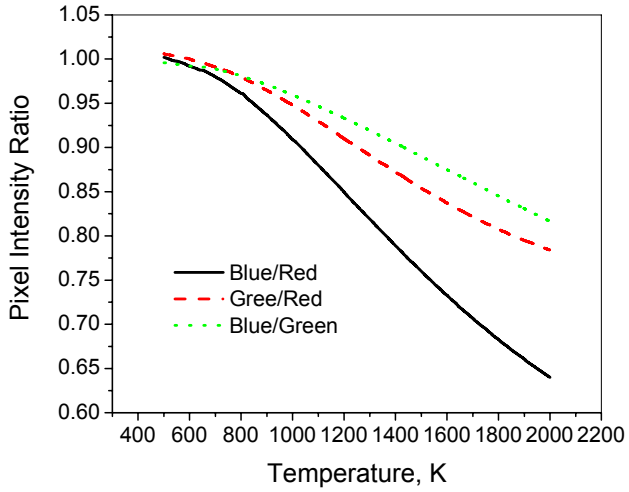

Figure 110 CMOS camera pixel intensity ratios as functions of temperature

It is commonly believed that CMOS sensors exhibit a slightly higher spectral responsivity than CCD sensors, especially at the near infrared (NIR) range. But CCD sensors commonly perform better than CMOS sensors with respect to uniformity, signal to noise ratio, and dynamic range. The low to moderate uniformity and signal to noise ratio may also contribute to the inaccuracy of temperature measurement of the SV2112 COMS camera at the low temperature range.

To obtain better temperature measurement results, a CCD camera was also used in this project.

CCD-Camera-Based Color-band Pyrometry

The SVS285CLCS camera uses a Sony Exview HAD CCD, which has very high sensitivity and low smear. This sensor shows higher sensitivity at the NIR range than traditional CCD due to the Exview HAD CCD technology. Similar to the CMOS camera, the IR filter was removed from the camera to maximize detectivity. The available spectral responsivity graph from the manufacturer appears in Figure 111, which only gives the visible spectral range.

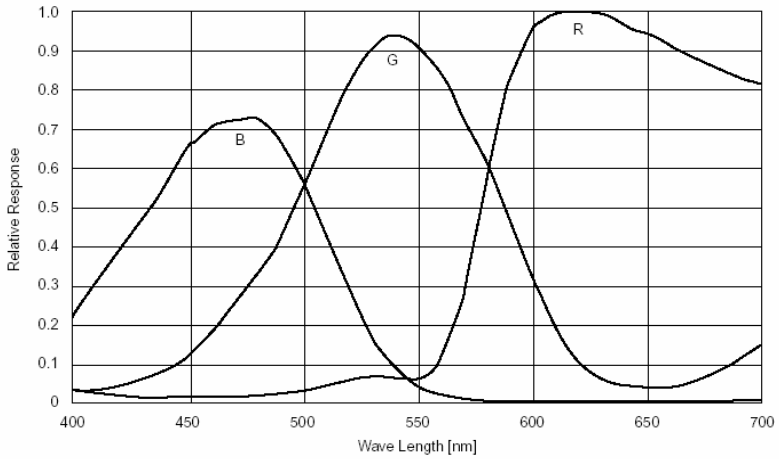

Figure 111 Manufacturer provided ICX285AQ CCD sensor spectral responsivity (Sony Inc 2005)

The complete spectral responsivity of each color/channel was measured with a black body as light source and a monochromator (CornerStone 130) separating the broad-band light into narrow-wavelength signals with a resolution of 0.5 nm. The black body temperature was set to 1600 ^{o}C to maximize the signal/noise ratio. The measured wavelength range is from 300 nm to 1150 nm. A high-pass filter (LPF750 Lot NNB) placed between the camera and the outlet of the monochromator blocked the second- and higher-order diffractions when measuring wavelengths longer than 750 nm. Both the spectral efficiency of the monochromator and the transmission efficiency of the filter impact the calculation of the spectral responsivity of the CCD sensor. Energy carried by a specific wavelength signal was calculated by Plank's law. The mathematical calculation of spectral responsivity for each color/channel appears as Equation (22).

$$S_{\lambda,color} = \frac{DN_{color,\lambda}}{\tau_{filter,\lambda} \quad \xi_{mono,\lambda} \quad \frac{C_1 \quad \lambda^{5}}{e^{C_2/\lambda \; T_B} \quad 1}}, \tag{22}$$

where, $color$ = Red, Green, and Blue. $\tau_{filter,\lambda}$ is the transmittance of the high pass filter, $\xi_{mono,\lambda}$ is the spectral efficiency of the monochromator, $DN_{color,\lambda}$ is the digital number or pixel intensity of each color at λ.

A complete relative spectral responsivity of each color/channel normalized by the maximum value, which occurred in the red color/channel, appears in Figure 112. The spectral responsivity data for each channel as a function of wavelength appears in Appendix B. The measured spectral responsivity curves of the CCD camera have similar shapes as those obtained from manufacturer for the CCD sensor. The small differences may arise from sample-to-sample variations in the sensors (manufacturer's data are typical but not obtained on each sensor), the camera characteristics, and the transmittance of the camera lens.

With the measured relative spectral responsivity curves, the pixel intensity ratios of any two colors/channels appear in Figure 113. The ratio of blue to red depends more strongly on temperature than the other two ratio values, as would be expected since they differ the greatest in average wavelength. This ratio should result in the most sensitive/accurate temperature measurement.

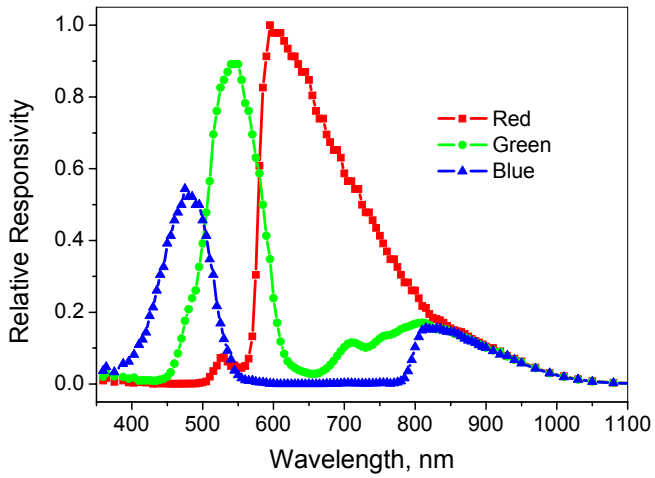

Figure 112 Measured relative spectral responsivity of the SVS285CSCL camera

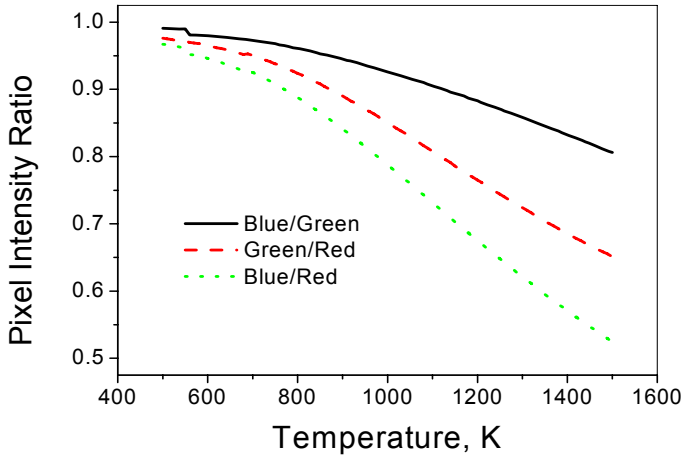

Figure 113 CCD camera pixel intensity ratios as functions of temperature

Figure 113 shows that the CCD camera is able to measure a wider temperature range compared with the CMOS camera since the CCD camera pixel intensity ratios approach 1.0 at lower temperature (~650 K). The black-body temperatures were then measured with this CCD camera and calculated using Equation (21) and the complete spectral responsivities. The camera measured data compared with thermocouple measurements appear in Figure 114, again without calibration. The results show that the CCD camera measurements were within 50 K of the thermocouple measured values when black-body temperature is lower than 1050 K, but with the sensor appears to begin to saturate at higher temperatures. So calibration might be necessary for more accurate and wider temperature measurements.

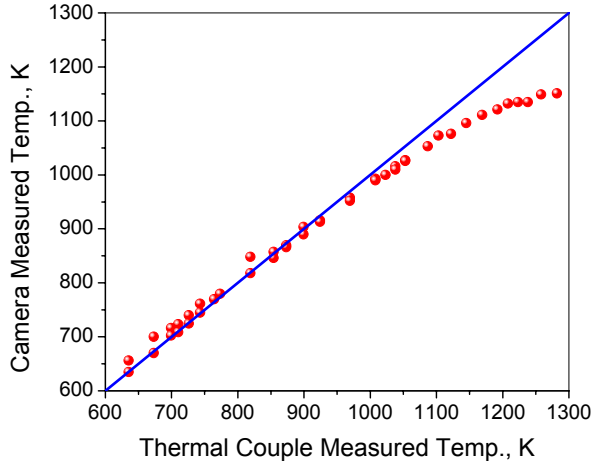

Figure 114 Temperature comparison of thermocouple and CCD camera measurements

To calibrate the CCD camera and make this method more robust, four variables have been studied: the square of lens aperture size divided by the square of the working distance, D^2/d^2; exposure time, Δt; black-body temperature, T; and camera gain value, g.

The first investigation explored the linearity implied by Equation (19) between the pixel intensity and D^2/d^2. Aperture size adjustments produced image pixel intensity data as a function of D^2 at a variety of temperatures and exposure times. Results indicated an almost perfectly linearity in all cases (Figure 115). Here only two cases appear: low temperature and long exposure time data appear in Figure 115 (a) and high temperature and short exposure time data appear in Figure 115 (b). In the calibration, working distance remained constant and only aperture size changed since D^2 and $1/d^2$ should have identical effects.

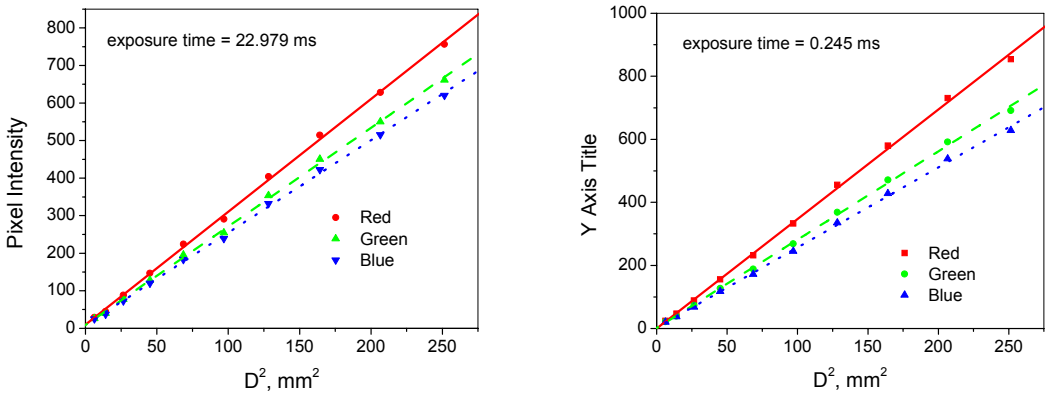

(a) low temperature at 927 K (b) higher temperature at 1224 K

Figure 115 Pixel intensity vs. effective aperture area

The camera gain value function, $f(g)$, was calibrated for each channel at different temperatures and exposure times. For each channel at any condition, the gain value function, $f(g)$, followed the form of $e^{\gamma \cdot g}$, as shown in Figure 116. The parameter γ in this function was found almost constant, so an average value was calculated for each channel: 3.424, 3.424, and 3.428, respectively for red, green, and blue channels. They can be treated as the same for each channel to simplify the color-band method.

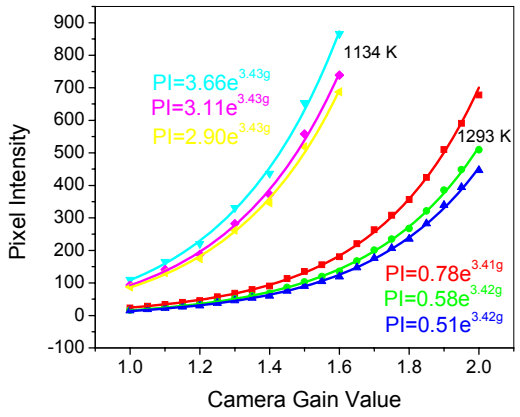

Figure 116 Camera gain value calibration

During the calibration, it was also found when black body temperature was higher than about 850 K, the image pixel intensity was nearly proportional to exposure time, but both the slope and intercept of the straight line started to increase with increasing black body temperature, as shown in Figure 117. The green channel and blue channel behaved similarly, and only the red channel appears here. These data follow a linear correlation but with a non-zero intercept, Equation (23), between the pixel intensity and exposure time when black body temperature is higher than 850

K. Both the slope and intercept are functions of the energy received by the CCD camera sensor, increasing with black body temperature increase.

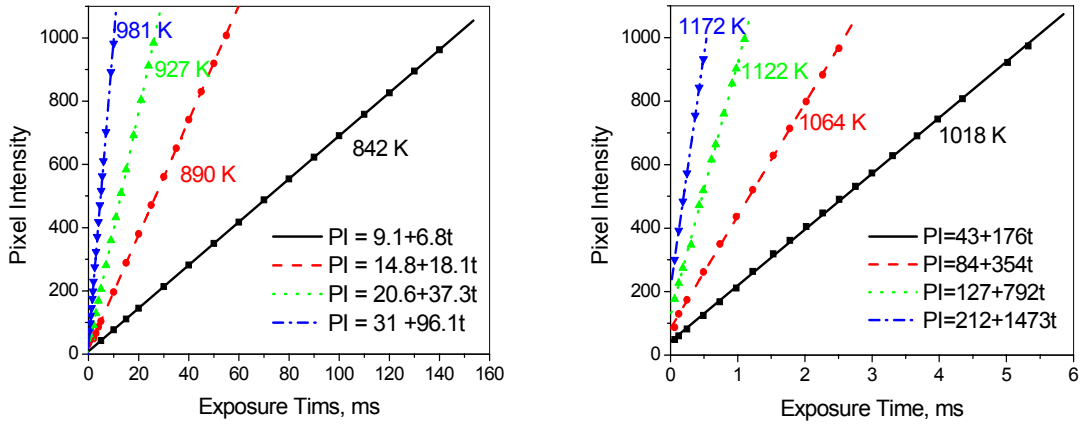

(a) low temperature (b)

higher temperature

Figure 117 Red channel pixel intensity vs. exposure time at different temperature

$$DN_{Red} = a_{Red}(E_{Red})\Delta t + b_{Red}(E_{Red})$$

where,

$$E_{Red} = \int_{\lambda_1}^{\lambda_2} S_{\lambda,Red} \cdot \frac{C_1 \cdot \lambda^{-5}}{e^{C_2/\lambda \cdot T} - 1} d\lambda \tag{23}$$

To determine the exact relation between the energy and slope, as well as that between the energy and intercept, black-body temperature was changed from about 850 K to 1312 K in increments of about 80 K. The slope and intercept in Equation (23) were calculated by adjusting the exposure time at each temperature. Both slope and intercept fit power functions of the energy, as shown in Figure 118. The camera was also calibrated at higher temperature range (>1273 K) with a high-power black body. The fitted functions were slightly different from what got in moderate temperature range, as shown in Figure 119.

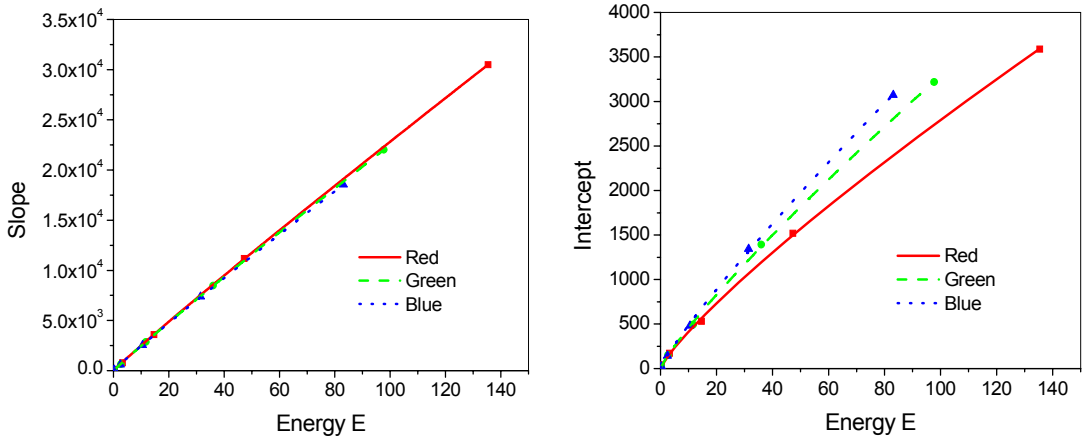

(a) Slope

Figure 118 Slope and intercept vs. energy at moderate temperature range

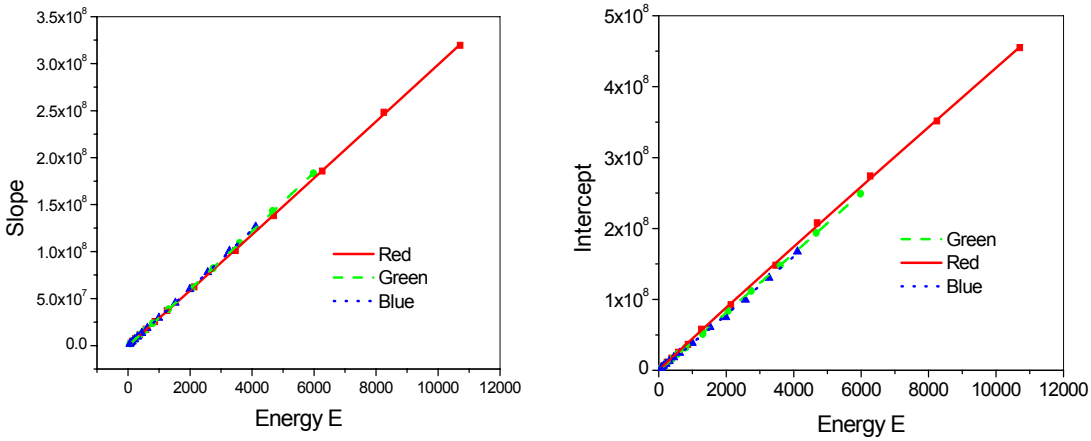

(a) Slope

Figure 119 Slope and intercept vs. energy at higher temperature range (>1273 K)

The final calibrations appear as Equation (24) for moderate- and Equation (25) for high-temperature ranges. The simplest form Equation (20) can be used to calculate low-temperature results by the color-band method.

$$DN_{\mathrm{Re}\,d} = \alpha \cdot \left(\frac{D}{d}\right)^2 \cdot e^{3.424 \cdot g} \cdot \left(\Delta t \cdot 280 \cdot E_{\mathrm{Re}\,d}(T)^{0.958} + 60.5 \cdot E_{\mathrm{Re}\,d}(T)^{0.83}\right)$$

$$DN_{Green} = \alpha \cdot \left(\frac{D}{d}\right)^2 \cdot e^{3.424 \cdot g} \cdot \left(\Delta t \cdot 272 \cdot E_{Green}(T)^{0.959} + 63.4 \cdot E_{Green}(T)^{0.86}\right) \quad (24)$$

$$DN_{Blue} = \alpha \cdot \left(\frac{D}{d}\right)^2 \cdot e^{3.428 \cdot g} \cdot \left(\Delta t \cdot 272 \cdot E_{Blue}(T)^{0.955} + 65 \cdot E_{Blue}(T)^{0.87}\right)$$

$$DN_{Red} = \alpha \cdot \left(\frac{D}{d}\right)^2 \cdot e^{3.424 \cdot g} \cdot \left(\Delta t \cdot 264 \cdot E_{Red}(T)^{1.013} + 526 \cdot E_{Red}(T)^{0.977}\right)$$

$$DN_{Green} = \alpha \cdot \left(\frac{D}{d}\right)^2 \cdot e^{3.424 \cdot g} \cdot \left(\Delta t \cdot 254 \cdot E_{Green}(T)^{1.022} + 344 \cdot E_{Green}(T)^{1.022}\right) \quad (25)$$

$$DN_{Blue} = \alpha \cdot \left(\frac{D}{d}\right)^2 \cdot e^{3.428 \cdot g} \cdot \left(\Delta t \cdot 252 \cdot E_{Blue}(T)^{1.024} + 307 \cdot E_{Blue}(T)^{1.032}\right)$$

If the CCD sensor spectral responsivities were measured accurately enough, all three colors/channels of the camera should have the same digital number vs. energy correlation. The discrepancy might be introduced by the errors in spectral responsivity measurements.

Both Figure 118 and Figure 119, as well as Equations (24) and (25) showed that the slope and intercept became more linear with respect to the received energy when black body temperature increased. With the equations obtained, the black-body temperature was measured by the color-band method at random working distance and random exposure time. Results compared with thermocouple data appear in Figure 120.

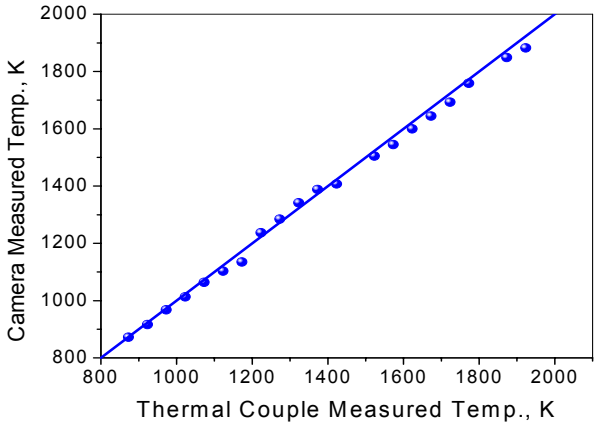

Figure 120 Black body temperature measured by the calibrated CCD camera

Particle Temperature Measurements Correction for Reflection Effects in Furnace

If the particle is heated in a furnace and the furnace wall temperature differs from the particle surface temperature, the measurement has to be corrected by taking surface reflection effects into account.

To simplify the correction, the following assumptions were made:

The wall temperature and surface properties are uniform;

All energy is emitted and reflected diffusely;

Both the particle and the wall surfaces are gray;

The particle surface is convex;

The incident and hence reflected energy flux is uniform over the surface area;

The reactor is considered as an enclosure and the particle is located in the center of the reactor.

Based on the above assumptions, a heat transfer diagram between the particle and the wall surface appears in Figure 121. The surface areas are A_1, A_2, and A_v for particle, reactor, and the view port hole, respectively. Particle surface temperature is T_1 and T_2 designates the reactor wall. It is also assumed that the surface areas of the particle and the view port are much less than that of the reactor wall: $A_1 << A_2$ and $A_v << A_2$.

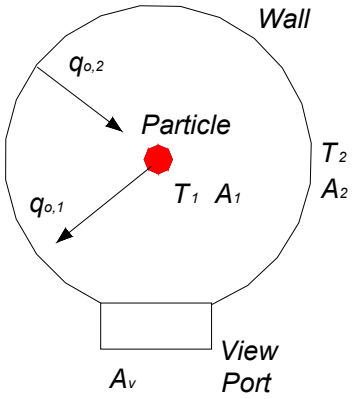

Figure 121 Radiant heat interchange between particle and reactor wall

Geometric configuration factors (Siegel and Howell 2002) of the particle surface and the reactor surface are $F_{1-1}, F_{1-2}, F_{2-1}, \text{and } F_{2-2}$. By analyzing the radiant energy interchange between the particle surface and the reactor wall, the radiant energy flux leaving the particle surface $q_{o,1}$ and that leaving the reactor wall surface $q_{o,2}$ were developed, as shown in Equations (26) and (27).

$$q_{o,1} = \varepsilon_1 \sigma T_1^4 + (1-\varepsilon_1)(F_{1-1} q_{o,1} + F_{1-2} q_{o,2}) \tag{26}$$

$$q_{o,2} = \varepsilon_2 \sigma T_2^4 + (1-\varepsilon_2)(F_{2-1} q_{o,1} + F_{2-2} q_{o,2}) \tag{27}$$

Substituting Equation (27) into Equation (26) results in Equation (28).

$$q_{o,1} = \frac{\left[1-(1-\varepsilon_2)F_{2-2}\right]\varepsilon_1\sigma T_1^4 + (1-\varepsilon_1)\varepsilon_2\sigma T_2^4}{\left[1-(1-\varepsilon_2)F_{2-2}\right] + \left[(1-\varepsilon_1)(1-\varepsilon_2)F_{2-1}\right]} \tag{28}$$

The above equation can be simplified for this system. The assumption of convex particle surface leads to $F_{1-1} = 0$ and $F_{1-2} = 1$ since $F_{1-1} + F_{1-2} = 1$. According to the reciprocity relation between any two radiant elements, $F_{1-2} \cdot A_1 = F_{2-1} \cdot A_2$, the radiant energy leaving the reactor wall that arrives the particle surface is $F_{2-1} = A_1/A_2$. Similarly, it is straightforward to get $F_{2-2} = 1 - A_1/A_2$. So, $F_{2-1} = 0$ and $F_{2-2} = 1$ since $A_1 << A_2$. Equation (28) then simplifies to Equation (29). Equation (28) also simplifies to Equation (29) if the emissivity of the reactor wall is 1.0.

$$q_{o,1} = \varepsilon_1\sigma T_1^4 + (1-\varepsilon_1)\sigma T_2^4 \tag{29}$$

Similarly, the spectral radiant energy flux leaving the particle surface may be obtained as Equation (30).

$$q_{o,1,\lambda} = \varepsilon_1 \frac{C_1 \cdot \lambda^{-5}}{e^{C_2/\lambda \cdot T_1} - 1} + (1-\varepsilon_1)\frac{C_1 \cdot \lambda^{-5}}{e^{C_2/\lambda \cdot T_2} - 1} \tag{30}$$

For color-band pyrometry with Equation (21), the corrected equation results from replacing the Plank's radiant energy with Equation (30). The result appears in Equation (31).

$$\frac{DN_{Blue}}{DN_{Red}} = \frac{\int_{\lambda_1}^{\lambda_2} S_{\lambda,Blue} \cdot \left(\varepsilon_1 \frac{C_1 \cdot \lambda^{-5}}{e^{C_2/\lambda \cdot T_1} - 1} + (1-\varepsilon_1)\frac{C_1 \cdot \lambda^{-5}}{e^{C_2/\lambda \cdot T_2} - 1} \right) d\lambda}{\int_{\lambda_1}^{\lambda_2} S_{\lambda,Red} \cdot \left(\varepsilon_1 \frac{C_1 \cdot \lambda^{-5}}{e^{C_2/\lambda \cdot T_1} - 1} + (1-\varepsilon_1)\frac{C_1 \cdot \lambda^{-5}}{e^{C_2/\lambda \cdot T_2} - 1} \right) d\lambda} \tag{31}$$

Similar equation is can be established for any other two channel combination: blue/green or green/red, and both particle emissivity and particle surface temperature can be obtained simultaneously.

Reflection effects corrections for any other calibration equation is straightforward.

3-D Particle Shape Reconstruction

Biomass particles usually present irregular shapes and larger size (~ 6+ mm) compared with pulverized coal. The surface-area-to-volume ratio of such a particle plays an important role in its combustion behaviors since its combustion process is mainly heat- and mass-transfer controlled

instead of kinetics controlled. A 3-dimensional (3D) particle shape reconstruction algorithm, developed in this project and applied for the first time to particle combustion, addresses experimental measurement and calculation of particle surface-area-to-volume ratios,.

Substantial studies have been done for object 3-D shape reconstruction. For human face shape reconstruction, with some featured points on the 2-D images, a curved surface model (Komatsu 1991) applies, which can reconstruct facial shape fairly well. Based on a projective grid space, multi-image projective reconstruction was developed from a large number of images (Saito and Kanade 1999). Space carving (Kutulakos and Seitz 2000) is another widely used shape reconstruction technique with multiple photographs taken at known but arbitrarily-distributed viewpoints. All above techniques or algorithms present nearly insurmountable challenges for particles burning in a reactor: only limited optical access can be provided and no detailed features can be found on the image except the edge contour of the particle. A more practical and simple algorithm developed in this project appears below.

Image Acquisition and Processing

The algorithm developed in this project uses three images of a particle or object taken from three orthogonal directions with known orientation, as illustrated in Figure 122. The direction of the z coordinate in this system is opposite from a regular coordinate (is a left-hand rather than a right-hand xyz diagram) for operation convenience, but this is immaterial to this method and the mathematical reconstruction. If any camera is set with the specific viewpoint and orientation shown in Figure 122, the image taken with the camera can be rotated or flipped to meet the orientation requirements.

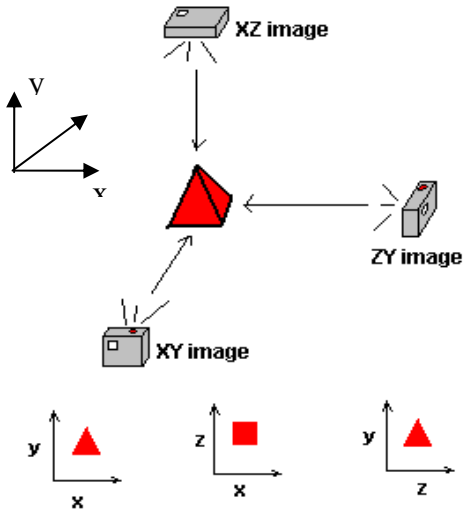

Figure 122 Camera setup orientation for imaging acquisition from three orthogonal direction

Three images taken for a popcorn ash (1-3 mm-sized fly ash) particle are named XY, XZ, and ZY, respectively, as shown in Figure 123. First, the edge contour in each image of the particle is detected using a color threshold which identifies those pixels that lie in the boundary between the

background and the particle image, illustrated in Figure 123 by red traces. If the three images have different scales due to camera setup difference, they must be rescaled based on one known image.

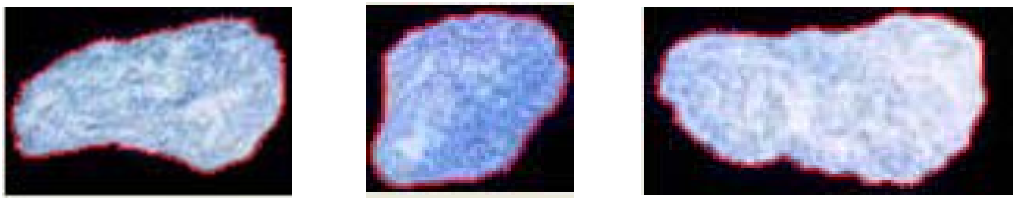

(a) XY image (b) XZ image (c) ZY

Figure 123 Three images of a popcorn ash particle taken from three orthogonal directions

Image Contour Alignment

On the edge contour trace in each 2-D image, four extreme points exist that have either minimal or maximum horizontal/vertical coordinates. A simple example is used to illustrate the image alignment using six common points. As shown in Figure 124, the four extreme points in the XZ image are marked as MinX, MaxX, MinZ, and MaxZ. A total of twelve extreme points appear in these three image contours. As a result, the space coordinates of six common points can be determined for a particle. Strictly speaking, these points will only be common in the limit of infinite focal lengths, but in this application focal lengths are long compared to particle size and this is a minor issue.

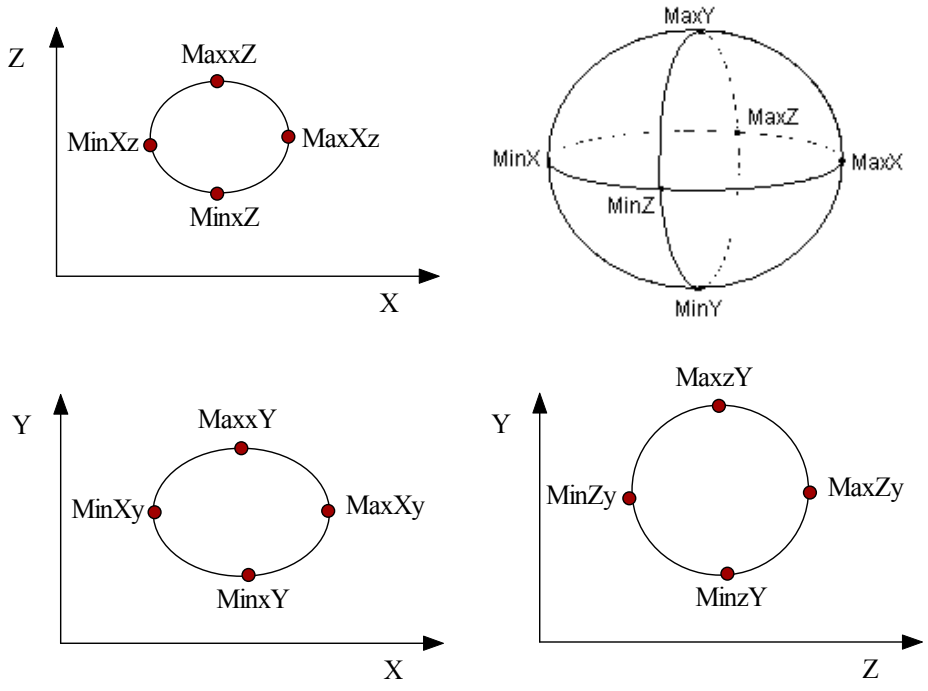

Figure 124 Image alignment illustration

For example, for the MinXy point in the XY image, its first two coordinates X and Y can be determined from the XY image. Assuming a convex particle surface, this point must correspond to the MinXz in image XZ. The third coordinate of this point must correspond to the point MinXz in the XZ image. Similarly, complete coordinates of another five points can be determined. With these six points, an approximate skeleton of the object is obtained, as shown in the right up corner in Figure 124. Only two coordinates (XY, or XZ, or ZY) for those points on the lines between any two adjacent extreme points are known, so the cubic spline interpolation algorithm approximates the third coordinate. A skeleton for the popcorn ash particle including eight surface segments (octants) results, as illustrated below.

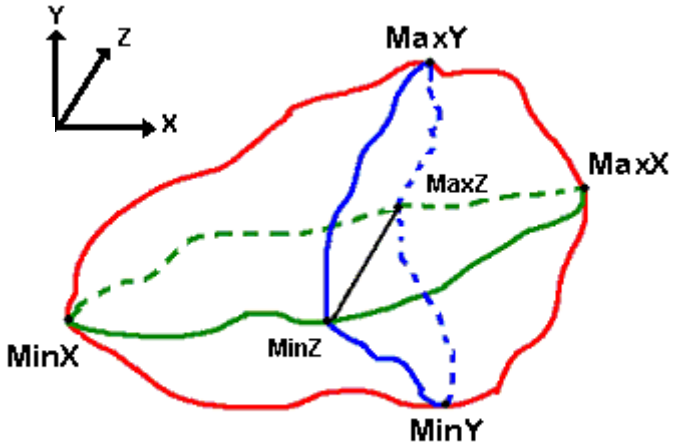

Figure 125 Popcorn ash particle skeleton after image contour alignment

Surface Generation

The exact locations of the points on the remaining particle surface lie between known bounds but cannot be precisely determined from this algorithm. In no case can the algorithm detect 3D concave features such as pits. However, the fixed or known points along the skeleton provide a means for estimating the remaining particle surface. An interpolation method called inverse distance weighting (IDW) generates surface point coordinates. IDW can be used both for curve fitting and surface fitting. A simple IDW weighting factor is $\omega(d) = 1/d^p$, where $\omega(d)$ is the weighting factor applied to a known value, d is the distance from the known value to the unknown value, and p is a user-selected power factor. Here weight decreases as distance increases from the known points. Greater values of p assign greater influence to values closest to the interpolated point. The most common value of p is 2.

A general form of interpolating a value using IDW is given in equation (32).

$$Z = \frac{\sum_i Z_i d_i^{-p}}{\sum_i d_i^{-p}} \tag{32}$$

where Z is the value of the interpolated point, Z_i is a known value,

$d_i = \sqrt{x_i^2 + y_i^2}$ is the distance from the known point i to the unknown point.

The alignment of the three traces divides the soon-to-be surface into eight areas, called octants. The inverse distance weighting (IDW) interpolation method applies to each octant separately, using the trace points that define the octant boundaries. The algorithm produces the same results along any boundary or at any fixed point independent of the direction from which it is approached, ensuring smooth transitions from one octant to the next. The interpolation only determines the z value for a surface point in the XY plane, and the XY image is used as an outline that is filled with a 2-D grid of points. These points are assigned a Z value in the IDW interpolation. This makes the XY image a backbone in the algorithm in that it has more influence in the final shape of the object 3-D model than the other two images. This is not inherent in the algorithm. In principle, similar interpolations could be applied to each of the other planar images generating additional surface points. However, this has thus far proven both unnecessary and too time consuming in this project.

Two variables are used to adjust the reconstructed shape. In addition to the power factor, p, in the original IDW method, the XY influence coefficient provides some flexibility. This variable is not in the original IDW algorithm, but the effect of increasing this value is that the XY image's trace will have a greater influence of the Z value of interpolated points. It was discovered that the IDW interpolation algorithm worked well at generating a spherical shape, but not so well with a cubic shape. By manipulating the power factor p and XY influence coefficient, a cube-like shape reconstruction can be improved.

A reconstructed 3-D shape of the popcorn ash particle appears in Figure 126, with surface points interpolated by the modified IDW method. This image is more readily appreciated on a computer screen where it can be rotated and examined from various angles than in this projection.

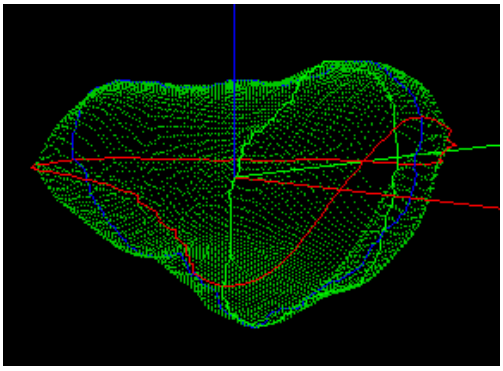

Figure 126 Reconstructed 3-D shape of a popcorn ash particle

Once the particle surface is generated, its surface area and volume can be calculated using the coordinates of all points on the surface. The calculated particle surface area of this popcorn ash particle is 1.59×10^{-4} m^2 and particle volume is 1.09×10^{-7} m^3.

For a reacting particle in a reactor, if its surface temperature distributions in all three 2-D images are calculated by the color-band method developed in this project, they can be mapped to the computer generated 3-D particle model surface.

The limitations of this particle shape reconstruction algorithm as well as its accuracy are discussed in Appendix C.

Both the particle shape reconstruction algorithm and temperature calculation algorithm are coded in the C++ computer language.

Summary

In this chapter, the experimental methods involved in investigating biomass particle or droplet combustion appear in reasonable detail. A sample preparation procedure to separate particle by shape and size is introduced. An entrained-flow reactor was designed and built to conduct sawdust particle combustion experiment; the structure and specifications of the entrained-flow reactor are explained. The operation procedure of a single-particle reactor for poplar dowel particle combustion experiment is presented.

A color-band imaging pyrometry has been developed to measure particle surface temperature with CCD or CMOS digital camera. In addition, a particle shape reconstruction algorithm was developed to calculate particle volume and surface area with three images taken from three orthogonal directions simultaneously.

Single Particle Combustion Model

As a biomass particle travels through the entrained-flow reactor or hovers in the single-particle reactor with air as carrier gas, it exchanges energy by both radiation and convective and potentially provides an energy source or sink through reactions. The biomass particle undergoes the following processes at different residence times: drying, devolatilization, volatiles combustion, and gasification and oxidation of char, as show in Figure 127. These processes may occur individually or simultaneously depending on particle properties and reactor conditions: particle type, density, size, shape, reactor temperature, heating rate, and etc.

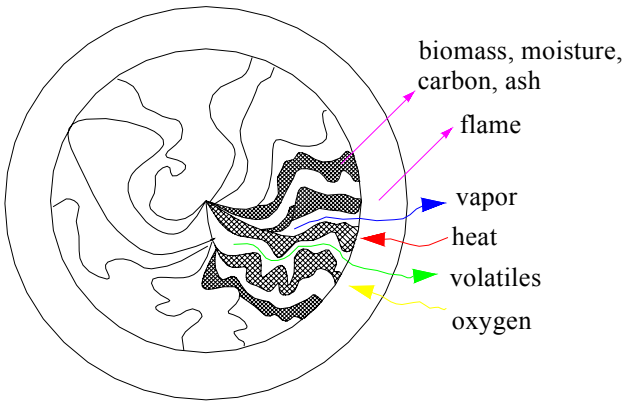

Figure 127 Particle combustion physical model with drying, devolatilization, char oxidation, gasification, and flame combustion

Mechanisms of drying, devolatilization, and char oxidation

Moisture in biomass occurs in two forms: free water and bound water (Forest Products Laboratory United States Department of Agriculture Forest Service 1999). Moisture content above the fiber saturation point (FSP) is free water, that is, exists in liquid form in pores and cells. Below the FSP moisture is bound water, that is, exists as moisture physically or chemically bound to surface sites or as hydrated species. The average FSP is 30% according to (Forest Products Laboratory United States Department of Agriculture Forest Service 1999), which is the weight of water in the wood as a percentage of the weight of ovendry wood (essentially water content on a dry basis). Traditionally, the forest products industries express moisture on this basis, so that 100% moisture means essentially half of the mass is water. Nuclear Magnetic Resonance (NMR) can determine free water and bound water contents (Guzenda and Olek 2000). Free moisture vaporizes from both the internal and external surface at a rate determined by the surface saturated vapor pressure, the partial pressure of vapor in the gas phase, and the specific surface area of the particle. Bound water does not vaporize in a manner similar to free moisture but rather is released as a result of chemical reactions releasing bound hydrates and similar processes. Four basic methods, including a thermal model, equilibrium model, and chemical reaction model, describe wood drying under combustion heat fluxes (Bryden and Hagge 2003). In this model, a mass transfer expression, with the difference between equilibrium vapor pressure and vapor partial pressure as the driving force, is used to describe both the evaporation of free water and recondensation of vapor. The evaporation rate of bound water is presented by a chemical reaction rate express (Chan, Kelbon et al. 1985). Figure 128 illustrates the drying

scheme of moisture. The biomass particles used in the entrained-flow reactor experiments were dried prior to use to maximize the particle size that can react in this residence-time-limited reactor. Drying of this nature removes all of the free moisture and bound water. Poplar particles used in the single-particle reactor usually have 6% moisture content, which is categorized as bound water. Samples with higher moisture content, up to 50%, were also prepared and used to collect free-water drying process data and validate the drying model.

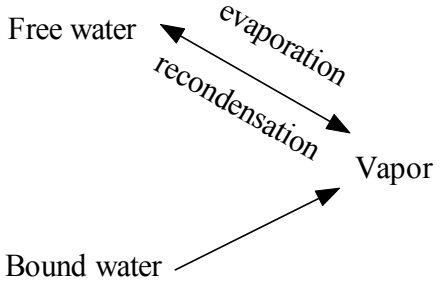

Figure 128 Moisture drying scheme

Devolatilization or pyrolysis involves heating of raw biomass components or organic materials in the absence of oxidizer, thermal degradation of the biomass components, mass transport of the devolatilization products by advection and diffusion, and escape of products at the surface of the particle. A few authors distinguish between pyrolysis and devolatilization, with the former occurring in a neutral or reducing environment and the latter in an oxidizing environment. Most particles thermally decompose within a volatile cloud (reducing environment) even when the overall environment is oxidizing, making this distinction somewhat ambiguous. The two terms are used interchangeably in this document, consistent with most of the literature. The two-stage wood pyrolysis kinetics model, shown in Figure 82, is chosen for this particle model since it is capable of predicting the product yields and distribution variations with temperature and heating rate which are significantly influenced by particle shape and size.

The volatile yield from pyrolysis includes a complex mixture and more than one hundred hydrocarbons were found (Evans and Milne 1987; Evans and Milne 1987; Demyirbas 2003). It is well known that pyrolysis product distribution depends strongly on reactor geometry, temperature, heating rate, residence time, and mass transfer velocity and pressure (Demyirbas 2003). This complex mixture mainly consists of CO, CO_2, H_2O, H_2, light hydrocarbons and heavy hydrocarbons. The first five components are classified as light gas, and the last one as tar. For the light gas composition, results from Thunman et. al (Thunman, Niklasson et al. 2001) are used here to predict wood pyrolysis volatile components, with the mass fraction of each species listed in Table 29. To simplify the combustion behaviors of volatiles, the light hydrocarbon and heavy hydrocarbon are lumped together as hydrocarbons in the current investigation, and the lumped hydrocarbon molecule is $C_6H_{6.2}O_{0.2}$, consistent with published results (Thunman, Niklasson et al. 2001). In this model, hydrocarbon combustion in the gas phase occurs through a one-step global reaction according to the approximate composition of hydrocarbon, even though the combustion chemistry of a simple gas could be a complex phenomena (Warnatz 2000). The reaction mechanism and kinetic parameters for the hydrocarbon combustion is based on Smoot et. al's (Smoot and Smith 1985) data.

Table 29 Light gas composition produced during devolatilization

Components	H2	CO	CO2	H2O	Light hydrocarbon
Mass fraction α	0.109	0.396	0.209	0.249	0.127

Char gasification and oxidation include five classic heterogeneous and homogeneous reactions, indicated as reactions 8 to 12 in Table 30. In coal char combustion, Reaction 8 is described by both first- and half-order expressions (Brewster, Hill et al. 1993; Smith, Smoot et al. 1994). Biomass char reactivity literature is less substantial than coal char but it is believed that biomass char has slightly higher reactivity than that of coal (Evans and Emmons 1977; Blackham, Smoot et al. 1994; Di Blasi, Buonanno et al. 1999; Wornat, Hurt et al. 1999). The oxidation rate of biomass char varies between a half- and first-order, as demonstrated by Janse et.al (Janse, de Jonge et al. 1998) .According to Bryden's (Bryden 1998) analysis, lignite's kinetic parameters are used for wood char oxidation since wood char more closely resembles lignite than other coal types. The oxidation kinetic mechanisms make this model more robust but in practice oxidation occurs mostly under diffusion-controlled conditions, in which case the details of the kinetics are immaterial.

Chemical reactions and phase changes, together with their corresponding rate expressions during drying, devolatilization, and char oxidation processes, appear in Table 30.

Table 30 Chemical reactions, phase change and rate expressions

Reaction index	Reaction description	Rate expression	Reference
1	Biomass → light gas	$r_1 = k_1 \rho_B$	
2	Biomass → tar	$r_2 = k_2 \rho_B$	
3	Biomass → char	$r_3 = k_3 \rho_B$	
4	Tar → light gas	$r_4 = \varepsilon k_4 \rho_g Y_T$	
5	Tar → char	$r_5 = \varepsilon k_5 \rho_g Y_T$	
6	H_2O (l, free) ↔ H_2O (g)	$r_6 = s_a \frac{\rho_{fw}}{\rho_{fw}^0} h_{m,pore} (\rho_v^{sat} - Y_V \rho_g)$	
7	H_2O (l, bound) → H_2O (g)	$r_7 = k_7 \rho_{bw}$	(Chan, Kelbon et al.

			1985)
8	$C + 1/2\ O_2 \rightarrow CO$	$r_8 = s_{a,char} \frac{\rho_C}{\rho_C + \rho_B + \rho_A} k_8 \varepsilon \rho_g Y_{O_2}$	(Evans and Emmons 1977)
9	$C + CO_2 \rightarrow 2CO$	$r_9 = s_{a,char} \frac{\rho_C}{\rho_C + \rho_B + \rho_A} k_9 \varepsilon \rho_g Y_{CO_2}$	(Brewster, Hill et al. 1993)
10	$C + H_2O \rightarrow CO + H_2$	$r_{10} = s_{a,char} \frac{\rho_C}{\rho_C + \rho_B + \rho_A} k_{10} \varepsilon \rho_g Y_V$	(Brewster, Hill et al. 1993)
11	$1/2\ O_2 + CO \rightarrow CO_2$	$r_{11} = k_{11} 10^3 M_{CO} \left(\frac{\rho_g Y_{CO}}{10^3 M_{CO}} \right) \left(\frac{\rho_g Y_{O_2}}{10^3 M_{O_2}} \right)^{0.25} \left(\frac{\rho_g Y_V}{10^3 M_V} \right)^{0.5}$	(Hautman, Dryer et al. 1981)
12	$H_2 + 1/2\ O_2 \rightarrow H_2O$	$r_{12} = k_{12} 10^3 M_{H_2} \left(\frac{\rho_g Y_{H_2}}{10^3 M_{H_2}} \right) \left(\frac{\rho_g Y_{O_2}}{10^3 M_{O_2}} \right)^{1.42}$	(Hautman, Dryer et al. 1981)
13	$C_6H_{6.2}O_{0.2} + 2.9O_2 \rightarrow 6CO + 3.1H_2$	$r_{13} = k_{13} 10^3 M_T \left(\frac{\rho_g Y_T}{10^3 M_T} \right)^{0.5} \left(\frac{\rho_g Y_{O_2}}{10^3 M_{O_2}} \right)$	(Smoot and Smith 1985)

Arrhenius expressions describe the temperature dependence of the kinetic rate coefficients for reactions 1-5 and 7-13, as indicated in Equations (33) and (34).

In reactions 1-5, 7, and 11-13,

$$k_i = A_i \exp\left(- \frac{E_i}{RT} \right); \tag{33}$$

and in Reactions 8 – 10,

$$k_i = A_i T \exp\left(-\frac{E_i}{RT}\right) \quad (34)$$

The literature-based kinetic parameters for wood pyrolysis vary widely. They are usually measured at low to moderate temperature (usually < 900 K). No high-temperature kinetic data for the two-stage scheme have been reported. Font et al. (Font, Marcilla et al. 1990) presented kinetic data for the three primary reactions that are found to be comparable to what Nunn et al. (Nunn, Howard et al. 1985) reported for the single reaction kinetic data for hardwood in the high-temperature range (573 ~ 1373 K). Font et al.'s results are used in this model for sawdust samples and Wagenaar's (Wagenaar, Prins et al. 1993) pine wood pyrolysis kinetics data are applied for poplar samples. The pre-exponential factors, activation energy, and standard heats of reaction for all the reactions used in this model appear in Table 31.

Table 31 Kinetics data and heat of reaction

Reaction index	A (1/s)	E (KJ/mol)	Reference	Temperature range (K)	ΔH (KJ/kg)	Reference
1 (hardwood sawdust)	1.52×10^{7}	139.2	(Font, Marcilla et al. 1990)	733-878	-418	(Chan, Kelbon et al. 1985)
1 (poplar)	1.11×10^{11}	177	(Wagenaar, Prins et al. 1993)	573-873		
2 (hardwood sawdust)	5.85×10^{6}	119	(Font, Marcilla et al. 1990)	733-878	-418	(Chan, Kelbon et al. 1985)
2 (poplar)	9.28×10^{9}	149	(Wagenaar, Prins et al. 1993)	573-873		
3 (hardwood sawdust)	2.98×10^{3}	73.1	(Font, Marcilla et al. 1990)	733-878	-418	(Chan, Kelbon et al. 1985)
3 (poplar)	3.05×10^{7}	125	(Wagenaar, Prins et al. 1993)	573-873		
4	4.28×10^{6}	107.5	(Liden, Berruti et al. 1988)	-	42	(Koufopanos, Papayannakos et al. 1991)

5	1.0×10^{5}	107.5	(Di Blasi 1993)	-	42	(Koufopanos, Papayannakos et al. 1991)
6	5.13×10^{10}	88	(Bryden and Hagge 2003)	-	-2,440	(Bryden and Hagge 2003)
8	0.658 (m/s.K)	74.8	(Evans and Emmons 1977)	-	9,212	(Bryden and Hagge 2003)
9	3.42 (m/s.K)	130	(Brewster, Hill et al. 1993)	-	14,370	(Turns 2000)
10	3.42 (m/s.K)	130	(Brewster, Hill et al. 1993)	-	10,940	(Turns 2000)
11	$10^{12.35}$	167	(Hautman, Dryer et al. 1981)	-	10,110	(Turns 2000)
12	$10^{12.71}$	171.3	(Hautman, Dryer et al. 1981)	-	120,900	(Turns 2000)
13	$10^{4.32}\times T\times P^{0.3}$	80.2	(Smoot and Smith 1985)	-	41,600	(Bryden 1998)

Heat, mass, and momentum transfer

The following assumptions allow tractable mathematical combustion model development:

all properties are assumed to be transient and one dimensional in space;

local thermal equilibrium exists between the solid and gas phase in the particle, so temperatures and their gradients are the same for the solid and gas;

gases behave as ideal gases, including both relationships between pressure, temperature, and specific volume and dependence of heat capacity on temperature only;

particle aspect ratios and shapes do not change during devolatilization, though size does change dynamically. The shape and aspect ratio is a simplifying assumption for this case but not required by the model in general;

heat and mass transfer at particle boundaries increase relative to that of a sphere by the ratio of the particle surface to that of a volume-equivalent sphere – a close approximation to results from more detailed analyses for similarly sized particles.

In the particle model, the particle shapes are represented by a parameter n. A spherical particle is described by $n = 2$, cylinder particles by $n = 1$, and flat plate particles $n = 0$. Before the biomass particle enters the reactor, it is assumed that it is filled by inert gas or air. So in total twelve species appear in the model: biomass, char, free water, bound water, ash, CO, CO_2, H_2O, H_2, O_2, lumped hydrocarbon (tar), and inert gas. The mass conservation of each species, the momentum, and the total energy equations, as well as the initial and boundary conditions appear as Equations (35) - (72).

The biomass temporal mass balance contains three consumption terms, one each for the reactions to light gas, tar, and char, where all terms in this expression and most terms in subsequent expressions depend on both time and position.

$$\frac{\partial \rho_B}{\partial t} = S_B$$
$$where, S_B = -(r_1 + r_2 + r_3) \quad (35)$$

Similarly, the char temporal mass balance contains five source terms, one from the conversion of biomass to char and one for the char yield from the secondary reactions of tar, as well as the gasification and oxidation reactions.

$$\frac{\partial \rho_C}{\partial t} = S_C$$
$$where, S_C = r_3 + r_5 - r_8 \frac{2M_C}{M_{O_2}} - r_9 \frac{M_C}{M_{CO_2}} - r_{10} \frac{M_C}{M_{H_2O}} \quad (36)$$

The temporal free-water mass balance contains a loss associated with conversion to vapor and a source term associated with water vapor readsorption into the particle, as determined by r_6 in Table 30. The free water also migrates due to the pressure gradient in the liquid phase (Ouelhazi, Arnaud et al. 1992; De Paiva Souza and Nebra 2000). The migration flux is based on Darcy's law for this porous media, which is proportional to the total liquid pressure gradient. The total liquid pressure is equal to the pressure of the gas phase minus the capillary pressure of the gas-liquid interface. An effective free water diffusivity $D_{eff,fw}$ is derived to describe the migration with Fick's law applied based on the Darcy's law results (De Paiva Souza and Nebra 2000). Equation (37) gives the mass balance for free water. The mass transfer coefficient of vapor in the pore $h_{m,pore}$, which appears in the evaporation rate r_6, is determined by Equation (38) (Incropera and Dewitt 1996).

$$\frac{\partial \rho_{fw}}{\partial t} = \frac{1}{r^n}\frac{\partial}{\partial r}\left(r^n D_{eff,fw}\frac{\partial \rho_{fw}}{\partial r}\right) + S_{fw} \qquad (37)$$
$$where, S_{fw} = -r_6,$$

$$h_{m,pore} = 3.66 \cdot \frac{D_{eff,H_2O}}{d_{pore\_hydraulic}} \qquad (38)$$

Bound water has similar migration in the radial direction but it is driven by a chemical potential gradient, and the phase change rate is described by the chemical reaction r_7, shown in Equation (39).

$$\frac{\partial \rho_{bw}}{\partial t} = \frac{1}{r^n}\frac{\partial}{\partial r}\left(r^n D_{eff,bw}\frac{\partial \rho_{bw}}{\partial r}\right) + S_{bw} \qquad (39)$$
$$where, S_{bw} = -r_7,$$

Several different correlations describe diffusivities of free water and bound water (Ouelhazi, Arnaud et al. 1992; De Paiva Souza and Nebra 2000; Olek, Perre et al. 2005), and Olek et. al.'s method is applied in this investigation. It is also believed that the diffusivities of both free water and bound water are direction dependent, and the diffusivity in the axial direction is larger than that in the tangential direction. Details can be found at the end of this section in the physical property list.

The ash in the particle is assumed to be inert, so that the ash density is constant,

$$\frac{\partial \rho_A}{\partial t} = 0 \qquad (40)$$

The conservation equations for all gas-phase components (CO, CO_2, H_2O, O_2, H_2, HC, and inert gas) include temporal and spatial gradients, convection, and source terms and can be written as follows

$$\frac{\partial}{\partial t}\varepsilon\rho_g Y_i + \frac{1}{r^n}\frac{\partial}{\partial r}(r^n \varepsilon\rho_g Y_i u) = \frac{1}{r^n}\frac{\partial}{\partial r}(r^n \varepsilon D_{eff,i}\rho_g \frac{\partial Y_i}{\partial r}) + S_i \tag{41}$$

Source terms for each gas phase species appear below.

$$\begin{aligned}
S_{CO_2} &= r_{11}\frac{M_{CO_2}}{M_{CO}} - r_9 + (r_1 + r_4)\alpha_{CO_2} \\
S_{CO} &= r_8\frac{2M_{C0}}{M_{O_2}} + r_9\frac{2M_{CO}}{M_{CO_2}} + r_{10}\frac{M_{CO}}{M_{H_2O}} + r_{13}\frac{6M_{CO}}{M_{HC}} - r_{11} + (r_1 + r_4)\alpha_{CO} \\
S_{O_2} &= -r_8 - r_{11}\frac{M_{O_2}}{2M_{CO}} - r_{12}\frac{M_{O_2}}{2M_{H_2}} - r_{13}\frac{2.9M_{O_2}}{M_{HC}} \\
S_{H_2} &= (r_1 + r_4)\alpha_{H_2} + r_{10}\frac{M_{H_2}}{M_{H_2O}} - r_{12} + r_{13}\frac{3.1M_{H_2}}{M_{HC}} \\
S_{H_2O} &= (r_1 + r_4)\alpha_{H_2O} + r_6 + r_7 - r_{10} + r_{12}\frac{M_{H_2O}}{M_{H_2}} \\
S_{HC} &= r_2 + (r_1 + r_4)\alpha_{HC} - r_4 - r_5 - r_{13} \\
S_I &= 0
\end{aligned} \tag{42}$$

The overall gas-phase continuity equation results from the sum of these species and has the form

$$\begin{aligned}
&\frac{\partial}{\partial t}\varepsilon\rho_g + \frac{1}{r^n}\frac{\partial}{\partial r}(r^n \varepsilon\rho_g u) = S_g, \\
&where, S_g = r_1 + r_2 - r_5 + r_6 + r_7 + r_8\frac{2M_C}{M_{O_2}} + r_9\frac{M_C}{M_{CO_2}} + r_9\frac{M_C}{M_{H_2O}}.
\end{aligned} \tag{43}$$

The gas-phase velocity in the particle obeys a Darcy-law-type expression

$$u = -\frac{\eta}{\mu}\frac{\partial p}{\partial r},$$
$$where, p = \frac{\rho_g R_g T}{M_W}. \tag{44}$$

The gas mixture is treated as ideal gas, and the average molecular weight is

$$M_W = \sum_j X_j \cdot M_j \,, \tag{45}$$

where the mole fraction of each gas species, X_j, is equal to

$$X_j = \frac{\left(\frac{Y_j}{M_j}\right)}{\left(\sum_i \frac{Y_i}{M_i}\right)} \tag{46}$$

The permeability, η, is expressed as a mass-weighted function of the individual solid-phase permeabilities

$$\eta = \frac{\rho_B}{\rho_{B,0}}\eta_B + \left(1 - \frac{\rho_B}{\rho_{B,0}}\right)\eta_C \tag{47}$$

The energy conservation equation includes the following terms

$$\begin{aligned} &\frac{\partial}{\partial t}\left[\sum_i \rho_i \hat{H}_i + \sum_k \rho_k \hat{H}_k + \varepsilon\rho_g \sum_j Y_j \hat{H}_j\right] + \frac{1}{r^n}\frac{\partial}{\partial r}\left[r^n \varepsilon \rho_g u \sum_j Y_j \hat{H}_j\right] \\ &= \frac{1}{r^n}\frac{\partial}{\partial r}(r^n K_{eff}\frac{\partial T}{\partial r}) + \frac{1}{r^n}\frac{\partial}{\partial r}\left[r^n\left(\rho_g \varepsilon \sum_j D_{eff,j}\frac{\partial Y_j}{\partial r}\hat{H}_j + D_{eff,k}\frac{\partial \rho_k}{\partial r}\hat{H}_k\right)\right] \end{aligned} \tag{48}$$

where,

$\hat{H}_l = \hat{H}^0_{l,f} + \int_{T_0}^{T} Cp_l(T)dT$, l is any species involved,

i = any species or component in the solid phase,

j = any species or component in the gas phase,

k = free water and bound water.

This form of the energy equation relates to standard theoretical analyses (Bird, Stewart et al. 2002) for multi-components systems. In Equation (48), the first term represents the energy accumulation; the second term represents energy convection; the third term (first term after the equals sign) accounts for conduction heat transfer, and the last term accounts for energy associated with diffusion of species in the gas phase and the liquid phase. The last term generally contributes only negligibly to the overall equations and is commonly justifiably ignored. No heats of reaction appear in the expression since the energy balances total enthalpy (both phases) and is not written in terms of temperature or separate particle and gas phases. Heats of reaction only become apparent when separately modeling the particle and gas phases or using temperature instead of enthalpy. Radiation between the gas and solid phase in the particle is incorporated into the effective conductivity, as explained below.

The effective diffusivity of gas species in the particle can be calculated by the parallel pore (Wheller) model, as shown in Equation (49).

$$D_{eff} = D\varepsilon/\tau$$
$$\text{where, } 1/D = 1/D_{AB} + 1/D_K \qquad (49)$$

An identical diffusivity for each species and Fickian diffusion assumptions, as implied here, avoid the complexity of more formal multi-component diffusion calculations.

The effective particle thermal conductivity includes radiative and conductive components with some theoretical basis (Robinson, Buckley et al. 2001; Robinson, Buckley et al. 2001) and with empirical verification for wood (Janse, Westerhout et al. 2000).

$$K_{eff} = K_{cond} + K_{rad}, \qquad (50)$$

where the particle structure is assumed to be close to the upper limit for thermal conductivity, that is, it is assumed to have high connectivity in the direction of conduction,

$$K_{cond} = \varepsilon K_{gas} + (1-\varepsilon)\left[\frac{\rho_B}{\rho_{B,0}}K_B + \left(1-\frac{\rho_B}{\rho_{B,0}}\right)K_C\right]$$
$$K_{gas} = \sum_j Y_j K_j \quad , \tag{51}$$

and where radiation contributes approximately to the third power of the temperature

$$K_{rad} = \frac{\varepsilon\sigma T^3 d_{pore}}{\omega} \tag{52}$$

The emissivity of the particle is the mass-weighted result of each solid component: biomass, ash, and char. A volume-weighted emissivity might be more appropriate, but it's not available in this case: all components are assumed to occupy the same total volume.

$$\omega = \frac{\rho_A}{\sum\rho_i}\omega_A + \frac{\rho_B}{\sum\rho_i}\omega_B + \frac{\rho_C}{\sum\rho_i}\omega_C \tag{53}$$

The thermal conductivity of wet biomass particle is based on Ouelhazi's (Ouelhazi, Arnaud et al. 1992) empirical correlation which states that the effective thermal conductivity is a function of temperature and moisture contents. Thermal conductivity in the axial direction is assumed to be 2.5 times that in the tangential direction. An average value of both the axial and tangential directions is adopted in this paper. Details of the thermal conductivity of the wet biomass particle appear at the end of this section.

Initial conditions are assumed from experimental conditions for a non-reacting particle. That is, at $t = 0$,

$$\begin{aligned} &p(t=0,r) = p_{atm} \\ &T(t=0,r) = 300K\,(typically) \\ &u(t=0,r) = 0 \\ &Y_l(t=0,r) = 1 \\ &Y_{i(j,k)}(t=0,r) = 0 \end{aligned} \tag{54}$$

Boundary conditions at the particle center are determined by symmetry, that is, at $r = 0$

$$\left.\frac{\partial p}{\partial r}\right|_{t,r=0} = 0,$$
$$u|_{t,r=0} = 0,$$
$$\left.\frac{\partial T}{\partial r}\right|_{t,r=0} = 0, \tag{55}$$
$$\left.\frac{\partial Y_{i(j,k)}}{\partial r}\right|_{t,r=0} = 0.$$

During biomass particle combustion, the flame surrounding the particle may affect particle surface temperature by heat generated in the flame that feeds back to the surface and further heats the particle. The model is capable of modeling both the particle domain and the boundary layer domain, which is assumed to include the flame during combustion. The boundary layer flame simulation, as with many other model features, can be turned on or off during simulation.

If the boundary layer domain is off, boundary conditions at the particle outer surface are defined by external conditions of pressure and heat and mass flux

$$p(t, r = r_p) = p_{atm},$$
$$\left.\frac{\partial Y_{i(j,k)}}{\partial r}\right|_{r=r_p} = \theta_m h_m R_{SA}\left(Y_{i(j,k),\infty} - Y_{i(j,k),S}\right) \tag{56}$$
$$k_{eff}\left.\frac{\partial T}{\partial r}\right|_{r=r_p} = \theta_T h_T R_{SA}\left(T_f - T\right) + R_{SA}\omega\sigma\left(T_w{}^4 - T^4\right)$$

where θ_m and θ_T represent the blowing factors (Bird, Stewart et al. 2002) for mass transfer and heat transfer, respectively. R_{SA} represents the exterior surface area ratio, which is the surface area of the particle divided by the characteristic surface area as follows

$$R_{SA} = SA/(4\pi R_P{}^2)$$
$$R_{SA} = SA/(4\pi R_P{}^2 AR) \tag{57}$$
$$R_{SA} = SA/(4R_P{}^2 AR^2)$$

for spheres, cylinders, and flat plates, respectively.

Each shape employs heat transfer coefficients developed for that particular shape. Correlations suitable for random particle orientation during flight appear in the literature for some particles

(Masliyah and Epstein 1972). Where such a model is not available, the characteristic length of the particle is calculated using the average length of the particle. For near-spherical particles, Masliyah's prolate spheroid model (Masliyah and Epstein 1972) provides a suitable correlation, as indicated in Equation (58).

$$Nu = 1.05 + 0.6\,\mathrm{Re}^{0.65}\,\mathrm{Pr}^{0.33} \tag{58}$$

Cylinders at low Reynolds numbers adopt the correlation of Kurdyumov (Kurdyumov and Fernandez 1998) (Equation (59)). .

$$Nu = W_0(\mathrm{Re})\mathrm{Pr}^{0.33} + W_1(\mathrm{Re}), \tag{59}$$

where,

$$Nu = 0.644\,\mathrm{Re}^{0.5}\,\mathrm{Pr}^{0.343} \tag{60}$$

$$W_0 = \begin{cases} 0.46271\exp\left(1.0 \\ 0.597\left(\mathrm{Re}/\ln\left(1/\mathrm{R}\right.\right. \end{cases}$$

$$W_1 = \begin{cases} 0.10666\exp\left(\begin{matrix} 0.4 \\ +0 \end{matrix}\right. \\ 0.0917, \quad \mathrm{Re} < 1 \end{cases}$$

The heat transfer coefficient for a flat plate appears in Equation (60).

Mass transfer coefficient calculations are analogous to heat transfer correlations respectively for each specific particle shape.

If the boundary layer domain is turned on, the boundary conditions assume those in the bulk flow (indicated by infinity subscripts), as shown in Equation (61).

$$\begin{aligned} p\big|_{r>=r_p} &= p_{atm}, \\ Y_{i(j,k)}\Big|_{r=r_p+BLT_m} &= Y_{i(j,k),\infty} \\ T\big|_{r=r_p+BLT_T} &= T_\infty \end{aligned} \tag{61}$$

where, BLT_m and BLT_T are boundary layer thickness of mass transfer and heat transfer, respectively. The determination of these two types of boundary layer thicknesses is straightforward if the particle stays in inert carrier gas (nitrogen). Two methods can be adopted to calculate the thickness: linear and exponential. Figure 129 illustrates each assumption, where

only mass-transfer-boundary-layer thickness is indicated. The heat-transfer-boundary-layer thickness has a similar form.

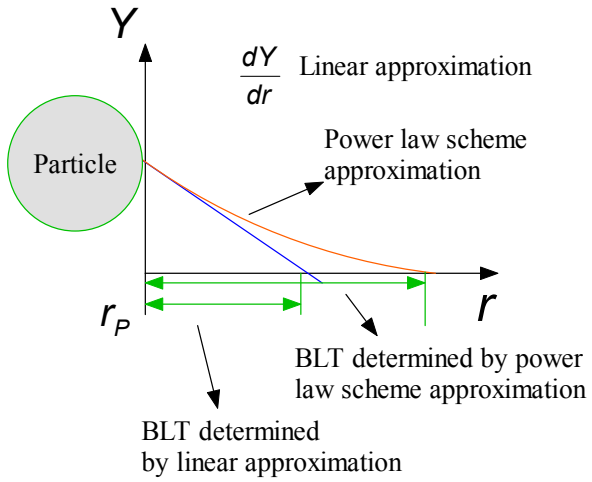

Figure 129 Boundary layer thickness determination

The linear approximation assumes that the gradient at the particle surface can be approximated by an algebraic difference

$$\frac{dY}{dr} \approx \frac{\Delta Y}{\Delta r} = \frac{Y_\infty - Y_S}{BLT_m} \tag{62}$$

The mass transfer at the particle surface is also correlated with the empirical mass transfer correlation

$$D_{AB}\frac{dY}{dr} = h_m \theta_m \left(Y_\infty - Y_s\right) \tag{63}$$

where, the mass transfer coefficient can be calculated by

$$Sh = \frac{d_P h_m}{D_{AB}} \tag{64}$$

So, substituting Equations (63) and (64) into Equation (62) leads to the boundary layer thickness for mass transfer

$$BLT_m = \frac{d_P}{Sh \cdot \theta_m} \tag{65}$$

Similarly, the boundary layer thickness of heat transfer based on the linear approximation is

$$BLT_T = \frac{d_P}{Nu \cdot \theta_T} \tag{66}$$

The exponential scheme (Roberts 2005) for boundary layer thickness calculation is based on a more exact solution for a convection-diffusion partial differential equation explained by Patankar (Patankar 1980). The exact solution better approximates the distribution in the boundary layer for any variable compared to the linear approximation, as shown in Figure 129. The exact solution of a steady one-dimensional convection and diffusion problem in Cartesian coordinates is

$$\frac{\phi - \phi_0}{\phi_L - \phi_0} = \frac{\exp(Px/L) - 1}{\exp(P) - 1}$$
$$\text{Peclet number } P = \frac{\rho u L}{\tau} \tag{67}$$

where *0-L* defines the boundary layer domain with *0* as the particle surface and *L* the infinity boundary. The derivative of φ at the particle surface with respect to x according to the above equation will be

$$\left.\frac{d\varphi}{dx}\right|_{x=0} = \frac{(\varphi_L - \varphi_0)}{\exp(P) - 1} \cdot \frac{P}{L} = \frac{(\varphi_L - \varphi_0)}{\exp(P) - 1} \cdot \frac{\rho u}{\tau} \tag{68}$$

Substituting the mass transfer correlation, Equation (63), into the above equation results in the boundary layer thickness

$$BLT_m = \frac{\tau}{\rho u} \ln\left(\frac{\rho u}{h_m \theta_m} + 1\right) \tag{69}$$

For any coordinate system, if both the strengths of convection and diffusion ($\rho u r^n$ and $\rho D_{AB} r^n$) are assumed be to constant, the boundary layer thickness for mass transfer appears in Equation (70).

$$BLT_m = \frac{\rho D_{AB} r^n}{\rho u r^n} \ln\left(\frac{\rho u r^n}{\rho D_{AB} r^n h_m \theta_m} D_{AB,x=0} + 1\right) \tag{70}$$

Similarly, the heat-transfer-boundary-layer thickness has the same formula as the mass-transfer-related parameters in Equation (70) replaced by heat-transfer-relevant parameters

$$BLT_T = \frac{kr^n}{\rho Cpur^n} \ln\left(\frac{\rho Cpur^n}{kr^n h_T \theta_T} k_{x=0} + 1\right) \tag{71}$$

When the particle is surrounded by air instead nitrogen, a flame forms in the boundary layer. The resulting temperature and species concentration distributions in the boundary layer may influence the boundary layer thickness, making it different from that calculated based on the heat and mass transfer correlations illustrated above. The determination of the exact boundary layer thickness for such a burning particle with surrounding flame could be complicated due to bulk flow convection (slip velocity) in the reactor axial direction and the offgases from the particle. A two-dimensional model might be needed to predict the exact boundary layer thickness. In this investigation, Equations (70) and (71) are applied for the boundary layer thickness determination for the boundary layer including flame and model predictions agree with experimental data well.

To simplify momentum conservation, constant boundary-layer pressure is assumed, equal to the atmospheric pressure. The secondary cracking reactions of tar and soot formation in the boundary layer are neglected, although combustion reactions are included. A radiation energy flux has to be added to the energy equation for the node on the particle physical surface due to the radiation between the particle surface and reactor wall.

Particle shrinking or swelling during drying, pyrolysis, and char gasification and oxidation is described and modeled using the following empirical correlation

$$\frac{v}{v^0} = 1 + x_M(\beta_M - 1.0) + x_B(\beta_B - 1.0) + x_C(\beta_C - 1.0) \tag{72}$$

,

which can be used to describe both shrinking and swelling behaviors of a burning solid particle or droplet. In Equation (72), v = current control volume of each cell, v^0 = initial control volume of each cell; x_m, x_B, x_C =conversion of moisture, biomass, and char; β_M =swelling/shrinking factor of moisture drying, 3.65 for black liquor swelling and 0.9 for wood particle drying shrinking; β_B =swelling/shrinking factor of biomass devolatilization, 30.0 for black liquor swelling and 0.9 for wood particle shrinking; β_C =shrinking factor of char burning, 0.0 for constant char density shrinking (conceptually consistent with the typically external diffusion controlled oxidation rates).

The physical properties of the biomass particles significantly affect the heat and mass transfer rates (Raveendran, Ganesh et al. 1995; Di Blasi 1997). In this work, temperature-dependent heat

capacity correlations are used for all species. The heat capacity of biomass and char adopt the model suggested by Merrick (Merrick 1983). Gronli et al. (Gronli and Melaaen 2000) suggested a correlation for tar heat capacity, which is based on some typical pyrolysis tar components (closely related to benzene). All physical properties appear in Table 32.

Table 32 Physical properties of biomass particles

Property		Value	Reference
Wood density ρ_B		650 kg/m^3 (sawdust) 580 kg/m^3 (poplar particle)	
Porosity ε		0.4	
Emissivity ω		ω_A=0.7 ω_B=0.85 ω_C=0.95	
Permeability (Darcy)	η	$\eta_B = 1$	(Gronli and Melaaen 2000)
		$\eta_C = 100$	(Gronli and Melaaen 2000)
Thermal conductivity (W/m.K)	K	k_j, gas species thermal conductivity is calculated based on DIPPR correlations	(DIPPR)
		$K_A = 1.2$	
		Wet biomass in tangential direction: if $C_w > 0.4$: $k_B = \left(9.32\times10^{-2} + 6.5\times10^{-3}C_w\right)$ $\left(1+3.65\times10^{-3}(T-273.15)\right)\left(0.986+2.695C_w\right)$ if $C_w \le 0.4$: $k_B = \left(0.129 - 4.9\times10^{-2}C_w\right)$ $\left(1+(2.05+4C_w)\times10^{-3}(T-273.15)\right)\left(0.986+2.695C_w\right)$ Thermal conductivity in axial direction is 2.5 times of the tangential one.	(Ouelhazi, Arnaud et al. 1992)

	$K_C = 0.071$	(Lee, Chaiken et al. 1976)
Biomass particle specific surface area S_a,(m^2/m^3)	9.04×10^4	BET
Char particle specific surface area $S_{a,char}$, (m^2/m^3)	1.0×10^6	BET
Pore size $d_{pore,}$ *(m)*	3.2×10^{-6}	BET
Hydraulic pore diameter, $d_{pore,hydraulic}$	$d_{pore,hydraulic} = \frac{4.0\varepsilon}{S_a(1.0-\varepsilon)}$	
Molecular weight *M (kg/kmol)*	$M_T = 145$	(Janse, Westerhout et al. 2000)
Viscosity μ, (Pa.s)	$\mu_{gas} = 3\times10^{-5}$ for all gas species	(Kansa, Perlee et al. 1977)
Diffusivity D_{AB} (m^2/s)	$D_{AB} = 3.0\times10^{-5}$ for all gas species	(Janse, Westerhout et al. 2000)
	$D_{eff,bw} = D_0 \exp(\frac{-E_b}{R \cdot T})$ $E_b = a_1 - a_2 \cdot C_{bw}$ where, C_{bw} is bound water content, $D_0 = 5\times10^{-5} m/s$ $a_1 = 31030 J/mol$ $a_2 = 10000 J/mol$	(Olek, Perre et al. 2005)

	$D_{eff,fw} = 6.1\times 10^{3}\left(\frac{k_{fw}}{\eta_{fw}}\right)\varepsilon^{0.61}\left(\frac{\rho_s C_{fw}}{\rho_{fw}}\right)$ *where* , $k_{fw} = \begin{cases} 0, \text{if } \left(\frac{\rho_s C_{fw}}{\varepsilon\rho_{fw}}\right) \le S_{ir} \\ k_{fw}^{\Phi}\left(1-\cos\frac{\pi}{2}\left(\frac{(\rho_s C_{fw}/\varepsilon\rho_{fw})-S_{ir}}{1-S_{ir}}\right)\right) \\ \text{if } \left(\frac{\rho_s C_{fw}}{\varepsilon\rho_{fw}}\right) > S_{ir} \end{cases}$ $S_{ir} = 0.1, \text{irreducibl e saturation}$ $k_{fw}^{\Phi} = 3.0\times 10^{-15}\, m^2$	(De Paiva Souza and Nebra 2000)
Heat capacity Cp (J/kg.K)	$Cp_B = \left(\frac{1000R_g}{7.72}\right)\left[g\left(\frac{380}{T}\right)+2g\left(\frac{1800}{T}\right)\right]$	(Merrick 1983)
	$Cp_C = \left(\frac{1000R_g}{11.3}\right)\left[g\left(\frac{380}{T}\right)+2g\left(\frac{1800}{T}\right)\right]$	(Merrick 1983)
	Where, $g(x) = \frac{x^2 e^x}{(e^x-1)^2}$	
	$Cp_T = -100+4.4\times T-0.00157\times T^2$	(Gronli and Melaaen 2000)
	Cp_j of all gas species except hydrocarbon is based on DIPPR database correlations	(DIPPR)

Particle Differential Equations Solution Procedure

This one-dimensional complete mathematical model for the combustion of a single biomass particle includes a set of partial differential equations (PDEs) to describe the mass, heat, and momentum transfer in the particle domain and the flame layer domain. A control volume method (Patankar 1980) reformulates these differential equations into a set of algebraic equations amenable to computer simulation. A fully implicit scheme is applied for the transient term in the energy conservation equation, each species conservation equation, and momentum equation; the convection and diffusion/conduction terms are solved by the power law scheme; control volume faces occur midway between the grid points; a staggered grid is used for velocity component; the SIMPLE algorithm is applied for the momentum transfer to calculate the flow field.

Standard solution for the general differential equation

This set of partial differential equations for heat, mass, and momentum transfer can all be presented by a standard general equation. If the dependent variable is denoted by φ, the general partial differential equation is

$$\frac{\partial}{\partial t}(\varepsilon\rho\Phi) + div(\varepsilon\rho u\Phi) = div(\Gamma grad\Phi) + S \quad , \tag{73}$$

where, $S = S_c + S_p\Phi$.

The calculation domain, including the particle and the boundary layer, is divided into a number of non-overlapping control volumes such that there is one control volume surrounding each grid point, as shown in Figure 130. The differential equation is integrated over each control volume. Piecewise profiles expressing the variation of φ between the grid points are used to evaluate the required integrals. The result is the discretization equation containing the values of φ for a group of grid points.

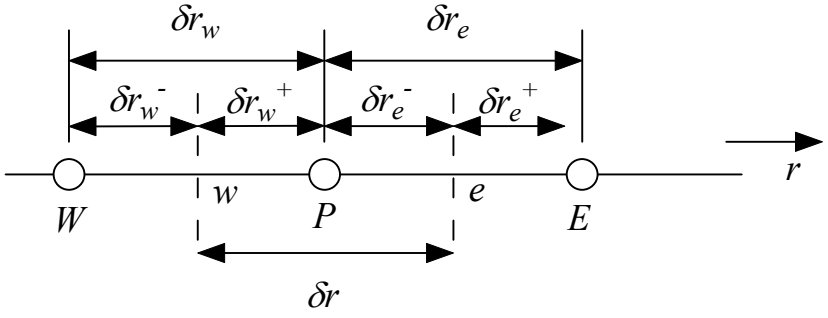

Figure 130 Grid-point cluster for one-dimensional problem

In Figure 130, point *P* is the current grid, and points *W* and *E* are the west neighbor point and the east neighbor point respectively for this one-dimensional problem. Faces *w* and *e* define the control volume surrounding the current grid point *P*. The integration form of the general equation with respect of time and the control volume is

$$\int_{dv}\int_{dt}\frac{\partial}{\partial t}(\varepsilon\rho\Phi)dtdv + \int_{dv}\int_{dt} div(\varepsilon\rho u\Phi)dtdv = \int_{dv}\int_{dt} div(\Gamma grad\Phi)dtdv + \int_{dv}\int_{dt} Sdtdv \quad . \tag{74}$$

$$a_P\Phi_P = a_W\Phi_W + a_E\Phi_E + b \quad , \tag{75}$$

The general discretization equation is now derived through the integration for the one-dimensional problem with shrinking/swelling included

where,

$$a_E = D_e A(|P_e|) + \max(-F_e, 0), \tag{76}$$

$$a_W = D_w A(|P_w|) + \max(F_w, 0), \tag{77}$$

$$A(|P|) = \max\left(0, (1 - 0.1|P|)^5\right), \tag{78}$$

$$b = a_P^0 \Phi_P^0 + \Delta v S_C, \tag{79}$$

$$a_P = a_P^1 + a_W + a_E - \Delta v S_P + (F_e - F_w). \tag{80}$$

This general discretization equation is similar to that described in Patankar's (Patankar 1980) analysis, with two differences: in this case, (1) the control volume shrinks/swells during combustion; (2) the continuity equation has a non-zero source term which is caused by mass change between different phases due to moisture evaporation/vapor recondensation, biomass pyrolysis/tar cracking, and char surface heterogeneous reactions.

With the general discretization equation established for each grid point in the calculation domain, a set of linear algebraic equations results. The solution of the discretization equations for this one-dimensional situation can be obtained by the standard Gaussian-elimination method, although in this case the matrix representation is triangular allowing the much more efficient TriDiagonal-Matrix Algorithm (TDMA) or Thomas algorithm. The detail process of the TDMA solution procedure is explained in (Patankar 1980).

Specific definitions of F_e, F_w, D_e, D_w, , P_e, P_w, a_P^0, a_P^1, S_C, *and* S_P are variable dependent, i.e., they are different for each species mass conservation and energy conservation equations, and the details are illustrated in the following sections.

Solution of solid species conservation equations

Solid species, including biomass, char, and ash, don't have convection and diffusion in the radial direction, so that

The source term of each solid species component is linearized as

$$F_e = F_w = D_e = D_w = a_W = a_E = 0, \tag{81}$$

Biomass:

$$S_C = 0,\ S_P = -(k_1 + k_2 + k_3);$$

$$a_P^0 = \frac{\Delta v^0}{\Delta t}, \qquad a_P^1 = \frac{\Delta V}{\Delta t}, \tag{82}$$

Char:

$$\Delta v^0 = \frac{r_e^{0\,n+1} - r_w^{0\,n+1}}{n+1}, \qquad \Delta V = \frac{r_e^{n+1} - r_w^{n+1}}{n+1} \tag{83} \quad (84)$$

$$S_C = k_3\rho_B + k_5\varepsilon\rho_g Y_H,$$

$$S_P = \frac{-s_{a,char}}{\rho_C^* + \rho_B + \rho_A}\left(k_8\varepsilon\rho_g Y_{O_2}\frac{2M_C}{M_{O_2}} + k_9\varepsilon\rho_g Y_{CO_2}\frac{M_C}{M_{CO_2}} + k_{10}\varepsilon\rho_g Y_V\frac{M_C}{M_V}\right);$$

Ash:

$$S_C = 0,\ S_P = 0.$$

The density of biomass, char, and ash can be solved explicitly and TDMA is not needed.

Solution of Liquid species conservation equations

The liquid species includes free water and bound water, which are assumed to migrate only through diffusion in the radial direction. Coefficients of the discretization equation are

The resulted discretization equations are solved with the TDMA explained above.

Solution of gas species conservation equations

$$F_e = F_w = P_e = P_w = 0, \tag{85}$$

$$a_P^0 = \frac{\Delta v^0}{\Delta t}, \qquad a_P^1 = \frac{\Delta v}{\Delta t}, \tag{86}$$

Free water ρ_{fw}:

$$D_e = r_e^n \frac{D_{eff,fw,e}}{\delta r_e}, \qquad D_w = r_w^n \frac{D_{eff,fw,w}}{\delta r_w};$$

$$S_C = s_a \frac{\rho_{fw}^*}{\rho_{fw}^0} h_{m,pore} Y_V \rho_g$$

$$S_P = -s_a \frac{1}{\rho_{fw}^0} h_{m,pore} \rho_v^{sat} \tag{87}$$

Bound water ρ_{bw}:

$$D_e = r_e^n \frac{D_{eff,bw,e}}{\delta r_e}, \qquad D_w = r_w^n \frac{D_{eff,bw,w}}{\delta r_w}.$$

$$S_C = 0, \qquad S_P = -k_7$$

Both convection and diffusion contribute the mass transfer of each individual gas species. Coefficients for the discretization equation of each gas species are listed in detail as follows.

For any gas species *j*:

$$D_e = r_e^n \frac{\varepsilon \rho_{g,e} D_{eff,j,e}}{\delta r_e}, \qquad D_w = r_w^n \frac{\varepsilon \rho_{g,w} D_{eff,j,w}}{\delta r_w} \tag{88}$$

$$F_e = r_e^n \varepsilon \rho_{g,e} u_e, \qquad F_w = r_w^n \varepsilon \rho_{g,w} u_w \tag{89}$$

$$P_e = \frac{F_e}{D_e}, \qquad P_w = \frac{F_w}{D_w} \tag{90}$$

$$a_P^0 = \frac{\varepsilon \rho_g^0 \Delta v^0}{\Delta t}, \qquad a_P^1 = \frac{\varepsilon \rho_g \Delta v}{\Delta t} \tag{91}$$

Linearization of the source terms of each gas species:

Oxygen Y_{O2}:

$$\begin{aligned}
&S_C = 0, \\
&S_P = -s_{a,char} \frac{\rho_C}{\rho_C + \rho_B + \rho_A} k_8 \varepsilon \rho_g \\
&-0.5 M_{w,O_2} \varepsilon k_{11} 10^3 \left(\frac{\rho_g Y_{CO}}{10^3 M_{CO}} \right) \left(\frac{\rho_g}{10^3 M_{O_2}} \right)^{0.25} \left(\frac{\rho_g Y_V}{10^3 M_V} \right)^{0.5} Y_{O_2}^{*\,-0.75} \\
&-0.5 M_{w,O_2} \varepsilon k_{12} 10^3 \left(\frac{\rho_g Y_{H_2}}{10^3 M_{w,H_2}} \right) \left(\frac{\rho_g}{10^3 M_{O_2}} \right)^{1.42} Y_{O_2}^{*\,0.42} \\
&-2.9 \varepsilon k_{13} 10^3 M_{W,O_2} \left(\frac{\rho_g Y_T}{10^3 M_T} \right)^{0.5} \left(\frac{\rho_g}{10^3 M_{O_2}} \right)
\end{aligned} \tag{92}$$

Carbon monoxide Y_{CO}:

$$S_C = s_{a,char}\frac{\rho_C}{\rho_C+\rho_B+\rho_A}\left(k_8\varepsilon\rho_g Y_{O_2}\frac{2M_{CO}}{M_{O_2}}+k_9\varepsilon\rho_g Y_{CO_2}\frac{2M_{CO}}{M_{CO_2}}+k_8\varepsilon\rho_g Y_V\frac{M_{CO}}{M_V}\right)$$
$$+\left(k_1\rho_B+\varepsilon k_4\rho_g Y_T\right)\alpha_{CO}+6\varepsilon k_{13}10^3 M_{CO}\left(\frac{\rho_g Y_T}{10^3 M_T}\right)^{0.5}\left(\frac{\rho_g}{10^3 M_{O_2}}\right), \quad (93)$$
$$S_P = -M_{CO}\varepsilon k_{11}10^3\left(\frac{\rho_g}{10^3 M_{CO}}\right)\left(\frac{\rho_g Y_{O_2}}{10^3 M_{O_2}}\right)^{0.25}\left(\frac{\rho_g Y_V}{10^3 M_V}\right)^{0.5}$$

Carbon dioxide Y_{CO2}:

$$S_C = \left(k_1\rho_B+\varepsilon k_4\rho_g Y_T\right)\alpha_{CO_2}+M_{CO_2}\varepsilon k_{11}10^3\left(\frac{\rho_g Y_{CO}}{10^3 M_{CO}}\right)\left(\frac{\rho_g Y_{O_2}}{10^3 M_{O_2}}\right)^{0.25}\left(\frac{\rho_g Y_V}{10^3 M_V}\right)^{0.5}, \quad (94)$$
$$S_P = -s_{a,char}\frac{\rho_C}{\rho_C+\rho_B+\rho_A}k_9\varepsilon\rho_g$$

Hydrogen Y_{H2}:

$$S_C = \left(k_1\rho_B+\varepsilon k_4\rho_g Y_T\right)\alpha_{H_2}+s_{a,char}\frac{M_{H_2}}{M_V}\frac{\rho_C}{\rho_C+\rho_B+\rho_A}k_{10}\varepsilon\rho_g Y_V$$
$$+3.1\varepsilon k_{13}10^3 M_{H_2}\left(\frac{\rho_g Y_T}{10^3 M_T}\right)\left(\frac{\rho_g Y_{O_2}}{10^3 M_{O_2}}\right)^{0.5}, \quad (95)$$
$$S_P = -\varepsilon k_{12}10^3 M_{H_2}\left(\frac{\rho_g}{10^3 M_{H_2}}\right)\left(\frac{\rho_g Y_{O_2}}{10^3 M_{O_2}}\right)^{1.42}$$

Vapor Y_{H2O}:

$$S_C = \left(k_1\rho_B+\varepsilon k_4\rho_g Y_T\right)\alpha_V+s_a\frac{\rho_{fw}}{\rho_{fw}^0}h_{m,pore}\rho_v^{sat}+k_7\rho_{bw}$$
$$+M_{H_2O}\varepsilon k_{12}10^3\left(\frac{\rho_g Y_{H_2}}{10^3 M_{H_2}}\right)\left(\frac{\rho_g Y_{O_2}}{10^3 M_{O_2}}\right)^{1.42}, \quad (96)$$
$$S_P = -s_{a,char}\frac{\rho_C}{\rho_C+\rho_B+\rho_A}k_{10}\varepsilon\rho_g-s_a\frac{\rho_{fw}}{\rho_{fw}^0}h_{m,pore}\rho_g$$

Carbon dioxide Y_{HC}:

$$S_C = k_1 \rho_B \alpha_{HC} + k_2 \rho_B,$$
$$S_P = -\varepsilon k_4 \rho_g (1-\alpha_{HC}) - \varepsilon k_5 \rho_g - \varepsilon k_{13} 10^3 M_T \left(\frac{\rho_g}{10^3 M_T}\right)^{0.5} \left(\frac{\rho_{O_2}}{10^3 M_{O_2}}\right) Y_T^{*-0.5} \qquad (97)$$

Inert gas Y_I:

$$S_C = 0, \qquad S_P = 0 \qquad (98)$$

Solution of energy conservation equation

The energy conservation equation (98) contains both enthalpy and temperature as the dependant variables. In the solid domain, the total enthalpy includes enthalpy of solid species, liquid species, and gas species, but only gas species enthalpy appears in the convection term. In addition, solid species enthalpy does not appear in the diffusion term. So temperature is chosen as the dependent variable for the energy conservation equation.

The original energy conservation equation is transformed so that it can be discretized by the control-volume method and solved by the standard TDMA.

Substituting the enthalpy expression of each species or component into Equation (98) results in Equation (99)

$$\begin{aligned}
&\sum_i \hat{H}^0_{i,f} \frac{\partial \rho_i}{\partial t} + \sum_k \hat{H}^0_{k,f} \frac{\partial \rho_k}{\partial t} + \sum_j \hat{H}^0_{j,f} \frac{\partial}{\partial t}\left(\rho_g \varepsilon Y_j\right) \\
&+ \frac{\partial}{\partial t}\left(\sum_i \rho_i \int_{T_0}^{T} Cp_i dT + \sum_k \rho_k \int_{T_0}^{T} Cp_k dT + \rho_g \varepsilon \sum_j Y_j \int_{T_0}^{T} Cp_j dT \right) \\
&+ \sum_j \hat{H}^0_{j,f} \frac{1}{r^n} \frac{\partial}{\partial r}\left[r^n \varepsilon \rho_g u Y_j \right] + \frac{1}{r^n} \frac{\partial}{\partial r}\left[r^n \varepsilon \rho_g u \sum_j Y_j \int_{T_0}^{T} Cp_j dT \right] = \frac{1}{r^n} \frac{\partial}{\partial r}\left(r^n K_{eff} \frac{\partial T}{\partial r}\right) \qquad (99) \\
&+ \sum_j \hat{H}^0_{j,f} \frac{1}{r^n} \frac{\partial}{\partial r}\left(r^n \rho_g \varepsilon \sum_j D_{eff,j} \frac{\partial Y_j}{\partial r} \right) + \sum_k \hat{H}^0_{k,f} \frac{1}{r^n} \frac{\partial}{\partial r}\left(r^n \sum_k D_{eff,k} \frac{\partial \rho_k}{\partial r} \right) \\
&+ \frac{1}{r^n} \frac{\partial}{\partial r}\left[r^n \left(\rho_g \varepsilon \sum_j D_{eff,j} \frac{\partial Y_j}{\partial r} \int_{T_0}^{T} Cp_j dT + \sum_k D_{eff,k} \frac{\partial \rho_k}{\partial r} \int_{T_0}^{T} Cp_k dT \right) \right]
\end{aligned}$$

The heat of formation of each species at standard state is independent of temperature and any other variable. Multiplying the heat of formation at standard state by both the left and right side of each of the species conservation Equations (35) ~ (41) respectively, and substituting them back into Equation (99), results in the following.

$$\sum_i \hat{H}^0_{i,f} S_i + \sum_k \hat{H}^0_{k,f} S_k + \sum_j \hat{H}^0_{j,f} S_j$$
$$+\frac{\partial}{\partial t}\left(\sum_i \rho_i \int_{T_0}^{T} Cp_i dT + \sum_k \rho_k \int_{T_0}^{T} Cp_k dT + \rho_g \varepsilon \sum_j Y_j \int_{T_0}^{T} Cp_j dT \right)$$
$$+\frac{1}{r^n}\frac{\partial}{\partial r}\left[r^n \varepsilon \rho_g u \sum_j Y_j \int_{T_0}^{T} Cp_j dT \right] = \frac{1}{r^n}\frac{\partial}{\partial r}(r^n K_{eff}\frac{\partial T}{\partial r}) \qquad (100)$$
$$+\frac{1}{r^n}\frac{\partial}{\partial r}\left[r^n \left(\rho_g \varepsilon \sum_j D_{eff,j} \frac{\partial Y_j}{\partial r} \int_{T_0}^{T} Cp_j dT + \sum_k D_{eff,k} \frac{\partial \rho_k}{\partial r} \int_{T_0}^{T} Cp_k dT \right) \right]$$

The source term S of each species are explained earlier in this section. Substituting these source terms into the first three terms in Equation (100), the sum of the first three terms is obtained in Equation (101).

$$\sum_i \hat{H}^0_{i,f} S_i + \sum_k \hat{H}^0_{k,f} S_k + \sum_j \hat{H}^0_{j,f} S_j = -\sum_m r_m \Delta H^0_m$$
$$\text{where, } m \text{ is reaction index} = 1, ..., 13 \qquad (101)$$
$$\Delta H^0_m \text{ is the heat of reaction at standard state, which is the enthalpy of reactants substracts that of products}$$

So, Equation (100) becomes to Equation (102).

$$\frac{\partial}{\partial t}\left(\sum_i \rho_i \int_{T_0}^{T} Cp_i dT + \sum_k \rho_k \int_{T_0}^{T} Cp_k dT + \rho_g \varepsilon \sum_j Y_j \int_{T_0}^{T} Cp_j dT \right)$$
$$+\frac{1}{r^n}\frac{\partial}{\partial r}\left[r^n \varepsilon \rho_g u \sum_j Y_j \int_{T_0}^{T} Cp_j dT \right] = \frac{1}{r^n}\frac{\partial}{\partial r}(r^n K_{eff}\frac{\partial T}{\partial r}) + \sum_m r_m \Delta H^0_m \qquad (102)$$
$$+\frac{1}{r^n}\frac{\partial}{\partial r}\left[r^n \left(\rho_g \varepsilon \sum_j D_{eff,j} \frac{\partial Y_j}{\partial r} \int_{T_0}^{T} Cp_j dT + \sum_k D_{eff,k} \frac{\partial \rho_k}{\partial r} \int_{T_0}^{T} Cp_k dT \right) \right]$$

Now, the above equation needs to be transformed to a generalized form so that it can be solved using a control-volume method with respect to temperature. With the transformation described in Equation (103), the first two terms in Equation (102) can be expressed as Equation (104), and the third term as Equation (105).

$$\frac{\partial}{\partial t}\left(\rho_i \int_{T_0}^{T} Cp_i dT\right) = \rho_i \frac{\partial}{\partial t}\left(\int_{T_0}^{T} Cp_i dT\right) + \int_{T_0}^{T} Cp_i dT \frac{\partial \rho_i}{\partial t}$$
$$\frac{\partial}{\partial t}\left(\int_{T_0}^{T} Cp_i dT\right) = Cp_i \frac{\partial T}{\partial t}$$
$$\frac{\partial}{\partial t}\left(\rho_i Cp_i T\right) = \rho_i Cp_i \frac{\partial T}{\partial t} + TCp_i \frac{\partial \rho_i}{\partial t} + T\rho_i \frac{\partial Cp_i}{\partial t} \tag{103}$$
$$\frac{\partial}{\partial t}\left(\rho_i \int_{T_0}^{T} Cp_i dT\right) = \rho_i Cp_i \frac{\partial T}{\partial t} + \int_{T_0}^{T} Cp_i dT \frac{\partial \rho_i}{\partial t}$$

$$\frac{\partial}{\partial t}\left(\rho_i \int_{T_0}^{T} Cp_i dT\right) = \frac{\partial}{\partial t}\left(\rho_i Cp_i T\right) + \left(\int_{T_0}^{T} Cp_i dT - TCp_i\right)\frac{\partial \rho_i}{\partial t} - T\rho_i \frac{\partial Cp_i}{\partial t} \tag{104}$$

$$\frac{\partial}{\partial t}\left(\varepsilon\rho_j Y_j \int_{T_0}^{T} Cp_j dT\right) = \frac{\partial}{\partial t}\left(\varepsilon\rho_j Y_j Cp_j T\right) + \left(\int_{T_0}^{T} Cp_j dT - TCp_j\right)\frac{\partial \varepsilon\rho_j Y_j}{\partial t} - T\varepsilon\rho_j Y_j \frac{\partial Cp_j}{\partial t} \tag{105}$$

Similarly, the convection term and the diffusion term in Equation (102) can be replaced by Equations (106), (107), and (108).

$$\frac{1}{r^n}\frac{\partial}{\partial r}\left[r^n \varepsilon\rho_g u Y_j \int_{T_0}^{T} Cp_j dT\right] = \frac{1}{r^n}\frac{\partial}{\partial r}\left(r^n \varepsilon\rho_g u Y_j Cp_j T\right)$$
$$+\left(\int_{T_0}^{T} Cp_j dT - TCp_j\right)\frac{1}{r^n}\frac{\partial}{\partial r}\left[r^n \varepsilon\rho_g u Y_j\right] - \frac{1}{r^n}\left(r^n \varepsilon\rho_g u Y_j T\right)\frac{\partial Cp_j}{\partial r} \tag{106}$$

$$\frac{1}{r^n}\frac{\partial}{\partial r}\left(r^n \rho_g \varepsilon D_{eff,j} \frac{\partial Y_j}{\partial r}\int_{T_0}^{T} Cp_j dT\right) = \frac{1}{r^n}\frac{\partial}{\partial r}\left[r^n \rho_g \varepsilon D_{eff,j} \frac{\partial Y_j}{\partial r} Cp_j T\right]$$
$$\left(\int_{T_0}^{T} Cp_j dT - TCp_j\right)\frac{1}{r^n}\frac{\partial}{\partial r}\left[r^n \rho_g \varepsilon D_{eff,j} \frac{\partial Y_j}{\partial r}\right] - \frac{1}{r^n}\left(r^n \rho_g \varepsilon D_{eff,j} \frac{\partial Y_j}{\partial r} T\right)\frac{\partial Cp_j}{\partial r} \tag{107}$$

$$\frac{1}{r^n}\frac{\partial}{\partial r}\left(r^n D_{eff,k} \frac{\partial \rho_k}{\partial r}\int_{T_0}^{T} Cp_k dT\right) = \frac{1}{r^n}\frac{\partial}{\partial r}\left[r^n D_{eff,k} \frac{\partial \rho_k}{\partial r} Cp_k T\right]$$
$$\left(\int_{T_0}^{T} Cp_k dT - TCp_k\right)\frac{1}{r^n}\frac{\partial}{\partial r}\left[r^n D_{eff,k} \frac{\partial \rho_k}{\partial r}\right] - \frac{1}{r^n}\left(r^n D_{eff,k} \frac{\partial \rho_k}{\partial r} T\right)\frac{\partial Cp_k}{\partial r} \tag{108}$$

The heat capacity of each species is usually just a function of temperature, and is not related to time and position. In the current physical model, the temperature is a function of both time and position, so the heat capacity would change with time and position. The following transformations are made, as illustrated in Equations (109) and (110).

$$\frac{\partial Cp}{\partial t} = \frac{\partial Cp}{\partial T}\frac{\partial T}{\partial t} \tag{109}$$

$$\frac{\partial Cp}{\partial r} = \frac{\partial Cp}{\partial T}\frac{\partial T}{\partial r} \tag{110}$$

Substituting Equations (103) ~ (108) back into Equation (102), and simplifying the resulted equation with Equations (35) ~ (41) and (109) ~ (110), Equation (102) becomes Equation (111).

$$\begin{aligned}
&\frac{\partial}{\partial t}\left[\left(\sum_i \rho_l Cp_i + \sum_k \rho_k Cp_k + \rho_g \varepsilon \sum_j Y_j Cp_j\right)T\right] \\
&+\frac{1}{r^n}\frac{\partial}{\partial r}\left\{\left[r^n \varepsilon \rho_g\left(u\sum_j Y_j Cp_j - \sum_j D_{eff,j}\frac{\partial Y_j}{\partial r}Cp_j\right) - r^n \sum_k D_{eff,k}\frac{\partial \rho_k}{\partial r}Cp_k\right]T\right\} \\
&=\frac{1}{r^n}\frac{\partial}{\partial r}(r^n K_{eff}\frac{\partial T}{\partial r}) + \sum_m r_m \Delta H_m^0 + \sum_l \left(Cp_l T - \int_{T_0}^{T} Cp_l dT\right)S_l \\
&+\left(\sum_i \rho_i \frac{\partial Cp_i}{\partial T} + \sum_k \rho_k \frac{\partial Cp_k}{\partial T} + \varepsilon\rho_g \sum_j Y_j \frac{\partial Cp_j}{\partial T}\right)T\frac{\partial T}{\partial t} \\
&+\left[\left(\sum_j Y_j \frac{\partial Cp_j}{\partial T}u - \sum_j D_{eff,j}\frac{\partial Y_j}{\partial r}\frac{\partial Cp_j}{\partial T}\right)\varepsilon\rho_g - \sum_k D_{eff,k}\frac{\partial \rho_k}{\partial r}\frac{\partial Cp_k}{\partial T}\right]T\frac{\partial T}{\partial r}
\end{aligned} \tag{111}$$

Substituting source terms of each species into the third term on the right side of Equation (111), the following equation is obtained.

$$\begin{aligned}
&\sum_l \left(Cp_l T - \int_{T_0}^{T} Cp_l dT\right)S_l = \sum_m r_m\left(\sum_{reac}\Psi_{reac}\int_{T_0}^{T} Cp_{reac}dT - \sum_{prod}\Psi_{prod}\int_{T_0}^{T} Cp_{prod}dT\right) \\
&+\sum_m r_m\left(\sum_{prod}\Psi_{prod}Cp_{prod} - \sum_{reac}\Psi_{reac}Cp_{reac}\right)T
\end{aligned} \tag{112}$$

, where, Ψ is the stoichiometric factor of each species in a specific reaction *m*.

So, a final general form of the energy equation, which can be solved by control volume method, is obtained in Equation (113).

$$
\begin{aligned}
&\frac{\partial}{\partial t}\left[\left(\sum_i \rho_i Cp_i + \sum_k \rho_k Cp_k + \rho_g \varepsilon \sum_j Y_j Cp_j\right)T\right] \\
&+\frac{1}{r^n}\frac{\partial}{\partial r}\left\{\left[r^n \varepsilon \rho_g \left(u\sum_j Y_j Cp_j - \sum_j D_{eff,j}\frac{\partial Y_j}{\partial r}Cp_j\right) - r^n \sum_k D_{eff,k}\frac{\partial \rho_k}{\partial r}Cp_k\right]T\right\} \\
&=\frac{1}{r^n}\frac{\partial}{\partial r}(r^n K_{eff}\frac{\partial T}{\partial r}) + \sum_m r_m\left(\sum_{reac}\Psi_{reac}\int_{T_0}^{T} Cp_{reac}dT - \sum_{prod}\Psi_{prod}\int_{T_0}^{T} Cp_{prod}dT\right) \\
&+\sum_m r_m\left(\sum_{prod}\Psi_{prod}Cp_{prod} - \sum_{reac}\Psi_{reac}Cp_{reac}\right)T + \sum_m r_m \Delta H_m^0 \\
&+\left(\sum_i \rho_i \frac{\partial Cp_i}{\partial T} + \sum_k \rho_k \frac{\partial Cp_k}{\partial T} + \varepsilon\rho_g \sum_j Y_j \frac{\partial Cp_j}{\partial T}\right)T\frac{\partial T}{\partial t} \\
&+\left[\left(\sum_j Y_j \frac{\partial Cp_j}{\partial T}u - \sum_j D_{eff,j}\frac{\partial Y_j}{\partial r}\frac{\partial Cp_j}{\partial T}\right)\varepsilon\rho_g - \sum_k D_{eff,k}\frac{\partial \rho_k}{\partial r}\frac{\partial Cp_k}{\partial T}\right]T\frac{\partial T}{\partial r}
\end{aligned}
\tag{113}
$$

The coefficients of the discretization equation for Equation (113) are quite complex compared with those of species conservation equations.

$$
D_e = r_e^n \frac{K_{eff,e}}{\delta r_e}, \qquad D_w = r_w^n \frac{K_{eff,w}}{\delta r_w} \tag{114}
$$

$$
\begin{aligned}
F_e &= r_e^n \varepsilon \rho_{g,e} \sum_j Cp_{j,e}\left(Y_{j,e}u_e - D_{eff,j,e}\frac{Y_{j,E}-Y_{j,P}}{\delta r_e}\right) - r_e^n \sum_k D_{eff,k,e}\frac{\rho_{k,E}-\rho_{k,P}}{\delta r_e}Cp_{k,e}, \\
F_w &= r_w^n \varepsilon \rho_{g,w} \sum_j Cp_{j,w}\left(Y_{j,w}u_w - D_{eff,j,w}\frac{Y_{j,P}-Y_{j,W}}{\delta r_w}\right) - r_w^n \sum_k D_{eff,k,w}\frac{\rho_{k,P}-\rho_{k,W}}{\delta r_w}Cp_{k,w}
\end{aligned}
\tag{115}
$$

$$
P_e = \frac{F_e}{D_e}, \qquad P_w = \frac{F_w}{D_w} \tag{116}
$$

$$
\begin{aligned}
a_P^0 &= \frac{\Delta v^0}{\Delta t}\left(\sum_i \rho_i^0 Cp_i^0 + \varepsilon\rho_g^0 \sum_j Y_j^0 Cp_j^0 + \sum_k \rho_k^0 Cp_k^0\right), \\
a_P^1 &= \frac{\Delta v}{\Delta t}\left(\sum_i \rho_i Cp_i + \varepsilon\rho_g \sum_j Y_j Cp_j + \sum_k \rho_k Cp_k\right)
\end{aligned}
\tag{117}
$$

The last five terms in Equation (113) are lumped as the source term of the energy equation. The source term is linearized so that it obeys Rule 3 (negative-slope linearization) of control volume method described in (Patankar 1980).

Calculation of the flow field

The momentum conservation of the gas phase is simply described by Darcy's law for the porous solid particle domain, shown in Equation (118). Discretization of the momentum equation in the staggered control volume leads

$$u_e = -\frac{\eta_e}{\mu_e}\frac{p_E - p_P}{\delta r_e} \quad . \tag{118}$$

The momentum equation can be solved only when the pressure field is given or is somehow estimated. The imperfect velocity field based on a guessed pressure field p^* is denoted by u^*, and it can be solved by

$$u_e^* = -\frac{\eta_e}{\mu_e}\frac{p_E^* - p_P^*}{\delta r_e} \quad . \tag{119}$$

To obtain the correct pressure p, the following formula is proposed

$$p = p^* + p' \quad , \tag{120}$$

where, p' is called the pressure correction. Similarly, the corresponding velocity correction is introduced

$$u = u^* + u' \quad . \tag{121}$$

Subtracting Equation (119) from Equation (118) results in

$$u_e' = -\frac{\eta_e}{\mu_e}\frac{p_E' - p_P'}{\delta r_e} \quad . \tag{122}$$

Assuming

$$d_e = \frac{\eta_e}{\mu_e \delta r_e} \quad , \tag{123}$$

the velocity-correction formula can be also written as

$$u_e = u_e^* + d_e\left(p_P' - p_E'\right). \tag{124}$$

Now, the gas-phase overall continuity equation is turned into a pressure-correction equation by integrating it over the control volume and the time interval, as illustrated below.

First, the discretization equation for the overall gas phase continuity equation is obtained after integration

$$\frac{\Delta v\rho_g - \Delta v^0\rho_g^0}{\Delta t} + \left(r_e^n\rho_{g,e}u_e - r_w^n\rho_{g,w}u_w\right) = \frac{\Delta v}{\varepsilon}S_g, \tag{125}$$

Substituting Equation (124) and the corresponding velocity at the west interface into Equation (125) and rearranging the resulted equation will lead a discretization equation for the pressure correction term p'.

$$a_P p_P' = a_W p_W' + a_E p_E' + b, \tag{126}$$

where,

$$a_W = r_w^n\rho_{g,w}d_w, \tag{127}$$

$$d_w = \frac{\eta_w}{\mu_w\delta r_w}, \tag{128}$$

$$a_E = r_e^n\rho_{g,e}d_e, \tag{129}$$

$$a_P = a_W + a_E, \tag{130}$$

$$b = \frac{\Delta v}{\varepsilon}S_g - \left[\left(\frac{\Delta v\rho_g - \Delta v^0\rho_g^0}{\Delta t}\right) + \left(r_e^n\rho_{g,e}u_e^* - r_w^n\rho_{g,w}u_w^*\right)\right]. \tag{131}$$

The discretization equation for pressure correction is solved with the standard TDMA.

Solution for the particle shrinking/swelling

To solve the particle/droplet shrinking/swelling model, Equation (132) is rearranged with the solid species mass conversion replaced by

$$x_i = 1 - \frac{\rho_i v}{\rho_i^0 v^0}, \tag{132}$$

where i = moisture, biomass, and char, and we obtain

$$\frac{v}{v_0} = 1 + \sum_i \left(1 - \frac{\rho_i v}{\rho_i^0 v^0}\right)(\beta_i - 1.0). \tag{133}$$

It can be further simplified to Equation (134)

$$\frac{v}{v_0} = \frac{1 + \sum_i (\beta_i - 1)}{1 + \sum \frac{\rho_i}{\rho_i^0}(\beta_i - 1)} \tag{134}$$

The derivative of volume with respect of time results in

$$\frac{1}{v}\frac{dv}{dt} = -\frac{\sum_i \frac{(\beta_i - 1)}{\rho_i^0}\frac{\partial \rho_i}{\partial t}}{1 + \sum_i \frac{\rho_i}{\rho_i^0}(\beta_i - 1)} \tag{135}$$

For each species in the solid phase in each control volume, the total mass is

$$m_i = \rho_i v. \tag{136}$$

The derivative of the above equation with respect of time is

$$\frac{\partial m_i}{\partial t} = \frac{\partial \rho_i v}{\partial t} = \rho_i \frac{\partial v}{\partial t} + v \frac{\partial \rho_i}{\partial t}, \tag{137}$$

which further results in Equation (138).

$$\frac{\partial \rho_i}{\partial t} = \frac{1}{V}\frac{\partial V \rho_i}{\partial t} - \frac{\rho_i}{V}\frac{\partial V}{\partial t}, \tag{138}$$

In Equation (138), the first term at the right side is the mass loss rate per unit volume, which is the source term S_i for this species in the solid phase, then Equation (138) becomes Equation (139).

$$\frac{\partial \rho_i}{\partial t} = S_i - \frac{\rho_i}{v}\frac{\partial v}{\partial t} \tag{139}$$

Substituting Equation (135) into Equation (139), and rearranging the equation leads to Equation (140).

$$\frac{\partial \rho_i}{\partial t} = S_i + \rho_i \sum_j \left(\frac{\beta_j - 1}{\rho_j{}^0} \right) \cdot S_j \tag{140}$$

,

where, j = *char, ash, and biomass*. Equation (140) shows that if the shrinking factor $\beta_j = 1.0$, which is the constant volume case, the density change rate of each species will be

$$\frac{\partial \rho_i}{\partial t} = S_i \tag{141}$$

.

The density change rate will slow down if the shrinking factor $0.0 < \beta_j < 1.0$ due to the volume shrinking; similarly, the density change rate will speed up if the shrinking factor $\beta_j > 1.0$ due to the volume swelling. A final case is constant-density shrinking, where $\beta_j = 0.0$. For the case, $\rho_j = \rho_j{}^0$ will be the only possible solution for Equation (140) since $\beta_j = 0.0$.

Now, substituting Equation (140) back into Equation (135), Equation (135) can be simplified to Equation (142).

$$\frac{1}{v}\frac{\partial v}{\partial t} = -\sum_i \left(\frac{\beta_i - 1}{\rho_i{}^0} \right) \cdot S_i \tag{142}$$

,

which can be similarly solved by the fully implicit algorithm described in (Patankar 1980).

With all partial differential equations for species mass fractions, temperature, and pressure being discretized to linear algebraic equations and solved by the TDMA method, the SIMPLE algorithm is chosen to calculate the flow field and ensure the convergence of all variables.

The solution of the mathematical model is coded in C/C++, and the computer time for a single biomass particle combustion simulation depends on particle size, usually 20 minutes for a 5 mm particle.

Summary

In this chapter, a one-dimensional, single-particle combustion model describing drying, devolatilization, and char oxidation and gasification has been developed. The mechanisms for each process have been analyzed in detail. The mathematical model was solved with control volume method.

The model is capable of simulating combustion of solid particle or droplet of any shape and size. It can predict the particle temperature distribution, species concentration distribution, and particle/droplet shrinking/swelling behaviors as function of residence time. Its predictions are compared with data derived from the experimental techniques described in the previous chapter to complete the analysis of biomass shape and size impacts on combustion.

Results and Discussions

In this project, biomass particle pyrolysis experiments were conducted in two entrained-flow reactors. Mass loss data of sawdust particle during pyrolysis was collected in a short entrained-flow reactor, which doesn't provide optical access and was operated at 1600 K. Biomass particle surface temperatures during pyrolysis and combustion were measured with the imaging pyrometry in a longer entrained-flow reactor, which provides optical accesses. With the single-particle reactor, poplar dowel particle data, including particle surface temperature, inner temperature, and particle mass loss during drying, devolatilization, and combustion, have been collected with type B or K thermocouples, the imaging pyrometry, and the balance.

All data are compared with the theoretical analysis results predicted by the single particle combustion model previously described.

In this chapter, the single particle combustion model is first validated with mass loss data and particle temperature data collected on the single-particle reactor. Then a series of model predictions with different levels of complexity illustrate the necessity of such a sophisticated structure model for biomass particle combustion modeling. Finally, more model studies and experimental data are presented and discussed.

The differences between measured and predicted data in most cases would be reduced if particle properties (pore sizes, densities, thermal conductivities, etc.) were altered within the range of their uncertainties. The presentation here includes no such optimization of results. The intention is to illustrate the level of agreement expected with a single set of properties based on independent measurements or literature values – the agreement expected in application of this approach in a predictive rather than a diagnostic mode.

Single particle combustion model validation

To validate the single particle combustion model, combustion experiments have been conducted in the single-particle reactor with poplar particles. Particle surface temperature, internal temperature, and mass loss during drying, devolatilization, and char oxidation are measured and compared with model predictions.

The single-particle reactor wall temperature is not uniform in the axial direction due to reactor configurations, so an average wall temperature determined at the location of the particle is used in the model as the reactor wall temperature. Both a type K thermocouple and the imaging pyrometer measure this temperature. The thermocouple readying was 1303 K and the average pyrometer measurement was 1276 K. The imaging pyrometer data are taken as the wall temperature here. A type K thermocouple monitors the center gas temperature. The actual gas temperature was corrected for radiative and other losses from the thermocouple bead based on the wall temperature, bulk gas velocity, and the thermocouple bead size. This resulted in a gas temperature of 1050 K.

Particle devolatilization

Data for a near-spherical particle (d = 11mm) with aspect ratio of 1.0 and a moisture content of 6.0 % (wt), including mass loss, center and surface temperature during pyrolysis appear with model predictions in Figure 131 and Figure 132. The nominal conditions of this experiment

include a reactor wall temperature of 1273 K and gas temperature of 1050 K. All the following validation experiments were conducted at the same conditions.

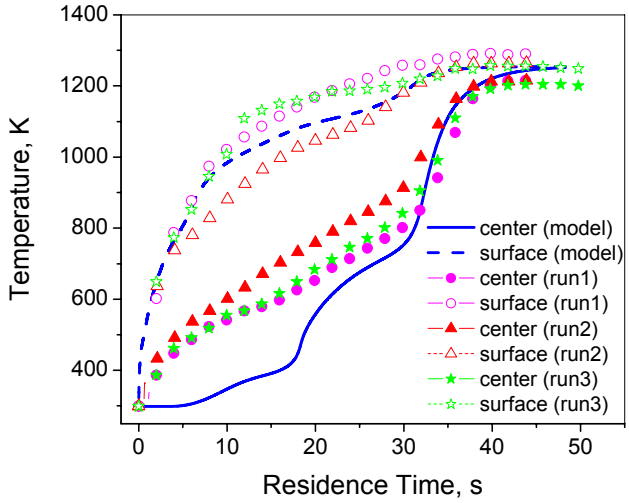

Figure 131 Temperature of near-spherical particle during pyrolysis, MC = 6 %(wt), T_w = 1276 K, T_g = 1050 K, d_p = 11 mm.

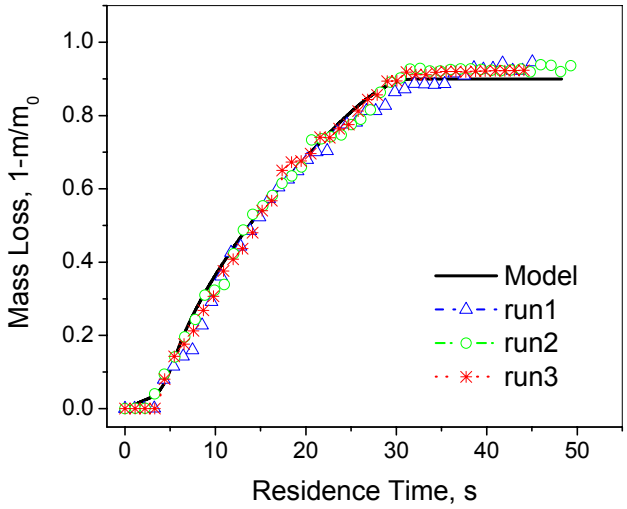

Figure 132 Mass loss of near-spherical particle during pyrolysis

The particle mass loss and particle surface temperature predictions generally agree with experimental data except that the measured particle center temperature increases faster than the model predictions at the beginning. This might be caused by the thermal conduction effects through the wire while measuring the particle center temperature. In principle, the measured particle surface temperature and center temperature should reach the same value at the end of pyrolysis, but a small discrepancy exists due to reactor temperature non-uniformity and differences in thermocouple bead size and shape. A more detailed discussion of the features of

these data appears after discussing the potential cause of the discrepancy in the center temperature data.

To determine the thermocouple lead wire impact on the measured center temperature, a second experiment at the same conditions used a cylindrical particle of the same diameter but with aspect ratio of 4.0. Two thermocouples monitored the center temperature, one passing axially and a second passing radially through the particle. The axial thermocouple should be less impacted by heat conduction through the leads since the particle provides some insulation from the radiation and bulk-flow convection. In Figure 133, lines 1 and 2 are particle center temperatures measured in the radial direction; lines 3 and 4 are results measured in axial direction. As indicated, the center temperature measured in the radial direction increases much faster than that measured in axial direction at the beginning, indicating that the thermocouple wire conduction influences initial center temperature measurements. The model prediction for the center temperature generally agrees with the average of the axial direction.

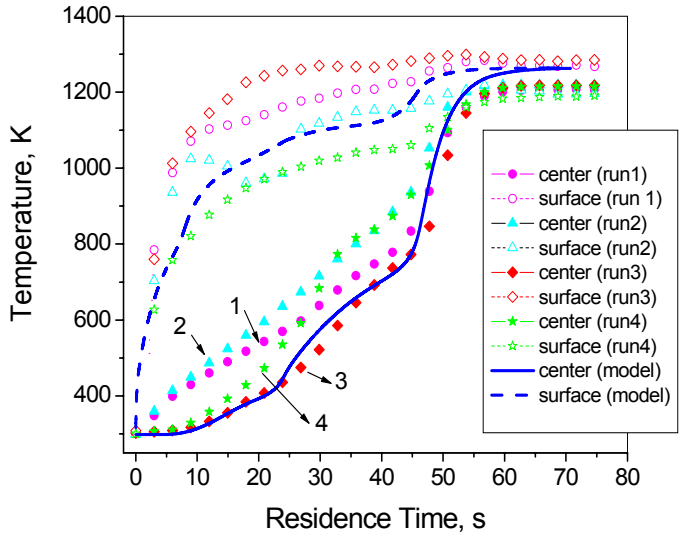

Figure 133 Temperature comparison of a cylindrical particle during pyrolysis. Lines 1 and 2 indicate radial thermocouple results and lines 3 and 4 represent axial thermocouple results, MC = 6 %(wt), T_w = 1276 K, T_g = 1050 K, d_p = 11 mm, AR = 4.0.

Mass loss data collected in several runs for the cylindrical particle are compared with model predictions in Figure 134.

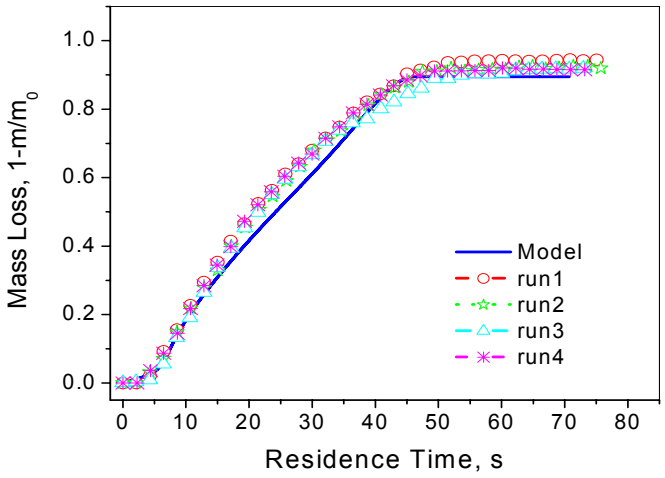

Figure 134 Mass loss comparison of a cylindrical particle during pyrolysis

The shapes of the temperature histories illustrate the complexity of this large-particle pyrolysis process even in the absence of complications arising from surface oxidation and surrounding flames. The initial low center temperature is associated with vaporization, which occurs at subboiling temperatures under nearly all conditions. Experiments with more moist particles reported later illustrate more clearly the impacts of vaporization. After vaporization, particles heat up relatively slowly, mainly because of devolatilization reactions in outer layers of the particle generate significant gas velocities in the pores (commonly reaching 0.2 m/s), thereby impeding internal heat transfer. After devolatilization, the rate of particle heating increases rapidly, mainly because the particle mass is greatly reduced relative to the early data by virtue of volatile losses but significantly because the internal heat transfer impediment from rapid outgassing also subsides. By contrast, the surface particle temperature increases rapidly and is less susceptible to slow heat transfer rates or even significant impacts from the blowing factor, in this case because radiation is the dominant heating mechanism. If convection were the primary heating mechanism, surface temperature heating rates would decrease by factors of up to 10 during rapid mass loss. These processes result in temperature differences between the surface and the center of many hundreds of Kelvins during particle heatup.

Particle drying and devolatilization

The drying model was further tested using wet particles with higher moisture content. Particle surface temperature and center temperature were measured with type K thermocouples in a cylinder particle with 40 % (wt) moisture (based on total wet particle mass) during drying and devolatilization. Similar to the previous experiments, particle center temperature was measured in both axial and radial directions. Results appear in Figure 135, which illustrates model predictions compared to data. Lines 1 and 2 indicate the center temperature measured in the radial direction and lines 3 and 4 indicate the axial measurement. Both the model prediction and experimental data showed that the particle temperature first rises to constant value near but below the boiling point, with evaporation mainly occurring in this stage. Following drying, the particle temperature again increases until biomass devolatilization slows the particle heating rate due to endothermic decomposition of biomass materials (minor impact) and the effect of rapid

mass loss on the heat transfer coefficient – often called the blowing parameter (major impact). Once all biomass material converts to char, light gas, and tar, the residual char undergoes a rapid temperature rise due to its lower mass (major impact), lower heat capacity (minor effect) and return of the blowing factor to near 1 (major effect). During most of the particle history, the predicted surface temperature is approximately 200 K below the average measured surface temperature. The predicted surface temperature depends primarily on radiative heating, convective heating, the impact of the blowing factor on heat transfer, and the rate and thermodynamics of water vaporization. As discussed later, the blowing factor in this radiation-dominated environment has little impact on the predictions. The thermodynamics of water vaporization are in little doubt, although the thermodynamics of the chemically adsorbed water losses are relatively uncertain. It is also possible that the reactions of the particle with its attendant changes in size and composition compromise the thermal contact between the surface thermocouple and the particle. There is no clear indication of whether the discrepancy arises from experimental artifacts or from uncertainties in emissivity and transport coefficients or other factors.

Figure 136 compares the predicted and measured mass loss data. The model does not predict the measured trend within its uncertainty though the predictions and measurements are in qualitative agreement. The disagreement is likely related to the temperature issues discussed above.

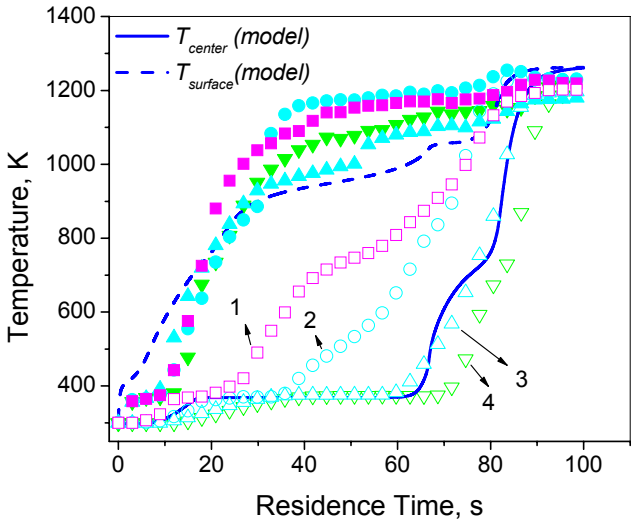

Figure 135 Temperature comparisons of a cylindrical particle during drying and pyrolysis, MC = 40 %(wt), T_w = 1276 K, T_g = 1050 K, d_p = 11 mm, AR = 4.0. All solid dots are measured surface temperature, and hollow dots are measured center temperature.

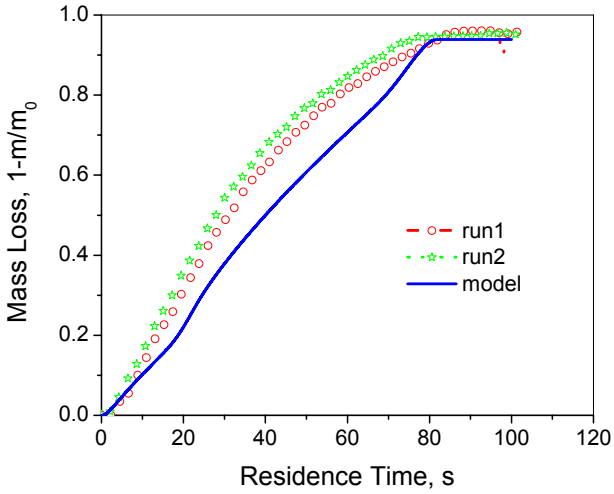

Figure 136 Mass loss of a cylindrical particle during drying and pyrolysis

The model was also validated with wet near-spherical particle drying and devolatilization data, as illustrated in Figure 137 and Figure 138. Results show that the predicted mass loss curve agrees with experimental data well. Both the surface temperature and center temperature profiles are similar to those for the wet cylinder particle illustrated above. The surface temperature data shows that the particle surface temperature rises to the water subboiling point and, presumably after the surface dries, rises rapidly. The center temperature data show qualitative behavior similar to that of the cylinder except that the impacts of heat conduction in the thermocouple leads remain in all of the data.

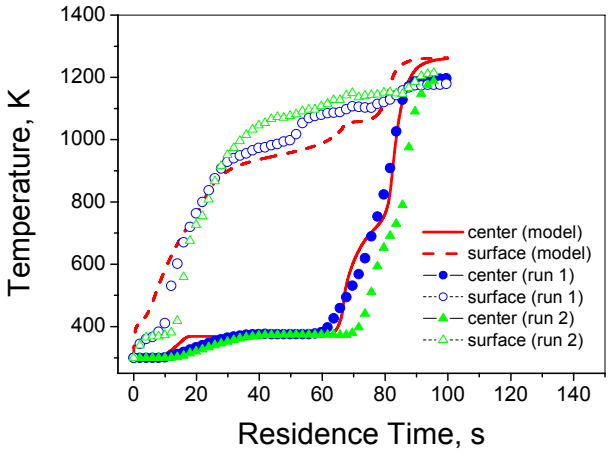

Figure 137 Temperature data of a wet near-spherical poplar particle during drying and pyrolysis, MC = 40 %(wt), T_w = 1276 K, T_g = 1050 K, d_p = 11 mm.

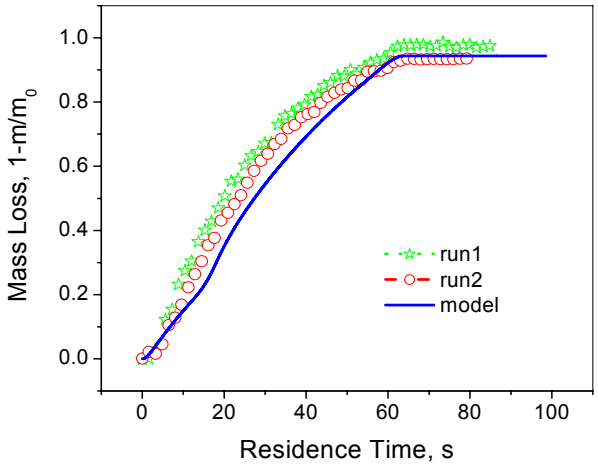

Figure 138 Mass loss of a wet near-spherical poplar particle during drying and pyrolysis processes

Figure 137 indicates measured surface and center temperatures increase more rapidly than the predicted values. The surface temperature discrepancy among the experimental data and model result can be explained by the experimental setup. When the wet particle was inserted into the reactor, the particle surface started to dry up. The thermocouple could not measure exactly the surface temperature since it was buried right next to the surface, which stayed near the boiling point as shown in the data. After the particle dried to some extent, the particle started to shrink and/or crack, compromising the contact efficiency of the thermocouple. On the other hand, for the center temperature measurement discrepancy, the heat conducted from the hot environment to the thermocouple bead through the thermocouple wire may still be the major influence in the temperature measurements when the particle is small as illustrated above for the dry cylinder particle.

Particle combustion

Figure 139 shows the temperature profiles of a wet, near-spherical particle with 40% (wt) moisture content (based on the total wet particle mass) and aspect ratio of 1.0 during combustion process.

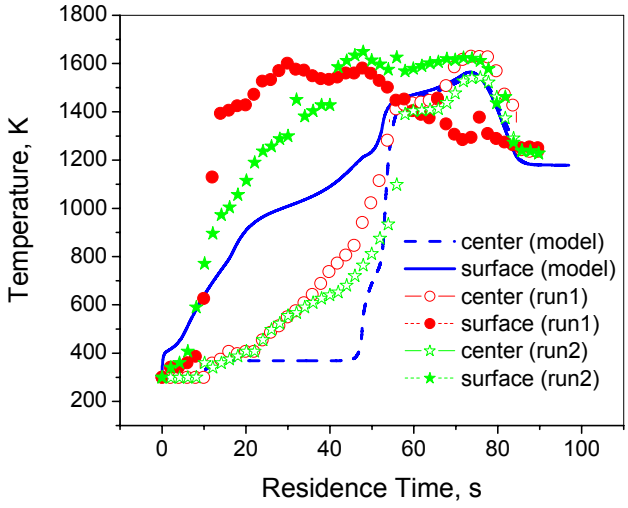

Figure 139 Temperature profiles of a near-spherical wet particle during combustion MC = 40 %(wt), T_w = 1276 K, T_g = 1050 K, d_p = 11 mm.

A Type-B thermocouple provides temperature data for combustion experiments since the peak temperatures exceed the reliable range of Type-K thermocouples. The measured particle surface temperatures are not consistent with model prediction due to experimental artifacts associated with a shrinking particle. The surface contact is lost as the particle shrinks and the bead becomes exposed to the surrounding flame. The measured particle center temperatures appear to disagree with model predictions, though the disagreement arises primarily from thermocouple wire conduction. Both experimental data and model predictions show that during the char burning stage the particle temperature increases to a peak value and then declines dramatically. This supports theoretical descriptions of large-particle combustion mechanisms. Oxidizer diffusion rates primarily control combustion rates in char consumption, which proceeds largely with constant density and shrinking particle diameter. The char particle oxidation front will finally reach the center of the particle as particle size gets smaller with ash built up in the outer layer of the particle. The pseudo-steady-state combustion rate/temperature of the particle first increases then decreases with size due to changes in the relative importance of radiation losses, convection, and diffusion. Once the char is completely consumed the particle (ash) cools rapidly to near the convective gas temperature, depending on the radiative environment. The mass loss curves as functions of time are shown in Figure 140.

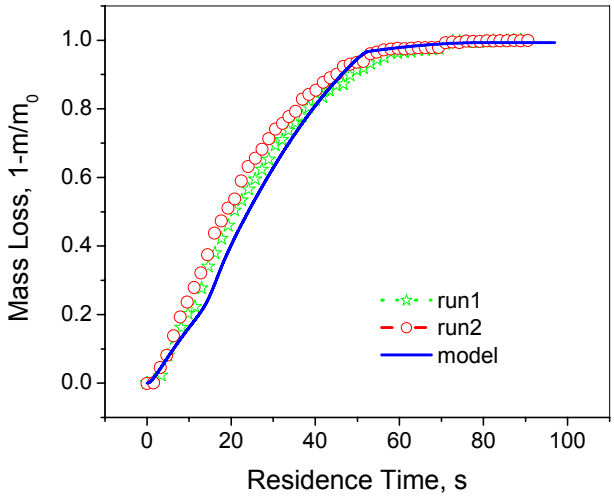

Figure 140 Mass loss of a near-spherical wet particle during combustion, MC = 40 %(wt), T_w = 1276 K, T_g = 1050 K, d_p = 11 mm.

For a low moisture content (6 %(wt)), near-spherical particle (equant diameter = 11 mm), the flame temperature are measured with both thermocouple and the camera pyrometry. A type B thermocouple mounted near the particle surface provides some measurements of the flame temperature surrounding the particle. The flame temperature was also measured by the imaging pyrometer. Both measured data are compared with model predictions in Figure 141, where the flame receded away from the thermocouple after devolatilization. The thermocouple measurements fluctuate due to the turbulence and two-dimensional effects caused by the bulk gas convection, which is not captured in this one-dimensional model. In the camera pyrometry measurements, soot was assumed as gray body emitter. The camera pyrometry measurements can be improved if spectral-dependent emissivity is applied in the calculation. The model prediction of the flame indicates the transition of combustion from devolatilization stage to char burning stage, appearing in Figure 141. Results show that model predictions generally agree with both the camera-measured data and thermocouple data, with difference within measurements uncertainty.

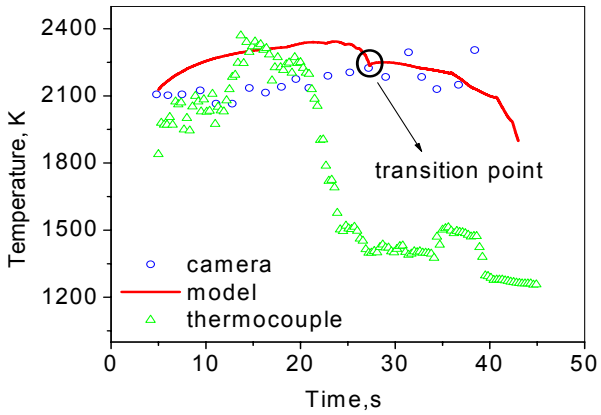

Figure 141 Flame temperature comparison during a near-spherical particle combustion, MC = 6 % (wt), Tw = 1273 K, Tg = 1050 K, dp = 11 mm

So far, the particle combustion model has been verified with each sub-process, including drying, devolatilization, and oxidation. It is ready to further investigate biomass particle combustion.

Effects of various factors on biomass particle combustion

With the validated particle model, a series of predictions of different levels of complexity are compared with some sets of experimental data collected in both the entrained-flow reactor and the single-particle reactor, starting with an isothermal, spherical particle model, which is appropriate to pulverized coal particle.

Non-isothermal effects

Both experimental data and model predictions showed that large temperature gradients exist in large biomass particles during combustion. An isothermal particle assumption incorrectly predicts both temperature and mass loss for large particles, as illustrated in Figure 142, where pyrolysis experimental data of a 11 mm dry, near-spherical particle are compared with model predictions with isothermal and non-isothermal assumptions. The isothermal assumption predicts overall conversion rates approximately three times faster than the non-isothermal predictions and data, the latter being in good agreement. In the isothermal prediction, the surface temperature, which controls the rate of convective and radiative heat transfer, is the same as the average particle temperature. The prediction with the temperature gradient indicates the surface temperature increases much faster than the average temperature, decreasing the average driving force for heat transfer and prolonging the reaction time of the particle. The difference between isothermal predictions and predictions with temperature gradients decreases with decreasing particle size, but the predicted conversion times do not become comparable (within 10 %) until the size is less than 100 micron – which is much smaller than the average particle size used in commercial operation.

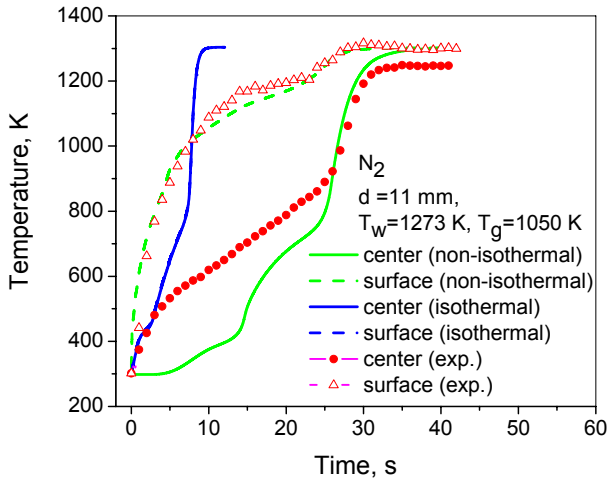

Figure 142 Effects of temperature gradients on particle pyrolysis

Effects of particle shape and size

Mass loss data of particles of varied shapes and sizes were collected in both the entrained-flow reactor and the single-particle reactor and modeled with different shape assumptions. Small size sawdust samples (Set I) were pyrolyzed in the entrained-flow reactor and large size poplar wood samples (Set II and Set III) were used in the single-particle reactor.

The wall and gas temperatures of the short entrained-flow reactor measured by type B thermocouples during sawdust pyrolysis experiments appear in Figure 21.

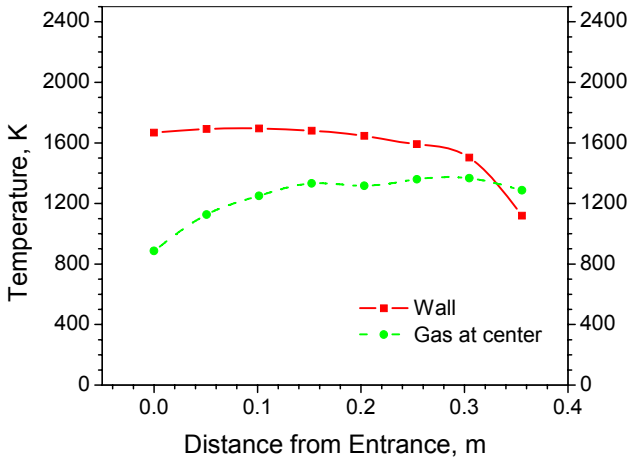

Figure 143 Entrained-flow reactor wall temperature and gas temperature along reactor center

To collect char samples at different residence times, the collection probe was fixed at the bottom of the reactor tube and the residence time was adjusted through moving the feed probe. Based on these average temperature profiles of reactor walls and gas, the mathematical model simulates devolatilization of the sawdust particle sample set I with the specific shapes described in the sample preparation section. Figure 22 illustrates the mass loss history of the three samples. Both the experimental data and model predictions show that the near-spherical particle looses mass more slowly compared with the other two shapes, while the flake-like particle devolatilizes slightly faster than cylinder-like particle. The model prediction indicates slightly more rapid mass loss the experimental data in each case. There are at least two possible explanations for this discrepancy. First, a slightly non-uniform size and/or shape distribution of the samples almost certainly exists, despite the relatively careful sample preparation procedures. These variations in shape and size tend to smooth the observed curve of mass loss vs. time as the small particles react faster than the larger particles. Secondly, actual devolatilization rates are much more complicated and involve reactions with a broader range of rates than is captured by the relatively simple model used here. Such simple models commonly capture the essence of the mass loss but not the details at either the initial or final stages, as reflected by our data compared to the model predictions. Despite these slight inconsistencies, the model and data generally agree, though not within the uncertainties of the data.

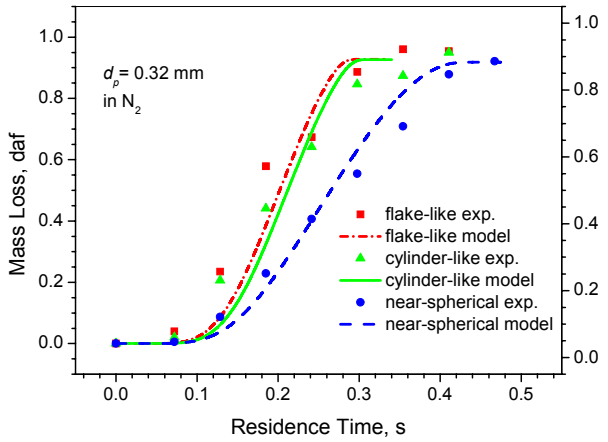

Figure 144 Mass loss histories of sawdust particles with different shapes but the same total mass/volume.

The flake-like and cylinder-like particles have larger surface areas and smaller thicknesses, which result in a higher heating rate and faster heat and mass transfer to the particle. The predicted surface and center temperatures for the three samples are illustrated in Figure 23. As expected, the near-spherical particle temperature rises more slowly than that of the other two shapes.

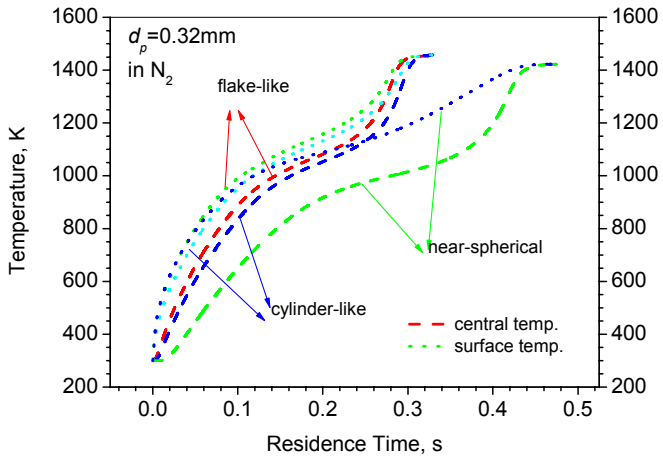

Figure 145 Particle temperature history comparison for sawdust particles with different shapes but the same total mass/volume.

The effect of particle shape on conversion time and product distribution should be more apparent for large particles than small particles. Large particles that sustain substantial internal temperature and composition gradients transfer heat and mass at rates that scale with surface area. Spheres have the lowest surface-area-to-volume ratio of all shapes and should therefore transfer heat and mass at slower rates than aspherical particles of the same volume/mass. By contrast,

particles with little or no internal temperature and compositions gradients transfer mass and heat at rates proportional to total particle volume. These typically small particles are less sensitive to shape than are larger particles of the same material in the same environment. These data and the analyses quantify these theoretical trends and indicate that particles as small as 0.3 mm equivalent diameter experience significant differences in conversion rate. This renders spheres poor choices for many if not most biomass fuels. This concept is similar to but not identical with using a Biot number to determine when internal temperature (and composition) gradients are significant. The Biot number determines when internal temperature (and composition) gradients can be ignored (Bi < 0.1) but does not in itself help determine how to treat the impacts of shape on such gradients when they shouldn't be ignored.

These figures include available data from the entrained flow reactor, but the data do not range over sufficient size to provide convincing experimental verification of the model predictions (because of reactor limitations). Investigations in the other facilities resolve this data gap. Specifically, the effects of particle shape on conversion time for large size particles will be shown and discussed (experimentally and theoretically) next with data collected in the single-particle reactor.

The mass loss rate difference between the near-spherical and aspherical particles increases with increasing size. As illustrated in Figure 146, particles with an equivalent diameter of 11 mm and different shapes, the near-spherical particle pyrolyze slowly compared with the two aspherical particles, consistent with model predictions.

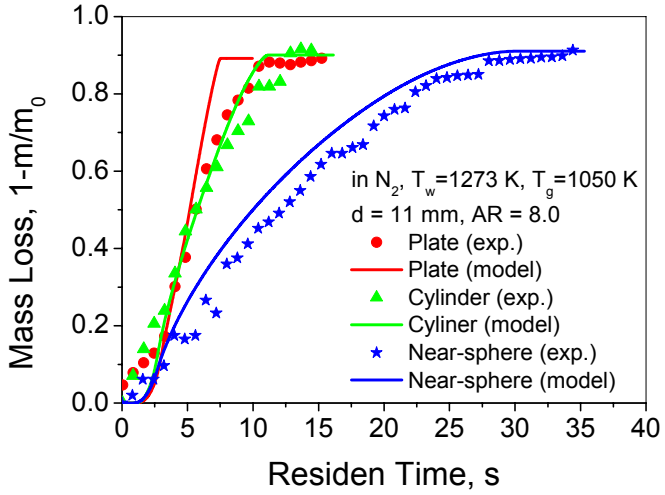

Figure 146 Mass loss profiles of particles with different shape and same mass

Relative to the objective of this investigation, the data and the model agree quantitatively and definitively that near-spherical particles react more slowly than do less symmetrical particles. The mass losses differ by as much as a factor of two during most of the particle histories based on both the predictions and the measurements. Small size sawdust pyrolysis data indicate that at these sizes, which are small relative to commercial uses of biomass, asphericity plays a

significant role in overall conversion. The effects of asphericity should increase with increasing size and increasing aspect ratio, appearing below.

In general, compared with aspherical particles with aspect ratios of 5.0, the conversion time of near-spherical particles can be twice that of aspherical particles for particle sizes larger than 10 mm, (Figure 147); the ratio becomes greater, up to 2.5 when the aspect ratio of aspherical particles increases to 8.0, as illustrated in Figure 148. Commercially significant biomass particles commonly have aspect ratios as large as 12. Less difference exists between the two aspherical shapes since they have about the same surface area to volume ratio.

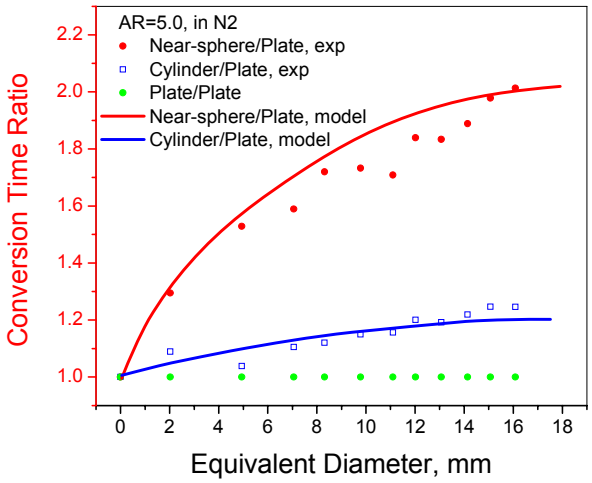

Figure 147 Effects of particle shape and size on conversion time (AR=5.0)

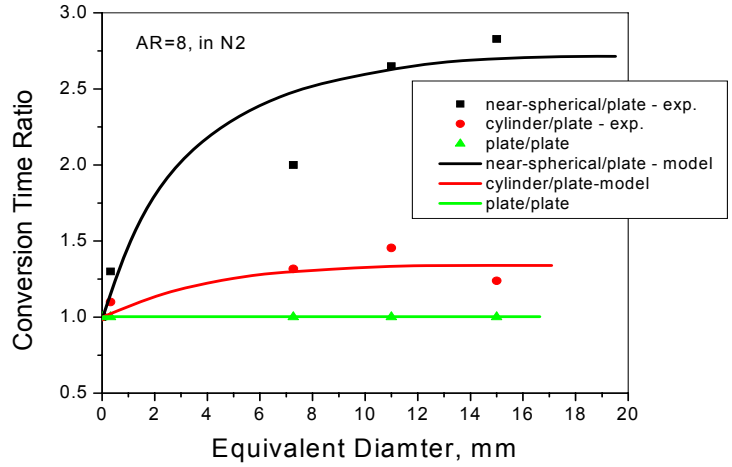

Figure 148 Effects of particle shape and size on conversion time (AR=8.0)

The above illustrations show that particle asphericity and sizes play important role in particle conversion process. A spherical particle would lead to substantial error in predicting combustion behaviors of biomass particles of commercial size and shape.

Effects of surrounding flame during particle combustion

The current single particle combustion model simulates the boundary layer and the flame formed around the particle surface in the boundary layer, as well as predicting the boundary layer thickness.

Figure 149 illustrates the effects of the boundary layer simulation and surrounding flame on the particle temperature profiles during combustion. Simulations both including and neglecting the surrounding flame appear in this graph. As expected, essentially no difference exists between the two simulations early in devolatilization (flame not yet ignited). Slight differences in the surface temperature start to appear during the late devolatilization stage and early oxidation stage of combustion, but the flame actually decreases the predicted surface temperature in this case. This counterintuitive decrease is associated with the flame consuming oxygen in the boundary layer that otherwise would have reacted with the particle. The relatively minor thermal feedback from the flame to the particle impacts the particle surface temperature less than the reduction in surface reaction associated with the decreased oxygen concentration. During the bulk of oxidation, the flame increases the predicted surface temperature by about 100 K.

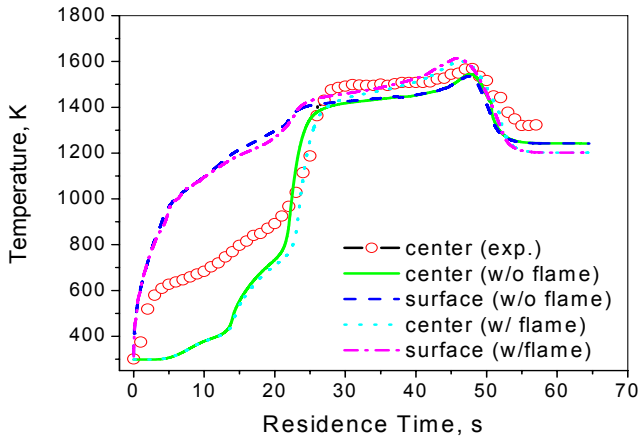

Figure 149 Effects of flame on particle temperature during combustion process

Model results also indicate that particle temperature becomes dramatically more uniform during char burning, although the flame feedback maintains a surface temperature greater than the center temperature, unlike theoretical predictions for particles with oxygen penetration but no flame feedback. These relatively subtle effects on flame temperatures are too small for accurate measurements by our techniques.

The comparisons between experimental data and model predictions with different levels of complexity demonstrate that, for biomass particle combustion a model with such a sophisticated structure is necessary.

Particle temperature measurements and comparison with model predictions

Particle surface temperature data were collected for both sawdust particles in the long entrained-flow reactor and poplar particles in the single-particle reactor during pyrolysis and combustion.

Sawdust particle surface temperature in the entrained flow reactor

Combustion experiments (air as carrier gas) for the sawdust particle sample set II were conducted on the long entrained-flow reactor with the imaging system. The reactor wall temperature distribution along the reactor appears in Figure 150.

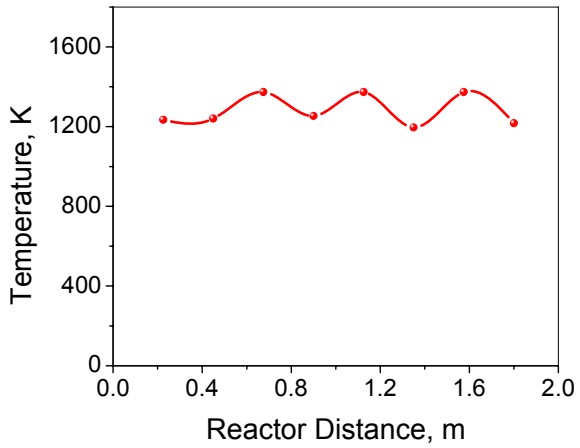

Figure 150 Reactor wall temperature distribution of the long entrained-flow reactor

The particle surface temperatures were measured with the camera pyrometry installed around the entrained-flow reactor through optical accesses. Particle traveling speed in the reactor was determined with the imaging system. Figure 151 illustrates the sawdust particle surface temperature distribution when the particle was heated up in the reactor before a flame was formed around. A relatively poor image was obtained since the particle traveled at an average speed of about 3.0 m/s and the particle surface temperature was not high enough to use a very short exposure time. The average particle surface temperature was 1173 K, as indicated in the temperature map.

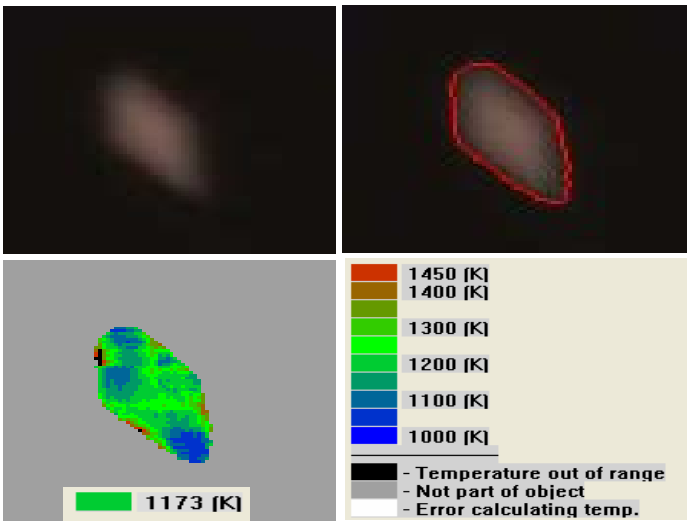

Figure 151 Particle surface temperature distribution during pyrolysis in entrained-flow reactor.

Once the particle starts to burn in the reactor, the particle itself will be surrounded by flame. The flame may not completely block the radiation from the char particle surface, so both the flame and the particle surface contribute the signal received by the pyrometer sensor. The measured temperature will be a value between the char surface temperature and the flame/soot temperature. It depends on the relative distance between soot cloud and the particle surface (which one is closer to the focus point of the imaging pyrometer), char surface temperature, flame temperature, soot absorption, etc. The temperature distributions of several burning particle in the entrained flow reactor are shown below.

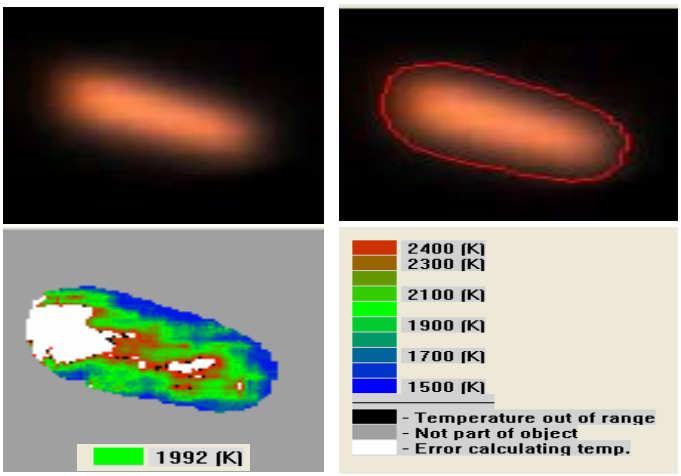

Figure 152 Temperature map of burning sawdust particle in entrained-flow reactor – particle 1

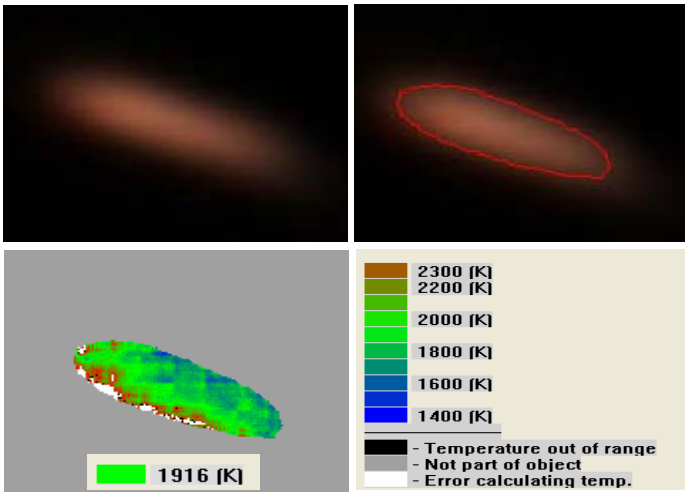

Figure 153 Temperature map of burning sawdust particle in entrained-flow reactor – particle 2

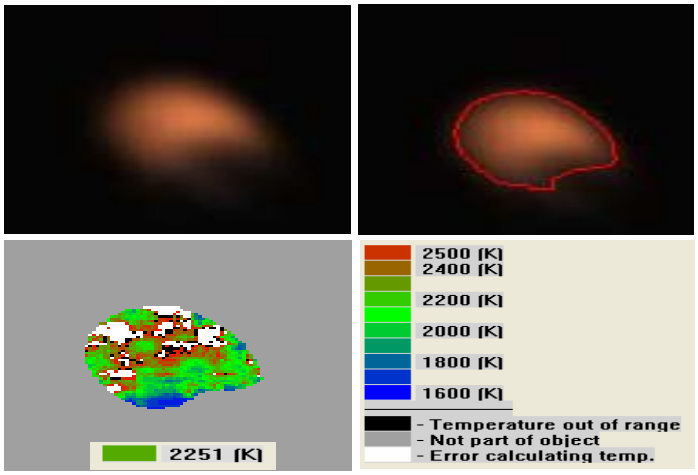

Figure 154 Temperature map of burning sawdust particle in entrained-flow reactor – particle 3

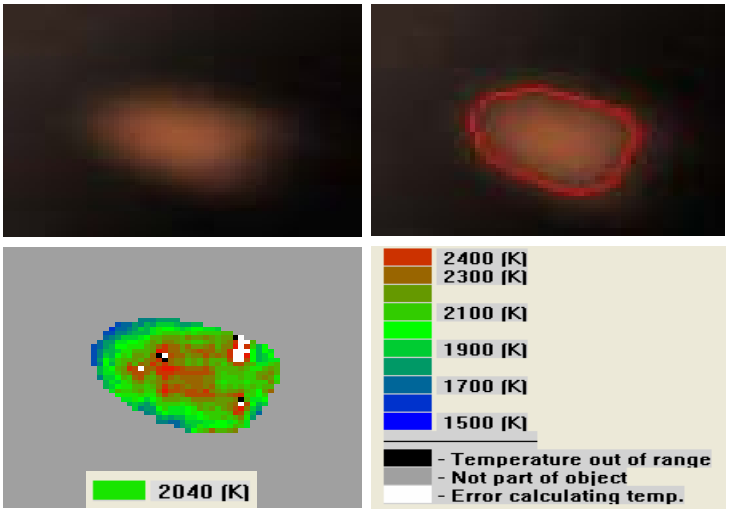

Figure 155 Temperature map of burning sawdust particle in entrained-flow reactor – particle 4

As illustrated in Figure 152 ~ Figure 155, the temperatures in all the maps range from 1500 K to 2500 K, with an average temperature of about 2000 K, which is reasonably close to the adiabatic flame temperature of most dry hydrocarbon fuels. Some areas in the maps are marked as errors, which can be caused by two situations: the pixel is saturated or the pixel intensity is too low to obtain reliable temperature data.

Poplar particle surface and flame temperature in single-particle reactor

The imaging pyrometers measure particle surface temperature and flame temperature during devolatilization and char burning through the optical accesses ports in the single-particle reactor wall. Thermocouples provide additional measurements of some of these data in many experiments.

When the wood particle is first inserted into the reactor, the particle surface immediately rises, but the reflection from the reactor wall dominates the particle surface radiance as explained in the imaging pyrometry development section. With the reflection effect accounted in the calculation of particle surface temperature, the pixel intensity ratio of any two channels differs from measurements without reflection, as illustrated in Figure 156, where the wall temperature is assumed to be 1300 K and the particle has an emissivity of 0.85. As shown in Figure 156, both the ratio of blue channel to the red channel and that of the green channel to the red channel first increase and then decrease with increasing temperature. As indicated, the temperature is uniquely defined by the pixel intensity ratio only when it exceeds the wall temperature. At low temperatures (< about 800 K in this case), the measurement is insensitive to temperature. Between these low-temperature and furnace-wall temperature limits, a given ratio of signals generally corresponds to two temperatures. At the lower of these two temperatures, surface reflections of wall radiation contribute to the measured signal more than particle surface emission, with the opposite being the case at the higher temperature. Determining which of the two temperatures is correct generally depends on additional information. The assumption that the surface temperature monotonically increases can often provide enough information to make such distinctions.

The specific results illustrated in this figure depend on temperatures and emissivities of walls and surfaces, but the general trends are characteristic of the analysis.

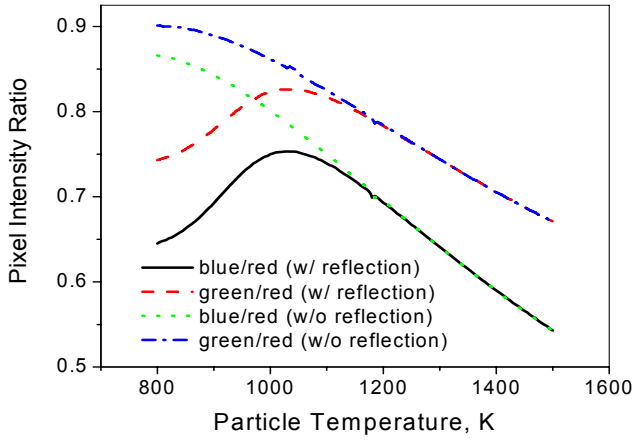

Figure 156 Pixel intensity ratios of a particle in furnace with reflection corrected

Based on the reflection correction analysis, time-resolved particle pyrolysis videos from three orthogonal cameras provide surface temperature of near-spherical poplar particles. The camera-measured particle surface temperatures as functions of time appear in Figure 157 and Figure 158 together with thermocouple measured results and model predictions.

For the pyrolysis of poplar particle, the particle surface emissivity was also calculated with the algorithm based on reactor wall reflection correction. An average of 0.99 was obtained, which is different from the typical wood emissivity of 0.85. This might be related with the reacting surface properties (charring). In cases where wall radiation is a not a factor, the pyrometry has to be calibrated with respect of working distance to measure particle surface emissivity, which is not done in this project.

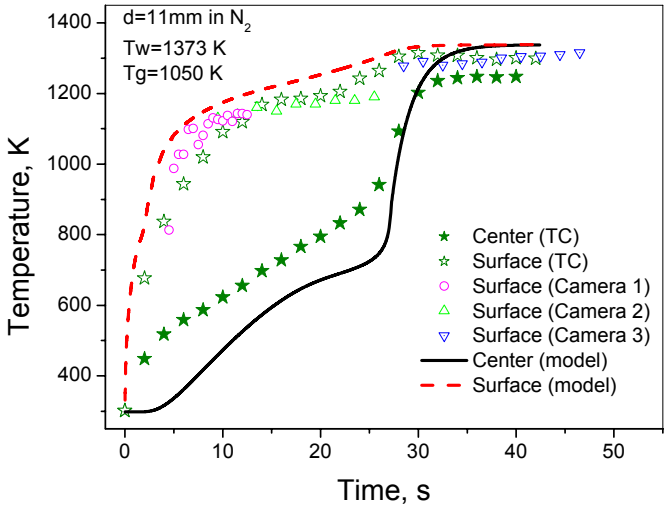

Figure 157 Particle surface temperature comparisons during pyrolysis – run 1

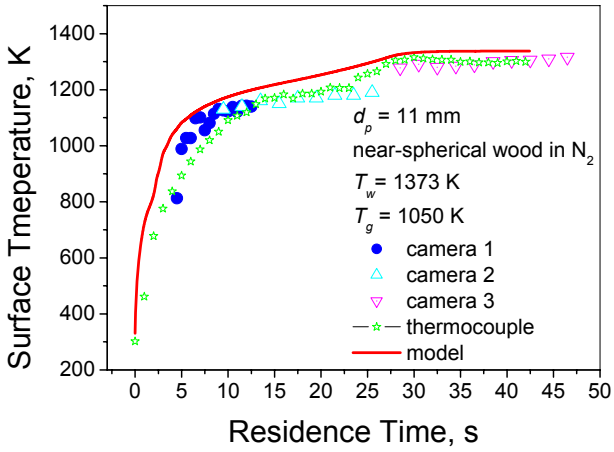

Figure 158 Particle surface temperature comparisons during pyrolysis – run 2

The spatially and temporally resolved imaging pyrometer results indicate that combustion proceeds with non-uniform particle surface temperature. Specifically, the particle surfaces exposed to the most intense radiation (bottom) and, during oxidation, those at the leading edge in the induced convective flow (also the bottom) generally heat faster and to higher temperatures than the remaining particle surfaces.

Three-dimensional rendering of these surface temperatures provides uniquely detailed data regarding combustion processes. To general such renderings, the particle surface temperature distribution is mapped onto two-dimensional images, as illustrated in Figure 159. This figure illustrates data from a single residence time and for a near-spherical poplar particle suspended in the single-particle reactor with an average particle surface temperature of 1312 K, approaching the end of particle devolatilization.

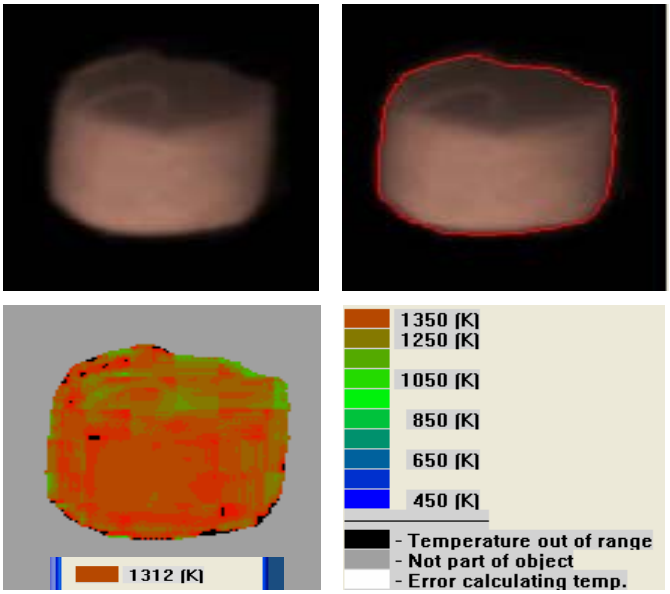

Figure 159 Poplar particle surface temperature during pyrolysis in a single-particle reactor

Particle surface and flame temperature distributions have also been measured and mapped to 2-D images for burning char particles, illustrated in Figure 160 to Figure 162.

Figure 160 shows the flame temperature distribution when volatiles burn next to the particle during devolatilization. The average temperature of the flame is about 2200 K. In Figure 161, both the images of the char particle and the flame next to the particle appear in one frame, and the flame temperature and particle surface temperature are calculated and mapped simultaneously. Obviously, the average temperature of the flame zone is much higher than that in the particle surface zone, i.e., during devolatilization the particle surface remains at a lower temperature than the surrounding flame. A char particle surface temperature map for a burning char particle appears in Figure 162.

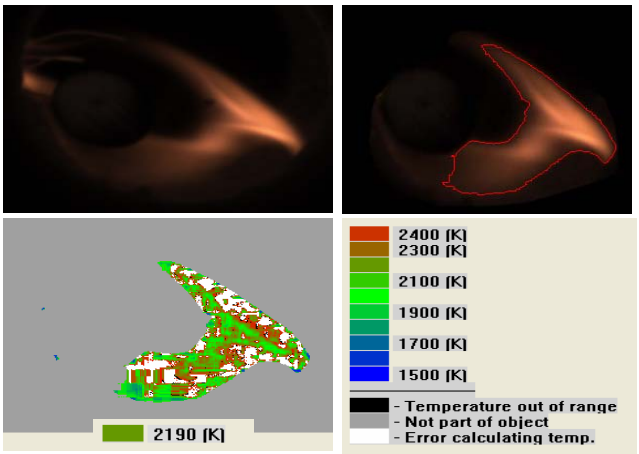

Figure 160 Flame temperature map during volatile combustion

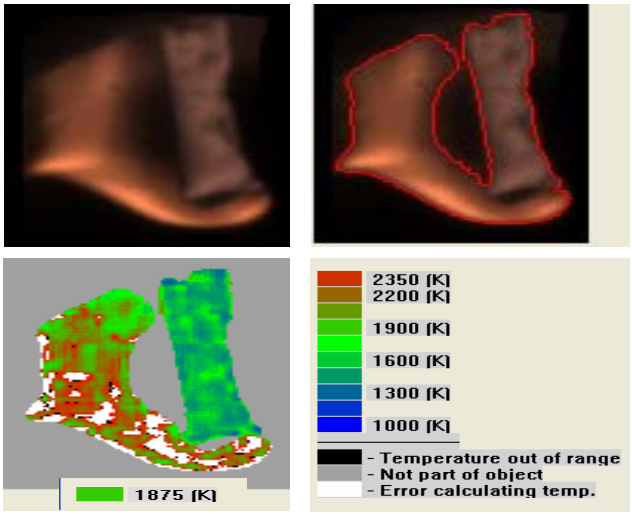

Figure 161 Char particle surface temperature and flame temperature map during particle devolatilization process

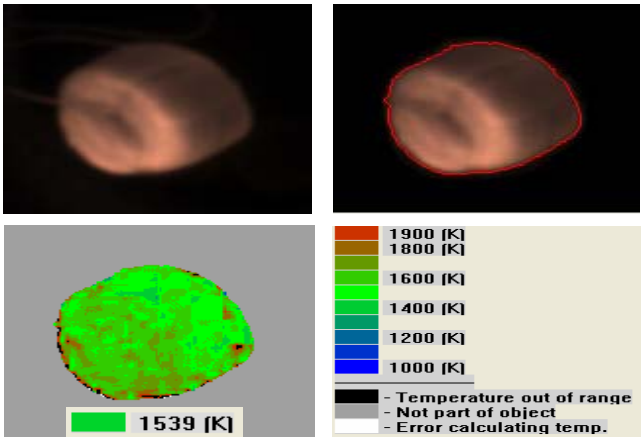

Figure 162 Char particle surface temperature map during char burning

Char particle surface temperature was also measured as a function of time during the char burning process with the multi-color band camera pyrometer and compared with thermocouple measured data and model predictions in Figure 163. The camera-measured temperatures exceed the measured center temperatures and the predicted and measured surface temperatures by about 100-200 K. The oxidizing and receding char surface precludes reliable surface temperature data from thermocouples. There are several complications in these temperature measurements. The optical measurements are potentially impacted by soot emission from the surrounding flame while the thermocouple data are potentially impacted from conduction along the wire. A detailed analysis of the flame temperature measurement and the potential impact of non-gray emission from soot particles appears in the appendix. However, no definitive method of separating flame interference from particle surface temperature data appears to exist. Nevertheless, the data, although potentially biased, still provide some insight into the particle combustion behavior.

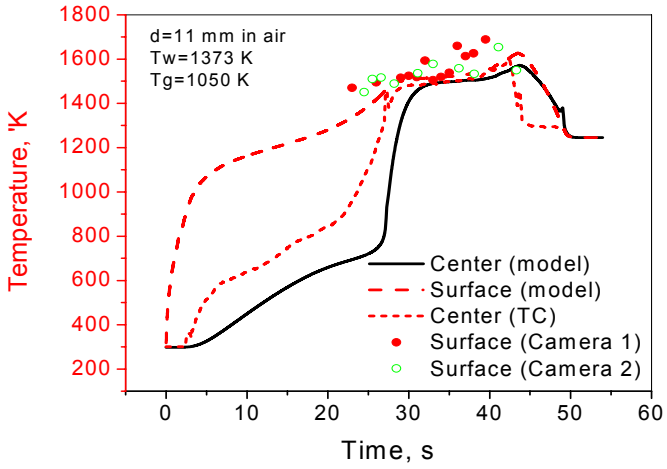

Figure 163 Char particle surface temperature as function of time

With the three camera pyrometers installed around the reactor, three images of a burning char particle were taken simultaneously from three orthogonal directions. The particle surface temperature from each angle was calculated individually for each image. The 3-D particle shape, reconstructed with the three images as previously described, combines with the particle surface temperature distribution data to provide spatially and temporally resolved 3-D particle data, as shown in Figure 164.

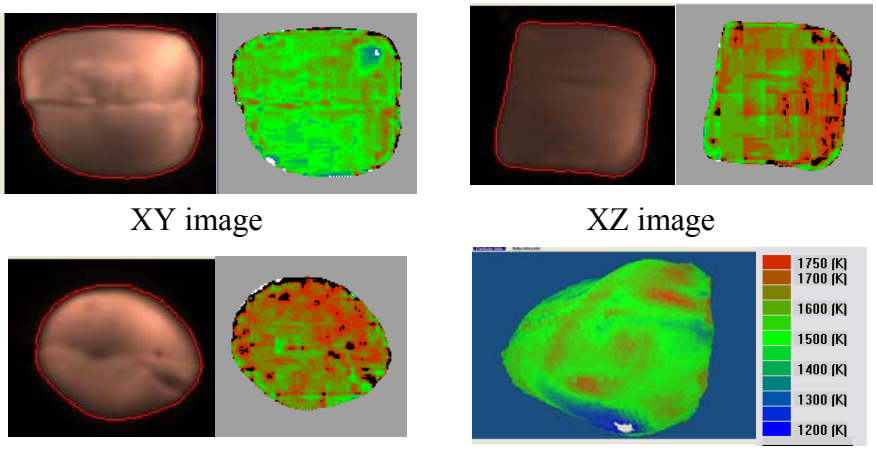

Figure 164 3-D particle surface temperature map of a burning char particle

Modeling studies

Pyrolysis and combustion of small sawdust particles and large poplar particles are further investigated with the single particle combustion model.

Composition gradients and effects of particle shape and size on volatile yields

The composition gradients inside the near-spherical particle are predicted using the model, as shown in Figure 165. Both the biomass density and the char density changes are illustrated at the particle center and surface boundary.

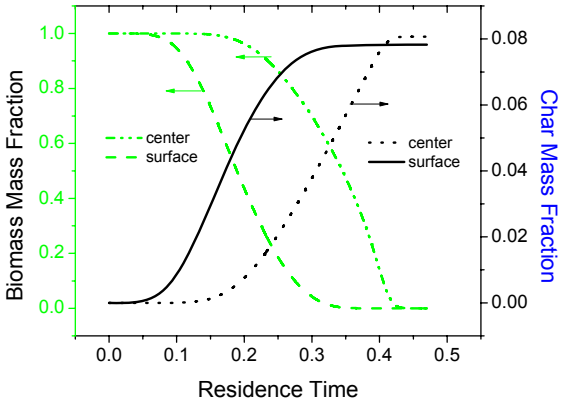

Figure 165 Composition of the near-spherical particle as functions of time

The effects of particle shapes and sizes on volatile yields are investigated using the model. As shown in Figure 25, the volatile yield of near-spherical particles decreases with increasing particle size. Both the experimental data and model predictions show that the near-spherical particles yield slightly lower volatiles relative to the other shapes. This is caused by a combination of different particle temperature histories due to the particle shape and longer average path lengths for tars to travel in spherical particles compared to their aspherical counterparts. Both flake-like and cylinder-like particles behavior similarly. However, the difference between the near-spherical and other shapes increases with increasing size.

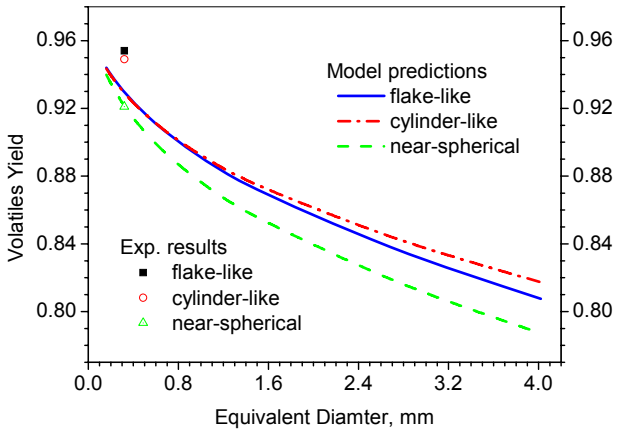

Figure 166 Volatile yields comparison of various particle shape and size

Effects of blowing on particle temperature

During pyrolysis, the blowing factor of the 11 mm particle becomes as low as 0.1, as shown in Figure 167. This pronounced impact on heat transfer is not observed when radiation dominates particle, as illustrated by the predicted temperature profiles of a biomass particle in the single-particle reactor with and without blowing factor correction in Figure 168. However, for environments dominated by convective heating, the blowing factor has a major impact on overall heat transfer rates, as indicated in Figure 169. The blowing factor slows down the particle thermal conversion by about 20 %.

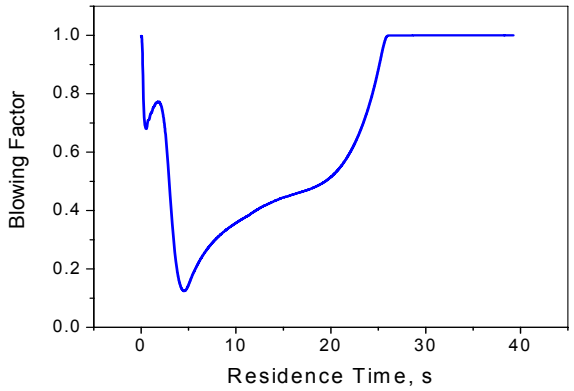

Figure 167 Blowing factor during pyrolysis process

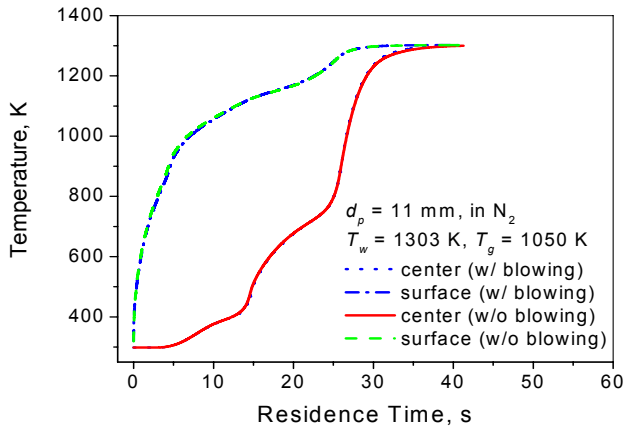

Figure 168 Particle temperature profile with and without blowing factor correction

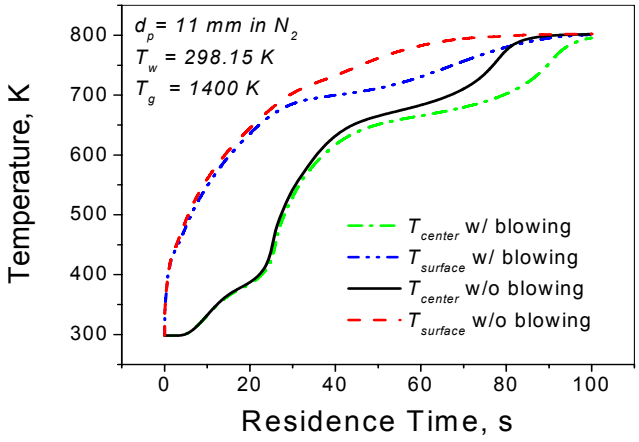

Figure 169 Effects of blowing factor on particle temperature during devolatilization when convection dominates

Temperature, pressure, and species concentration profiles

The complete combustion of poplar particles has been further comprehensively investigated using the single particle combustion model. An 11 mm near-spherical poplar particle forms the basis for illustrating the predictions. Experimental verification for most of the information illustrated in this section is beyond the scope of this project, though some of it in principal could be accomplished with the facilities developed and described earlier.

Combustion modeling results for a particle with 6 %(wt) of moisture content show that after the particle enters hot gas and wall radiation, moisture starts to evaporate immediately, shown in Figure 170. Biomass begins to pyrolyze after about 3 seconds and the char mass ratio (with respect to the original particle mass) increases with increasing pyrolysis. The char mass ratio peaks slightly prior to the end of pyrolysis, with the latter occurring at about 20 seconds. Usually for this poplar particle, its char yield can be as high as 10 % (wt) (with respect to the original wet particle mass) in inert gas, but here it shows the maximum char yield is only about 7 %(wt). This is caused by the overlap of the three processes; drying, pyrolysis, and char burning occurs simultaneously for this large size particle.

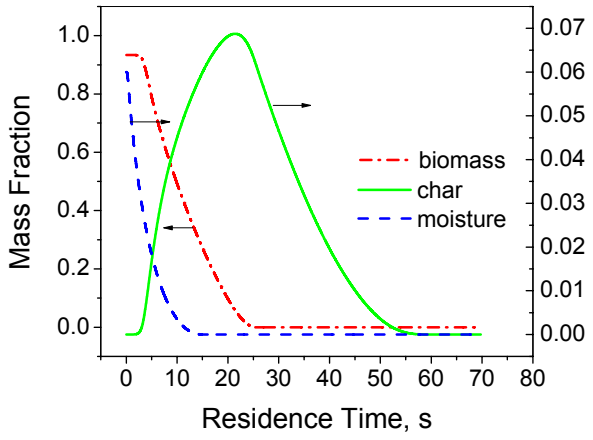

Figure 170 Mass fraction of each species as functions of time

Particle (Zone A) and gas (Zone B) temperature profiles for a particle with higher (40%) moisture content appear in Figure 171 and Figure 172, where the abscissa indicates the relative distance from the center of the particle to the infinity boundary. The sizes of both the particle and boundary layer zone change during combustion. Figure 171 indicates that most of the particle remains at subboiling temperatures when volatiles ignite and form a flame surrounding the particle in the boundary layer. Strong temperature gradients exist between the drying and devolatilization zones in the particle. The maximum flame temperature can reach about 2400 K in this simulation (furnace wall temperatures 1276 K). During char burning, the flame shifts close to the particle surface as the blowing effect decreases. The temperature gradient in the particle also flattens during char oxidation, as shown in Figure 172.

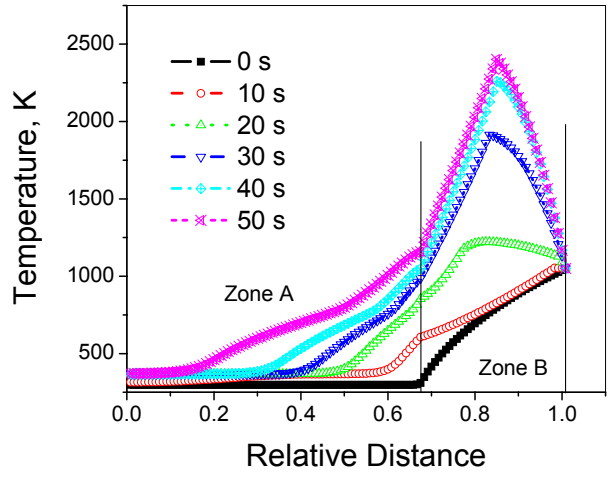

Figure 171 Temperature distributions during drying and pyrolysis

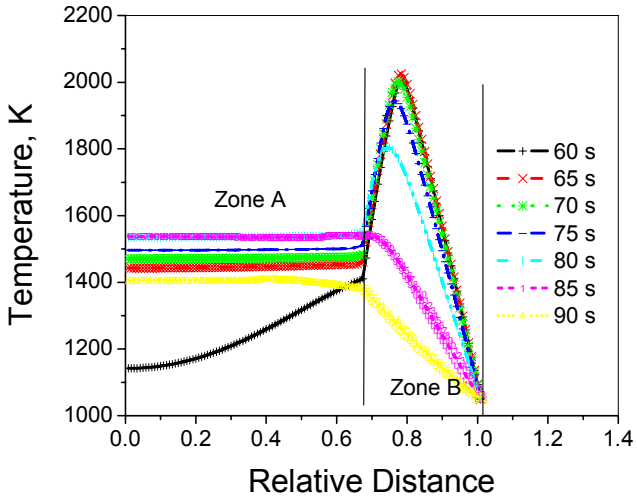

Figure 172 Temperature distributions during char burning

The modeled particle radius, boundary layer thickness, and off-gas velocity as functions of residence time during the drying, devolatilization, and char burning processes appear in Figure 173.

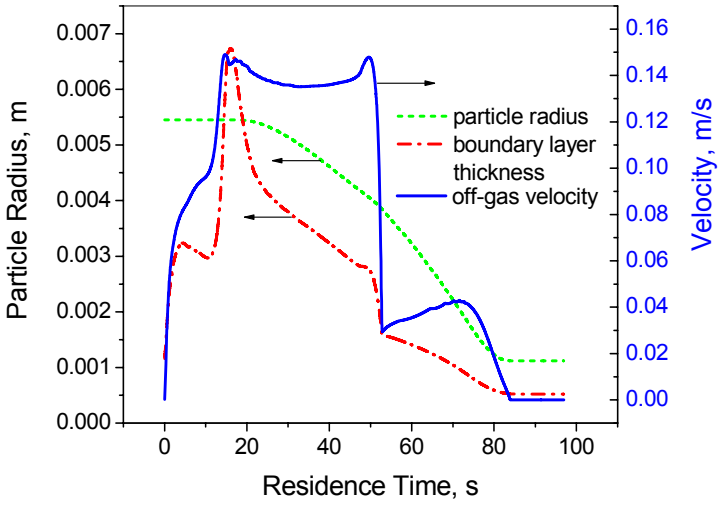

Figure 173 Particle radius, boundary layer thickness, and off-gas velocity during a wet particle combustion process

Although the three processes of drying, devolatilization, and char oxidation occur simultaneously for large particles such as the 11 mm poplar particle used in this investigation, they can still be approximately identified from both experimental data and model predictions, as shown in Figure 139 and Figure 173. Drying mainly finishes in the first 20 seconds followed by primary devolatilization that lasts about 30 seconds; char oxidation requires an additional 30 seconds.

The modeling results also show that the particle shrinks slightly during drying and shrinks more rapidly during char burning.

The pressure profile in the particle during drying and the first half of devolatilization appears in Figure 174. The particle pressure of the inner part first starts to drop due to vapor recondensation during drying, and then it increases as devolatilization begins at the outer layer of the particle. The particle pressure continues increasing through the end of the particle devolatilization. When the particle devolatilization is almost finished, the particle pressure drops but does not reach atmospheric pressure until the completion of char burning, as illustrated in Figure 175.

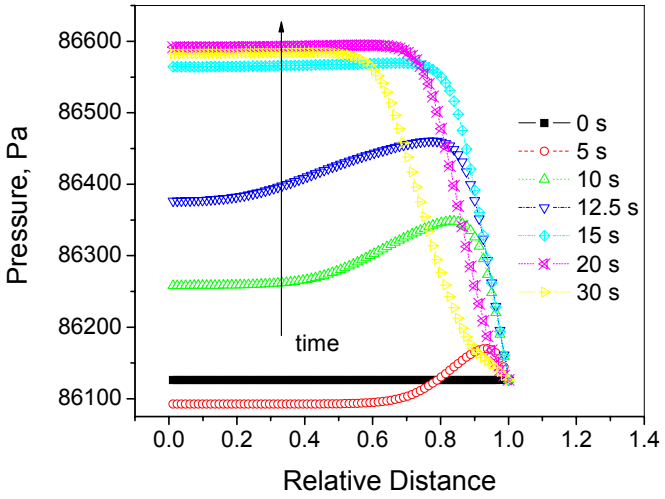

Figure 174 Particle pressure distribution during drying and first half of devolatilization

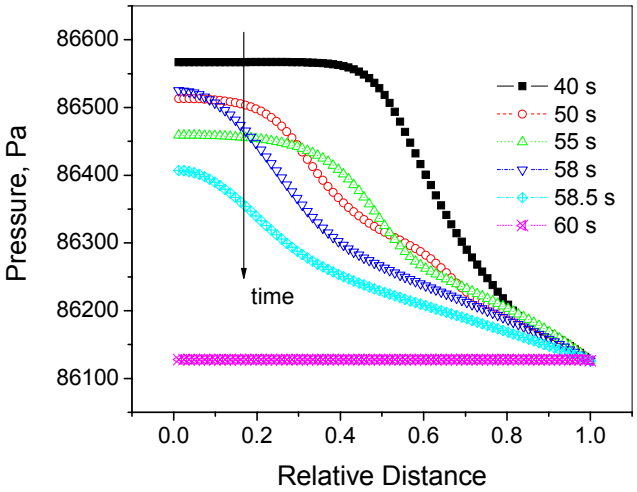

Figure 175 Particle pressure distribution at the end of devolatilization

The species concentrations profiles for several major species provide additional insight. The free water concentration profiles inside the particle as functions of time appear in Figure 176. When free water in the outer layer starts to evaporate, moisture in the gas phase diffuses both directions and the free water density in the inner layer starts to increase due to the vapor recondensation since the inner part of the particle remains at a low temperature.

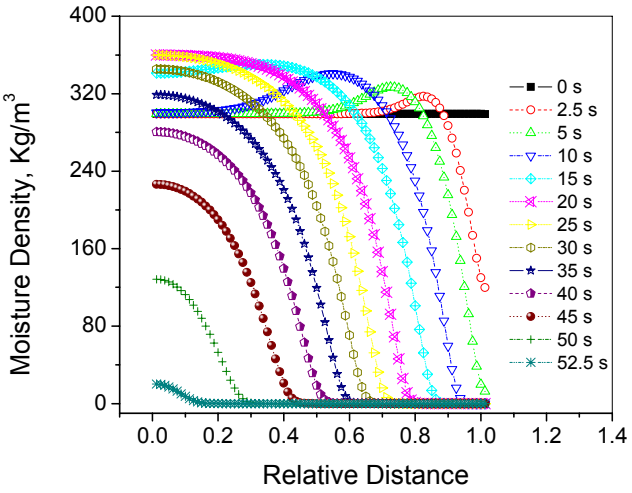

Figure 176 Free water concentration profiles during drying

The concentration profiles of the other two solid species at different residence times appear in Figure 177 and Figure 178. The pyrolysis front moves from the outer layer to the particle center with increasing time and a monotonic decrease in biomass (as opposed to char) concentration. The pyrolysis front is steep, reasonably approaching a step function through most of the particle history.

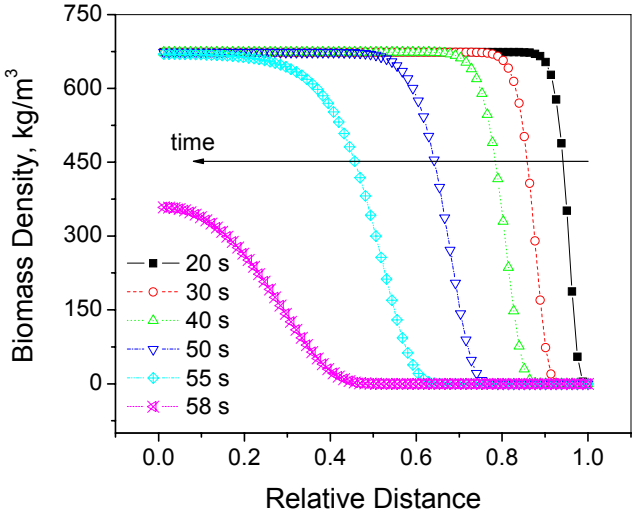

Figure 177 Biomass concentration profile at different residence time

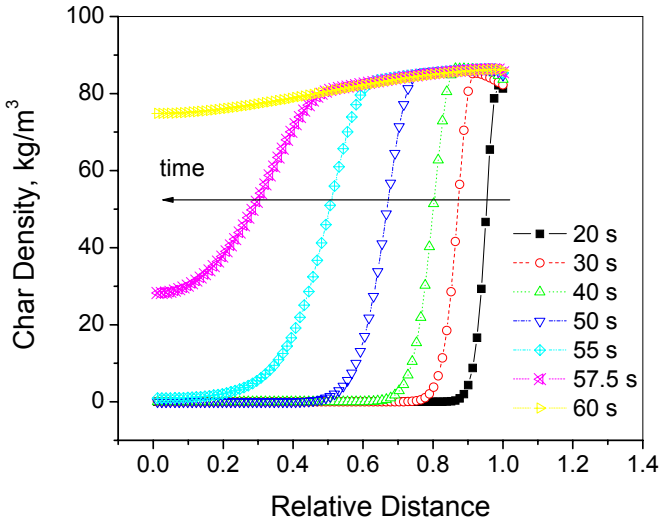

Figure 178 Char concentration profile at different residence time

Figure 179 is the concentration distribution of hydrocarbon gases and oxygen during devolatilization process. The flame position in the boundary layer corresponds to the location where these two profiles simultaneously approach zero.

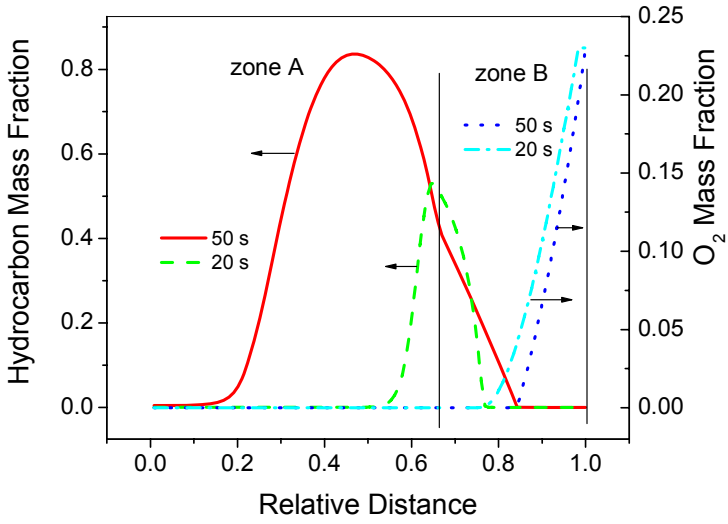

Figure 179 Hydrocarbon gases and oxygen profiles during devolatilization

The concentration profiles of carbon monoxide and oxygen during char burning appear in Figure 180. The oxidizer is nearly consumed before it reaches the surface of the char particle, and the oxidation rate of the char particle is diffusion controlled. These O_2 and CO concentration profiles

are similar to what predicted by a two-film model explained in (Turns 2000) for coal char particle combustion.

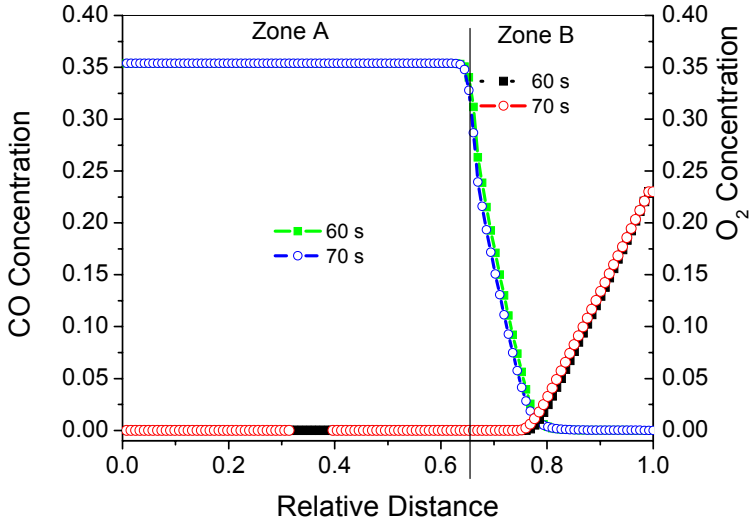

Figure 180 CO and oxygen concentration during char burning

Preliminary black liquor combustion simulation

The single particle combustion model has been used to preliminarily model combustion of a 3.3 mm black liquor droplet. The black liquor droplet has 30%(wt) moisture content and 15%(wt) inorganic material. In this simulation, inorganic material is assumed to be inert, and no smelt reactions are considered – a poor assumption that will be relaxed by other students working in this area. The same conditions as the biomass combustion are used with a wall temperature of 1276 K and a bulk gas temperature of 1050 K. The swelling and mass loss of the particle during drying and devolatilization appear in Figure 181. Modeling results show that the droplet starts to swell during drying and reaches a peak value at the end devolatilization. The swelling ratio is about 2.5. The droplet shrinks dramatically during the char burning stage. The modeled particle surface temperature and center temperature appear in Figure 182.

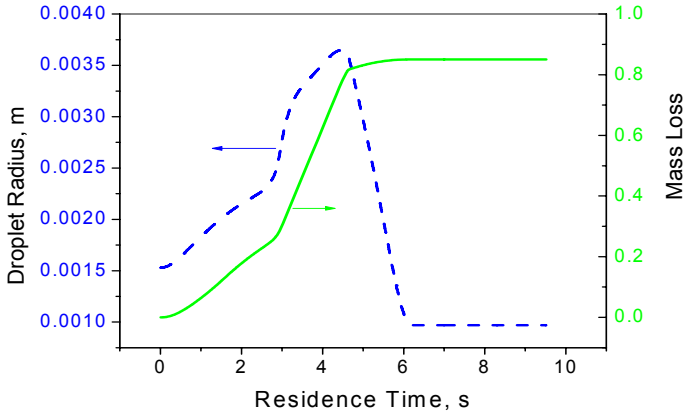

Figure 181 Mass loss and swelling of a black liquor droplet combustion

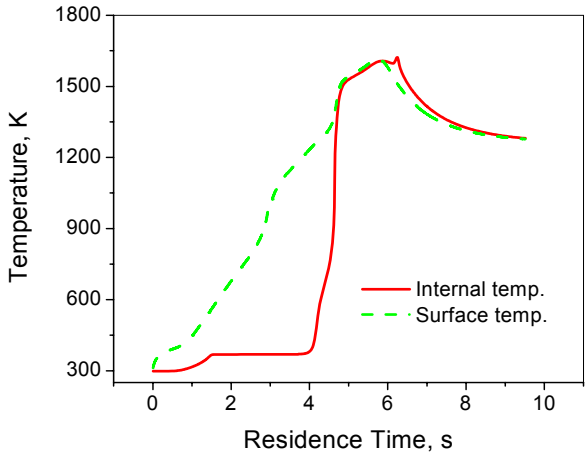

Figure 182 Black liquor temperatures as function of time during combustion

Similar predictions for particle of various shapes and sizes qualitatively indicate the same behavior as those illustrated for near-spherical particles.

Combustion of wheat straw

In this project, knees and stalks of wheat straw were also burned in the single-particle reactor. Mass loss data as function of residence time were recorded for both knees and stalks. Results that stalks burn about three times faster than knees due to the larger surface area and lower particle density of stalks than those of knees, as shown in Figure 183.

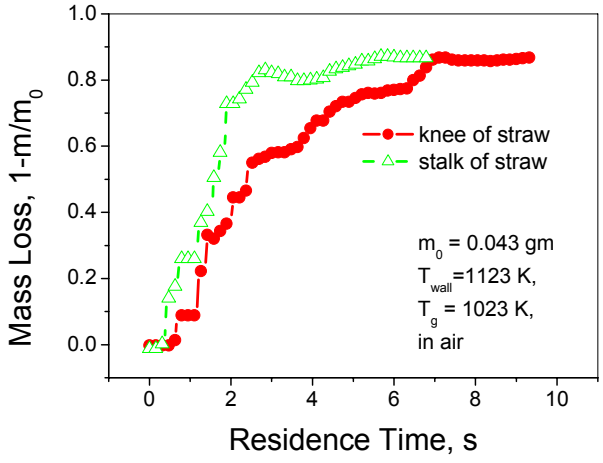

Figure 183 Mass loss of wheat straw knee and stalk during combustion

Summary

In this chapter, experimental data, including particle temperature and mass loss, for sawdust particle samples and poplar dowel particle samples of different shape and size are presented. The single particle combustion model has been validated using experimental data collected in the single-particle reactor and the entrained-flow reactor.

Biomass particle combustion including drying, devolatilization, and char burning and has been comprehensively studied both experimentally and theoretically using two reactors and a single particle combustion model. The effects of solid particle shape and size on particle combustion reactivity have been studied and discussed with experimental data and modeling results.

Effect of particle density on combustion rate is also demonstrated with experimental data collected with wheat straw knees and stalks.

Conclusions and Recommendations

Principal Conclusions

In this project, experimental data and a single particle combustion model describe drying, devolatilization, and char oxidation of biomass particles of varied shape and size. Experimental data are collected in both an entrianed-flow reacotr and a single-particle reactor. Particle surface and flame temperature are measured with a color-band imaging pyrometry developed and applied in the investigation. Particle volumes and surface areas of irregular particles are measured with a particle shape reconstruction algorithm developed in this investigation. The last two diagnostics represent the first-ever application of such tools to particle combustion experiments to our knowledge.

Each part of this project is concluded as follows:

A single particle combustion model has been developed

A relatively general purpose particle combustion model capable of simulating drying, recondensation, devolatilization, and char oxidation and gasification, and swelling/shrinking as well as gas-phase combustion surrounding biomass particles is described in detail and validated with original data. Validation relies primarily on particle center and surface temperature data and overall mass loss. Model predictions include many additional features of biomass combustion less amenable to direct measurement.

An entrained-flow reactor was designed and built

An entrained-flow reactor designed, constructed, and used in this project provides unique access to combustion characterization of aspherical particles. The combustor provides optical access at three levels in three orthogonal directions. A particle residence time of up to 2 seconds can be obtained in this reactor. The reactor can provide a maximum wall temperature of 1600 K. An imaging system associated with this reactor provides raw data that, when combined in alorgithms described below, captures three-dimensional combustion features of aspherical particles.

A color-band pyrometry was developed and successfully applied to meausre particle surface and flame temperature

A color-band pyrometry has been developed in this investigation based on a CCD/CMOS digital cameras. Particle surface temperature and flame temperature measurements generally agree with thermocouple measurements and model predictions when artifacts from each are removed, although there remain small differences in predictions and measurements. This new diagnostic provides pixel-by-pixel particle (and flame) temperature and emissivity data from widely available and relatively inexpensive cameras. Depending on magnification, shutter speed, etc., useful temperature and emissivity data are obtainable at temperatures greater than about 750 K, with the lower limit based on signal intensity. Cameras more sensitive in the infrared produce useful data at lower temperatures.

These non-contact particle temperature data compare reasonably well with both predicted and thermocouple measurements for both suspended and entrained-flow systems. The images allow three-dimensional reconstruction of particle temperature profiles that reveal large spatial differences in particle surface temperature – a feature that cannot be captured in one-dimensional transient models of any complexity. To our knowledge, this investigation represnts the first-ever development or application of this technique to particle combustion investigations.

An particle shape reconstruction algorithm has been developed to meaure particle external surface area and volume for particles with irregular shape

This investigations developed an algorithm that reconstructs a three dimensional representation of a particle based on three orthogonal profiles of the particle shape. Cooridnates of six extreme points are determined based on the orientation of the images, and points on particle surface are interpolated with the inverse distance weighting method. The average error of this algorithm is about 10% based on measurement of rock surface area and volume. To our knowledge, this investigation represnts the first-ever development or application of this technique to particle combustion investigations.

Particle shape and size impact fuel reactivity substaneously

This investigation reports a comprehnensive dataset of biomass particle reaction as a function of sample shape, size, and composition obtained with the entrained-flow reactor and the single-particle reactor, the color-band pyrometer, and the particle reconstruction algorithm. The single particle combustion model provides a theoetical basis for analyzing the experimental results.

Both experimental and theoretical investigations indicate particle shape and size both impact overall particle reactivity. Experiments conducted on biomass particles at relevant temperatures and a variety of well-characterized shapes indicate that particle shape impacts overall reaction rates relative to those of spheres with the same mass/volume by factors of two or more at sizes and shapes of commercial relevance. Data and theoretical models indicate that the impact of shape increases with increasing size and increasing asphericity and is large at sizes relevant to biomass utilization in industry. Generally speaking, spherical mathematical approximations for fuels that either originate in or form aspherical shapes during combustion poorly represent

combustion behavior when particle size exceeds a few hundred microns. This includes a large fraction of the particles in both biomass and black liquor combustion.

Shape impacts on combustion also impact overall convesion times by factors of two to three, depending on size and combustion conditions. In particular, composition and temperature gradients in particles strongly influence the predicted and measured rates of temperature rise and combustion, with large particles reacting more slowly than is predicted from isothermal models.

The data and model developed in this investigation describe single-particle biomass combustion rates reasonably well. Generally agreement within a few percent of the measured values is achieved, though in most cases there remain generally small but statistically signficant differences between predictions and measurements. However, relative to the factors of 2 or more errors associated with isothermal, spherical, or other common assumptions, this investigation provides substantial improvement in predicting biomass behavior. Most of the remaining difference between measurement and predictions may be related to uncertainties in physical properties, experimental artifacts, or model assumptions inherent in this approach (see below).

Recommendations

The model developed in this investigation provides detailed predictions of biomass combustion behavior. However, the data suggest some features of biomass combustion that require fundamentally different modeling approaches. For example, the three-dimensional reconstruction of shape and size routinely show that large or aspherical particle combustion (and possibly small particle combustion) is at least two dimensional. Particle reaction rates and temperatures differ markedly at different regions on the particle surface, a feature that cannot be resolved with a one-dimensional model of any complexity. This also suggests that the conceptual model of char oxidation, for example, may be fundamentally flawed. It is possible (likely in the cases investigated here) that oxidation does not occur by oxygen diffusion to the surface and product diffusion back to the bulk along similar paths, but rather by oxygen diffusion/convection to one side of the particle (typically the windward side) and product diffusion/convection to the bulk gas from a separate region (typically the leeward side). This fundamentally changes concepts of diffusion limitations, maximum burning rates, temperature profiles, and peak particle temperatures during combustion. Further investigation of this phenomenon is highly recommended.

Many of the diagnostics innovated and demonstrated here have much greater potential application than has been exploited for this investigation. The color-band reconstruction algorithm and the reconstruction techniques, as well and the reactors, are highly versatile instruments that can be applied to many investigations in and out of combustion. These are being pursued by colleagues in several contexts but could be developed much further in many areas.

The particle model described here could make essential contributions to combustion simulators. While the efficiency of the current code increased dramatically as part of this investigation, it still may not be (probably is not) sufficiently efficient to incorporate into such codes. Efforts currently underway by colleagues to increase the efficiency could make these results much more useful. In a related matter, the C++ coding of this model is in general compliance with our research group's coding standards but could be improved significantly.

Finally, some of the predictions made by the particle model here could be more thoroughly verified through additional experimentation. Specifically, the particle and gas composition data predicted by the code possibly could be verified by creative particle characterization and in situ gas characterization techniques. Such verification would prove useful in extending the validation beyond temperature and mass loss data.

Appendix A Sawdust sample preparation procedure

Step 1 Separation with sieve shaker ---- This step preliminarily separates the sample by size. A series of standard sieves were put in a sieve shaker in order from 25 to 80 mesh, with the 80 mesh sieve at the bottom of the stack. The top sieve is filled with sawdust particles and the sieve shaker operates for 40 – 45 minutes. Samples left in each sieve are collected in sample bags respectively.

Step 2 Aerodynamic classification ---- A tunnel separator was built to aerodynamically classify sawdust samples by shape and density (Figure 184). Compressed air is introduced from the air inlet at the bottom of the air distribution pipe. Sawdust particles are fed from the top of the tunnel. Drag forces and gravity determine the trajectory of each particle. Less dense and fuzzy particles end up in tray four or out the end of the tunnel. Trays two and three are normally mixed together and used to get flakes and cylinders, while tray one is used to primarily get cubical/spherical particles. Samples collected in these four trays may have to run through the tunnel separator more than once.

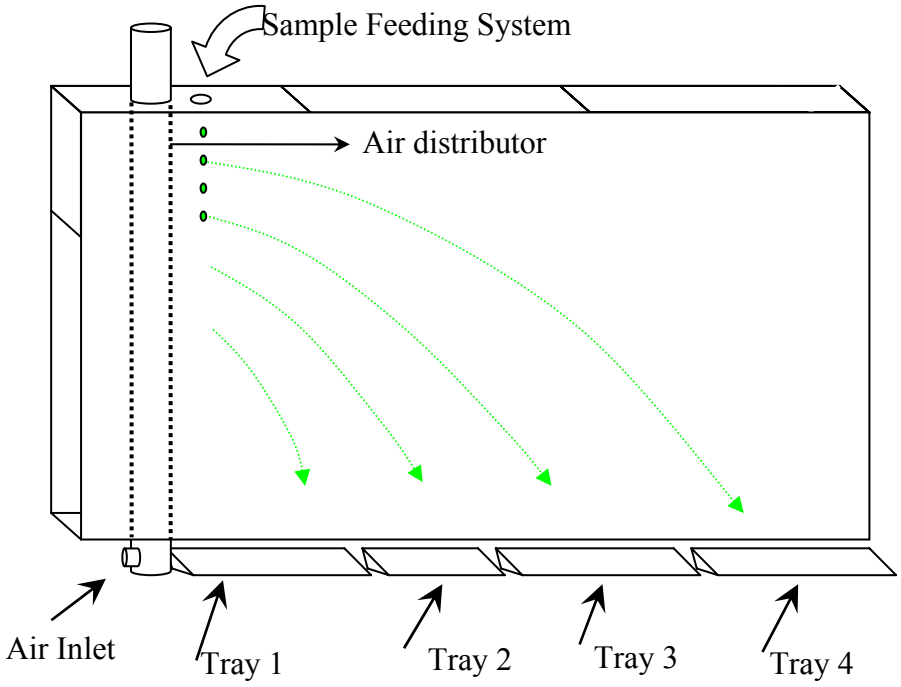

Figure 184 Tunnel separator schematic diagram

Step 3 Shape separation by sieve---- In this step, samples collected with the tunnel separator in tray one, tray two, and tray three are separated into near-spherical, flake-like, and cylinder-like particles. While shaking the sieve with samples in, particles with smaller aspect ratios fall

through the sieve before the larger ones. Based on the residence time difference, particles with different shapes and aspect ratios can be separated. Usually near-spherical particles are pass through the sieve most quickly, followed by flake-like and cylinder-like particles. Samples with different residence time are collected separately.

Step 4 Further shape separation by friction plate ---- A two-foot-long board with 600 grit sand paper along the length of it refines the particle shape separation so that more uniform particles with specific shape and size can be obtained,. The board is held at about a thirty degree angle and one or two grams of sample are poured at the top. Sawdust samples proceed to fall the length of the board, with only the most cubical/spherical particles making it all the way to the bottom. The sand paper has the effect of increasing the frictional resistance to the sawdust particles. Those with the smallest surface-area-to-volume ratio travel the furthest along the length of the board.

Parts or all of these procedures sometimes must be repeated to improve separation.

Appendix B Spectral responsivity data of the CCD camera

Spectral responsivity data of the CCD camera

Red channel		Green channel		Blue channel	
Wavelength	Response	Wavelength	Response	Wavelength	Response
0.35	0	0.35	0	0.35	0
0.353	0	0.353	0.00181	0.353	0.0065
0.369	0	0.368	0.013	0.37	0.068
0.386	0	0.386	0.024	0.386	0.149
0.394	0	0.394	0.026	0.392	0.e196
0.405	0	0.404	0.032	0.403	0.24
0.412	0.00157	0.412	0.036	0.411	0.304
0.419	0.00214	0.419	0.04	0.42	0.374
0.438	0.00488	0.438	0.054	0.429	0.455
0.449	0.00723	0.449	0.067	0.444	0.563
0.459	0.00895	0.458	0.076	0.453	0.68
0.468	0.00952	0.468	0.099	0.467	0.724
0.476	0.00952	0.476	0.143	0.479	0.701

0.484	0.01	0.484	0.229	0.49	0.563
0.492	0.013	0.492	0.36	0.495	0.482
0.502	0.016	0.502	0.539	0.502	0.325
0.516	0.024	0.513	0.721	0.516	0.199
0.529	0.029	0.524	0.845	0.529	0.116
0.54	0.026	0.54	0.906	0.54	0.057
0.55	0.023	0.553	0.859	0.55	0.035
0.56	0.032	0.563	0.785	0.56	0.016
0.57	0.136	0.57	0.683	0.57	0.016
0.58	0.572	0.58	0.569	0.58	0.012
0.59	0.919	0.59	0.419	0.59	0.00679
0.6	1	0.6	0.248	0.6	0.00588
0.61	0.997	0.61	0.12	0.61	0.00197
0.62	0.96	0.62	0.065	0.62	6.83E-04
0.63	0.941	0.63	0.045	0.63	9.16E-04
0.64	0.908	0.64	0.036	0.64	7.58E-04
0.65	0.88	0.65	0.03	0.65	8.44E-04
0.66	0.831	0.66	0.031	0.66	0.00202
0.67	0.784	0.67	0.039	0.67	0.00219
0.68	0.734	0.68	0.058	0.68	0.00284
0.69	0.705	0.69	0.086	0.69	0.00387
0.699	0.658	0.7	0.114	0.7	0.00464
0.71	0.623	0.71	0.126	0.71	0.00375
0.72	0.595	0.72	0.12	0.72	0.00276
0.73	0.55	0.73	0.113	0.73	0.00234

0.74	0.52	0.74	0.125	0.74	0.00345
0.75	0.471	0.75	0.144	0.75	0.00399
0.76	0.439	0.76	0.156	0.76	0.00396
0.77	0.397	0.77	0.164	0.77	0.00469
0.78	0.352	0.78	0.177	0.78	0.011
0.79	0.323	0.79	0.189	0.79	0.046
0.8	0.3	0.8	0.2	0.8	0.123
0.81	0.271	0.81	0.205	0.81	0.178
0.82	0.238	0.82	0.199	0.82	0.189
0.83	0.219	0.829	0.193	0.83	0.19
0.84	0.207	0.84	0.188	0.84	0.185
0.85	0.193	0.849	0.182	0.85	0.178
0.86	0.183	0.859	0.175	0.859	0.172
0.87	0.172	0.87	0.165	0.87	0.162
0.88	0.16	0.88	0.155	0.88	0.152
0.89	0.147	0.89	0.143	0.89	0.141
0.9	0.135	0.9	0.131	0.9	0.13
0.911	0.126	0.91	0.123	0.91	0.121
0.92	0.117	0.92	0.114	0.92	0.113
0.93	0.104	0.93	0.102	0.93	0.101
0.94	0.093	0.94	0.091	0.94	0.09
0.95	0.084	0.95	0.082	0.95	0.08
0.96	0.071	0.96	0.07	0.96	0.069
0.97	0.061	0.97	0.06	0.97	0.059
0.98	0.051	0.98	0.05	0.98	0.049

0.99	0.043	0.99	0.041	0.99	0.041
1	0.035	1	0.034	1	0.034
1.01	0.029	1.01	0.029	1.01	0.028
1.02	0.023	1.02	0.023	1.02	0.022
1.03	0.018	1.03	0.017	1.03	0.017
1.04	0.014	1.04	0.013	1.04	0.013
1.05	0.01	1.049	0.01	1.05	0.00991
1.06	0.0079	1.06	0.0077	1.06	0.00774
1.07	0.00596	1.07	0.00577	1.07	0.00566
1.08	0.00471	1.08	0.00451	1.08	0.00441
1.09	0.00368	1.09	0.0036	1.09	0.00358
1.1	0.0028	1.1	0.0025	1.1	0.0022
1.11	0.00221	1.11	0.002	1.11	0.0018
1.13	0.00123	1.13	0.0012	1.13	0.00115
1.15	0	1.15	0	1.15	0

Appendix C Limitations and accuracy of the particle shape reconstruction algorithm

When creating tetrahedrals out of the interpolated points, concavity presents a challenge. When modeling a hand, for example, the tetrahedralization algorithm does not know where the edge of one finger begins and the other starts. This results in a volume and surface area that would include the space between the fingers as well as an inaccurate surface area and surface rendering. This challenge might be resolved with the idea that every object with concavity can be broken down into smaller convex objects.

The current algorithm needs to know the orientation of the camera with which the three images are taken and the three images have to be taken from three orthogonal directions.

To examine the accuracy of this algorithm for a randomly shaped particle with respect of volume and surface area, two pieces of randomly chosen rocks were used since it is difficult to directly measure small sawdust particle. The volumes of the two rocks were measured with containers filled with water and the surface areas were measured with paper wrapped around the rock surface. The surface-area to volume ratios of the two rocks were calculated using the particle shape reconstruction algorithm with several sets of images taken from different positions, and compared with measured results in Figure 185. Errors of the current algorithm appear in Figure

186. Results show that the average volume calculation error is - 5.1 % and the average surface area calculation error is + 6.2 %. So it results in an average surface-area to volume ratio error of about 10.3 %.

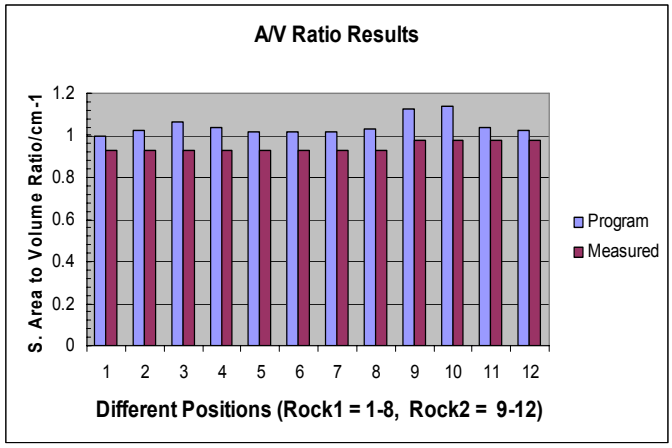

Figure 185 Comparisons of measured and calculated surface-area to volume ratios for two rocks

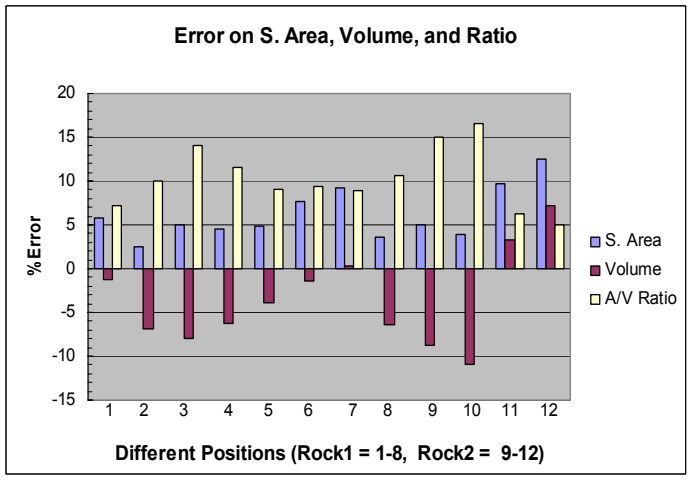

Figure 186 Error analysis of surface area, volume, and surface-area to volume of the particle shape reconstruction algorithm

CONDENSED PHASE THERMOCHEMICAL EQUILIBRIUM MODEL

Abstract

A knowledge of the solid-liquid phase equilibrium of salts and silicates is important to understand ash deposition and slagging problems in black liquor, biomas and coal thermal processing equipment. Computer codes simulating combustion/gasification processes require a good thermodynamic subprogram to describe the effect of slagging on the process. While ash deposits are generally not in equilibrium, thermochemical equilibrium represents the endpoint of their reaction and differences between current conditions and equilibrium conditions affect both chemical and physical (sintering, melting, vaporization) reaction rates. In the present work, a

modified quasichemical model correlates the equilibrium phase diagrams of binary and ternary systems of significance to black liquor, biomass, and coal conversion equipment. Examples of $NaCl-Na_2CO_3$, Na_2S-K_2S, K_2O-SiO_2, and $FeO-SiO_2$ systems validate the model and phase equilibrium algorithm by comparison with literature data. The model is discussed and a comparison of the model predictions and data is given.

Introduction

Biomass and coal thermal conversion equipment (combustors, gasifiers, pyrolyzers, etc.) represent the primary technologies based on ash-forming fuels for power generation. These technologies convert fuel, air/oxygen, and steam to lighter molecules such as water, carbon dioxide, hydrogen, carbon monoxide, and various pollutants. Depending on the technology and fuel, the systems typically operate at temperatures (T) from 600 to 2500 K and at pressures (P) from 0.1 to 50 atmospheres (Smoot and Smith 1985). Due to their high energy conversion efficiency and improving environmental performance, these systems commonly represent large and long-term capital investments at the heart of power production or processing industries. However, converting the organic portion of the fuel to light gases generally impacts both design and operation of such technologies less than the behavior of inorganic compounds. These elements include Si, Al, Fe, Ca, Mg, Na, K, H, Ti, S, P, C, and O. These minerals and oxides form deposits and fly ash that often result in serious operational problems. If fixed beds or entrained beds are used, slagging may be even more serious. Despite the importance of inorganic transformation processes, the chemistry, , phase behavior, and other thermodynamic properties of these inorganic systems are poorly characterized, especially at high temperatures. The difficulty in constructing phase diagrams becomes even more pronounced as the number of components increases and the experiments necessary to obtain the required data become more time-consuming and costly. Models can, in principle, describe chemical equilibria in multicomponent systems. However, the complexity and non-ideality of condensed-phase equilibrium calculations thus far prove too great to yield to the comparatively simple models used to describe gas-phase phenomena In the present work, a modified quasi-chemical model is used to correlate properties of many molten salt and silicate systems of interest to these technologies. This model, together with a generalized phase equilibrium algorithm programmed at BYU, can be used to calculate the phase equilibria of many binary systems. As a subprogram in the BYU ash deposition project, the present model will be integrated into a software package to supplement existing and developing fouling/slagging models in thermal conversion equipment.

Modeling Approach

Salt and silicate properteies in liquid/solid phases depend only weakly on pressure. Therefore, the Gibbs energy (G) in most equation-of-state models for condensed salts and silicates are usually expressed as functions of concentration and temperature (T). However, the complexity of molten salts and silicates leads to phase diagram models involving molten salts and silicates at high *temperatures* that are usually system-dependent. Even for a given modeling approach, the equation forms and the number of modeling parameters used in the model vary with components. This variety increases the difficulty of developing a generalized model to correlate phase equilibria of multicomponent systems. In the present work, we used the modified quasichemical theory initially developed by Pelton and Blander (Pelton and Blander 1986; Blander and Pelton 1987) and later further modified by Pelton et al. (Pelton, Degterov et al. 2000) to model binary liquid solutions. This model allows us to use one uniform approach to model various binary

liquids. The model of Pelton et al. can be used to correlate many different types of binary systems. In this model, Pelton et al. used the "first-nearest-neighbor pairs" as the pair approximation. The atoms or molecules A and B are assumed to be distributed over the sites of a quasilattice. The interactions between different atoms/molecules can be obtained using the pair exchange reaction shown in Equation (1),

$$(\mathrm{A}-\mathrm{A})+(\mathrm{B}-\mathrm{B})=2(\mathrm{A}-\mathrm{B}) \tag{1}$$

where (A−A), (B-B), and (A-B) represent the first-nearest-neighbor pairs of A-A, B-B, and A-B, respectively. The change in G for reaction (1), Δg_{AB}, accounts for the nonconfigurational change in G for the formation of two moles of (A−B) pairs, and is a function of T and mole fraction (x). The molar G value of the system is shown in Equation (2),

$$g=(x_{\mathrm{A}}g_{\mathrm{A}}^{\mathrm{o}}+x_{\mathrm{B}}g_{\mathrm{B}}^{\mathrm{o}})-T\Delta s^{\mathrm{config}}+(n_{\mathrm{AB}}/2)\Delta g_{\mathrm{AB}} \tag{2}$$

where g is the G value per mole of mixture for the binary system, x_{A} and x_{B} are the mole fractions of components A and B, respectively, $g_{\mathrm{A}}^{\mathrm{o}}$ and $g_{\mathrm{B}}^{\mathrm{o}}$ are the molar G values of the pure components A and B, respectively, and $\Delta s^{\mathrm{config}}$ is the configurational entropy change and is defined in Equation (3),

$$\Delta s^{\mathrm{config}}=-R(x_{\mathrm{A}}\ln x_{\mathrm{A}}+x_{\mathrm{B}}\ln x_{\mathrm{B}})-R\left(n_{\mathrm{AA}}\ln\frac{x_{\mathrm{AA}}}{Y_{\mathrm{A}}^2}+n_{\mathrm{BB}}\ln\frac{x_{\mathrm{BB}}}{Y_{\mathrm{B}}^2}+n_{\mathrm{AB}}\ln\frac{x_{\mathrm{AB}}}{2Y_{\mathrm{A}}Y_{\mathrm{B}}}\right) \tag{3}$$

where R is the gas constant, x_{AA}, x_{BB}, and x_{AB} are the mole fractions of A-A, B-B, and A-B pairs, respectively, n_{AA}, n_{BB}, and n_{AB} are the numbers of moles of A-A, B-B, and A-B pairs, respectively, in one mole of solution, and Y_{A} and Y_{B} are the equivalent fractions of pairs containing components A and B, respectively. Equation (4) defines the Y_{A} and Y_{B} terms.

$$Y_{\mathrm{A}}=x_{\mathrm{AA}}+\frac{x_{\mathrm{AB}}}{2}\quad\text{and}\quad Y_{\mathrm{B}}=x_{\mathrm{BB}}+\frac{x_{\mathrm{AB}}}{2} \tag{4}$$

Most terms thus far discussed involve no explicit interactions. The Δg_{AB} term defined in Equation (1), which encapsulates the interactions, is usually divided into two terms: the enthalpy change due to mixing, Δh_{AB}, and the nonconfigurational entropy change, Δs_{AB}. Equation (5) gives the expression for Δg_{AB}

$$\Delta g_{\mathrm{AB}}=\Delta h_{\mathrm{AB}}-T\Delta s_{\mathrm{AB}}. \tag{5}$$

Both Δh_{AB} and Δs_{AB} in Equation (5) are assumed to be independent of T and are usually expressed as polynomial functions of x_{A} and x_{B}, or functions of Y_{A} and Y_{B}, or functions of x_{AA} and x_{BB}, with the coefficients of each polynomial function determined from experimental data using a least-squares fitting method.

Solids may be modeled as pure minerals or solid solutions, depending on the crystal structures of the compounds in the solid phase. Some intermediate compounds may also exist in the solid phase. The thermodynamic properties of stable compounds can be found in thermodynamic

databases (Bale, Chartrand et al. 2002; McBride, Zehe et al. 2002) or in published articles. Values for the thermodynamic properties of unstable or intermediate compounds result by fitting them to experimental. Solid solutions can also be modeled using the modified quasi-chemical approach. However, this approach is seldom used for solid solutions. Instead, the Bragg-Williams approach (Bragg and Williams 1934) with an ideal configurational entropy is often used and the excess *G* values are expressed as polynomial functions of mole fractions or equivalent fractions as shown in Equations (6) through (8). Most solid solutions have more than one sublattice and require more complex models within the framework of the sublattice compound energy formalism.

$$\Delta g_{AB} = \sum_{i=0}^{n} g_i x_A^i, \tag{6}$$

$$\Delta g_{AB} = g_0 + \sum_{i=1}^{n} g_i Y_A^i + \sum_{j=1}^{n} g_j Y_B^i, \tag{7}$$

$$\Delta g_{AB} = g_0 + \sum_{i=1}^{n} g_i x_{AA}{}^i + \sum_{j=1}^{n} g_j x_{BB}{}^i \tag{8}$$

When the liquid and solid phases have been modeled and the modeling parameters have been determined, optimizes their values. This analysis uses a program initially presented by Greenberg (Greenberg 1986) and programmed at BYU for the minimization process. Many simpler algorithms either neglect ion formation or implicitly assume that activity scales with mole fraction, or both. A computation process diagram is shown in Figure 187.

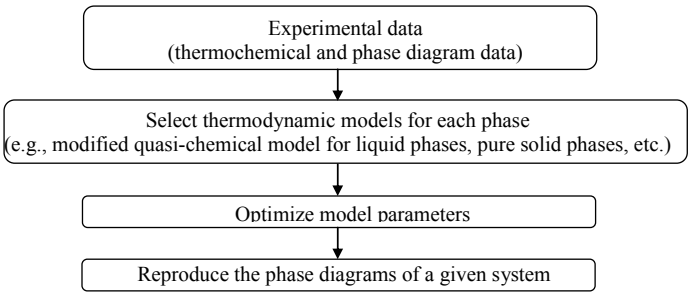

Figure 187: Diagram of phase equilibrium computation

Modeling Results

Many binary salt and silicate phase diagrams have been modeled and are available from the ash deposition group at Brigham Young University (Liu, Oscarson et al. 2006): NaCl-Na_2CO_3, KCl-K_2CO_3, NaCl-Na_2SO_4, KCl-K_2SO_4, K_2CO_3-KOH, KCl-$MgCl_2$, Na_2O-SiO_2, CaO-SiO_2, Al_2O_3-SiO_2, FeO-SiO_2, Na_2S-K_2S, etc. In this paper, phase diagrams of NaCl-Na_2CO_3, Na_2S-K_2S, K_2O-SiO_2, and FeO-SiO_2 are shown and discussed.

Error! Reference source not found. illustrates the phase diagram of a liquid NaCl-Na_2CO_3 solution in equilibrium with pure solid NaCl and/or pure solid Na_2CO_3. The Δs_{AB} term in Equation (5) was assumed to be zero in the modified quasi-chemical model. The coefficients in the Δh_{AB} polynomial expression were optimized and Δh_{AB} is expressed as a function of the mole fraction of NaCl-NaCl pairs as shown in Equation (9)

$$\Delta h = 238.384 + 85.7575 x_{AA} + 96.6826 x_{AA}^2, \tag{9}$$

where x_{AA} represents the mole fraction of NaCl-NaCl pairs. The results calculated using the model agree well with the measured values, and the calculated eutectic point (0.449, 633 ºC) is well within the reported eutectic point region (0.41−0.47, 632−645 ºC) (Amadori 1914; Niggli 1919; Belyaev and Sholokhovich 1953).

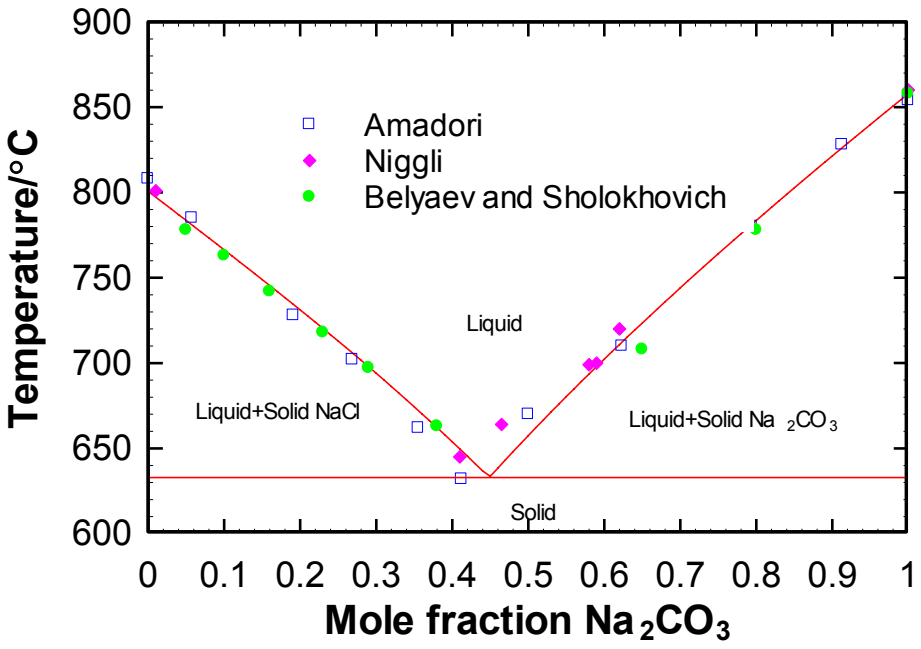

Figure 188: *T-x* phase diagram of the Na_2CO_3-NaCl system. □ Amadori data (Amadori 1914), ♦ Niggli data (Niggli 1919), ● Belyaev and Sholokhovich data (Belyaev and Sholokhovich 1953), (—) Results calculated using the model.

Even though the ionic diameters of K^+ and Na^+ are rather different, it is quite common to find complete solid solutions over the whole composition range for binary salt systems with a common anion (Lindberg, Backman et al. 2006). Thus, solid solutions containing Na_2S and K_2S may form. Mäkipää and Backman (Mäkipää and Backman 1998) tentatively constructed the liquid-solid phase diagram of the K_2S-Na_2S system. A minimum solidus point at $x_{K_2O} \approx 0.65$ and T = 1009 K was reported (Mäkipää and Backman 1998). With no further experimental data available, Lindberg et al. (Lindberg, Backman et al. 2006) pointed out that the binary liquid and solid Na_2S-K_2S systems can be modeled using the ideal solution and the regular solution approaches, respectively. The ideal mixing G equation for both phases (liquid and solid

solutions) and the excess G equation for the solid solution used in the study of Lindberg et al. are shown in Equations (10) and (11), respectively.

$$\Delta g^{\text{ideal}} = 2RT(x_{K_2S} \ln x_{K_2S} + x_{Na_2S} \ln x_{Na_2S}) \tag{10}$$

$$g^{\text{ex}} / (\text{J} \cdot \text{mol}^{-1}) = 26776 x_{Na_2S} x_{K_2S} \tag{11}$$

where Δg^{ideal} and g^{ex} represent the ideal mixing and excess G values, respectively. There is a constant number "2" on the right side of Equation 12 because each mole of Na_2S or K_2S contributes 2 moles of alkali cations.

In Figures and, the pure-species G values used to compute the phase diagrams are based on the NASA thermodynamic database (McBride, Zehe et al. 2002). Liquid heat capacities were assumed constant at T values below the melting points because these heat capacities are nearly independent of T at conditions above the melting points.

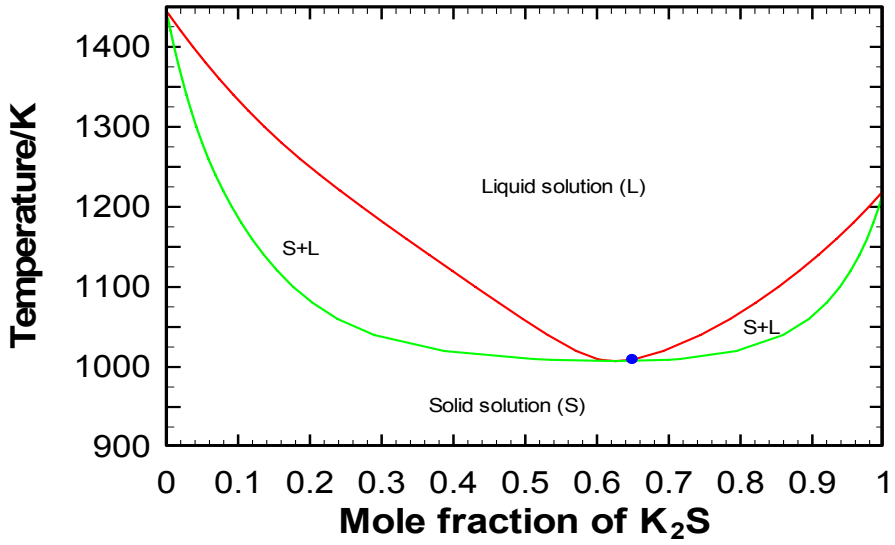

Figure 189: Liquid-solid solution phase diagram of the K_2S-Na_2S system. The solidus line is calculated using the regular solution theory (Lindberg, Backman et al. 2006) and the liquidus line is calculated using the ideal solution assumption. ● Reported lowest solidus temperature point (Mäkipää and Backman 1998).

Many fuel deposits have large fractions of oxides and silicates. In Figure 190, a phase diagram of a binary oxide/silicate system (K_2O-SiO_2) is given. The parameters in the liquid solution model were optimized using measured data (Kracek, Bowen et al. 1937) for liquid solutions in equilibrium with K_2SiO_3(s) and SiO_2(s), respectively. The G values of pure liquid species, pure solid K_2SiO_3, and pure solid SiO_2 use the equations reported by Wu et al. (Wu, Eriksson et al. 1993). The G value of pure $K_2Si_2O_5$(s) was calculated from the measured data (Kracek, Bowen et al. 1937) of $K_2Si_2O_5$(s) in equilibrium with the liquid solution (Equations (12) and (13)). Equation (14) shows the optimized Gibbs energy equation of $K_2Si_2O_5$(s) used in the present work.

$$K_2O(l) + 2SiO_2(l) = K_2Si_2O_5(s) \tag{12}$$

$$G_{K_2Si_2O_5(s)}(T) = u_{K_2O(l)}(x,T) + 2u_{SiO_2(l)}(x,T) \tag{13}$$

$$\frac{G_{K_2Si_2O_5(s)}}{\text{J/mol}} = -2.549\times10^6 + 1068T - \frac{11623}{T} - 191.4T\ln(T) + 1.435\times10^{-6}T^3 \tag{14}$$

where u in Equation (13) represents the chemical potential.

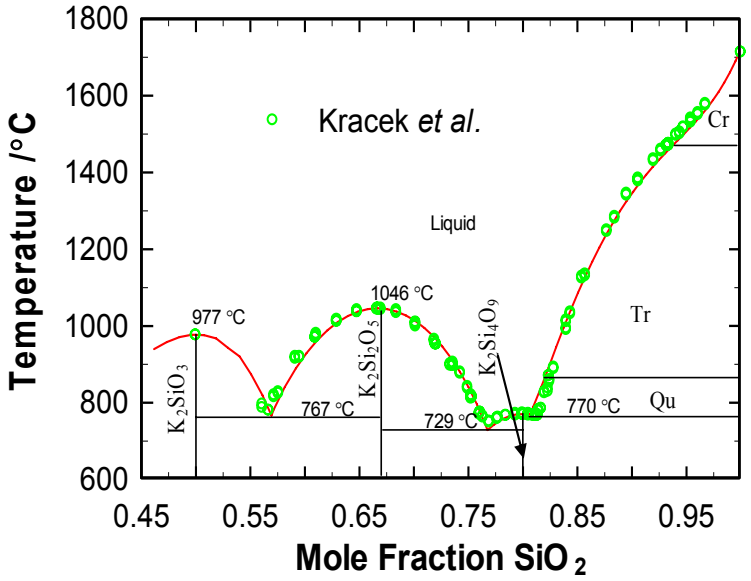

Figure 190: *T-x* phase diagram of K_2O-SiO_2. ○ Kracek et al.(Kracek, Bowen et al. 1937). Cr, Tr, and Qu represent the three forms of crystalline SiO_2. (—) Results calculated using the model.

Phase diagrams of silicate systems are more complex than those of salts (Figures). One possible reason is that silica is highly polymerized. When silica mixes with some other oxides, the structure of the mixture becomes highly networked resulting in large property changes. Another possible reason derives from the formation of many intermediate compounds during the mixing process. Depending on their stability, these intermediate compounds may decompose or change into other compounds as T and x change. The high melting point (1046 ºC) of $K_2Si_2O_5$(s) in Figure 190 relative to other intermediate compounds implies that solid $K_2Si_2O_5$ is more stable at compositions 0.57~0.77 than other reported solid compounds (K_2SiO_3, $K_2Si_4O_9$, etc.) (Kracek, Bowen et al. 1937).

Figure 191 illustrates a phase diagram involving iron and silicates (FeO-SiO_2). The G values of pure components were calculated using the equations reported by Romero-Serrano and Pelton (Romero-Serrano and Pelton 1999). The parameters of the liquid solution model were optimized using the phase equilibrium data of liquid solution in equilibrium with $FeSiO_4$(s), FeO(s), and SiO_2(Tr). In the phase diagram for FeO-SiO_2, only one intermediate compound, $FeSiO_4$, has

been reported (Bowen and Schairer 1932). The relatively small flat region around $x_{SiO_2} \approx 0.33$ implies that the association between SiO_2 and FeO results in species of limited stability which can easily decompose as T increases or composition changes. An immiscible liquid region was found using the liquid solution model at $x_{sio2} \approx 0.6$~0.99 and may partially account for the variety of mineral types in the slags.

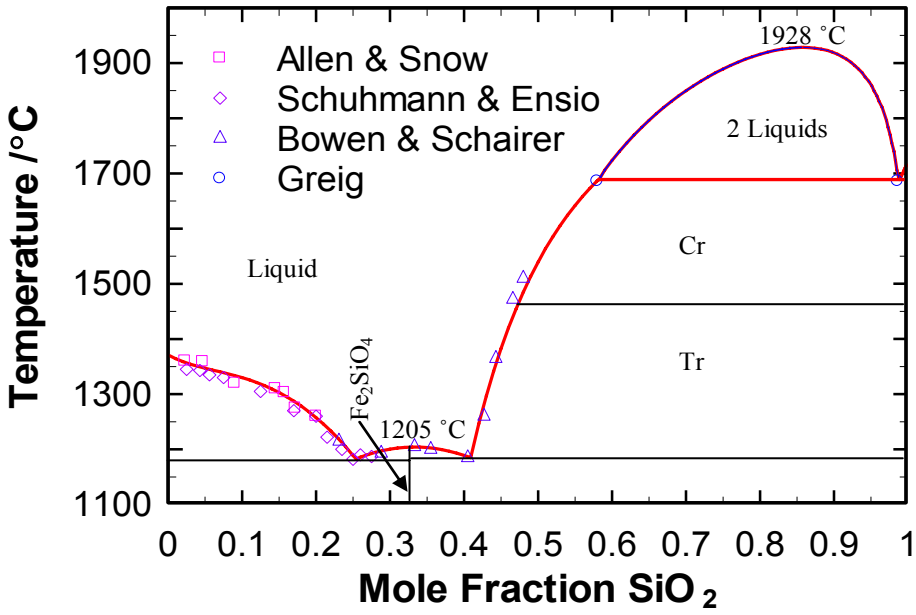

Figure 191: *T-x* phase diagram of FeO-SiO_2. Experimental data: □ Allen and Snow (Allen and Snow 1955), ◊ Schuhmann and Ensio (Schuhmann and Ensio 1951), Δ Bowen and Schairer (Bowen and Schairer 1932), ○ Greig (Greig 1927). (—) Results calculated using the model.

Conclusions

A modified quasi-chemical model and a generalized Gibbs energy algorithm can calculate phase behavior of salt and silicate systems of importance to biomass and coal thermal process systems. The NaCl-Na_2CO_3, Na_2S-K_2S, K_2O-SiO_2, and FeO-SiO_2 systems reported in this paper validate the model and phase diagram algorithm and provide evidence that the *G* models of the low-order phases can be used in extrapolations to multi-components in high-order phases once proper mixing rules are found.

References

[1] L.D. Smoot, P.J. Smith, Coal Combustion and Gasification, Plenum Press, New York, New York, N. Y., 1985.

[2] A.D. Pelton, M. Blander, "Thermodynamic Analysis of Ordered Liquid Solutions by a Modified Quasi-Chemical Approach - Application to Silicate Slags," *Metallurgical Transactions B-Process Metallurgy* 17 (1986) 805-815.

[3] M. Blander, A.D. Pelton, "Thermodynamic Analysis of Binary-Liquid Silicates and Prediction of Ternary Solution Properties by Modified Quasi-Chemical Equations," *Geochimica et Cosmochimica Acta* 51 (1987) 85-95.

[4] A.D. Pelton, S.A. Degterov, G. Eriksson, C. Robelin, "The Modified Quasichemical Model I - Binary Solution," *Metallurgical And Materials Transactions B-Process Metallurgy And Materials Processing Science* 31 (2000) 651-659.

[5] C. Bale, P. Chartrand, S.A. Degterov, G. Eriksson, K. Hack, R. Ben Mahfoud, J. Melancon, A.D. Pelton, S. Petersen, "FactSage Thermochemical Software and Database,". *Calphad-Computer Coupling of Phase Diagrams and Thermochemistry* 26 (2002) 189-228.

[6] B. J. McBride, M.J. Zehe, S. Gordon, *NASA Glenn Coefficients for Calculating Thermodynamic Properties of Individual Species*, Glenn Research Center, Cleveland, Ohio, 2002.

[7] W.L. Bragg, E.J. Williams, " Effect of thermal agitation on atomic arrangement in alloys," *Proceedings of the Royal Society (London)* A145 (1934) 699-730.

[8] J.P. Greenberg, *The Design of Chemical Equilibrium Computation Algorithms and Investigations into the Modeling of Silicate Phase Equilibria*, Ph. D. Dissertation, University of California, San Diego, San Diego, CA, 1986.

[9] B. Liu, J. L. Oscarson, R. M. Izatt, Larry L. Baxter, *Unpublished Data*, Brigham Young University: Provo, UT, 2006.

[10] M. Amadori, Atti della Accademia Nazionale dei Lincei, Classe di Scienze Fisiche, Matematiche e Naturali, Rendiconti 22 (1914) 366-372.

[11] P. Niggli, "Carbonate and Chloride Melts" *Zeitschrift Anorganische Allgemeine Chemie*., 106 (1919) 126-142.

[12] I.N. Belyaev, M. L. Sholokhovich, "Reciprocal System of Sodium and Barium Chlorides and Carbonates," *Sbornik Statei Obshchei Khimiya Akadamie Nauk S.S.S.R* 1 (1953) 134-143.

[13] D. Lindberg, R. Backman, M. Hupa, P. Chartrand, "Thermodynamic Evaluation and Optimization of the (Na+K+S) System" *Journal of Chemical Thermodynamics* 38 (2006) 900-915.

[14] M. Mäkipää, R. Backman, "Corrosion of Floor Tubes in Reduced Kraft Smelts: Studies on the Effect of Chlorine and Potassium," in: *9th International Symposium on Corrosion in the Pulp and Paper Industry* 1998.

[15] F.C. Kracek, N.L. Bowen, G. W. Morey, "Equilibrium Relations and Factors Influencing Their Determination in the System K_2SiO_3-SiO_2," *Journal of Physical Chemistry* 41 (1937) 1183-1193.

[16] P. Wu, G. Eriksson, A.D. Pelton, "Optimization of the Thermodynamic Properties and Phase-Diagrams of the Na_2O-SiO_2 and K_2O-SiO_2 Systems," *Journal of the American Ceramic Society* 76 (1993) 2059-2064.

[17] A. Romero-Serrano, A.D. Pelton, "Thermodynamic analysis of binary and ternary silicate systems by a structural model," *Isij International*, 39 (1999) 399-408.

[18] N. L. Bowen, J.F. Schairer, "The System: FeO-SiO_2" *American Journal of Science* 24 (1932) 177-213.

[19] W. C. Allen, R.B. Snow, "The Orthosilicate-Iron Oxide Portion of the System CaO-"FeO"-SiO_2," *Journal of the American Ceramic Society* 38 (1955) 264-280.

[20] R. Schuhmann, Jr., P.J. Ensio, "Thermodynamics of Iron Silicate Slags: Slags Saturated with γ Iron," *Journal of Metals* 3 (1951) 401-411.

[21] J.W. Greig, "Liquid Immiscibility in the System: FeO-Fe_2O_3-$Al2O_3$-SiO_2," *American Journal of Science* 14 (1927) 473-484.

Entrained Flow Gasifier Model Design

This document outlines the design of the entrained-flow gasifier model (EFGM). EFGM provides rapid (< 60 s) estimates of gasifier performance suitable for monitoring and eventually control of pilot and commercial entrained-flow coal gasification systems.

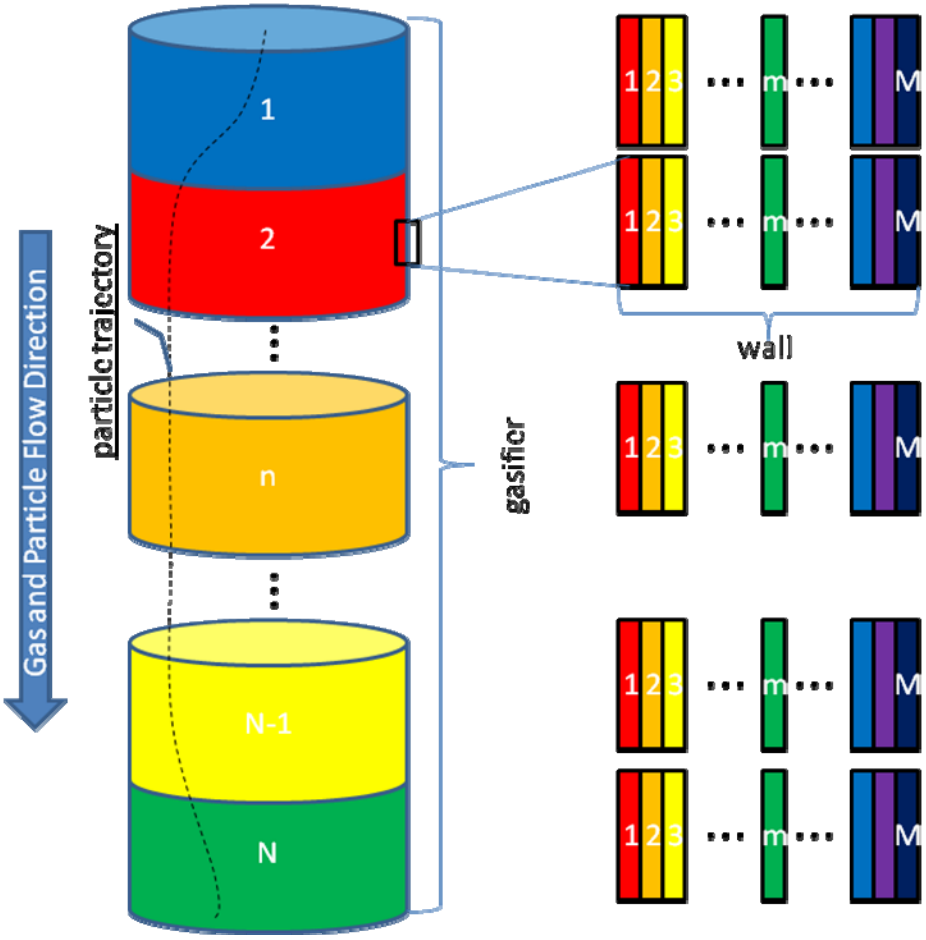

Figure 192 Schematic diagram of the gasifier model domain.

Figure 192 illustrates the geometry and computational domain of the model which is described as follows. The model describes the gas-phase compositions, temperatures, and velocity in an Eulerian framework with one independent spatial dimension (assumes rapid and perfect mixing in the other two dimensions) and as a function of time, where the dimension is along the dominant flow path. Figure 192 illustrates the first and last two of N nodes in this flow direction and an arbitrary intermediate node labeled n, all indicated as cylinders along the generally down-fired flow direction. The colors correspond approximately to the temperatures in a typical gasifier, beginning with cool inlets, producing high gas temperatures as the volatiles combine with oxygen, and decreasing temperature as the endothermic gasification reactions proceed and as heat is lost from the vessel. The flow field is more accurately described as axisymmetric and radially invariant (no gradients in either the tangential or radial directions) than one dimensional.

That is, velocities are defined in all three dimensions, but there are no gradients in velocity in the tangential or radial directions. Thus, flows expand from a central inlet and contract to a central exit and may swirl, but the only dimension that shows variation in the expanding, contracting, or swirling flow is the axial dimension.

The model also describes the particle temperatures, compositions, and trajectories within gas flow field. The particle trajectories are three dimensional and depend on residence time and Eulerian time. Figure 192 illustrates a single particle trajectory. Typically there would be multiple trajectories representing different particle sizes, starting locations, or types.

Finally, the model includes a two dimensional, time dependent Eulerian wall model, with one dimension associated with the gas-phase nodes and a second dimension orthogonal to the gas flow direction. Figure 192 illustrates the first and last three and an arbitrary intermediate node of M wall nodes at each of the N gas nodes. The color again represents typical temperature variation within the wall, with the inside being the hottest and a monotonic but non-linear temperature decrease with increasing radial distance. The inside boundary of this node is the edge of the deposit or slag layer generated by the particles and the outside extends through the deposit/slag layer, the ceramic liner, to the outer edge of the metallic containment vessel where a boundary condition can be identified. The wall model includes deposit accumulation and chemical and physical interactions with the gasifier liner, including its dissolution and spalling. As indicated, the physical dimensions of the each slag layer are very small compared to those of the overall reactor.

The model is designed in UML and written primarily in C++ according to object-oriented design principles. This document steps through the overall design and designs of the principle packages using Use Case diagrams and related UML constructs.

Overall Model Design

Figure 193 illustrates the overall model structure. All of the components shown at this level are packages, i.e., generic aggregates of model capability without specific attributes or methods. A user interface provides information needed to describe the particle and gas models. This interface may be a GUI interfacing with a person or a set of subprogram calls from a supervisory control or other computer-based algorithm. The combination of the particle and gas models provides estimates of the wall behavior, specifically the slagging and liner degradation rates. These three components (particle, wall, and gas models) constitute the essential model components. They are interdependent and time variant, although early implementations of the model ignore the time variation. The time variation included here represents relatively long (many minutes to a few hours) time steps during which the gas and particle models change little. Only the boundary conditions of the gas and particle models change, and these changes are dominated by temperature. The wall model, however, changes dramatically, with deposit thickness, slag formation, etc. changing at each time step.

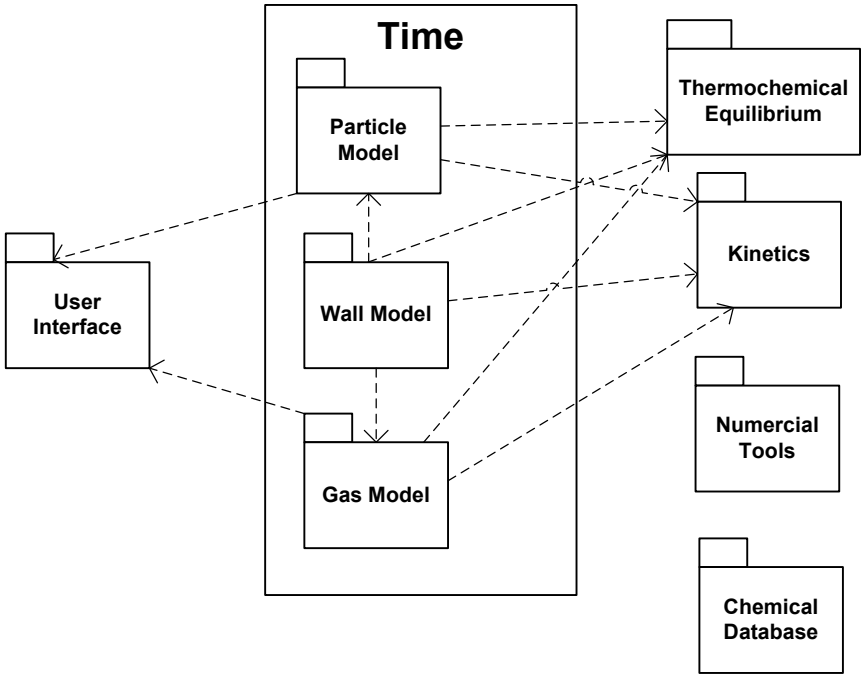

Figure 193 Use Case diagram of EFGM

There are many utility-style model components that support this core. The utility packages shown in Figure 193 include equilibrium models, kinetic rate models, numerical tools (matrix inversions, ODE solvers, etc.), and chemical databases. These interact with most or all major portions of the model in generic ways, and their dependencies do not appear directly in this figure.

The results of the model include spatially (one dimension along the flow path) dependent gas composition, temperature, and velocity estimates with corresponding residence-time-dependent particle composition, position, velocity, and temperature estimates and, at each flow node, one-dimensional (orthogonal to the flow direction) wall composition, phase, thickness, heat flux, flow velocity (for slag), thermal conductivity, strength, porosity, and temperature estimates. The wall model also includes emissivity estimates at the innermost node, Node 1. The remainder of this document discusses each of the major model subcomponents.

Particle Model

The core of the particle model (Figure 194) is the trajectory class. This class stores the essential particle properties as a function of residence time, including: the particle position vector (three components) and corresponding turbulent variations, the particle velocity vector (three components) and corresponding turbulent fluctuations, the n-dimensional particle composition vector, the particle size, temperature, burnout, mass, density, emissivity, and viscosity scalars. These are computed as a function of time using the ordinary differential equation (ODE) solver from the numerical methods package. This solution requires supporting subroutines that calculate the rate of change of each variable as a function of position in the reactor and time. These appear in the diagram as separate classes that compute, for example, the various forms of heat transfer (convective, radiative, and reaction-driven), the major organic reactions (drying, devolatilization,

oxidation/gasification), the primary inorganic reactions, the drag force, etc. In fact, some or all of these computations may be incorporated as part of the ComputeProperties subprogram. There is rarely an explicit time dependence, but there is a strong dependence on position in the reactor. The subprogram that computes all of these values as a function of time is called ComputeLagProperties.(compute Lagrangian properties).

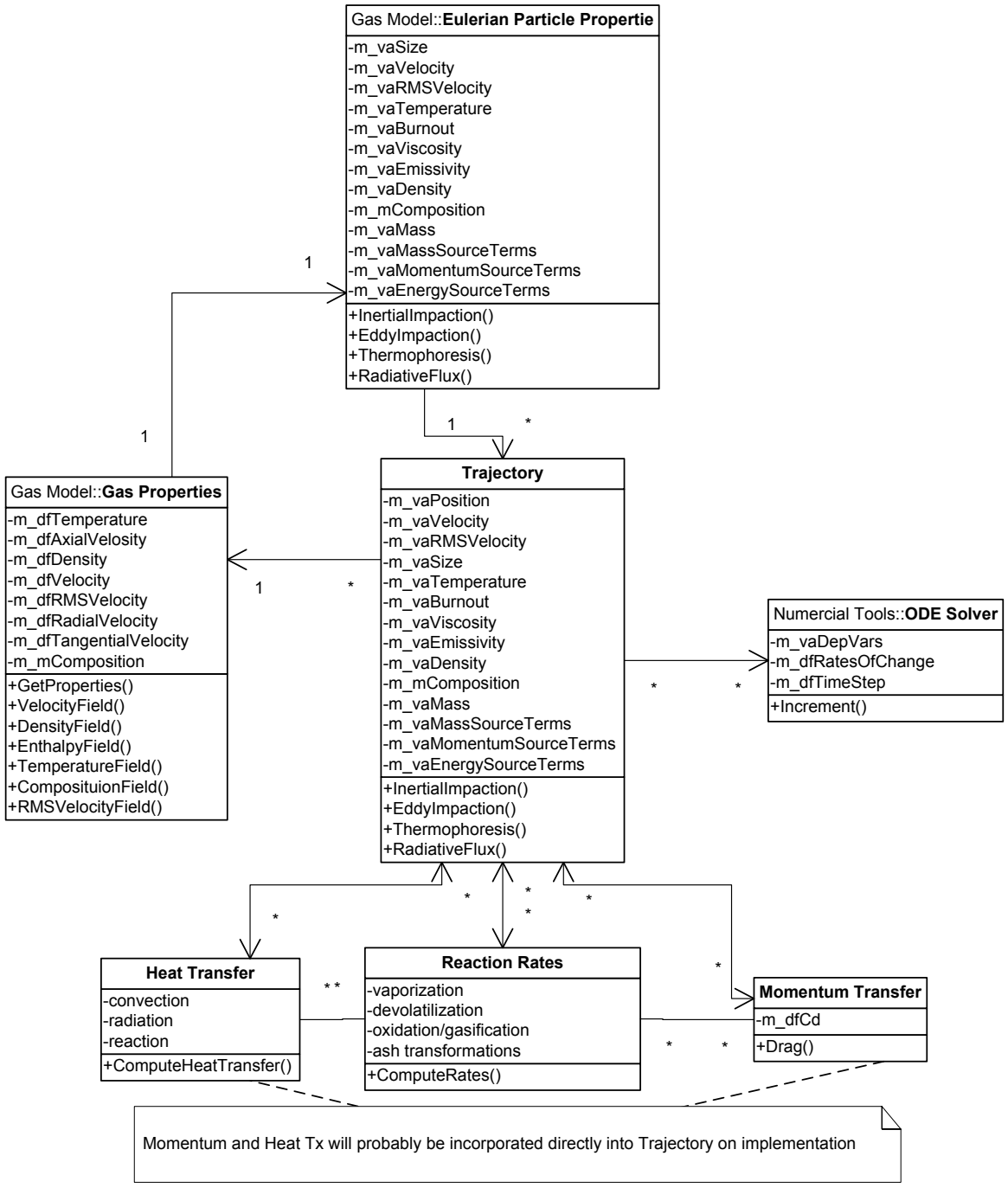

Figure 194 Particle Use Case Diagram

During the computation, the Eulerian grids store statistical particle information such that most of the particle properties can be represented as Eulerian variables. These appear in the Eulerian Particle Properties class, which is part of the gas-phase package (discussed next). Not shown but essential for he computations are the variances of each of the properties listed. That is, both average particle size at a given location in the reactor and the variance/standard deviation in the size are stored. This information and source terms(mass, momentum, and energy) for the gas phase computations are the major contributions of the particle model to the gas-phase model. The gas-phase model provides the gas property field information (gas velocities, temperatures, composition, turbulence, etc.) for the particle model.

As indicated in the diagram, the particle and gas models are interdependent. Computing consistent descriptions of both requires iteration between the particle and gas models.

Gas Model

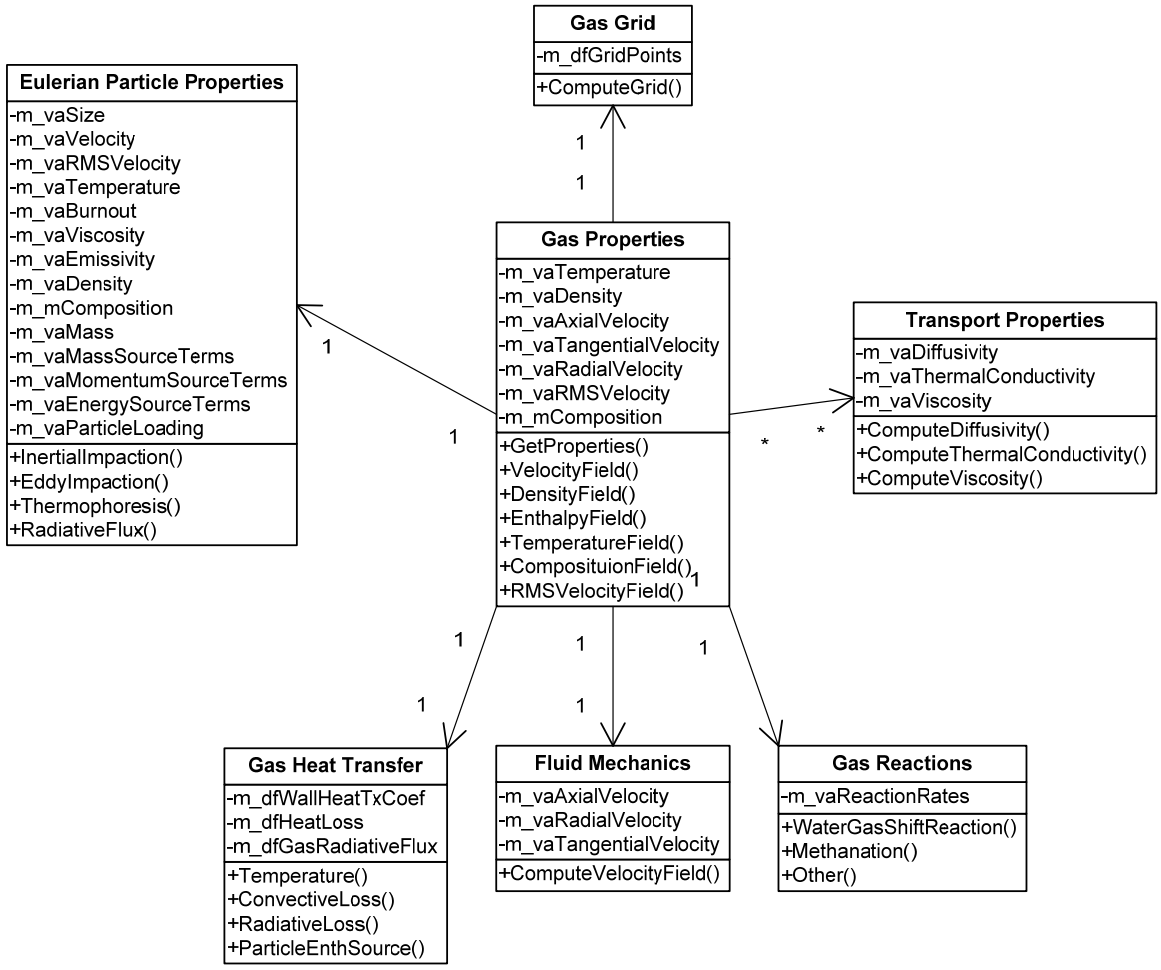

Figure 195 Gas Model Use Case Diagram

The essential elements of the gas model appear in Figure 195. The central component of this model is the Gas Properties class. This class computes, stores, and provides an interface for the

Eulerian gas-phase properties of temperature, velocity and root-mean-square (rms) velocity vectors in three dimensions,

Wall Model

Figure 196 illustrates the Use Case diagram for the most essential components of the wall model. As shown, a wall grid establishes the location of each node, which may vary with time and axial position in the model. At each of the wall node locations, the wall model includes the attributes listed in the first section of the Wall Properties class.

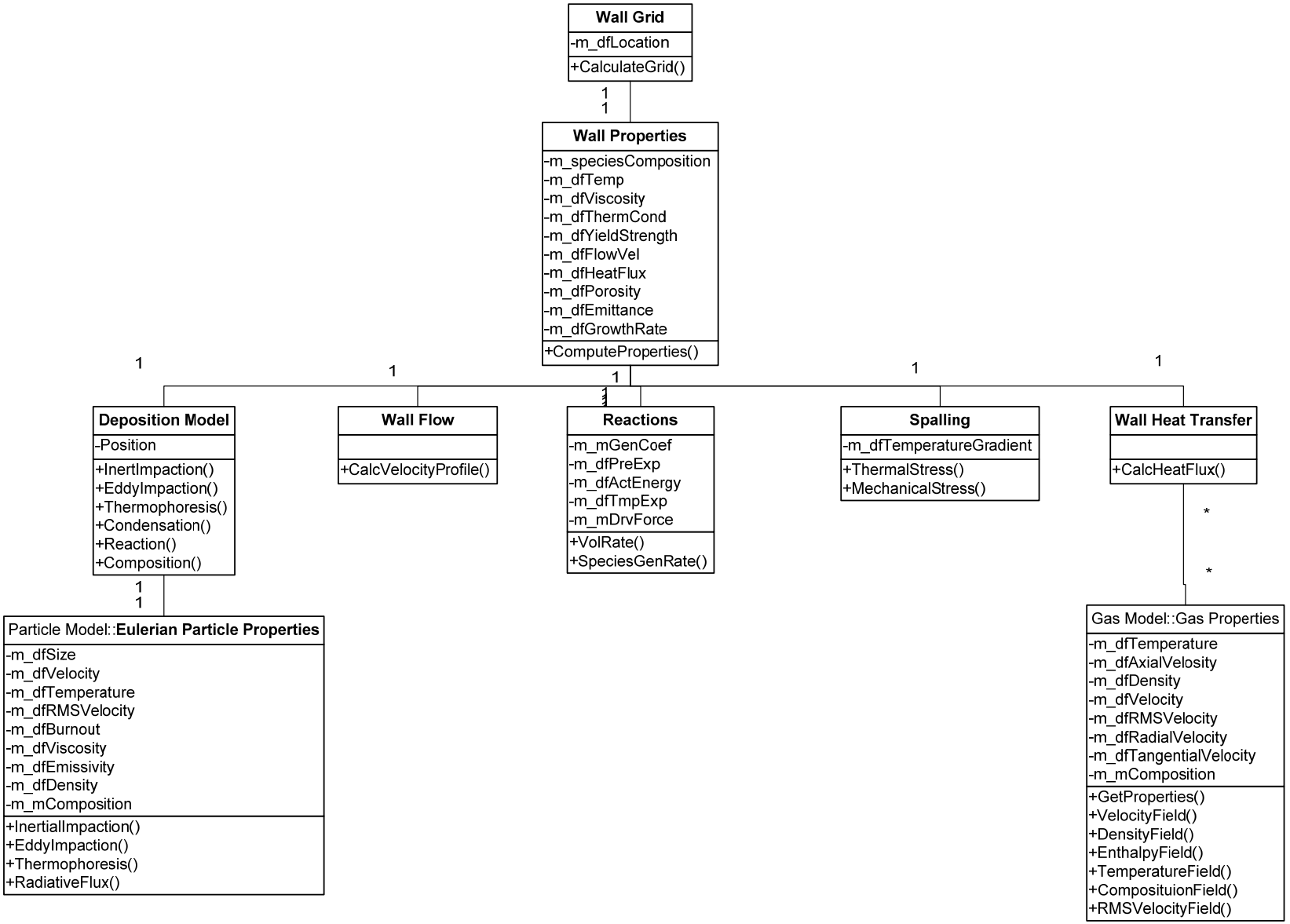
Wall Grid
-m_dfLocation
+CalculateGrid()
1
1
Wall Properties
-m_speciesComposition
-m_dfTemp
-m_dfViscosity
-m_dfThermCond
-m_dfYieldStrength
-m_dfFlowVel
-m_dfHeatFlux
-m_dfPorosity
-m_dfEmittance
-m_dfGrowthRate
+ComputeProperties()
1
1
1
1
1
1
1
Deposition Model
-Position
+InertImpaction()
+EddyImpaction()
+Thermophoresis()
+Condensation()
+Reaction()
+Composition()
1
1
Particle Model::Eulerian Particle Properties
-m_dfSize
-m_dfVelocity
-m_dfTemperature
-m_dfRMSVelocity
-m_dfBurnout
-m_dfViscosity
-m_dfEmissivity
-m_dfDensity
-m_mComposition
+InertiallImpaction()
+EddyImpaction()
+Thermophoresis()
+RadiativeFlux()
Wall Flow
+CalcVelocityProfile()
Reactions
-m_mGenCoef
-m_dfPreExp
-m_dfActEnergy
-m_dfTmpExp
-m_mDrvForce
+VolRate()
+SpeciesGenRate()
Spalling
-m_dfTemperatureGradient
+ThermalStress()
+MechanicalStress()
Wall Heat Transfer
+CalcHeatFlux()
*
*
Gas Model::Gas Properties
-m_dfTemperature
-m_dfAxialVelosity
-m_dfDensity
-m_dfVelocity
-m_dfRMSVelocity
-m_dfRadialVelocity
-m_dfTangentialVelocity
-m_mComposition
+GetProperties()
+VelocityField()
+DensityField()
+EnthalpyField()
+TemperatureField()
+ComposituionField()
+RMSVelocityField()

Figure 196 Use Case diagram of the essential wall model components

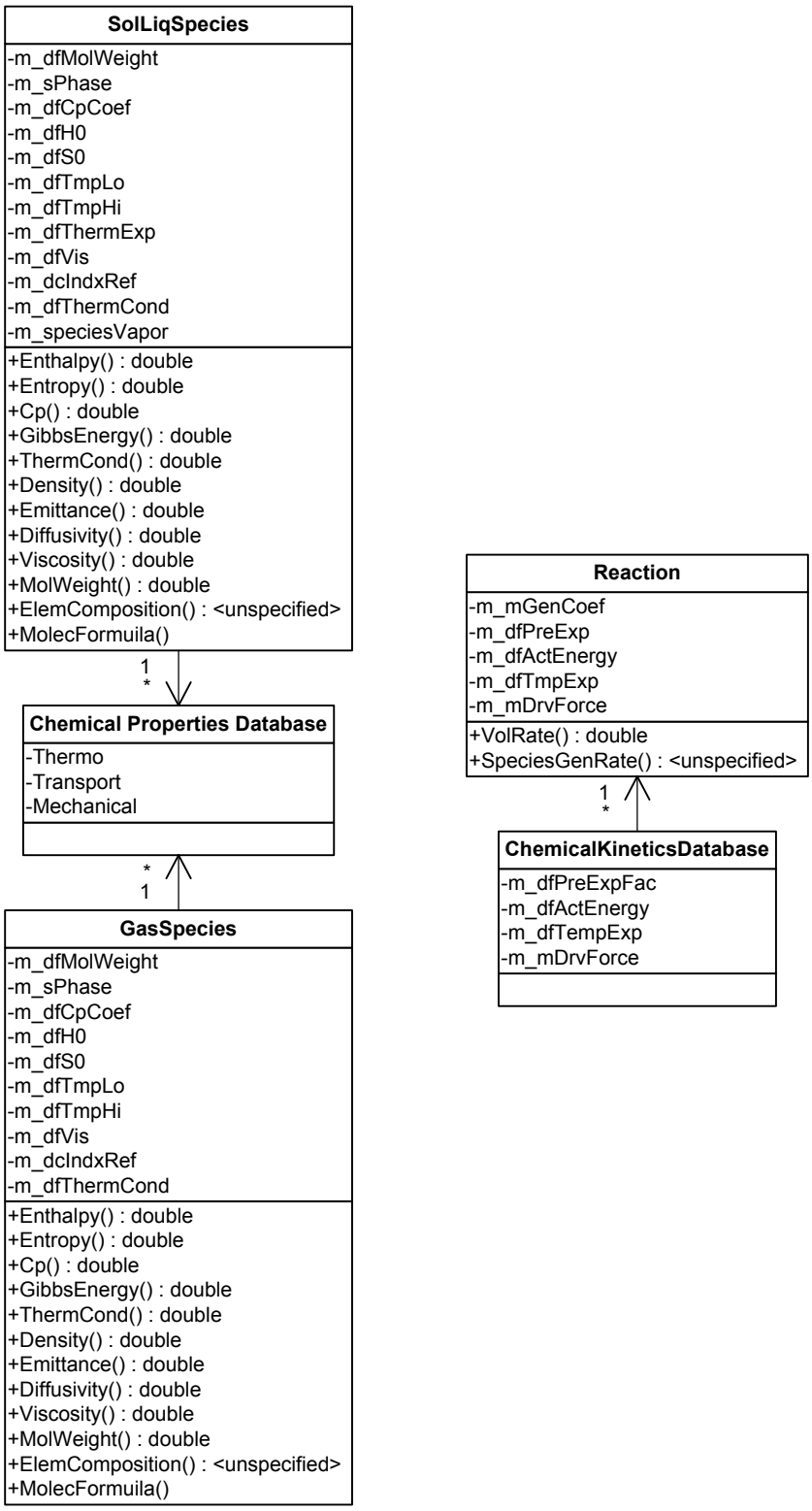
SolLiqSpecies
-m_dfMolWeight
-m_sPhase
-m_dfCpCoef
-m_dfH0
-m_dfS0
-m_dfTmpLo
-m_dfTmpHi
-m_dfThermExp
-m_dfVis
-m_dcIndxRef
-m_dfThermCond
-m_speciesVapor
+Enthalpy() : double
+Entropy() : double
+Cp() : double
+GibbsEnergy() : double
+ThermCond() : double
+Density() : double
+Emittance() : double
+Diffusivity() : double
+Viscosity() : double
+MolWeight() : double
+ElemComposition() : <unspecified>
+MolecFormuila()
1
*
Chemical Properties Database
-Thermo
-Transport
-Mechanical
*
1
GasSpecies
-m_dfMolWeight
-m_sPhase
-m_dfCpCoef
-m_dfH0
-m_dfS0
-m_dfTmpLo
-m_dfTmpHi
-m_dfVis
-m_dcIndxRef
-m_dfThermCond
+Enthalpy() : double
+Entropy() : double
+Cp() : double
+GibbsEnergy() : double
+ThermCond() : double
+Density() : double
+Emittance() : double
+Diffusivity() : double
+Viscosity() : double
+MolWeight() : double
+ElemComposition() : <unspecified>
+MolecFormuila()
Reaction
-m_mGenCoef
-m_dfPreExp
-m_dfActEnergy
-m_dfTmpExp
-m_mDrvForce
+VolRate() : double
+SpeciesGenRate() : <unspecified>
1
*
ChemicalKineticsDatabase
-m_dfPreExpFac
-m_dfActEnergy
-m_dfTempExp
-m_mDrvForce

User Interface

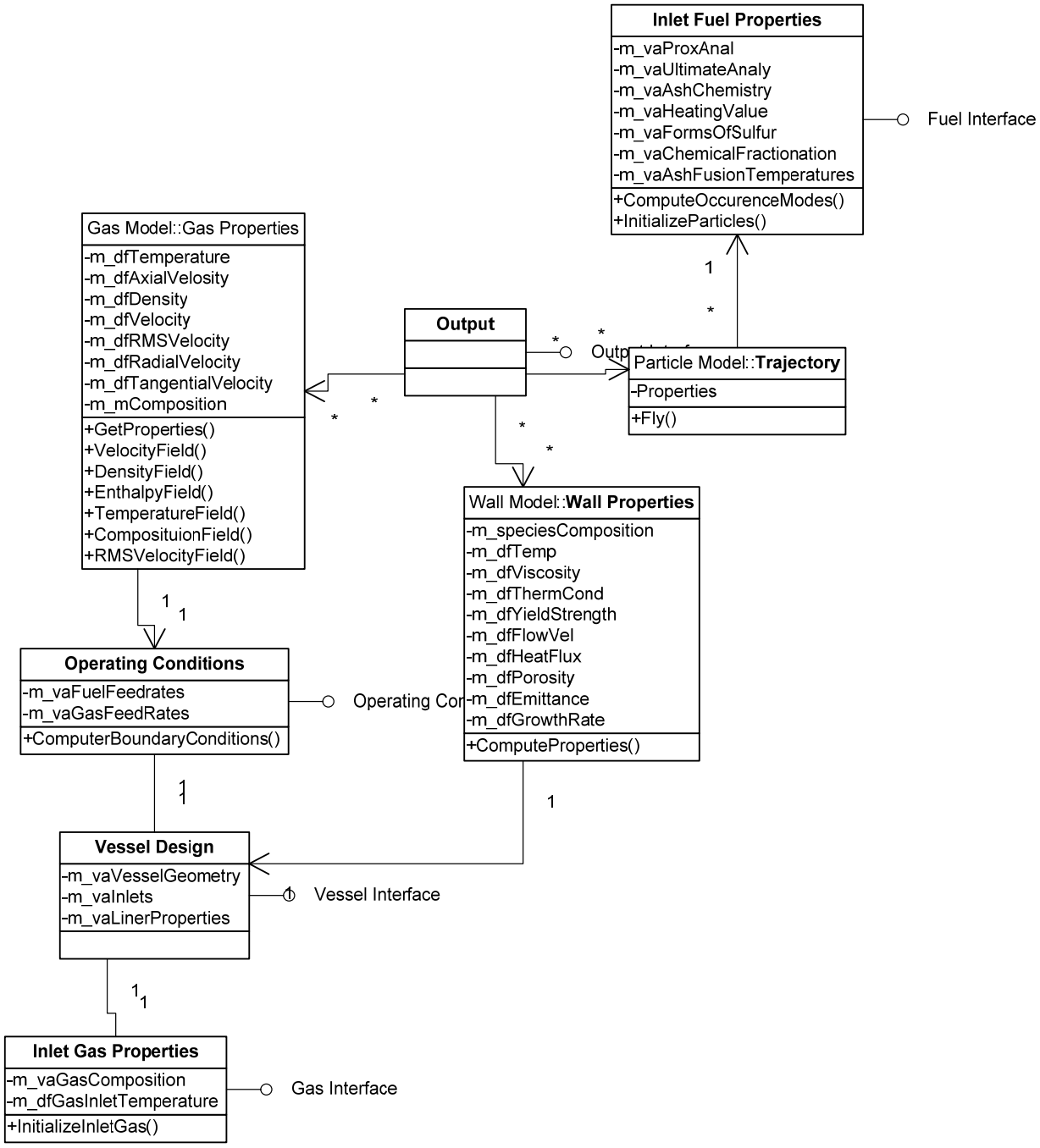

Figure 197 User Interface Use Case Diagram

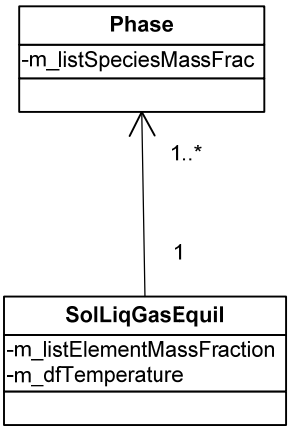

Figure 198 Condensed-phase equilibrium model.

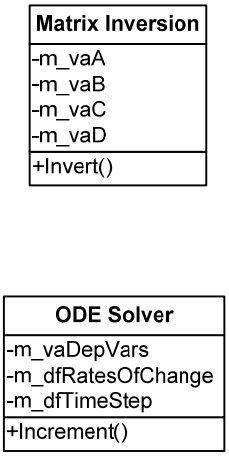

Figure 199 Numerical tools class structures.

Model Results

A dissolution model has been developed to account for the refractory wear due to chemical corrosion in entrained-flow slagging gasifiers. This model is based on the diffusion-dominant mass transport assumption, and incorporates the effects of slag flow and heat transfer on the corrosion rate. The boundary layer theory is used to derive an analytical equation form of the mass transfer coefficient. The effects of temperature, composition, and slag flow are analyzed and discussed based on a CaO-Al_2O_3-SiO_2 slag and an Al_2O_3-dominant refractory material. Results indicate that temperature and slag composition have significant effects on the corrosion rate. This model, combined with the spalling and coal gasification models, will be used to support the development of monitoring capabilities to on-line access the wear of refractory liners in entrained-flow gasifiers.

1. Introduction

Entrained-flow gasification has proven to be a high efficient technology to convert solid fuel (coal, biomass, etc.) into energy-rich gaseous chemicals. This technology partially

oxidizes pulverized coal, petcoke, or biomass into light molecules like hydrogen, carbon monoxide, and carbon dioxide. During the gasification processes, the inorganic impurities in fuel are oxidized and accumulate on the internal surface of the gasifier. Due to the highly corrosive nauture of liquid slag, refractory liners installed in the gasifier are continuously dissolved by the slag. Slag also penetrates into refractories through the refractory pores or fractures, which accelerates corrosion rates and leads to spalling occurrences (Bakker 1993; Bennett and Kwong 2004). Due to serious refractory wear, typical gasifiers can only be normally operated up to 4-18 months, and it takes 2-3 weeks and costs more than 1 million dollars to shutdown, uninstall the damaged refractory liners, and install new ones. Because of the high-temperature, high-pressure, and harsh operating conditions, it is difficult to on-line measure refractory wear. Models are needed to simulate the refractory degradation, monitor the refractory remaining useful life, and control/improve the operational performance for the gasification process. In this study, a chemical corrosion model combined with slag flow and heat transfer effects has been developed to predict the corrosion rate of refractory liners. A ternary slag system, CaO-Al_2O_3-SiO_2 is used as an example to attentively describe the corrosion of an Al_2O_3-based refractory material.

2. Slag Flow along the Refractory Liner

The slag flow along the refractory is a complex phenomenon since fly ash continuously deposits on the flowing slag. To model the slag flow, three assumptions are made in the present work:

1. Slag is Newtonian fluid and uniformly distributed around the refractory at a given axial position.
2. Slag flow is fully developed and is 1-D laminar along the flow direction.
3. The shear force between the slag and syngas is neglected.

In slagging gasifiers, accumulated slag forms a molten film on the hot-face surface of the refractory and flows under gravity. The Reynolds number, Re, is small since the slag viscosity is large and the flow is in the creeping regime. As a result, the nonlinear convective terms in the equation of motion is neglected. Hence, the Navier-Stokes equation reduces to:

$$0 = \frac{1}{r}\frac{d}{dr}\left(r\mu \frac{dv_z}{dr} \right) + \rho g \sin\theta, \tag{15}$$

where μ is the slag viscosity, r is the radial coordinate with an origin at the gasifier center line , v_z is the slag velocity along the flow direction (i.e., z direction), ρ is the slag density, g is the gravity, and θ is the angle between the normal direction of the flow and the axial direction.

The boundary conditions for Equation (15) are:

$$\begin{aligned} r &= R - r_s & \frac{\partial v_z}{\partial r} &= 0, \\ r &= R & v_z &= 0, \end{aligned} \tag{16}$$

where R is the internal radius of the refractory liner, and r_s is the slag thickness at a given axial position. The first boundary condition in Equation (16) results from the negligible shear stress between the slag and syngas.

During gasification processes, the oxidized inorganic matters in gasifiers continuously merge into the flowing slag film. Therefore, r_s is not a constant but a function of the axial position as the slag flows downwards.

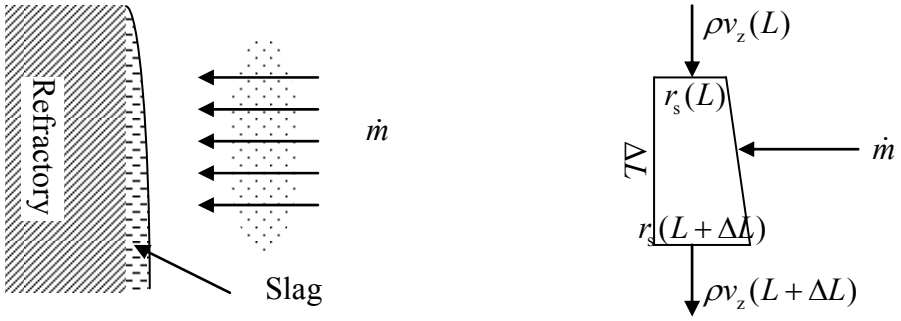

Figure 200: Slag flow and fly ash addition into the slag along the refractory surface

At steady state, the mass balance on the flowing slag is:

$$2\pi R\int_0^L \dot{m}dz = \int_{R-r_s}^{R} 2\pi r\cdot\rho v_z(L)dr \tag{17}$$

where L is the film length at the inflow position, and $\dot{m}$ is the mass flux of joined fly ash. When $\dot{m}$ is a function of axial positions, we use

$$\dot{m}_i\Delta L_i + \int_{R-r_s(L)}^{R} \rho v_z dr = \int_{R-r_s(L+\Delta L)}^{R} \rho v_z dr \tag{18}$$

as the mass balance equation, where $\dot{m}_i$ is the mass flux in the ith computational zone, and ΔL is the axial length for a given computational zone. The assumption of $2\pi r \approx 2\pi R$ is used in Equation (18) due to $r_s \ll R$.

In the above, no assumptions have been made on the slag properties (i.e., μ and ρ). Iterations are needed to solve Equations (15)-(17) to obtain the flow velocity and slag thickness if large temperature gradients are present through the slag layer. In such a case, a reasonable initial guess of r_s at the bottom of the kth computational zone ($r_{s,k}$) can be obtained using Equation (19) which is approximated at constant μ and ρ values (See Appendix A).

$$r_{s,k} = 2\sqrt{\frac{\mu_k \sum_{i \le k} \dot{m}_i \Delta L_i}{R \rho_k^2 g \sin\theta_k}} \tag{19}$$

If the wall temperature is too low (e.g., for Shell gasifiers where water-cooling jackets are used), slag can be frozen at positions adjacent to the internal refractory surface. In such as case, the critical viscosity temperature is used to divide the slag flow into two regions: Newtonian flow region and non-Newtonian flow region. If slag temperature is lower than the critical viscosity temperature, it is assumed that slag is motionless due to the large viscosities. However, this phenomenon is not considered for the refractory wear model since chemical corrosion is insignificant at low temperatures.

3. Heat Transfer through the Slag, Refractory, and Steel Layers

The temperature profiles of the slag and refractory are needed to solve the slag flow and chemical corrosion. Figure 201 illustrates a typical gasifier layer structure and a temperature profile through the heat transfer layers. Typical air-cooling gasifiers have one anti-corrosion refractory liner and several insulation refractory layers. The refractory liner layer usually has higher thermal conductivities than those of insulation layers to minimize refractory wear due to creep or thermal expansion effects. The insulation layers are made of materials with low thermal conductivities to keep high cold gas efficiency.

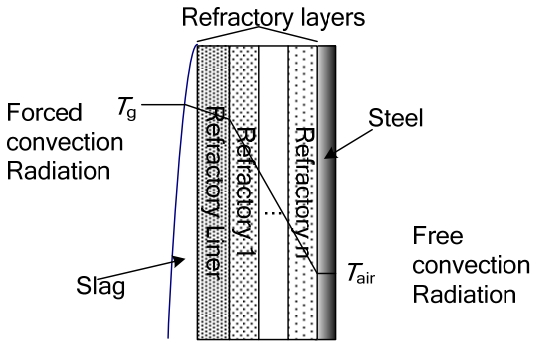

Figure 201: Scheme of heat transfer layers in the coal-based gasifiers

At low Reynolds numbers, the heat transfer due to slag convection and viscous dissipation is negligible, and the heat conduction along the radial direction dominates the energy transport mechanism. Therefore, the slag layer, refractory layer, and steel shell layer can be modeled using the same governing equation. At steady state, the 1-D heat equation can be simplified into

$$\frac{d}{dr}\left(kr\frac{dT}{dr}\right) = 0, \tag{20}$$

where T is the temperature and k is the thermal conductivity. Equation (20) can be further simplified into

$$\frac{dT}{dr} = \frac{q}{kr}, \tag{21}$$

where q is a constant and can be taken as the heat flow rate (In fact, $2\pi q$ is the exact heat flow rate through the layer for the 1-D steady state radial heat conduction). Equation (21) can be solved analytically if the value of k is known, or can be solved numerically at given boundary conditions.

The volume fraction of flying particles is small compared with the reactor volume. Therefore, only the radiation and the forced convection effects between the syngas and slag are considered for the energy balance at the gas-slag interface. The boundary conditions of Equation (20) at the gas-slag and steel shell-air interfaces are expressed in Equations (22) and (23),

$$r = R - r_s \qquad k_{slag}\left(\frac{dT_{slag}}{dr}\right) = h_g(T_{slag} - T_g) + \varepsilon_{slag}\sigma\left(T_{slag}^4 - T_g^4\right), \tag{22}$$

$$r = R_o \qquad -k_{st}\left(\frac{dT_{st}}{dr}\right) = h_{air}(T_{st} - T_{air}) + \varepsilon_{st}\sigma\left(T_{st}^4 - T_{air}^4\right), \tag{23}$$

respectively, where R_o is the external radius of the steel shell, k_{slag} and k_{st} are the thermal conductivities of the slag and steel shell, respectively, h_g and h_{air} are the convective heat transfer coefficients of the gas and environmental air at the interface, respectively, T_{slag}, T_g, T_{st} and T_{air} are the temperatures of the slag, gas, steel shell, and environmental air, respectively, ε_{slag} and ε_{st} are the emissivities of the slag to the gas and the steel shell to the air, respectively, and σ is the Stefan's constant. Strictly speaking, the value of R is not a constant but a function of time due to continuous refractory wear. However, the wear rate is significantly slow when compared with the heat transfer, and thus, the energy transport can be taken as a quasi-steady state process. The value of R, therefore, can be taken as a constant at a given computational time interval.

In practical applications, the temperature profiles through the slag and gasifier layers can be obtained based on the energy balance without any temperature measurements in the gasifiers (i.e., in pure gasification modeling work), or can be solved using some measurable boundary conditions (e.g., using T_{st} values measured with thermocouples) if on-line measurements are available. If measured boundary conditions are used, it will greatly decrease the computational complexity since the heat transfer rate can be computed directly without extensive iterations.

4. Chemical Corrosion Model

The following assumptions are used in the chemical corrosion model:

1. Direct dissolution mechanism dominates the corrosion rate.
2. Slag concentration is uniform along the radial direction unless in a thin transport boundary layer adjacent to the slag-refractory interface.
3. The composition and structure of refractories are uniform

Bui et al. (Bui, Ha et al. 2005) and Sandhage et al. conducted chemical corrosion experiments using the rotating cylinder method. They reported that chemical corrosion may also occur by the indirect dissolution mechanism where oxides diffuse through the reaction solids formed along the liquid-solid interface. However, this mechanism is not considered in this study because the indirect dissolution is much slower than the direct dissolution that occurs on the slag-refractory interface. Because the useful life of refractory liners is determined by the local refractory wear, only the direct dissolution mechanism needs to be considered in slagging gasifiers.

The chemical corrosion rate of refractories is affected not only by chemical reactions between the molten slag and refractory, but also by the diffusion of refractory materials into the slag. Most refractory liners used in coal gasification processes are made of alumina or chromia-based materials. Taira (Taira, Nakashima et al. 1993), Samaddar et al.(Samaddar, Kingery et al. 1964) and Yu et al. (Yu, Pomfret et al. 1997) reported that the corrosion rate of alumina in liquid slag is controlled by the diffusion mechanism. Similar conclusion has been reported for Cr_2O_3-based materials by Hirata et al.(Hirata, Morimoto et al. 2003) and Greenberg and Poeppel (Greenberg and Poeppel 1986). Hence, only the diffusion effect is considered in the present work. Bennett (Bennett and Kwong 2003) claimed that dissolving of particle bonds accelerates the corrosion rate in non-uniform refractory materials. This effect, however, is not considered in the present work due to the lack of proprietary information on commercial refractory structures.

Based on the above assumptions, Equation (24) is used to calculate the molar flux for a solute species, *A*, dissolved into a liquid phase

$$N_{\mathrm{A}} = k_{\mathrm{A}} \Delta C_{\mathrm{A}} \tag{24}$$

where N_{A} is the molar flux of *A*, k_{A} is the mass transfer coefficient, and ΔC_{A} is the solute concentration difference between the solid-liquid interface and the bulk liquid, which can be calculated using a phase equilibrium program.

The value of k_{A} in Equation (24) is a function of the slag flow and solid-liquid interface properties, and can be obtained using the boundary layer theory (See Appendix B). After simplification, k_{A} can be expressed as:

$$k_{\mathrm{A}} = 0.538 \frac{\eta D_{\mathrm{As}}}{\sqrt[3]{\int_0^L \frac{\mu D_{\mathrm{As}}}{\rho g r_{\mathrm{s}} \sin\theta} dz}} \tag{25}$$

where ρ, μ, and D_{As} are computed at the interface temperature, and η is the correction factor used to account for the high net mass transfer rate and is defined as

$$\eta = \frac{\ln(1+R_x)}{R_x} \tag{26}$$

with R_x being

$$R_x = \frac{x_A^* - x_{Ab}}{1 - x_A^*} \tag{27}$$

where x_A^* is the saturated mole fraction of A at the boundary, and x_{Ab} is the bulk mole fraction of A.

The corrosion rate of the refractory in the slag is then determined by

$$v_{corr,L} = \left. \frac{M_A N_A}{\rho_A (1-\varepsilon_{ref})} \right|_L \tag{28}$$

where $v_{corr,L}$ is the corrosion rate of refractories at L, M_A is the molecular weight of A (kg/mol), ρ_A is the density of solid A, and ε_{ref} is the porosity of the refractory material.

5. Baseline and Data Specification

A single-stage entrained down-flow gasifier is used in the present work to simulate a G.E. coal gasification process (Figure 202). Because most coal ashes are abundant of Ca, Al, Si, and O elements, a ternary slag system, CaO-Al_2O_3-SiO_2, is used in this study to compute refractory wear. The refractory material is assumed to be Greencast 94 (2007) (Al_2O_3 > 94%) since many properties of Al_2O_3-related slag and refractory materials have been publicly reported (e.g., solubility, viscosity, diffusion coefficients, etc.).

To simplify the computation, only one refractory layer is considered here (although typical commercial gasifiers have multiple refractory layers). Similarly, the steel shell is assumed to be exposed in the air directly, although a cooling jacket/heat exchanger may be present in commercial gasifiers. However, the model does have the capability to compute cases with more than one refractory layer or with cooling systems.

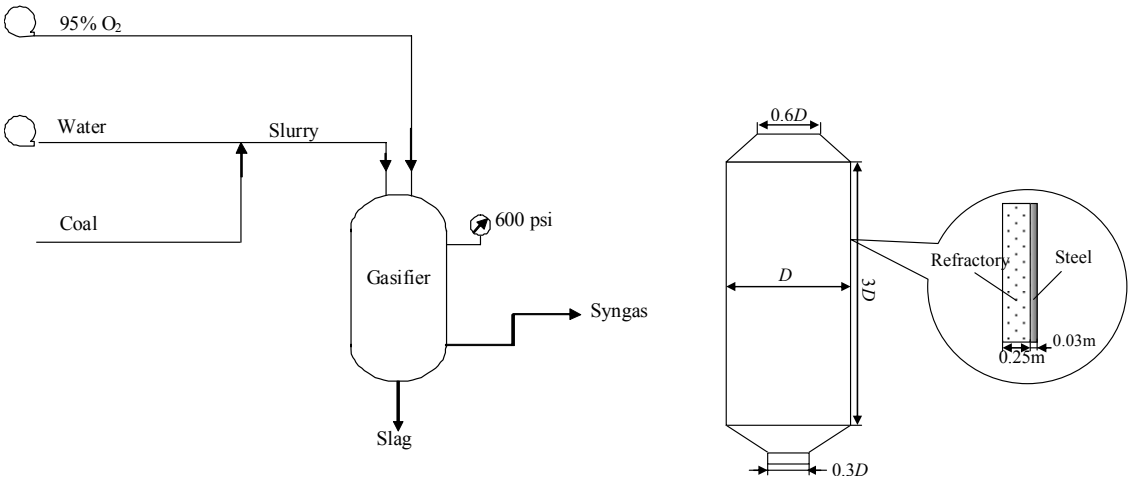

Figure 202: Scheme of one-stage entrained-flow gasifier. The internal diameter D = 2.8 m.

6. Results and Discussion

Chemical corrosion in slagging gasifiers is a complex phenomenon influenced by such factors as coal type, refractory material, gasifier geometry, ash/slag deposition rate, heat transfer, and operating conditions etc. Figures 203 and 204 depict the temperature and gas composition profiles in the gasifier at the flowrate of Wyodak coal 5500 tons/day and water/coal (mass) = 0.50 and oxygen/coal (mass) = 0.87, computed using the gasification package (Liu, Baxter et al. 2008). Because refractory wear is most serious in the slagging chamber where temperature is high and slag is mostly liquid (above the fusion temperature line in Figure 203, corresponding to L= 0.2~0.6m in this study), more attention is paid here to the corrosion around the highest temperature zone where slag freezing effect is not significant. With this consideration, a position at L ~ 0.36 m from the top of the gasifier is used as the default analyzing position in the following discussion. For analysis convenience, the averaged value of $\dot{m}$ is assumed to be 0.1 kg/m^2·s along the axial direction and the mass fraction of the default slag is assumed to be 40%CaO-20%Al_2O_3-40%SiO_2 through the gasifier unless the variants are specified in a specific section. The thermodynamic data reported by Eriksson and Pelton (Eriksson and Pelton 1993) are used in the present work to calculate the liquid-solid phase equilibrium of the slag (e.g., solubility and melting points of slag at given compositions).

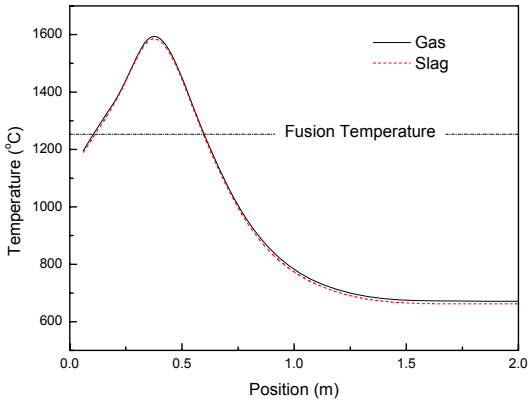

Figure 203: Averaged temperature profiles of gas and slag vs. position

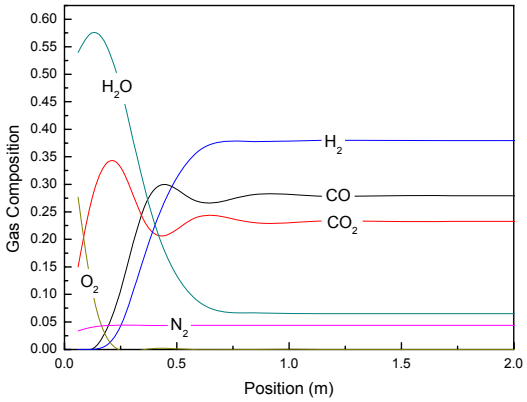

Figure 204: Averaged composition profiles of gas vs. position

6.1. Temperature and thickness of the slag in the slagging chamber

Figure 205 depicts the temperature profiles of slag at the hot-face (slag-gas interface) and the cold-face (slag-refractory layer) boundaries, computed using the models developed in this study. In the slagging chamber, the slag layer is thin and mostly liquid and has a relatively higher thermal conductivity than typical ash. Hence, the cold-face temperature profile is close to the hot-face temperature profile. The temperature difference between the two profiles is most appreciable around the highest temperature region where the heat transfer flux is largest.

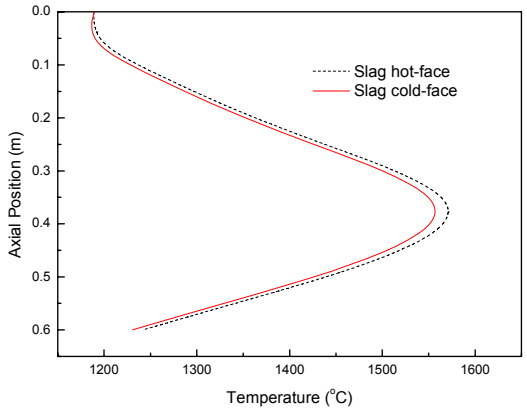

Figure 205: Slag temperature vs. axial position

Figure 206 illustrates the slag thickness as a function of the axial position. The typical computed liquid slag thickness is in an order of millimeters, which is similar to those reported by Benyon et al.(Benyon, Inumaru et al. 2000), Wang et al.(Wang, Zhao et al. 2007), and Bockelie et al.(Bockelie, Denison et al. 2002).

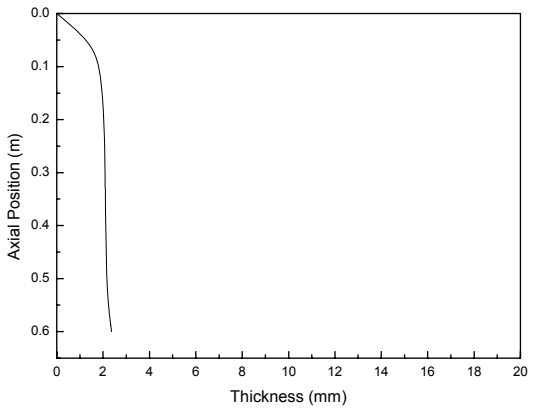

Figure 206: Slag thickness vs. axial position

Figure 207 reports the predicted slag velocity in the slagging chamber. The highest velocity occurs where the slag temperature is highest. A possible explanation is that the velocity is strongly dependent on the viscosity of the slag. Because the slag viscosity decreases exponentially with increasing temperature (Figure 208), the slag velocity profile is significantly influenced by the temperature.

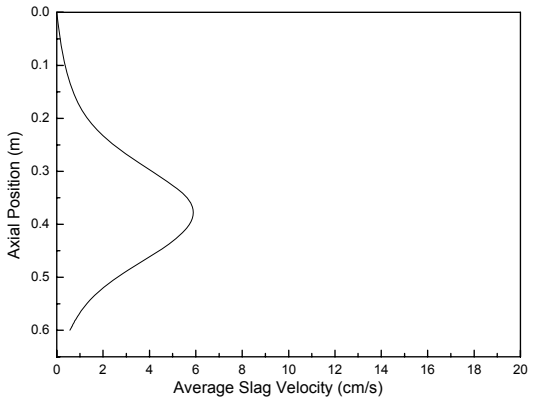

Figure 207: Slag velocity vs. axial position

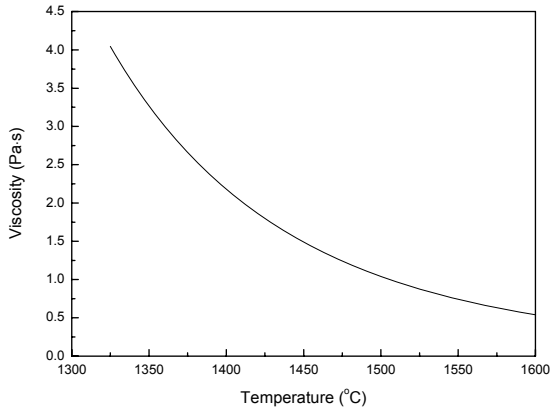

Figure 208: Viscosity of liquid slag vs. temperature, computed using the Kalmanovitch and Frank model (Kalmanovitch and Frank 1988).

6.1. Effect of temperature on corrosion rate

Figure 209 reports the corrosion rate as a function of temperature. The diffusivity of Al_2O_3 is calculated with the Stokes-Einstein equation using a reference point reported by Samaddar et al (Samaddar, Kingery et al. 1964). The corrosion curve can be divided into two smooth regions according to temperature: the 1325~1423 ˚C region and 1423~1600 ˚C region. In each region, the corrosion rate increases with increasing temperature. The curve becomes flat and close to zero as temperature approaches 1325 ˚C. The trend of the corrosion rate can be explained using the solute solubility and diffusivity changes with temperature (Figures 210 and 211). The solute solubility is a highly nonlinear function of temperature since different high-melting point solid compounds may be formed as more solute is dissolved into the unsaturated liquid slag. Depending on the temperature and composition, the saturated liquid slag can be in equilibrium with different solid compounds. For example, the saturated liquid slag is in equilibrium with $Ca_2Al_2SiO_7$, $CaAl_{12}O_{19}$, and Al_2O_3 over temperature ranges of 1325~1423 ˚C, 1423~ 1593 ˚C, and 1593~1600 ˚C, respectively. The change of the solubility trend at 1593 ˚C is not as distinct as that at 1423 ˚C because both $CaAl_{12}O_{19}$ and Al_2O_3 have large fractions of Al_2O_3 and therefore have similar Gibbs energy changes based on per mole of Al_2O_3. Around 1425 ˚C, the corrosion rate varies not as abruptly as the solubility curve because the corrosion curve is smoothed by the contribution of solute diffusivity with respect to temperature (Figure 211). As temperature approaches1325 ˚C, the slag becomes saturated with respect to Al_2O_3 (Figure 210) and cannot hold more solute in the liquid, resulting in a zero corrosion rate.

Due to the significant effect of temperature on chemical corrosion, Chen and Buyukozturk (Chen and Buyukozturk 1985) expressed the corrosion rate as an exponential function of temperature. Samaddar et al. (Samaddar, Kingery et al. 1964) pointed out that the temperature-function modeling approach is ineffective and misleading in general. the saturated solute concentration and the solute diffusivity are dependent not only on temperature, but also on the liquid composition. For example, the

zero corrosion rate at temperatures close to 1325 ˚C and the non-smooth curve of the corrosion rate shown in Figure 209 cannot be accounted for by a simple temperature function alone. In addition, the effect of slag flow on the corrosion rate is ignored in Chen and Buyukozturk's work.

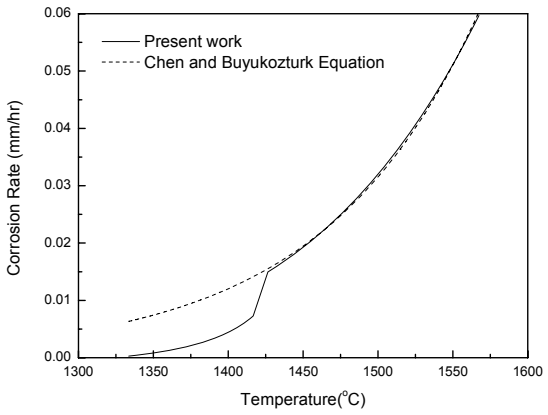

Figure 209: Corrosion rate vs. temperature

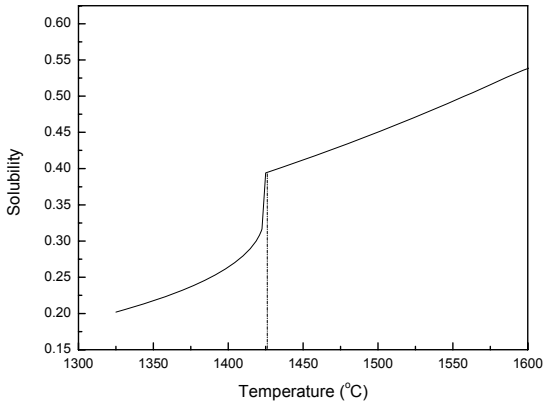

Figure 210: Solubility of the default slag as a function of temperature

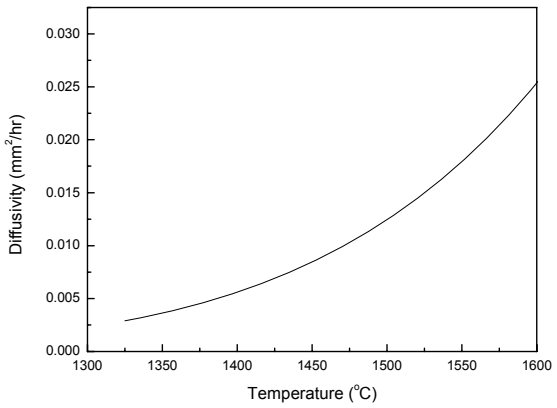

Figure 211: Diffusivity of the default slag as a function of temperature

6.2. Effect of slag composition on corrosion rate

To separate the effect of temperature on the corrosion rate, the gas temperature at L = 0.36 m is fixed in the present section. Figure 212 illustrates the effect of Al_2O_3 composition on the corrosion rate. The corrosion rate decreases with increasing Al_2O_3 composition and approaches zero as the composition of Al_2O_3 is close to 0.5. A possible explanation is that the corrosion rate is significantly influenced by the solute solubility. The slag becomes more and more close to the saturated point with the addition of solute in the slag, and thus, the ΔC_A term defined in Equation (24) approaches zero as the composition of Al_2O_3 increases. The corrosion rate is zero at Al_2O_3 compositions above 0.5 because the slag is saturated/oversaturated.

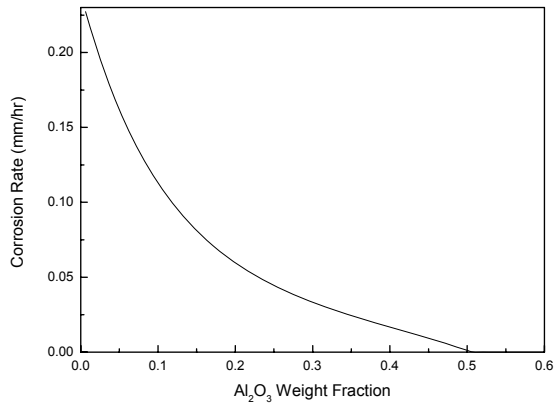

Figure 212: Corrosion rate vs. Al_2O_3 composition at $CaO/SiO_2 = 1$

Figure 213 depicts the corrosion rate as a function of CaO composition. The corrosion rate is zero at CaO compositions below 0.13 or above 0.52. The zero corrosion rate can be explained using the melting point curve as shown in Figure 214. At CaO compositions below 0.13 or above 0.52, the melting points of stable solid compounds

are higher than that of the computed slag cold-face temperature. In other words, the liquid slag is saturated/oversaturated resulting in a zero corrosion rate. The vertical distance between the melting point and the slag cold-face temperature in Figure 214 reflects the soluble capacity. However, the transition points of the corrosion rate curve (e.g., the peak point) do not occur at the corresponding CaO compositions where the transition of the melting point curve does. A possible explanation is that the corrosion rate is a combination result of both the solute solubility and diffusivity. The diffusivity curve (Figure 215) increases dramatically with increasing CaO composition, and thus, results in the shift of the transition points of corrosion rate curve to higher CaO compositions. Similar trends can be expected in the curve of the corrosion rate vs. SiO_2 composition at fixed CaO/Al_2O_3 ratio, though the figures are not shown here due to the similar mechanism to the CaO effect; however, the corrosion rate-SiO_2 composition curve "shifts" to the lower SiO_2 composition side because the diffusivity of Al_2O_3 decreases with increasing SiO_2 composition.

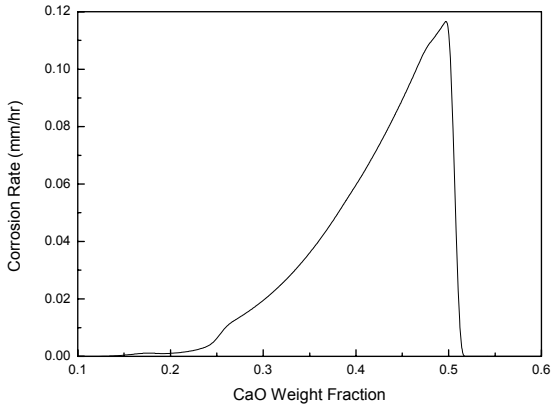

Figure 213: Corrosion rate vs. CaO composition at Al_2O_3/SiO_2=0.5

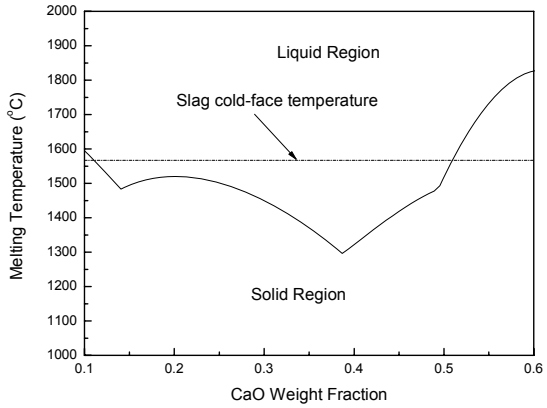

Figure 214: Melting point of Al_2O_3-CaO-SiO_2 slag at Al_2O_3/SiO_2 = 0.5, calculated using the BYU phase equilibrium package (Liu, Oscarson et al. 2007).

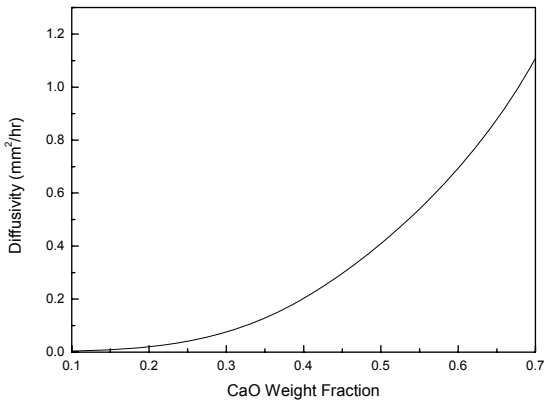

Figure 215: Diffusivity of Al_2O_3 at $Al_2O_3/SiO_2 = 0.5$.

6.3. Effect of slag flow on corrosion rate

The corrosion kinetics of oxides in the slag has been studied by many researchers using the rotating cylinder (Taira, Nakashima et al. 1993; Bui, Ha et al. 2005) or immersing method. The rotating cylinder method, though is widely used to evaluate refractory resistance and qualitatively study corrosion mechanisms, often overestimates the corrosion rate when it is used in slagging gasifiers since the slag flow effect is not properly estimated. The immersing method (diffusion in stationary slag), on the other hand, underestimates the corrosion rate in slagging gasifiers due to the ignorance of the slag flow effect. An example of the slag flow effect is shown in Figure 216. The without-slag-flow curve is computed using the pure radial diffusion assumption through the slag layer. The difference of corrosion rates increases with increasing temperature. A possible explanation is that the slag velocity increases with increasing temperature resulting in a thinner mass transfer boundary layer. As a result, the transport resistance in the slag becomes much smaller and the solute is more quickly removed by the flowing slag.

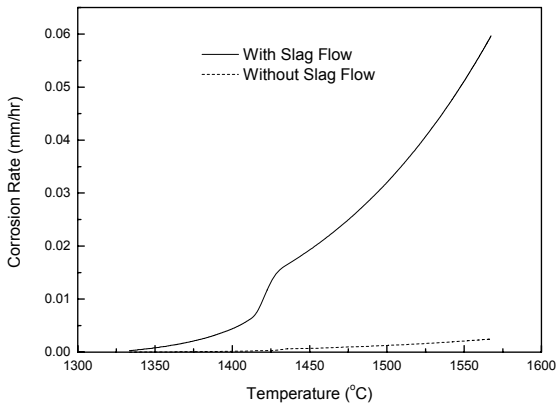

Figure 216: Comparison of corrosion rates with and without the slag flow effect

Figure 217 depicts the refractory wear as a function of axial position from the top of the gasifier. For analysis convenience, the syngas temperature and composition profiles are fixed at those shown in Figure 203. It can be found that not all positions in the slagging chamber are of appreciable chemical corrosion. A possible explanation is that temperature has a significant effect on corrosion rates. At low gas temperatures (and therefore low slag-wall temperatures), slag is either nearly saturated with the refractory material or the solute diffusivity is too small to appreciable dissolution occurrence (If temperature is lower than the melting point of the slag, ash deposition will occur which protects the refractory from direct contact with the liquid slag). Refractory wear is most serious around L=0.36m since the corresponding slag-refractory interface temperature is highest. Temperature also has a significant effect on the slag flow due to the strong dependence of slag viscosity on temperature. However, compared with the direct effect of temperature on solute solubility and diffusivity, the slag flow effect on the corrosion rate is much less pronounced. The significant effect of temperature on refractory wear implies that the remaining useful life of refractory liners can be prolonged by installing thicker liner materials or installing a cooling jacket around the highest temperature region.

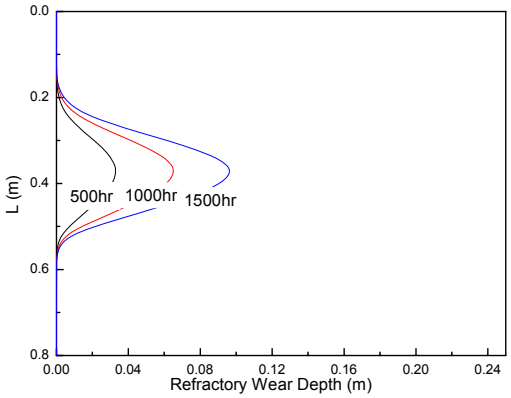

Figure 217: Refractory wear distribution along the axial direction

7. Conclusions

In this study, a comprehensive dissolution model has been developed to predict the chemical corrosion behavior that occurs in slagging gasifiers. The effects of temperature, slag composition, and slag flow have been analyzed and discussed based on an Al_2O_3-CaO-SiO_2 slag and the Greencast 94 refractory material.

The corrosion rate increases dramatically with increasing temperature. Both the diffusion coefficient and the solute solubility increase as temperature increases. However, a temperature function alone cannot correctly describe the corrosion phenomenon. Slag composition has a strong influence on both the slag thermo and transport properties, and thus on the corrosion rate. Slag flow also influences the corrosion rate. The flow effect, however, is less pronounced than the slag temperature and composition effects. Rotating cylinder or immersing techniques can be used to analyze the transport and corrosion mechanisms, but are not appropriate to be directly used in slagging gasifiers to evaluate the solute dissolution behavior.

Not all positions in the slagging chamber are of significant chemical corrosion. The corrosion rate is highest at the position where the temperature is highest. Because the remaining useful life of refractories is determined by the severity of local wear, more attention should be paid to the region where combustion reactions are dominant and gas temperature is highest.

It should be pointed out that the predicted corrosion rate is higher than the recently reported industrial values (Bakker 1993) because more anti-corrosive Cr_2O_3-based refractory materials are more widely used in these years. However, the presented modeling approach can be easily used to predict Cr_2O_3-based refractory wear once the needed Cr_2O_3-related properties are obtained.

The model presented in this study has been integrated with the coal gasification package (Liu, Baxter et al. 2008) developed at INL to investigate refractory wear.

Acknowledgement

The research reported in this paper was supported by the U.S. Department of Energy contract DE-AC07-05ID14517.

Appendix A. Derivation of Equation (5)

At constant μ and ρ values, an explicit solution to the slag flow defined in Equations (15) and (16) can be obtained by

$$v_z = \frac{\rho g \sin\theta (R^2 - r^2)}{4\mu} + \frac{\rho g \sin\theta (R - r_s)^2}{2\mu} \ln\frac{r}{R} \qquad (.29)$$

Summation of Equation (18) over *k* computational zones results in

$$\int_{R-r_{s,k}}^{R} \rho v_z dr = \sum_{i \le k} \dot{m}_i \Delta L_i, \qquad (.30)$$

where $r_{s,0} = 0$ is used since no ash deposition is assumed to exist at the initial flowing position. Substituting Equation (.29) into Equation (.30), after simplification, results in

$$\frac{\rho^2 g \sin\theta}{4\mu}\left(R r_s^2 - \frac{1}{3} r_s^3 + 2\left(R - r_s\right)^2 \left((R - r_s) \ln\frac{R}{R - r_s} - r_s \right) \right) = \sum_{i \le k} \dot{m}_i \Delta L_i \qquad (.31)$$

The value of r_s is a small number compared with *R*. Hence, the term in the parentheses of Equation (.31) can be further simplified into

$$\begin{aligned} & R r_s^2 - \frac{1}{3} r_s^3 + 2\left(R - r_s\right)^2 \left((R - r_s) \ln\frac{R}{R - r_s} - r_s \right) \\ & \approx R r_s^2 - \frac{1}{3} r_s^3 + 2\left(R - r_s\right)^2 \left((R - r_s) \frac{r_s}{R - r_s} - r_s \right), \\ & \approx R r_s^2 \end{aligned} \qquad (.32)$$

where the approximation of $\ln\frac{R}{R - r_s} = \ln\left(1 + \frac{r_s}{R - r_s}\right) \approx \frac{r_s}{R - r_s}$ is used in the above derivation. Equation (19) can be obtained by substituting Equation (.32) into Equation (.31).

For slag flow with large temperature gradients along the *r* direction, the values of μ and ρ evaluated at the hot-face temperature of the slag can be used as initial guesses.

Appendix B. Derivation of Mass Transfer Coefficient

For the interfacial mass transfer through the flowing slag, the steady-state governing equation is

$$\frac{\partial N_{Az}}{\partial z}+\frac{1}{r}\frac{\partial (rN_{Ar})}{\partial r}=0 \qquad (.33)$$

where N_{Az} and N_{Ar} are the mass fluxes of A along the z and r directions, respectively. Due to the slowness of slag corrosion (typically ~ 10^{-9} m/s), the bulk slag concentration can be assumed to be constant during the dissolution process. The N_{Az} and N_{Ar} terms can then be expressed as

$$N_{Az}=-D_{As}\frac{\partial C_A}{\partial z}+x_A N_{Az}\approx C_A v_z \qquad (.34)$$

$$N_{Ar}=-D_{As}\frac{\partial C_A}{\partial r}+x_A N_{Ar}=-\frac{D_{As}}{1-x_A}\frac{\partial C_A}{\partial r} \qquad (.35)$$

where C_A is the concentration of A, D_{As} is the effective diffusion coefficient of A in the slag, and x_A is the mole fraction of A in the slag. The $C_A v_z$ term in Equation (.34) results from the dominance of convection on the transport of A along the flow direction.

Substituting Equations (.34) and (.35) into Equation (.33) results in:

$$v_z\frac{\partial C_A}{\partial z}=\frac{1}{r}\frac{\partial}{\partial r}\left(\frac{rD_{As}}{1-x_A}\frac{\partial C_A}{\partial r}\right) \qquad (.36)$$

with the boundary conditions of

$$\begin{aligned} &z=0 && C_A=C_{Ab}\\ &r=R && C_A=C_A^* \\ &r=R-r_s && \frac{\partial C_A}{\partial r}=0 \end{aligned} \qquad (.37)$$

where C_{Ab} is the bulk concentration of A, and C_A^* is the saturated concentration of A at the slag-refractory boundary.

For slow diffusion (~10^{-9} m/s for typical dissolution rates in slagging gasifiers), the distance through which solute can penetrate is much small compared with the slag thickness (i.e., r_s). The governing equation and the boundary conditions defined in Equations (.36) and (.37) can be replaced by

$$v_z\frac{\partial C_A}{\partial z}=\frac{1}{R-y}\frac{\partial}{\partial y}\left(\frac{(R-y)D_{As}}{1-x_A}\frac{\partial C_A}{\partial y}\right)\approx\frac{\partial}{\partial y}\left(\frac{D_{As}}{1-x_A}\frac{\partial C_A}{\partial y}\right), \qquad (.38)$$

and

$$\begin{aligned} z &= 0 \qquad & C_{\mathrm{A}} &= C_{\mathrm{Ab}} \\ y &= 0 \qquad & C_{\mathrm{A}} &= C_{\mathrm{A}}^{*} \\ y &= \infty \qquad & C_{\mathrm{A}} &= C_{\mathrm{Ab}} \end{aligned} \quad , \tag{.39}$$

where $y = R - r$. The *R*-*y* term in Equation (.38) is approximated to be a constant due to $R \gg r_s \gg y$ (The approximated expression in Equation (.38) can also be taken as the transport equation in Cartesian coordinates).

If *A* is dilute in the slag (i.e., $x_{\mathrm{A}} \ll 1$), the bulk flow effect of *A* along the *r* direction is negligible and Equation (.38) can be simplified into

$$v_{\mathrm{z}} \frac{\partial C_{\mathrm{A}}}{\partial z} = \frac{\partial}{\partial y}\left(D_{\mathrm{As}} \frac{\partial C_{\mathrm{A}}}{\partial y} \right) \tag{.40}$$

In general, Equation (.36) is used to calculate the solute dissolution rate.

We first consider the diffusion case in dilute solutions as shown in Equation(.40). According to the boundary layer theory, a mass transfer boundary layer with a thickness, δ_{A}, is present in the vicinity of the slag-refractory interface which dominates the mass transport resistance along the *r* direction. Due to the slow velocity change within δ_{A}, v_{z} can be approximated using its first-order derivative (from Equation (15)) with respect to *y* which gives

$$v_{\mathrm{z}} \approx \frac{\rho g \sin\theta (r_{\mathrm{s}} - y) y}{\mu} \approx a y, \tag{.41}$$

where

$$a = \frac{\rho g r_{\mathrm{s}} \sin\theta}{\mu} \tag{.42}$$

Equation (.40) can then be transformed into

$$a y \frac{\partial C_{\mathrm{A}}}{\partial z} = \frac{\partial}{\partial y}\left(D_{\mathrm{As}} \frac{\partial C_{\mathrm{A}}}{\partial y} \right) \tag{.43}$$

Substituting $C_A/C_A^* = f(\xi)$ and $\xi = y/\delta_A$ into Equation (.43) results in

$$\frac{d^2 f}{d\xi^2} + \left(\frac{a\delta_A^2}{D_{AB}} \frac{\partial \delta_A}{\partial z} \right) \xi^2 \frac{df}{d\xi} = 0 \qquad (.44)$$

with the boundary conditions of

$$\begin{aligned} f(0) &= 1 \\ f(\infty) &= 0 \end{aligned} \qquad (.45)$$

A realistic solution of Equation (.44) exists only if the term in the parentheses is a constant since all other terms in Equation (.44) are dimensionless. For a particular case where ρ, μ, and D_{As} are constant, Equation (.43) can be simplified into

$$\frac{d^2 f}{d\xi^2} + 3\xi^2 \frac{df}{d\xi} = 0 \qquad (.46)$$

by assuming $\xi = y(a/9D_{As}z)^{1/3}$ without using the boundary layer theory. Therefore, the thickness of δ_A can be found by solving

$$\frac{a\delta_A^2}{D_{AB}} \frac{\partial \delta_A}{\partial z} = 3, \qquad (.47)$$

which results in

$$\delta_A = \sqrt[3]{\int_0^L \frac{9D_{As}}{a} dz}, \qquad (.48)$$

or

$$\delta_A = \sqrt[3]{\sum_{i=1}^{n} \frac{9\mu_i D_{As,i}}{\rho_i g r_{s,i} \sin\theta} \Delta L_i} \qquad (.49)$$

for the solution solved using the finite difference method.

The solution to Equation (.44) is

$$\frac{C_A}{C_A^*} = f(\xi) = \frac{\int_\xi^\infty e^{-\zeta^3} d\zeta}{\Gamma\left(\frac{4}{3}\right)}, \qquad (.50)$$

where $\Gamma(4/3) = 0.8930\ldots$ is the value of the gamma function at 4/3.

The diffusion flux at the slag-refractory boundary in dilute solutions at the axial position L can then be found by

$$-N_{\mathrm{Ar}}(L)\big|_{r=R} = N_{\mathrm{Ay}}(L)\big|_{y=0} = \left.\frac{D_{\mathrm{As}}C_{\mathrm{A}}^{*}}{\Gamma\left(\frac{4}{3}\right)\delta_{\mathrm{A}}}\right|_{L} \qquad (.51)$$

For a general solution, the diffusion flux at the boundary can be obtained by inserting the effects of C_{Ab} as shown in Equation (.52).

$$-N_{\mathrm{Ar}}(L)\big|_{r=R} = N_{\mathrm{Ay}}(L)\big|_{y=0} = \frac{\eta D_{\mathrm{As}}(C_{\mathrm{A}}^{*} - C_{\mathrm{Ab}})}{\Gamma\left(\frac{4}{3}\right)\delta_{\mathrm{A}}} \qquad (.52)$$

The k_{A} term can therefore, after simplification, be expressed using Equation (25).

BIBLIOGRAPHY

(2007). "ANH Refractories." from www.hwr.com/.

Abreu, H. D. S., A. M. D. Nascimento and M. A. Maria (1999). "Lignin structure and Wood Properties." Wood and Fiber Science **31**(4): 426-433.

Adanez, J., L. F. de Diego, F. Garcia-Labiano, A. Abad and J. C. Abanades (2001). "Determination of Biomass Char Combustion Reactivities for FBC Applications by a Combined Method." Ind. Eng. Chem. Res. **40**(20): 4317-4323.

Allen, W. C. and R. B. Snow (1955). "The Orthosilicate-Iron Oxide Portion of the System CaO-"FeO"-SiO_2." Journal of the American Ceramic Society **38**: 264-280.

Amadori, M. (1914). "The Tendency of Halides and Other Salts of the Same Metal to Combine Fluorides, Chlorides and Carbonates." Atti della Accademia Nazionale dei Lincei, Classe di Scienze Fisiche, Matematiche e Naturali, Rendiconti **22**(II): 366-72.

Antal, M. J. J. and V. Gabor (1995). "Cellulose Pyrolysis Kinetics: the Current State of Knowledge." Ind. Eng. Chem. Res. **34**: 703-717.

Antal, M. J. J., G. Varhegyi and E. Jakab (1998). "Cellulose pyrolysis kinetics: Revisited." Industrial & Engineering Chemistry Research **37**(4): 1267-1275.

Babu, B. V. and A. S. Chaurasia (2003). "Modeling, simulation and estimation of optimum parameters in pyrolysis of biomass." Energy Conversion and Management **44**(13): 2135-58.

Backman, R., W. J. Frederick and M. Hupa (1993). "Basic Studies on Black-Liquor Pyrolysis and Char Gasification." Bioresource Technology **46**: 153-158.

Bakker, W. T. (1993). "Refractories for Present and Future Electric Power Plants." Key Engineering Materials **88**: 41-70.

Bale, C., P. Chartrand, S. A. Degterov, G. Eriksson, K. Hack, R. Ben Mahfoud, J. Melancon, A. D. Pelton and S. Petersen (2002). "FactSage Thermochemical Software and Databases." Calphad-Computer Coupling of Phase Diagrams and Thermochemistry **26**(2): 189-228.

Baxter, L. L. (2000). "Physical and combustion properties of biomass." from http://www.et.byu.edu/%7Elarryb/Biomass.htm.

Baxter, L. L. (2005). "Biomass-coal co-combustion: opportunity for affordable renewable energy." Fuel **84**(10): 1295-1302.

Baxter, L. L., T. Lind, M. Rumminger and E. Kauppinen (2001). Particle Size Distributions in Recovery Boilers. International Chemical Recovery Conference, Whistler, British Columbia, Canada, TAPPI.

Baxter, L. L. and A. L. Robinson (2000). Engineering Models of Biomass Combustion Processes. Biomass for Energy and Industry: 1st World Conference and Technology Exhibition, Seville, Spain.

Belyaev, I. N. and M. L. Sholokhovich (1953). "Reciprocal System of Sodium and Barium Chlorides and Carbonates." Sbornik Statei Obshchei Khim., Akad. Nauk S.S.S.R. **1**: 134-43.

Bennett, J. P. and K.-S. Kwong (2004). "Refractory Liner Materials Used in Slagging Gasifiers." Refractories Applications and News **9**(5): 20-25.

Bennett, J. P. and K. Kwong (2003). "Refractory Liner Materials Used in Slagging Gasifiers." Refractories Applications and News **9**(5): 20-25.

Benyon, P., J. Inumaru, M. Otaka, S. Hara, H. Watanabe and J. Kent (2000). Engineering Modeling of High Pressure and Temperature Entrained-Flow Gasifiers. Japan-Australia Joint Technical Meeting on Coal Fukuoka, Japan.

Bird, R. B., W. E. Stewart and E. N. Lightfoot (2002). Transport Phenomena. New York, Wiley.

Bird, R. B., W. E. Stewart and L. E. N. (2002). Transport Phenomena. New York / Chichester / Weinheim / Brisbane / Singapore / Toronto, John Wiley & Sons, Inc.

Blackham, A. U., L. D. Smoot and P. Yousefi (1994). "Rates of oxidation of millimetre-sized char particles: simple experiments." Fuel **73**(4): 602-612.

Blander, M. and A. D. Pelton (1987). "Thermodynamic Analysis of Binary-Liquid Silicates and Prediction of Ternary Solution Properties by Modified Quasi-Chemical Equations." Geochimica Et Cosmochimica Acta **51**(1): 85-95.

Blasiak, W., L. Tao, J. Vaclavinek and P. Lidegran (1997). "Modeling of Kraft recovery boilers." Energy Conversion and Management **38**(10-13): 995-1005.

Bockelie, M. J., M. Denison, Z. Chen, T. Linjewile, C. Senior and A. Sarofim (2002). CFD Modeling for Entrained Flow Gasifiers. Gasification Technologies Conference San Francisco, CA USA.

Bowen, N. L. and J. F. Schairer (1932). "The System: FeO-SiO_2." American Journal of Science **24**: 177-213.

Bradbury, A. G. W., Y. Sakai and F. Shafizadeh (1979). "A Kinetic Model for Pyrolysis of Cellulose." Journal of Applied Polymer Science **23**: 3271-3280.

Bragg, W. L. and E. J. Williams (1934). "Effect of thermal agitation on atomic arrangement in alloys." Proc. Roy. Soc. (London) **A145**: 699-730.

Brewster, B. S., S. C. Hill, P. T. Radulovic and L. D. Smoot (1993). Fundamentals of Coal Combustion for Clean and Efficient Use. London, Elsevier Applied Science Publishers.

Broido, A. (1976). Kinetics of Solid-Phase Cellulose Pyrolysis. Thermal Uses and Properties of Carbohydrates and Lignins. New York, Academic Press**:** 19-35.

Broido, A. and M. A. Nelson (1975). "Char Yield on Pyrolysis of Cellulose." Combustion and Flame **24**: 263-268.

Brown, A. L., D. C. Dayton and J. W. Daily (2001). "A Study of Cellulose Pyrolysis Chemistry and Global Kinetics at High Heating Rates." Energy & Fuels **15**: 1286-1294.

Brown, A. L., D. C. Dayton and J. W. Daily (2001). "A study of cellulose pyrolysis chemistry and global kinetics at high heating rates." Energy and Fuels **15**(5): 1286-1294.

Brown, A. L., D. C. Dayton, M. R. Nimlos and J. W. Daily (2001). "Design and Characterization of an Entrained Flow Reactor for the Study of Biomass Pyrolysis Chemistry at High Heating Rates." Energy & Fuels **15**: 1276-1285.

Brown, A. L., D. C. Dayton, M. R. Nimlos and J. W. Daily (2001). "Design and Characterization of an Entrained Flow Reactor for the Study of Biomass Pyrolysis Chemistry at High Heating Rates." Energy and Fuels **15**(5): 1276-1285.

Bryden, K. M. (1998). Computational Modeling of Wood Combustion. Mechanical Engineering Department Madison, University of Wisconsin-Madison.

Bryden, K. M. and M. J. Hagge (2003). "Modeling the combined impact of moisture and char shrinkage on the pyrolysis of a biomass particle." Fuel **82**: 1633-1644.

Bryden, K. M. and M. J. Hagge (2003). "Modeling the combined impact of moisture and char shrinkage on the pyrolysis of a biomass particle." Fuel **82**(13): 1633-1644.

Bui, A.-H., H.-M. Ha, I.-S. Chung and H.-G. Lee (2005). "Dissolution Kinetics of Alumina into Mold Fluxes for Continuous Steel Casting." ISIJ International **45**(12): 1856-1863.

Canavos, G. C. (1984). Applied probability and statistical methods. Boston, Little, Brown and Company.

Cannon, S. M., B. S. Brewster and L. D. Smoot (1999). "PDF modeling of lean premixed combustion using in situ tabulated chemistry." Combustion and Flame **119**(3): 233-252.

Chan, W.-C. R., M. Kelbon and B. B. Krieger (1985). "Modeling and experimental verification of physical and chemical processes during pyrolysis of a large biomass particle." Fuel **64**(11): 1505-1513.

Chan, W.-C. R., M. Kelbon and B. B. Krieger (1985). "Modelling and experimental verification of physical and chemical processes during pyrolysis of a large biomass particle." Fuel **64**(11): 1505-1513.

Chang, D. P. Y., R. E. Mournigham and G. L. Huffman (1991). "An equilibrium analysis of some chlorinated hydrocarbons in stoichiometric to fuel-rich post-flame combustion environments." Journal of the Air & Waste Management Association **41**: 947-955.

Chen, E.-S. and O. Buyukozturk (1985). "Modeling of Long Term Corrosion Behavior of Refractory Linings in Slagging Gasifiers." American Ceramic Society Bulletin **64**(7): 995-1000.

Chen, G., Q. Yu and K. Sjostrom (1997). "Reactivity of Char from Pyrolysis of Birch Wood." Journal of Analytic and Applied Pyrolysis **40-41**: 491-499.

Chen, Y. G., S. Charpenay, A. Jensen and M. A. Wojtowicz (1998). Modeling of Biomass Pyrolysis Kinetics. Twenty-seventh Symposium (International) on Combustion / The Combustion Institute.

Dasappa, S. and P. J. Paul (2001). "Gasification of char particles in packed beds: analysis and results." International Journal of Energy Research **25**(12): 1053-1072.

De Diego, L. F., F. Garcia-Labiano, A. Abad, P. Gayan and J. Adanez (2002). "Modeling of the devolatilization of nonspherical wet pine wood particles in fluidized beds." Industrial and Engineering Chemistry Research **41**(15): 3642-3650.

De Paiva Souza, M. E. and S. A. Nebra (2000). "Heat and mass transfer model in wood chip drying." Wood and Fiber Science **32**(2): 153-163.

Demirbas, A. (2000). "Mechanism of Liquefaction and Pyrolysis Reactions of Biomass." Energy Conversion & Management **41**: 633-646.

Demyirbas, A. (2003). "Hydrocarbons from Pyrolysis and Hydrolysis Processes of Biomass." Energy Sources **25**: 67-75.

Di Blasi, C. (1993). "Analysis of convection and secondary reaction effects within porous solid fuels undergoing pyrolysis." Combustion Science and Technology **90**: 315-340.

Di Blasi, C. (1994). "Numerical simulation of cellulose pyrolysis." Biomass and Bioenergy **7**(1-6): 87-98.

Di Blasi, C. (1996). "Heat, Momentum and Mass Transport through a Shrinking Biomass Particle Exposed to Thermal Radiation." Chemical Engineering Science **51**(7): 1121-1132.

Di Blasi, C. (1996). "Kinetic and heat transfer control in the slow and flash pyrolysis of solids." Industrial & Engineering Chemistry Research **35**(1): 37-46.

Di Blasi, C. (1996). "Kinetics and Heat Transfer Control in the Slow and Flash Pyrolysis of Solids." Ind. Eng. Chem. Res. **35**: 37-46.

Di Blasi, C. (1997). "Influences of Physical Properties on Biomass Devolatilization Characteristics." Fuel **76**: 957-964.

Di Blasi, C. (1997). " Influences of Physical Properties on Biomass Devolatilization Characteristics." Fuel **76**: 957-964.

Di Blasi, C. (1998). "Comparison of semi-global mechanisms for primary pyrolysis of lignocellulosic fuels." Journal of Analytical and Applied Pyrolysis **47**(1): 43-64.

Di Blasi, C., F. Buonanno and C. Branca (1999). "Reactivities of Some Biomass Chars in Air." Carbon **37**: 1227-1238.

DIPPR. "Design Institute of Physical Property Data." http://dippr.byu.edu/index.asp, from http://dippr.byu.edu/index.asp.

EIA (2003). Renewable energy annual 2002 with preliminary data for 2002 Washington, DC, Office of Coal, Nuclear, Electric and Alternate Fuels, U.S. Department of Energy.

Eriksson, G. and A. D. Pelton (1993). "Critical-Evaluation And Optimization Of The Thermodynamic Properties And Phase-Diagrams Of The Cao-Al2o3, Al2o3-Sio2, And Cao-Al2o3-Sio2 Systems." Metallurgical Transactions B-Process Metallurgy **24**(5): 807-816.

Evans, D. H. and H. W. Emmons (1977). "Combustion of wood charcoal." Fire Research(1): 57-66.

Evans, R. J. and T. A. Milne (1987). "Molecular Characterization of the Pyrolysis of Biomass. 1. Fundamentals." Energy & Fuels **1**(2): 123-137.

Evans, R. J. and T. A. Milne (1987). "Molecular Characterization of the Pyrolysis of Biomass. 2. Applications." Energy & Fuels **1**(4): 311-319.

Fjellerup, J., U. Henriksen, A. D. Jensen, P. A. Jensen and P. Glarborg (2003). "Heat transfer in a fixed bed of straw char." Energy & Fuels **17**(5): 1251-1258.

Fletcher, D. F., B. S. Haynes, F. C. Christo and S. D. Joseph (2000). "CFD based combustion model of an entrained flow biomass gasifier." Applied Mathematical Modelling **24**(3): 165-182.

Fletcher, T. H., A. R. Kertein, R. J. Pugmire and D. M. Grant (1992). "Chemical Percolation Moddel for devolatilization. 3. Direct used of 13C NMR data to predict effects of coal type." Energy & Fuels **6**(4): 414-431.

Fletcher, T. H., H. R. Pond, J. Webster, J. Wooters and L. L. Baxer (2003). Prediction of Tar and Light Gas during Pyrolysis of Black Liquor and Biomass. 3rd Annual Joint Meeting of the U.S. Sections of the Combustion Institute, Chicago, IL.

Font, F., A. Marcilla, E. Verdu and J. Devesa (1990). "Kinetics of the pyrolysis of almond shells and almond shells impregnated with CoCl2 in a fluidized bed reactor and in a pyroprobe 100." Ind. Eng. Chem. Res. **29**: 1846-1855.

Font, R., A. Marcilla, E. Verdu and J. Devesa (1990). "Kinetics of the pyrolysis of almond shells and almond shells impregnated with CoCl₂ in a fluidized bed reactor and in a Pyroprobe 100." Industrial & Engineering Chemistry Research **29**(9): 1846-1855.

Forest Products Laboratory United States Department of Agriculture Forest Service (1999). Chapter 3, Physical Properties and Moisture Relations of Wood. Wood Handbook: Wood as an Engineering Material. Madison, Wisconsin, Forest Products Society**:** 3-5.

Frederick, W. J., K. J. Wag and M. M. Hupa (1993). "Rate and Mechanism of Black Liquor Char Gasification with Co2 At." Industrial & Engineering Chemistry Research **32**: 1747-1753.

Friedlander, S. K. (2000). Smoke, Dust, and Haze. New York, Wiley.

Gelbard, F. (1984). "Computer-Program and Algorithm Review - Maeros." Aerosol Science and Technology **3**(1): 117-118.

Gelbard, F. (1990). "Modeling Multicomponent Aerosol-Particle Growth by Vapor Condensation." Aerosol Science and Technology **12**(2): 399-412.

Gelbard, F., J. W. Fitzgerald and W. A. Hoppel (1998). "A one-dimensional sectional model to simulate multicomponent aerosol dynamics in the marine boundary layer - 3. Numerical methods and comparisons with exact solutions." Journal of Geophysical Research-Atmospheres **103**(D13): 16119-16132.

Gelbard, F. and J. H. Seinfeld (1980). "Simulation of Multicomponent Aerosol Dynamics." Journal of Colloid and Interface Science **78**(2): 485-501.

Grace, T. M. (1999). "Bed cooling following an ESP." Tappi Journal **82**(9): 85-92.

Grace, T. M., H. N. Tran and M. Kawaji (2002). "Mill trial on accelerated char bed cooling following an ESP." Pulp & Paper-Canada **103**(6): 49-54.

Greenberg, J. P. (1986). The Design of Chemical Equilibrium Computation Algorithms and Investigations into the Modeling of Silicate Phase Equilibria. Chemistry San Diego, University of California, San Diego. **Ph.D.:** 271.

Greenberg, S. and R. B. Poeppel (1986). Corrosion of Refractories in a Synthetic Coal Slag. EPRI AP-4589 Project 2048-4 Argonne, Illinois, Argonne National Laboratory.

Greig, J. W. (1927). "Liquid Immiscibility in the System: FeO-Fe_2O_3-$Al2O_3$-SiO_2." American Journal of Science **14**(5): 473-84.

Gronli, M. G. and M. C. Melaaen (2000). "Mathematical model for wood pyrolysis - comparison of experimental measurements with model predictions." Energy and Fuels **14**(4): 791-800.

Gronli, M. G. and M. C. Melaaen (2000). "Mathematical model for wood pyrolysis - comparison of experimental measurements with model predictions." Energy & Fuels **14**(4): 791-800.

Guo, J. and A. C. Lua (2000). "Kinetic study on pyrolysis of extracted oil palm fiber. Isothermal and non-isothermal conditions." Journal of Thermal Analysis and Calorimetry, 1st Brazilian Congress on Thermal Analysis and Calorimetry (I CBRATEC), Mar 29-Apr 2 1998 **59**(3): 763-774.

Guzenda, R. and W. Olek (2000). Identification of free and bound water content in wood by means of NMR relaxometry. 12th International Symposium on Nondestructive Testing of Wood, Sopron, Hungary.

Hagge, M. J. and K. M. Bryden (2002). "Modeling the impact of shrinkage on the pyrolysis of dry biomass." Chemical Engineering Science **57**(14): 2811-2823.

Hautman, D. J., L. Dryer, K. P. Schug and I. Glassman (1981). "A multiple-step overall kinetic mechanism for the oxidation of hydrocarbons." Combustion Science and Technology **25**: 219-235.

Hinds, W. C. (1999). Aerosol Technology: Properties, Behavior and Measurements of Airborne Particles. New York, John Wiley & Sons, Inc.

Hirata, T., T. Morimoto, S. Ohta and N. Uchida (2003). "Improvement of the corrosion resistance of alumina-chromia ceramic materials in molten slag." Journal of the European Ceramic Society **23**(12): 2089-2096.

Horbaj, P. (1997). "Model of the Kinetics of Biomass Pyrolysis." Drevarsky Vyskum **42**(4): 15-23.

Incropera, F. P. and D. P. Dewitt (1996). Fundamentals of Heat and Mass Transfer, John Wiley & Sons.

Ingle Jr., J. D. and S. R. Crouch (1988). Chapter 4. Optical Sources, Transducers, and Measurement Systems. Spectrochemical Analysis. Upper Saddle River, New Jersey 07458, Prentice-Hall, Inc.**:** 88.

Ip, L.-T. (2005). Comprehensive black liquor droplet combustion studies. Chemical Engineering Provo, Brigham Young University.

Jalan, R. K. and V. K. Srivastava (1999). "Studies on Pyrolysis of a Single Biomass Cylindrical Pellet Kinetic and Heat Transfer Effects." Energy Conversion & Management **40**: 467-494.

Jalan, R. K. and V. K. Srivastava (1999). "Studies on Pyrolysis of a Single Biomass Cylindrical Pellet Kinetic and Heat Transfer Effects." Energy Conversion & Management **40**(5): 467-494.

Janse, A. M. C., H. G. de Jonge, W. Prins and W. P. M. van Swaaij (1998). "Combustion kinetics of char obtained by flash pyrolysis of pine wood." Industrial & Engineering Chemistry Research **37**(10): 3909-3918.

Janse, A. M. C., R. W. J. Westerhout and W. Prins (2000). "Modelling of Flash Pyrolysis of a Single Wood Particle." Chemical Engineering and Processing **39**: 239-252.

Jensen, A., K. Dam-Johansen, M. W. Wojtowicz and M. A. Serio (1998). "TG-FTIR Study of Influence of Potassium Chloride on Wheat Straw Pyrolysis." Energy & Fuels **12**: 929-938.

Jokiniemi, J. K., J. Pyykonen, P. Mikkanen and E. I. Kauppinen (1996). "Modeling fume formation and deposition in kraft recovery boilers." Tappi Journal **79**(7): 171-181.

Kalmanovitch, D. P. and M. Frank (1988). An Effective Model of Viscosity for Ash Deposition Phenomena. Proceedings of Mineral Matter and Ash Deposition from Coal, Santa Barbara, CA, US, Engineering Foundation Conference.

Kansa, E., J., H. E. Perlee and R. F. Chaiken (1977). "Mathematical model of wood pyrolysis including internal forced convection." **29**(3): 311-324.

Kauppinen, E., P. Mikkanen and J. Jokiniemi (1993). "Aerosol Capture of Sulfur and Sodium in Recovery Boilers." Paperi Ja Puu-Paper and Timber **75**(3): 122-125.

Kochesfahani, S. H., H. Tran, A. K. Jones, T. M. Grace, S. J. Lien and W. Schmidl (2000). "Particulate formation during black liquor char bed burning." Journal of Pulp and Paper Science **26**(5): 180-187.

Komatsu, K. (1991). "3-D shape reconstruction of human face from a 2-D facial image and provision for change of expression." Systems and Computers in Japan **22**(7): 63-74.

Koufopanos, C. A., G. Maschio and A. Lucchesi (1989). "Kinetic Modelling of the Pyrolysis of Biomass and Biomass Components." The Canadian Journal of Chemical Engineering **67**: 75-84.

Koufopanos, C. A., N. Papayannakos, G. Maschio and A. Lucchesi (1991). "Modelling of the Pyrolysis of Biomass Particles. Studies on Kinetics, Thermal and Heat Transfer Effects,." The Canadian Journal of Chemical Engineering **69**(4): 907-915.

Koufopanos, C. A., N. Papayannakos, G. Maschio and A. Lucchesi (1991). "Modelling of the Pyrolysis of Biomass Particles. Studies on Kinetics, Thermal and Heat Transfer Effects,." The Canadian Journal of Chemical Engineering **69**: 907-915.

Kracek, F. C., N. L. Bowen and G. W. Morey (1937). "Equilibrium Relations and Factors Influencing Their Determination in the System K_2SiO_3-SiO_2." Journal of Physical Chemistry **41**: 1183-93.

Kurdyumov, V. N. and E. Fernandez (1998). "Heat transfer from a circular cylinder at low Reynolds numbers." Journal of Heat Transfer, Transactions ASME **120**(1): 72-75.

Kutulakos, K. N. and S. M. Seitz (2000). "A theory of shape by Space Carving." International Journal of Computer Vision **38**(3): 199-218.

Lee, C. K., R. F. Chaiken and J. M. Singer (1976). "Charring pyrolysis of wood in fires by laser simulation." Symp (Int) on Combust, 16th, MIT, Aug 15-20 1976: 1459-1470.

Lee, S. R. and K. N. Nichols (1997). "CO2 gasification of kraft black liquor char in a fixed-bed reactor." Journal of Pulp and Paper Science **23**(3): J132-J138.

Li, J. and A. R. P. Vanheiningen (1989). "Reaction-Kinetics of Gasification of Black Liquor Char." Canadian Journal of Chemical Engineering **67**(4): 693-697.

Li, J. and A. R. P. Vanheiningen (1990). "Kinetics of Co2 Gasification of Fast Pyrolysis Black Liquor Char." Industrial & Engineering Chemistry Research **29**(9): 1776-1785.

Li, J. and A. R. P. Vanheiningen (1991). "Kinetics of Gasification of Black Liquor Char by Steam." Industrial & Engineering Chemistry Research **30**(7): 1594-1601.

Liden, C. K., F. Berruti and D. S. Scott (1988). "A kinetic model for the production of liquids from the flash pyrolysis of biomass." Chemical Engineering Communications **65**: 207-221.

Liliedahl, T. and K. Sjostrom (1998). "Heat transfer controlled pyrolysis kinetics of a biomass slab, rod or sphere." Biomass and Bioenergy **15**(6): 503-509.

Lind, T., M. Rumminger and L. L. Baxter (2000). Characterisitics of Salt Particles in a Recovery Boiler. Behavior of Inorganic Material In Recovery Boilers, Bar Harbor, Maine, AIChE.

Lindberg, D., R. Backman, M. Hupa and P. Chartrand (2006). "Thermodynamic Evaluation and Optimization of the (Na+K+S) System." Journal of Chemical Thermodynamics **38**(7): 900-915.

Liu, B., L. L. Baxter and H. E. Garcia (2008). Refractory Wear in Entrained-flow Coal Gasifiers, Unpublished Work Idaho Falls, Idaho, Idaho National Laboratory.

Liu, B., J. L. Oscarson, L. L. Baxter and R. M. Izatt (2006). Unpublished Data Provo, Utah, Brigham Young University.

Liu, B., J. L. Oscarson, L. L. Baxter and R. M. Izatt (2007). Modeling Multicomponent Solid-Liquid Phase Equilibrium of Salts and Silicates in Biomass and Coal Thermal Conversion Processes. 5th US Combustion Meeting San Diego, California, US, the Western States Section of the Combustion Institute.

Lu, H., W. Robert, L. Werret, G. Peirce and L. L. Baxter (2006). Comprehensive study of biomass particle combustion. 31st International Symposium on Combustion Heidelberg, Germany (submitted).

Mäkipää, M. and R. Backman (1998). Corrosion of Floor Tubes in Reduced Kraft Smelts: Studies on the Effect of Chlorine and Potassium. 9th International Symposium on Corrosion in the Pulp and Paper Industry.

Mann, M. (2001). "A Comparison of the Environmental Consequences of Power from Biomass, Coal, and Natural Gas." from http://www.nrel.gov/analysis/pdfs/2001/nov_dc.pdf.

Masliyah, J. H. and N. Epstein (1972). "Numerical solution heat and mass transfer from spheroids in steady axisymmetric flow." Prog. Heat Mass Transfer **6**: 613-632.

Masliyah, J. H. and N. Epstein (1972). "Numerical solution of heat and mass transfer from spheroids in steady axisymmetric flow." Prog. Heat Mass Transfer **6**: 613-632.

McBride, B. J., M. J. Zehe and S. Gordon (2002). NASA Glenn Coefficients for Calculating Thermodynamic Properties of Individual Species. Cleveland, Ohio, Clenn Research Center.

Merrick, D. (1983). "Mathematical models of the thermal decomposition of coal - 2. Specific heats and heats of reaction." Fuel **62**(5): 540-546.

Merrick, D. (1983). "Mathematical models of the thermal decomposition of coal. 2. Specific heats and heats of reaction." Fuel **62**(May): 540-545.

Mikkanen, M. P., E. I. Kauppinen, J. K. Jokiniemi, S. A. Sinquefield and W. J. Frederick (1994). "Bimodal Fume Particle-Size Distributions from Recovery

Boiler and Laboratory-Scale Black Liquor Combustion." Tappi Journal **77**(12): 81-84.

Miller, R. S. and J. Bellan (1996). "Analysis of Reaction Products and Conversion Time in the Pyrolysis of Cellulose and Wood Particles." Combustion Science and Technology **119**: 331-373.

Miller, R. S. and J. Bellan (1997). "A Generalized Biomass Pyrolysis Model Based on Superimposed Cellulose, Hemicellulose and Lignin Kinetics." Combustion Science and Technology **126**: 97-137.

Niggli, P. (1919). "Carbonate and Chloride Melts." Z. Anorg. Allgem. Chem. **106**: 126-42.

Niksa, S. (2000). Predicting the rapid devolatilization of diverse forms of biomass with bio-FLASHCHAIN. 28th International Symposium on Combustion, Edinburgh, United Kingdom, Combustion Institute.

Niksa, S., A. R. Kerstein and T. H. Fletcher (1987). "Predicting Devolatilization at Typical Coal Combustion Conditions with the Distributed-Energy Chain Model." Combustion and Flame **69**(2): 221-228.

Northey, B. (1998). "Wood Chemistry." from http://depts.washington.edu/pse406/40inter.htm.

Nunn, T. R., J. B. Howard, J. P. Longwell and W. A. Peters (1985). "Ind. Eng. Chem. Process Des. Dev.": 24:844.

Nunn, T. R., J. B. Howard, J. P. Longwell and W. A. Peters (1985). "Product compositions and kinetics in the rapid pyrolysis of sweet gum hardwood." Industrial & Engineering Chemistry, Process Design and Development **24**(3): 836-844.

O'Dowd, W., D. Gera, M. Mathur and M. Freeman (2001). "Moisture and char reactivity modeling in pulverized coal combustors." Combustion Science and Technology **172**(1): 35-69.

Olek, W., P. Perre and J. Weres (2005). "Inverse analysis of the transient bound water diffusion in wood." Holzforschung **59**(1): 38-45.

Orfao, J. J., F. J. A. M. Antunes and J. L. Figueiredo (1999). "Pyrolysis Kinetics of Lignocellulosic Materials, Three Independent Reactions Model." Fuel **78**: 349-358.

Ouelhazi, N., G. Arnaud and J. P. Fohr (1992). "A Two-dimensional study of wood plank drying. The effect of gaseous pressure below boiling point." Transport in Porous Media **7**(1): 39-61.

Patankar, S. V. (1980). Numerical Heat Transfer and Fluid Flow, Taylor & Francis.

Pelton, A. D. and M. Blander (1986). "Thermodynamic Analysis of Ordered Liquid Solutions by a Modified Quasi-Chemical Approach - Application to Silicate Slags." Metallurgical Transactions B-Process Metallurgy **17**(4): 805-815.

Pelton, A. D., S. A. Degterov, G. Eriksson, C. Robelin and Y. Dessureault (2000). "The Modified Quasichemical Model I - Binary Solutions." Metallurgical And Materials Transactions B-Process Metallurgy And Materials Processing Science **31**(4): 651-659.

Pond, H. R., T. H. Fletcher and L. Baxter (2003). Prediction of Tar and Light Gas During Pyrolysis of Black Liquor and Biomass. 3rd Annual Joint Meeting of the U.S. Sections of the Combustion Institute, Chicago, IL.

Pyykonen, J. and J. Jokiniemi (2000). "Computational fluid dynamics based sectional aerosol modelling schemes." Journal of Aerosol Science **31**(5): 531-550.
Raveendran, K., A. Ganesh and K. C. Khilar (1996). "Pyrolysis Characteristics of Biomass and Biomass Components." Fuel **75**(8): 987-998.
Raveendran, K., A. Ganesh and K. C. Khilart (1995). "Influence of Mineral Matter on Biomass Pyrolysis Characteristics." Fuel **74**(12): 1812-1822.
Roberts, W. (2005). Brigham Young University, Provo, Utah, Personal Communication.
Robinson, A. L., S. G. Buckley and L. L. Baxter (2001). "Thermal Conductivity of Ash Deposits 1: Measurement Technique." Energy & Fuels **15**: 66-74.
Robinson, A. L., S. G. Buckley, N. Y. C. Yang and L. L. Baxter (2001). "Thermal Conductivity of Ash Deposits 2: Effects of Sintering." Energy & Fuels **15**: 75-84.
Robinson, A. L., H. Junker and L. L. Baxter (2002). "Pilot-scale investigation of the influence of coal-biomass cofiring on ash deposition." Energy & Fuels **16**(2): 343-355.
Romero-Serrano, A. and A. D. Pelton (1999). "Thermodynamic analysis of binary and ternary silicate systems by a structural model." Isij International **39**(5): 399-408.
Saaddjian, E., N. Midoux, M. I. Gastou Chassaing, J. C. Leprevost and J. C. Andre (1996). "Chaotic mixing and heat transfer between confocal ellipses: experimental and numerical results." Phys. Fluids **8**(3): 677-691.
Saito, H. and T. Kanade (1999). "Shape reconstruction in projective grid space from large number of images." Proceedings of the 1999 IEEE Computer Society Conference on Computer Vision and Pattern Recognition (CVPR'99) **2**: 49-54.
Samaddar, B. N., W. D. Kingery and A. R. Cooper (1964). "Dissolution in Ceramic Systems: II, Dissolution of Alumina, Mullite, Anorthite, and Silica in a Calcium-Aluminum-Silicate Slag." Journal of the American Ceramic Society **47**(5): 249-254.
Saviharju, K., A. Moilanen and A. R. P. Van Heiningen (1998). "New high-pressure gasification rate data for fast pyrolysis of black liquor char." Journal of Pulp and Paper Science **24**(7): 231-236.
Schuhmann, R., Jr. and P. J. Ensio (1951). "Thermodynamics of Iron Silicate Slags: Slags Saturated with γ Iron." Journal of Metals **3**: 401-11.
Serio, M. A. (1997). A Comprehensive Model of Biomass Pyrolysis.
Shen, M. S., A. P. Lui, L. J. Shadle, G. Q. Zhang and G. J. Morris (1991). "Kinetic Studies of Rapid Oil Shale Pyrolysis. 2. Rapid pyrolysis of Oil Shales in a Laminar-flow Entrained Reactor." Fuel **70**(11): 1277-1284.
Sheng, C. and J. L. T. Azevedo (2002). Modeling Biomass Devolatilization Using CPD for Main Components. 29th International Symposium on Combustion.
Siegel, R. and J. Howell (2002). Chapter Six - Radiation exchange in enclosures composed of black and/or diffuse-gray surfaces. Thermal radiation heat transfer, Taylor & Francis.
Smith, K. L., L. D. Smoot, T. H. Fletcher and R. J. Pugmire (1994). The structure and reaction processes of coal. New York and London, Plenum Press.
Smoot, L. D. and P. J. Smith (1985). Coal Combustion and Gasification. New York, Plenum Press.
Solomon, P. R., T. H. Fletcher and R. J. Pugmire (1993). "Progress in Coal Pyrolysis." Fuel **72**(5): 587-597.
Solum, M. S. (2002).

Solum, M. S., R. J. Pugmire and D. M. Grant (1989). "Energy & Fuels." Energy & Fuels **3**: 187-193.

Sony Inc. (2005). "ICX285AQ CCD sensor spectral responsivity." from http://products.sel.sony.com/semi/PDF/ICX285AQ.pdf.

Sricharoenchaikul, V. (2001). Fate of Carbon-Containing Compounds from Gasification of Kraft Black Liquor with Subsequent Catalytic Conditioning of Condensable Organics, Gerogia Institute of Technology.

Stenius, P. (2000). Forest Products Chemistry, Fapet Oy.

Sutinen, J., R. Karvinen and W. J. Frederick (2002). "A chemical reaction engineering and transport model of Kraft char bed burning." Industrial & Engineering Chemistry Research **41**(6): 1477-1483.

Taira, S., K. Nakashima and K. Mori (1993). "Kinetic Behavior of Dissolution of Sintered Alumina into CaO-SiO_2-Al_2O_3 Slags." ISIJ International **33**(1): 116-123.

Tamminen, T., J. Kiuru, R. Kiuru, K. Janka and M. Hupa (2002). "Dust and flue gas chemistry during rapid changes ion the operation of black liquor recovery boilers: Part 1 - Dust formation." Tappi Journal **1**(5): 27-32.

Tavares, A. J., H. Tran and T. P. Reid (1998). "Effect of char bed temperature and temperature distribution on fume generation in a kraft recovery boiler." Tappi Journal **81**(9): 134-138.

Thunman, H., F. Niklasson, F. Johnsson and B. Leckner (2001). "Composition of Volatile Gases and Thermochemical Properties of Wood for Modeling of Fixed or Fluidized Beds." Energy & Fuels **15**: 1488-1497.

Thurner, F. and U. Mann (1981). "Kinetic investigation of wood pyrolysis." **20**(3): 482-488.

Turns, S. R. (2000). An Introduction to Combustion: Concepts and Applications, Thomas Casson.

Vanheiningen, A. R. P., V. T. Arpiainen and R. Alen (1994). "Effect of Liquor Type and Pyrolysis Rate on the Steam Gasification Reactivities of Black Liquors - Complex Relationships Are Revealed." Pulp & Paper-Canada **95**(9): 55-60.

Varhegyi, G., M. J. J. Antal, T. Szekely and P. Szabo (1989). "Kinetics of the thermal decomposition of cellulose, hemicellulose, and sugar cane bagasse." Energy & Fuels **3**(3): 329-335.

Versteeeg, H. K. and W. Malalasekera (1995). An Introduction to Computational Fluid Dynamics. London, Prentice Hall.

Wagenaar, B. M., W. Prins and W. P. M. Van Swaaij (1993). "Flash pyrolysis kinetics of pine wood." Fuel Processing Technology **36**: 291.

Wang, X. H., D. Q. Zhao, L. B. He, L. Q. Jiang, Q. He, Y. Chen and Ss (2007). "Modeling of a Coal-fired Slagging Combustor: Development of a Slag Submodel." Combustion and Flame **149**(3): 249-260.

Warnatz, J. (2000). "Hydrocarbon oxidation high-temperature chemistry." Pure Appl. Chem. **72**(11): 2101-2110.

Warnqvist, B. (1994). "Char Bed and Smelt Properties Mill Studies." Pulp & Paper-Canada **95**(8): 34-36.

Wessel, R. A., K. L. Parker and C. L. Verrill (1997). "Three-dimensional kraft recovery furnace model: implementation and results of improved black-liquor combustion models." Tappi Journal **80**(10): 207-220.

Whitty, K. (1997). Pyrolysis and Gasification Behavior of Black Liquor under Pressurized Conditions, Åbo Akademi.

Williams, P. T. and P. A. Horne (1994). "Role of Metal Salts in the Pyrolysis of Biomass." Renewable Energy **4**(1): 1-13.

Wornat, M. J., R. H. Hurt, K. A. Davis and N. Y. C. Yang (1999). Single-Particle Combustion of Two Biomass Chars. Twenty-Sixth Symposium (International) on Combustion / The Combustion Institute.

Wu, P., G. Eriksson and A. D. Pelton (1993). "Optimization of the Thermodynamic Properties and Phase-Diagrams of the Na_2O-SiO_2 and K_2O-SiO_2 Systems." Journal of the American Ceramic Society **76**(8): 2059-2064.

Yang, W. R., R. R. Horton and T. N. Adams (1994). "Effects of Boundary Geometries on Cfd Simulations of Recovery Furnace Char Beds." Tappi Journal **77**(8): 189-199.

Yu, X., R. J. Pomfret and K. S. Coley (1997). "Dissolution of Alumina in Mold Fluxes." Metallurgical and Materials Transactions B-Process Metallurgy and Materials Processing Science **28**(2): 275-279.

Zhang, X., A. Dukhan and I. I. Kantorovich (1996). Structural changes of char particles during chemically controlled oxidation. Twenty-Sixth Symposium (International) on Combustion / The Combustion Institute, Napoli, Italy.